R-14-13

The Greenland Analogue Project:

Data and Processes

Harper J[1], Hubbard A[2], Ruskeeniemi T[3], Claesson Liljedahl L[4], Kontula A[5], Hobbs M[6], Brown J[1], Dirkson A[1], Dow C[7], Doyle S[2], Drake H[8], Engström J[3], Fitzpatrick A[2], Follin S[9], Frape S[10], Graly J[11], Hansson K[12], Harrington J[11], Henkemans E[10], Hirschorn S[6], Humphrey N[11], Jansson P[13], Johnson J[1], Jones G[7], Kinnbom P[14], Kennell L[6], Klint K E[15], Liimatainen J[5], Lindbäck K[13], Meierbachtol T[1], Pere T[5], Pettersson R[13], Tullborg E-L[16], van As D[15]

1 University of Montana
2 Aberystwyth University
3 Geological Survey of Finland
4 Svensk Kärnbränslehantering AB
5 Posiva Oy
6 Nuclear Waste Management Organization
7 Swansea University
8 Linnæus University
9 Golder associates
10 University of Waterloo
11 University of Wyoming
12 Geosigma AB
13 University of Stockholm
14 PKM Innovation AB
15 Geological Survey of Denmark and Greenland
16 Terralogica

August 2016

Svensk Kärnbränslehantering AB
Swedish Nuclear Fuel
and Waste Management Co

Box 250, SE-101 24 Stockholm
Phone +46 8 459 84 00

ISSN 1402-3091
SKB R-14-13
ID 1545041

August 2016

The Greenland Analogue Project:

Data and Processes

Harper J[1], Hubbard A[2], Ruskeeniemi T[3], Claesson Liljedahl L[4], Kontula A[5], Hobbs M[6], Brown J[1], Dirkson A[1], Dow C[7], Doyle S[2], Drake H[8], Engström J[3], Fitzpatrick A[2], Follin S[9], Frape S[10], Graly J[11], Hansson K[12], Harrington J[11], Henkemans E[10], Hirschorn S[6], Humphrey N[11], Jansson P[13], Johnson J[1], Jones G[7], Kinnbom P[14], Kennell L[6], Klint K E[15], Liimatainen J[5], Lindbäck K[13], Meierbachtol T[1], Pere T[5], Pettersson R[13], Tullborg E-L[16], van As D[15]

1 University of Montana
2 Aberystwyth University
3 Geological Survey of Finland
4 Svensk Kärnbränslehantering AB
5 Posiva Oy
6 Nuclear Waste Management Organization
7 Swansea University
8 Linnæus University
9 Golder associates
10 University of Waterloo
11 University of Wyoming
12 Geosigma AB
13 University of Stockholm
14 PKM Innovation AB
15 Geological Survey of Denmark and Greenland
16 Terralogica

Preface

This Data and Processes report is, together with the accompanying Final Report (SKB report TR-14-13), one of two top documents summarising the results from the Greenland Analogue Project (GAP). The idea and planning of the GAP was started by SKB in 2005 and the project itself was formalised and launched in 2008 when the national nuclear waste management organisations in Sweden (SKB), Finland (Posiva) and Canada (NWMO) joined forces to support the project. The present report is the result of collaboration among the three organisations and the GAP project members, which include scientists and technical experts from Sweden, Finland, Canada, Denmark, the US and the UK. The GAP was initiated to increase the knowledge on glacial hydrological processes and their influence on both surface and subsurface environments relevant to the long term performance of geological repositories for nuclear waste. To this end, a Greenland site, with an existing ice sheet in a crystalline bedrock setting, serves as a natural analogue to future conditions expected for selected repository sites in previously glaciated terrain, such as in Sweden. This Data and Processes report presents the methods applied and compiles and evaluates the datasets collected within the project, whereas the accompanying Final Report (SKB report TR-14-13) presents key findings of the GAP and the increased scientific understanding that has been obtained. The results presented in the two reports will be used in ongoing and future safety assessment work performed at SKB. The structure of the report reflects the way the GAP was implemented, and the results from each subproject are presented in the succeeding chapters.

Summary

This report presents the methods, collected datasets, and the interpretations completed for the Greenland Analogue Project (GAP), a collaborative research project conducted between 2008 and 2013 by the national nuclear waste management organisations in Sweden (SKB), Finland (Posiva) and Canada (NWMO). The primary aims of the GAP were to enhance scientific understanding of glacial processes and their influence on both surface and subsurface environments relevant to deep geological repository (DGR) performance in crystalline shield rock settings. Based on its size, relative accessibility, and crystalline shield bedrock, the Greenland Ice Sheet (GrIS) was selected by the GAP as a natural analogue for glaciation processes expected to reoccur in Fennoscandia and Canada over DGR safety-relevant timeframes.

The GAP study area is located east of Kangerlussuaq village on the west coast of Greenland and covers approximately 12 000 km^2, of which approximately 70% is occupied by the GrIS. To advance understanding of glacial hydrogeological processes, GAP research activities included both extensive field work and modelling studies of the GrIS, focused into three main subprojects: SPA) surface-based ice sheet studies; SPB) ice drilling and direct studies of basal conditions; and SPC) geosphere studies. The main objectives and activities of these subproject areas are provided below:

SPA) Surface-based ice sheet studies aimed to improve the current understanding of ice sheet hydrology and its relationship to subglacial hydrology and groundwater dynamics. This work was based primarily on *indirect* observations from the ice sheet surface of the basal hydrological system, to obtain information on the parts of the ice sheet which contribute water for groundwater infiltration. Project activities included quantification of ice sheet surface-water production, as well as an evaluation of how water is routed from the ice surface to the interface between the ice and the underlying bedrock. Methods employed include: remote sensing, automatic weather station network, GPS measurements of ice motion, ground-penetrating radar and seismics.

SPB) Ice drilling and direct studies of basal conditions also aimed to improve understanding of ice sheet hydrology and groundwater formation based on *direct* observations of the basal hydrological system, paired with numerical ice sheet modelling. Specific processes were investigated, including: 1) thermal conditions within and at the base of the ice sheet; 2) generation of meltwater at the ice/bedrock interface; and 3) hydrologic conditions at the base of the ice sheet. Activities included ice drilling of multiple holes at three locations on the ice sheet, at distances up to thirty kilometers from the ice sheet terminus, to assess drainage, water flow, basal conditions and water pressures at the interface between the ice and bedrock.

SPC) Geosphere investigations focused on groundwater flow dynamics and the chemical and isotopic composition of water at depths of 500 metres or greater below ground surface, including evidence on the depth of permafrost, redox conditions and the infiltration of glacial meltwater into the bedrock. Deep and inclined bedrock boreholes were drilled through the permafrost in the vicinity of the ice sheet margin. The boreholes were hydraulically tested and instrumented to allow hydrogeologic and hydrogeochemical monitoring. The nature of ground conditions under a proglacial lake was also investigated, to assess if areas of unfrozen ground within the permafrost (taliks) may act as a potential pathway for exchange of deep groundwater and surface water. A wide range of methods were applied by SPC to study the above including: geological, geophysical and surface water investigations, as well as bedrock borehole investigations.

Contents

1 Introduction 11
1.1 Context for undertaking the Greenland Analogue Project 12
1.2 Scope and objectives of the Greenland Analogue Project 14
1.3 Structure of the report 16

2 GAP study area description 17
2.1 Geological setting 19
2.2 Topography and Quaternary geology 19
2.3 Climate, permafrost and deglaciation history 20
2.4 The Greenland Ice Sheet (GrIS) in the GAP study area 23

3 Subproject A – Ice sheet hydrology and subglacial groundwater formation 25
3.1 Introduction and objectives of SPA 25
3.2 Remote sensing 26
  3.2.1 Data sources 26
  3.2.2 Data processing 26
  3.2.3 Data outputs and conclusions 27
3.3 Supraglacial meltwater production and runoff 33
  3.3.1 Introduction and objectives 33
  3.3.2 Weather station observations 34
  3.3.3 Surface energy balance modelling 39
  3.3.4 Meltwater production and runoff 40
  3.3.5 Remote sensing and AWS data that contributes to addressing the GAP questions 42
3.4 GPS measurements of ice motion 42
  3.4.1 Introduction and objectives 42
  3.4.2 Data collection 43
  3.4.3 GPS processing methods 47
  3.4.4 Results 47
  3.4.5 GPS data that contributes to addressing the GAP questions 51
3.5 Radar 53
  3.5.1 Radar data 53
  3.5.2 Results 58
  3.5.3 Radar data that contributes to addressing the GAP questions 62
3.6 SPA Seismic aquisitions 63
  3.6.1 Reflection seismic acquisitions 63
  3.6.2 Summary of reflection seismic data 70
3.7 Passive seismics experiments 70
  3.7.1 Introduction 70
  3.7.2 Background and methods 72
  3.7.3 Event location and testing procedure 76
  3.7.4 Results 77
  3.7.5 Discussion 80
3.8 3D Modelling of subglacial water flow and its impact on ice dynamics 83
3.9 Summary of understanding of ice sheet surface ablation, flow dynamics, hydro-thermal regime and their impact on subglacial waters, its pressure, extent and composition developed through SPA 89
  3.9.1 Background 89
  3.9.2 SPA observations and datasets 90
  3.9.3 SPA observations on the quality, quantity and distribution of subglacial water available for groundwater recharge 91
  3.9.4 Surface meltwater production, transfer and storage 94
  3.9.5 Surface to bed coupling 95
  3.9.6 Subglacial hydrological impacts of surface melt 96

3.9.7 Indirect observations of subglacial conditions 98
3.9.8 Subglacial complications 100
3.9.9 Synopsis of SPA contributions towards the GAP project questions 100

4 Subproject B – Subglacial hydrology 103
4.1 Introduction and objectives of SPB 103
4.1.1 Background 103
4.1.2 SPB project goals 104
4.2 SPB study sites and ice boreholes 106
4.2.1 Site and Borehole Notation 106
4.2.2 Margin case-study region: (sites GL10-1, GL10-2, GL10-3, GL12-1) 107
4.2.3 Interior case-study region: (sites GL11-1, GL11-2) 108
4.2.4 Interior trough case-study region: (site GL12-2) 110
4.2.5 Borehole drilling 111
4.3 Borehole impulse test experiments 112
4.3.1 Methods 113
4.3.2 Results 114
4.3.3 Summary and discussion of the borehole impulse test experiments 119
4.4 Basal water pressure 121
4.4.1 Water pressure methods 121
4.4.2 Boreholes and records 123
4.4.3 Water pressure results 124
4.4.4 Summary and discussion of the basal water pressure 126
4.5 Chemistry of basal water and sediment 129
4.5.1 Sampling strategy 129
4.5.2 Sampling methods and field measurements 129
4.5.3 Laboratory analyses 131
4.5.4 Results 132
4.5.5 Summary of chemistry and basal water and sediment 134
4.6 Ice temperature 136
4.6.1 Methods 136
4.6.2 Results 138
4.6.3 Summary and discussion of ice temperatures 140
4.7 Ice surface velocity 145
4.7.1 Methods 145
4.7.2 Results 147
4.7.3 GL11-1 147
4.7.4 Summary and discussion of ice surface velocity 149
4.8 Surface meteorological measurements 150
4.8.1 Methods 150
4.8.2 Results 151
4.8.3 Summary and discussion of surface meterological measurements 155
4.9 Numerical modelling 155
4.9.1 Modelling requirements 155
4.9.2 Modelling methods 156
4.9.3 Source of error 162
4.9.4 Modelling results 164
4.9.5 Conclusions/findings 170
4.10 Summary of understanding of ice sheet basal boundary developed through SPB 170
4.10.1 The ice-bed contact 170
4.10.2 Configuration of the subglacial hydrological system 171
4.10.3 Pressure of the subglacial boundary condition 175

5 Subproject C – Hydrogeology and hydrogeochemisty 181
5.1 Introduction and objectives of SPC 181
5.1.1 Aims and background of SPC 181
5.1.2 Implementation of SPC work 182

5.2 Geological setting 182
5.3 Drilling and instrumentation of research boreholes 184
  5.3.1 Purpose of drilling bedrock boreholes in GAP study area 184
  5.3.2 Instrumentation of the boreholes 191
5.4 Geological investigations in the GAP study area 195
  5.4.1 Overall mapping and logging 195
  5.4.2 Bedrock geology 196
  5.4.3 Drill core observations 199
  5.4.4 Structural geology 200
  5.4.5 Petrophysical properties 214
5.5 Permafrost 217
  5.5.1 Temperature profiling in GAP boreholes 218
  5.5.2 Electromagnetic soundings for permafrost investigations 223
  5.5.3 Taliks and their development 227
  5.5.4 Geothermal properties of the bedrock 229
  5.5.5 Main conclusions from the permafrost investigations 230
5.6 Hydrogeology 231
  5.6.1 Hydrogeology in the glacial-periglacial system 231
  5.6.2 Evaluation of hydraulic tests in DH-GAP01 231
  5.6.3 Evaluation of hydraulic tests in DH-GAP04 232
  5.6.4 Fluid pressure, density and hydraulic head 242
  5.6.5 Downhole long term monitoring of boreholes DH-GAP01 and DH-GAP04 244
  5.6.6 Summary of downhole monitoring observations 255
5.7 Hydrogeochemistry 262
  5.7.1 General methods for hydrogeochemical samples 262
  5.7.2 Surface water geochemistry 266
  5.7.3 Ice and meltwaters 272
  5.7.4 Groundwaters 273
  5.7.5 Porewater studies 280
  5.7.6 Main conclusions from hydrogeochemical investigations 285
  5.7.7 Microbial investigations 286
5.8 Mineralogical studies 290
  5.8.1 Fracture infillings 290
  5.8.2 Preliminary isotope results on sulphate infillings 293
  5.8.3 Observations on redox conditions based on fracture infillings 294
  5.8.4 Main conclusions from the fracture infilling investigations 304
5.9 Summary of understanding developed through SPC 305
  5.9.1 Conceptual model for DH-GAP04 area 305
  5.9.2 Source areas for meltwater recharge 305
  5.9.3 The role of permafrost and taliks in the periglacial hydrogeology 308
  5.9.4 Depth of meltwater penetration and flow in bedrock 310
  5.9.5 Hydraulic conditions in the bedrock 313
  5.9.6 Surface water evolution in periglacial environment 315
  5.9.7 Meltwater characteristics 316
  5.9.8 Deep groundwater evolution and penetration of meltwater 316
  5.9.9 Geochemistry of talik waters 318

6 Summary of GAP datasets and key outputs 319
6.1 Subproject A (SPA) 319
  6.1.1 Remote sensing 319
  6.1.2 Automatic weather station network 319
  6.1.3 GPS measurements of ice motion 320
  6.1.4 Ground-penetrating radar 320
  6.1.5 Seismics – reflection and passive seismics 320
6.2 Subproject B (SPB) 321
  6.2.1 Summary of testing in SPB 321
  6.2.2 Key outputs from SPB 322

6.3 Subproject C (SPC) 324
  6.3.1 Bedrock geology 324
  6.3.2 Geophysics 325
  6.3.3 Surface water characterisation 325
  6.3.4 Bedrock borehole investigations 326
  6.3.5 Groundwater and porewater characterisation 329

Acknowledgement 331

References 333

Appendix A Measured variables from automatic weather stations KAN_L, KAN_M and KAN_U, respectively. 355

Appendix B Borehole DH-GAP04 monitoring equipment, installation of the instruments and uncertainties related to pressures and evaluated heads. 365

1 Introduction

The *Greenland Analogue Project* (GAP): Data and Processes (Data Report 2016) is the first of two final technical reports documenting the results from the GAP. The fieldwork was conducted during 2008 to 2013 near Kangerlussuaq in Western Greenland (Figure 1-1). The Data Report presents the methods, collected datasets, and the interpretations completed for each of the three subprojects within the GAP. The GAP Final Report (Claesson Liljedahl et al. 2016, from here on referred to as the Final Report 2016) is a synthesis report which aims to summarise and integrate the findings and understanding gained from the three subprojects, as presented in this Data Report.

The main authors and experts who contributed to this report are listed in Table 1-1.

Table 1-1. Contributors to individual chapters in the present report in alphabetical order. The GAP was initiated and funded by Svensk Kärnbränslehantering AB (SKB) in Sweden, Posiva Oy (Posiva) in Finland and the Nuclear Waste Management Organization (NWMO) in Canada.

Author	Organisation	Chapter(s)
Brown, Joel	University of Montana	4
Claesson Liljedahl, Lillemor	SKB	1, 2, 5, 6
Dirkson, Arlan	University of Montana	4
Dow, Christine	Swansea University	3
Doyle, Sam	Aberystwyth University	3
Drake, Henrik	Linnæus University	5
Engström, Jon	Geological Survey of Finland	5
Fitzpatrick, Andrew	Aberystwyth University	3
Follin, Sven	Golder associates	5
Frape, Shaun	University of Waterloo	5
Graly, Joseph	University of Wyoming	4
Hansson, Kent	Geosigma AB	5
Harper, Joel	University of Montana	4, 6
Harrington, Joel	University of Wyoming	4
Henkemans, Emily	University of Waterloo	5
Hirschorn, Sarah	NWMO	5
Hobbs, Monique	NWMO	1, 5, 6
Hubbard, Alun	Aberystwyth University	3
Humphrey, Neil	University of Wyoming	4
Jansson, Peter	University of Stockholm	3,
Johnson, Jesse	University of Montana	4
Jones, Glenn	Swansea University	3
Kinnbom, Pär	PKM Innovation AB	5
Kennell, Laura	NWMO	5
Klint, Knud Erik	Geological Survey of Denmark and Greenland	5
Kontula, Anne	Posiva	1, 2, 5, 6
Liimatainen, Jyrki	Posiva	5
Lindbäck, Katrin	University of Stockholm	3
Meierbacthol, Toby	University of Montana	4
Pere, Tuomas	Posiva	5
Pettersson, Rickard	University of Stockholm	3
Ruskeeniemi, Timo	Geological Survey of Finland	5
Tullborg, Eva-Lena	Terralogica	5
van As, Dirk	Geological Survey of Denmark and Greenland	3

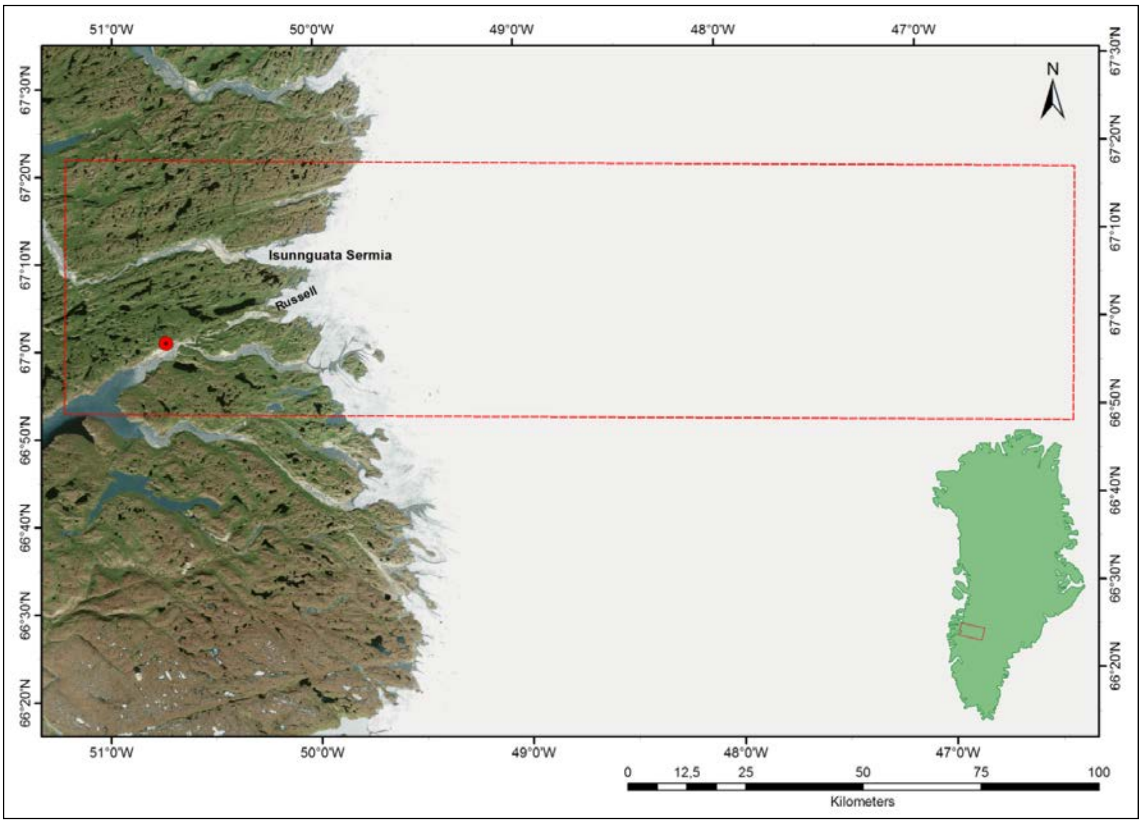

Figure 1-1. *Overview map showing the GAP study area (red dashed rectangle). Background image is a World Imagery ESRI satellite image acquired October 2, 2012. Inset map shows the location of the study area on Greenland scale. The key outlet glaciers in the GAP study area, Isunnguata Sermia and Russell glacier are indicated. Red circle =Kangerlussuaq International Airport.*

1.1 Context for undertaking the Greenland Analogue Project

Deep Geological Repositories (DGRs) for spent nuclear fuel are being considered in a number of countries that are designing and/or implementing practical solutions for the long term safety and isolation of spent nuclear fuel. The DGR concept (Figure 1-2) is based on a multi-barrier principle. For example, in Sweden and Finland, the DGR concept (the KBS-3 vertical deposition concept shown to the left in Figure 1-2) includes copper canisters, each with a cast iron insert and containing spent nuclear fuel, that are emplaced in individual deposition holes bored in the floors of deposition tunnels. To seal the deposition holes, the canisters are to be surrounded by a swelling clay buffer material (bentonite). The deposition tunnels, the central tunnels and the other underground openings, including the main access shafts and/or ramps, are to be backfilled with materials of low permeability.

Long term safety in nuclear waste management requires that the spent nuclear fuel, including its original radionuclide inventory and associated decay by-products, is kept isolated from the biosphere on a time scale of 100 000 years up to one million years. Over this time frame, glacial conditions are expected to occur repeatedly in regions that have been glaciated from the mid Pliocene onwards. Climate-induced changes, such as the advance and retreat of ice sheets and development of permafrost, will influence and alter the surface and subsurface environment, including its hydrology, hydrogeology, geochemistry and stress state, which may impact repository performance. In assessments of glacial impacts on repository safety, simplified models and cautious assumptions are used, e.g. in relation to the representation of ice sheet hydrology, generation of dilute meltwater and the penetration of that dilute meltwater into the underlying rock. Observations from existing ice sheets may help to reduce uncertainties and provide a stronger scientific basis for the treatment of glacial impacts in safety assessments (e.g. SKB 2011, NWMO 2012, Posiva 2012).

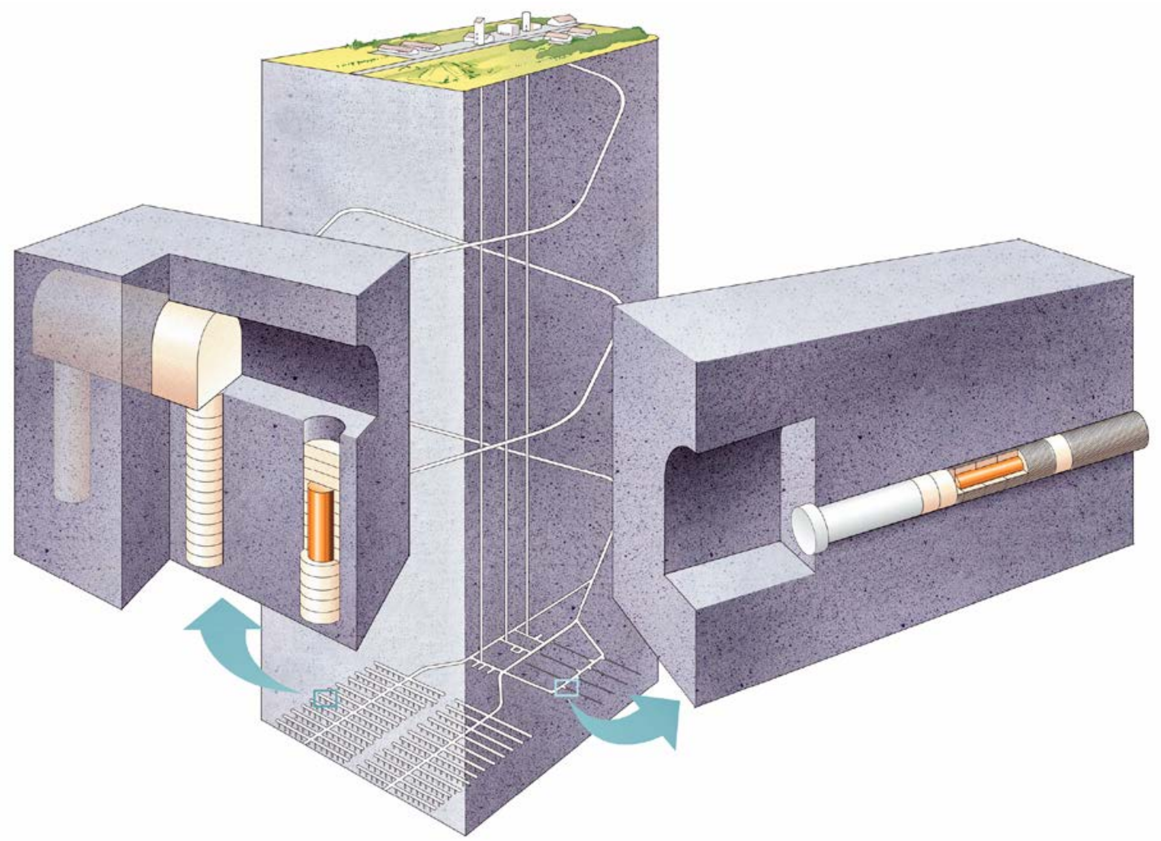

Figure 1-2. *The multi-barrier deep geologic repository concept (here illustrated by the KBS-3 concept), showing the vertical deposition concept to the left and the horizontal deposition concept to the right. SKB ©.*

In 2008, the international GAP was initiated collaboratively by *Svensk Kärnbränslehantering AB* (SKB) in Sweden, *Posiva Oy* (Posiva) in Finland and the *Nuclear Waste Management Organization* (NWMO) in Canada. The goal of the GAP is to advance the understanding of processes associated with glaciation and their impacts on the long term performance of a DGR. An additional aim of the GAP is to contribute to an increased understanding of a glaciated environment by obtaining an integrated view of ice sheet hydrology and groundwater flow and chemistry. Using the *Greenland Ice Sheet* (GrIS) as a modern analogue for future continental-scale ice sheets in previously glaciated regions, field and modelling studies of the GrIS and subsurface conditions were undertaken. The GrIS was chosen because it is of about the same size as those ice sheets known to have formed, and expected to form in the future in Fennoscandia, which suggests that the scale of processes and response times could be similar during the glaciation and deglaciation phases. Moreover, the bedrock in the study area is crystalline, with similarities to the crystalline bedrock in Sweden, Finland and Canada in terms of composition, fracturing and age. These characteristics make the study site an appropriate analogue of the conditions that are expected to prevail in Fennoscandia and, to some degree, in Canada during future glacial cycles. However, the suggested repository sites in Finland and Sweden are located in regions of low topography, whereas the GAP study area is characterised by moderate relief (few hundreds of metres), which among other things, needs to be considered when transferring knowledge obtained from GAP to other regions.

The study area chosen for GAP is located close to the Kangerlussuaq village (in Danish Søndre Strømfjord) on the west coast of Greenland, just north of the Polar Circle at 67°N and 51°W and ~ 160 km from the Atlantic Ocean (Figure 1-1, Figure 1-3 and Figure 2-1). The GAP study area measures ~ 200 km from east to west, extending from the ice sheet to the Kangerlussuaq fjord and measures 60 km from north to south (Figure 1-1 and Figure 1-3). This study area was chosen to meet the following criteria: 1) the field area is logistically easy to reach compared with other areas in Greenland; 2) its long axis is parallel to the general ice flow direction; 3) it includes frozen and wet conditions at the base of the ice sheet; and 4) the proglacial area is within continuous permafrost and includes larger lakes.

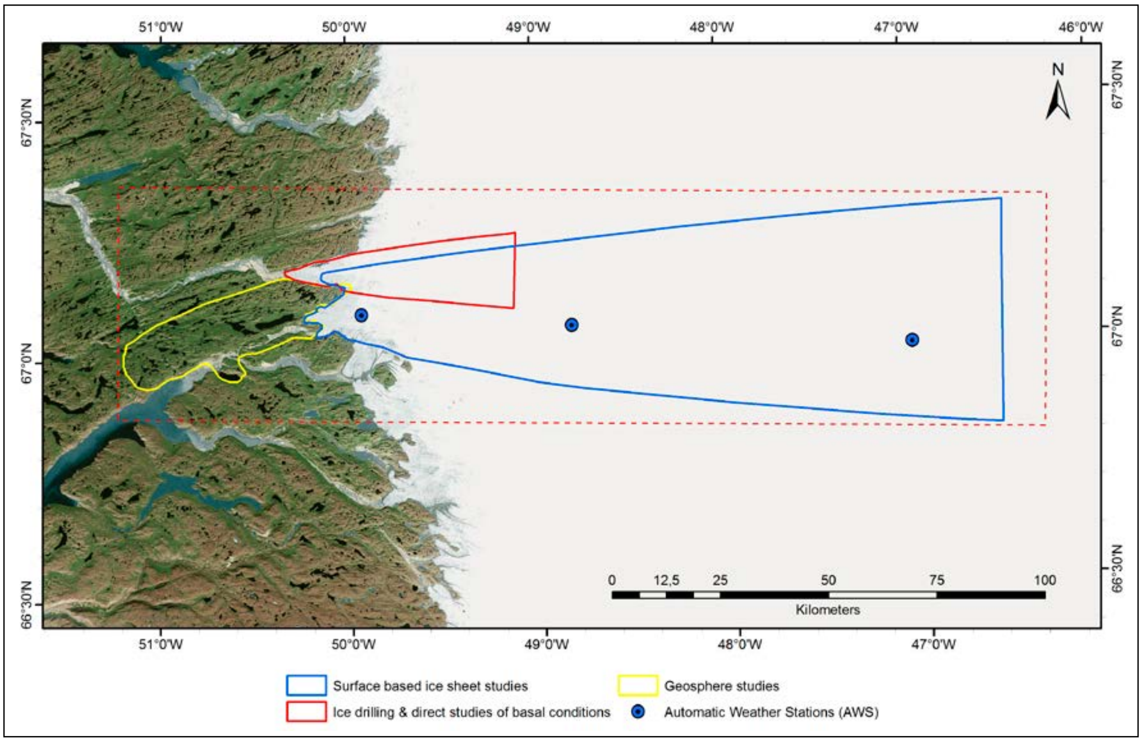

Figure 1-3. *Satellite image of the GAP study area (red dashed line) and the borders of the different field study areas within the GAP. The SPA (surface-based ice sheet investigations) were carried out in the blue bordered area (see Chapter 3), the SPB (ice drilling and direct studies of basal conditions) was carried out in the red bordered area which overlaps with the surface-based ice sheet investigation area (see Chapter 4). The yellow bordered area shows where the SPC (geosphere investigations) was carried out (see Chapter 5). Blue circles show the locations of the three GAP automatic weather stations (AWS), which form part of the surface-based ice sheet investigations (for details see Section 3.3). Background image is a World Imagery ESRI satellite image acquired October 2, 2014.*

1.2 Scope and objectives of the Greenland Analogue Project

Safety assessment of geological disposal of nuclear waste is a multidisciplinary and iterative approach (IAEA 2012) used to develop an overall understanding of the long term performance of the repository and its surroundings. The repository system includes multiple engineered barriers which, together with the surrounding geosphere, are designed to contain and isolate nuclear waste. Features, events and processes (natural and anthropogenic) that could potentially affect the safety of the repository system are identified and possible releases to the environment are assessed, as well as the consequences of such potential release events.

Given the long time span covered by safety assessments of DGRs for nuclear waste (100 000 years up to one million years), scientific information and knowledge on processes related to cold climate conditions are required. Previous safety assessments have shown that, for sites located in previously glaciated terrain, the impact of glacial (ice sheet) and periglacial (permafrost) processes need to be included and addressed in these assessments. These processes influence the environment around a repository and have the potential to directly or indirectly affect the engineered barrier system, the geosphere and, consequently, repository safety (e.g. SKB 2011, NWMO 2012, Posiva 2012). In this context, specific factors of importance for repository safety include changes in groundwater flow, hydrogeochemistry, hydrostatic pressure and bedrock stresses.

Scientific research to better understand processes associated with continental-scale glaciation, in terms of both glacial and periglacial conditions, has increased in the past decade (e.g. Kleman et al. 2008, Pitkäranta 2009, Vizcaíno et al. 2010, Jansson 2010 and references therein, SKB 2010a and references therein). Reference information on permafrost characteristics and development and groundwater flow and chemical composition are the most limited. However, conducting such research remains challenging due to the remote nature and extreme environmental conditions associated with ice sheets in both Greenland and Antarctica. Within fields where available scientific information has been limited, uncertainties have been handled using conservative assumptions in safety assessments. To reduce these uncertainties and in order to better evaluate the assumptions made in safety assessments, the GAP aimed to advance scientific understanding of hydrological, hydrogeological and geochemical processes during glacial conditions. To achieve this advanced understanding, GAP research focused on obtaining information that contributes to answering the following six overall project questions:

1) Where is the meltwater generated under an ice sheet?
2) What is the hydraulic pressure situation under an ice sheet, driving groundwater flow?
3) To what depth does glacial meltwater penetrate into the bedrock?
4) What is the chemical composition of glacial water when, and if, it reaches repository depth?
5) How much oxygenated water will reach repository depth?
6) Does discharge of deep groundwater occur in the investigated proglacial talik in the study area?

These questions cover areas where process understanding based on observations from a real ice sheet setting or the extent of the process (as for duration, magnitude or scale) were limited prior to the GAP. These questions also highlight areas where considerable conservative assumptions have been necessary in safety assessment analyses. Specifically, the first two questions relate to reducing uncertainties associated with the influence of the ice sheet on the groundwater system (including seasonality) and to better constrain the hydraulic boundary conditions to be used in groundwater modelling. Questions 3 through 5 are posed to better understand potential changes in groundwater chemical composition that could affect conditions at repository depth (e.g. oxygen in the infiltrating/penetrating meltwater which may influence bentonite stability through an adverse change in pH and/or ionic strength). The final question may contribute to a better understanding of periglacial processes (especially hydrogeological) where permafrost occurs. In the final question the term “deep groundwater” is used and in this study, it refers to the groundwater system found at depths greater than 300 m. Groundwaters from the surface to ~ 300 m depth are here denoted “shallow groundwaters”. The contributions of the GAP towards answering these questions are documented in the Final Report (2016).

The six project questions were formulated in a condensed and simplistic way and they are used only as general guidelines for planning research conducted in the GAP. In reality, each question encompasses a range of specific research goals that were included in activities conducted in the GAP. The project was divided into three subprojects (SPA, SPB, and SPC), each with specific individual objectives that collectively aimed at contributing knowledge and input towards the six project questions. The specific objectives of the three subprojects are described below. Figure 1-3 shows the extent of the GAP study area and highlights the field areas in which the subprojects carried out fieldwork.

Subproject A (SPA): Ice sheet hydrology and subglacial groundwater formation

Subproject manager: Alun Hubbard, Aberystwyth University.

SPA aims to improve the understanding of interactions between ice sheet hydrology and subglacial hydrology in order to gain insight into the prerequisites for groundwater formation. This was done by indirect observations from the ice sheet surface to increase the understanding of the basal hydrological system and specifically, to identify which parts of the ice sheet contain basal water available for bedrock infiltration. The latter aspect includes quantification of ice sheet surface-water production, as well as how water is routed from the ice surface to its basal interface. This subproject included remote sensing, as well as direct measurements of vertical ice displacement and horizontal velocity fluctuations, and examined the variation of these parameters in space and time with variable surface meltwater production and routing.

Subproject B (SPB): Subglacial ice sheet hydrology

Subproject manager: Joel Harper, University of Montana.

Similar to SPA, SPB aims to improve understanding of ice sheet hydrology and groundwater formation. SPB focused on *direct* observations and measurements to investigate the characteristics of the basal boundary conditions of the GrIS. The following specific processes are investigated by SPB: 1) thermal conditions at the base of the ice sheet, with a particular focus on delineating frozen and melted conditions; 2) generation of water at the ice/bedrock interface by mechanisms such as melting from ice pressure and geothermal heat flux, and friction from basal sliding; 3) hydrologic conditions of the base of the ice sheet, such as water storage, water pressure, water pressure variations; and 4) chemical composition and geochemical processes of water at the ice sheet base. The main activity in SPB was drilling through the ice sheet at a number of locations where the ice sheet is known to be wet-based. The purpose of the drilling and borehole monitoring installations was to observe water pressures at the interface between the ice and the bedrock. In addition to ice drilling, collection of remote sensing data on ice sheet surface conditions was performed. This information provides important input for the conceptualisation of hydraulic gradients during glacial conditions for groundwater models applicable in Fennoscandia and Canada, including spatial and temporal variation.

Subproject C (SPC): Bedrock drilling, hydrogeochemistry and hydrogeology

Subproject manager: Timo Ruskeeniemi, Geological Survey of Finland (GTK)

SPC focused on studying the infiltration of glacial meltwater into the bedrock, as well as groundwater flow dynamics and the chemical composition of water when, and if, it reaches typical repository depths (~ 500 m b.g.s. or more). The main activities within SPC involve deep bedrock drilling in front of the ice sheet for subsequent downhole surveys and hydrogeological/hydrogeochemical instrumentation, sampling and monitoring. Bedrock drilling provides information on geology, hydrology, hydrogeochemistry and permafrost extent in a glaciated environment. In order to investigate whether or not taliks may act as discharge points for deep groundwater formed under an ice sheet, a borehole was also drilled into an area where a talik was interpreted to exist.

1.3 Structure of the report

There are six main chapters included in this report.

- Chapter 1 gives an introduction to the report.
- Chapter 2 presents a summary of the GAP study area.
- Chapter 3 presents a description and summary of the datasets collected by SPA throughout 2008–2013. The understanding of ice sheet hydrology and groundwater formation developed based on findings from SPA is also summarised.
- Chapter 4 presents a description and summary of the datasets collected by SPB throughout 2010–2013. The understanding of subglacial hydrology and groundwater formation developed based on the findings of SPB is also summarised.
- Chapter 5 presents a description and summary of the datasets collected by SPC throughout 2008–2013. The understanding of groundwater hydrology and hydrogeochemistry based on the results of SPC are summarised.
- Chapter 6 summarises the datasets collected during the GAP and the key findings (or outputs) from each of the three subprojects (A, B and C).

A list of abbreviations is presented at the end of the report.

Throughout the present report, unless otherwise stated, all geographical data are presented by the *World Geodetic System 1984* (WGS-84) latitude and longitude. Elevations are presented relative to the WGS-84-datum reference ellipsoid. The elevation of the geoid (sea-level surface) is located 34 m above the WGS-84 reference ellipsoid in the GAP study area. Time is presented as Coordinated Universal Time (UTC).

2 GAP study area description

The GAP study area (Figure 1-1, Figure 1-3, Figure 2-1 and Figure 2-2) encompasses a land terminus portion of the GrIS, east of the Kangerlussuaq village (Søndre Strømfjord) and on the west coast of Greenland, located just north of the Polar Circe at 67°N and 51°W. Kangerlussuaq is a settlement situated in the Qeqqata municipality at the head of the Kangerlussuaq fjord, just north of the polar circle and 160 km from the Atlantic Ocean. The study area measures ~ 200 km from east to west and 60 km from north to south. Approximately 70 % of the study area is covered by the GrIS. The area in front of the ice sheet is a gentle WSW-ENE trending hilly landscape, with bare bedrock, sparse vegetation cover and river valleys in the lower parts of the area (Figure 2-3). The bedrock consists of glacially-scoured gneiss, with relief up to 600 m a. s. l. The ice-free part of the study area has a large number of proglacial lakes (Figure 2-2).

The Kangerlussuaq International Airport (IATA: SFJ; ICAO: BGSF) is one of two international civilian airports in Greenland. From Copenhagen airport it takes ~ 4.5 hours to reach Kangerlussuaq village. The ease of travel to the village of Kangerlussuaq, in combination with a gravel road that provides direct access to the ice sheet (at Point 660), makes the village an international research hub not only for the GAP but also for a variety of other international research programs.

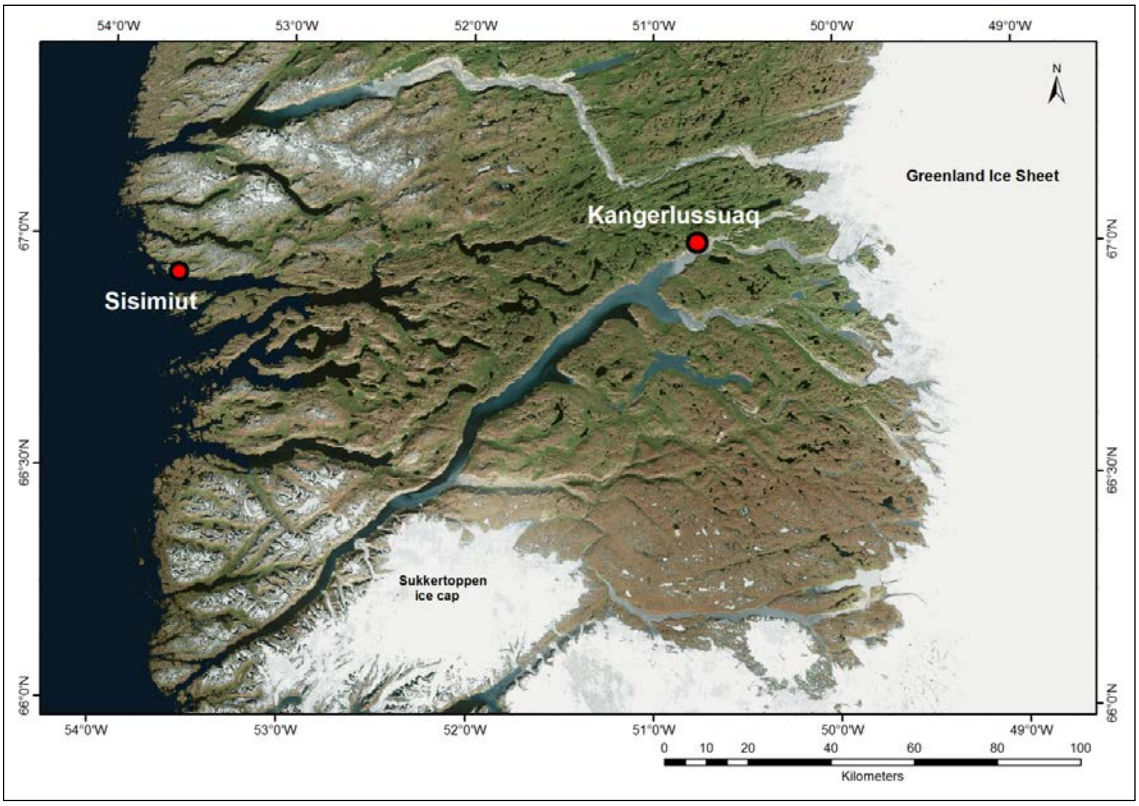

Figure 2-1. *Map of the Kangerlussuaq region, including the ~170 km long Søndre Strømfjord/Kangerlussuaq fjord, extending from the Atlantic Ocean in the SW to the Kangerlussuaq village. Background image is a World Imagery ESRI satellite image acquired October 2, 2014.*

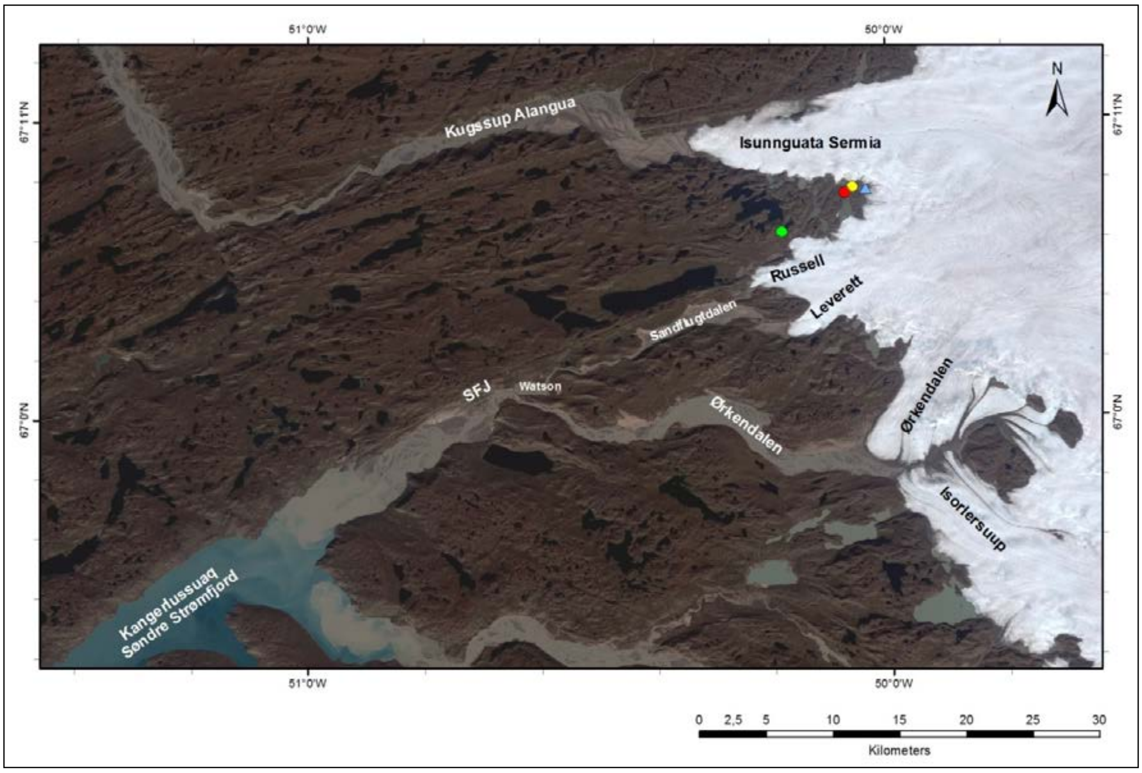

Figure 2-2. *Map of the ice marginal and proglacial areas, including the many proglacial lakes. Light grey coloured lakes are glacial meltwater lakes, dark blue lakes are lakes without inflow of glacial meltwater. The northernmost tip of the ~ 170 km long Søndre Strømfjord is shown in the lower left corner. Isunnguata Sermia, Russell, Leverett, Ørkendalen and Isorlersuup form the major outlet glaciers in the area. Sandflugtdalen and Ørkendalen are the major valleys and meltwater rivers in the area. The Watson river extends from the head of the Søndre Strømfjord and up through the Sandflugtdalen to the Russell and Leverett outlet glaciers. Locations of the bedrock boreholes drilled by the GAP are indicated as coloured circles. Green circle = DH-GAP01, red circle = DH-GAP03, and yellow circle = DH-GAP04. Blue triangle shows the location of Point 660. SFJ = Kangerlussuaq International Airport. Background Landsat image was acquired August 23, 2000.*

The landscape in the Kangerlussuaq area is typical of central west Greenland, which is a fjord landscape with numerous long (typically around 25 km), narrow and up to 600 m deep fjords that terminate in U-shaped valleys. Some of these valleys contain an outlet glacier and terraces, whereas others are partially filled with terraces of glaciofluvial and marine sediments (Ten Brink 1975). The latter is true for the valley where Kangerlussuaq is located. The Kangerlussuaq fjord is ~ 170 km long and 1 to 6 km wide, and receives the majority of the meltwater discharge from the large area south of the Russell Glacier, whereas the majority of the meltwater from the terminus of Isunnguata Sermia is transported via Kugssup Alangua (Figure 2-2) to the Sisimiut Isortuat fjord, north of Kangerlussuaq.

The proglacial area constitutes a gentle WSW–ENE trending hilly landscape, hosting numerous lakes of varying size, river valleys in the lower parts, abundant bare bedrock and sparse vegetation cover (Figure 2-2 and Figure 2-3). Two valleys running roughly east-west extend from the end of the Kangerlussuaq fjord to the ice sheet, i.e. Sandflugtdalen (which translates to Sand drift valley) and Ørkendalen (which translates to Desert Valley), and merge 3 km east of Kangerlussuaq (Figure 2-2).

The rivers are often frozen from October/November until April/May. Maximum discharge occurs from June to August. Abrupt drainage of ice dammed lakes occurs frequently in the area. The timing of these outburst floods, often at the end of the runoff season, is attributed to a sudden reduction of subglacial water pressure, caused by the annual reduction in meltwater production, which facilitates inflow of lake water to the glacier plumbing system (Russell et al. 1990, 2011, Mikkelsen et al. 2013).

Figure 2-3. *The rolling hills directly east of Kangerlussuaq. The river transports meltwater from the Russell and Leverett glaciers to the Kangerlussuaq fjord (Søndre Strømfjord). Photograph is from 2009 and was taken by Lillemor Claesson Liljedahl.*

2.1 Geological setting

Kangerlussuaq is situated within the southern part of the Nagssugtoqidian Orogen, which consists of an ~ 1900–1800 Ma old fold belt that formed in a collision zone between two parts of a previously rifted large Archaean continent. The rocks in the Nagssugtoqidian Orogen are predominantly Archaean ortho-gneisses, with minor amounts of amphibolite and metasedimentary rocks that were reworked under high grade metamorphic conditions in the Palaeo-proterozoic (van Gool et al. 2002, Garde and Hollis 2010). The primary structures reflect the ductile to semi-ductile nature of the regional deformation, including macro scale folds, a penetrative gneissic fabric and evidence of shearing. Occasional intrusions of mafic dykes occur in the area. The more brittle structures, such as open faults and fractures, are regarded to have formed in a younger shallow, colder and, hence, more rigid environment.

2.2 Topography and Quaternary geology

The landscape in the Kangerlussuaq area is typical of central west Greenland, characterised by long and narrow, up to 600 m deep, fjords and summits with an elevation of 600 m. The fjords terminate in stream valley basins, which likely extend under the ice sheet. Major bedrock structures have a clear control on the fjord paths. The Søndre Strømfjord receives the majority of the meltwater discharge from the large area south of the Russell Glacier, whereas the majority of the meltwater from the terminus of Isunnguata Sermia is transported via Kugssup Alangua (Figure 2-2) to the Sisimiut Isortuat fjord, i.e. there is a regional groundwater divide between the two glacial tongues (Figure 1-1 and Figure 2-2).

The relief in the Kangerlussuaq region is typically a few tens of metres and some peaks reach 200–300 m above the lowest stream valley, but the total elevation range is from 0 m (at the Watson river in Kangerlussuaq) to 600 m (close to the ice margin). The same kind of highly variable relief exists under the ice sheet, where the ice bed is locally depressed hundreds of m b.s.l. (for details see Section 3.5).

Bedrock surfaces are often striated and erratics are common in the area. Till cover on elevated areas is usually rather thin and eroded by heavy winds. Fresh bedrock faces with striations are typical of surfaces that have been exposed for only a relatively short period of time. Periglacial features, such as patterned ground, hummocks and ice-wedges, as well as erratics with honeycomb weathering and loss characteristics, are observed in lowlands (Aaltonen et al. 2010). Valley floors and bedrock depressions are typically filled with till. Due to the arid conditions, and the supply of fine-grained sediments, various types of eolian deposits are widespread in the area (Willemse et al. 2003).

Meltwaters from the Russell Glacier and the Leverett Glacier are drained through the two branches of the Watson River. They merge at a 2–3 km wide flood plain, called Sandflugtdalen, at the terminus of the Russell Glacier. The thickness of the glaciolacustrine and glaciofluvial deposits in this valley range from 40 to 80 m (Storms et al. 2012). Southwest from the Sandflugtdalen, the valley narrows, resulting in thinner deposits. Close to the village, the sediments are typically 30 m thick. The head of the Søndre Strømfjord is filled with terraces of glaciofluvial and marine sediments of Holocene age (Storms et al. 2012).

The highest marine limit (based on the elevation of marine clays terraces) is located at an elevation of 40 ± 5 m a.s.l. (Ten Brink 1974). However, since marine clays do not necessarily refer to a palaeo coastline elevation, this is considered a minimum value on the highest marine limit (Storms et al. 2012). The vertical displacement rate of the bedrock during Neoglacial time (i.e. the last 4000 years of the Holocene) has varied between 20 mm/a (Weidick 1993, 1996) and −5.8 mm/a (Wahr et al. 2001). The vertical subsidence displacement is attributed to the Neoglacial re-advance of the ice sheet during the past 3000–4000 years (Tarasov and Peltier 2002, Dietrich et al. 2005). Dietrich et al. (2005) report a current subsidence rate of −3.1 mm/a for Kangerlussuaq.

2.3 Climate, permafrost and deglaciation history

The present-day climate in the GAP study area is considered low Arctic continental, with continuous permafrost (Willemse et al. 2003). The region is characterised by a steep climate gradient from the coast to the inland, with mild winters, cool summers and varying weather in the coastal zone, and warm (and stable) summers and cold winters in the inland zone. The GrIS, reaching an elevation of 3000 m a.s.l., has a dominant influence on precipitation and winds (Jørgensen and Andreasen 2007). The *Danish Meteorological Institute* (DMI) operates a weather station in Kangerlussuaq. Figure 2-4 shows the mean monthly air temperatures from this station for the period 1961–2013 (Cappelen et al. 2001, Cappelen 2012). The *mean annual air temperatures* (MAAT) at the Kangerlussuaq International Airport average –5.1 °C, ranging from –9.1 to –0.3 °C (temperature record spanning 1977–2011; Cappelen 2012), whereas the *mean annual ground temperature* (MAGT) close to the airport is ~ –2 °C at 1.25 m below ground surface (van Tatenhove and Olesen 1994). The temperature is below zero between October to May, with winter temperatures down to −40 °C and summer temperatures up to 20 °C (Russell 2007). Although the weather naturally fluctuates from year to year, the GAP was carried out during a period with significantly warmer temperatures than during the 1961–1990 period (Figure 2-4). The 1961–1990 period is considered to represent a period during which the GrIS was in approximate mass balance (e.g. van Angelen et al. 2012).

A clear decreasing precipitation gradient is present from the coast towards the inland. At Sisimiut, situated by the coast (Figure 2–1), the annual mean precipitation is 383 mm (long term normal 1961–1990). The corresponding value at Kangerlussuaq, ~ 160 km from the coast, (DMI weather station) is 173 mm (measured 1977–2011), i.e. a desert-like annual precipitation (Cappelen 2012). At Kangerlussuaq 40 % of the precipitation falls as snow and 60 % as rain. Mean surface wind speeds are low (< 5 m/s) in the ice free regions of the GAP study area. Winds are dominantly easterly at ground level and are an effect of thermally induced katabatic winds and airflow channelling in the valleys (van den Broeke and Gallée 1996). The vegetation near the ice sheet margin consists of dwarf-shrub tundra and steppe, with fell fields present throughout the region (Willemse et al. 2003).

Kangerlussuaq is located within the continuous permafrost zone (Weidick 1968, Christiansen and Humlum 2000). Based on the MAAT and MAGT, permafrost at the Kangerlussuaq airport was previously modelled to be 100–160 m thick (van Tatenhove and Olesen 1994). Based on Greenland's glaciation history during the Pleistocene-Holocene, there have been periods when permafrost was more widespread and deeper in the Kangerlussuaq area than it is today, but long permafrost-free periods have also existed (e.g. Ten Brink 1975, van Tatenhove et al. 1995, Forman et al. 2007). Periglacial features such as pingos and ice-wedges are found in the area (e.g. Scholz and Baumann 1997).

During the *Last Glacial Maximum* (LGM), the GrIS was considerably more extensive and the ice sheet margin extended offshore, at least onto the continental shelf (Funder 1989, Bennike and Björk 2002). By the beginning of the Holocene, the ice margin had retreated towards the east to a position close to the modern outer coast (Funder and Hansen 1996). Due to increasing air temperatures, and low annual precipitation (Anderson and Leng 2004, Aebly and Fritz 2009), the ice margin started to retreat, which resulted in a series of regional moraine systems formed during temporal halts of the retreat phase. These moraine systems have been mapped and dated by Ten Brink and Weidick (1974), van Tatenhove et al. (1996), Forman et al. (2007) and Levy et al. (2012). Deglaciation of the southern West Greenland (Figure 2-5) present-day coastal area started around 12 300 years BP, and most of the ice sheet margin reached its present position between 6500 and 7000 years BP (Ten Brink and Weidick 1974, van Tatenhove et al. 1996). The retreat was fast and, at ~ 6000 years BP, the ice margin was behind the present position and remained there until the *Little Ice Age* (LIA) re-advance (van Tatenhove et al. 1996, Forman et al. 2007). It is assumed that the minimum position was reached by 5000 years BP (Weidick 1993). Neoglacial advance may have started as early as 4800 years BP and culminated about 2000 years BP (van Tatenhove et al. 1996, Forman et al. 2007). The climate then started to warm and, around 1000 years BP, it was warmer than present temperatures. The ice sheet advanced again during the LIA, when the ice margin of western Greenland was ~ 1–2 km west from its current position (Csatho et al. 2005).The Isunnguata Sermian edge of the ice margin was only 50–200 m beyond its present margin (Forman et al. 2007). The maximum position was reached around 1850 AD. Forman et al. (2007) reported that the ice sheet has retreated to its present position over the past 100 years. Thinning of the ice sheet at elevations below 1500 m a.s.l. has accompanied this retreat (Krabill et al. 2000, Johannessen et al. 2005).

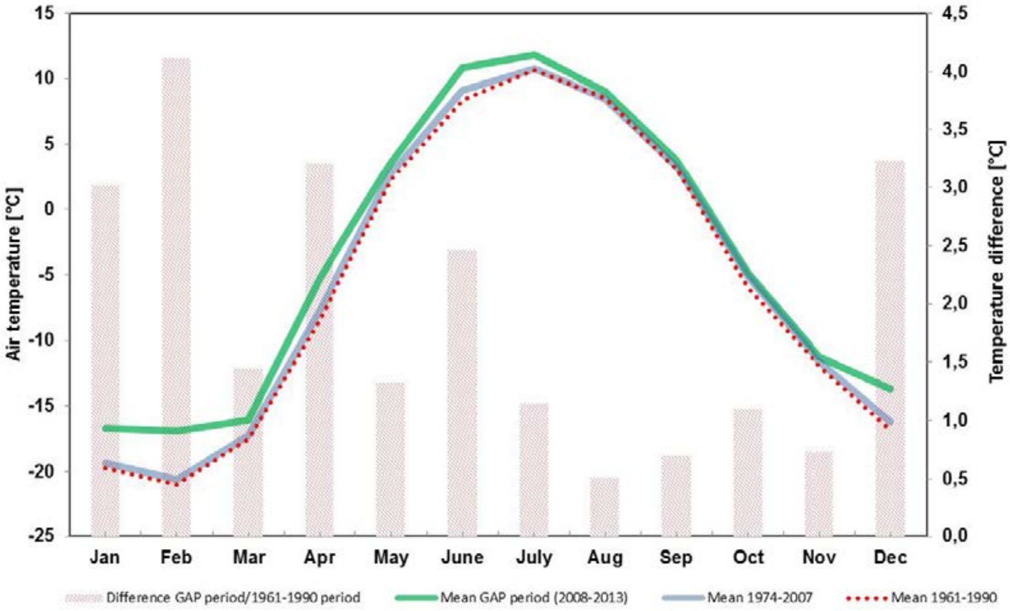

Figure 2-4. *Monthly mean air temperatures from the DMI weather station in Kangerlussuaq for the periods 1961–1990, 1974–2007 and the GAP period 2008–2013. The 1961–1990 period is considered to represent a period during which the GrIS was in approximate mass balance (e.g. van Angelen et al. 2012). The temperature difference between the GAP period and the 1961–1990 period is shown as coloured bars.*

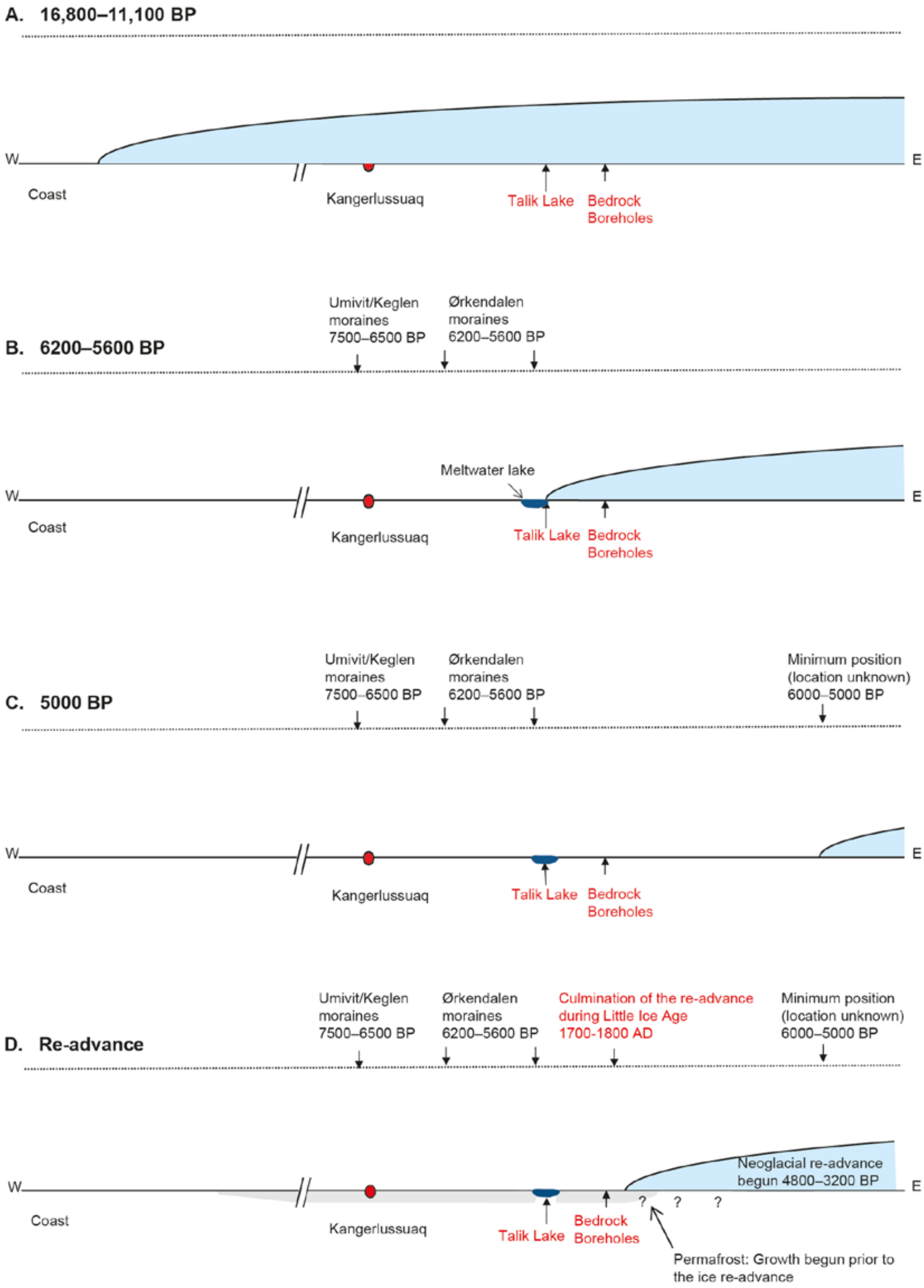

***Figure 2-5.** Cartoon showing the deglaciation history of the Kangerlussuaq area since the LGM. Many of the present lakes were likely formed as soon as the area was exposed from the retreating ice sheet. These lakes were first filled with meltwaters and later turned into non-glacial lakes. This implies that the growth of permafrost was prevented under these lakes when the climate started to cool during the neoglacial re-advance. Moraine ages are presented as ^{14}C BP and are from van Tatenhove et al. (1996).*

Unfrozen ground, known as taliks, occurs beneath large lakes, rivers and fjords only. Through taliks, i.e. taliks extending through the permafrost, provide exchange of water between the unfrozen groundwater system below the permafrost and the shallow groundwater in the active layer, and are thus flow pathways potentially allowing both recharge and discharge. The ice-free part of the GAP study area encompasses several hundreds of proglacial lakes (Figure 2-6). About 20 % of these lakes have a diameter larger than 400 m (these lakes covers 6 % of the land surface area), which suggests that the permafrost in this area is perforated by through taliks (SKB 2010a), and flow pathways available for exchange of surface water and deep groundwater through the permafrost are abundant.

2.4 The Greenland Ice Sheet (GrIS) in the GAP study area

The GrIS is the largest reservoir of ice in the Northern Hemisphere and marine records suggest that the GrIS has existed for millions of years. However, the timing of onset of glaciation on Greenland remains undetermined. It is believed that the Northern hemisphere only experienced ephemeral glaciations during late Eocene to early Pliocene, and the onset of extensive glaciations occurred around mid-Pliocene ~ 3 Ma (Maslin et al. 1998, Kleiven et al. 2002, Bartoli et al. 2005). The present-day ice divide runs near the eastern ice sheet margin, so that most of the ice sheet flows towards the west. The GrIS contains ~ 11 % of all fresh water on Earth , and has the potential of contributing up to 7.4 m of global mean sea level rise, if it was to entirely melt (Bamber et al. 2013a, IPCC 2013). Because of the GrIS's high elevation and north-south orientation the mean westerly atmospheric circulation is affected and as a result the GrIS impacts the climate in the entire Northern Hemisphere (Clark et al. 1999). The maximum ice thickness is 3400 m, with an average thickness of 1600 m (Thomas et al. 2001), and a total volume of 2.9 million km^3 (Bamber et al. 2001). The current ice in the ice sheet is 110 000 years old at a depth of 2800 m (Meese et al. 1997) at the Summit location in central Greenland. The current mass balance of the GrIS is negative, and over the time period January 2011 to January 2014 the volume loss for the entire GrIS was –375 ± 24 km^3/yr (Helm et al. 2014). The ice sheet part of the GAP study area includes the Isunnguata Sermia, Russell, Leverett, Ørkendalen and Isorlersuup outlet glaciers and their catchment areas (see Figure 2-2 and Chapter 3). The ice thickness in the study area reaches ~ 1500 m with a mean value of ~ 800 m, but is highly variable due to the steep and undulating subglacial topography (Lindbäck et al. 2014). The ice-flow direction in the area is generally directed from east to west, with a mean surface velocity of ~ 150 m/yr (Joughin et al. 2010). The glaciated part of the GAP study area is one of the most studied regions of the GrIS including previous and parallel studies of mass balance (e.g. van de Wal et al. 2012) and ice dynamics (e.g. van de Wal et al. 2008, Bartholomew et al. 2011, Palmer et al. 2011, Sole et al. 2013). One reason for the research interest in this area is related to the fact that the land-terminating outlet glaciers here are isolated from marine influences and exhibit changes in ice dynamics that are remote from tidewater influences and are directly attributable to surface-melt forcing (Fitzpatrick et al. 2014). The period 1961–1990 is often used as a reference to when the GrIS was considered to be in approximate steady state, whereas during the past 20 years the mass balance has turned negative (van Angelen et al. 2012). A recent strong warming over the western part of the GrIS is recorded by weather stations in the GAP study area (van As et al. 2012, van Angelen et al. 2014). The negative mass balance has resulted in a larger melt extent of the GrIS, increased surface runoff and discharge (Ettema et al. 2009, Fettweis et al. 2011, Hanna et al. 2008, van As et al. 2012).

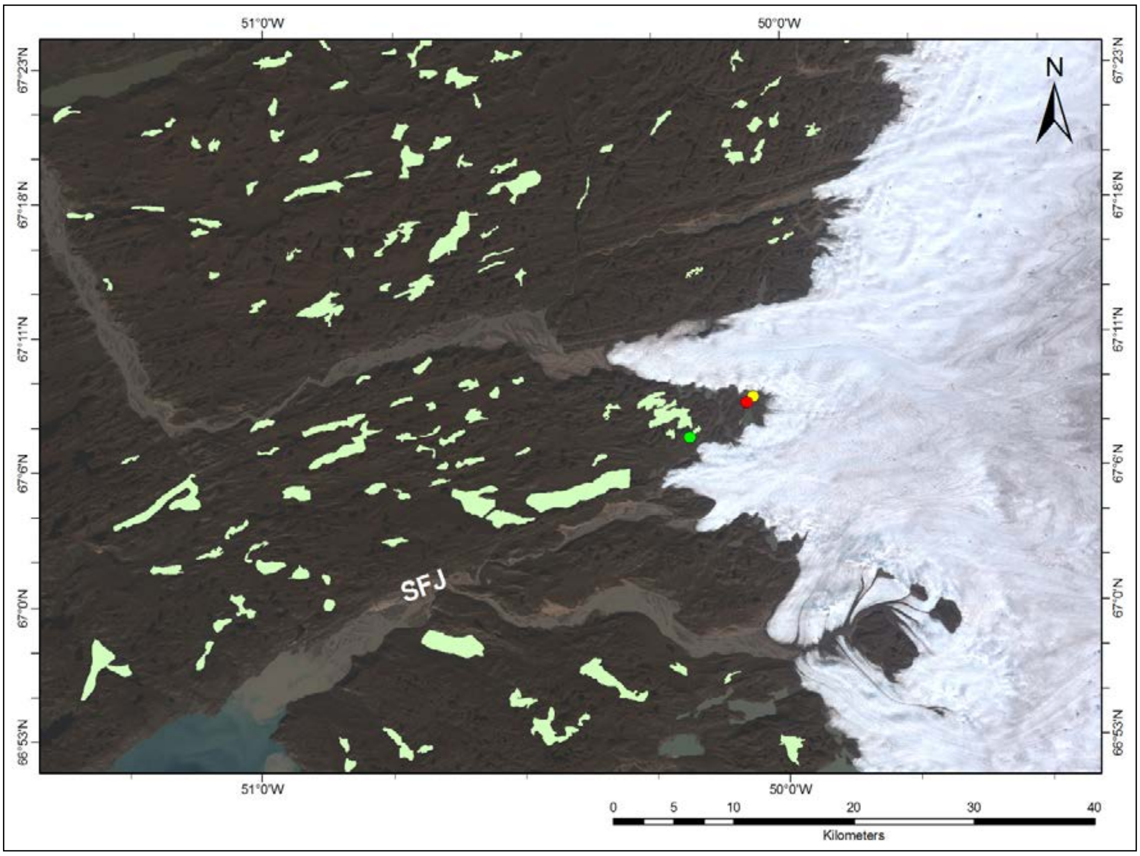

Figure 2-6. Map of the proglacial region of the GAP study area where lakes with a diameter ≥400 m, and thus may host through taliks, are shown in light green. Bedrock boreholes are shown as coloured circles. Green circle = DH-GAP01, red circle = DH-GAP03, yellow circle = DH-GAP04. SFJ = Kangerlussuaq International Airport. Background Landsat image was acquired August 23, 2000.

3 Subproject A – Ice sheet hydrology and subglacial groundwater formation

3.1 Introduction and objectives of SPA

A decade ago, knowledge and understanding was poor regarding the dynamics, processes and boundary conditions of the GrIS (IPCC-WG1 2007). The subglacial relief and basal interface, in particular its composition, character, thermal structure and concomitant hydraulic conditions and impact on ice flow were inferred only at the broadest of scales and corroborated by few indirect observations. For example, the formative and high impact paper of Zwally et al. (2002) linking seasonal ice flow acceleration to summer surface melt is representative and neatly sums up the state of this knowledge. In it, Zwally et al. (2002) determine from a multi-year time series of GPS measurements, that the magnitude of enhanced summer-flow was proportional to the cumulative *positive degree-day* (PDD) sum via a speculative mechanism by which surface meltwater enters the subglacial environment and drives enhanced, lubricated basal motion.

No explicit subglacial hydrological model or deterministic process linkage between surface melt and basal water pressure is implied in the paper, but an attractive conceptual model invoking a flat, hard-bedded subglacial topography flooded by an extensive and homogenous water-film fed from the surface via crevasses and moulins is implied.

Over the last six years, SPA has focused on *Russell Glacier Catchment* (RGC) (see Figure 3-1), a land terminating outlet of the western margin of the GrIS to glean empirical-based insight into subglacial conditions using a combination of remote sensing, meteorological, hydrological and geophysical/geodetic techniques. These techniques have been used not only to elucidate the character and processes operating at the ice sheet bed but also crucially, how they inter-connect and feedback to the patterns and processes operating at the ice surface. In this manner, extensive observations made at the ice surface, when used judiciously, can help inform and provide process insight on conditions in the subglacial environment.

Project goals

The main focus of SPA are direct observations of the surface and indirect observations of the subglacial properties and bed topography, monitoring of ice speeds and vertical displacement using fixed kinematic-(k) GPS stations and meltwater production across the ice surface of what is referred to as the "wider RGC". These datasets are critical prerequisites for robust ice dynamics or subglacial hydrological modelling efforts and to aid development of an integrated understanding of the interactions between the ice sheet hydrology, subglacial hydrology and subglacial/groundwater geochemistry and thus important for the GAP project as a whole.

This subproject is directed at addressing three of the GAP driving questions: *Question 1: Where is the meltwater generated under an ice sheet? Question 2: What is the hydraulic pressure situation under an ice sheet, driving groundwater flow? and Question 4: What is the chemical composition of glacial water when, and if, it reaches repository depth?* In addition, SPA provides basic information and datasets to address the GAP driving questions.

Implementation of the SPA work

The cornerstone of SPA geophysical effort has been radar surveys to establish high resolution distributions of bedrock topography beneath the ice sheet, basal character/conditions (i.e. identifying where sediments and/or water exist beneath the ice sheet in the GAP study area) and to derive proxy measures of thermo-hydrological conditions. Site specific seismic reflection experiments have been used to characterise the subglacial sedimentary environment; that is the presence/absence of sediment, its thickness and to infer porosity and water-content. Passive seismic experiments provide insight into the mode, mechanisms and rates of water-routing from the ice sheet surface to bed. Geodetic (GPS) records yield high resolution time series of ice surface displacement. These can be partitioned into components of horizontal velocity and vertical uplift, which, when decomposed through time can be used as proxies for changing subglacial hydraulic conditions. These observations are complimented by a suite of remote sensing, meteorological and hydrological measurements, which crucially defines an envelope of environmental forcing to which the ice sheet system is exposed and responds.

3.2 Remote sensing

The objective of the remote sensing work within SPA is to establish good spatial coverage of surface boundary conditions of the ice sheet in the GAP study area that can be used to direct/target the detailed field-based research and to provide specific inputs (e.g. supraglacial lake water flux to the bed/surface flow distributions/surface elevation change) for other analyses and modelling within the project. Remotely sensed data collected for this project has been used to determine the fluxes of surface meltwater to the bed of the ice sheet and the extent to which catchment-wide spatial and temporal variations in glacier acceleration are linked to these changes reflecting the basal boundary condition of the ice sheet.

3.2.1 Data sources

A considerable archive of remotely sensed data has been assembled to meet the project aims, utilizing data from satellite and aerial platforms, using optical and radar sensors, summarised in Table 3-1.

Table 3-1. Characteristics of remotely sensed data sources, their usage and coverage.

Satellite/Sensor	Image resolution (m)	Temporal Coverage	Usage	Russell Glacier coverage
Landsat	16	Every 16 days May–September 2000–2012 (see Table 2-2)	Mapping/velocities	Up to 140 km inland
Advanced Spaceborne Thermal Emission and Reflection Radiometer (ASTER)	16	April/May 2009	Mapping/velocities	First 30 km
Moderate resolution imaging spectroradiometer (MODIS)	250	Daily May-September 2002–2012	Mapping supraglacial lakes	Up to 140 km inland
Système Pour l'Observation de la Terre (SPOT)	5	2008	Structural mapping/ DEM	Up to 100 km inland
TerraSAR-X (TSX)	100	Summer 2009/2010	Surface velocities	Extend 57 km inland
GIMP DEM v1	30	2007	Fine resolution DEM	Complete
Light image detection and radar (LIDAR)	1.5	July 2007 and August 2009	Fine resolution DEM	1.5 km wide swath extending 107 km
Terrestrial Laser Scanner (TLS)	Varies (up to 1.5 m)	July 2010	Fine resolution DEM	Ice front

3.2.2 Data processing

3.2.2.1 Lake drainage data

Supraglacial lake (SGL) areas were calculated using multi-temporal *Moderate Resolution Imaging Spectroradiometer* (MODIS) imagery from the Terra satellite. The level 2 (MOD09) product was used, which provides un-gridded swaths of atmospherically corrected, calibrated and geolocated surface reflectance. Although the region experiences 24-h daylight in summer, illumination conditions alter with changing solar zenith angle, therefore scenes used in this study were restricted to those captured at nadir. Scenes covering the entire melt season were obtained from 2002 to 2012 from *day of year* (DOY) 121 (May 1) to DOY 274 (September 30).

Given the size of RGC, a semi-automatic strategy was used to classify SGL extents, using the Normalized Difference Water Index (Huggel et al. 2002) and freely available RSGISlib software (http://www.rsgislib.org). SGL volume was calculated using an empirically derived depth-reflectance relationship using the bathymetry of two SGLs surveyed in July 2010. The depth-reflectance relationship was then applied to all water classified pixels across the study region to yield depth estimates and were subsequently integrated over the SGL area to calculate water volume.

3.2.2.2 Structural maps

Using a variety of optical satellite imagery (Table 3-1 and Table 3-2) major structural features on the ice surface were mapped using ArcGIS software. The structural map, combined with velocity maps from previous studies (Palmer et al. 2011, Sundal et al. 2011) and a preliminary basal DEM (Pettersson R 2010, personal communication) were used to determine the flow lines of each of the major outlets covered in the velocity data.

Table 3-2. Details of the Landsat temporal coverage

Year	Dates DD/MM/YY
2000	22/07/00, 23/08/00
2001	04/04/01, 09/07/01
2002	22/03/02, 25/05/02, 13/08/02
2003	09/03/03, 10/04/03, 26/04/03, 23/05/03, 15/07/03
2004	14/05/04, 30/05/04, 17/07/04
2005	14/03/05, 17/05/05
2006	08/08/06, 24/08/06, 25/09/06, 11/10/06
2007	04/03/07, 23/05/07, 10/07/07, 11/08/07, 27/08/07, 12/09/07
2008	09/05/08, 10/06/08, 26/06/08, 28/07/08
2009	05/05/09, 12/05/09, 21/05/09, 28/05/09, 13/06/09, 15/07/09, 31/07/09
2010	16/06/10, 02/07/10, 18/07/10, 19/08/10
2011	28/06/11
2012	16/07/12, 17/08/12, 23/07/12

3.2.2.3 Velocity data

Velocity data were derived from the TerraSAR-X (TSX) datasets using a combination of conventional interferometry and speckle tracking techniques (Joughin 2002). The 11-day repeat pairs of SAR data provided by the TSX platform exhibit a strong sensitivity to displacement. Average error margins in the TSX velocity data were calculated to be ~ 5 m/a by measuring the average difference from zero of stationary (off-ice) areas in each of the images.

Surface velocity maps produced by the TSX data encompass four major outlets including Russell Glacier and Isunnguata Sermia. To illustrate these ice flow patterns for each outlet, surface velocity profiles were extracted.

3.2.2.4 High-resolution DEMs

The 2007 and 2009 LIDAR data were processed by Cambridge Unit for Landscape Modelling and Plymouth Marine Laboratory respectively using Optech REALM v3.5 software. The high-resolution point clouds were gridded to 20 m resolution for computation efficiency and to minimise the effect of high frequency returns caused by migrating crevasses. Using optical satellite data (Table 3-2) the location of supraglacial lakes were identified and masked out of the LIDAR data to remove any potential inaccuracies due to differences in lake height between years. The change in surface height was calculated by subtracting the 2007 data from the 2009 data in areas where the datasets overlapped (> 503 000 points). LIDAR data were compared with NASA's IceBridge dataset and Terrestrial Laser Scanner data collected at the front of Russell Glacier in 2011.

3.2.3 Data outputs and conclusions

3.2.3.1 Lake drainage data

Using 502 optical satellite images, the storage and drainage of ~ 200 seasonally occurring lakes across RGC was quantified as part of GAP, producing detailed maps of lake recurrence and drainage patterns (Figure 3-1). Although SGLs in the GAP study area occupy a relatively small portion of the catchment (2 %), they store a disproportionately large volume of bulk runoff (13 %). They have important implications for ice dynamics through the release of surface meltwater into the subglacial hydrological system via rapid *in situ* drainage or through overflow into moulins.

Lake volumes were compared with air temperature, surface melt (van As et al. 2012) and discharge data (Hasholt et al. 2013). SGL drainage coincides with short term increases in discharge indicating that supraglacial water storage does impact on catchment wide hydrological dynamics (Figure 3-2). In years of high summer temperatures, SGLs form and drain earlier in the season (e.g. 38 and 20 days earlier than the 11 year mean during 2010 and 2012, respectively), and cover a larger surface area (e.g. 40 % greater in the record melt year of 2012 compared with e.g. the cooler year of 2006). Furthermore, inland expansion of SGLs is strongly correlated with air temperature (r^2=0.78), with lakes occupying a greater area within the upper ablation zone. For example, in 2012, lake area was

49 % greater above 1400 m (compared with the 11 yr mean) and extending farther inland (>1800 m) than previously recorded. In a warming climate, spatial and temporal expansion of SGLs with concomitant surface to bed coupling will likely impact on inland ice sheet flow dynamics and drawdown.

Evidence of SGLs draining in clusters was found, potentially impacting on bulk discharge gauged at Watson River. It was inferred that one drainage event dynamically triggered rapid tapping in neighbouring lakes. Lake size was found to not influence the drainage mechanism, and no evidence was found supporting the need for a critical lake depth or volume threshold to initiate rapid drainage.

3.2.3.2 Structural maps

Structural mapping (Figure 3-3) reveals that patterns of foliation on the ice surface is longitudinally extended in areas of faster ice flow corresponding to the location of subglacial troughs. The results of the study are concurrent with other work (Joughin et al. 2013) suggesting that the spatial patterns of accelerated ice flow can be attributed to the slope of both the ice sheet surface and the underlying bedrock, acting in unison to determine subglacial hydrological pathways.

3.2.3.3 Velocity data

The TSX data provide snapshots of the highly variable ice flow distribution observed across Russell Glacier extending at least 57 km up-glacier (Figure 3-4). Specific spatial and temporal coverage of available velocity maps are shown in Table 3-3. The observed seasonal flow variations are in broad agreement with previous studies (Joughin et al. 2008, 2010, Bartholomew et al. 2010) though the large initial perturbation followed by rapid deceleration of the ice within the 2400 km^2 catchment, indicates the basal drainage system responds rapidly to changes in supraglacial inputs.

The large spatial variability of the observed velocity trends in this region (Figure 3-4), highlighted by the differences in ice flow between neighbouring outlets, suggests a complex relationship between the routing of water from the surface to the bed and illustrates the importance that other forces such as bedrock geometry are considered. Previous work proposes the concept that a positive feedback exists between meltwater production and ice velocity, which would lead to a more rapid response to projected future warming trends (Zwally et al. 2002). However the hydraulic evolution of the basal drainage system acts to regulate ice flow, therefore self-limiting this positive feedback. Recent studies (Sundal et al. 2011) support this hypothesis; in warmer years the period of melt-induced summer acceleration is shorter than in cooler years, as equilibrium subglacial hydrological conditions are reached earlier in the season. Modelling studies including a 'dynamic switching' threshold determine that above a critical rate of meltwater input, channelisation and surface deceleration occurs, indicating that sustained high meltwater rates would suppress dynamic response (Schoof 2010). However, analysis made in GAP during two contrasting melt seasons do not completely concur with these findings, suggesting that a more complex relationship between meltwater availability and accelerated flow exists.

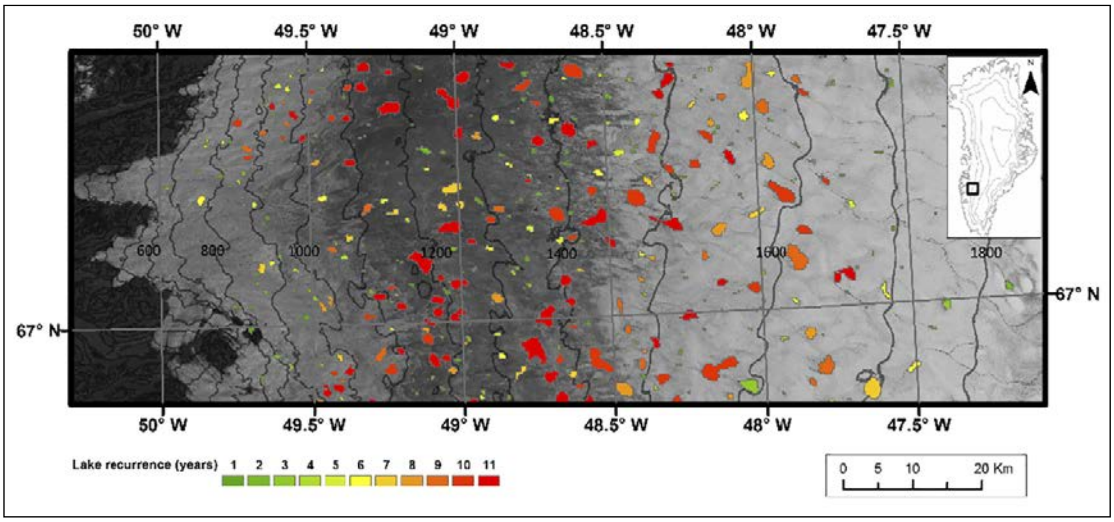

Figure 3-1. The location of all SGL's within the study area between 2002–2012, coloured by their recurrence.

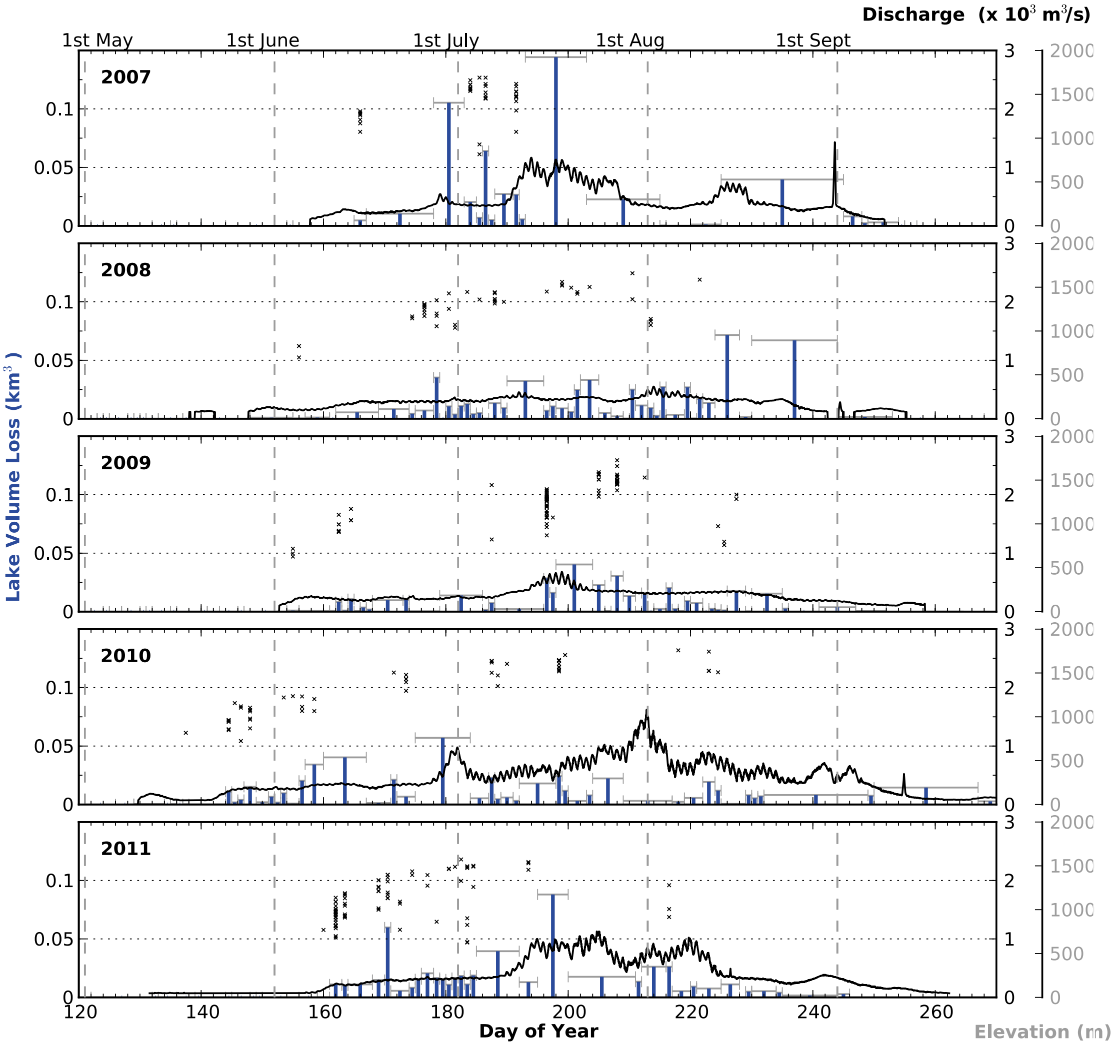

Figure 3-2. Lake volume loss within RGC and Watson River discharge between 2007 and 2012. The drainage date and elevation of rapidly draining lakes are also shown (black crosses).

Table 3-3. Details of 11-day averaged velocity maps revealing their spatial and temporal coverage. TSX coverage of Russell Glacier consists of two scenes, which include the upper and lower catchment (see Figure 3-4), and both scenes were not always recorded by the sensor.

Date (11 day midpoint) DD/MM/YY	Spatial coverage over Russell Glacier catchment
25/03/09	Complete
04/08/09	Complete
26/08/09	Complete
11/11/09	Complete
07/02/10	Upper
25/04/10	Lower
06/05/10	Complete
19/06/10	Lower
30/06/10	Lower
11/07/10	Lower
22/07/10	Lower
24/08/10	Upper
29/10/10	Complete
09/11/10	Lower
20/11/10	Complete

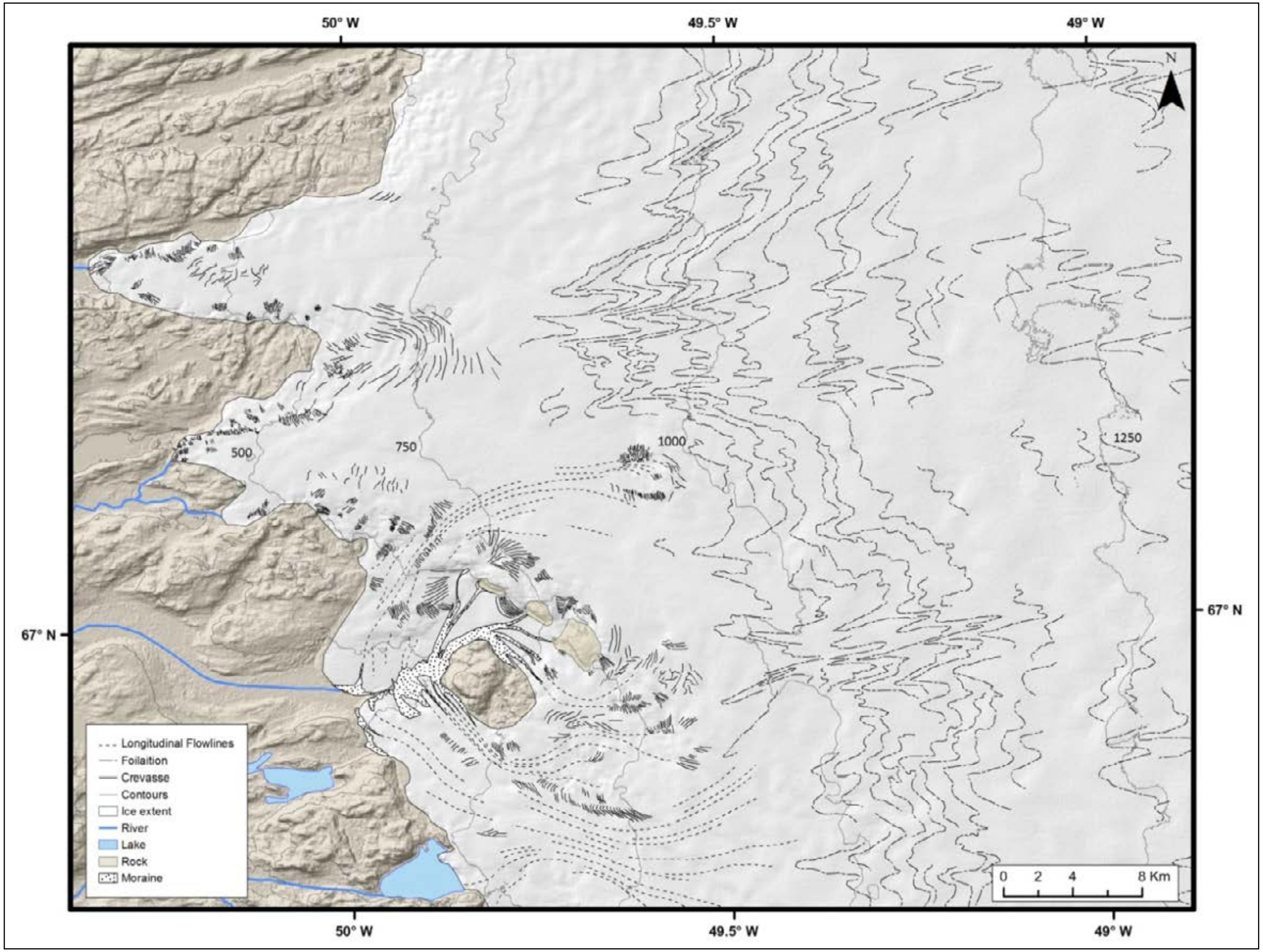

Figure 3-3. *Structural map of the study area revealing deformation of internal glacial structures owing to differences between fast and slow flowing regions.*

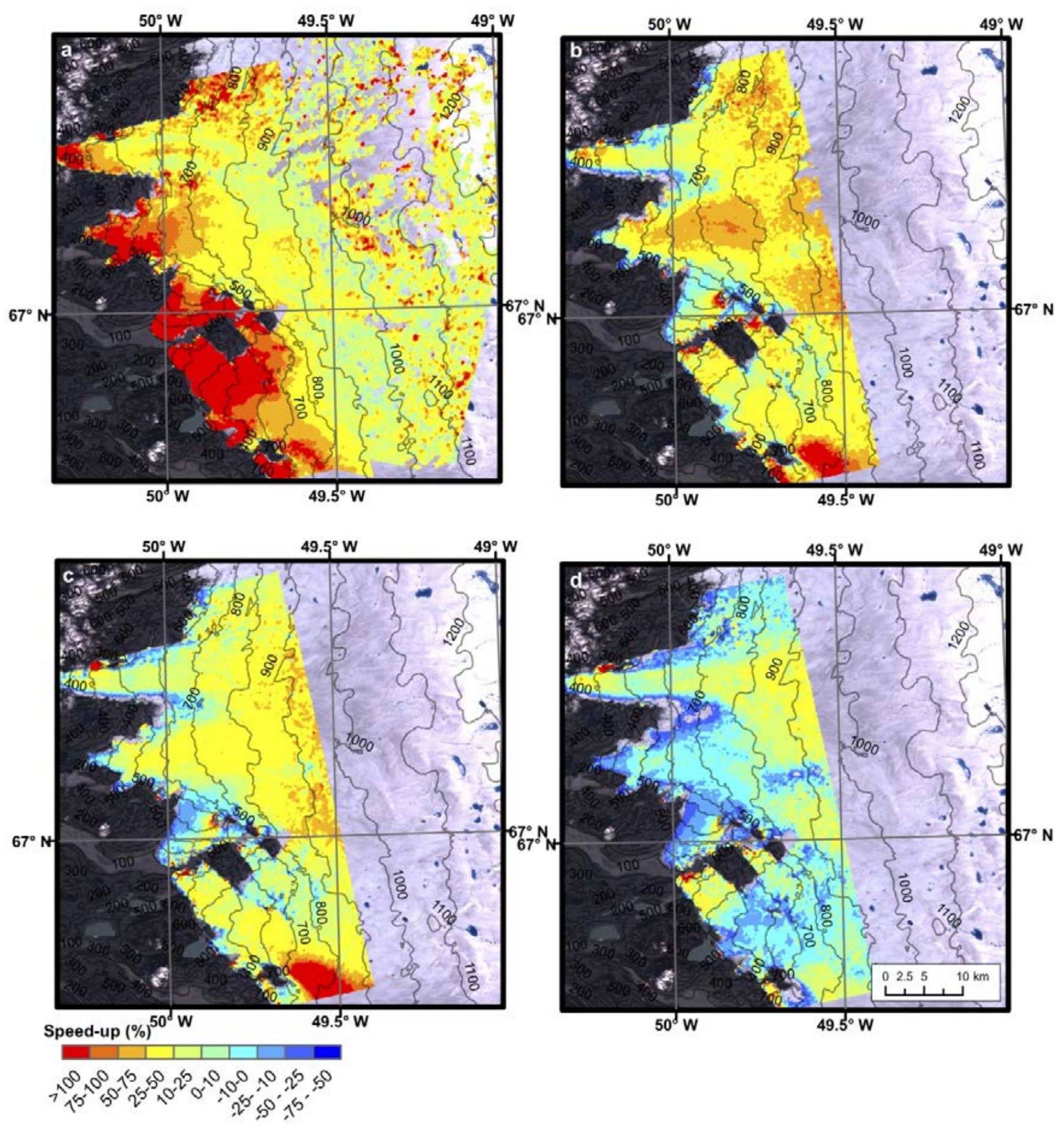

Figure 3-4. *Surface velocities expressed as a percentage relative to the winter mean throughout summer 2010 over 11-day periods with mid-points a) May 6, b) June 19, c) June 30, d) July 22. Elevation contours derived from a SPOT DEM are also shown.*

3.2.3.4 High-resolution DEMs

High-resolution DEMs have been generated covering the margin of Russell Glacier (Figure 3-5) extending 107 km up-glacier (Figure 3-6). Analysis of repeat DEMs has revealed evidence of extensive thinning extending ~ 80 km inland (~1500 m ice thickness) in line with previous studies (e.g. Krabill et al. 2000, Abdalati et al. 2001, Thomas et al. 2001). Over the entire survey area mean thinning rates during 2007-09, 2010 and 2011 were −0.59 ± 0.39 m/yr, −2.29 ± 0.085 m/yr and −1.13 ± 0.085 m/yr respectively (Figure 3-7). The combined LIDAR and IceBridge surveys reveal a trend of increased rates of thinning over time, with the greatest thinning rates at the ice sheet margins (< 20 km, where ice thickness range between ~ 220–800 m), with decreasing magnitude farther up-glacier. Where data is available, the greatest rates of thinning occur in marginal zones and along the centre of outlet flowlines, coinciding with the regions which undergo the greatest magnitudes of melt-induced accelerated flow. The observed elevation changes may be attributed to continued dynamic thinning as a result of accelerated flow comparable to previous studies (Pritchard et al. 2009), and implies that this western portion of the GrIS is continuing to undergo a period of sustained dynamic imbalance driven by subglacial-dynamic processes.

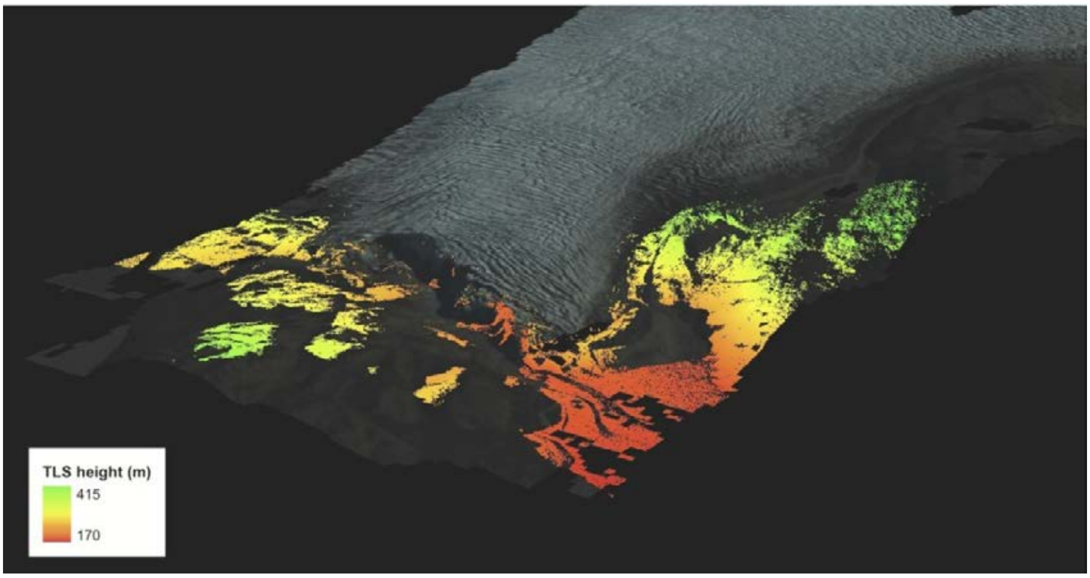

Figure 3-5. *Colour scaled TLS coverage at the margin of Russell Glacier (gridded at 2m resolution) draped over the LIDAR coverage (gridded at 20m resolution).*

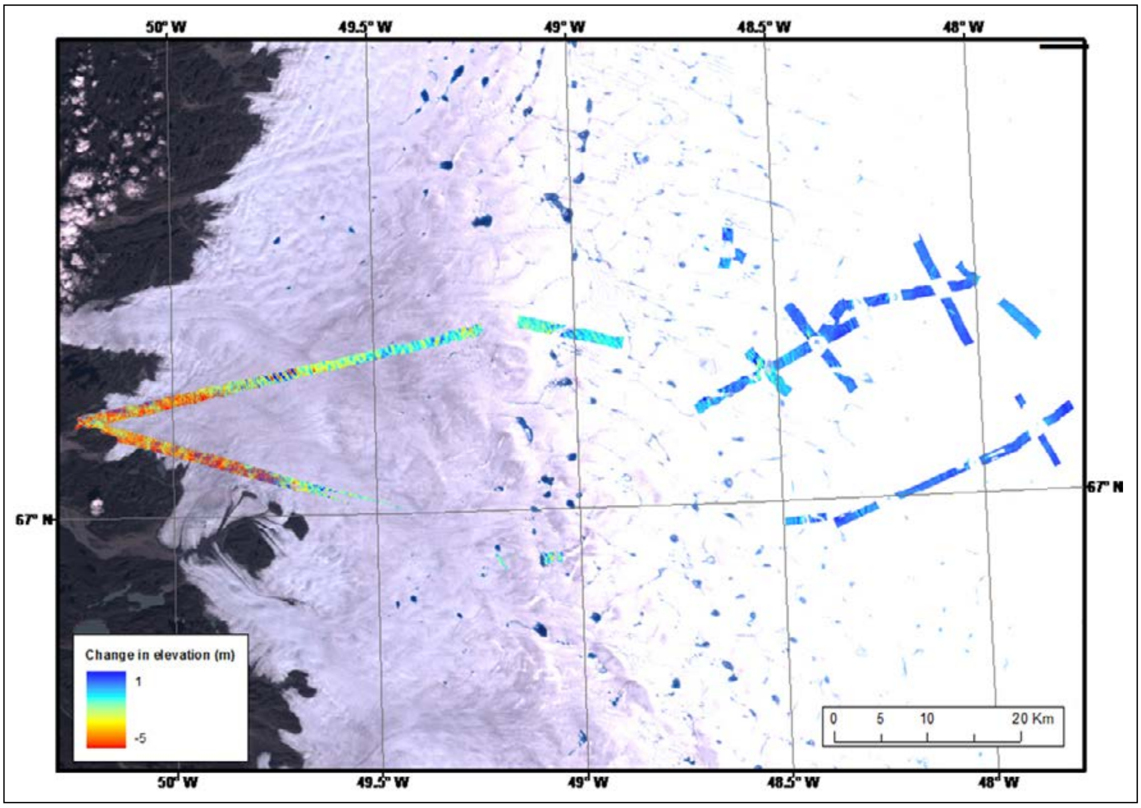

Figure 3-6. *Repeat LIDAR tracks revealing change in surface elevation (m) between 2007 and 2009, overlaid onto a Landsat 7 image from late June 2008.*

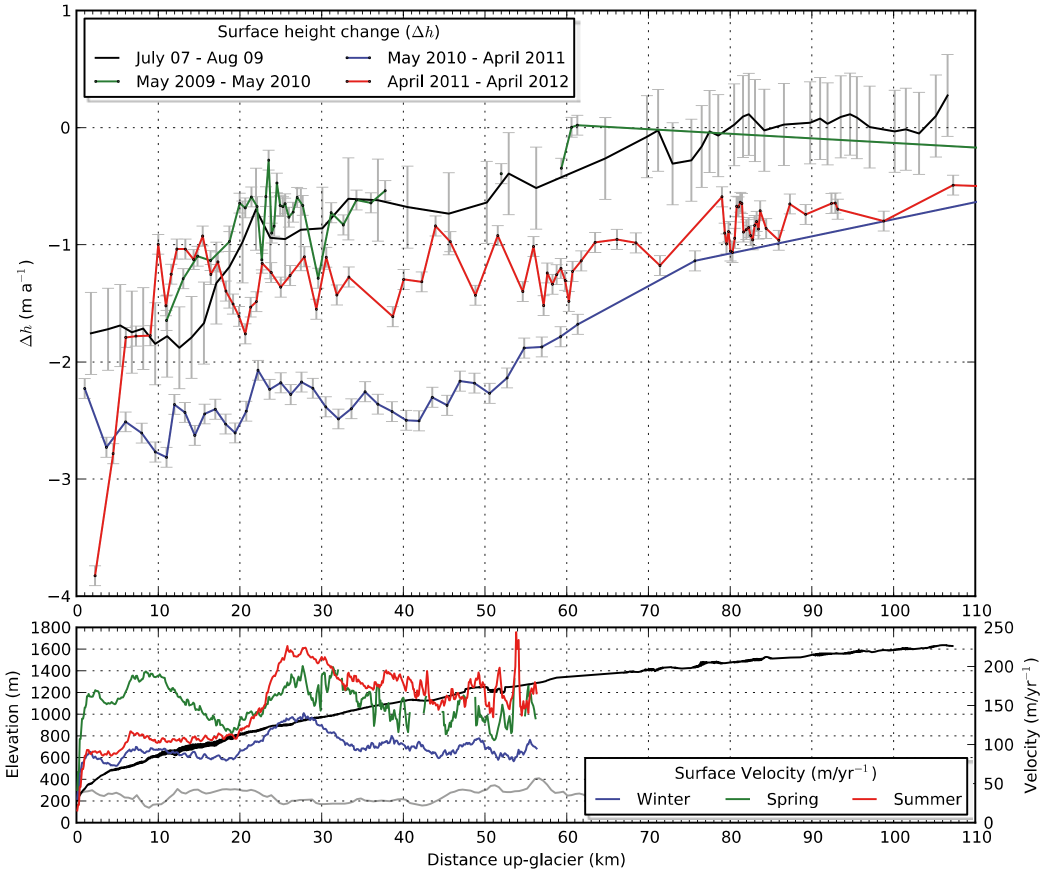

Figure 3-7. *Change in ice surface elevation (1000 point running mean) (m) with increasing distance up-glacier over between 2007–2011 (top), and surface and basal topography with ice speed during winter, spring and summer (bottom).*

3.3 Supraglacial meltwater production and runoff

3.3.1 Introduction and objectives

Determining the availability of meltwater in the supra-, en- and subglacial system was one of the goals of the GAP. Most meltwater originates at the surface of the ice sheet, where ice melt is caused by energy received from the sun and atmosphere. Net mass input by snow accumulation in higher regions occurs in order to compensate for the melting at low elevations. Cooling climates reduce the rate of surface melting, and warming climates, such as Greenland is presently experiencing, enhance the rate of surface meltwater production. Water is also generated at the bed from melting of ice due to heat energy supplied from geothermal sources, friction from the ice mass sliding over its bed, and deformation of the ice.

A common, observation-based method was used by GAP to determine the surface meltwater production. On glaciers around the globe, *automatic weather stations* (AWS) are used to quantify the energy exchange at snow and ice surfaces. Surface energy balance models use the observations by AWS to calculate the separate heat sources and sinks, not only providing an accurate melt estimate, but also offering the possibility to investigate the relative contributions of heat sources and changes therein in a warming climate.

Three AWS were installed in the Kangerlussuaq sector of the GrIS in September 2008 and April 2009 (Table 3-4, Figure 3-8, Figure 3-9 and Appendix A). The lower station (KAN_L) is positioned in the lower ablation area at 710 m (D-WGS84), the middle station (KAN_M) is in the upper ablation area at 1310 m (D-WGS84), and the upper station (KAN_U) is placed in the accumulation area at 1880 m (D-WGS84). The AWS measure barometric pressure, air temperature, humidity, wind speed and direction, solar and terrestrial radiation (vertical components), snow accumulation, ablation, subsurface temperatures down to 10 m, GPS position, and a number of diagnostic parameters such as battery voltage, station tilt and the current drawn by the ventilator in the radiation shield of the temperature and humidity assembly (see Table 3-5 for details on instrumentation). Measurements are taken every ten minutes and stored in the logger memory. Hourly averaged data are transmitted by Iridium satellite link between mid-April to late October (days 100–300 in the calendar year), and daily averages are transmitted during the remaining days of the year when solar power for battery recharge is less abundant. GPS measurements follow the transmission schedule.

Table 3-4. Locations and deployment dates of the AWS.

Station name	Latitude (°N)	Longitude (ºW)	(D-WGS84) (m)	Placement date
KAN_L	67.097	49.933	710	September 1, 2008
KAN_M	67.066	48.818	1310	September 2, 2008
KAN_U	67.000	47.017	1880	April 4, 2009

Table 3-5. AWS instrumentation.

Instrument (measured units)	Manufacturer	Model
Barometer (hPa)	Setra	CS100
Thermometer (°C)	Rotronic	MP100H
Hygro/thermometer (%, °C)	Rotronic	Hygro Clip S3
Ventilated radiation shield (mA)	Rotronic	multiple parts
Wind monitor (m/s, °)	Young	05103-5
Radiometer (W/m^2)	Kipp and zonen	CNR1/4
Sonic ranger × 2 (m)	Campbell Scientific	SR50A
Pressure transducer (m)	Ørum and Jensen, Geological Survey of Denmark and Greenland (GEUS) assembly	NT1400/1700
Thermistor, 8 in 10 m string (°C)	RS Components, GEUS string	151-243 100k
Inclinometer (°)	HL Planar, GEUS enclosure	NS-25/E2
GPS antenna (°N, °W, m)	Trimble	SAF5350-A
Satellite antenna	NAL Research	SAF5350-A
Modem	NAL Research	9601-DG
Data logger (°C)	Campbell Scientific	CR1000
Multiplexer	Campbell Scientific	AM16/32B
CF card reader	Campbell Scientific	CFM100
Solar panel	BP Solar	SX10U
Batteries, 4 × 28 Ah (V)	Panasonic	LC-XC1228AP

3.3.2 Weather station observations

The AWS measurement success rate is high, with all of the primary sensors continuing to function properly as of April 2014. Secondary measurement records such as station tilt and GPS position exhibit data gaps of up to several tens of percent, but these gaps have no significant consequences to the melt product. A common issue with surface height measurements by fairly delicate sonic rangers, used for melt model validation, is caused by stake assemblies melting out several metres until they cannot endure high wind stress any longer and collapse. In general, the success rate of these three GAP AWS is higher than elsewhere in Greenland due to the relatively mild atmospheric conditions in the region. An issue that was encountered was a problematic memory card swap at KAN_U in 2010, only providing transmitted data at hourly or daily measurement frequency for a 17.5 month period (September 8, 2010–January 21, 2012).

The AWS data are processed to remove unrealistic values and calculate hourly, daily and monthly mean values. Prior to averaging and use by the surface energy balance model a number of standard and custom recalculations take place, such as adjusting sonic ranger height for dependence of sound velocity on air density, removing air pressure variability from the surface ablation measurements by pressure transducer, and correcting shortwave radiation for sensor tilt. Table 3-6 lists the sizes and locations of the processed data files. A selection of daily-mean measured AWS variables are illustrated in Figure 3-10. The measurements that are most important to the melt calculations are discussed here.

Figure 3-8. *AWS a) KAN_L, b) KAN_M and c) KAN_U on April 2, 3 and 4, 2009 respectively. Photographs taken by Dirk van As.*

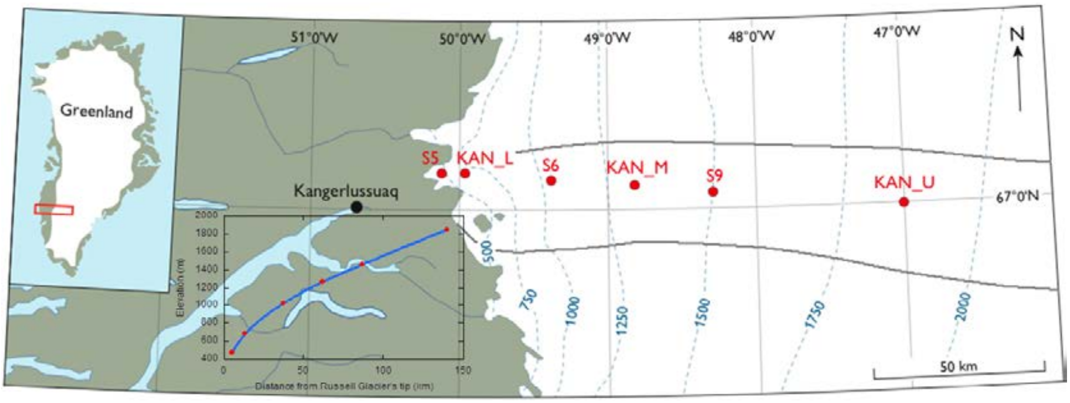

Figure 3-9. *Map of southwest Greenland including the positions of the GAP and Institute for Marine and Atmospheric Research in Utrecht (IMAU) (S5, S6 and S9) AWS and catchment delineation (grey lines).*

Measurements of accumulation and ablation in Figure 3-10a reveal some of the difficulty in obtaining continuous data series for this parameter, and therefore it is measured with multiple sensors. Sudden jumps are due to redrilling of instrumentation. At KAN_L, nearly 4 m of ice ablated in the summer of 2009, while more than 6 m ablated in 2010, when the melt season was relatively warm and long. Whereas the surface mass budget at KAN_M was in near-balance in 2009, about 2 m ablated in 2010 and 2012. Note that ablation does not equal mass loss; gravity-driven ice-dynamic transport balances the ablated ice on an ice sheet in steady state. Even at KAN_U in the accumulation area, the surface lowered in 2010 and 2012 due to ablation by melting exceeding the wintertime accumulation. However, this should not be interpreted as net ablation since in the accumulation area of any ice mass meltwater will partly or fully refreeze in the snow and firn. Compared to other GrIS regions, little or no snow accumulates in the lower regions of the Kangerlussuaq region in winter. Also the upper station receives relatively little precipitation; the Kangerlussuaq sector of the ice sheet is orographically shielded from precipitation by the high Sukkertoppen ice cap towards to southwest (see Figure 2-1).

The amplitude of the annual cycle in near-surface temperature is about 20 °C (Figure 3-10b). The largest variability occurs in winter. In summer, temperatures are a few degrees above freezing, most frequently at KAN_L. The lowest daily-mean temperature occurred at KAN_U (–43.8 °C on March 1, 2012), with the lowest hourly-mean value measured the following day (–47.9 °C). In summer, thermal regulation of the melting 0 °C surface prohibits the near-surface atmosphere to follow free-atmospheric temperatures, which can be relatively high for the continental climate of the Kangerlussuaq region (Cappelen 2013). Summer (June, July, August) temperatures were equally high in 2010 and 2012, followed by 2011, 2014, 2009 and coldest summer 2013. Overall, the last decade has been warm in Greenland, but record-setting high temperatures were recorded around the country in 2010 and 2012, most notably along the western and southern coasts (Hanna et al. 2012, van As et al. 2013).

Also other meteorological parameters display an annual cycle (Figure 3-10b–f). Most interesting is wind speed, which is higher in winter and at higher elevation (Figure 3-10e). More frequent wintertime storms are due to the more frequent passage of low-pressure systems. Also, the radiative cooling of the surface in winter produces an atmospheric inversion layer with larger temperature deficit, resulting in stronger gravity-driven katabatic winds. The ever-present katabatic forcing can be recognised in the year-round non-zero wind speed. The strongest winds during the measurement period were recorded on 8 January 2014, when the daily-mean values at KAN_U reached 28.9 m/s (104 km/h). The highest wind speed measured at KAN_U was 36.3 m/s (131 km/h) on December 14, 2009.

The Kangerlussuaq sector of the GrIS is positioned just north of the polar circle, so it experiences a short period of midnight sun in summer and polar night in winter (Figure 3-10g). Daily-mean downward radiative fluxes of solar radiation in summer exceed 400 W/m^2 and act as the largest source of melt energy. Measured values are fairly similar at the three AWS though solar radiation is commonly lowest at KAN_L, mostly due to the more frequent presence of clouds. Due to differences in albedo (Figure 3-10h), a larger fraction of the solar radiation is absorbed by the ice surface at low elevation. Interestingly, the middle station KAN_M measures the lowest mid-summer albedo in most years.

Longwave radiation emitted downward by the atmosphere and upward by the ice surface (Figure 3-10i and j, respectively), reflect the annual cycle in temperature. Note the upward longwave is limited to ~ 316 W/m^2, as the ice surface cannot warm beyond 0 °C. The deeper ice layers remain well below freezing, lagging atmospheric temperatures by several months. Figure 3-10k plots the deepest thermistor measurements, at 10 m depth at the moment of (re)drilling, and illustrates that ice temperatures decrease slowly with surface elevation. The exception is the summer of 2012, when latent heat released by refreezing in the firn at depth caused KAN_U ice temperature to exceed that at KAN_M (Charalampidis et al. 2015).

Finally, to illustrate the good vertical distribution of the weather stations and that they record GPS-determined postion, in Figure 3-10l daily-mean GPS elevation is plotted. A plotting criteria was applied in which only the most accurate values are shown, putting emphasis on summer values when the GPS readings are performed hourly rather than once every day, to preserve power in winter.

Table 3-6. AWS data files and melt modelling output files.

Data description	File name	Size	Location
Hourly data KAN_L	KAN_L_hour.txt	< 20 MB	SKB database
Daily data KAN_L	KAN_L_day.txt	< 1 MB	SKB database
Hourly data KAN_M	KAN_M_hour.txt	< 20 MB	SKB database
Daily data KAN_M	KAN_M_day.txt	< 1 MB	SKB database
Hourly data KAN_U	KAN_U_hour.txt	< 20 MB	SKB database
Daily data KAN_U	KAN_U_day.txt	< 1 MB	SKB database
Daily surface meltwater production per 100 m elevation bin	meltwater(mm).txt	< 1 MB	SKB database
Daily surface meltwater runoff per 100 m elevation bin	runoff(mm).txt	< 1 MB	SKB database
Daily surface meltwater production per 100 m elevation bin, summed over the bins	meltwater(m^3).txt	< 1 MB	SKB database
Daily surface meltwater runoff per 100 m elevation bin, summed over the bins	runoff(m^3).txt	< 1 MB	SKB database

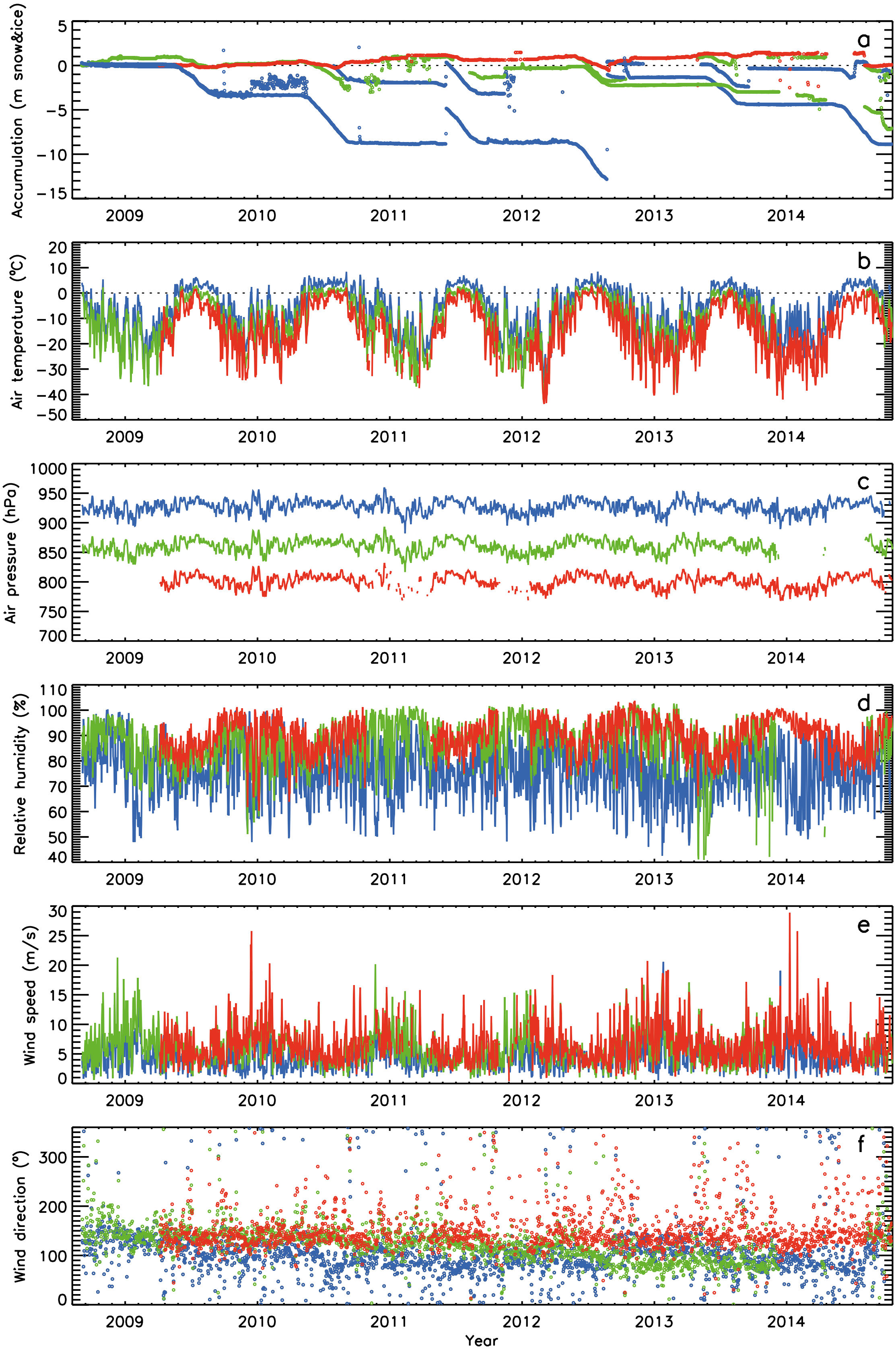

Figure 3-10a–f. *Daily-mean AWS data for KAN_L (blue), KAN_M (green) and KAN_U (red). a) Surface height measured by sonic rangers and pressure transducers, b) Air temperature, c) Air pressure, d) Relative huidity, e) Wind speed, f) Wind direction. Continues on next page.*

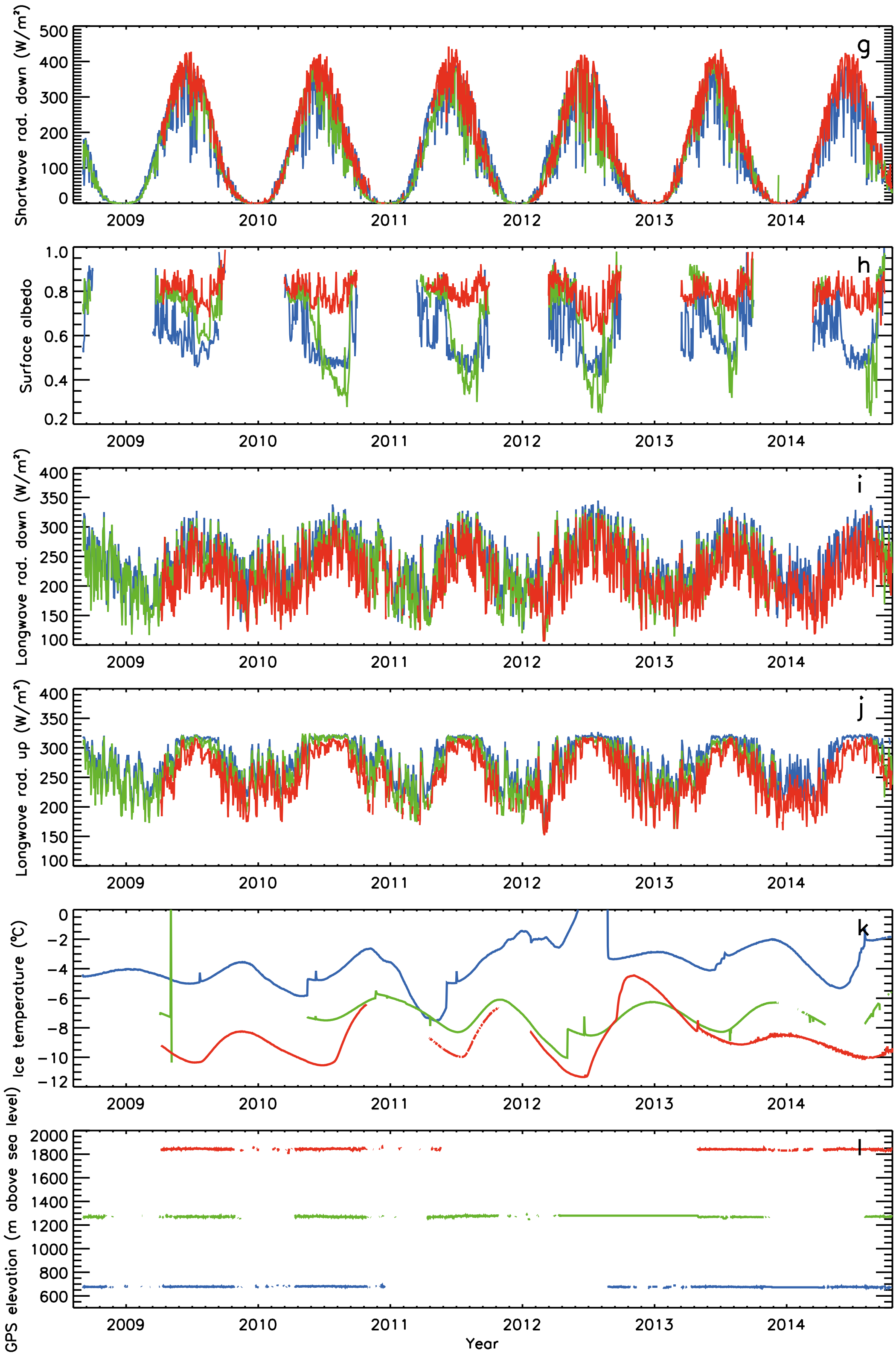

Figure 3-10g–l. *g) Downward shortwave radiation, h) Surface albedo, i) Downward longwave radiation, j) Upward longwave radiation, k) Ice temperature at 10 m (depth changes due to ablation/accumulation), l) GPS elevation in m a.s.l.*

3.3.3 Surface energy balance modelling

The surface meltwater production in the Kangerlussuaq sector of the GrIS is calculated using AWS measurements as input for a surface energy balance model. The model used is similar to that applied by van As (2011) and has proven robust and accurate for various snow and ice surfaces in, among others, Greenland high melt regions and the Antarctic plateau. Barometric pressure, temperature, humidity, wind speed, and the incoming radiation components are required to calculate the separate energy fluxes between the atmosphere/sun and ice sheet surface. These energy sinks and sources are SR_{net}: the solar (shortwave) radiative flux (downward minus reflected), LR_{net}: the terrestrial (longwave) radiative flux (emitted downward by the atmosphere minus emitted by the ice sheet surface), SH: the sensible turbulent heat flux, LH: the latent turbulent heat flux, SSH: the sub-surface heat flux, and RH: the heat flux by rain. Added together, any surplus of energy is either used for the heating of the near-surface snow and ice layers, or is consumed by melting (M):

$$M = SR_{net} + LR_{net} + SH + LH + SSH + RH$$

The calculation of the turbulent heat fluxes (SH and LH) is based on near-surface gradients of temperature, humidity and wind speed, using the surface as the lower level for gradient calculation, and makes use of well-tested stability correction functions and common values for aerodynamic surface roughness length for momentum (1×10^{-4} m for snow and 1×10^{-3} m for ice). Calculation of emitted longwave radiation, as well as SH, LH and SSH makes use of the unknown variable of surface temperate, for which the surface energy balance can be solved iteratively. The model time step is daily.

In order to calculate spatially distributed surface melt over the catchment (Figure 3-9) (van As et al. 2012), the AWS variables measured at various elevations are interpolated into 100 m elevation bins. Because surface albedo (defined as the fraction of the reflected and downward shortwave radiative fluxes) is highly spatially variable, yet a dominant parameter for surface meltwater production, interpolating albedo between AWS sites is not justified. Instead satellite (MODIS) derived albedo is used (e.g. Box et al. 2012), calibrated by AWS measurements.

The modelled surface mass balance is the sum of solid precipitation, melt, sublimation/deposition, and condensation/evaporation. Liquid precipitation and meltwater produced at the surface refreeze in underlying snow layers if temperature and density requirements are met, i.e. when sub-surface grid cells are at sub-freezing temperatures and not at ice density. The remaining water is assumed to run off. All but one of the mass balance components are products of the energy balance model. Precipitation, however, is unknown, as it is not measured at the AWS on the ice sheet, and cannot be accurately extrapolated from distant or even nearby off-ice measurements due to its high spatial variability. Whereas solid precipitation could be estimated from the accumulation measured at the three AWS, liquid precipitation cannot and has to be parameterised. A 1 mm water equivalent per hour precipitation rate was prescribed in the parameterisation for periods with a heavy cloud cover, which the model identifies from occurrences when downward longwave radiation values exceed blackbody radiation calculated using near-surface air temperature. This precipitation rate was tuned to fit accumulation observations, assuming solid precipitation to occur for subfreezing temperatures.

Several factors contribute to the uncertainty in the *Surface Energy Balance* (SEB) calculations. Firstly, measurement errors vary per sensor and can accumulate in non-linear ways in the surface energy balance calculations. The largest sensor uncertainty, as reported by the manufacturer, is for the radiometer (10 % for daily totals, see van As 2011), which is actually shown to be smaller (van den Broeke et al. 2004). Secondly, a number of assumptions are made in the model (van As 2011), most importantly for the aerodynamic surface roughness length. Assuming these to be constant in time is a simplification, as outlined by Smeets and van den Broeke (2008). Using a daily time step in the model calculations instead of a temporal resolution resolving the daily cycle is justified, given the ablation validation for the AWS positions shown below. Also, a reduced temporal resolution ensures a more robust spatial interpolation of measured variables since local atmospheric variability on short time scales is averaged out. The linear interpolation in itself contributes to model uncertainty, but also keeps measurement errors by single AWS in check by the measurements of other stations. Finally, in calculating the integrated runoff from the ice sheet, the error in the delineation of the Kangerlussuaq catchment translates directly into runoff errors. In all, the causes of uncertainty in this study are not exceptional and allow for catchment-wide runoff calculations that are more accurate than in previous studies given the reliance on observational data, in particular on MODIS albedo.

Evaluation of the calculations is performed using three independent methods. Firstly, it is determined whether there is a close agreement between the modelled surface temperatures and those calculated from measured emitted longwave radiation assuming black-body radiative properties. *Root mean square* (RMS) difference values of 1.0–1.7 °C were found for the six stations and their corresponding elevation bins, which is 4–6 times smaller than the uncertainty derived from the 10 % uncertainty quoted by the radiometer manufacturer (van As et al. 2012). Secondly, observed and modelled surface height changes due to ablation and accumulation at the AWS sites were compared, giving acceptable differences (see next paragraph). Thirdly, the quantitative agreement between the surface meltwater runoff for the Kangerlussuaq catchment and the freshwater discharge measurements in the Watson river at the Kangerlussuaq bridge was assessed (see Section 3.3.4).

The cumulative ablation at the AWS in the ablation zone and the model results in the corresponding elevation bins disagree by 4 % (van As et al. 2012), although the difference at individual stations can be larger (RMS error of 16 % of the cumulative ablation). If the cumulative AWS ablation measurements are assumed to be representative for the runoff from entire catchment, and take into account the uncertainty in catchment size (up to 13 % for extreme melt years such as 2010), a model uncertainty for runoff totals of 6–14 % can be calculated. Thus, a conservative estimate of uncertainty in daily catchment wide meltwater runoff is 15 %. The catchment delineation yields the largest contribution to uncertainty in catchment-wide runoff due to uncertainties in subglacial topography, englacial water pressure and poor performing automated delineation tools in ArcGIS (van As et al. 2012).

3.3.4 Meltwater production and runoff

Surface water on the ice sheet is largely provided by melting; condensation and rain contribute relatively small amounts in the Kangerlussuaq sector of the GrIS. For simplicity, here the term “surface meltwater” is used for all surface water. Meltwater can either run off through the surface drainage network of channels and lakes, or refreeze, the latter of which occurs when there is snow or firn present with sufficient pore space and cold content available, i.e. mostly in the accumulation area.

The surface energy balance model results for both surface meltwater generation and runoff are shown in Figure 3-11. Nearly all melt takes place during the three summer months (Figure 3-11). Interannual variability is large, though, both in length of the melt season, and the melt intensity. A large melt peak in the summer of 2009 was surpassed by longer periods of more intense melting in the following three years. In 2010, the melt season was relatively long, lasting from early May to well into September, and peaking in August. In 2012 the melt season started later, but high surface melting took place in July, leading to large meltwater runoff and the destruction of the bridge in Kangerlussuaq. During these few days nearly the entire ice sheet surface was reported to melt (Nghiem et al. 2012). Figure 3-11 illustrates that most of the meltwater ran off the ice sheet according to the model, thus only a smaller part refroze in snow and firn.

The majority of the meltwater running off the ice sheet is also illustrated in Figure 3-11, in which cumulative meltwater generation and runoff are plotted for the four melt seasons. Melt and runoff initiated one to five weeks earlier in 2010 than in the other three years. After DOY ~ 170 the meltwater generated in 2012 had exceeded the high 2010 values. Towards the end of the melt season more melt occurred in 2010. The difference in total melt between 2010 and 2012 is roughly 15 %. The difference between 2010 and 2012 is smaller in terms of meltwater runoff, since a relatively large share of melt in 2012 occurred in the accumulation area, where the model calculated a larger share to have refrozen in the firn.

This is illustrated in Figure 3-11, which shows the generated meltwater and runoff for the four year period, per 100 m elevation bin. With increasing elevation an increasing amount of meltwater refreezes. Below the long term *equilibrium line altitude* (ELA) (~ 1550 m, van de Wal et al. 2012) little snow accumulates in wintertime and thus there is little (capacity for) refreezing at the start of the melt season. At high elevation all meltwater refreezes according to the model. Most meltwater is generated around 1100 m a.s.l. This is due to the flattening of the ice sheet at higher elevation and thus the increase in size of the elevation bins; local melt is largest at the lowest elevations. The interannual variability in meltwater generation per elevation bin is largest at higher elevation. 2012 experienced a large amount of melt as high up as 2000 m a.s.l. Remarkably, below 1300 m a.s.l. elevation 2010 melt and runoff exceeded that of 2012.

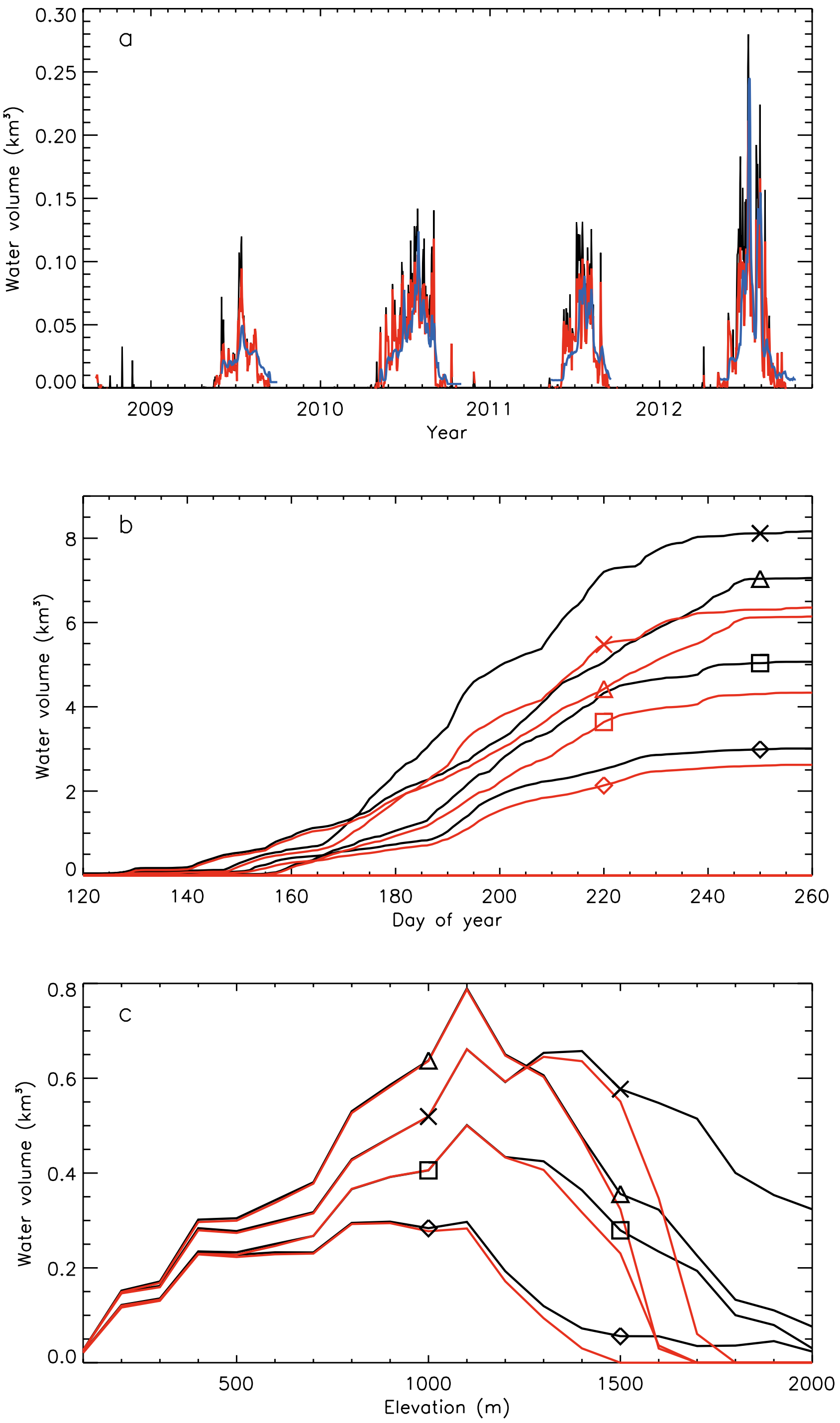

Figure 3-11. *a) Surface meltwater production (black), surface meltwater runoff (red) and proglacial river discharge (blue) versus time, b) Same, but cumulative per year, c) Same, but per 100 m elevation bin per year (diamonds: 2009, triangles: 2010, squares: 2011, crosses: 2012).*

The runoff is compared to the discharge measured at the proglacial Watson river in Kangerlussuaq in Figure 3-11. There is a good quantitative agreement between the calculated and measured values, giving confidence in the model output. The slight overestimation by the model can be due to errors in catchment delineation. The surface runoff is more variable than the river discharge as atmospheric conditions differ from day to day; the internal drainage system of the ice sheet removes variability in discharge because it cannot immediately accommodate the large amounts of meltwater. In the beginning of the melt season, when the drainage channels within and underneath the ice are still being developed by the increasing water pressure, the transit time of water from the ice sheet surface to the melt river is up to a few days. Past the peak of the melt season, when the channels are larger and efficiently drain surface meltwater, the peaks in meltwater runoff at opposite ends of the glacier's drainage system are more closely timed.

3.3.5 Remote sensing and AWS data that contributes to addressing the GAP questions

The results described in this section directly address the first of the GAP questions – *how much meltwater is generated where and when?*. The meltwater runs off over the surface of the ice sheet, where it converges into channels or lakes. These water bodies release the water into moulins or crevasses, transporting it into the en- and subglacial environment. In combination with other SPA findings, it is possible to assess where and when which quantity of meltwater accesses the ice sheet. This allows an estimate of the subglacial water budget, linking SPA and SPB, and providing an estimate of meltwater available to enter into the bedrock, i.e. the domain of SPC.

The recent extreme melt years in Greenland provide an excellent setting for studying the relatively large meltwater fluxes from an ice sheet in retreat. These atmospheric conditions are in part caused by an unusual North Atlantic Oscillation (NAO) (Fettweis et al. 2013) and may not be fully representative of the Greenland climate in coming years. However, these warm years offer a convenient analogue for a warmer future climate (IPCC-WGI 2007). Importantly, catchment-wide runoff will be amplified by a hypsometric effect: as melt reaches higher elevations on the ice sheet where the surface is flatter, larger surface areas are affected. Also, increased melt will darken the ice sheet surface as snow undergoes heat-driven metamorphoses or melts off to reveal darker ice. This in turn will increase absorption of solar radiation and thus melt (the melt-albedo feedback, e.g. Box et al. 2012). Finally, as the firn covering the higher regions of the ice sheet retain and refreeze increasing amounts of meltwater, it will lose pore space and thus retention capacity (Harper et al. 2012). Because of this, the buffering effect of the firn zone weakens, and larger pulses of meltwater are received at the glacier margin. The GrIS hydrology in 2012 showed all these symptoms, leading to the destruction of the bridge in Kangerlussuaq, which was never expected to receive this much meltwater discharge during the construction in the previous century. It proves that meltwater release from the ice sheet can be disproportionally large compared to the amount of atmospheric warming, setting the context for potential future scenarios.

3.4 GPS measurements of ice motion

3.4.1 Introduction and objectives

Observations of surface ice motion provide an indirect method for investigating the role of water at the ice sheet's basal interface. Pressurised subglacial water reduces the effective pressure at the bed causing hydraulic ice-bed separation and enhanced basal motion. These rapid, transient accelerations and vertical displacement events are detectable using geodetic-quality Global GPS receivers. Measurements of ice motion from a network of GPS receivers deployed across RGC can be used to constrain when water accesses the bed and how basal water pressure and ice motion respond to it.

GPS receivers measure the range between their antenna and a number of satellites (>4 required to obtain a 3D position). These ranges are used to calculate the antennas position (X, Y, Z), which are then differentiated and summed in quadrature to calculate horizontal speed. The GPS receiver measures the motion of a pole drilled 2 m into the ice sheet surface. Ice sheet surface velocity (u_s) is the combined effect of internal ice deformation (u_d) and sliding at the ice-bed interface (u_b), see Figure 3-12. Over short time-scales, internal deformation (u_d) is assumed to be constant, and variations in surface velocity u_s are attributed to basal motion (u_b). Basal motion is a function of subglacial water pressure (p_w) in a non-linear relationship that evolves in response to subglacial water inputs and the capacity of the basal drainage system to remove it. GPS measurements at the ice surface quanitfy these processes through vertical change (directly reflecting ice-bed separation) and horizontal acceleration indirectly reflecting the degree of basal decoupling, though these relationships are far from straight forward.

3.4.2 Data collection

Initially four on-ice GPS receivers were deployed across RGC in 2007 (Figure 3-13). Two recievers were added in 2008 and a further five were added in 2009 (Table 3-7). In 2010 the network was increased to 24 receivers, which was then reduced to 12 in September 2011 (Table 3-8 and 3-9, Figure 3-13). From 2013 onwards the network was further reduced to 7 on-ice receivers optimised to coincide with *Geological Survey of Denmark and Greenland* (GEUS) and *Institute for Marine and Atmospheric Research in Utrecht* (IMAU) long term weather station monitoring sites. Power, memory capacity and antenna problems have led to some interruptions in the data acquisition. Throughout, the network has been calibrated against a permanently mounted base-station which was located overlooking the terminus of Russell Glacier in 2008.

Table 3-7. GPS data collected between 2007 and 2009. Off-ice reference stations are highlighted in green. Data for on-ice receivers is highlighted in blue.

Site	**Month of 2009**											
	J	**F**	**M**	**A**	**M**	**J**	**J**	**A**	**S**	**O**	**N**	**D**
base			🟩				🟩	🟩	🟩	🟩		
skb3		🟦	🟦	🟦	🟦	🟦	🟦	🟦				
disc						🟦	🟦	🟦				
gf15							🟦	🟦				
gf21							🟦	🟦				
gf22							🟦	🟦				
isum	🟦											
skb1	🟦	🟦	🟦	🟦	🟦	🟦						
hapy						🟦						
s10a				🟦								
skb4					🟦							
lake						🟦						
Site	**Month of 2008**											
	J	**F**	**M**	**A**	**M**	**J**	**J**	**A**	**S**	**O**	**N**	**D**
base			🟩	🟩	🟩	🟩	🟩	🟩	🟩	🟩		
skb3									🟦	🟦	🟦	
s4aa					🟦	🟦	🟦	🟦				
isum					🟦	🟦	🟦	🟦	🟦	🟦	🟦	🟦
hapy	🟦	🟦	🟦	🟦								
lake				🟦			🟦	🟦	🟦	🟦	🟦	🟦
Site	**Month of 2007**											
	J	**F**	**M**	**A**	**M**	**J**	**J**	**A**	**S**	**O**	**N**	**D**
base												
dope							🟦	🟦				
disc							🟦	🟦				
hapy							🟦					
isum							🟦	🟦	🟦	🟦	🟦	🟦

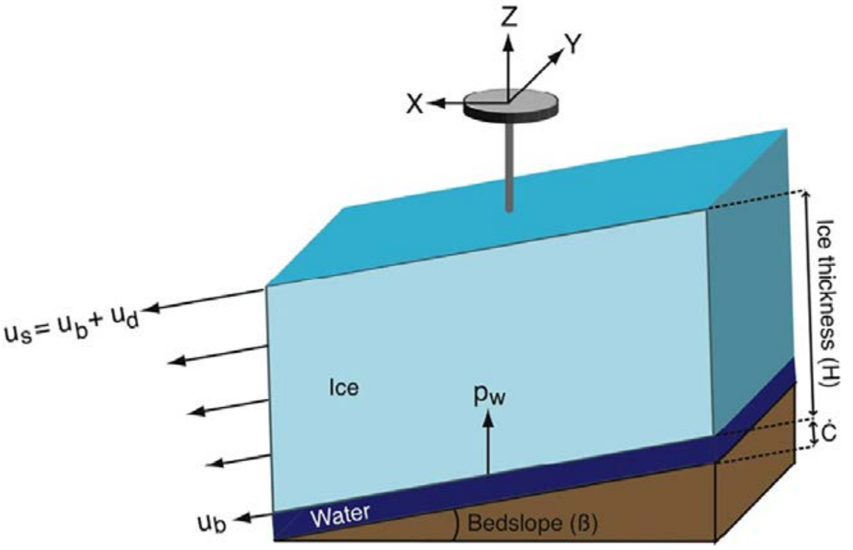

Figure 3-12. *Conceptual diagram of GPS measurements of ice motion. Ċ denotes ice-bed separation due to cavity opening.* u_b, u_d *and* u_s *denote basal motion, internal deformation and surface motion respectively. Subglacial water pressure is denoted* p_w.

Table 3-8. Summary of GPS data collected in 2010.

	Month of 2010											
	J	**F**	**M**	**A**	**M**	**J**	**J**	**A**	**S**	**O**	**N**	**D**
base	🟩	🟩	🟩	🟩	🟩	🟩	🟩	🟩	🟩	🟩	🟩	🟩
skb3		🟦	🟦	🟦	🟦	🟦	🟦	🟦	🟦	🟦	🟦	🟦
disc	🟦	🟦	🟦	🟦	🟦	Removed by third party						
sudd							🟦	🟦	🟦	🟦	🟦	🟦
nord							🟦	🟦	🟦	🟦	🟦	🟦
east							🟦	🟦	🟦	🟦	🟦	🟦
skb1				🟦	🟦	🟦	🟦	🟦	🟦	🟦	🟦	🟦
s4aa					🟦	🟦						
s10a			🟦	🟦	🟦	🟦			🟦		🟦	
skb4					🟦	🟦	🟦	🟦	🟦			
shrr				🟦	🟦	🟦	🟦	🟦	🟦	🟦	🟦	
shrn							🟦					
shrs							🟦	🟦	🟦	🟦	🟦	🟦
shre				🟦	🟦	🟦	🟦	🟦				
shrw				🟦	🟦	🟦	🟦	🟦				
blow						🟦	🟦					
moul			🟦	🟦	🟦	🟦						
zlak						🟦	🟦					

Table 3-9. Summary of GPS data collected in 2011. An X indicates the GPS was installed but not running. A dash indicates the GPS was not installed. Question marks indicate that the GPS is still in operation and therefore the amount of data recorded since the last visit is unknown. The last column indicates the percentage of data recorded between installation and the date of last service or removal, or for GPS installed before 2011 from the first day of 2011. A p indicates that pre-processing is required before the amount of data recorded is known. Data recorded at off-ice reference stations is highlighted in green; data for on-ice receivers is highlighted in blue. Site kely is a reference station maintained by UNAVCO and located in Kellyville, which is ~10 km SE of Kangerlussuaq (see Figure 3-41 for location). Due to an antenna fault the Russell Glacier reference station base had poor tracking on the L2 frequency between DOY 190 2010 and DOY 149 2011. At the end of 2011 eleven on-ice kGPS stations remain in operation and these are highlighted in bold. Positions and elevations are given in WGS-1984.

Site	**Month of 2011**											
	J	**F**	**M**	**A**	**M**	**J**	**J**	**A**	**S**	**O**	**N**	**D**
base	🟩 <---- No L2 data---- >	🟩	🟩	🟩	🟩	🟩	🟩	🟩	🟩	🟩	X	X
s4aa	X	X	🟦	🟦	🟦	🟦	🟦	🟦	🟦	🟦	X	X
skb4	X	X	X	X	X	🟦	🟦	🟦	🟦	X	X	X
isum	X	X	X	X	X	🟦	🟦	🟦	🟦	?	?	?
shrs	X	X	X	X	X	🟦	🟦	X	X	–	–	–
shrr	X	X	X	X	X	🟦	🟦	🟦	🟦	🟦	X	X
moul	X	X	X	X	X	🟦	X	X	X	X	X	X
lgbl	–	–	–	–	🟦	🟦	X	X	X	–	–	–
rf1a	–	–	–	–	🟦	🟦	🟦	–	–	–	–	–
rf2a	–	–	–	–	🟦	🟦	🟦	–	–	–	–	–
rf3a	–	–	–	–	🟦	🟦	🟦	–	–	–	–	–
lgbm	–	–	–	–	🟦	🟦	X	X	X	?	?	?
lgbu	–	–	–	–	🟦	🟦	🟦	X	X	–	–	–
icet	X	X	X	🟦	🟦	🟦	🟦	?	?	?	?	?
sudd	p	p	p	p	p	P	p	p	p	–	–	–
east	p	p	p	🟦	🟦	🟦	🟦	X	🟦	🟦	–	–
nord	p	p	p	🟦	🟦	🟦	🟦	🟦	🟦	–	–	–
skb3	X	🟦	🟦	🟦	🟦	🟦	🟦	🟦	🟦	X	X	X
sgll	X	X	X	X	🟦	🟦	🟦	🟦	🟦	🟦	X	X
skb1	🟦	🟦	🟦	🟦	X	X	X	X	🟦	?	?	?
s10a	X	🟦	X	X	🟦 X	🟦 X	🟦 X	🟦 X	🟦 X	🟦 X	X	X
kely	🟩	🟩	🟩	🟩	🟩	🟩	🟩	🟩	🟩	🟩	🟩	🟩

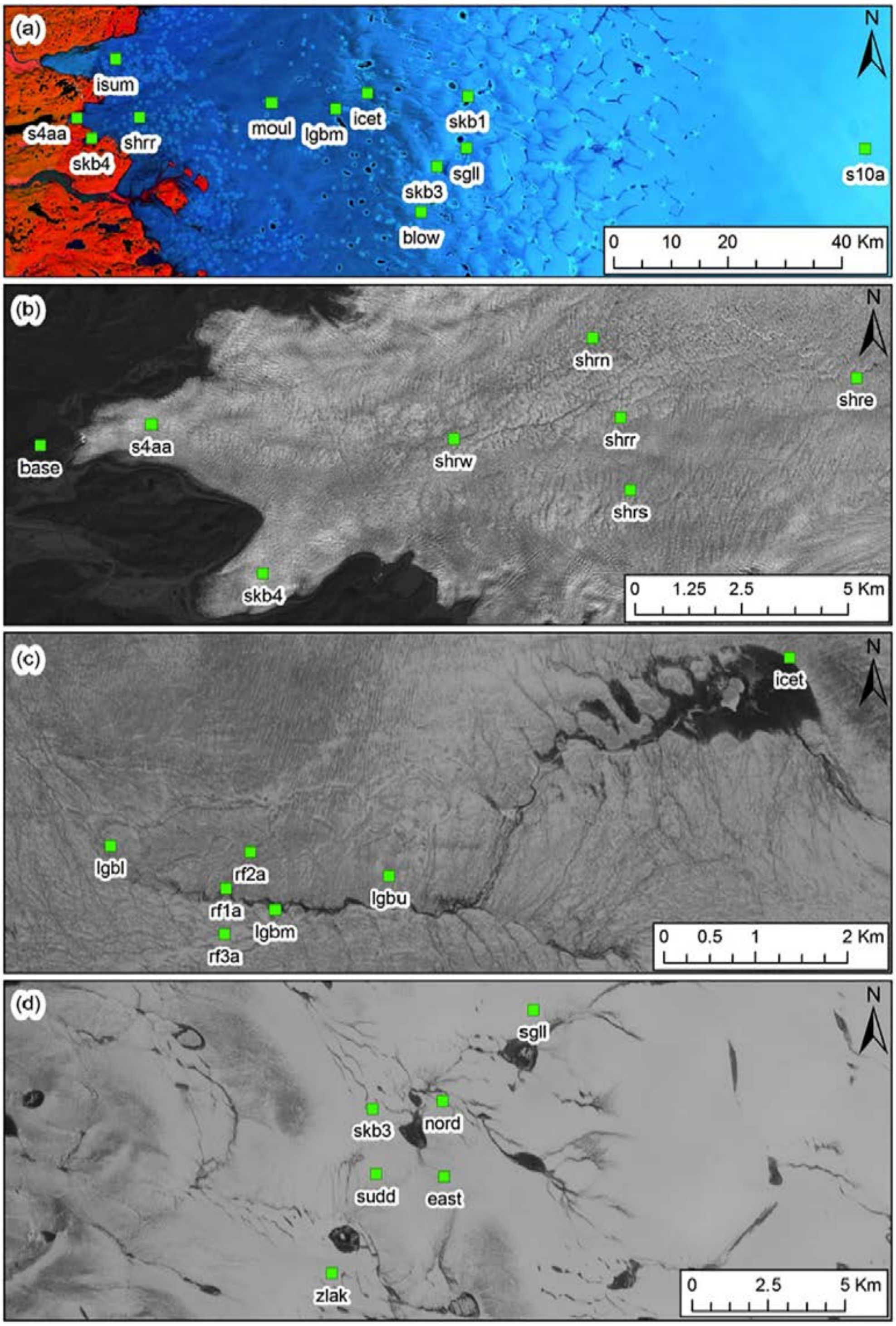

Figure 3-13. *(a) Map of the RGC GPS network with close-up views of: (b) the SHR strain diamond and GPS on Russell and Leverett Glacier; (c) the moulin initiation experiment; and (d) the SKB3 lake strain diamond and sgll and zlak GPS. Background images are a 2001 false colour Landsat (a) and 5 m resolution SPOT imagery acquired on July 7, 2008 (b) and June 27, 2008 (c) and (d). Note that base station kely, located ~ 30 km SE of the base station, is not shown on this map (for location see Figure 3-41).*

3.4.3 GPS processing methods

Data were processed kinematically (King 2004) at a 30-second interval relative to bedrock-mounted reference stations using the carrier phase differential positioning software Track v. 1.24 (Chen 1999) and final precise ephemeris from the International GNSS Service (Dow et al. 2009). Reference stations were located 1 km from the terminus of Russell Glacier (*base*) and at Kellyville (*kely*) giving baseline lengths of 5 to 170 km (Figure 3-13). Assuming steady ice motion, uncertainties in the positions were estimated at < 0.02 m in the horizontal and < 0.05 m in the vertical by examining the detrended position time series for SHR GPS receiver in October 2011. High frequency noise in the position time series was reduced by filtering with a two-pole, low-pass Butterworth filter with a 12-h cut-off period. Daily-averaged horizontal velocity is calculated by differencing the filtered positions at a daily time step.

3.4.4 Results

The seasonal velocity cycle, which is characterised by an initial maxima at melt onset (the so called 'spring event') followed by a gradual decline to an all year minimum in autumn, provides insight into the hydraulic situation at the ice-bed interface. Ice2Sea (http://www.ice2sea.eu/) borehole water pressure is high at the end of the winter (~ 97 % of overburden; Figure 3-14) as the basal drainage system is formed of high-pressure but isolated cavities. The first melt of the season is delivered to this inefficient, distributed basal drainage system, which cannot accommodate it. Hence pressurised water is forced out over a wide area of the bed promoting basal sliding. The ice sheet basal hydrological system then adapts to continued water inputs by developing a more efficient, channelised system, at least within 40 km of the ice margin (Chandler et al. 2013). Efficient flow through channels results in low subglacial water pressures over a small area of the bed and therefore low ice velocities (Figure 3-14). Imprinted on the seasonal cycle of ice velocities is the diurnal melt cycle (Shepherd et al. 2009), rapid lake drainage events (e.g. Das et al. 2008, Doyle et al. 2013), moulin initiation and rainfall events. Each was investigated.

3.4.4.1 Diurnal velocity cycle

At s4aa GPS strong coupling between ice velocity and the diurnal melt cycle is evident in the good correlation with ice-velocity lagging air temperature by ~ 4 h in June 2010 (Figure 3-15 and Figure 3-16). The evolution of this coupling through the melt season was investigated by cross-correlating runoff (melt) with ice velocity over daily intervals for the SHR/KAN_L site (Figure 3-17). At the start of the melt season (early June) the lag between runoff and velocity is > 7 h (Figure 3-18). This lag reduces gradually as the season progresses and the efficiency of the glaciers hydrological system is developed. In early July 2011 the lag had reduced to 4.1 h and by early August had reduced further to 3.8 h. Brief periods of reduced melt are followed by an increased lag time on the following day, indicating rapid closure of the subglacial hydrological system.

3.4.4.2 Lake drainage events

Lake drainage events deliver large (10^7 m^3) volumes of surface water to the ice-bed interface over short time-scales (~ 2 h). They cause significant ice sheet-bed hydraulic jacking and ice tectonic deformation, opening up surface-to-bed hydraulic pathways via hydrofracturing, which deliver water to the subglacial environment for the remainder of the melt season (Das et al. 2008). In 2010, the opening and closure of a ~ 3-km-long hydraulic fracture that drained a 7.4×10^7 m^3 SGL in ~ 2 h was captured, see Figure 3-19 and Figure 3-20 (Doyle et al. 2013). Decimetre-scale surface uplift indicates subglacial water pressures above the ice overburden pressure and transient water storage at the bed (Figure 3-19). The lake opened up several moulins, the largest of which was ~ 10 m in diameter, some of which remained open until autumn.

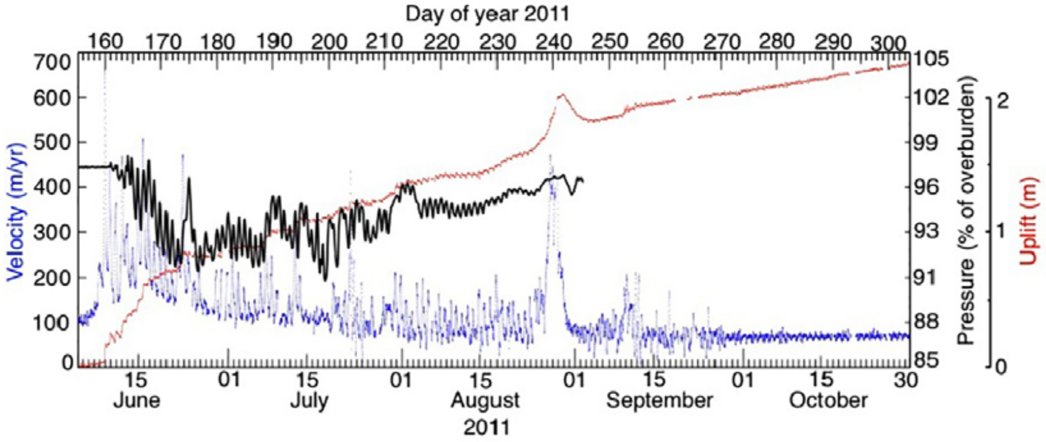

Figure 3-14. *Ice velocity, relative uplift and borehole water pressure expressed as a percentage of overburden at SHRR in 2011.*

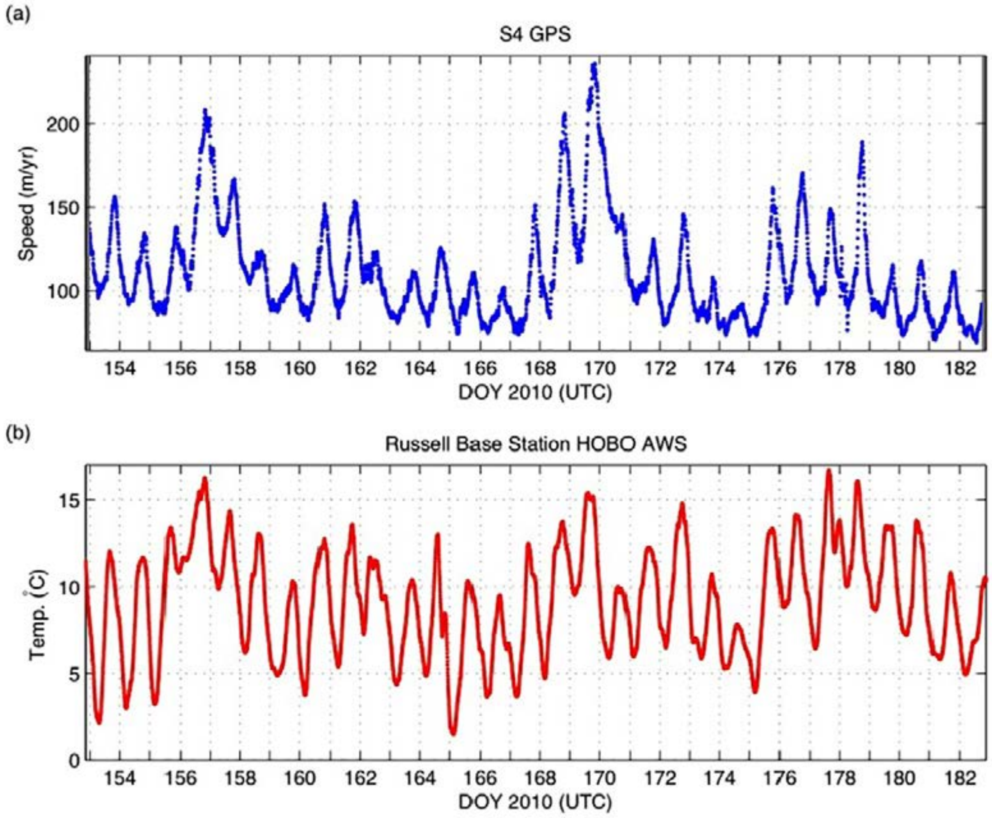

Figure 3-15. *Time series of velocity and air temperature at S4 GPS in June 2010.*

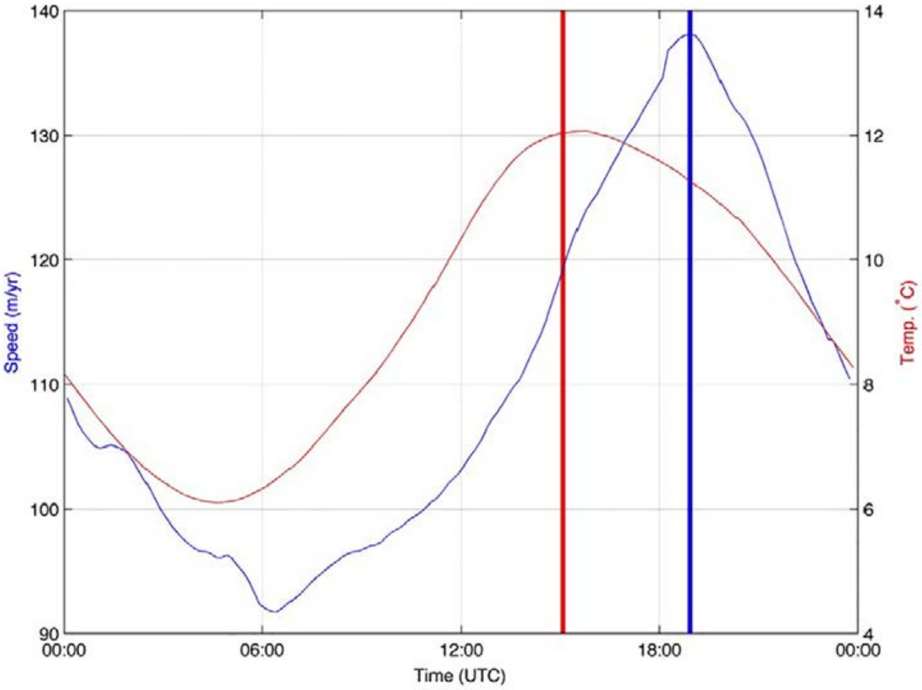

Figure 3-16. The average daily cycle of air temperature and ice velocity at S4 over the same period as in June 2010. Peak ice velocity lags peak air temperature by ~ 4 h.

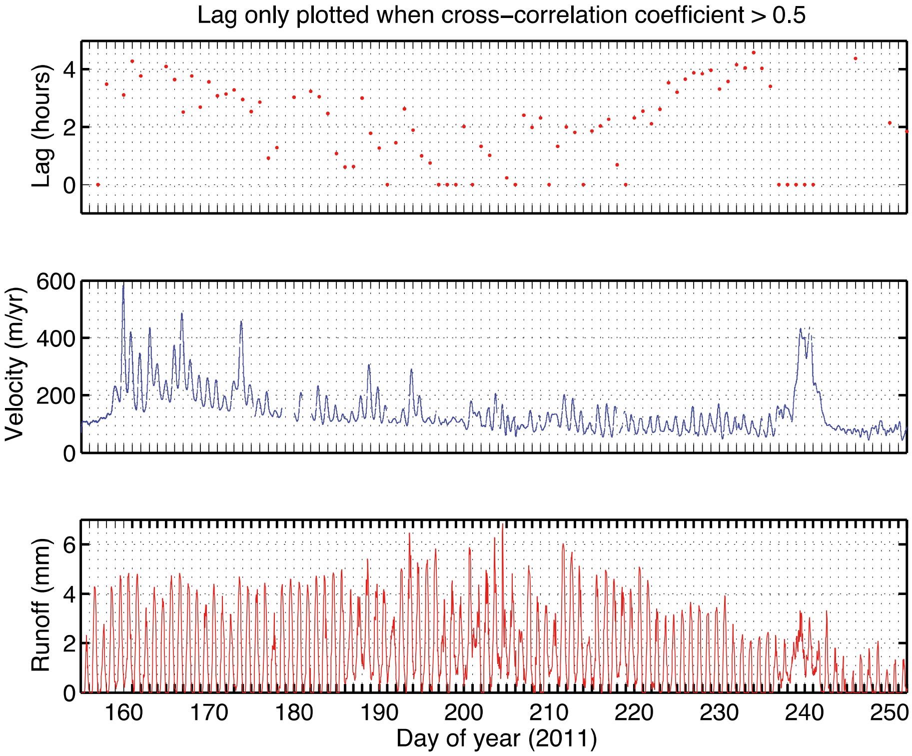

Figure 3-17. The evolution of the time lag between runoff and ice velocity at SHR estimated for three time periods in 2011 using cross-correlation.

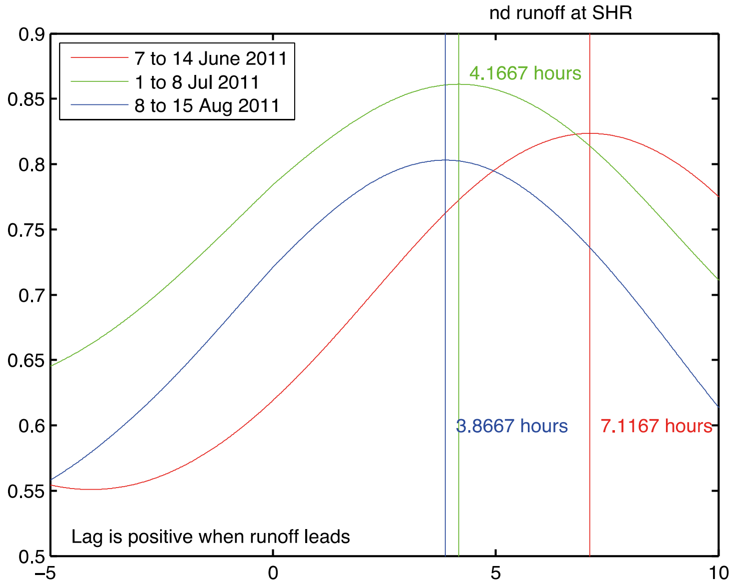

***Figure 3-18.** The time lag between runoff and ice velocity at SHR reduces from 7.1 h in early-June to 3.8 h in August.*

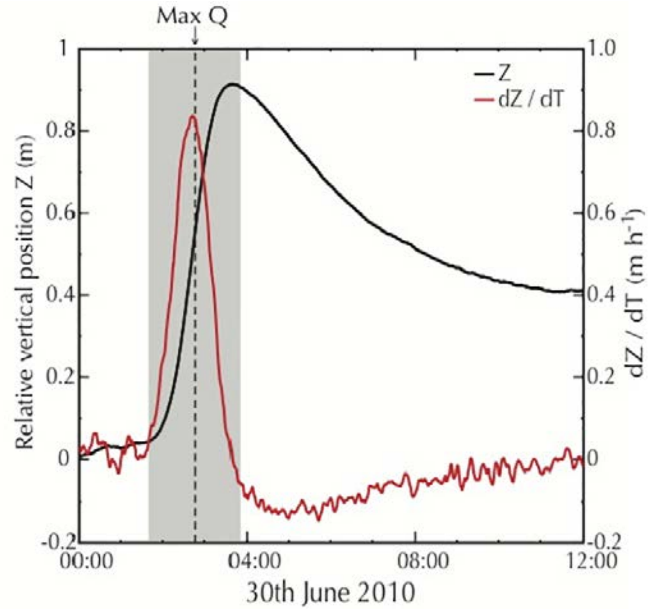

***Figure 3-19.** GPS uplift (Z) and uplift rate (dZ/dt) during the rapid in situ drainage of a SGL. The time of rapid drainage is shaded grey and peak discharge (Q = 3300 m^3 /s) is marked with a vertical dashed line.*

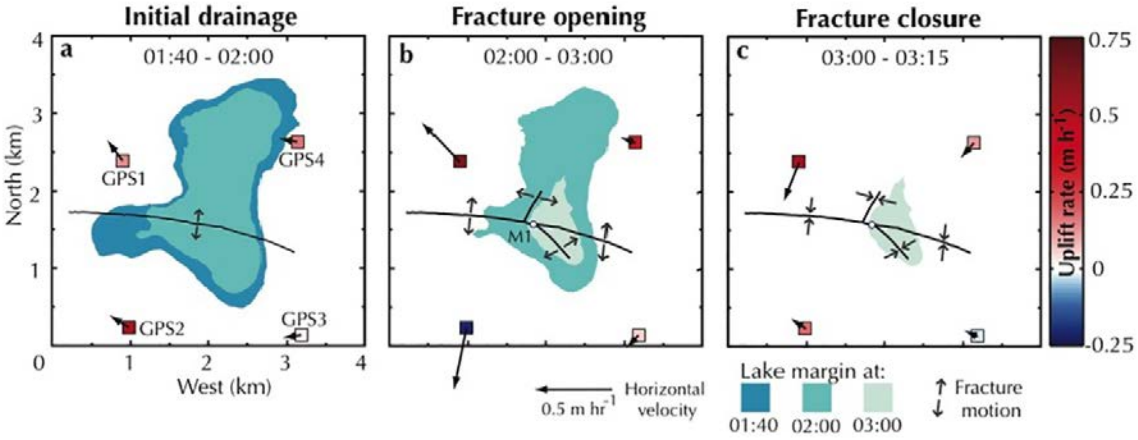

Figure 3-20. *GPS receivers recorded the opening and closure of a hydraulic fracture during the rapid drainage of a SGL. Black arrows represent horizontal velocity vectors. The red arrow represents the mean ice flow direction and is not scaled by magnitude. The colour of each GPS symbol represents the mean uplift rate during each stage. The lake margin at each time step is shown.*

3.4.4.3 Rainfall events

A prominent acceleration occurred in late August 2011, driven by melt and rainfall resulting from cyclonic weather conditions (Figure 3-21). The magnitude and spatial scale of the late August acceleration is unprecedented: the acceleration occurred simultaneously at all GPS sites and at one site, *shrr*, daily averaged velocity exceeded the spring event maximum. Although a fifth of the annual total precipitation fell as rain during the event, the runoff was predominantly sourced from widespread melt brought about by the advection of warm moist air by a cyclonic weather system. Such events will become more common in the future due to a warmer regional climate and a northward shift in North Atlantic storm tracks (Fettweis et al. 2011, Franco et al. 2013, Schuenemann and Cassano 2010).

3.4.4.4 Moulin initiation

In 2011, a combined GPS/passive seismic experiment was performed to investigate the dynamic response of the ice sheet to the re-initiation of a large moulin. Initial results indicate decimetre scale ice sheet-bed hydraulic jacking and substantial acceleration coincident with high rates of seismicity when the moulin reactivated (Figure 3-22).

3.4.5 GPS data that contributes to addressing the GAP questions

The following section describes where data collected from GPS contribute information towards the GAP project questions. The GPS data provides information relating to the following GAP questions:

Where is water generated within the ice sheet system?

Data collected by SPA confirms that water is predominantly generated at the surface of the GrIS from the melt of snow and ice, although rainfall was also found to make a small contribution. Water may be stored in SGLs, or within the snowpack, before it forms runoff and is eventually delivered to the ice-bed interface via moulins or crevasses.

What is the hydraulic pressure situation under an ice sheet?

GPS observations reveal that the hydraulic pressure situation under the ice sheet is variable in space and time. High-pressure events (inferred from surface accelerations) occur at the seasonal onset of melt (the so called ‘spring event’), during lake drainage and rainfall events. The highest magnitude velocity events occur when the difference between the water inputs and the capacity of the ice sheets hydrological system is large, that is predominately in the early part of the melting season.

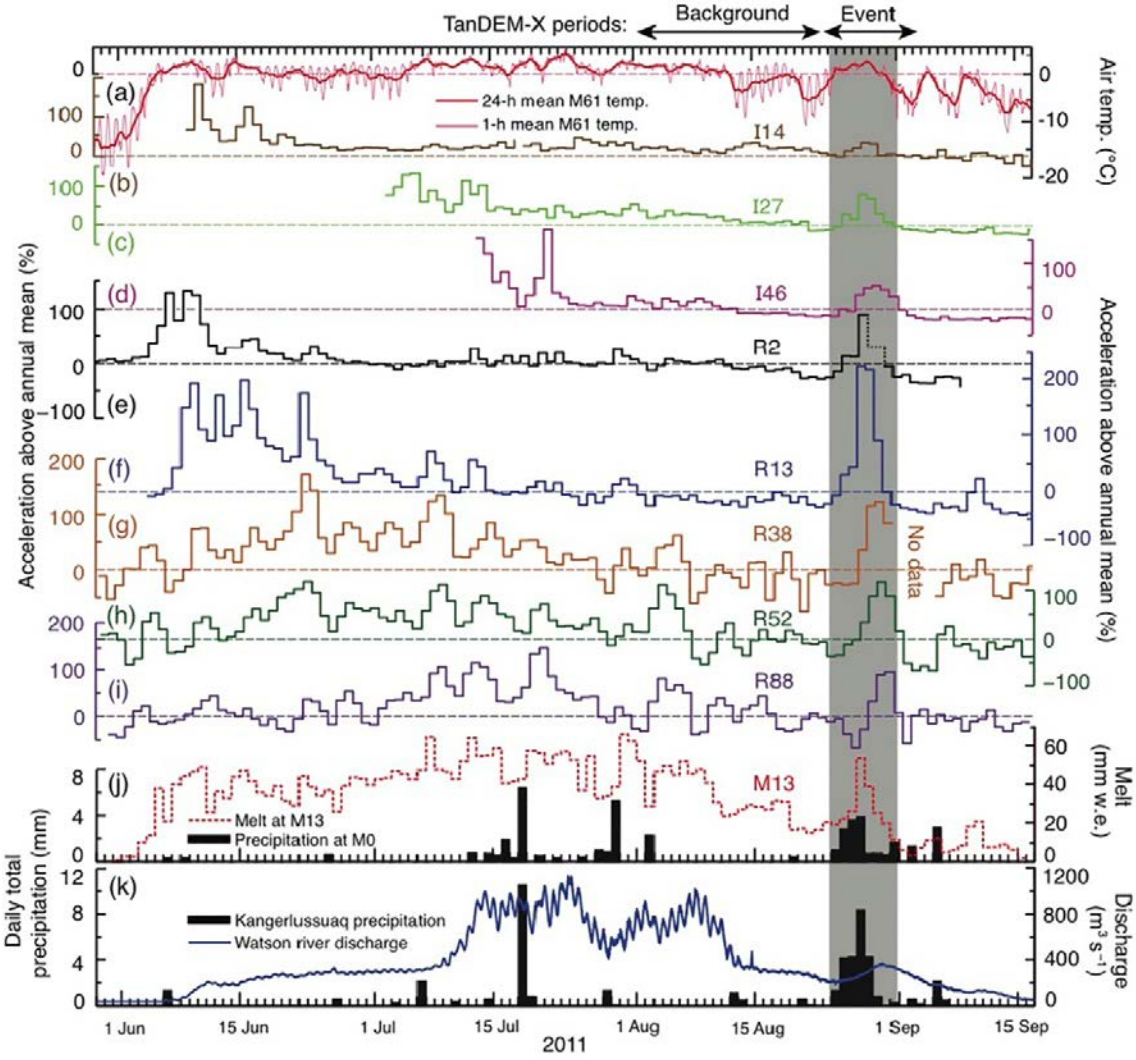

Figure 3-21. *Records of ice motion, meteorology and Watson river discharge revealing a prominent and widespread acceleration in late August 2011, which was driven by warm, wet cyclonic weather. (a) air temperature at M61 (KAN_M) with a 1- and 24-hour average applied, (b–i) daily averaged ice-surface velocity at eight GPS sites expressed as acceleration above the annual mean, (j) daily total melt at M13 (KAN_U) and corrected daily total precipitation at M0, and (k) corrected daily total precipitation in Kangerlussuaq and proglacial Watson River discharge.*

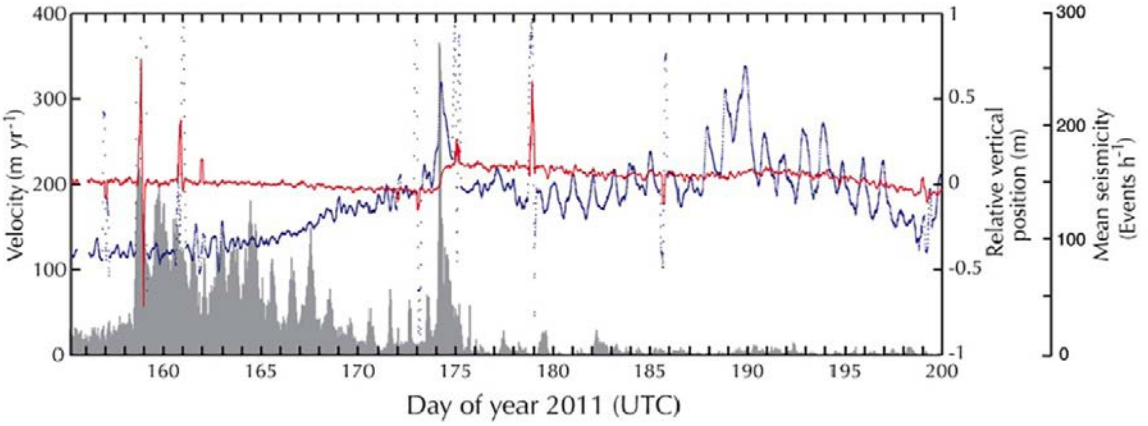

Figure 3-22. *Velocity, relative uplift and mean seismicity showing the acceleration and decimetre-scale vertical uplift during the re-initiation of a large moulin on ~ DOY 174.*

Continued water flow (as in summer) was observed to develop efficient (channelised) subglacial drainage at least within 40 km from the margin (Chandler et al. 2013), resulting in low velocities in autumn (Bartholomew et al. 2011, Fitzpatrick et al. 2013, Sundal et al. 2011). However, even during mid-summer there is strong coupling between ice velocities (and therefore subglacial water pressure) with the diurnal melt cycle, indicating partial closure of the basal drainage system during low water inputs at night.The decline of the lag time between peak melt and peak velocity through the melt season indicates the progressive development of efficient subglacial drainage.

Lake drainage events rapidly deliver large volumes of water to the ice-bed interface and dm-scale uplift indicates high subglacial water pressures. Lake drainage events open up hydraulic pathways through km-thick ice, which continue to deliver water to the subglacial environment for the remainder of the melt season. Rainfall events, which have to date not been considered for the GrIS, produce sufficient melt and rainfall to overwhelm the ice sheets basal hydrological system, driving pronounced, sustained and widespread flow accelerations up to 88 km inland.

During the rapid drainage of SGLs, rainfall-driven accelerations and spring events subglacial water pressure exceeds the ice overburden pressure and the ice sheet is hydraulically decoupled from its bed – promoting rapid basal sliding. The subsequent release of highly turbid, sediment-rich water from the ice sheet into proglacial rivers indicates that the water accessed a large area of the bed.

3.5 Radar

3.5.1 Radar data

The objective of the radar work within the GAP was to establish good spatial coverage of subglacial topography and basal conditions of the ice sheet in the study area that will be used for modelling efforts and other analyses within the project.

The radar data can be used to derive potential flow paths and hydraulic head distribution under the ice, provided that the subglacial topography and ice surface could be determined with accuracy. The returned power from the bed reflections in the radar data can also give an indication of the distribution of meltwater and the basal thermal boundaries.

For this purpose, two low-frequency impulse radar systems were built, which have been operating on Greenland as part of GAP during two field seasons (2010–2011). The collected data was combined with previously collected radar data from other sources to create the best available topographic information and derive basal conditions.

3.5.1.1 Radar acquisition

During April to May 2010 and 2011, ~ 1500 km of common-offset radar profiles were collected with two ground-based low-frequency impulse radar systems. Each system consists of resistively-loaded dipole antennas with a center frequency of 2.5 MHz, a transmitter with average output power of 35 W and a pulse repetition frequency of 5 kHz, and a 16-bit receiver with 200 MHz bandwidth and a capacity of collecting 5000 traces per second. The trace acquisition was triggered by the direct wave between transmitter and receiver. The radar systems were towed by snowmobiles at a speed of ~ 10 km/h, giving a trace interval distance of ~ 6 m with a stacking of 3000 traces to reduce incoherent noise. The profiles where positioned using a carrier-phase two-frequency GPS receiver.

The profiles were arranged in a pattern of 45 km long profiles perpendicular to the general glacier flow direction and each profile was separated by 2 km (Figure 3-23). The profile grid was placed to optimise the coverage in the GAP investigation area and taking into account other existing datasets (see Section 3.5.1.3).

3.5.1.2 Processing

The GPS data were processed using a Precise Point Positioning service maintained by the Canadian Natural Resource Agency (Natural Resources Canada 2013), giving an estimated horizontal accuracy of ± 0.02 m and an error of surface elevation of ± 0.03 m. The GPS receiver was located at the radar receiver and the position was adjusted to the common-depth point of the radar by linear interpolation along the travelled trajectory. Due to the interpolation to correct for the displacement between the common-mid point and the GPS receiver, the accuracy is reduced to ± 2 m.

The collected radar data have been processed following the processing flow in Figure 3-24 using customised tools written in Matlab/C++. The radar traces were geolocated using the collected GPS data and high noise and static traces were removed. All data was zero-time adjusted to account for variable trigger-time due to different antenna separation during different surveys. A 5th order Butterworth band-pass filter with cut-off frequencies of 0.75 and 10 MHz was used to remove undesired frequency content in the data. Normal move-out correction (Yilmaz 2001) was applied with a constant wave speed of 168 m/µs to correct for antenna separation. Rubber-band correction (Jol 2009) was used to interpolate the data to uniform trace spacing as this is required for migration of the data. 2D frequency-wavenumber migration (Stolt 1978) was used to collapse hyperbolic reflectors back to their original points in the direction of the profile using a constant velocity of 168 m/µs. The bed returns were picked semi-automatically using a cross-correlation picker (Irving et al. 2007). Ice thickness was calculated from the picked travel-times of the bed using a constant radar signal speed of 168 m/µs. Using a constant wave speed for depth conversion and processing is a commonly used assumption in glaciology due to the fact that ice is a homogenous material (Lythe et al. 2001, Bamber et al. 2013a). However, the wave speed can vary spatially to some degree depending on variations of density and impurities in the ice. A typical variation of 2 % of ice density and impurities in glaciers (Navarro and Eisen 2009) gives an uncertainty of ± 8.4 m in the depth calculations. In combination with the inherited accuracy of the radar signal (i.e. bandwidth of signal and sampling interval) an estimated accuracy of ± 18.8 m for the depth values is achievable.

3.5.1.3 Integration of radar data with other available datasets

Besides the collected radar data (GAP ground based radar; Lindbäck et al. 2014), three other datasets of subglacial topography is available within the GAP study area, including data collected by *Danish Technical University* (DTU) and GEUS (DTU dataset (Christensen et al. 2000)) and NASA through the project IceBridge (IceBridge dataset (Leuschen and Allen 2010). All available datasets are shown in Figure 3-25. The DTU dataset consists of ~ 3000 km of data collected in 2005 from a Twin Otter aircraft. Data acquisition took place along flight tracks separated by ~ 3 km, with a trace spacing of ~ 25 m. The system used is a 60 MHz impulse system (Christensen et al. 2000). The bed return in the data was not detectable in some parts of the tracks, primarily close to the ice margin. The IceBridge dataset covers a large portion of Greenland and approximately 5000 km in the vicinity of the GAP study area. The dataset was collected in 2010–2012 from aircraft with a multichannel frequency modulated system with a center frequency of 194 MHz (Leuschen and Allen 2010). The profiles are separated by a minimum of 500 m and up to several km (see Figure 3-25), and with a trace spacing along flight lines of ~ 15 m. Similar to the DTU data, the IceBridge dataset does not include good coverage close to the ice margin.

All three external datasets (DTU, IceBridge, CReSIS) were provided with already picked bed returns as ice thickness and surface elevation and their geographical coordinates. The ice thickness values were adjusted because slightly different wave speed in the ice was used in the transformation between radar signal travel time and ice thickness. All datasets, including the GAP dataset, were combined after a quality check of the four individual datasets (including removal of duplicate points and points with obviously incorrect ice thickness values) and finally transformed into a common coordinate system. The Polar Stereographic projection was used (standard latitude of 71°N, standard longitude of 39°W with no translation) with the WGS84 datum as elevation reference. UTM projection recommended by the GAP project guidelines is impractical as the GAP area is divided between two UTM zones which causes uneven distortion of the spatial coordinates over the area.

Crossover analysis

Crossover analysis was made of the ice thicknesses to estimate digitization and positioning errors within each dataset and to test the consistency between datasets. Two measurements from different profiles were rarely available for precisely the same location and thus the crossing point values were determined by linear interpolation along each profile.

The GAP dataset had an average crossover misfit of 16.0 m and a standard deviation of 20.3 m (based on 159 crossing points). Approximately 80 % of the total crossover locations in the ground based data had a difference of less than 19 m, the theoretical minimal resolution of the radar system. This indicates that the majority of the misfit is within navigational, instrumental and depth conversion uncertainties. The DTU dataset had an average crossover misfit of 12.0 m, with a standard deviation of 13.0 m (based on 97 crossing points) and IceBrigde dataset 19.6 m with a standard deviation of 27.5 m (based on 745 crossing points). The crossover analysis within the same dataset does not capture systematic errors and therefore a comparison between the datasets is essential. When running a crossover analysis on all the datasets there is an average misfit of 19.7 m with a standard deviation of 24.6 m, based on 1900 crossing points.

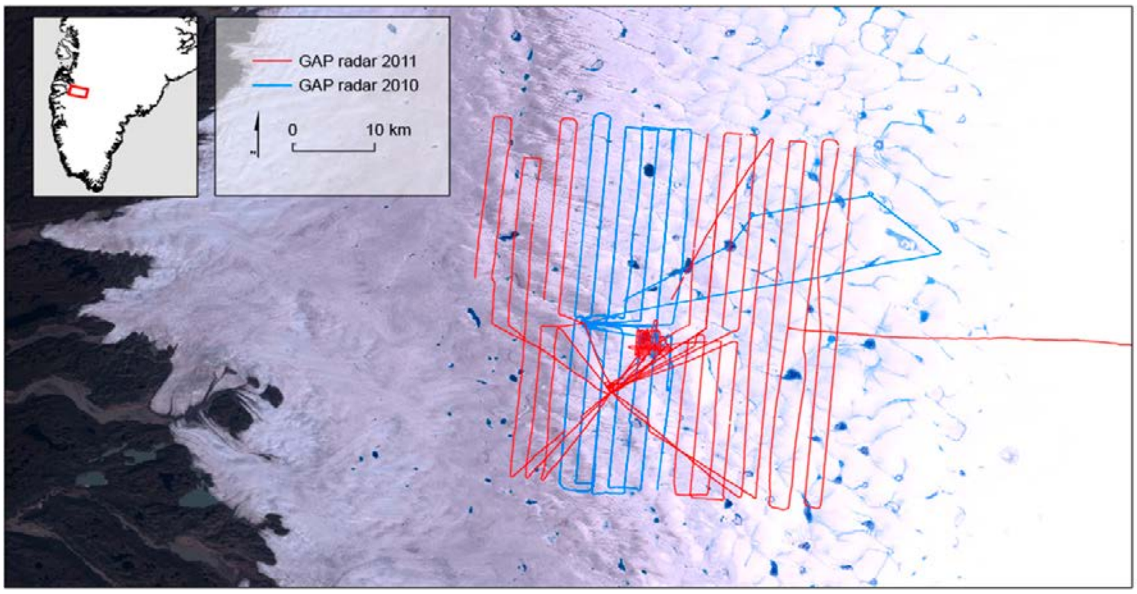

Figure 3-23. *GAP-SPA radar data during spring field campaigns 2010 and 2011.*

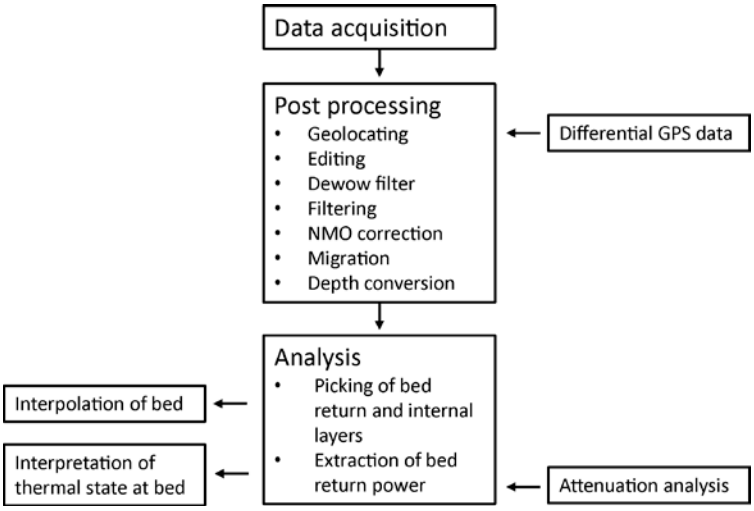

Figure 3-24. *Processing and analysis scheme for radar data.*

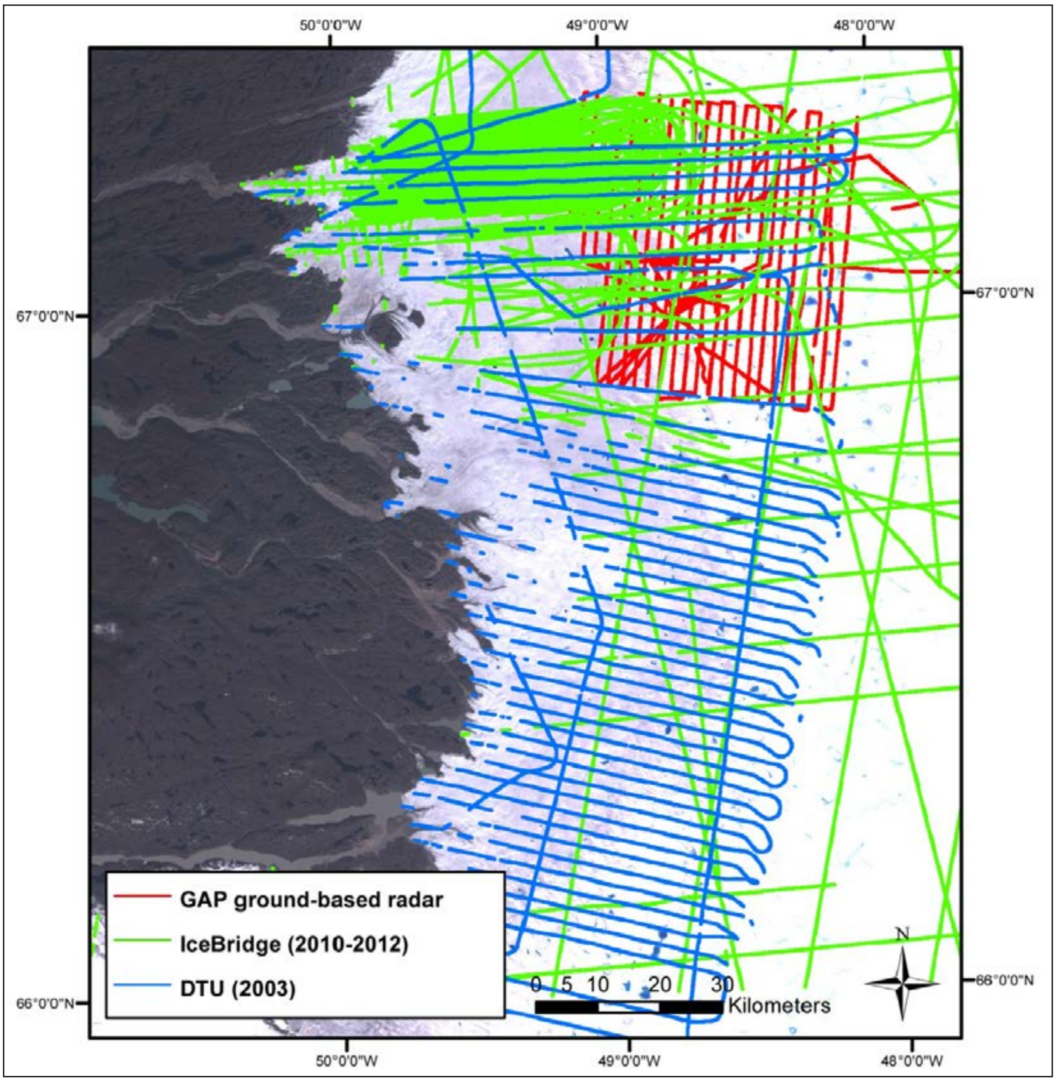

Figure 3-25. *Available datasets for the GAP area.*

Interpolation of ice thickness and bed elevation

The different datasets were combined to produce ice thickness and bed elevation grids. The datasets have high spatial density along the profiles, with a data point spacing of 10 to 25 m, compared to 500 to 2500 m spacing between individual profiles. This clustering along lines is not optimal for gridding algorithms. The GAP dataset is particularly dense (~ 3 m trace separation) and was re-sampled to a data point spacing of 20 m, corresponding to the spacing of the airborne datasets. Thereafter, the data was sub-gridded into 100 m bins along the profiles to reduce the data density further. Before the data was interpolated a zero ice thickness boundary-condition along the edge of the ice sheet was added, which was derived from SPOT-5 satellite image acquired in August 2008.

The ice thickness was interpolated at 250 m resolution in the northern section of the study area, with high spatial density of profiles, and 500 m in the southern part where spacing between profiles was larger. The interpolation was done using universal kriging (e.g. Isaaks and Srivastava 1989), with a bilinear drift applied to remove large-scale trends. The interpolation model was based on an anisotropic spherical variogram (Figure 3-26) representing the spatial variability of the dataset (Figure 3-26). A nugget effect of 20 m was applied, causing a smoothing effect, to account for the accuracy of the data points (see crossover analysis).

The bed elevation was calculated by subtracting the ice thickness from the surface elevation in every grid point. For surface elevation the *Greenland Mapping Project* (GIMP) surface elevation model was used (Howat et al. 2012). The GIMP surface elevation model is constructed from a combination of ASTER and SPOT-5 DEMs for the peripheral areas of the ice sheet, with a resolution of 30 m.

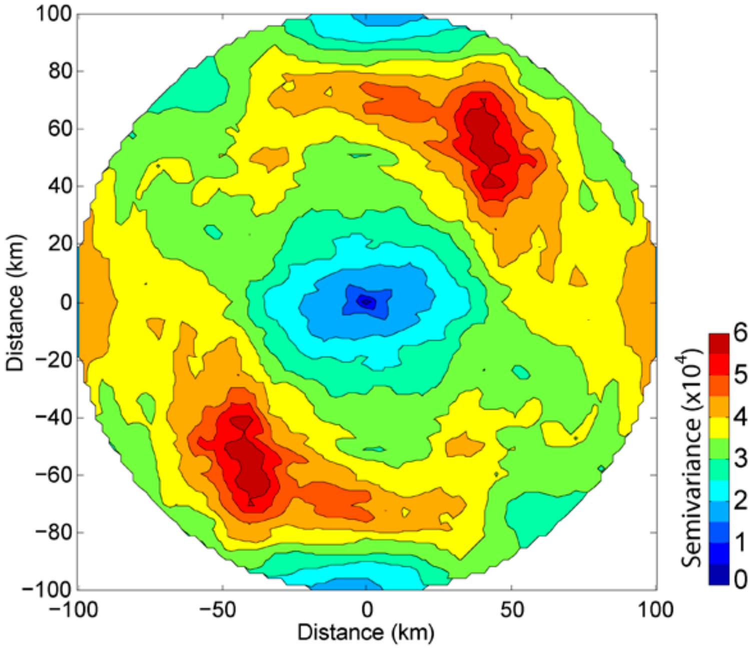

Figure 3-26. *2D variogram map showing the spatial correlation of ice thickness over distance.*

3.5.1.4 Extraction of bed reflectivity

Relative reflectivity of the bed was estimated using the method of Gades et al. (2000) and Jacobel et al. (2009). Relative intensity of the bed echo has been used as a proxy of bed conditions where a strong bed return is interpreted to be a result of a wet bed (Bentley et al. 1998, Peters et al. 2005, Jacobel et al. 2009). The recorded basal echo intensities depend also on losses within the ice and the spherical spreading of the signal, which must be corrected. The geometrical spreading is affected by antenna radiation pattern that may vary along the profiles, but a spatially constant spherical-spreading relationship was assumed for this analysis. The signal attenuation rate can be used to compensate for signal losses within the ice. The spatial variations of returned bed power as a function of signal path-length in the ice (i.e. ~ double the ice depth) were used to estimate the attenuation rate following the method of Gades et al. (2000), Winebrenner et al. (2003), Jacobel et al. (2009) and Matsuoka et al. (2010). After correcting for geometrical spreading and englacial attenuation using the estimated attenuation rate, the returned bed power mainly depends on the dielectric contrast at the bed and thus can be a proxy for changes in basal conditions. Bed reflectivity was derived only along the ground-based profiles because of uncertainty in flight elevation and antenna gain, as well as uncertainties in the calibration of the digitization of the airborne data.

The attenuation rate can also be modeled if temperature and conductive impurities in the ice are known (Macgregor et al. 2007). The contribution from conductive impurities are of secondary order due to often low concentrations in polar ice and can be ignored (Matsuoka 2011), thus the attenuation can be estimated based only on a temperature profile. As part of the GAP, SPB collected several temperature profiles through the ice (Section 4.6), and these measurements were used to verify the radar-derived attenuation rates.

3.5.1.5 Hydraulic potential

As a proxy for routing of subglacial water the hydraulic potential is calculated, which is the sum of the elevation potential and pressure potential (Shreve 1972) as:

$$\Phi = \rho_w g z_{bed} + k\rho_i g h_{ice},$$

Where ρ_w and ρ_i is density of water and ice, z_{bed} is elevation of the subglacial topography, h_{ice} is ice thickness and g is the gravity acceleration of Earth. The factor $k = 0$ corresponds to atmospheric pressure in subglacial channels and $k = 1$ corresponds to subglacial water pressures being equal to the overburden ice pressure. A sensitivity analysis was done using different values for the subglacial water pressure as a fraction of the overburden pressure in the calculations.

The GIMP surface elevation (Howat et al. 2012) and the interpolated bed elevation grid (see Interpolation of ice thickness and bed elevation) was used to calculate the hydraulic potential using ArcGIS 10.1 (ESRI 2013). Based on the resulting hydraulic potential grid, the major subglacial drainage basins were calculated using the built in tool in ArcGIS. The major flow paths were also derived, based on flow accumulation calculations in ArcGIS. Spectral analysis of bed roughness was also carried out (see Section 3.5.1.6).

3.5.1.6 Spectral analysis of bed roughness

The spectral analysis of bed roughness follows the method described by Taylor et al. (2004). To do spectral analysis the data had to be pre-processed in various steps. The data is divided into straight lines (i.e. turns along the profiles were removed). A low-pass filter is applied to smooth the GAP-data, since the picking of the bed was done in high detail compared to the airborne datasets. All datasets are spatially re-sampled to a common trace interval of 30 m using a sinc interpolation (Schanze 1995, Lyons 2004) to avoid introducing any unwanted frequency in the data. The spectral analysis was done using a Fast Fourier Transform (FFT) over a moving window of 2^n blocks. The minimum window used was set to n=5, which which yields segments that are 32 data-points-long, or 960 m, Before the FFT, long wavelength topographic variations were removed from the raw data by de-trending the data using a least-square linear regression. The spectral power spectrum for each window was calculated as:

$$S = \frac{1}{l}\left|FFT\left(Z(x)\right)\right|^2,$$

where $Z(x)$ is the bed elevation variations of a window with length l along the profiles. The roughness index, ξ, is obtained by integrating the spectral power density S in a specific wavelength intervals,:

$$\xi = \int_{k_1}^{k_2} S dk,$$

where k_1, k_2 are the limits of each interval given in Hz. When k_1 is zero and k_2 is infinity, the total roughness value for the window is obtained. Integration is carried out using the trapezoidal rule between all adjacent power density values. The roughness calculations were done along profiles, since the interpolation of a bed map would add values where no data have been taken. This makes an assessment of the roughness, i.e. wavelength-related undulation of the bed from a gridded map, problematic (Siegert et al. 2005). However, to visualise the data, the calculated roughness values were interpolated into a grid using inverse distance weighting, where the inverse-weighting was limited to a searching radius of 20 km, a method applied by Rippin et al. (2011, Rippin 2013). Roughness in the proglacial area was calculated using elevation from the GIMP DEM for a set of artificial profiles having the same orientation and spacing as the radar profiles over the proglacial area. Points falling on lakes or fjords were removed along the profiles to avoid a bias towards smooth surface.

3.5.2 Results

3.5.2.1 Ice thickness and bottom topography

The ice thickness and bed topography is shown in Figure 3-27. Ice thickness generally increases towards the ice divide, as expected, and the maximum ice depth is 1460 m in the gridded data. The mean ice thickness in the area is 830 m. The bed topography shows a highly variable subglacial topography that resembles the landscape in front of the ice sheet. The geological deformation zone west of the ice (with the continuation of the Kangerlussuaq fjord) continues for several tens of kilometres under the ice. Major valleys are going in NE-SW or SE-NW diagonal directions likely following the dominant geological weakness zones. The deepest trough lies under the Isunnguata Sermia Glacier with a minimum gridded elevation of −510 m (corresponds to 544 m below sea level) and a difference of ~ 1000 m between the valley floor and the elevated areas on each side. The highest subglacial peak in the area reaches 1060 m above the ellipsoid (1026 m a.s.l.) and is located in a generally higher area in the south. The southern part of the dataset shows a higher mean elevation, probably due to more resistant bedrock. The relief of the bed topography decreases towards the ice divide, but is generally variable throughout the whole dataset. This smoothing of the landscape towards the interior of the ice sheet is consistent with previous studies (Layberry and Bamber 2001).

3.5.2.2 Basal reflectivity

The attenuation rate is estimated from a plot of returned bed power as a function of depth to 23.3 dB/km (Figure 3-28). The modeled attenuation based on temperature profiles from ice boreholes in the area (see Section 4.6) gives an attenuation of 25 dB/km, which is very similar to the attenuation rate obtained from the radar data. Basal reflectivity is shown in Figure 3-29. The reflectivity shows high frequency variability along the profiles, but also a general reduction of the reflectivity towards the ice divide. The general pattern follows the basal roughness (see Section 3.5.2.4). The difference in reflectivity between the high reflectivity zone in west and the low reflectivity zone in east is comparable to the theoretical Fresnel reflectivity difference of ~ 15 dB between water and dry bedrock interface. Figure 3-29 shows the variability of the reflectivity on a local spatial scale by normalising with the mean reflectivity. The range in variability within individual profiles is less than the theoretical reflectivity difference between wet and dry (frozen) bedrock.

3.5.2.3 Hydrological potential

Hydraulic potential shows a decreasing trend towards the front as a consequence of the thinner ice at the margin (Figure 3-30). Second order variations show close similarities with the bedrock topography due to the smooth ice surface. Different fractions of overburden pressure (*k* value) for the hydraulic potential calculations give similar results, with decreasing hydraulic potential towards the front. However, the delineated subglacial drainage basins varied substantially at different *k*-values with almost doubling of drainage basin area when *k* changes from 0.9 to 1.1. The major subglacial routing pathways follow the main subglacial valleys. The major flow pathways end where major streams emerge at the front giving confidence in the calculated flow paths. There are several closed sinks in the hydraulic potential where subglacial ponding may occur. Subglacial ponding can be important features of ice sheets as they affect the hydrological regime by acting as storage of subglacial water and smooth subglacial water discharge over time.

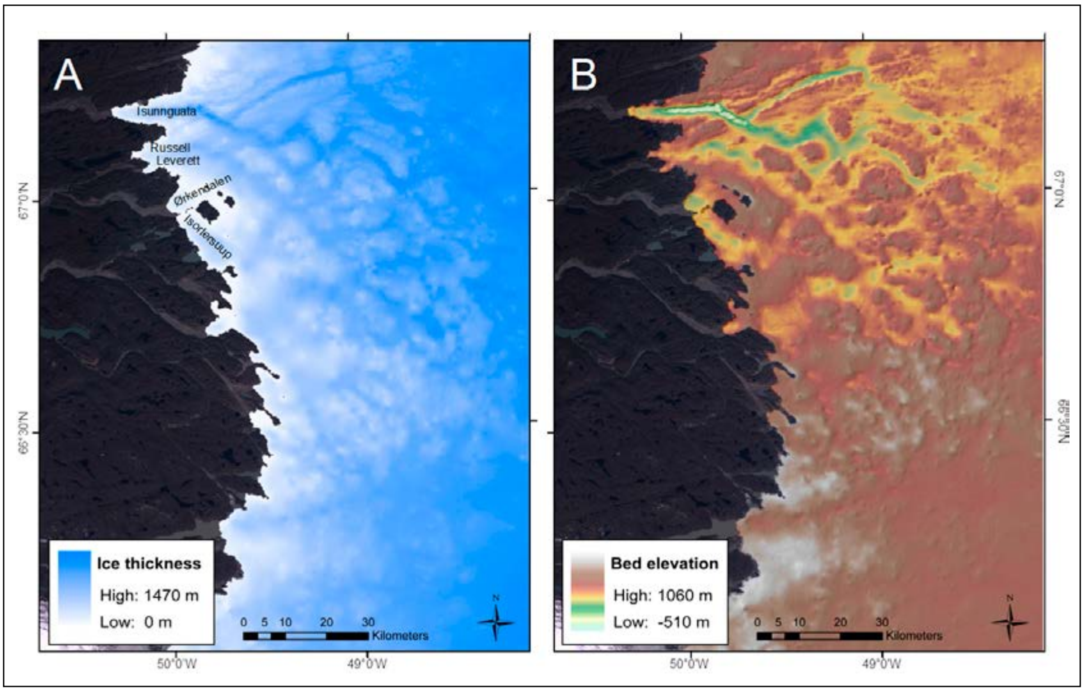

Figure 3-27. *A) Ice thickness, and B) basal topography over part of the GAP area (in m above the WGS-84 ellipsoid) (Figure 3-25). The ice thickness and basal topography maps extend farther south than the GAP study area since the DTU airborne radar was available for this part of the ice sheet.*

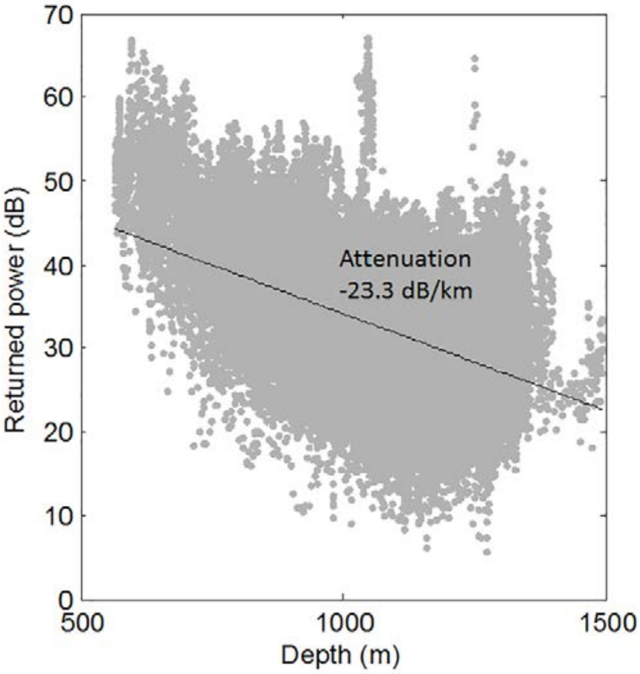

Figure 3-28. Plot of bed return echo strength against depth. The slope of a fitted line indicates the attenuation rate within the ice.

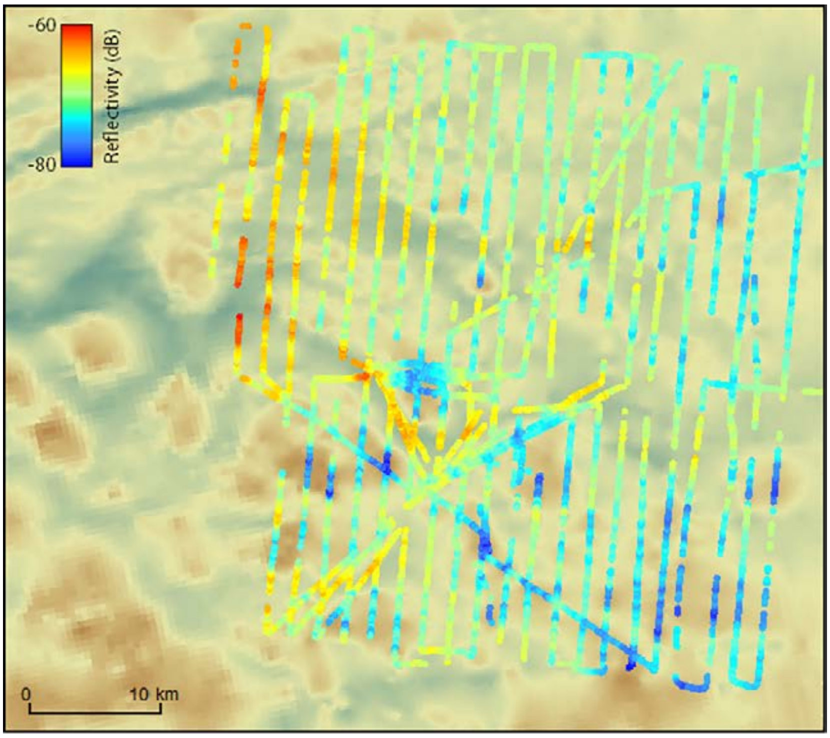

Figure 3-29. Preliminary basal reflectivity for the GAP dataset. There is an indication of a lower reflectivity towards the interior of the ice sheet. This could possibly indicate a transition to bottom frozen conditions.

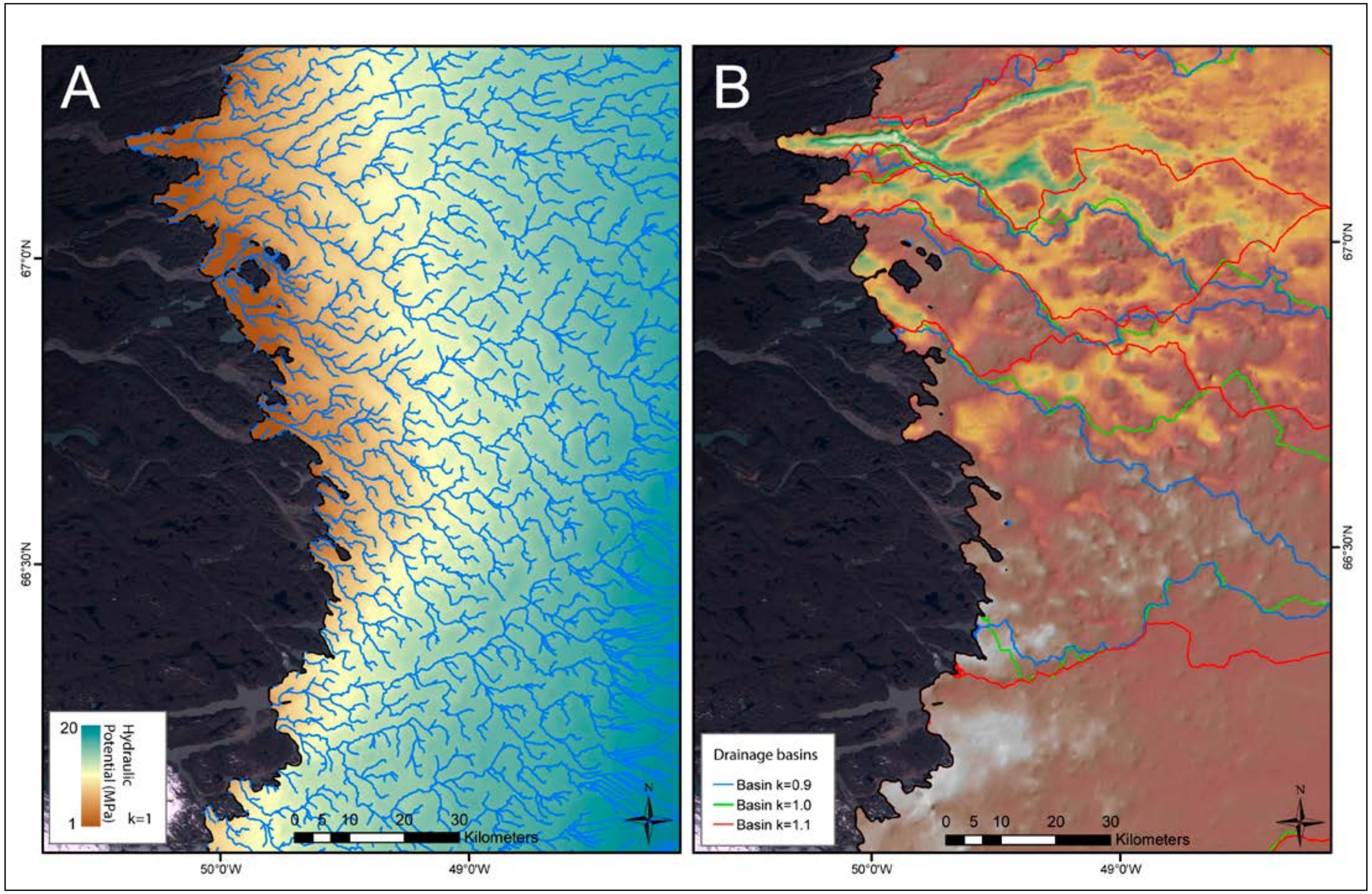

Figure 3-30. *A) Calculated hydraulic potential with pathways of accumulated water flow. The shadowed map in the background depicts bed topography. B) Map showing the topography of the study area and subglacial drainage basins for major proglacial river derived using various assumptions about basal water pressure (k values represent basal water pressure as a fraction of overburden, see inset); colouring depicts elevation with brown colours higher than blue colours. Note the large changes (up to 100 % area change) of subglacial drainage basins that occur for different scenarios of basal water pressure.*

3.5.2.4 Basal roughness

Figure 3-31 illustrates the interpolated bed roughness in the area and shows that the subglacial topography is rough to the west close to the ice margin but gets slightly smoother to the east towards the ice divide. This might reflect the density of the radar profiles, as the spatial density is reduced higher up on the glacier. However, spatial frequency analysis of individual profiles supports that the subglacial landscape does get smoother towards the interior of the ice sheet. The roughness is also higher in the central-southern part of the investigated area where ice thickness is low and subglacial bed elevation is high (Figure 3-31). This probably reflects that this area consists of erosion resistant bedrock giving a rougher topography. Figure 3-32 shows the correlation between the spectral distribution of the subglacial and proglacial topography with elevation. It is clear that there is a close correlation with rougher terrain at high elevation. This suggests that more erosion has taken place at lower elevations, while terrain in higher elevation areas is more preserved.

3.5.3 Radar data that contributes to addressing the GAP questions

The collected radar data provide possibilities to interpret the distribution of water and its general routing under the glacier, providing information to address two of the GAP project questions. The following provides a short summary of preliminary key findings related to these questions:

Where is the meltwater generated under an ice sheet?

Reflectivity of the bed returns in the radar data can be used as a proxy for the hydro-thermal state at the bed of the ice sheet, provided the attenuation rate of the radar signal travelling through the ice is known and that radar-system specific parameters can be normalised. The similarity between modeled and the radar derived attenuation rate gives confidence in the estimation of the attenuation rate. The estimated value is comparable to what is found in cold ice areas in Antarctica, indicating that the majority of the ice column might be cold.

The reflectivity data cannot discriminate the amount of water under the ice and is limited to be a proxy for the presence and distribution of any water along the subglacial boundary. However, the reflectivity of the bed returns in the collected GAP data is higher within ~ 80 km from the margin or up the long term equilibrium line (~ 1500 m above WGS84 ellipsoid) compared with farther inland towards the ice divide. The reflectivity difference between these two regions is comparable to the theoretical difference of −15 dB between a water and a dry bedrock interface. This suggests that the base of the ice sheet is wet (at the melting point) up to approximately the long term equilibrium line but becomes considerably drier farther inland. A dry condition is not necessary indicating cold (i.e. frozen) subglacial conditions, but rather water-limited conditions. This interpretation of a dry condition inland of the long term equilibrium line is supported by the observation that ice motion variations at the highest GPS stations (see Section 3.4) do not show any strong diurnal or seasonal changes which indicate a non-active subglacial hydrological environment. Ice temperature profiles of SPB (Section 4.6) also indicate a diminishing basal layer of temperate ice towards the interior of the ice sheet.

The variability of the reflectivity on a local scale (< km) in the two regions of high and low reflectivity is lower than the theoretical difference between reflections from water and dry sediment/bedrock. It is possible that the variability is a result of patchiness in the water distribution at the base of the ice sheet, but the variability might also be an artifact by convergent (increased strength) or divergent (reduced strength) ray paths within the radar footprint. There is no clear correlation between reflectivity and bedrock topography. This is expected because the hydraulic potential calculations indicate that subglacial water is directed to main subglacial valleys (Figure 3-30).

What is the hydraulic pressure situation under an ice sheet?

The derived map of the hydraulic potential and the flow accumulation developed by SPA indicate the regional hydraulic pressure and water routing in the subglacial environment in the GAP study area. Although the hydraulic potential calculation is simplistic and has limitations, it can provide an overview picture of regional trends. The hydraulic potential (Figure 3-30) has decreasing trend towards the terminus but is modified with lower hydraulic potential in major subglacial valleys, and the subglacial water will be focused into these main valleys as indicated by the flow accumulation calculation.

Based on the hydraulic potential, preliminary subglacial drainage basins can be delineated. The catchments change considerably at different overburden pressure values (k-values), which indicate that subglacial water emerging in the proglacial rivers might come from variable areas over time depending on the subglacial pressure.

3.6 SPA Seismic aquisitions

3.6.1 Reflection seismic acquisitions

The objective of the reflection seismics was to establish detailed spatial coverage of subglacial topography and basal sediment character under the ice sheet in the GAP study area. Reflection seismic techniques involve imaging the elastic properties of the ice sheet subsurface. A shockwave of elastic strain energy is produced that travels through the ice and reflects from boundary layers back to a series of geophones on the ice surface. Reflection seismic techniques on the *RGC* was applied to determine the geometry and characteristics of material at the ice-bed interface. *Amplitude versus angle* (AVA) analysis provides further information on the substrate characteristics, such as sediment porosity, sediment density and changes in water content, through exmination of the reflection angles from subsurface layers in relation to individual shot gathers.

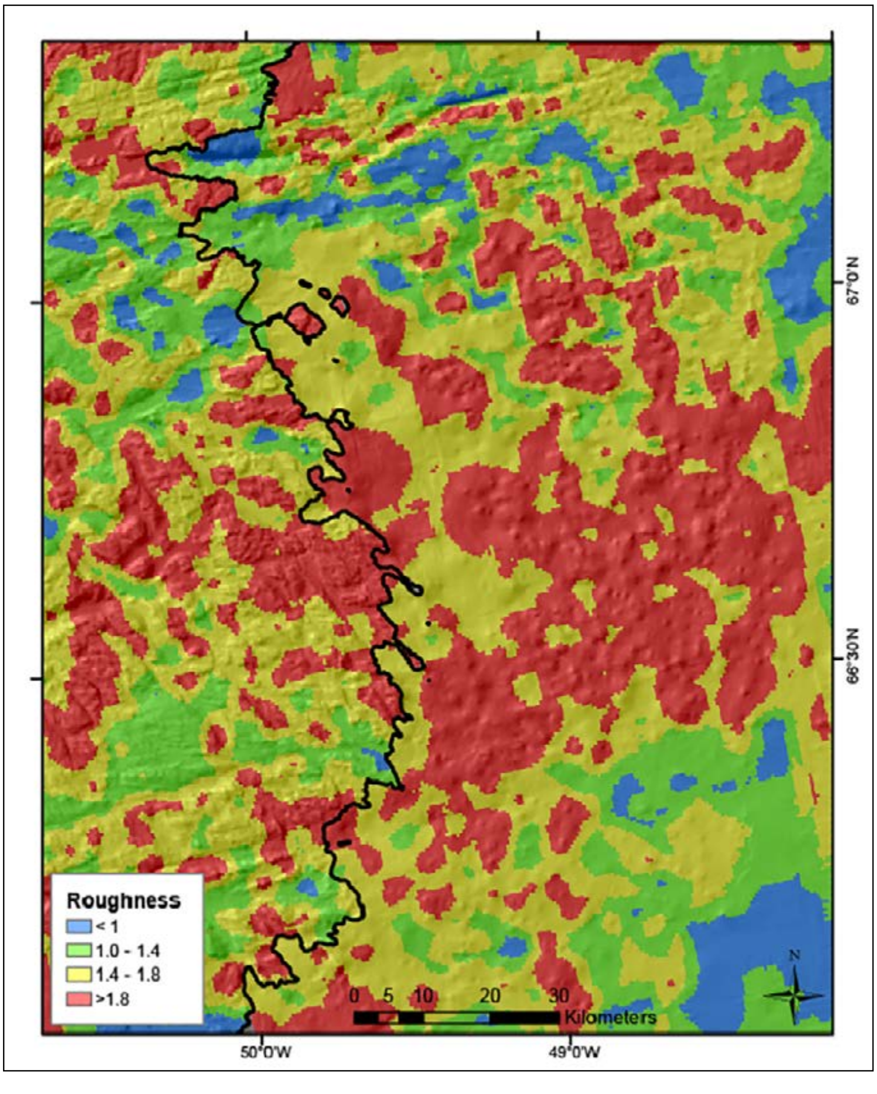

Figure 3-31. Bed roughness calculated from spectral analysis of all datasets including the proglacial areas derived from GIMP DEM. The ice margin is indicated by a black line.

Reflection seismic field data were collected in July and August 2010 at four sites shown in Figure 3-33. The aim of the reflection seismic campaign was to determine characteristics of the basal material underlying the ice at each site. In total, six seismic lines were gathered using 236 shots covering ~ 18 km on the ice surface; using these techniques a total length of 9.3 km of the subsurface has been imaged. For each line, a seismic stacked section has been produced and AVA analysis carried out. The seismic reflectivity of an interface is determined by the physical contrast on either side of it, and also by the incidence angle at which seismic energy arrives. By plotting this angle against the observed reflectivity, an 'AVA curve' is produced, which can be highly diagnostic of mechanical properties of the subsurface. The four sites are as follows:

Site 1: SEISLINE, BANG and BOOM collected around F-lake (red lines in Figure 3-33).

Site 2: PLOP collected in the region of a potential subglacial lake (yellow line in Figure 3-33).

Site 3: SHBAM collected downstream from the Z-lake Moulin (orange line in Figure 3-33).

Site 4: SHR collected ~ 13 km from Russell Glacier terminus (green line in Figure 3-33).

At each site, 48 vertical component geophones, with a spacing of 10 m, were set into concrete slabs (of dimensions 15 × 15 cm) and buried with ice chips to reduce surface noise (except for site 4 where 24 geophones were used). Shot holes were drilled to ~ 3 m depth at a spacing of 80 m. At the sites, the thickness of ice required the use of explosive sources to reflect energy off the bed. To reflect energy off the bed. The holes were loaded with one detonator and one or two charges of Pentex and dynamite. Most charges were left to freeze overnight in order to produce better coupling so that energy from the explosions would travel primarily down into the ice. Shotboxes for firing were provided under a peer-reviewed equipment loan from *Seismic Equipment Infra-Structure in the UK* (SEIS-UK), *Natural Environment Research Council* (NERC) Geophysical Equipment Facility. Accurate differential GPS locations of the shot holes (using a Leica SR520 receiver processed against either a static on- or off-ice receiver) were collected in order to both establish the exact location of the shots and the elevation change along the line. Table 3-10 gives information about the line characteristics.

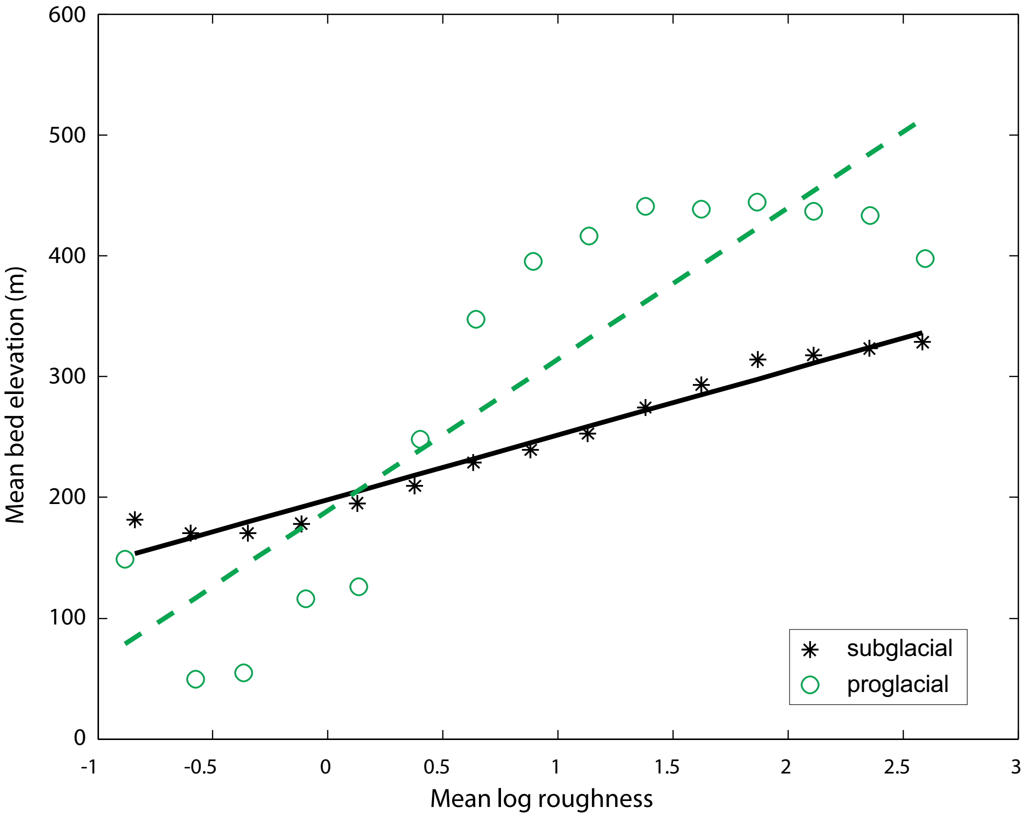

Figure 3-32. *Mean bed elevation calculated for each logarithmic roughness bin of 0.5 intervals for subglacial (black asterisks) and the proglacial area (green circles). A linear regression fit show the general trend with an R2 value of 0.91 for the subglacial area and 0.58 for the proglacial.*

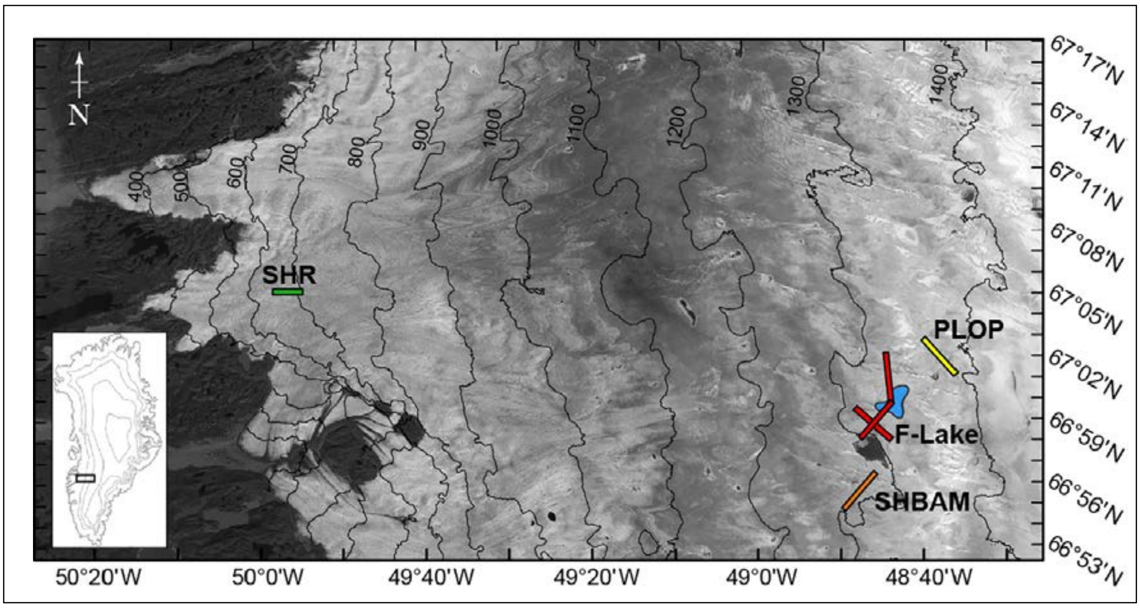

__Figure 3-33.__ Landsat image from July 18, 2010 with the the active seismic lines marked in colour. F-lake is marked at the maximum extent prior to drainage.

Table 3-10. Reflection seismic line properties.

	SEISLINE	BANG	BOOM	PLOP	SHBAM	SHR
Line length (m)	3040	3600	4240	3920	1040	1920
Line direction	S-N	NE-SW	SE-NW	WNW-ESE	NE-SW	W-E
Shotline start location (N,W)	67.02888 −48.7269	66.99832 −48.7237	66.96989 −48.7226	67.04922 −48.648	66.931 −48.834	67.09998 −49.96061
Shotline end location (N,W)	67.00158 −48.72583	66.97515 −48.7812	66.9964 −48.7925	67.02154 −48.5926	66.9360 −48.815	67.10005 −49.93841
Start offset (from phone 1)	2480	2000	2000	1760	470	1140
End offset (from phone 1)	560	1600	2240	2160	570	780
No. of shots	39	46	54	50	14	33
No. of charges	1	1	1	2 (9 holes +1)	3	2 (27 holes +1)
Misfired shots	39 not triggered	n/a	24, 25, 28 re-fired	30 re-fired	n/a	n/a
Date fired (July 2010)	3, 4, 5	9, 10	16, 17	19	27	31
Mean ice thickness (m)	1271	1054	1070	1160		~ 600
Mean elevation (m D-WGS84)	1367.55	1355.23	1359.92	1395.36		709.82
Surface elev. change (m)	20.5	36	25.5	20.5		41.5
Section length (m)	1750	2079	2450	2000		1075
Section start (N,W)	67.02672 −48.7269	66.99213 −48.7391	66.9759 −48.7384	67.04186 −48.6333		67.08347 −49.92319
Section end (N,W)	67.01024 −48.7263	66.97876 −48.7723	66.9909 −48.778	67.02777 −48.6051		67.08336 −49.95505

F-Lake

Three reflection seismic lines were carried out at F-Lake, called SEISLINE, BOOM and BANG (with locations relative to F-Lake shown in Figure 3-34). The seismic profiles were processed using *ProMAX*™ software. Outputs from pre-stack time migrated are shown in Figure 3-34 for the respective lines; the depths were estimated assuming a seismic velocity of 3800 ± 40 m/s.

The ice thickness at SEISLINE is between 1.15–1.32 km with no indication of a basin under the initial ice-bed reflection. Ice thickness at BANG and BOOM is around 1–1.1 km with a basin structure intersected by both lines. The basin is several hundred metres wide, 10–20 m deep and lies beneath the main basal reflector. This basin could be interpreted as an isolated pocket of subglacial till or a local inhomogeneity within a more extensive till unit. AVA analysis was applied at the locations indicated in Figure 3-34, to quantify physical properties of the substrate.

The AVA outputs are shown in Figure 3-35. The AVA output over the basin in BANG and BOOM (a and b) is substantially different from that identified in SEISLINE and outside the basin at BANG (c and d). The zero-incidence reflection and reflectivity decrease with increasing angle in SEISLINE and BANG (outwith the basin); this result is indicative of lodged, dry till. However, although the basin structures show a similar reflection at zero-incidence, reflectivity increases with angle. Such an increase is indicative of material with high water-content but is not consistent with a positive zero-incidence reflection value. As a result, the material in the BANG and BOOM basin appears to suffer from thin-layer effects where layers with a thickness less than the seismic resolution interferes with the reflection signal. An in-depth thin layer analysis for the F-Lake site was carried out and is reported in Booth et al. (2012).

Preliminary analysis of the AVA curves suggests that the F-Lake site is underlain by extensive till units. A minimum acoustic impedance for a subglacial till is ~ 3.0×10^6 kg/m^2 s (in the cases of highest water content), and would not be expected to exceed 5.0×10^6 kg/m^2 s (more indicative of lithified sediment; Vaughan et al. 2003); respective Poisson's ratios would approach 0.5, and would not be expected to be less than 0.18 (Gercek 2007).

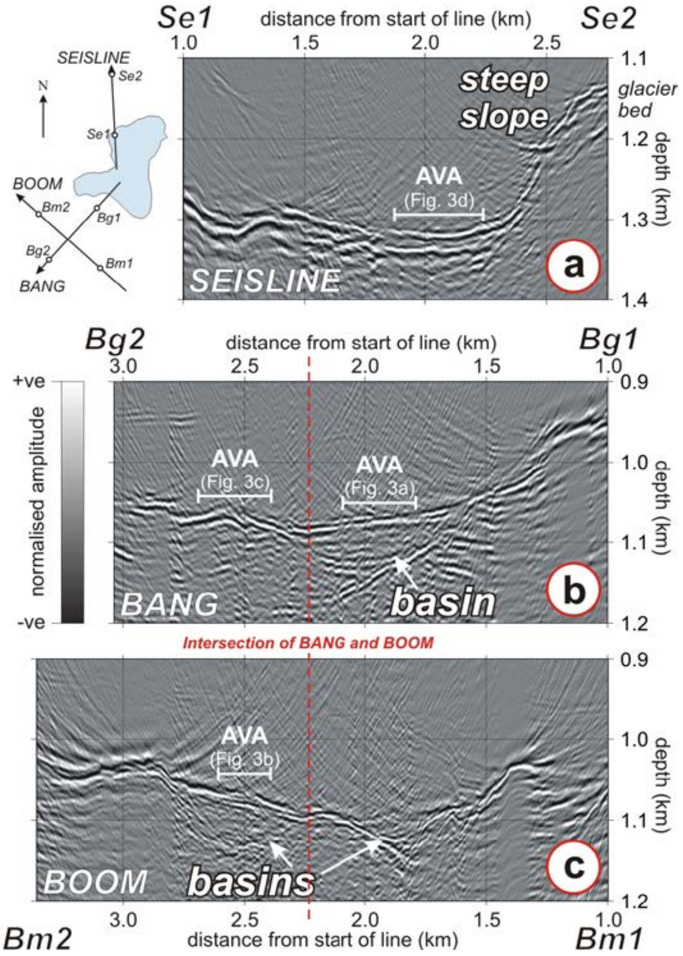

Figure 3-34. *Processed seismic profiles: a) SEISLINE, b) BANG and c) BOOM. Depth conversion assumes seismic velocity of 3800 ± 40 m/s (depth error ± 1 %); depths are referenced to surface datum. AVA annotations show ranges of traces used in reflectivity analysis in Figure 3-35. Inset, top left: location map for reference.*

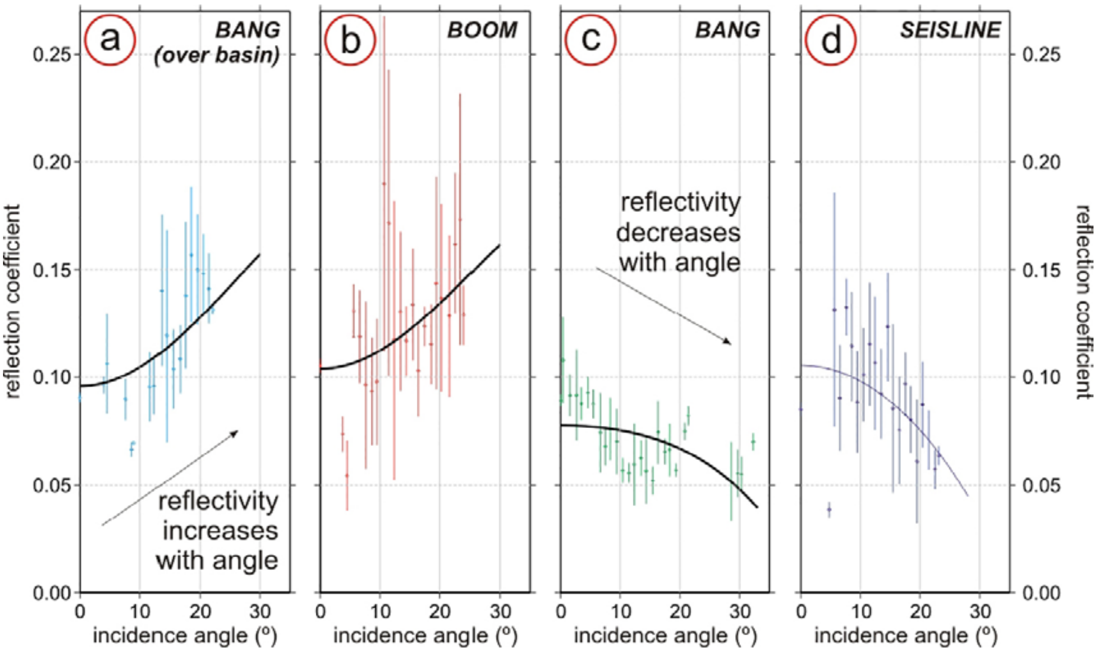

Figure 3-35. *AVA reflectivity analysis for locations marked in Figure 3-34. Panels a) and b) show basal AVA responses over basin-form structures in BANG and BOOM, respectively. Panels c) and d) show basal AVA responses, elsewhere, in BANG and SEISLINE. Heavy lines through the responses show best-fit AVA curves.*

The AVA response from SEISLINE (Figure 3-35d) gives acoustic impedance and Poisson's Ratio of $4.32 \pm 0.45 \times 10^6$ kg/m^2 s and 0.202 ± 0.06, suggestive of lodged till with low water content. Outside the basin in BANG, (Figure 3-35), acoustic impedance and Poisson's Ratio are $4.09 \pm 0.41 \times 10^6$ kg/m^2 s and 0.356 ± 0.06, suggestive of subglacial till with a somewhat higher water content. The thin-layer interpretation of the AVA responses over the subglacial basins (Figure 3-35) is consistent with a composite AVA response from a stratified till unit, where a cap of deforming till (less than 1 m thick) overlies a thicker non-deforming unit (Booth et al. 2012); the acoustic impedance of the deforming and non-deforming till is $3.0–3.4 \times 10^6$ kg/m^2 s (assumed) and $4.20–4.39 \times 10^6$ kg/m^2 s, respectively, and the Poisson's Ratio of the deforming till is 0.492 ± 0.015.

PLOP

A GPR campaign run by GAP in May 2010, upstream of the F-Lake study site identified an area with a bright flat reflector underlying the ice. When compared to surrounding reflective indices it was determined that the substrate causing the flat reflector was likely water. Due to the high absorption of radar energy by water, the GPR returns can give little information on the depth of the potential water feature or the characteristics of the material. By running a seismic line over this area, the aim was to determine the P-wave and S-wave speeds through the substrate and also the density of the basal material, allowing the depth and contents of the basin to be estimated (assuming the bottom of the basin could be detected).

PLOP was set up in a ~WNW to ESE direction covering 3920 m on the surface (Figure 3-33). Approximately 2 km of the ice-bed interface was illuminated with this deployment. The seismic stack was processed using ReflexW (Sandmeier Software) and is shown in Figure 3-36. As indicated by the dashed line in Figure 3-36, there is a basin of around 900 m length beneath a bright reflection that represents the ice-bed interface. The topography in the ESE side of the section beyond the basin is significantly sloped with a maximum gradient of ~ 20 degrees. The mean ice thickness is ~ 1160 m and the mean elevation above sea level is ~ 1395 m. Prior to AVA analysis it is not possible to determine the true thickness of the material in the basin because the image was created using a constant velocity stack (and the velocity of the material in the basin is likely to be different than that of ice). Two englacial reflections can be seen at a distance of between 900 and 1250 m along the section.

The outputs of AVA analysis of the basin (over the region indicated by the red arrow in Figure 3-36) are shown in Figure 3-37. The high zero-offset reflection coefficient is normally associated with stiff till. However the AVA curve is positive suggesting the presence of water in the sediment. As a result it is likely that thin layers below the seismic resolution are merged within the AVA signal and prevent accurate interpretation of the seismic returns.

As there is a high Poisson's ratio suggested by the AVA range (because of the positive gradient), one of the sub-ice layers is likely to be soft and saturated. It is not likely that a consolidated, dry material would overlie a soft, wet material and therefore it can be assumed that the overlying thin layer is soft. Such an assumption puts an upper constraint on the thin layer acoustic impedance of ~ 3.5×10^6 kg/ m^2 s. The thin layer will not have an acoustic impedance lower than that of water (i.e. 1.5×10^6 kg/m^2 s). These thin layer acoustic impedance constraints output acoustic impedance values for the underlying layer of $3.36–7.27 \times 10^6$ kg/m^2 s. The lower value would suggest a thin (2.5 m) layer of water overlying dilatant till, whereas the upper value would suggest dilatant till (with a thickness of ~ 3 m) overlying very stiff (approaching lithified) sediment. Using these techniques it is not possible to elucidate further information about the substrate.

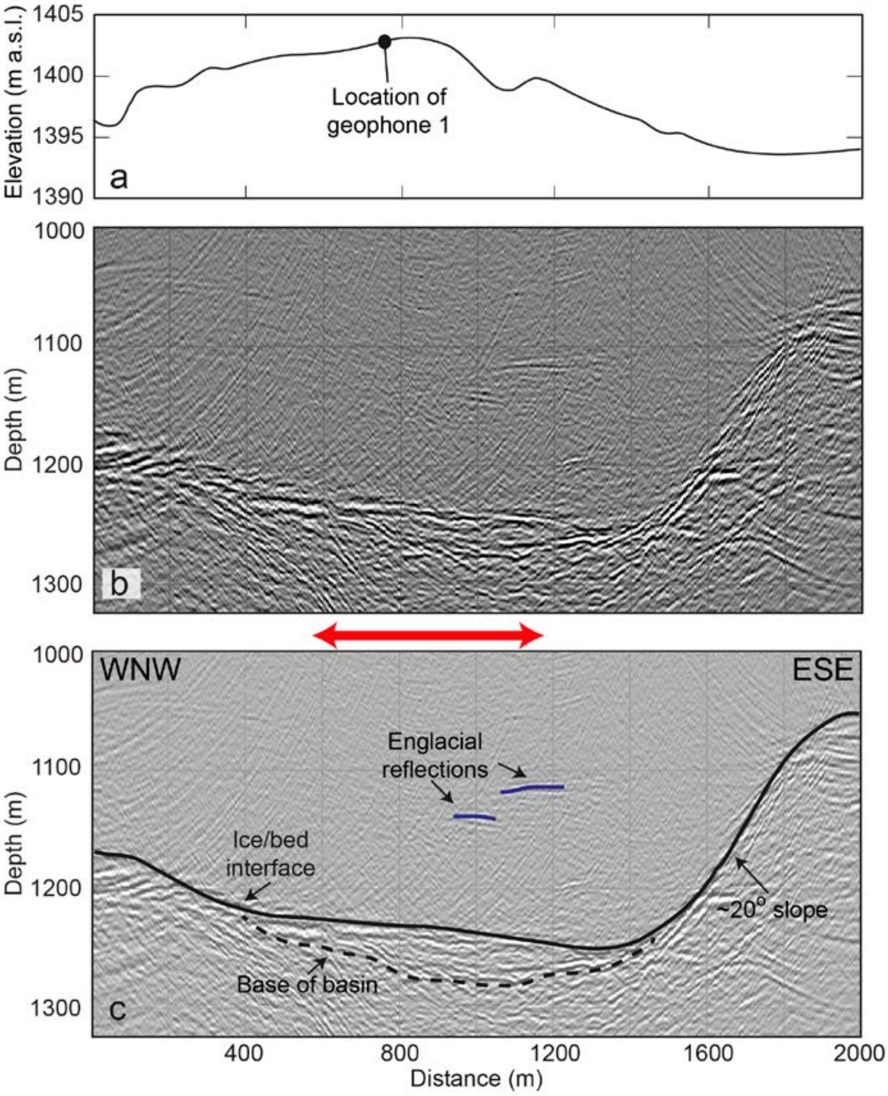

Figure 3-36. *a) Ice surface elevation at PLOP. Note the vertical exaggeration and scale on the elevation axis. b) Seismic profile of the field site. The depth is based on a seismic velocity of 3800 m/s and is relative to the surface elevation in a). c) Interpretation of the main features in the seismic profile. AVA analysis is applied to the area shown by the red double arrow.*

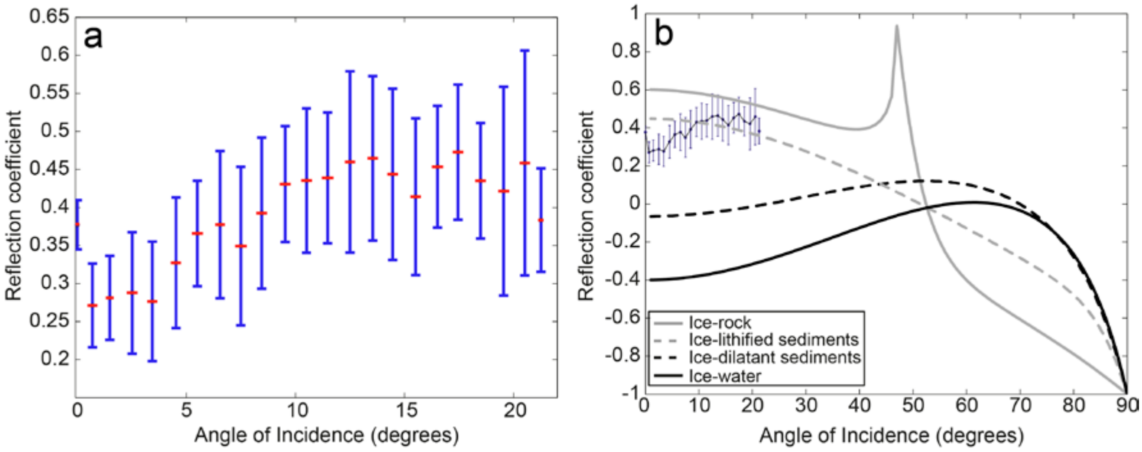

Figure 3-37. *AVA outputs for primary reflector picks over the basin at the PLOP site. a) AVA outputs averaged in 1 degree bins, including error from variations in ice velocity, ice attenuation value and angle binning. b) AVA output range with examples of reflection coefficient outputs for typical ice-interface boundaries. Here, AVA curves for ice with bedrock, sediment and water interfaces are plotted.*

SHR

The SHR active seismic line was located ~ 13 km from the terminus of Russell Glacier at an average surface elevation of 710 m a.s.l in the vicinity of the *Alfred Wegener Institute* (AWI)/IMAU (Ice2Sea project) borehole drilled through ~ 600 m thick ice. The purpose of the SHR seismic line was to provide basal conditions for the bedrock drilling team at this site. The seismic line ran near west to east at a bearing of 50°, covering 1920 m on the surface; ~ 1100 m of the bed was illuminated. The surface topography at SHR is substantially undulating with ice hummocks of several metres. In addition the site has numerous crevasses, moulins and surface streams. As a result, much of the seismic energy was lost to near-surface defocusing and the seismic returns are noisy.

The seismic stacked section was processed using ReflexW (Sandmeier Software) and the final stack is shown in Figure 3-38. The bed appears to be flat with minor undulations of ~ 10 m. The mean ice thickness from the stacked section is 640 m. There is a sloping reflector that cross-cuts the base-ice event in the west that is interpreted as an out-of-plane reflection.

Substantial noise in the data meant that only primary amplitudes (and no multiple amplitudes) could be picked. As multiple amplitudes are necessary to perform standard AVA analysis, a new technique was developed for this site using a forward model with known primary amplitudes and simulated multiple amplitudes. The resulting AVA range is shown in Figure 3-39. A lack of polarity reversal illustrates that thick layers of water or deformable sediment were not present at SHR. However, a positive gradient of the AVA reflection coefficients illustrates that sediment is present. If the primary amplitudes are assumed to represent thick layers of sediment (with no thin-layer effects), the modelled AVA outputs for SHR give an acoustic impedance range of $3.50–3.68 \times 10^6$ kg/m^2 s and a Poisson's ratio range of 0.36–0.49. These results suggests that the material at SHR was composed of till which was not stiff enough to be lodged but had a high porosity between 30 % and 40 % and water within the sediment matrix. As the shear strength of sediment reduces exponentially with increasing porosity (Tulaczyk et al. 2000), the till was likely weak, although not dilated. The new AVA processing technique and results from SHR have been published in Dow et al. (2013).

SHBAM

The SHBAM seismic reflection line was configured so that a temporal AVA survey could be carried out in order to record diurnal changes in the water content of the englacial and basal system downstream of the Z-lake drainage moulin. SHBAM ran in a NE-SW direction with a total line length of 1040 m with 15 shots. The length of the line was limited by surface undulations and several large, impassable water channels. The shot configuration was adapted for the short line length and near-offset analysis by setting out a square array of 16 shots at 10 m intervals (see Figure 3-40). Following initial detonation of the seismic line on July 27, the entire 16-shot seismic array were loaded and fired every ~ 2 hours over 30 hours between 20:55 UTC on July 27 and 01:10 UTC on July 28 in alphabetical sequence (see Figure 3-40). By repeating the shot firing sequence, temporal changes in the basal water content should be identifiable in AVA responses. The SHBAM active seismic line and temporal AVAdata have not yet been analysed.

3.6.2 Summary of reflection seismic data

Reflection seismic data collected from five sites on RGC indicate the widespread occurrence of till with varying material characteristics. Soft till is seen in basins to the south (BANG and BOOM) and north (PLOP) of the F-lake field site with a third line near the lake (F-lake) indicating the presence of lodged till. Closer to the terminus, analysis of seismic data from the SHR site suggests that weak and wet (although not dilating) sediment is present in the region.

3.7 Passive seismics experiments

3.7.1 Introduction

Passive seismic analysis provides a technique for listening to and triangulating specific energy signatures associated with material fracture, movement and/or the flow of fluids within a medium. In this context, the objective of the passive seismic experiments conducted within the GAP was to primarily confirm and establish linkages between surface meltwater production and its transmission englacially to the ice sheet basal interface, and secondly, to determine the subsequent destination of that water and how it impacts on the ice sheet's subglacial hydro-thermal environment.

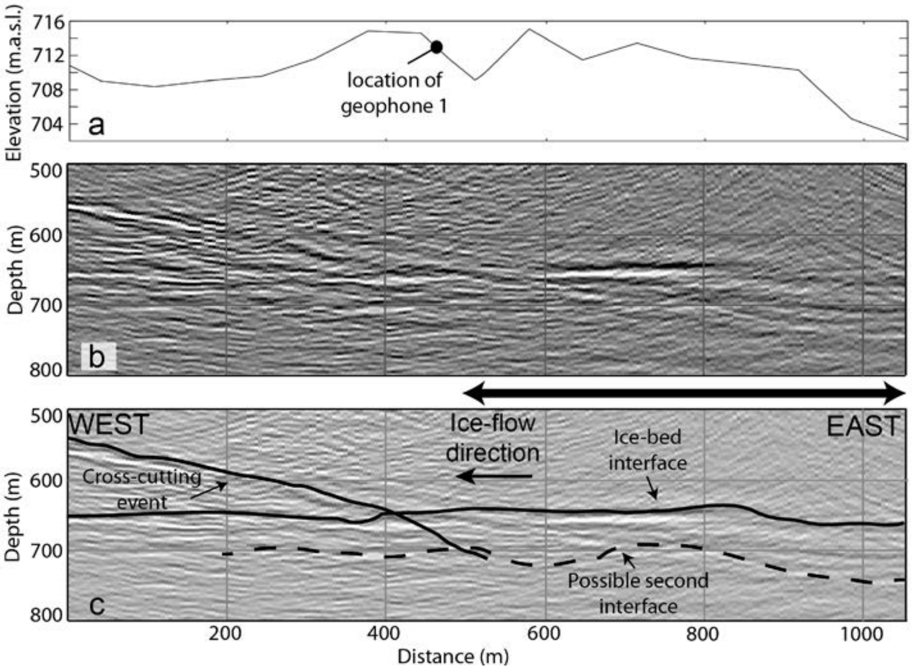

Figure 3-38. a) Ice surface elevation at SHR. Note the vertical exaggeration and scale on the elevation axis. b) Seismic profile of the field site. The depth is based on a seismic velocity of 3800 m/s and is relative to the surface elevation in a). c) Interpretation of the main features in the seismic profile. AVA analysis is applied to the area shown by the black double arrow.

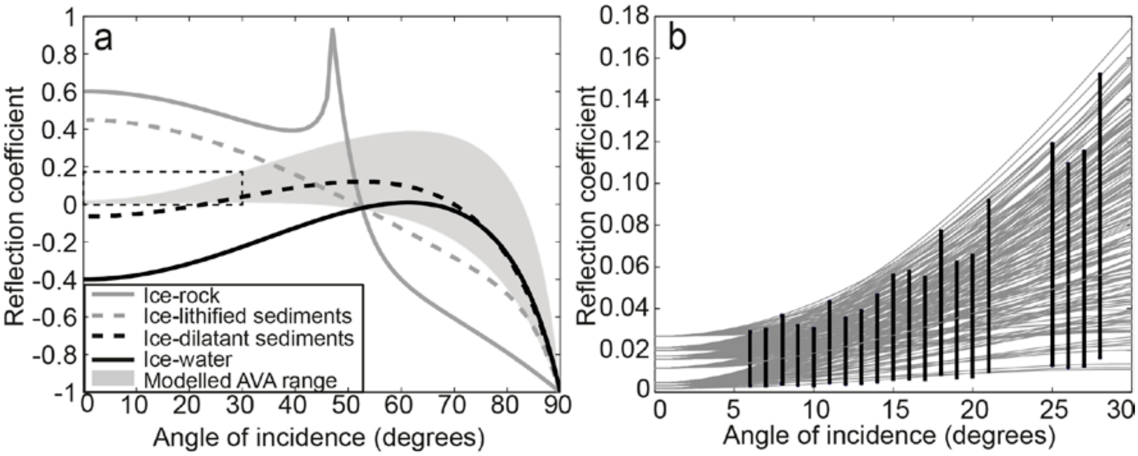

Figure 3-39. *a) The range of models that correspond with the simulated AVA range at SHR (grey shaded zone) along with examples of reflection coefficient outputs for typical ice-interface boundaries. Here, AVA curves for ice with bedrock, sediment and water interfaces are plotted. The dashed box indicates the area depicted in b). b) A close-up of the simulated AVA range (black bars) that correspond to models (grey curves) within the simulated AVA range.*

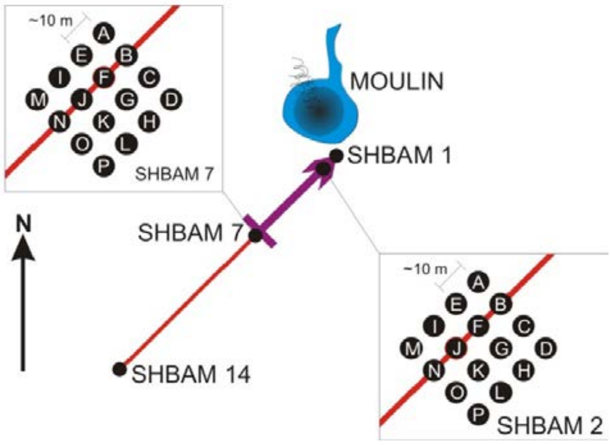

Figure 3-40. *Schematic ground-plan of SHBAM seismic line with the letters indicating shot positions.*

For this purpose, two passive seismic experiments were conducted over two field seasons. Location of these field-experiments are shown in Figure 3-41. In June, 2010 a target SGL was instrumented with 6 geophones prior to its drainage to determine the triggering mechanism by which it would rapidly tap, along with the hydraulic pathways, processes and consequences of that drainage event. In May, 2011 a moulin was instrumented with three pairs of geophones to identify to what extent such surface to bed hydraulic connections persist and reactivate year-to-year, remaining open over winter with no meltwater inputs, and to understand the impact on the subglacial hydraulic environment. The moulin, ~ 30 m in diameter was identified as being fed via a large, deeply-incised surface channel from a large supraglacial lake 7 km up-glacier which in previous years drained slowly, over a week, by over-topping and channel back-incision. In order to facilitate interpretation of passive seismic experiments, ice displacement was also recorded at intervals between 1 and 10 s through co-deployment of continuous geodetic-GPS stations with passive geophones. Key meteorological and hydrological parameters were also measured at these sites, for example, air-temperature and pressure, rainfall, lake-depth, and down-moulin pressure level and englacial temperature.

3.7.2 Background and methods

A hydrofracture will propagate once the stress concentration at its tip exceeds both the confining pressure and tensile strength of its constraining medium (Mandl and Harkness 1987). When a vertical water-filled crack either builds sufficient hydrostatic head or the stress-field within the surrounding medium is perturbed, then the tip-stress exceeds its confining threshold and the fracture propagates (van der Veen 2007). Since water is ~ 10 % denser than ice and hydrostatic pressure acts perpendicular to the sidewalls at the tip, then the mechanical advantage of the lever increases proportionally as the fracture unzips. Hence, once initiated, a self-propagating hydrofracture is theoretically only limited by available water supply to maintain head (Weertman 1973). The SGLs which cover up to 4 % (Fitzpatrick et al. 2013) of the melt-zone of the GrIS are therefore ideal candidates for hydrofracture as they store sufficient water to sustain the mechanism through potentially thousands of metres of ice (Krawczynski et al. 2009). Despite this, and considerable speculation on the role of hydrofracture in the rapid drainage of SGLs, the mechanism is yet to be directly observed and its impact on subglacial hydrology and dynamics determined. Moulins, which are likely point remnants of pervasive hydrofractures and continue to be active by inflow of meltwater, are recognised as the second mode of effective water transmission from the ice surface to the bed. Moulins appear to persist not only through individual summer melt seasons, but also appear to re-activate perennially despite being continually advected away from the vicinity of the supraglacial lakes which feed them and from which they likely originate.

The passive network deployed in both experiments consisted of six GS-11D velocity geophones (Figure 3-42 and Figure 3-43) with a natural frequency of 4.5 Hz and a bandwidth of 5–1000 Hz, continuously recording micro-seismic velocity at sampling rate of 1 kHz on a RefTek-130 digitiser. For optimal coupling, geophones were mounted on concrete slabs and buried to an approximate depth of 0.3 m. At each site, a Leica SR1200 geodetic GPS was also installed with the antenna and a 40 W solar panel mounted on a 3 m scaffold pole drilled 2 m into the ice surface. At the SGL, geophones were deployed equidistant around the lake with a separation of ~ 800 m (Figure 3-43). At the moulin, the geophones were deployed in three pairs (Rf 1-3 (a-b)) (Figure 3-42) with a separation of ~ 500 m between each pair of stations and ~ 20 m between each geophone in a station pair. Each geophone pair was co-located with a high rate (1 Hz) geodetic GPS and a further three GPS stations were deployed (with a sampling rate of 10 s) to measure the spatial evolution of ice strain as the moulin activated.

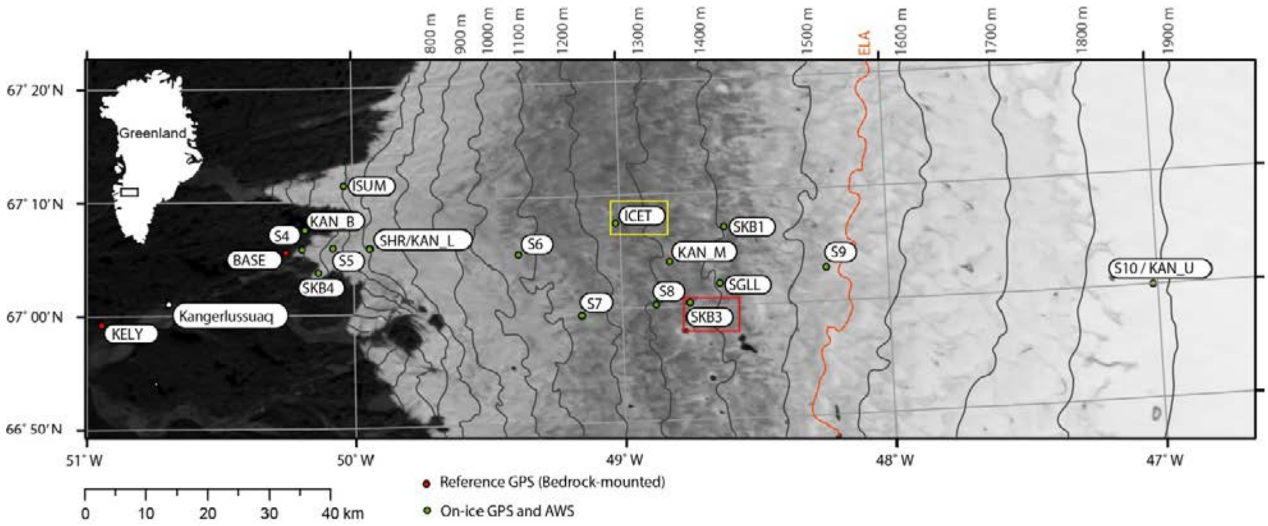

Figure 3-41. Map of the GAP GPS network showing the locations of a) GPS receivers, b) K-transect sites (S4, S5, SHR, S6, S7, S8, S9 and S10), c) the GAP AWS (KAN_B, KAN_L, KAN_M and KAN_U), d) Kangerlussuaq town and airport, e) the bedrock-mounted Kellyville reference GPS maintained by UNAVCO and f) the locations of two passive seismic experiments around a SGL (SKB3, red box9) and moulin (ICET, yellow box). The twenty-one (1990-2011) year mean mass-balance equilibrium line altitude (ELA) estimated by van de Wal et al. (2012) at 1553 m a.s.l. is indicated with a red line. The elevation contours are based on the DEM of Howat et al. (2013). The MODIS background image was acquired on August 17, 2011.

The first processing stage is the detection of seismic arrivals at each of the six geophone stations. The data were pre-processed with a Butterworth bandpass filter of 10–200 Hz and arrival times were automatically picked using a short term/long term-average (STA/LTA) algorithm whereby an event is detected when the ratio of the STA/LTA exceeds a threshold (e.g. Nippress et al. 2010). The parameters of the detection algorithm were STA window length = 0.7 s, LTA window length = 7 s, threshold = 3. Once an event has been detected, that channel is paused for 2.5 s. The second stage of the processing is the co-detection of associated arrivals at multiple stations from a common seismic event using a four step procedure based on that used by Bassis et al. (2007): 1) sort all arrival times in ascending order, independent of the station triggered, 2) calculate the difference in arrival times between i^{th} and j^{th} station assuming a constant velocity $V_s = 2000$ m/s which defines the upper limit in travel time difference between an event recorded at different stations, 3) for each arrival time, search for other arrivals at other stations which fall within the temporal bounds defined in stage 2, and finally, 4) an event is recorded if a predefined number of arrivals is exceeded simultaneously (i.e. within bounds) at different stations.

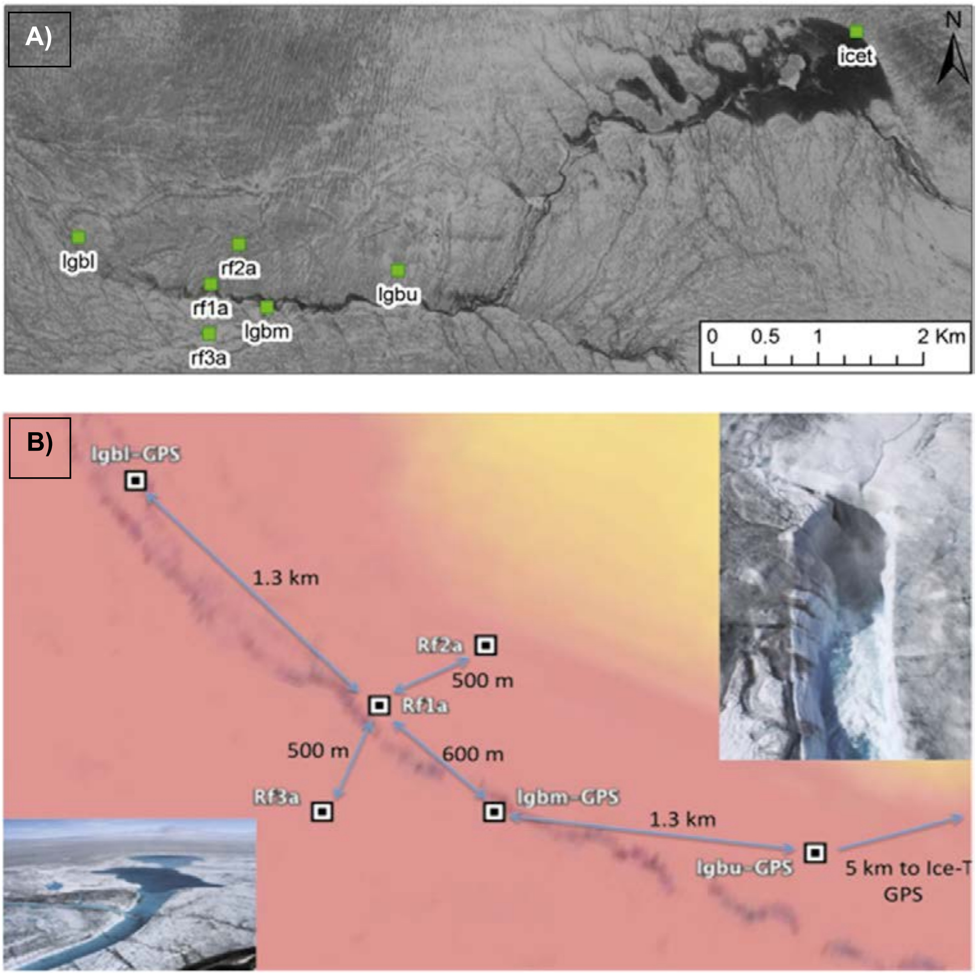

Figure 3-42. *Location and setup of the moulin experiment: A) shows the overall configuration of the catchment with labelled GPS stations from the source lake (Icet – top left) via the supraglacial channel to the moulin (lgbm). B) shows the local setup around the moulin (inset) under investigation and the SGL which feeds it (also photographed). Passive seismic stations Rf 1-3a and GPS units deployed shown with their separation.*

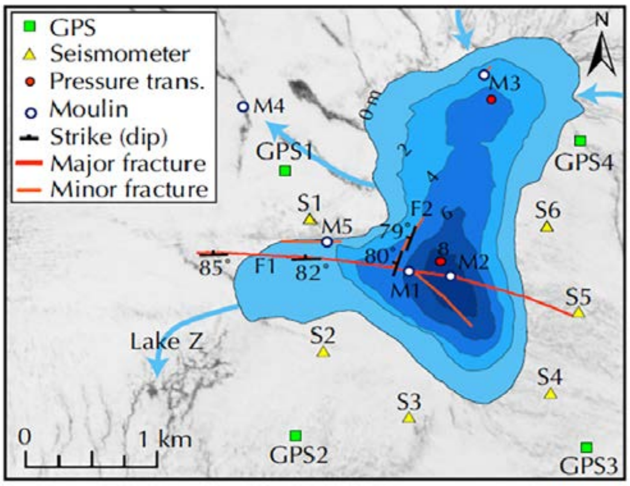

Figure 3-43. *Location of the geophones (S1–S6) and geodetic GPS for the 2010 SGL tapping experiment. Main structural fractures observed after the drainage are also shown, along with in and outflow channels, location of subsequent moulins (M1-3), lake bathymetry (to 10 m depth) and pressure sensors.*

An example of a typical event recorded during the experiment is illustrated in Figure 3-44. A change in wave characteristics is apparent across the array with greater separation of different seismic phases with distance from the source. As expected there is a high degree of similarity between seismograms recorded at common station pairs (e.g. Rf1 a and b) which can be exploited to obtain high precision arrival time picks. There is a significant drop in the measured amplitude of the recorded waveforms with distance from the source which will ultimately affect the performance of the STA/LTA event detection algorithm. Figure 3-44 reveals a magnified image of the 3 components of Rf2b from Figure 3-44a showing both P- and S-waves arrivals. The observed P-waves are weak and the majority of seismic energy is concentrated in the later S-wave arrival.

The weakness of the P-wave arrival can be seen in Figure 3-44a where it is present on stations Rf1 and Rf2 but not on Rf3. The majority of triggered events in this study are S-waves, justifying the use of V_s for event arrival association.

Having built an event catalogue, an automated procedure is applied to define precise arrival times. Due to the large impulsive nature of the S-waves these are picked first by filtering the data using a 2-pass Butterworth filter in the ranges 60–250 Hz and subsequently running a finer STA/LTA picking algorithm with an STA window = 20 ms and LTA window = 250 ms. The threshold is selected as 85 % of the maximum value of STA/LTA function to attain the precise arrival. A similar procedure is also applied to the P-wave arrival picking whereby a 150–350 Hz Butterworth is applied before the STA/LTA algorithm (STA=20 ms, LTA=500 ms). Should multiple arrivals be recorded, the trigger closest to the P- or S-wave is selected. The next stage is the generation of consistent and precise arrival-times across each pair of associated stations Rf1-3. The close proximity of the station pairs means that similarity in the characteristics of the waveforms can be exploited using cross-correlation to improve the consistency of the arrival times.

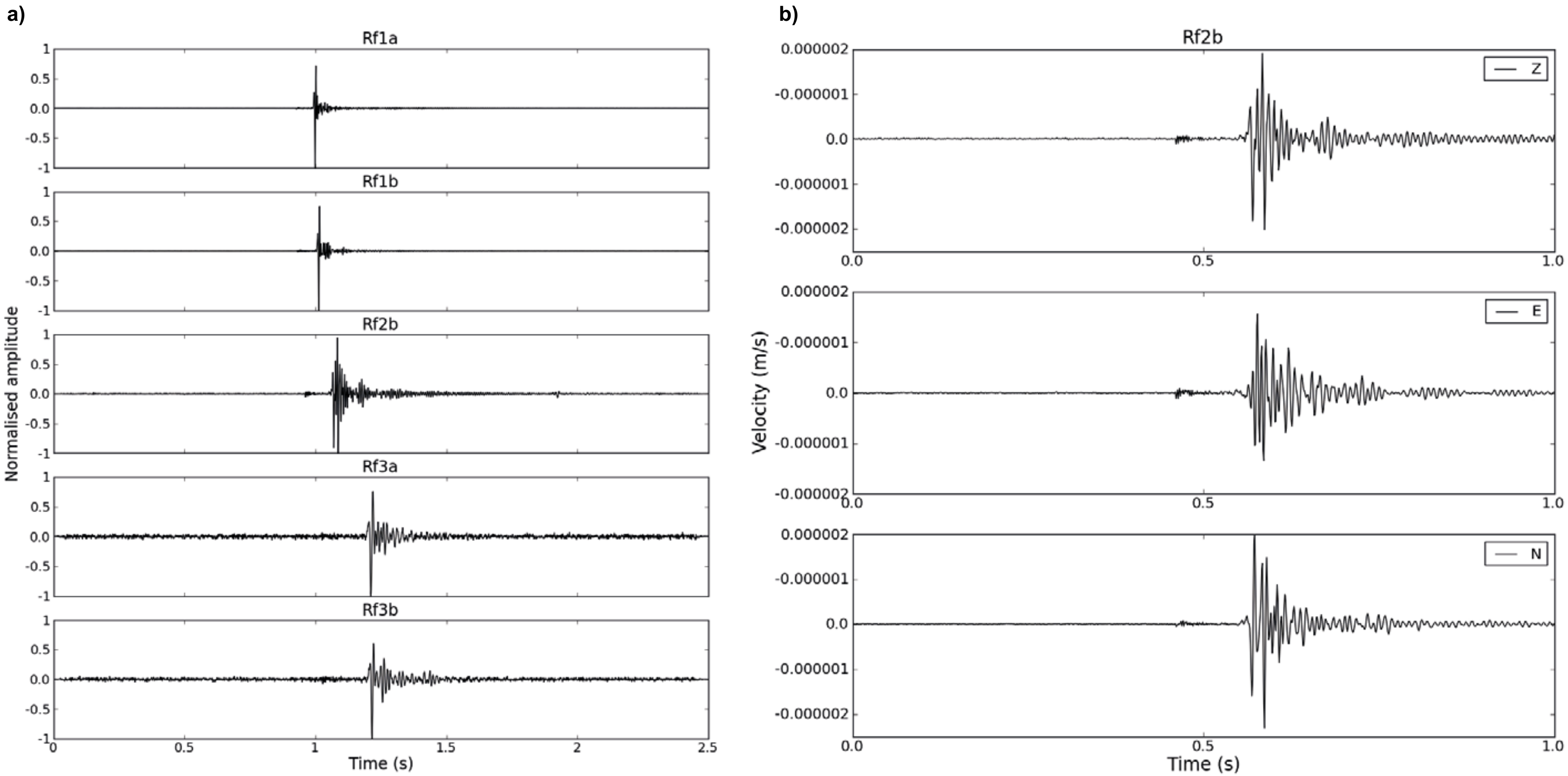

Figure 3-44. *a) and b) Typical example of vertical component recording of a seismic event during the moulin experiment at the three pairs of passive seismic geophones showing both P- and S-wave arrival at stations Rf1 and Rf2 but P-waves are absent from the more distant Rf3 stations. The right panel shows three component seismogram of the event seen in Figure a recorded at station Rf2b. Note that the P-wave is weak compared to the S-wave.*

3.7.3 Event location and testing procedure

Localisation of the seismic event hypocentre in space (x, y, z) and time (t0) is approached as a non-linear optimisation problem where the source position is defined as a point which minimises the misfit between observed phase arrival times with theoretical predictions from a number of stations. A two-step approach was utilised similar to that of of Sambridge and Kennett (1986) to determine the hypocentre of an event. Stage 1 employed an extensive grid search procedure in conjunction the Equal Distance Time (EDT) method. For a perfectly determined event hypocentre, r, the modelled travel times Cri and Crj calculated at two stations i and j and the measured travel times Ti and Tj are equal (Zhou 1994, Jones et al. 2013). Since the travel time Ti is defined as the sum of the arrival time (ti) and origin time (t0) the measured travel time difference at sensors i and j is therefore equal to the difference in measured travel times. In practice these differences in arrival times define a curved surface through space independent of the origin time – the EDT. The EDT procedure may be generalised to all N arrival time picks within an array leading to M=N(N-1)/2 independent EDT surfaces (Zhou 1994, Jones et al. 2013). The hypocentre is finally defined by the grid point with the maximum number of intersecting EDT surfaces. In practice, errors are present both with the arrival time picks and the velocity model, which can be accounted for within the EDT surface. The second stage of the procedure involves refining and rejecting calculated hypocentres using the residuals between modelled and actual arrival times through an iteratively damped least-squares method where the point with the minimum misfit is deemed the event hypocentre or is otherwise rejected if not sufficiently small.

P- and S-waves from seismic reflection experiments recorded across the SGL network in 2010 can be used to calculate and validate the localisation procedure and ice velocity model. For the initial EDT localisation a tolerance error of ± 2.5 ms was selected and a grid with a spatial resolution of 50 m in x, y, z. The source location algorithm yields good coincidence with the actual seismic shots ($\Delta x = 43$ m, $\Delta y = 75$ m, $\Delta z = 3$ m: Figure 3-45). A Monte Carlo error analysis was also conducted to assess the stability of the inversion whereby the arrival times were perturbed using a zero mean Gaussian distribution with a standard deviation of 5 ms (5 samples). The majority of the events are confined to regions of high EDT intersection from the pre-perturbed data, thus highlighting the stability of the inversion scheme. Arrival time perturbation test gave an interquartile range errors of $\Delta x = 24$ m, $\Delta y = 81$ m and $\Delta z = 311$ m.

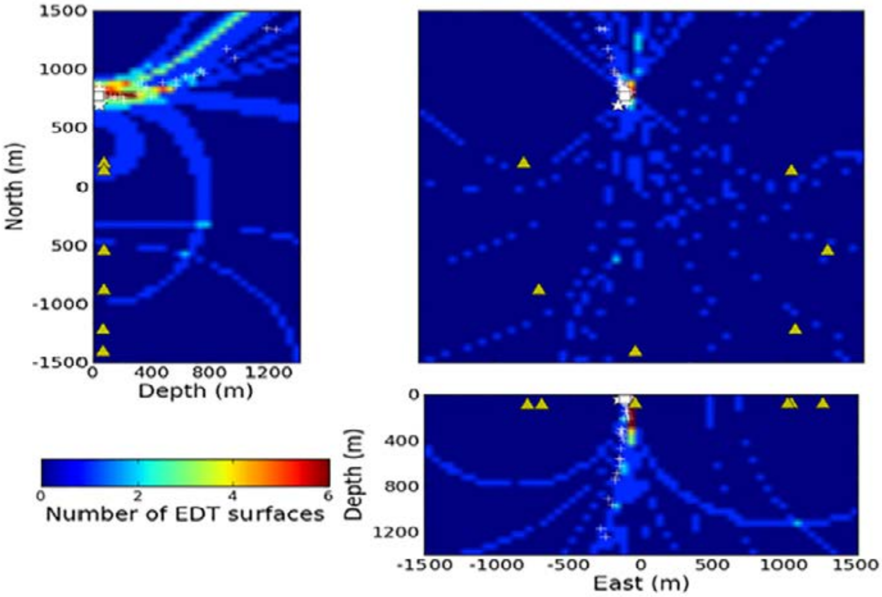

Figure 3-45. Location of a seismic reflection shot (white star) and the inverted events (yellow triangles) recorded during the microseismic experiment in 2010 (see Jones et al. 2013). Colour code indicates the number of intersecting EDT surfaces. Note that results from the Monte Carlo test (white crosses) are mostly confined to regions of high EDT intersection.

3.7.4 Results

3.7.4.1 Moulin Experiment

The frequency of triggered arrivals detected between the June 5 (DOY 157) and June 26 (DOY 176) 2011 closely match horizontal and vertical motion recorded by the geodetic GPS (Figure 3-46). An abrupt increase in the background seismicity is observed on DOY 158, which decays slowly with daily intermittent pulses of activity until DOY 170 (Figure 3-46). This is followed by a large spike in seismicity on DOY 174 which is sustained until DOY 176 (Figure 3-46). These spikes in the number of detected seismic arrivals are attributed to increased melt, and delivery of water to and activation of the moulin. After DOY 176 there is a drop-off in seismic arrivals, which can be attributed to increased environmental noise levels associated with the re-opened moulin. The increased water content in the firn layer will increase attenuation of incoming microseismic energy, thus reducing the ability to detect impulsive seismic arrivals. A total 41 662 events were located during the moulin experiment, of which 1438 events have RMS residuals < 5 ms (Figure 3-47). This initial microseismic location analysis delineates a suite of co-located vertical structures indicative of likely moulin reactivation concentrated around DOY 159 (June 7 – green circles).

3.7.4.2 Supraglacial lake experiment

Early on June 30, 2010, the 2 km wide, 10 m-deep lake drained completely via a 3 km long fracture, which opened up within the lake-bed. The event lasted 2 hours and accounted for 7.4×10^6 m^3 of rapid meltwater drainage and was accompanied by loud noises, low-frequency rumbling and a series of shock-waves associated with abrupt surface displacements. These were felt at the lake edge and at a camp ~ 1.5 km away. Based on the acquired passive seismic, lake pressure and GPS record, the rapid lake drainage event has been characterised into four key stages:

Stage 1 01:40–02:20 UTC. Rapid tapping (defined when SGL discharge exceeds 50 m^3/s) first commenced at 01:40 UTC marked by a steady increase in seismicity (black line Figure 3-48) and discharge up to 1400 m^3/s (red line in Figure 3-48). Although there is little change in the vertical displacement of GPS, horizontal perturbations led to a net transverse (cross-flow) extensional regime across the SGL (Figure 3-48). Throughout this initial stage, seismicity is restricted to less than 100 m below the surface (Figure 3-49) and waveforms closely resemble those observed during volcanic swarms, with many simultaneous and overlapping events.

Seismicity was initiated to the west of the SGL, and propagated eastward along a series of surface fractures – the principal fracture F1, and two sub-fractures F2 and F3, all of which formed during this stage. Mapping reveals that fracture F2 intersects F1 at 60° and F3 intersects F1 at 50° resulting in a set of antithetic fractures at high incidence angles. Such fracture suites are characteristic of compressional tectonic environments where deformation is accommodated by shear and extension along the main fault. Such large-scale ice tectonic deformation has been observed once previously on the GrIS, and this model has been adopted for the specific interpretation of the GAP GPS records which represent the 3D displacement of the four discrete blocks.

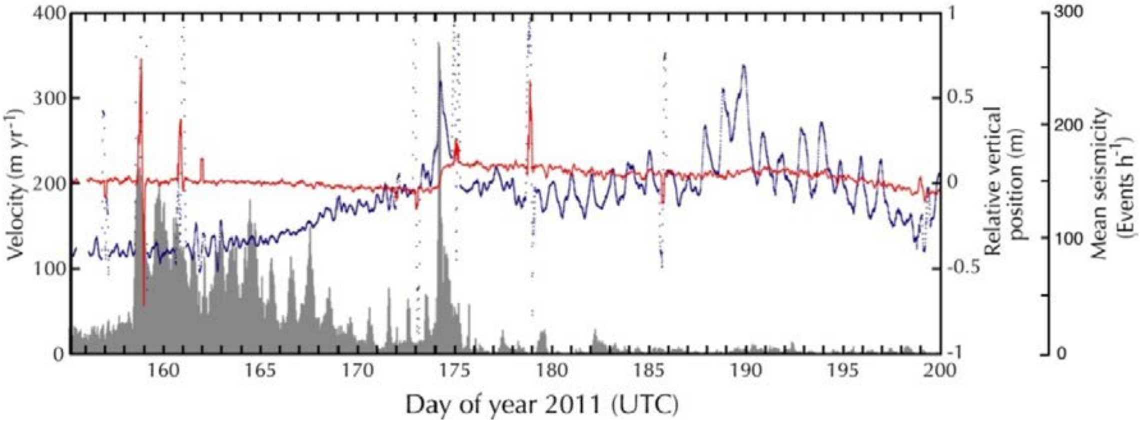

Figure 3-46. Horizontal velocity (red line) and vertical motion (blue line) time series for GPS Rf 1a. The grey histogram is the mean number of triggered seismic events per hour across the network. Note the correlation between the increase in GPS deformation and the number of triggered seismic events.

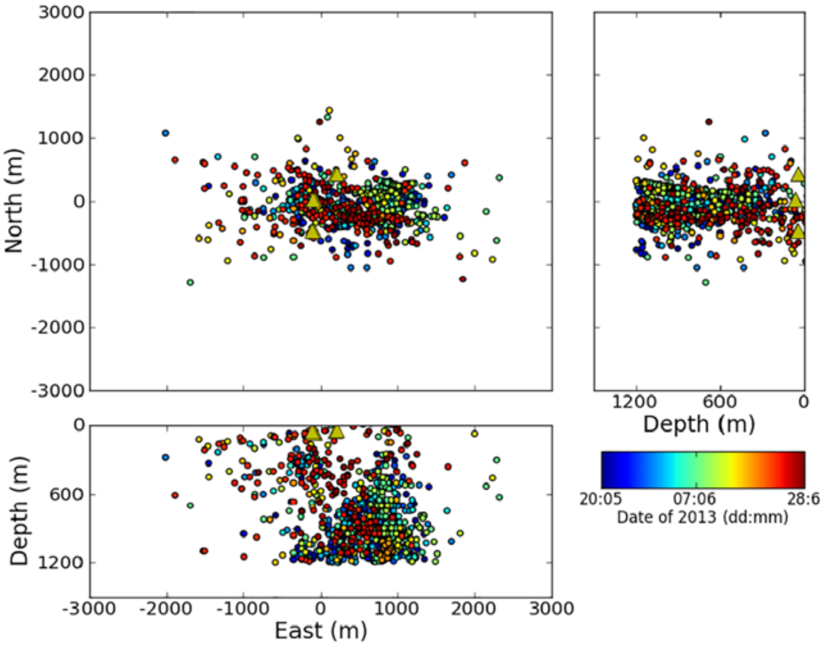

Figure 3-47. Plot of 1438 located events coloured by time between June 20 and July 28, 2013. Note the vertical structure at 1000 m easting corresponding to the moulin.

Based on the temporal evolution of seismicity with depth, and the extensional regime between the NW, NE and southern blocks (Figure 3-48), it is hypothesised that drainage of the SGL was achieved by the activation of hydrofractures at the intersection between and along fractures F1 and F2, and that the seismic surface waves were induced by draining lake water entering these hydrofractures. The lack of seismicity along the eastern extension of F1 is consistent with minimal inter-GPS separation (~ 14 cm) across the NE and SE blocks and can be attributed to a pronounced subglacial topographic pinning-point which stabilised the overlying ice and supressed fracture development to the east.

Stage 2 02:20–03:00 UTC. The secondary and main stage of drainage occurred between 02:20 and 03:00 UTC (Figure 3-48), coincident with widespread uplift and migration of the seismicity from the eastern flank of the principal fracture towards the centre of the lake to where fractures F1 and F2 intersect. During this stage, SGL volume decreased by 75 %, with a maximum flux of 3.3 × 103 m^3/s observed at 02:47 UTC (red line in Figure 7-8). The rate of separation between the NW and SW blocks was greatest at this time, with an inferred widening of F1 by 0.5 m. Extension of 0.3 m between the NW and NE blocks along F2 is also apparent. The temporal trajectory of seismic event locations is consistent with the downward propagation of a hydrofracture tip to the ice sheet bed at a depth of ~ 1150 m in less than 3 min (Figure 3-49). The inferred hydrofracture plane defines an approximately linear sub-vertical (80°) axis, consistent with the surface dip angle of 82–85° observed post-drainage along the principal fracture F1 (Figure 3-49).

The hydrofracture propagated through the ice sheet in a series of discrete steps; initially rapidly downwards to a depth of ~ 400 m followed by an accumulation of seismicity at ~ 400–600 m concurrent with lateral advancement along the strike of F1 to the west (Figure 3-49). Two inferred hydrofractures subsequently propagate from a depth of ~ 600 m to the ice-bed interface, dipping at angles of ~ 45° (Figure 3-49). Back-projected seismic source amplitudes indicate that significantly larger stresses were necessary to perpetuate these intermediate fractures to the ice-bed interface (Figure 3-49). It is likely that these fractures only initiated when the surrounding ice matrix was sufficiently weakened by lateral fracturing and accumulation of water at intermediate depth.

Stage 3 03:00–03:25 UTC. Seismic amplitudes increase from 03:00 to 03:25 UTC (Figure 3-48) when GPS receivers on the NW and NE blocks indicate closure of the principal fracture F1. Maximum uplift at the north-western GPS receiver is attained (blue line in Figure 3-48), consistent with the drainage of the remaining lake water. Total SGL water loss during this stage was 4.9×10^5 m^3 (7 % of initial volume), and the foci of seismicity along the plane of fracture F1 at depth is consistent with water continuing to access the bed.

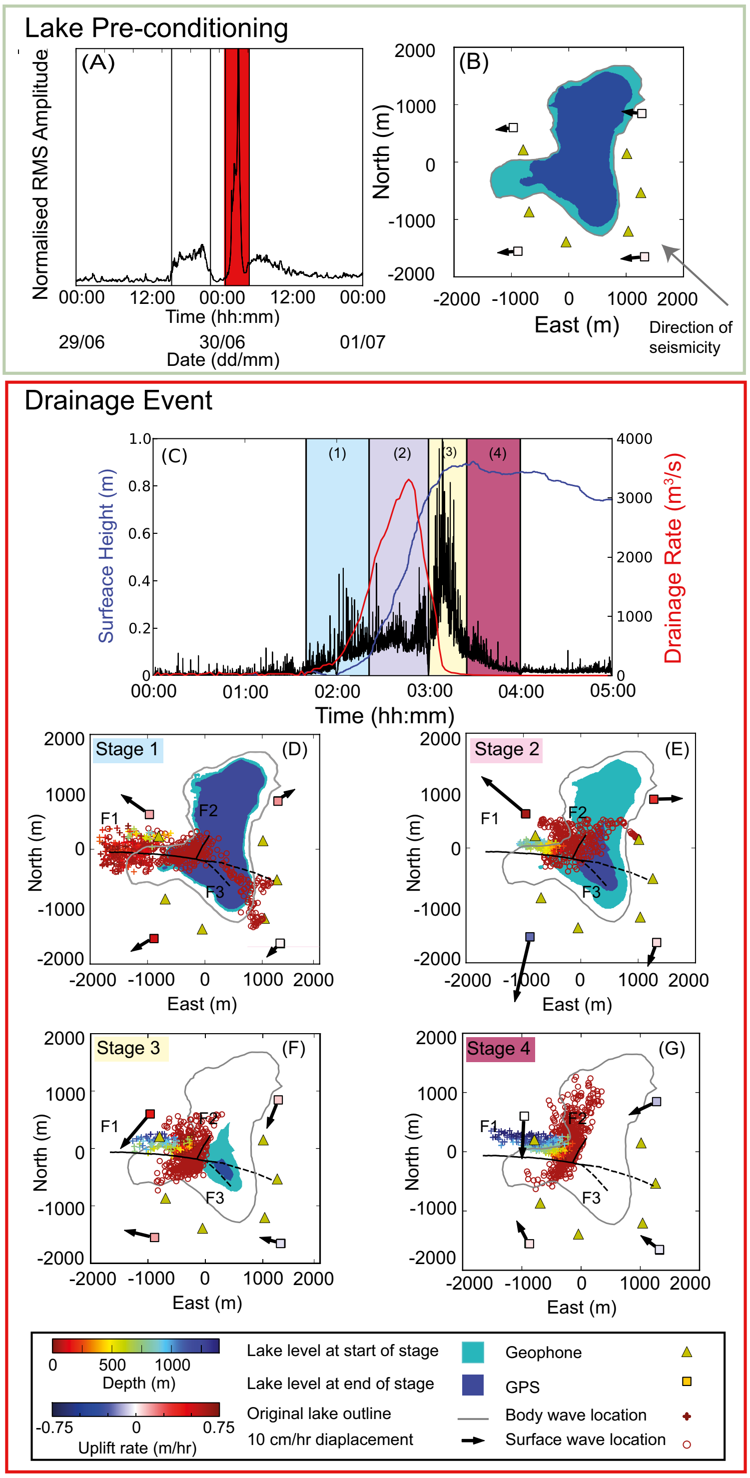

Figure 3-48. *Summary of the progression of SGL drainage. A) Two day time series of the normalised RMS seismic amplitudes. The grey shading indicates the time period of increased seismicity in response to an enhanced ice-flow event, inferred as preconditioning the lake for rapid drainage (see text). The red shading highlights the time period 00:00 to 05:00 UTC. B) Map of the lake outline at its maximum extent (light blue) and during the lake pre-conditioning stage (dark blue). Location of the GPS units (squares) and their associated horizontal velocity vectors (black arrows). The direction of incoming seismic activity during this period is shown by a grey arrow. C) Five hour time series of the lake drainage rate (red line), vertical displacement from the north-west GPS (blue line) and the mean normalised seismic amplitude measured at all 6 geophones (black line). D–G) The four stages of drainage are identified between 01:00 and 04:00. Imaged hydraulic fracture occurs during stages 2–4. Note that the seismicity located in stage 2 E) delineates the fracture propagating from the surface of the ice to ~ 1100 m depth at a rate of 6–7 m/s.*

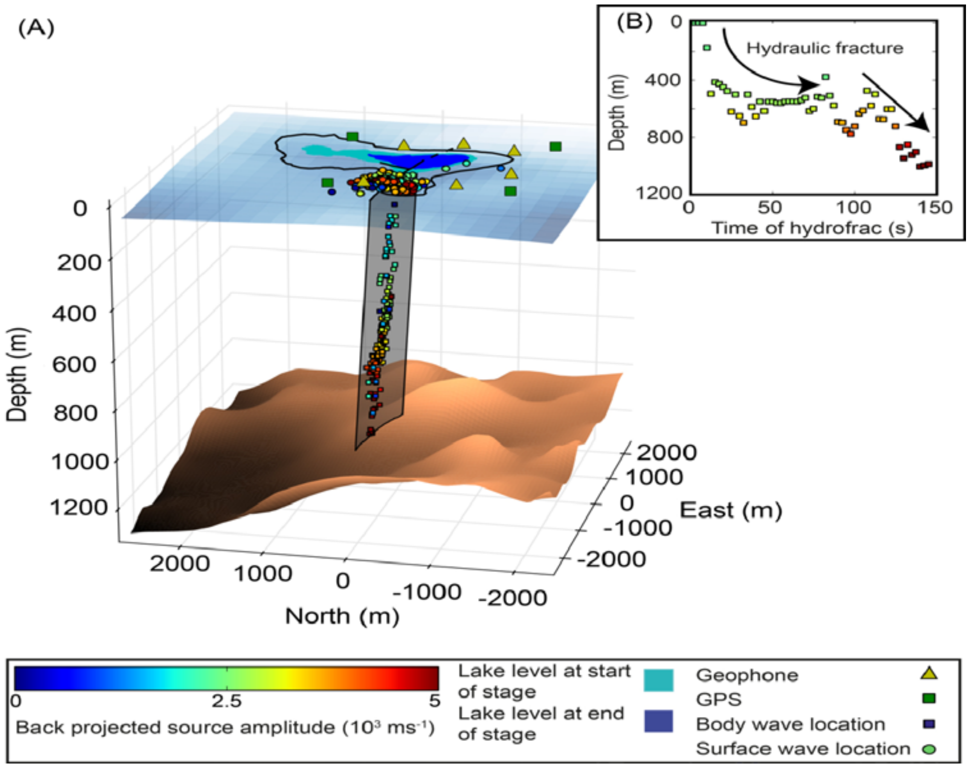

Figure 3-49. *3D image of hydraulic fracture. A) 3D image of the hydraulic fracture in stage 2 (02:20 to 03:00) defining a sub-vertical fracture plane dipping at 80° to the north, consistent with the post-drainage measured dip of F1 (82–85°). The colored squares and circles are the body and surface wave locations respectively. The seismic events are colored by their back-projected amplitudes. Note that there is a general increase in source amplitude with depth. B) Image of depth progression of the hydraulic fracture with time. The 3 stages of hydraulic fracture are highlighted: (1) Vertical propagation of the hydraulic fracture to a depth of 400 m. (2) Vertical deceleration and lateral advance of the hydraulic fracture along the strike of F1. (3) Secondary hydraulic fractures that propagate from 600m depth to the ice sheet bed.*

Stage 4 03:25–04:00 UTC. The final 35-minute stage between 03:25 and 04:00 UTC coincides with complete closure of F1 and F2 as the SGL empties altogether (Figure 3-48). Seismic surface waves locate along fracture F2 whilst body waves indicate continued water-flow to the bed, followed by rapid rising of seismicity upwards along the fractures associated with final suture. Post-drainage, a permanent displacement of 0.78 m of the NW block over the SW block (Figure 3-48) was mapped at the centre of the SGL. Meltwater continued to drain via three moulins which developed along the intersection of the principal fracture F1 with F2 and F3, and which for the reminder of the melt season were fed by a network of supraglacial channels flowing from the east.

3.7.5 Discussion

The two passive seismic experiments conducted enable analysis of the factors effecting the timing, delivery and potential impact of surface meltwater to the base of the GrIS. Specifically, they enable the impact of surface lake drainage on basal ice dynamics to be investigated with respect to the mode of drainage mechanism: either 1) relatively slow overspill drainage via an existing channel to an existing moulin; or 2) relatively fast bottom drainage via hydrofracture and the creation of new moulins.

Analysis of the moulin GPS and passive seismic datasets reveals that the moulin was reactivated with the onset of local melt at this elevation (1250 m a.s.l.) in early June, 2011 (Figure 3-46 and Figure 3-47). A slow buildup in seismicity culminating in the abrupt peak on June 7 (DOY 159) is indicative of pervasive percolation of meltwater through an increasingly saturated snowpack which over the course of a number of days drains into and fills a closed moulin. It is apparent from the GPS and passive seismic data that over-winter, with no meltwater inputs, creep-closure completely shuts down the englacial pathway at some depth within the moulin. On June 7, sufficient local meltwater completely filled the moulin and sufficient head pressure had accumulated to trigger and propagate micro-fractures down the pre-existing vertical structure to the ice sheet bed thereby fully reactivating it. The vertical structures delineated by the seismic location analysis confirm this interpretation. Rapid, but short-lived vertical uplift and rebound (to ~ 1.0 m) and what appears to be an elastic response in the horizontal GPS record indicates rapid hydraulic pressurisation of the subglacial environment followed by rapid recovery as this initial meltwater pulse dissipated. That the event was not accompanied by any prolonged horizontal flow acceleration suggests that the meltwater flux to the bed was small, likely limited to the volume contained within the moulin itself when it was reactivated, and, as yet, the surface meltwater runoff and delivery into the moulin was small. The net result was that even though the surface to bed connection was reactivated and established, the localised subglacial hydrological system was now receptive to surface meltwater yet remained inefficient and undeveloped. Hence the basal hydrological environment responded to increased meltwater inputs over the following two weeks as surface temperatures and runoff inputs into the moulin gradually increased.

Continued meltwater delivery raised basal water pressures, gradually increasing ice-bed separation, expressed by steady uplift in the GPS sited at the moulin surface. This uplift continued until June 24 (DOY 174), when the SGL sited 7 km upstream commenced overspill, activating and supplying the supraglacial meltwater channel directly feeding the moulin. The seismic and dynamic impact of the onset of SGL overspill was immediate with a major spike in seismic activity, accompanied by short-lived 0.5 m vertical uplift and a 25 % (~ 52 m/yr) increase in horizontal surface velocity which persisted for the following 10 days. It is interpreted that SGL overspill led to direct flooding of the subglacial environment in the vicinity of the moulin, thereby for a short, 1-day episode, subglacial water pressures were abruptly elevated, triggering ice-bed decoupling and accelerated flow. However, under sustained surface meltwater delivery from the overflowing SGL and continuous moulin delivery into the basal hydrological environment, an efficient drainage system developed which, despite continuous high discharge, reduced subglacial water pressures and ice velocity.

Various trigger mechanisms have been proposed for the initiation of rapid drainage of SGLs. Several studies invoke a critical lake-depth trigger, whereby a hydrofracture is initiated when the hydrostatic pressure exceeds a critical threshold. Observation of rapid drainage 4 days after, as opposed to concurrent with maximum lake-level on the June 26, 2010 discounts such a threshold in the current study as the singular prerequisite for triggering drainage. Instead, it appears that down-glacier acceleration and the ensuing reactivation of a healed crevasse via longitudinal-mechanical coupling served as the principal trigger. A downstream GPS receiver (G053), located on a major fast-flow axis, accelerated notably on June 24, followed by a marked acceleration of upstream receiver G070 a day later. Such succession of up-glacier flow acceleration concurrent with the evolution of the basal drainage system is consistent both with previous studies of Alpine glacier behaviour and recent observations at the GrIS (Bartholomaus et al. 2008, Bartholomew et al. 2010, Fitzpatrick et al. 2013). The target SGL is located on the upper eastern boundary of a fast-flow axis rendering it susceptible to a longitudinally-coupled response, be it lagged, to down-glacier flow acceleration. It is significant that the efficacy of longitudinal-stress coupling over length-scales of 10 s of km in ice sheets is dependent on basal lubrication/slip conditions and such mechanical effects rapidly decay across stiff/sticky beds with high traction (Hindmarsh 2006, Price et al. 2011). Hence, stress/strain perturbations are preferentially transferred along low-traction, fast-flow pathways which are, at the margins of the GrIS, determined by subglacial relief, composition and water-pressure state.

It is inferred that on June 29 the target SGL was subject to a strong tensile-stress perturbation originating down-glacier, which triggered strain localisation and damage accumulation along a healed crevasse within the SGL bed. In accordance with models of Linear Elastic Fracture Mechanics that require an initial flaw as a prerequisite for initiation, once sufficient mechanical damage had accumulated, reactivation of the crevasse was inevitable given the hydrostatic pressure acting from the 10 m head lying above. Such an interpretation is confirmed by the sudden local increase in seismicity on June 29, the west-to-east propagation of subsequent activity and north-westward acceleration of GPS receiver G065 (Figure 3-48).

Analysis of daily MODIS imagery indicates that several lakes drained concurrently in the vicinity of the target SGL, consistent with the hypothesis of a down-glacier originating stress perturbation preferentially transferred longitudinally along a fast-flow axis. Such a mechanism explains the spatial and temporal clustering of rapidly draining SGLs observed both here (Fitzpatrick et al. 2013) and elsewhere across the margin of the GrIS (Joughin et al. 2013, Lampkin 2011), establishing efficient surface-to-bed hydraulic pathways and leading to regional-scale, concurrent flooding of the subglacial environment. The drainage of multiple SGLs over the entire sector of RGC around June 29, 2010 delivered ~ 6×10^7 m^3 (0.056 giga tonnes (GT)) of surface water into the subglacial environment and contributed a notable, though lagged, peak in proglacial discharge gauged at Watson River within 40 hours.

The impact of SGL tapping on the subglacial environment can be examined from a mass and energy conservation perspective, assuming that such large meltwater fluxes from the surface to the bed cause ice-bed separation and uplift which enables water-flow to be routed following the subglacial hydraulic gradient indicated by the hydraulic potential map (Figure 3-30). Our results indicate that 7.4×10^6 m^3 of water were directly decanted to the bed below the target SGL over 2 hours and was likely dispersed downstream along discrete subglacial drainage pathways which reached the ice margin, 70 km, within a day. The absolute subglacial discharge rate likely decays quite rapidly over this length scale, as the flood-pulse becomes attenuated through basal sediments and cavities. The discharge rate is dominated by pervasive surface runoff entering the basal drainage system by moulins already established down-stream and activated in the weeks preceding the SGL tapping event. Despite this, the energy delivered to the subglacial environment from the two hour SGL tapping event still exceeds 7.25×10^{13} Joules, capable of melting ~ 2.5×10^5 m^3 of ice at pressure melting point or otherwise warming a ~ 20 km^2 area of 0.25 m thick basal ice by over 4 K.

The relative roles of lake-overflow supplying moulins via supraglacial channels versus rapid drainage of SGLs via hydrofracture has also been investigated by Tedesco et al. (2013), who conclude that even though SGL hydrofracture leads to abrupt and large-scale delivery of meltwater to, and perturbation of, the basal environment, moulins play a more pervasive role because the majority of SGLs across the GrIS drain gradually by overspill. The existence of two drainage mechanisms with differing dynamic impacts suggests that assuming all drainages are due to the previously identified hydrofracture mechanism would result in an overestimation of the ice dynamic effect of lake drainage at short and seasonal time scales, since lakes that drain by overspill have a more muted dynamic impact. A number of studies have identified rapid drainage as a small fraction of all SGL outcomes. In a study of supraglacial lakes detectable in MODIS imagery across the entire GrIS over 10 years, Fitzpatrick et al. (2013) find that 30 % of SGLs drain rapidly in under four days. Slow drainage, by contrast, accounts for 34 % of lake drainage events over the same period (Selmes et al. 2013). Thus, the hydrofracture-induced rapid drainage mechanism may be relatively rare (Selmes et al. 2011, Fitzpatrick et al. 2013) consistent with the observation that lake drainage associated speedups account for less than 5 % of all summer ice motion. Despite these conclusions, the role of SGL hydrofracture is highly significant by both 1) delivering large fluxes of meltwater and energy directly to the base of the ice sheet, and 2) preconditioning the englacial pathway which moulins subsequently exploit in successive years as they advect down-glacier away from the SGLs at which they originally formed.

The two passive seismic investigations carried out here provide the first direct evidence for the initiation and propagation of both a hydrofracture and the reactivation of a moulin to the bed of the GrIS. In the former investigation, enhanced distal ice-flow led to a tensile perturbation in the local stress regime, thereby triggering strain localisation and damage accumulation along a previously healed crevasse. Once sufficient damage was accumulated across the crevasse, drainage was accomplished by a number of step-like hydraulic fractures, with the ice deforming as semi-independent tectonic blocks. The displacement of these blocks during rapid drainage triggered the drainage of adjacent SGLs through longitudinal stress coupling which was coincident with and possibly led to regional subglacial flooding on the order of 7×10^7 m^3 over a few days. Once meltwater accessed the subglacial environment, it was transferred over 70 km to the ice sheet margin along major subglacial pathways determined by basal relief, where it had a discernible impact on ice flow dynamics.

3.8 3D Modelling of subglacial water flow and its impact on ice dynamics

A 3D higher order, thermo-mechanical model was employed to estimate the spatial and temporal patterns of meltwater flow through the subglacial environment once it has been delivered from the surface via moulins and hydrofractures, and to quantify its impact on ice dynamics through interaction with a layer of deformable subglacial till (Bougamont et al. 2014). Observational data on lake volume loss and velocity from SPA were used to provide constraints on the surface and basal boundary conditions.

Quantifying the response of the GrIS to warming climate is paramount for predicting global sea-level rise, but the task is challenged by complex and uncertain feedbacks between ice flow and surface meltwater delivery to the bed. Recent studies argue that ice flow across the ablation zone is stabilised by the development of an efficient subglacial conduit system in summer (Schoof 2010, Sole et al. 2013). Observations have, however, cast doubts on the ability of conduits to form > 35 km inland of the ice sheet margin_ENREF_7 (Chandler et al. 2013, Meierbachtol et al. 2013), as greater ice thickness there promotes conduit closure while lower surface slopes hinder conduit growth. Of particular relevance is the drainage of SGL water to the bed through hydro-fracturing (Das et al. 2008, Doyle et al. 2013), causing large perturbations to the basal environment, and pronounced, though short-lived ice-flow acceleration when the drainage system is overwhelmed. This occurs rapidly and frequently across the entire margin of the ice sheet, and significantly enhances ice flow on timescales from a few hours to several days. It has been suggested that SGL discharge modulates ice flow because water supplied to the basal environment causes a sudden increase in basal water pressure resulting in reduced basal traction, yet the exact mechanism of basal lubrication is unclear.

In the modelling conducted by Bougamont et al. (2014) and summarised here, the higher-order *Community Ice Sheet Model* (CISM) was coupled with a model of a subglacial sediment layer and a model of subglacial hydrology which was previously used to estimate routing and fluxes of water associated with episodic drainage of subglacial lakes in Antarctica (Carter et al. 2011). SGL volumes from the wider RGC during summer 2010 (Fitzpatrick et al. 2013) were used to drive the model. This representation of the glacier bed integrates recent geophysical observations, showing that Russell Glacier flows in places over deep troughs underlain by coarse-grained, water-saturated sediment (Booth et al. 2012, Dow et al. 2013), similar to tills produced by glaciers in Canada, Scandinavia and Svalbard (Clarke 1987, Murray 1998). The inclusion of subglacial sediment in the model is consistent with the extremely high suspended sediment load observed in proglacial streams of Russell Glacier (Cowton et al. 2012).

Current understanding of SGL dynamics suggest that rapid, high magnitude influx of water to the bed, considering peak fluxes as high as 5000 m^3/s (Fitzpatrick et al. 2014), is unlikely to be instantaneously accommodated by any channelised basal hydrological system that is established. Instead, the accelerated flow observed in late summer when an efficient drainage system has already developed_ENREF_12 points to subglacial evacuation of SGL water in a distributed, high-pressure system. The possibility that SGL water travels down-glacier in such a system, following the hydraulic potential surface was explored in the modelling by Bougamont et al. 2014. It was argued that this high-pressure pulse would allow water to interact with subglacial sediment. More specifically, the evolution of the sediment strength relates to variations in the sediment effective pressure, which, in the model, is reduced when the sediment receives water from an expanded basal water system following SGL discharge. After SGL water passes on, the effective pressure increases again because water flows out of the subglacial sediment when pressure conditions readjust towards equilibrium. Details on the methods used for the ice sheet, basal sediment and basal water system models, as well as information on the boundary conditions in the sediment layer, model initialisation and testing are given in Bougamont et al. 2014. The subglacial water fluxes and associated spatial and temporal changes in basal drag were calculated at a model resolution of 1 km.

In Figure 3-50, maps of surface velocity derived from TerraSAR-X satellite image pairs acquired with 11-day separation and centered on June 19, July 22 and November 11, 2010 (Fitzpatrick et al. 2013) are shown, together with maps of modelled surface velocity averaged over the same periods (Bougamont et al. 2014). Ice flow acceleration, observed as well as modelled, is very distinct on June 19, ~ 30 km inland from the margin of Russell Glacier, and for Ørkendalen Glacier (RG and OG on Figure 3-50f), south of Russell Glacier. The velocity then declines over the course of summer, approaching the previous winter average on November 11. The modelled response to SGL drainage events is thus consistent with observed spatio-temporal ice flow variation in the RGC.

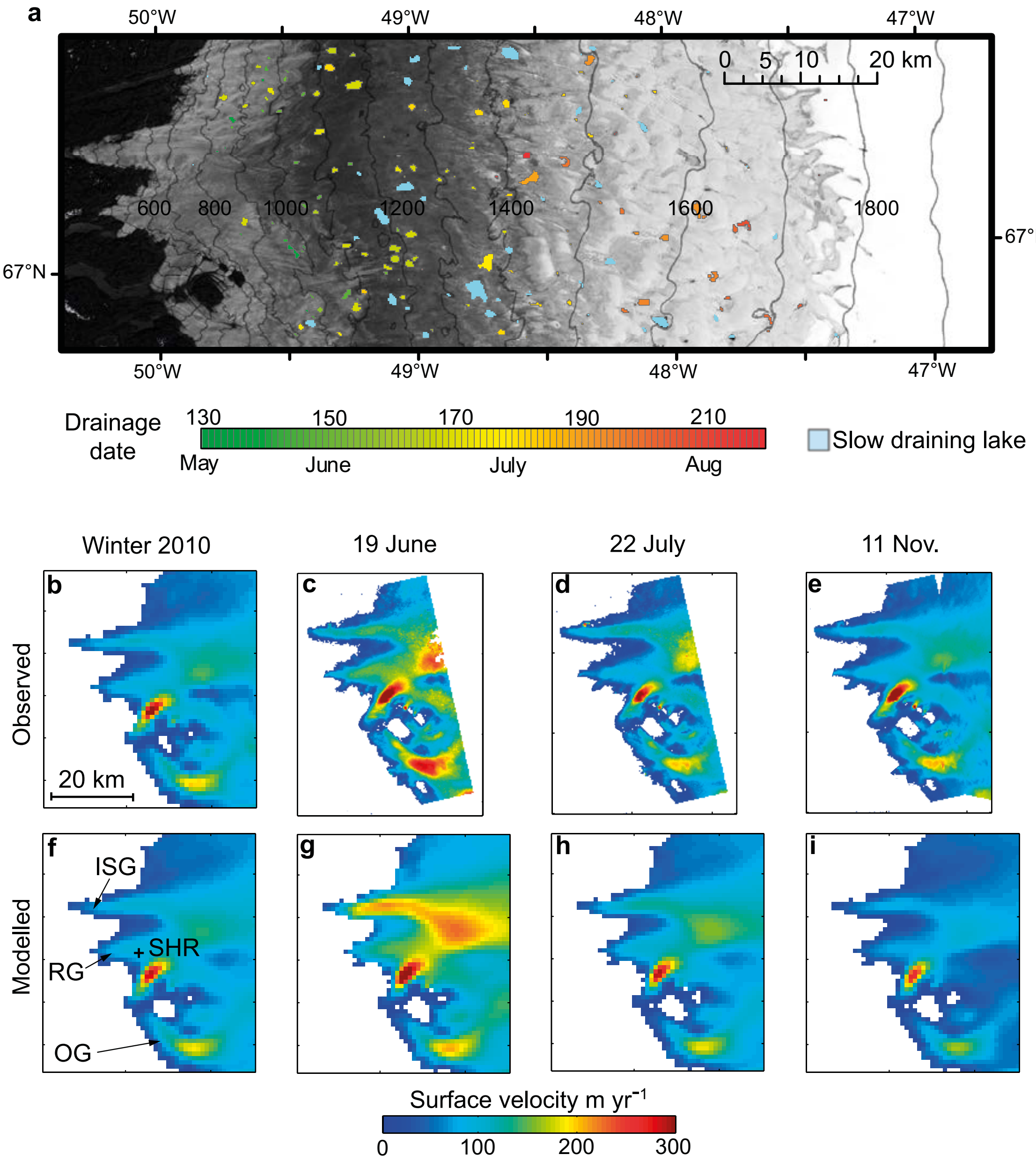

Figure 3-50. *a) Colour coded summer 2010 lake drainage map, with elevation contours (m). b) Composite winter 2010 velocity map (m yr^{-1}). c-e) Velocity maps (m yr^{-1}) derived from TerraSAR-X satellite data, showing the average velocity over 11-day periods centered over the date indicated above each panel. f) Modelled initial ice flow for winter 2010 (m yr^{-1}). g-i) Modelled ice flow (m yr^{-1}) averaged over the same 11-day periods used to generate TerraSAR-X velocity maps as shown in (c-e). The locations of Russell Glacier (RG), Isunngata Sermia Glacier (ISG), Ørkendalen Glacier (OG), and SHR site are indicated on f).Figure from Bougamont et al. 2014, reprinted with permission from Nature Communications.*

Similarly, a time series of modelled daily mean surface velocity at the SHR site (Figure 3-51), ~ 15 km from the margin of Russell Glacier, also compares favourably with mean daily velocities acquired with GPS at this location (Figure 3-51). On June 10, the modelled velocity reaches a maximum of 326 m/yr, which is within 6% of the GPS-measured velocity. On June 25 the modelled velocity reaches a maximum of 248 m/yr, which is within 15% of the GPS-measured velocity. It was noted that the timing of modelled peak velocities is influenced by the uncertainty of observing lake drainage (e.g. ± 3.5 days for the June 10 event and ± 4.5 days for the event on June 25, Fitzpatrick et al. 2013).

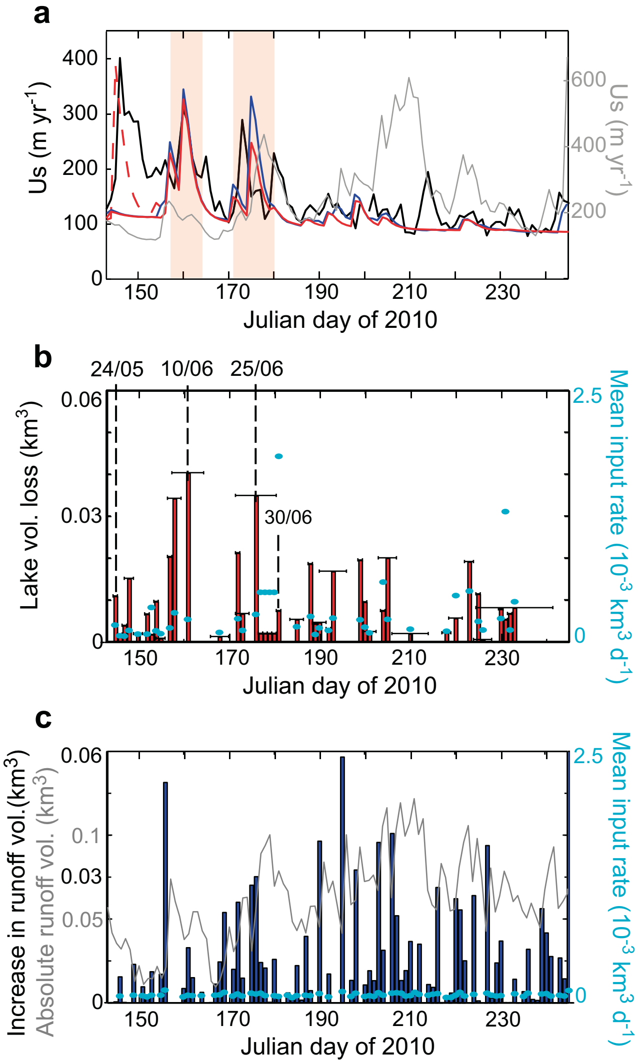

Figure 3-51. *a) Time series of observed mean daily velocity acquired with GPS at SHR site (black), and comparison with model output at the same location, when forced with SGL-only volumes (red), with SGL volumes plus runoff rates (blue), and with absolute runoff volumes (grey, RHS scale). The speed-up event on May 24-27 is reproduced assuming a three-fold increase in SGL volume loss (red dashed line). This can be explained, as in reality, the ice flow may be more sensitive to water input early in the season, when the basal water system is not yet fully developed. Alternatively, the observed ice flow may have responded to SGL water loss combined to the basal meltwater produced over winter and released early in the season. The shaded red zone corresponds to uncertainties in observing the timing of SGL drainage on June 10 and June 25, due to cloud cover. b) SGL volume loss data used to drive the model. For periods of time where no satellite data were available (horizontal bars), the timing of drainage is centered over that period. c) Daily runoff rates (blue bars), calculated from the total runoff volume estimated for 2010 (grey line). The daily mean water input rates (RHS scale, cyan dots on b,c) are highest for SGL volume loss. Figure from Bougamont et al. 2014. Figure reprinted with permission from Nature Communications.*

It was also noted that the first "spring-event" was not captured by the model, unless the lake volume loss on May 24 to 27 is three times that indicated on Figure 3-51. While early season SGL volumes may be underestimated (Fitzpatrick et al. 2014), the discrepancy also points to a limitation in the assumed uniform flow sensitivity to basal lubrication, in space and time. For instance, the response of ice flow to water input may be more sensitive in the lower ablation zone and early in the melt season when the basal system is not yet fully developed (Bartholomew et al. 2010)_ENREF_13.

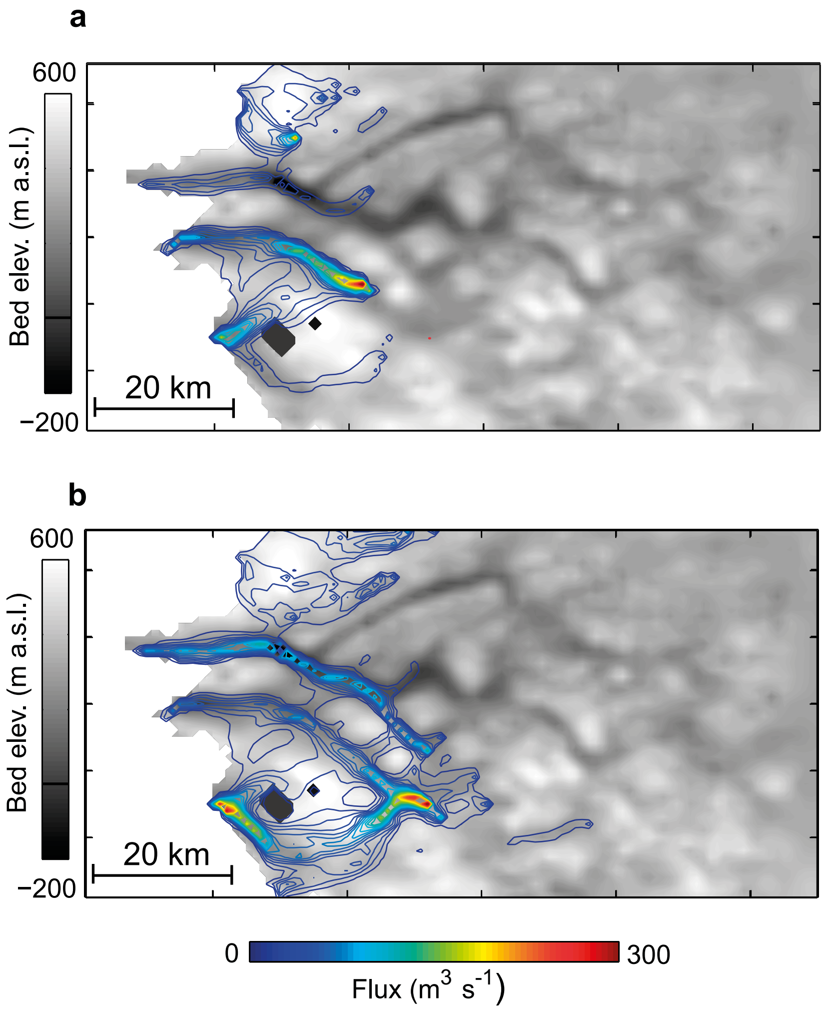

***Figure 3-52.** Bed elevation (m a.s.l., grey scale) overlain with subglacial water fluxes calculated on a) May 24 and b) May 27.*

The modelling conducted by Bougamont et al. 2014 provides insights into the dynamic impact of lake drainage for the June 10 events. In their simulations, water is routed 20 to 70 km down glacier in one day (i.e. the model timestep); this is consistent with subglacial water velocities from 22 to > 86 km/d measured using SF6 gas tracing experiments (Chandler et al. 2013). As water travels down the hydraulic potential gradients, some of it flows into the subglacial sediment. On June 10, the predicted water fluxes reach locally 570 m^3/s and averaged 57 m^3/s over a distance of ~ 65 km. The volume of water entering the sediment is 3.8 × 10^6 m^3, ~ 10% of the total lake volume loss on that date. The remaining ~ 90% is simply routed away with no effect on ice flow (Bougamont et al. 2014). Subsequently, basal traction locally falls by up to ~ 50 kPa, or about 33% of the pre-discharge value (Figure 3-53), as effective pressure in the sediment drops with the water intake (Figure 3-54). This leads to a 200% surface acceleration in the region of water input (Figure 3-55). Furthermore, basal strengthening takes place over the next few days (June 12–15, Figure 3-54), when water flows out of the expanded and over-saturated sediment layer, as pressure conditions within it re-adjust towards a post-pulse equilibrium. In response, the ice flow slows down by ~ 75% (Figure 3-55).

A feature of the robust model employed by Bougamont et al. 2014 is that a more sensitive response to SGL drainage events leads to earlier and subsequently greater slow-down (Figure 3-55). This flow characteristic is consistent with GPS records acquired on Russell Glacier, showing that flow enhancement from increased surface melting during warm summers is negated by reduced winter velocities (Sole et al. 2013). The latter could result from increased effective pressure in enlarged subglacial channels if the bed was hard (Schoof 2010, Cowton et al. 2013, Röthlisberger 1972), although the existence of conduits appears inconsistent with observations in SPB ice boreholes located

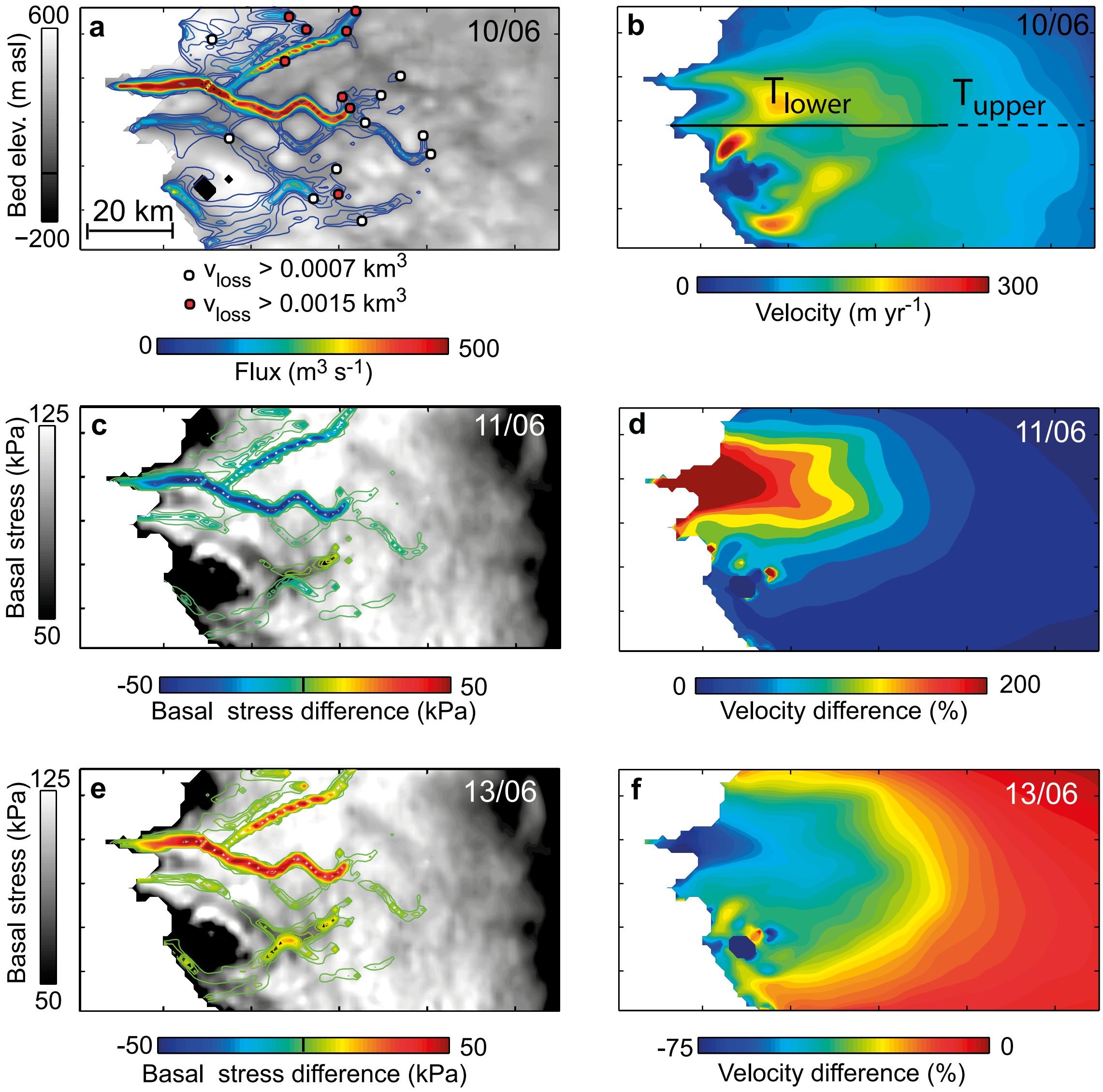

Figure 3-53. *a) Bed elevation (m a.s.l., grey scale) overlain with modelled water flux (m^3 s^{-1}, colour scale) from lakes draining on June 10 (red and white dots, v_{loss}). b) Modelled (pre-discharge) mean daily velocity on June 10 (m yr^{-1}). c) Modelled basal shear stress (kPa, grey scale) overlain with basal stress reduction calculated on June 11 (kPa, colour scale) and d) associated speedup (%). e) Modelled basal shear stress (kPa, grey scale) overlain with increase in basal stress calculated on June 13 (kPa, colour scale), relative to that calculated on June 11, and f) associated slowdown (%). The location of transects (T_{lower}, T_{upper}) used to calculate velocities on Figure 3-55 is shown on (b). Figure from Bougamont et al. 2014. Figure reprinted with permission from Nature Communications.*

> 16 km inland of the margin (Meierbachtol et al. 2013). The modelling results of Bougamont et al. 2014 provide an alternative theoretical explanation, consistent with these observations. Summer ice flow is greater with higher SGL discharge, because higher gradients in excess pore pressure (e.g. the difference between the total pore pressure and the hydrostatic pressure) drive a proportionally larger volume of water into the sediment layer. Upon termination of SGL drainage, reversed but equally high gradients in excess pore pressure develop at the ice-sediment interface, driving water out of the sediment. With sufficiently high gradients, the new state of pressure equilibrium in the sediment is attained with an overall sediment strengthening compared to pre-summer state (Figure 3-54).

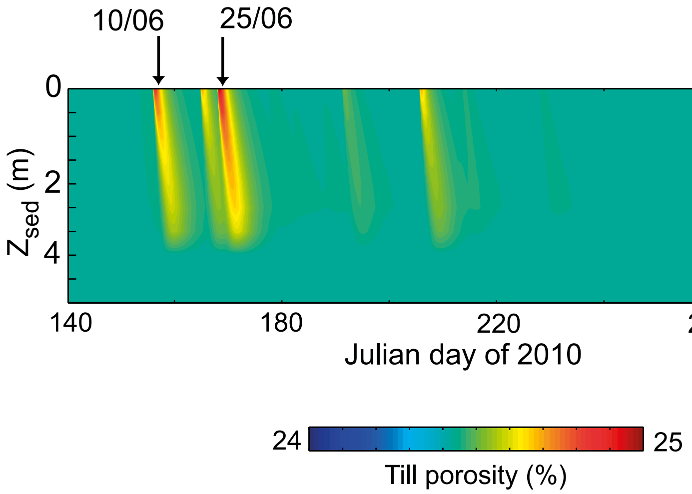

***Figure 3-54.** Evolution of the porosity distribution (%) in the sediment layer (Z_{sed}), at the SHR location. Lake-tapping events on June 10 and June 25 are clearly visible, with up to just 5% increase in porosity.*

In a final set of comparative experiments, Bougamont et al. (2014) suggest that the subglacial processes in place in the model are highly sensitive to the spatial distribution and frequency of high water-discharge events. As explained above, when the model is forced using the 2010 record of SGL drainage, which comprises ~ 500 discrete high-rate discharge events, the modelled flow is such that the mean annual velocity decreases. This trend changed when the model was forced using a drainage record based on enhanced runoff discharge, which included ~ 2500 discrete high-rate discharge events. In that case, the modelled winter slow-down could not compensate for the discrete summer acceleration events, thus resulting in a net positive increase in mean annual flow.

The modelling presented by Bougamont et al. 2014, which was strengthened by the use of SPA high-resolution ice sheet geometry and a detailed record of water input to the bed, quantitatively reproduces the flow evolution at the western GrIS margin over a complete ablation season. The model accurately replicates complex temporal and spatial characteristics of the seasonal flow variation, simply as a result of changes in basal drag caused by cumulative SGLs drainage events. The results of the study confirm that SGL drainage events exert the primary control on GrIS seasonal ice-flow variability, as has been previously hypothesized and demonstrate that the effect of SGL drainage can be effectively described by bed weakening ensuing rapid routing of lake water according to the hydraulic potential surface. The results, derived for a soft-bedded glacier, provide an estimate of the pattern and amplitude of change in basal resistance subsequent to SGL drainage.

The modelling confirms a strong hydrological control on ice flow and it also suggests that this control may occur through its interaction with subglacial sediment and not exclusively from switches between distributed and channelised drainage system configuration. The results demonstrate that the effect of water flowing into and out of soft subglacial sediment may resemble the anticipated effect of drainage system switches (Bougamont et al. 2014), replicating a faster summer flow followed by a slower winter flow as recently observed. However, it was also found that the future evolution of the annual velocity may depend on the spatial distribution and frequency of SGL events. If numbers of SGL drainage events increase, the summer speed-up would be such that it would not be compensated for by winter slow-down, overall resulting in an year-on-year increase in mean annual velocity. The accurate long term prediction of the fate of the GrIS in a warmer climate requires a better understanding of the subglacial environment.

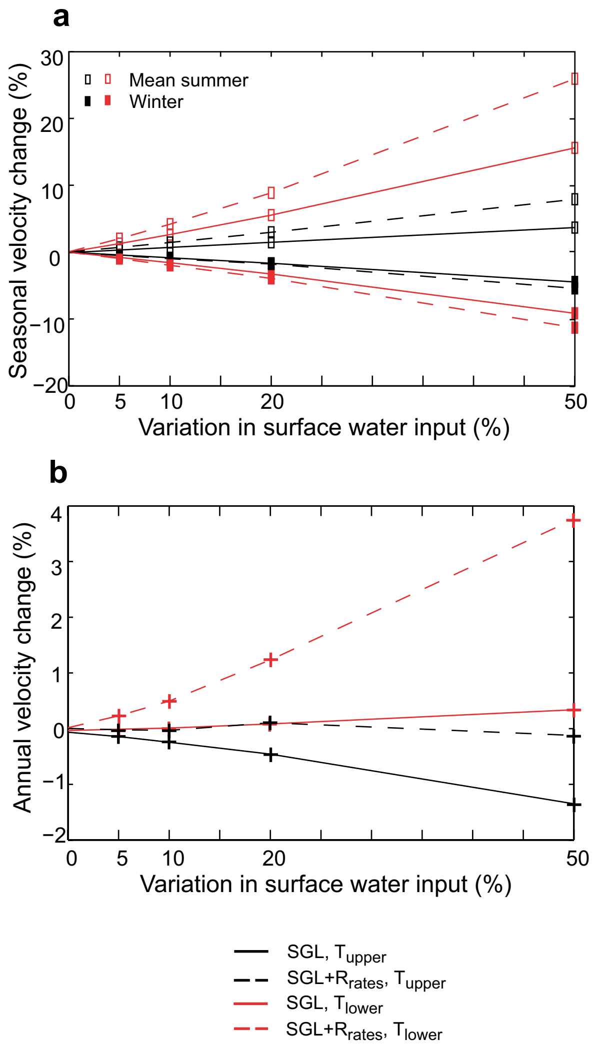

Figure 3-55. *Modelled velocity along the transects T_{lower} (red) and T_{upper} (black), using SGL-only volumes (solid lines) and runoff rates in addition to SGL volumes (dashed lines). See Figure 3-53b for transects location. a) Mean summer velocity (open squares) and winter velocity (coloured squares). The latter is assumed to be represented by the end-of-run (November 15) value. b) Mean annual velocity. Figure from Bougamont et al. 2014. Figure reprinted with permission from Nature Communications.*

3.9 Summary of understanding of ice sheet surface ablation, flow dynamics, hydro-thermal regime and their impact on subglacial waters, its pressure, extent and composition developed through SPA

3.9.1 Background

A decade ago, knowledge was poor regarding the dynamics, processes and boundary conditions of the GrIS (IPCC-WG1 2007). The subglacial relief and basal interface, in particular its composition, character, thermal structure and concomitant hydraulic conditions and impact on ice flow, were inferred on the broadest scales and corroborated by sparse, indirect observations. For example, the formative and high impact paper of Zwally et al. (2002) linking seasonal ice flow acceleration to summer surface melt is representative and neatly sums up the state of knowledge at the time. Zwally et al. (2002) determine, from a multi-year time series of GPS measurements, that the magnitude of enhanced summer-flow was proportional to the cumulative PDD sum via a mechanism which they speculate is driven by surface meltwaters that enter the subglacial environment and result in enhanced lubricated basal motion (Figure 3-56).

No explicit subglacial hydrological model or deterministic process linkage between surface melt and basal water pressure is implied in the paper, but a simple conceptual model invoking a flat, hard-bedded subglacial topography flooded by an extensive and homogenous film of water fed from the surface via crevasses and moulins, is implied.

Over the last six years, SPA has focused on RGC, a land terminating outlet of the western margin of the GrIS to glean empirical-based insight into subglacial conditions using a combination of remote sensing, meteorological, hydrological and geophysical/geodetic techniques. These techniques have been used not only to elucidate the character and processes operating at the ice sheet bed but also crucially, how they inter-connect and feedback to the patterns and processes operating across the ice surface. In this manner, extensive observations made at the ice surface, when used judiciously, can help inform and provide insight on the processes and conditions within the subglacial environment.

3.9.2 SPA observations and datasets

The cornerstone of SPA geophysical effort has been radar surveys (Lindbäck et al. 2014) to establish at high resolution the bedrock topography beneath the ice sheet, basal character/conditions (i.e. sediments/water) and to derive proxy measures of thermo-hydrological conditions (Lindbäck et al. 2014). Site specific seismic reflection experiments (Booth et al. 2012, Dow et al. 2013) have been used to characterise the subglacial sedimentary environment; that is the presence/absence of sediment, its thickness and to infer its thermal, porosity and hydrological character. Passive seismic experiments (Jones et al. 2013) provide insight into the mode, mechanisms and rates of meltwater-routing from the ice sheet surface to bed. Geodetic (GPS) records yield high resolution time series of ice surface displacement (Doyle et al. 2013, 2014). These can be resolved into components of horizontal velocity and vertical uplift which, when partitioned through time can be used as a proxy for changing subglacial hydraulic conditions. These observations are complimented by a suite of remote sensing (Fitzpatrick et al. 2013, 2014), meteorological (van As et al. 2012) and hydrological measurements (Mikkelsen et al. 2013), which crucially defines an envelope of environmental forcing to which the ice sheet system is exposed and responds.

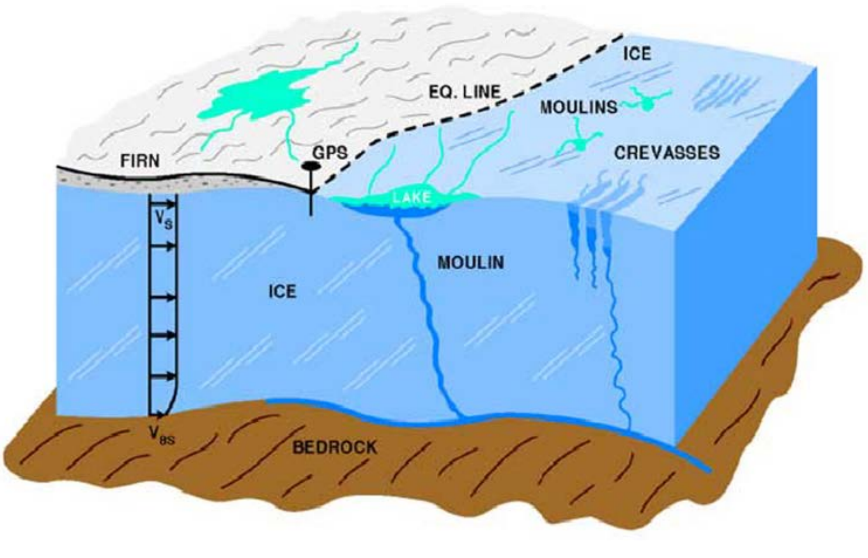

Figure 3-56. *Conceptual model from Zwally et al. (2002) with pervasive flooding of a flat, hard basal interface by surface derived meltwater transferred via moulins and hydrofractures. Figure from Zwally et al. 2002. Reprinted with permission from AAAS.*

3.9.2.1 Field data collected by SPA:

- Remote-sensing datasets from Aster, MODIS, SPOT, Landsat, TerraSarX (+LIDAR/TLS) yielding: time-slice distributions of ice surface structure, elevation, albedo, velocity, hydrological routing, location and volume of SGL, and changes in these quantities over time.
- ~ 2200 km total radar profiles orientated perpendicular to ice flow spaced at 2 km.
- Meteorological records from a network of three AWS.
- Temporal records of horizontal and vertical ice surface displacement from up to 24 GPS receivers.
- Passive seismic imaging of rapid SGL drainage and moulin initiation.
- Seismic reflection profiling at six locations from 10 to 100 km from the ice margin.
- Integrated catchment runoff modelling, bulk discharge gauging and surface hydrological measurements.

3.9.2.2 Data available to complement SPA data:

- High frequency radar of firn stratigraphy and accumulation history in a 1 × 1 km grid.
- Subglacial water pressure and englacial temperature from two boreholes drilled at KAN_L/SHR by the Ice2Sea project through ~ 600 m thick ice.
- Meteorological data from three IMAU AWS and two off-ice AWS (DMI/GRASP).
- NERC *Airborne Research and Survey Facility* (ARSF) airborne LIDAR surveys of RGC in 2007 and 2009.
- NASA IceBridge airborne radar surveys over the lower part of Isunnguata Sermia. These profiles were collected parallel to ice flow with a transect spacing of ~ 500 m.
- GEUS/DTU airborne radar surveys over ~ 100 × 100 km with variable transect spacing but usually > 2 km.
- A suite of ~ 30 Rhodamine and SF6 tracer experiments conducted by Bristol University at injections points located 2 to 51 km from the ice margin.
- 2007–2012 Watson River gauging/discharge measurements.

3.9.3 SPA observations on the quality, quantity and distribution of subglacial water available for groundwater recharge

Theory and associated modelling (e.g. Hooke 1989, van der Veen 2001) of the subglacial heat budget and resulting *in situ* basal meltwater production is well founded on a closed system (conservation of energy) bounded by 1) incoming geothermal heat flux through the substrate, 2) diffusion of the atmospheric (cold) signal from the surface through the ice column, 3) advected (cold) ice originating upstream from the surface, and, 4) frictional heating generated from internal deformation and basal motion.

Over the very short (geo/glaciologically speaking) time-scales involved in contemporary ice sheet study it can be assumed that geothermal heat flux, ice thickness, and to lesser extent, mean surface temperature and ice deformation rates, are relatively static quantities. Under these assumptions, at RGC, items 1 to 4 above can be relatively well constrained once the required spatial distributions are established and estimates of *in situ* subglacial meltwater production ranges from ~mm to ~cm per year (van der Veen 2001). To this end, SPA observations of surface climate, ice thickness and ice motion form critical inputs to such a modelling effort. Furthermore, the relative strength of the reflections from the ice-bed interface (bed return power) in calibrated radar signals can be used as a proxy for the basal hydro-thermal state of the ice sheet, provided that the attenuation rate of the radar signal travelling through the ice is known and that radar-system specific parameters can be normalised. In this manner SPA observations also provide rigorous input to any subglacial thermomechanical model, as well as providing a robust validation of outputs.

However, since Zwally et al. (2002) it has been increasingly recognised that the basal thermo-hydrological system (at least within the broad zone up to and probably some way above the ELA) is accessible to surface meltwater inputs and this introduces significant complications into any thermo-mechanical modelling effort based on a closed and isolated basal system. GAP (SPA and SPB) observations, in concert with an ever increasing body of scientific publications on the GrIS, confirm that this is indeed the case. Throughout the melt season large excursions of surface derived meltwater (orders of magnitude greater than *in situ* basal melt) penetrate and impact on the subglacial environment through: 1) direct transfer and redistribution of energy and 2) associated perturbations in the subglacial hydrological system (water pressure distribution), which drives enhanced basal motion and associated frictional heating. Furthermore, it has also been recognised that the subglacial topography (at least within 100 km of the margin at RGC) is far from flat and is characterised by high magnitude relief of the order of 100 s m of vertical change within similar horizontal length scales with upland plateau areas (at 500–700 m a.s.l.) intersected by fault-derived/deeply incised valley systems, up to 5 km wide and over-deepened to below sea-level (Figure 3-57). This critical insight – brought home for RGC in a number of SPA papers (Fitzpatrick et al. 2013, Lindbäck et al. 2014, Lindbäck and Pettersson 2015) should come as no surprise given the character and roughness scales of RGC proglacial relief and its geological control, which is reworked Archaen orthogneiss with minor metavolcanic and metasedimentary rocks metamorphosed under high grade conditions over 1.75 Ga ago (Engström and Klint 2014).

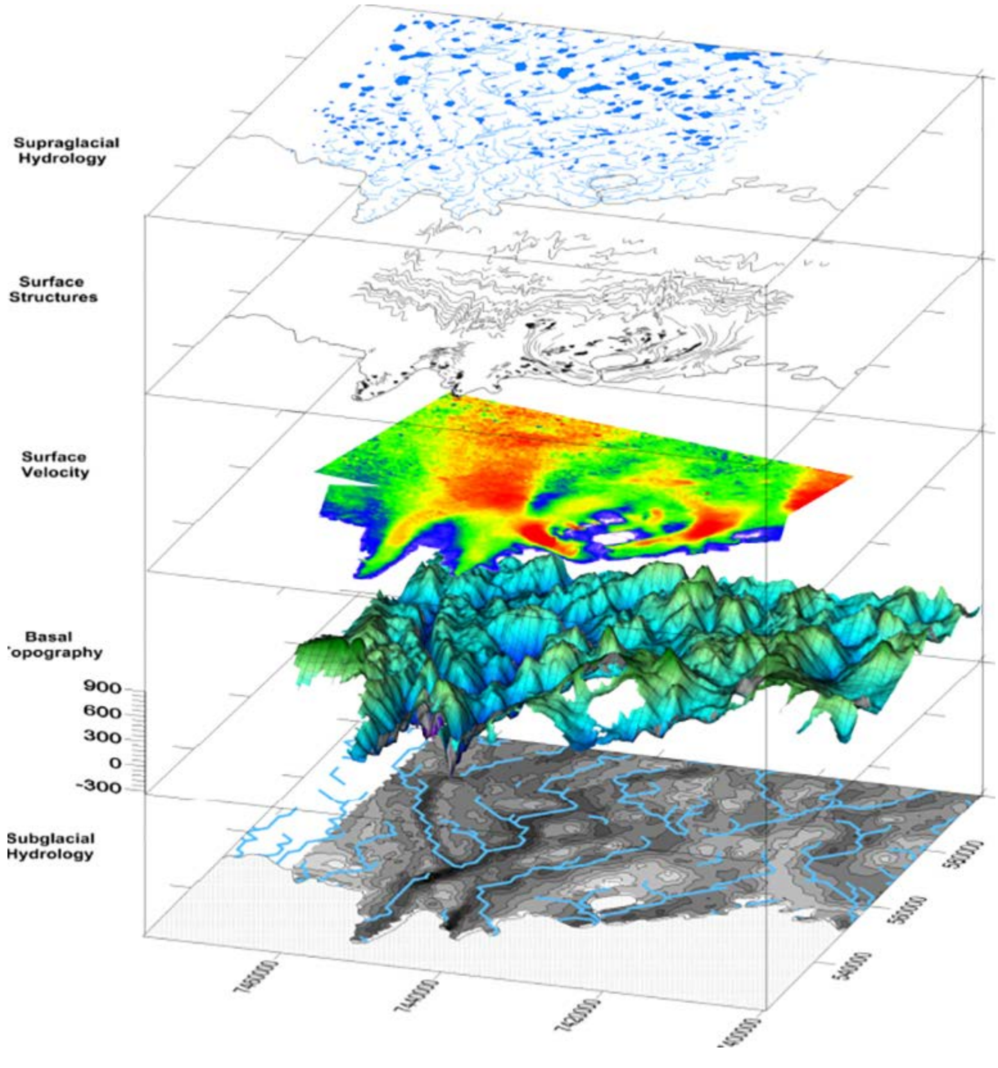

Figure 3-57. *3D GIS Multiview of RGC basal topography, inferred subglacial drainage pathways, ice velocity, surface foliation/crevassing and associated structure and supraglacial lakes, moulins and drainage network. Compiled by A. Fitzpatrick (2013) from SPA outputs.*

Recent radar compilations and analysis (e.g. Rippin 2013) of the entire Greenland subglacial topography reveals that much of the margin of the ice sheet is underlain by large, over-deepened glacial troughs (up to 1 km deep and below present sea-level) and high amplitude roughness zones, many of which are likely to have been fluvial in origin and inherited from the pre-Quaternary, providing preferential fast-flow pathways for both the ice sheet and subglacial water drainage (Figure 3-58). For example, Bamber et al. (2013b) identify a 1 km deep subglacial canyon which extends over 800 km to the ice divide and into the central, accumulation zone, forming the main outlet trough of Petermann Glacier in the far northern sector.

These linkages have long been recognised and investigated in glaciology with much of the work and accompanying theory developed in the 1970s, 80s and 90s through the intensive field-study of small temperate and polythermal case study glaciers in the Alps, Scandinavia and North America (see, for example, the review of Chu 2013 and Jansson 2010) but understanding of the impact of these processes on the ice sheet thermal and hydrological regimen and associated dynamics is still emerging. Advances in understanding made by SPA, as relevant to the GAP project questions, is presented below.

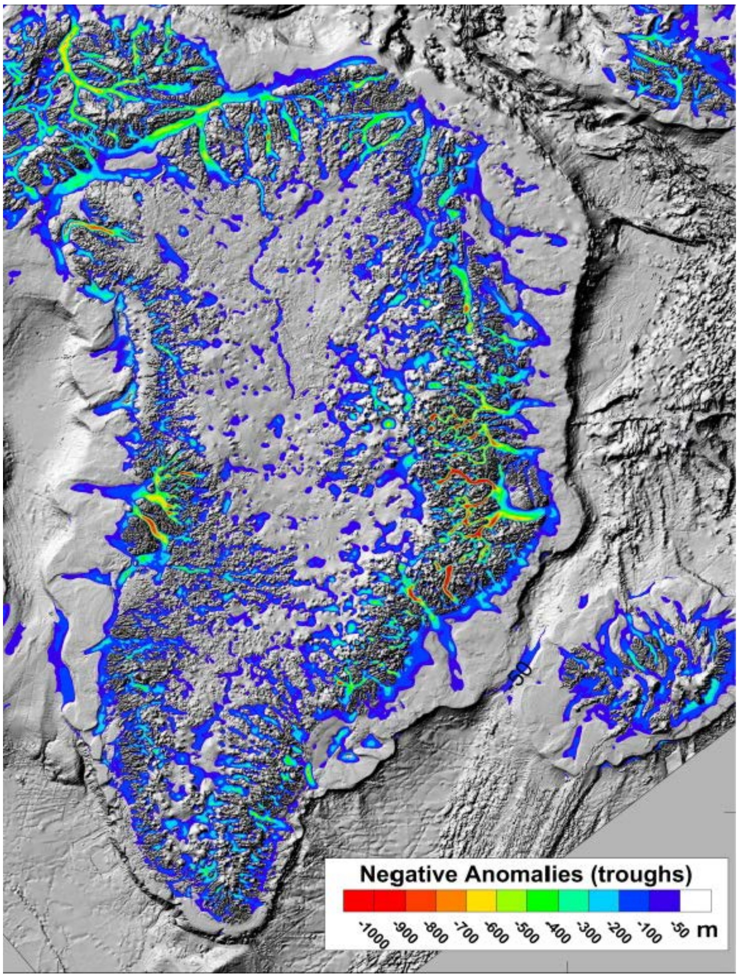

Figure 3-58. *GrIS subglacial topographic anomalies revealing sectors of high amplitude subglacial roughness and relief. The 800 km long, sinuous, 1000 m deep subglacial trough draining Petermann Glacier that extends into the heart of the ice sheet in the far north is clear, as is the Jakobshavn Isbrae trough complex in the west. Credit: A. Hubbard, 2014.*

3.9.4 Surface meltwater production, transfer and storage

SPA and other AWS measurements (e.g. van den Brooke et al. 2011), energy-balance modelling and remote sensing confirm that large seasonal variations of surface meltwater production occur over RGC to elevations that include much of the accumulation area (Figure 3-59a). Such meltwater generated over the ice sheet can be transported in a variety of ways. It can move through supraglacial channel networks and lakes or alternatively, above the ELA it may be retained through refreezing in the snowpack or become stored interannually in SGLs or water filled crevasses. Complex processes of melting and firn refreezing govern the proportion of surface meltwater production that becomes meltwater runoff across the wet snow zone. Field and modelling investigations by, for example Harper et al. (2012), indicate that local high elevation melt should be retained and refrozen within the firn as it percolates downward and fills the pore space, leading to firn densification. Record (high) temperature years have been observed across RGC, characterised by extreme melt and runoff in 2002, 2007, 2010 (van As et al. 2012) and culminated in 2012 when proglacial discharge at Watson River exceeded 3000 m^3/s for a short period in mid-July destroying the Kangerlussuaq road-bridge (Figure 3-59b).

During this 5-day flood event, there was no recorded rainfall or ice-marginal lake drainage and furthermore, analysis of SGL volume changes indicates that such drainage contributed less than 2 % to the overall hydrograph (Fitzpatick et al. 2014). The majority of the record high discharge, which peaks at 3100 m^3/s can hence be attributed to surface meltwater runoff alone. Analysis of melt partitioned into 300 m elevation bands (Mikkelsen et al. 2013, Figure 3-59) indicates that the ice sheet topography at higher elevations (hypsometry) played an important role in amplifying the bulk runoff due to the large increase in contributing area when the melt encroaches farther into the ice sheet interior. However, such hypsometry can only be a controlling factor if the buffering of surface meltwater by firn retention (superimposed ice storage) is hampered within the wet-snow zone of the accumulation area. Bulk runoff and discharge accounting (Figure 3-59) suggest that the effect of meltwater runoff buffering by firn retention was severely reduced during 2012. It appears that percolation of local surface melt within this zone may have been intercepted by perched superimposed ice layers formed during previous warm summers – which is an unexpected observation and somewhat contrary to the hypothesis of Harper et al. (2012). Under such conditions, when downward percolating melt encounters a horizontally extensive yet perched superimposed ice layer within the firn, horizontal water-flow and channelisation will be encouraged within this high elevation zone, thereby contributing to runoff and proglacial discharge. Such an event appears to have occurred in mid-July, 2012 and can be identified by distinctive surface meltwater routing from the KAN_U area as observed within Landsat imagery from this period (Figure 3-59).

Surface water residence timescales vary from hours (in channels) to many weeks (in SGLs) over the summer. Surface melt, percolation and runoff are apparent to at least 140 km from the ice margin (Figure 3-59) and likewise, significant surface ponding of water is also apparent above the ELA revealing that meltwater may be accessing the subglacial environment well within the ice sheet interior, through up to ~ 1500 m thick ice (Fitzpatrick et al. 2014) by a process of hydraulic fracture (see next section; Doyle et al. 2013, 2014).

Satellite MODIS analysis aided by field measurements indicating that ephemeral SGLs cover under 2 % of the ablation zone of RGC, range in size up to ~ 8 km^2, and are over 25 m deep with a volume of 10^6 to 10^7 m^3. The surface hydrological network and location of SGLs and moulins are dictated by the surface topography. SGLs have formed at successively higher elevations during the warmer summers over the last decades (Fitzpatrick et al. 2014) and play an important role in establishing the hydraulic pathways that enable surface water to directly access the ice-bed interface through kilometre thick ice (e.g. Das et al. 2008, Doyle et al. 2013).

Concurrent with increased melt production, runoff and formation of SGLs at higher elevations over the last decades has been the observed darkening of much of the ice sheet surface, including the RGC ablation area (e.g. see Box et al. 2012, Figure 3-59) leading to a net lowering of surface albedo, which itself exerts a primary control on the surface energy balance and hence net melt production (van As 2012). The darkening emanates from surface accumulation of both englacial and aeolian-dust and soot which accumulate over much of the ablation zone as distinct cryoconite holes. Microbial activity appears to flourish in cryoconite holes as sediment, carbon and water interactions create a nutrient source for organic matter, which further reduces albedo and also impacts runoff water quality (Stibal et al. 2012).

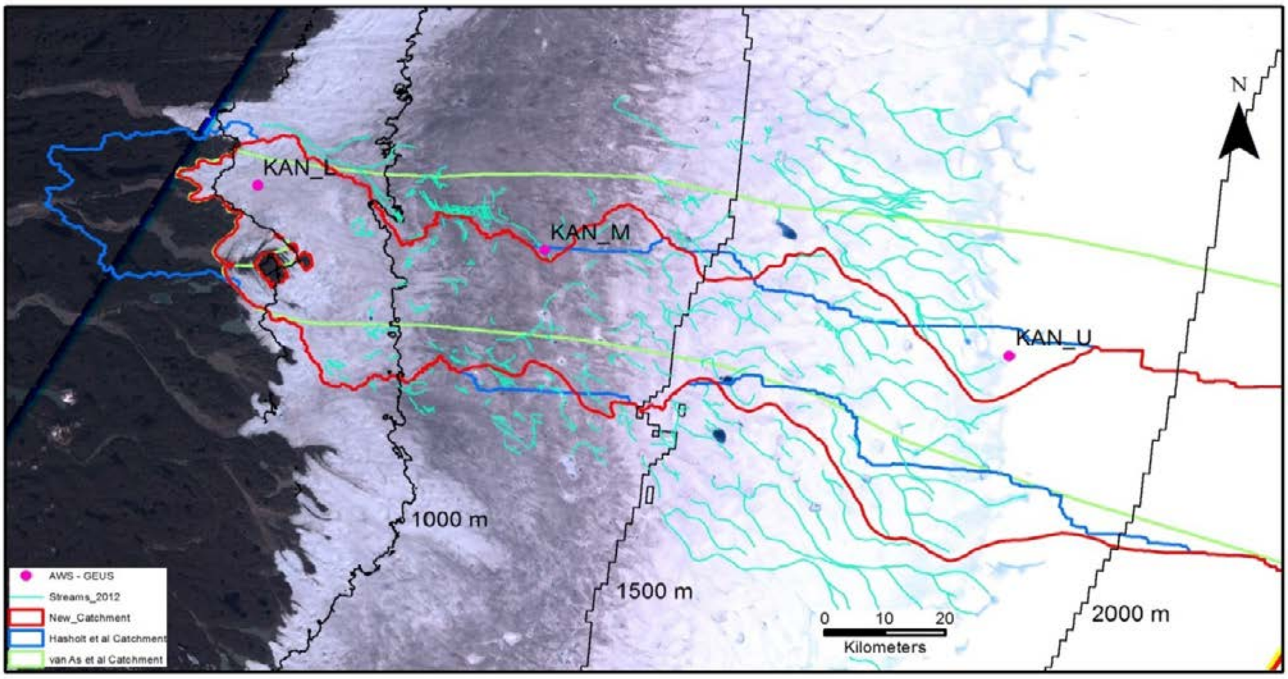

Figure 3-59. *Landsat TM image of RGC on July 10, 2014 indicating the active surface drainage network (cyan) with channels emerging within the wet snow zone well above the ELA at 1550 m and extending almost as far at KAN_U, ~140 km from the margin and underlain by at least 30 m of low density firn. Also shown are the Watson River contributing catchments areas delineated (in blue) by van As (2012) and (in red) by Fitzpatrick et al. (2014).*

3.9.5 Surface to bed coupling

Although melt is inherently diffuse, the delivery of surface water to the bed is focused – in both space and time – by its flow in surface channels and SGLs (Figure 3-60). Passive seismic imaging of hydrofracture by SPA during rapid SGL drainage and moulin initiation confirms that large fluxes ($10^{6–7}$ m^3) of surface meltwater directly access the subglacial environment over very short timescales (hours). GPS observation of rapid SGL drainage (tapping) indicate that short term vertical displacement, a proxy for ice-bed separation and by inference basal water-pressure, is substantial at between ~dm to 1 m in under an hour (Das et al. 2008, Doyle et al. 2013). The accompanying hydro-mechanical impulse (instantaneous shock loading) on the subglacial system, when a water filled hydraulically driven fracture which originates from the ice sheet surface unzips and intercepts the bed through over 1000 m of ice, is likely to be substantial and could potentially be many times overburden pressure for short periods during the event.

A hydrofracture will propagate once the stress concentration at its tip exceeds both the confining pressure and tensile strength of its constraining medium (Mandl and Harkness 1987). When a vertical water-filled crack either builds sufficient hydrostatic head or the stress-field within the surrounding medium is perturbed, then the tip-stress exceeds its confining threshold and the fracture propagates (van der Veen 2007). Since water is ~ 10 % denser than ice and hydrostatic pressure acts perpendicular to the sidewalls at the tip, then the mechanical advantage of the lever increases proportionally as the fracture unzips. Hence, once initiated, a self-propagating hydrofracture is theoretically only limited by water supply to maintain head (Weertman 1973). The SGLs which cover up to 4 % (Fitzpatrick et al. 2013) of the melt-zone of the GrIS are therefore ideal candidates for hydrofracture as they store sufficient water to sustain the mechanism through potentially thousands of metres of ice (Krawczynski et al. 2009).

Furthermore, the large fluxes of mass and energy accompanying such SGL tapping events will likely have a wider regional impact on subglacial dynamics and thermal regimen (Dow et al. 2013).

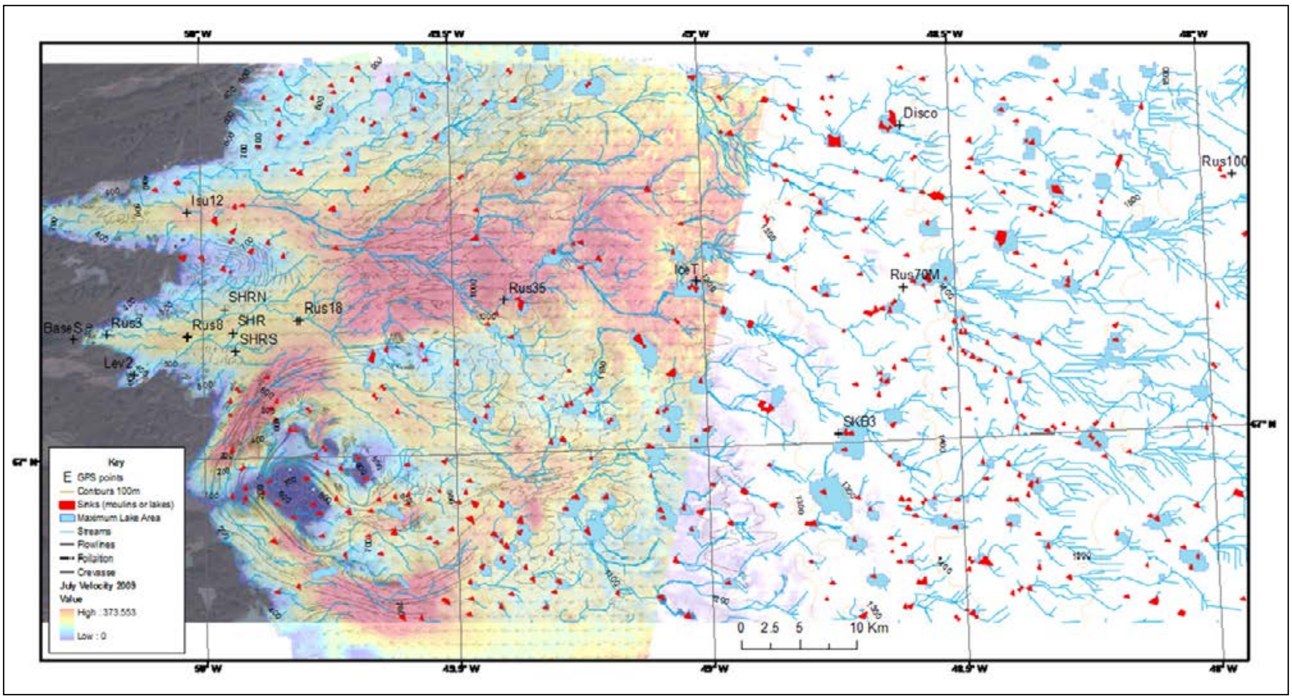

Figure 3-60. *Supraglacial lakes, hydrological network and sinks (moulins) mapped from satellite imagery and ground verified imposed over 2010 surface flow derived from TerraSAR-X feature tracking (Fitzpatrick et al. 2013).*

Cryo-Hydrologic Warming (CHW) has recently been proposed as a potent mechanism that increases the sensitivity and reduces the resilience of ice sheets to climate forcing by changing their 3D thermal structure (Phillips et al. 2010). CHW is based on the concept that across the melt-zone, large fluxes of energy are transferred by surface meltwater as it transits through and beneath the ice sheet via moulins, hydrofractures and associated hydrological network. The effect is a net warming of both the englacial environment and basal interface which reduces ice viscosity, weakens cold-based 'sticky-spots' and facilitates enhanced basal motion over an expanding zone.

Phillips et al. (2010) note that CHW can impact on englacial and basal temperatures in a time-frame of years, which is contrasts with the conventional thermal response time for ice sheets via vertical conduction and advection of centuries to millennia (van der Veen 2001). Satellite (Phillips et al. 2013) and GPS observations (Doyle et al. 2014) from the interior sectors of the GrIS and RGC provide strong evidence for CHW and reveal both year-on-year increases in ice flow at KAN_U (S10) from 51.78 ± 0.01 m/yr in 2009 to 52.92 ± 0.01 m/yr in 2012, or a net increase of 2.2 % (Doyle et al. 2014). This is a key site 140 km from the margin which has shown consistent increases in winter flow over the last 5 years (Figure 3-61).

3.9.6 Subglacial hydrological impacts of surface melt

Diurnal and seasonal fluctuations (up to 250 %) in GPS displacement are phase-correlated with cycles of ablation and subglacial water pressure. This phase-correlation indicates strong spatially-driven perturbations in the subglacial hydrological system along preferential drainage axes as a result of SGL drainage and melt runoff into moulins (Figure 3-61). Borehole water pressure and moulin records indicate that subglacial water pressures for the most part vary within ~ 10 % of ice over-burden pressure (Figure 3-62). Large surface velocity fluctuations are widespread, and it is apparent that basal motion is sensitive to subglacial water pressure. Observed velocity fluctuations are spatially heterogeneous and their magnitude decreases towards the ice sheet interior. Site KAN_U/S10 GPS for example, shows no diurnal variability (to instrument precision of ± 2 cm) though significant seasonal variability up to ~ 4 % (Figure 3-62).

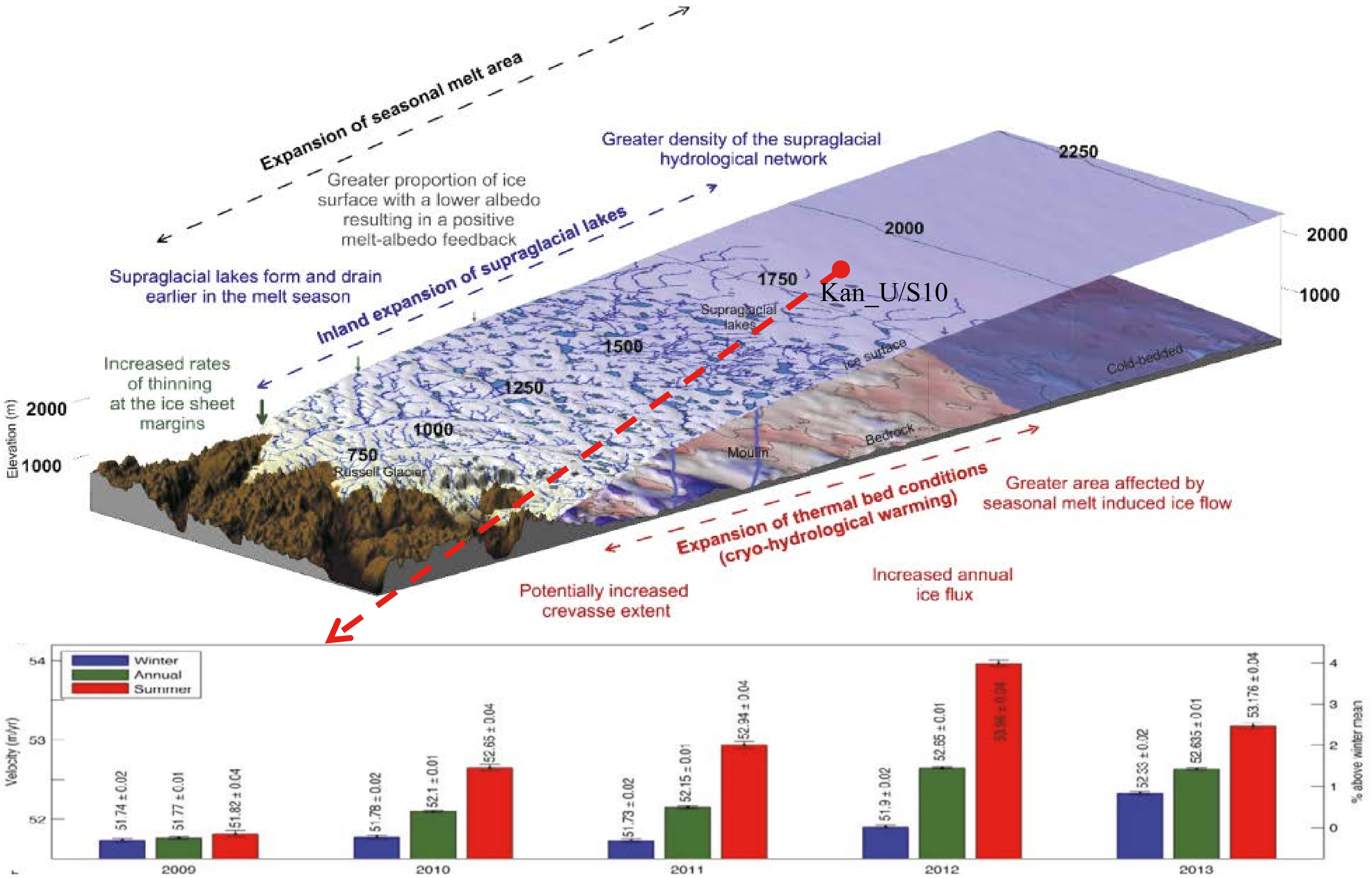

***Figure 3-61.** a) Cross section of RGC showing the location of KAN_U/S10 AWS station. The surface elevation is from Howat et al. (2014), the bed topography is from Bamber et al. (2013), and the basal thermal regime is conceptual. The maximum SGL and stream extent between 2002 and 2012, adapted from Fitzpatrick et al. (2014). b) GPS velocity relative to winter mean at KAN_U/S10.*

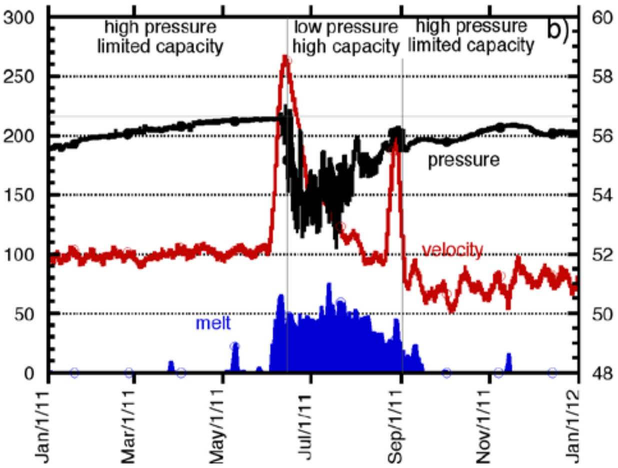

Figure 3-62. *Time series of seasonal water pressure, melt and velocity at KAN_L (SHR), 12 km from the margin of RGC in 2011. The onset of significant melt in late-May leads to high magnitude acceleration and a short period of water pressure in excess of the overburden pressure (horizontal grey line). Later in the ablation season variability in the water pressure remains, but its amplitude is diminished. During the melt season an efficient hydraulic system of channels develops, phase 1, and closes under hydrostatic pressure once the melt decreases, phase 3 in the figure. Note that even in autumn and early winter, single melt events affect water pressure and ice velocity. Ablation rates are vary from 0 to 8.5 cm water equivalent/d. The Y2-axis indicates percentage pressure scaled to overburden. From van de Wal et al. (2015).*

3.9.7 Indirect observations of subglacial conditions

Analysis of subglacial hydraulic potential indicates that basal water flow is likely routed into the main subglacial troughs as revealed in radar compilation (Figure 3-63). Based on the hydraulic potential calculations, specific subglacial drainage basins can be delineated. These can be fed by surface meltwater runoff and storage terms providing individual subglacial catchments with associated hydrographs of groundwater recharge potential. The hydraulic potential reconstruction assumes that water can move freely; thermal zonation at the base of the ice sheet will restrict these flow pathways. Although the calculated subglacial hydraulic potential has major limitations with respect to actual processes and mechanisms by which basal water flows, be it through pervasive film, cavities, conduits/channels or through sediment, it does provide an overview of the most probable regional patterns and are indicative of preferential subglacial pathways/hydraulic axes. A combination of the spatial reflectivity data and hydraulic potential would reveal a more realistic view of the regional subglacial water flow. Reflectivity of the bed returns indicate that the base of the ice sheet is at the melting point to at least ~ 75 km from the margin. Radar analysis also indicated that reflectivity is reduced towards the ice sheet interior which likely indicates frozen subglacial conditions (Lindbäck et al. 2014) in general accordance with the flowline thermo-mechanical modelling presented in SPB. The variability of the reflectivity on a local scale (< km) in these two zones is within the theoretical difference between reflections from water and dry sediment/bedrock. It is possible that the variability is a result of patchiness in the thermal state at the base of the ice sheet, as the reflectivity of water saturated sediments/wet bedrock is less than the Fresnel reflectivity of a water interface. However, the small differences do not give a clear answer and the patchiness of the reflectivity could also result from variations in amount of water at the bed. Attenuation rate of the radar signal within the ice beyond 75 km from the RGC margin is comparable to what is found in cold ice areas in Antarctica, indicating that majority of the ice column is likely cold.

SPA remote sensing observations of surface velocity further reveal high spatio-temporal structure strongly coupled to subglacial topography, ice thickness, meltwater runoff and its routing (Palmer et al. 2011, Fitzpatrick et al. 2013, Figure 3-60 and Figure 3-64). Superimposed on this inherent spatial structure are large, surface driven temporal variations in velocity (from both remote sensing and GPS) with spring acceleration (‘speed-up’) events which are accompanied by widespread surface uplift and storage of subglacial water as observed at KAN_L/SHR (Figure 3-64, Fitzpatrick et al. 2013).

Comparison of the likely subglacial routing, derived from calculated hydraulic potential (Figure 3-63) with the 24 hour residual change in surface velocity derived from InSAR remote sensing (Figure 3-64), enables speculative demarkation of lateral zones of basal water-pressure influence along and away from the preferential subglacial hydraulic pathways. Such a lateral zonation of hydrologic influence away from these pathways has been observed at Haut Glacier d'Arolla by Hubbard et al. (1998) where a suite of instrumented boreholes were drilled and monitored at intervals perpendicular (across the glacier) to the inferred subglacial water channel (termed variable pressure axis) and overall ice flow. Following such a scheme, it would be possible to zone RGC into three sub-sectors: 1) those in the immediate vicinity of a basal hydrological pathway which experience large (e.g. up to ~ 10 %) fluctuations in subglacial water pressure (such as SHR/KAN_L,Figure 3-62); 2) those more distal (beyond ~ 5 km) from the hydrological pathway which are linked, be it dampened, through pressure wave transfer and impulses from the main axes, and 3) zones that are either frozen, distill (beyond ~ 15 km) or located on high subglacial topography with relatively thin ice that are completely isolated from any preferential hydrological axes.

To quantify basal transit times and infer subglacial hydrological conditions, Chandler et al. (2013) supported by SPA carried out rhodamine and sulphur hexafluoride (SF6) tracer experiments. Tracers were injected into the RGC drainage system via moulins over three melt seasons, to observe subglacial drainage properties and evolution up to 57 km from the margin. The results indicate evolution from a slow, inefficient drainage system to a fast, efficient channelised drainage system over the course of the melt season, concurrent with increased meltwater inputs. Farther inland, evolution to efficient drainage occurs later and more slowly, with efficient routing of water established up to 41 km or more from the margin of RGC to where the ice is ~ 1000 m thick (Figure 3-65).

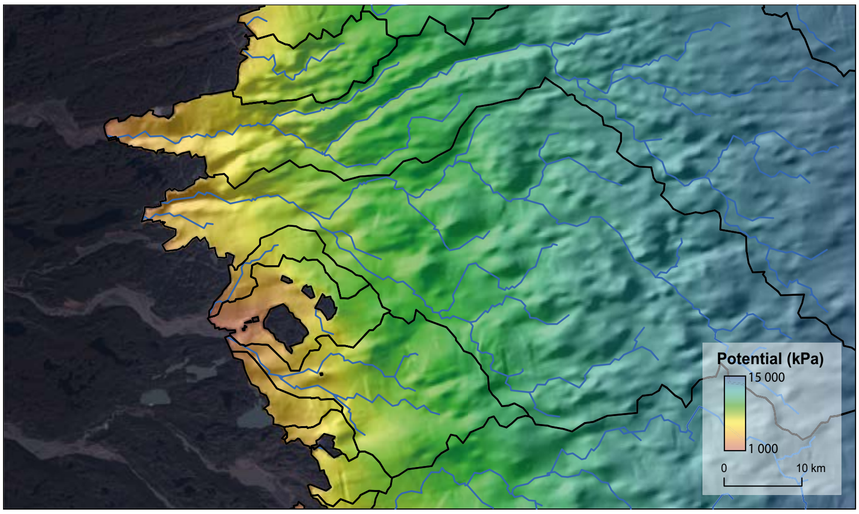

Figure 3-63. *Calculated hydraulic potential for RGC indicating preferential subglacial drainage pathways (blue) and possible catchment boundaries (black).*

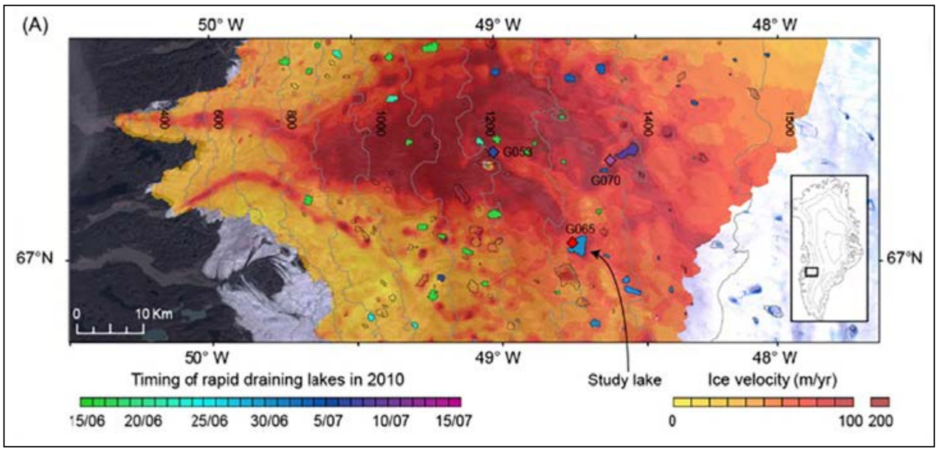

Figure 3-64. *Surface velocity for a 24 hr period derived from Tandem-TSX data in 2012 overlain with the location and timing of rapid SGL drainage in 2010.*

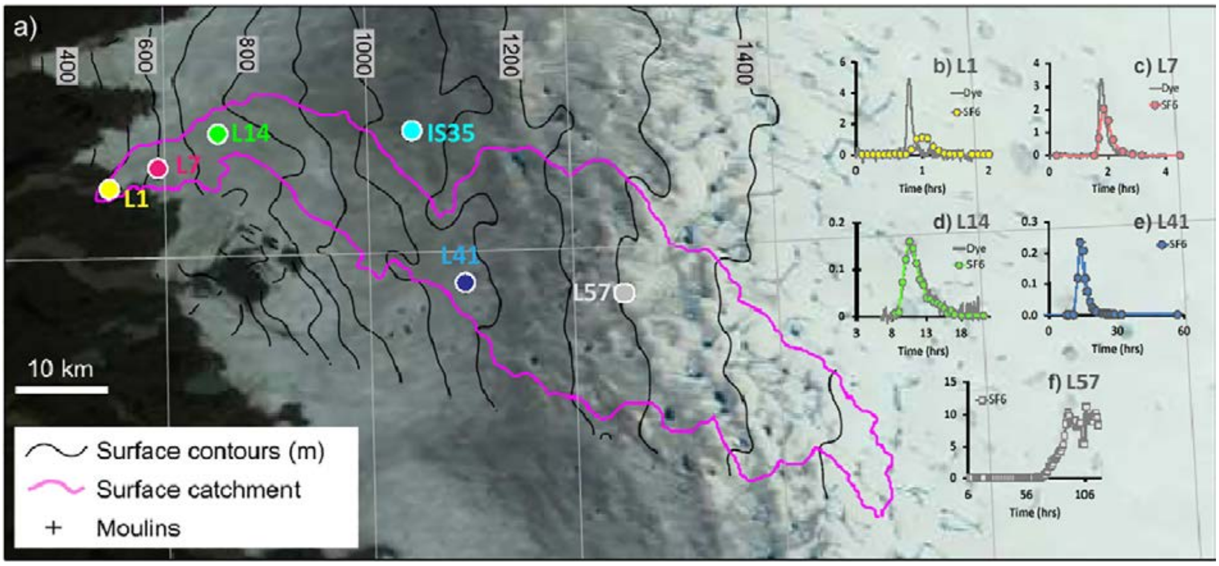

Figure 3-65. *a) Location map of rhodamine and SF6 injection sites. b to f) tracer return curves revealing an efficient hydrological system developing over the ablation season and maintained to 41 km from the margin.*

The inference here is that there is a strong temporal evolution of the subglacial hydrological system from an inefficient/distributed one to an efficient system which modulates water pressure and basal motion. It is suggested by Schoof (2010), Chandler et al. (2013) and many others that this evolution is governed by the rate and quantity of meltwater input and ice thickness/basal motion which will govern conduit closure rate.

3.9.8 Subglacial complications

Seismic reflection experiments strongly indicate that basal sediment sequences of many metres thickness exist up to 70 km inland from the ice margin, and are primarily located within the major troughs (Booth et al. 2012, Dow et al. 2013). Such spatial heterogeneity in subglacial sediment distribution comes as no surprise given the proglacial till distribution that is observable and mapped across the RGC forefield by SPC (see Chapter 5).

Radar and seismic reflection analysis confirms the existence of a perennial subglacial lake of at least 2 km^2 located 75 km from the ice margin under 1100 m of ice. Such elongated/flow parallel subglacial water-bodies are likely to be common under this and other regions of the GrIS (Livingstone et al. 2013, Palmer et al. 2013) given the relief and character of the subglacial topography, and it follows that such localised zones of the bed are at over-burden pressure over long (annual) time-scales.

3.9.9 Synopsis of SPA contributions towards the GAP project questions

The data collected by SPA can provide information towards addressing three of the GAP project questions. A summary of that information is provided below.

Where is the meltwater generated under an ice sheet?

- *In situ* basal meltwater is generated across zones of thick, rapidly-moving ice subjected to high geothermal heating.
- These waters appear to be routed into a subglacial hydrological system which closely maps onto the subglacial topography. The resulting pattern of ice flow is spatially and temporally heterogeneous.
- Above and beyond the ELA, predominantly frozen bed conditions are encountered and coupled with decreasing surface meltwater production (and opportunity to access the bed) yield a relatively frigid/stable basal environment.

What is the hydraulic pressure situation under an ice sheet?

- Tapping of SGLs through over 1200 m of ice to the base of the ice sheet delivers large quantities of meltwater to bed in a short period of time, having potential to alter basal water pressure and drainage system characteristics.
- Perennial SGLs provide a long term groundwater supply at overburden pressure.

What is the chemical composition of glacial water when, and if, it reaches repository depth?

- Throughout the summer melt season large fluxes of rainfall, meltwater and runoff which interchange freely with the atmosphere, transit the supraglacial environment on time-scales between hours and weeks across the ablation area of the ice sheet. However, currently with increased atmospheric temperatures and moisture availability, the temporal and spatial footprint of 'the ablation area' is expanding into the ice sheet interior and also into the equinoctial, autumnal season.
- Runoff is a catalyst for microbial activity through exposure to surface accumulations of cryoconite.
- Thick and extensive layers of sediment lie beneath some regions of the ice sheet and likely within the deep troughs that dissect the marginal zone. Subglacial water quantity, quality and pressure will be modulated by contact with such basal sediment.

To understand the context of the information collected by SPA, and how it can be used to address the GAP project questions, it is important to understand the following qualifications. The GrIS is deglaciating; retreat has been ongoing since the last glacial maximum when it extended to the continental shelf edge and converged in the far NW sector (Humbolt and Petermann Glaciers) with the Laurentide Ice Sheet across Nares Strait and the Kane Basin (Figure 3-66). This retreat has been punctuated by short periods of relative stability or advance during short lived cool episodes. Despite this, over the last decade Greenland has experienced record warm atmospheric and oceanic temperatures which have led to an episode of widespread ice thinning and retreat. In light of this, SPA findings must be viewed most cautiously within the context of extrapolating conditions over an entire ice sheet cycle. The highly dynamic behavior of the subglacial environment that is evident from SPA observations, is quite possibly confined to such short but intense episodes of rapid deglaciation and retreat. During the prolonged cool periods of ice sheet buildup, advance and stability, the ablation zone will be much reduced both in area and intensity. A larger proportion of the subglacial environment will be frozen with significantly less surface meltwater available to impact on it. Hence, caution must be exercised when extrapolating contemporary conditions at the margin of the GrIS both in time and space. Despite this, SPA observations indicate a highly dynamic subglacial hydrological environment across much of the ablation zone of the SPA study area. This behaviour is observed elsewhere across the GrIS and hence can be considered typical. Even if this behavior is not representative over an entire ice sheet cycle, the impact of even short-lived episodes of rapid-retreat on groundwater quality and recharge capacity will be substantial.

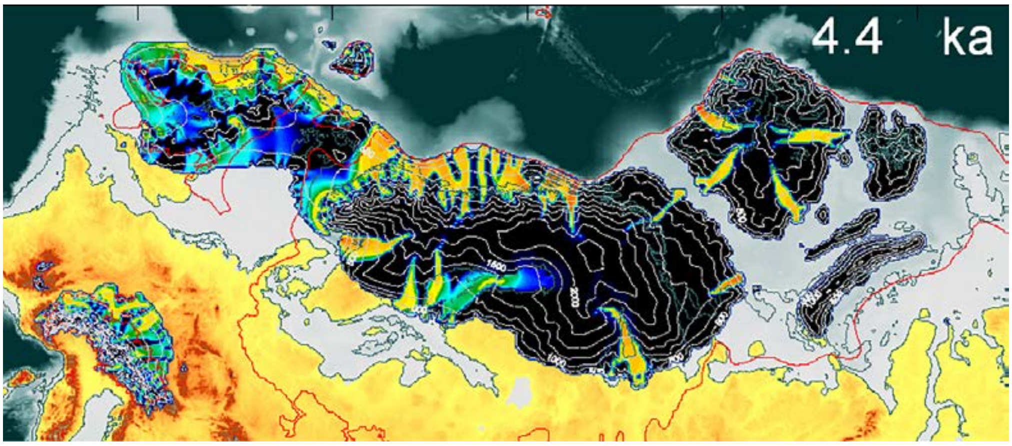

Figure 3-66. *Simulated advance of the European and Fennoscandian/Barrents Sea Ice Sheets during the last glacial. Even though rapid, fast-flowing ice streams are dominant the dynamics and mass-transfer of the ice sheet indicate that the majority of the subglacial enrvironment is frozen. Credit: A. Hubbard, 2014.*

4 Subproject B – Subglacial hydrology

4.1 Introduction and objectives of SPB

4.1.1 Background

Substantial meltwater exists on the ice surface of the GrIS ablation zone, and, over the last decade, substantial scientific attention has focused on the fate of this meltwater and its impacts on the ice sheet's glaciological processes. Some authors have noted that water could not easily penetrate the ice located around the margins of the GrIS, where thickness often exceeds 1 km and temperatures are well below 0 °C (e.g. Alley et al. 2005, Catania et al. 2008); however, other authors have observed that large streams rarely pour off the surface of the ice sheet around its edges, but very large streams frequently emerge from beneath the ice at terrestrial margins (e.g. Thomsen and Braithwaite 1987, Zwally et al. 2002). The latter implies that a substantial fraction of ice surface melt, perhaps nearly all of it, does find rapid access to the bed well inward from the margin of the GrIS.

Basal melt from geothermal heating was clearly present in early ice sheet model output (e.g. Huybrechts 1996), but had not been a targeted focus of modelling efforts. Unlike Antarctica, Greenland has a very high snow accumulation rate, which drives fast vertical flow, thereby transferring cold from the atmosphere to the ice-bedrock interface (e.g. Parizek and Alley 2004). The interface (i.e. the glacier "bed") near the centre flow-divide was believed to be well below freezing, while the margins were thought to be melted, but without substantial sliding motion. Deeper understanding of the GrIS basal thermal conditions was not of high scientific interest until recently.

The final source for water at the bed of the GrIS is melting due to frictional heating from ice sliding over bedrock, which has only recently been included in ice sheet models (Brinkerhoff et al. 2011, Meierbachtol et al. 2011). This is because sliding processes previously had been considered unimportant to the GrIS. A series of ground observations (e.g. Zwally et al. 2013) and remote sensing work (e.g. Rignot and Kanagaratnam 2006, Joughin et al. 2008), however, shifted this paradigm by demonstrating that the ice sheet undergoes time-variable velocity variations, which can only be attributable to high rates of basal sliding. Melting from frictional heat is now recognised as an important source of basal meltwater.

An inaccurate assessment is that 'what used to be thought correct about the GrIS basal conditions and hydrology has now been proven wrong'. Rather, a more accurate description is that there were few scientific investigations and discussions of the role of water in the GrIS until the last decade. Recent acknowledgment that water is present at the base of the ice sheet, originating from both the penetration of surface melt and from *in situ* melt, yields numerous important questions related to the distribution and characteristics of the water.

4.1.1.1 Transferability of existing information

Prior to the GAP, there had been extremely limited direct observation of the hydrologic processes at the base of an ice sheet, allowing no firm conclusions to be made about subglacial conditions. If the extensive observations and interpretations from mountain glaciers were extended to the ice sheet setting, large temporal and spatial gradients in subglacial water pressure could be hypothesised; however, the uniquely thick and cold ice found in ice sheets might result in substantially different hydrologic processes from those observed in a mountain glacier setting. The temporal and spatial gradients in water pressure were, therefore, unclear. Recent interpretations of ice sheet hydrology have frequently invoked ideas developed from prior studies of mountain glaciers (e.g. Schoof 2010, Sole et al. 2011, Sundal et al. 2011, Bartholomew et al. 2012). These studies have sought to link observed temporal variations in surface velocity to inferred changes in the basal drainage system, based on conceptual models developed from studies of mountain glaciers.

An important body of early work conducted for SKB addressed the interaction between subglacial conduits and groundwater flow (Boulton et al. 2001, 2007, 2009). Large conduit drainage features at the bed, termed R-channels, are theorised to be the dominant form of basal water drainage at the base of the ice (Figure 4-1). Such features have been well documented in mountain glaciers from both theoretical (e.g. Shreve 1972) and observational (e.g. Nienow et al. 1998) perspectives; widespread eskers left behind by ice sheets indicate this form of drainage is common, at least in certain places and/or times of glaciation. The conduits are suggested to carry surface melt that penetrates to the bed and water generated from basal melt of ice, as well as substantial quantities of upward flowing groundwater due to the low water pressure within the conduits relative to adjacent areas. The latter, if confirmed, implies that groundwater flow conditions at a given location are highly altered when ice sheets are present relative to when they are absent.

Distinct differences, however, potentially exist between the hydrology of an ice sheet versus that of a mountain glacier. Water can reach the bed of a typical mountain glacier almost anywhere due to the relatively thin (often temperate) ice, and due to water's ability to flow inward from the valley walls, either along the ice/bed contact or as groundwater baseflow. Steep topography of the glacier and the surrounding landscape provide high elevation head gradients for water in both the glacier and groundwater systems. The time/space distribution of water delivery to the bed of the GrIS is less clear and it is likely to be more limited also, as there is no terrestrial topography standing above the ice surface interior from the margin. The difference in depth-scales between mountain glaciers and ice sheets also implies a potentially greater role for pressure effects in driving basal physics. For example, the higher pressures in ice sheets may change melting or phase-change phenomena, such as heat pumping, and there is potentially faster basal system reorganisation under higher differential stresses, as present in ice sheets.

Despite many decades of research, many poorly understood aspects of the hydrology of mountain glaciers remain. Nevertheless, mountain glaciers provide a wide body of literature presenting extensive field observations from numerous different glaciers and detailed theoretical work. All scientific results derived from mountain glaciers are not necessarily representative of ice sheets because the size, geometry and thermal conditions are so different between the two types of ice masses. The primary goal of this research is to investigate the GAP study area, representing a continental ice sheet instead of a system of mountain glaciers. Existing understanding of glaciological processes, derived mainly from the study of mountain glaciers, must be incorporated into the interpretation and/or contrasted with observations from the study site.

4.1.2 SPB project goals

The purpose of SPB is to conduct comprehensive research on the basal hydrological system of the GrIS. Motivation stems from the need for basic information on the water conditions at the base of ice sheets for use in safety assessment considerations for DGRs for nuclear waste. The goal is to further the fundamental understanding of how continental ice sheets potentially influence groundwater system behaviour, both chemical and physical aspects, in crystalline rock settings at proposed repository depths (i.e. up to 500 m b.g.s.).

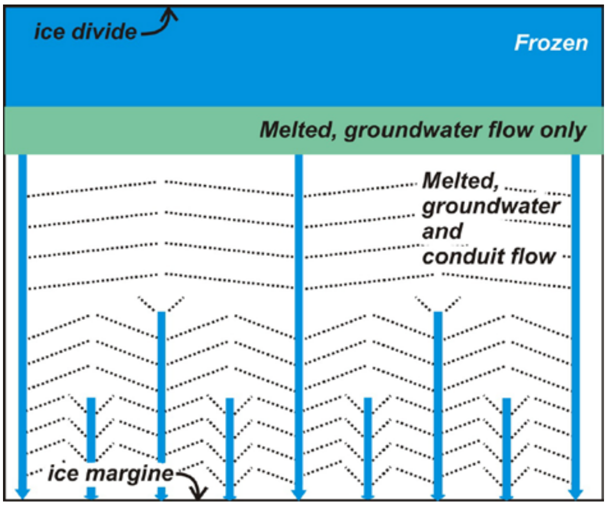

Figure 4-1. Boulton's conduit network. Frozen and melted areas of the bed shown. Blue lines represent major conduit pathways. The conduits are believed to have low pressure relative to the remaining ice/bed interface. Dotted lines show pathways for flow in the groundwater system, contributing water to, and driven by, a pressure gradient created by the low pressure conduits.

This subproject is focused on providing information to address two of the GAP questions: *Question 1) Where is the meltwater generated under an ice sheet*? and *Question 2) What is the hydraulic pressure situation under an ice sheet, driving groundwater flow?*

In addition, SPB aims to provide basic information and datasets to SPA and SPC. Specifically, SPB provides direct observation and modelling of basal conditions, which is relevant to surface conditions addressed by SPA and groundwater/chemical conditions addressed by SPC. Also, a focus for SPB is the characterisation of the region near the bedrock borehole extending under the ice (DH-GAP04), which is drilled and monitored as part of SPC (see Chapter 5).

4.1.2.1 Implementation

Direct measurement of basal conditions everywhere on the GrIS is not possible. Remote sensing techniques have, thus far, been unsuccessful at quantifying basal temperature or the quantity of water at the bed, and there is little progress to-date to suggest that science is close to solving this problem. Modelling is, therefore, the only mechanism for extending the understanding of basal conditions away from the handful of point measurements. In the case of ice sheet hydrology, where all processes are not fully understood, the processes that are numerically simulated by models need to be derived from observational and theoretical arguments. Further, model representation of the GrIS basal conditions is governed by numerous assumptions and prescribed conditions, such as geothermal heat flux at the bed, ice deformation rate, basal sliding rate, surface climate and surface mass balance. Relatively minor adjustments to the model representation of these various parameters can have a dramatic impact on model results. A key step to successfully modelling basal conditions is to collect field datasets and a thorough interpretation of those datasets to improve understanding of glacial processes. The datasets both drive the theory behind the model simulations and constrain the models with real world observations.

The goals of this project are achieved through a combination of direct field observation and numerical modelling. No single observational campaign reveals all relevant aspects of interest with respect to basal water. Consequently, an observational campaign with a multi-faceted approach was necessary. The core of the observational campaign was direct measurement of basal water via borehole experiments and monitoring. Ancillary observations, such as ice velocity, surface meteorological conditions, and geochemical analysis of basal water and sediment, are essential to advancing understanding as well. For example, ice velocity alone is of little concern to the basic constraints on the safety of nuclear waste repository sites, but changes in ice velocity can act as an indicator of the distribution of water at the bed, which is relevant to the overall project goals. In addition, ice sheet models are too under-constrained to run in isolation without feedback from as many different types of field observations as possible, such as surface velocity, ice temperature, etc.

The basic measurements and their purpose with respect to overall goals of this project are as follows.

1) Basal water pressure – a direct measure of the pressure within the basal hydrological system. This is measured by placing a water pressure transducer at the base of boreholes. These data are relevant to characterising the basal boundary condition, which serves as a boundary to groundwater flow near and beneath ice sheets.
2) Borehole impulse tests – experiments conducted by artificially perturbing the water level in open boreholes. Results provide information about the state of the hydrological system and its ability to respond to transient perturbations.
3) Basal water and sediment chemistry – geochemical analysis of subglacial waters and subglacial sediment collected in boreholes drilled to the bed of the ice sheet, and by sampling of outlet streams. These data can reveal basic water flow processes at the bed, as well as chemical conditions at the groundwater/ice interface.
4) Surface velocity – measured by installation of continuously logging GPS stations mounted on the ice and referenced to a station in front of the ice margin (these GPS stations are individual GPS stations installed in the ice drilling study area and are not part of the SPA GPS network described in Section 3.4). Although poorly constrained, time changes in sliding velocity often indicate changing basal hydrological conditions. However, constraining the changing hydrological conditions exactly is difficult.

5) Surface meteorology – measured by installation of sensors on the glacier surface. These data are used for simplistic comparison with meltwater generation and forcing on basal processes.
6) Ice temperature – measured by installation of temperate sensors at intervals along boreholes. Data are used for comparison to numerical model output; models used to investigate frozen versus melted conditions at the ice sheet bed.

In addition to the field measurements, numerical simulations (ice sheet modelling) of e.g. basal temperature and basal water production were done for comparison to field observations and to provide boundary conditions for groundwater modelling.

4.2 SPB study sites and ice boreholes

Field research by SPB at the GAP field sites was conducted each year from 2010–2013. Ice boreholes were drilled and instrumentation was installed during the months of June and July of each of the study years. The sites were revisited each September to download data and to prepare some instruments for over-wintering. Because the various study sites were installed in different years, and the instrumentation collected data for limited time periods, there is not complete time overlap between the datasets from all sites.

The field efforts were focused on data collection at three different case-study regions located around the GAP study area of the western GrIS (Figure 4-2). Each of the case-study regions was selected to represent specific glaciological settings based on ice thickness, basal and surface topographic gradients, and proximity to the ice margin (Figure 4-3). The case-study regions included sites located 1) close to the ice margin, 2) within the ice sheet interior, and 3) over a deep bedrock trough. Four margin region sites were installed 0.1–3 km from the ice margin, and two interior region sites were installed 15 and 30 km inland from the nearest exposed land. Multiple boreholes were installed at each study site, and various other experiments were conducted as well. Data exist for a total of seven sites spread among the three case-study regions.

4.2.1 Site and Borehole Notation

Drilling sites and boreholes are summarised in Table 4-1 and identified with the schema "GLXX-YZ",

where:

'GLXX' = Greenland GAP study site and year site was installed,

'Y' = site number for the given year, and

'Z' = specific boreholes drilled at a site, given alphabetically in order of drilling.

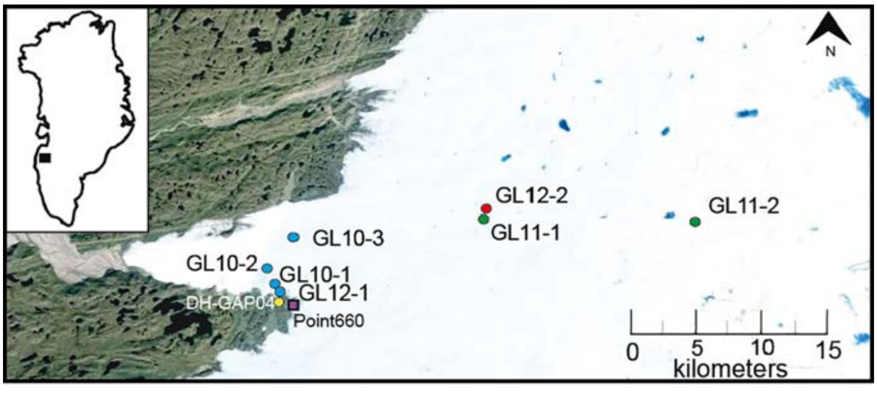

Figure 4-2. *Map showing GAP study sites; colour of each circle on the ice indicates the site region: margin = blue, interior = green, trough = red. Yellow circle = location of bedrock borehole DH-GAP04. Purple square = location of Point 660. Dark blue areas show the location of supraglacial lakes (SGL).*

Table 4-1. Information on all boreholes; Showing hole ID, site name, region, drill date, latitude (UTM/WGS84 ellipsoid), longitude (UTM/WGS84 ellipsoid), x-easting (UTM/WGS84 ellipsoid), y-northing (UTM/WGS84 ellipsoid), zone (UTM/WGS84 ellipsoid), hole depth, bed elevation (above UTM/WGS84 ellipsoid). N/A under the bed elevation column refers to boreholes that did not successfully reach the bed.

ID	Site	Region	Drill Date YYYY/MM/DD	Lat.	Long.	X-east	Y-north	Zone	Elev. (m)	Depth (m)	Bed (m)
1A	GL10	Margin	2010-06-12	67.1622	−50.0643	540527	7449768	22 N	520	98.0	422.0
1B	GL10	Margin	2010-06-13	67.1621	−50.0644	540520	7449760	22 N	519	92.5	426.5
1C	GL10	Margin	2010-06-14	67.1625	−50.0633	540570	7449803	22 N	523	91.0	432.0
1D	GL10	Margin	2010-06-14	67.1624	−50.0633	540568	7449788	22 N	523	98.5	424.5
1E	GL10	Margin	2010-06-16	67.1625	−50.0629	540585	7449804	22 N	525	91.9	433.1
1F	GL10	Margin	2010-06-17	67.1627	−50.0620	540623	7449820	22 N	532	102.0	430.0
2A	GL10	Margin	2010-06-20	67.1670	−50.0665	540420	7450304	22 N	554	144.0	410.0
2B	GL10	Margin	2010-06-21	67.1671	−50.0665	540421	7450311	22 N	554	148.7	405.3
2C	GL10	Margin	2010-06-23	67.1670	−50.0663	540429	7450305	22 N	555	146.3	408.7
2D	GL10	Margin	2010-06-23	67.1671	−50.0662	540436	7450314	22 N	555	145.6	409.4
2E	GL10	Margin	2010-06-25	67.1671	−50.0664	540427	7450317	22 N	556	148.7	407.3
3A	GL10	Margin	2010-06-30	67.1917	−50.0293	541991	7453081	22 N	618	577.3	N/A
3B	GL10	Margin	2010-07-02	67.1916	−50.0295	541984	7453065	22 N	619	700.4	N/A
1A	GL11	Interior	2011-07-02	67.1952	−49.7195	555381	7453708	22 N	848	457.5	390.5
1B	GL11	Interior	2011-07-04	67.1953	−49.7191	555397	7453720	22 N	850	466.0	384.0
1C	GL11	Interior	2011-07-06	67.1951	−49.7189	555407	7453695	22 N	849	459.5	389.5
2A	GL11	Interior	2011-07-13	67.2016	−49.2891	573975	7454867	22 N	1095	254.5	N/A
2B	GL11	Interior	2011-07-14	67.2014	−49.2888	573987	7454854	22 N	1092	821.0	271.0
2C	GL11	Interior	2011-07-17	67.2013	−49.2893	573966	7454837	22 N	1087	816.0	271.0
2D	GL11	Interior	2011-07-18	67.2013	−49.2891	573974	7454843	22 N	1088	814.5	273.5
1A	GL12	Margin	2012-06-07	67.1593	−50.0593	540748	7449447	22 N	482	116.7	365.4
1B	GL12	Margin	2012-06-07	67.1592	−50.0593	540748	7449434	22 N	479	114.5	364.6
2A	GL12	Trough	2012-06-13	67.2042	−49.7179	555429	7454718	22 N	849	701.3	147.7
2B	GL12	Trough	2012-06-15	67.2040	−49.7179	555432	7454688	22 N	849	715.3	133.7
2C	GL12	Trough	2012-06-17	67.2037	−49.7178	555437	7454660	22 N	849	691.5	157.5
2D	GL12	Trough	2012-06-20	67.2039	−49.718	555430	7454688	22 N	849	697.7	151.3

The digital elevation model (DEM) from SPA (see Section 3.2.3) used to create surface and bedrock topographic maps was mined to best represent topographic features with respect to particular regions (Figure 4-3 and Figure 4-6). Discrepancies between the 500 × 500 m DEM pixels and GPS/borehole derived data (averaged for each site) are compared in Table 4-2. The largest discrepancy in ice thickness existed for GL12-2, where the DEM fails to estimate the bed elevation within the trough. Although there is a trough feature in the DEM, the elevation of the bed is overestimated by about 275 m.

4.2.2 Margin case-study region: (sites GL10-1, GL10-2, GL10-3, GL12-1)

This case-study region addresses ice sheet conditions located adjacent to the land terminating margin of the GrIS. The rationale for selecting this case-study region is two-fold. First, study sites in this region are used to investigate ice sheet basal conditions near the ice margin, where the ice is thinner and the climate is warmer relative to the interior. Second, the study sites in this region are used to provide constraining information for the deep bedrock borehole extending under the ice, and drilled and monitored as part of SPC activities (Chapter 5). These sites represent the near-field boundary conditions in the deep bedrock borehole.

Table 4-2. A comparison of DEM topography and data collected topography from GPS and borehole drilling. Surface and bed elevation are given by metres above the WGS84 ellipsoid. Ice thickness is then derived from ice surface and bed elevations. The difference between the DEM and GPS/borehole data is given by subtracting DEM results from GPS/borehole results. Since each site is represented by its own DEM pixel (excluding GL10-1 and GL10-2, which share one), GPS/borehole data were averaged for each site in order to be reasonably comparable. N/A is for boreholes which terminated before reaching the bed.

		DEM			**GPS and Boreholes**			**Difference**		
Region	Site ID	Surface	Bed	Thickness	Surface	Bed	Thickness	Surface	Bed	Thickness
Margin	GL10-1	506	506	0	523.7	428	95.7	17.7	−78	95.7
	GL10-2	506	506	0	554.8	408.1	146.7	48.8	−97.9	146.7
	GL10-3	567	546	21	618.5	N/A	N/A	51.5	N/A	N/A
	GL12-1	465	465	0	480.5	365	115.5	15.5	−100	115.5
Interior	GL11-1	839	464	375	849	388	461	10	−76	86
	GL11-2	1116	366	750	1090.5	271.8	818.7	−25.5	−94.2	68.7
Trough	GL12-2	813	423	390	849	147.6	701.4	36	−275.4	311.4

Data were collected from this case study region in 2010 (sites GL10-1, GL10-2, GL10-3) and 2012 (GL12-1). These sites are located from 100 m to ~ 3 km from the ice margin. All sites are located on the ice sheet adjacent to a marginal area commonly referred to as "Point 660". This is the area where the gravel road from Kangerlussuaq terminates at the ice margin. This is also the area where SPC drilled a deep angled bedrock borehole (DH-GAP04, ~ 700 m length and 650 m deep) that extends beneath the ice sheet (see Chapter 5).

The ice thickness in the margin case-study region ranges from zero at the margin to 100–200 m ~ 1 km inward from the margin, and then rapidly increases towards the main truck of Isunnguata Sermia where the ice thickness is many hundreds of metres just 3 km inland from the margin. The bed topography is also variable, with locally steep slopes (Figure 4-3). The surface topography in this area is steep and hummocky within 2 km of the ice sheet margin. The surface slope is highly variable, and sometimes averages 10 degrees over distances of hundreds of metres. The area has many crevasses. There are no large supraglacial lakes in this area, but there are occasional small ponds on order of 10 m in diameter. The surface has many small streams; some terminate in small moulins, while others run off the ice margin. Surface ablation is very high, though spatially variable; ablation of > 3 m/yr is common.

A total of 15 boreholes were drilled in this region, and 13 of these holes reached the bed. Measurements collected include:

- Basal water pressure.
- Ice temperature.
- Results from borehole impulse experiments.
- Borehole water samples.
- Stream outlet water samples (these samples represent a natural averaging of subglacial conditions collected from the terminal outlet of the Isunnguata Sermia Glacier).
- GPS surface velocity values.
- Meteorological data.

4.2.3 Interior case-study region: (sites GL11-1, GL11-2)

The interior region was selected to represent ice sheet basal conditions beneath thick ice and away from the margin. This is representative of a high degree of glaciation, analogous to having thick ice overlying a repository site (but does not necessarily represent conditions at the ice divide where the ice can be > 2000 m thick and frozen to the bed). In addition, with straight-line distances of 15 and 30 km from DH-GAP04, these sites represent the far-field boundary conditions for the deep bedrock borehole (see Section 5.3.1.3).

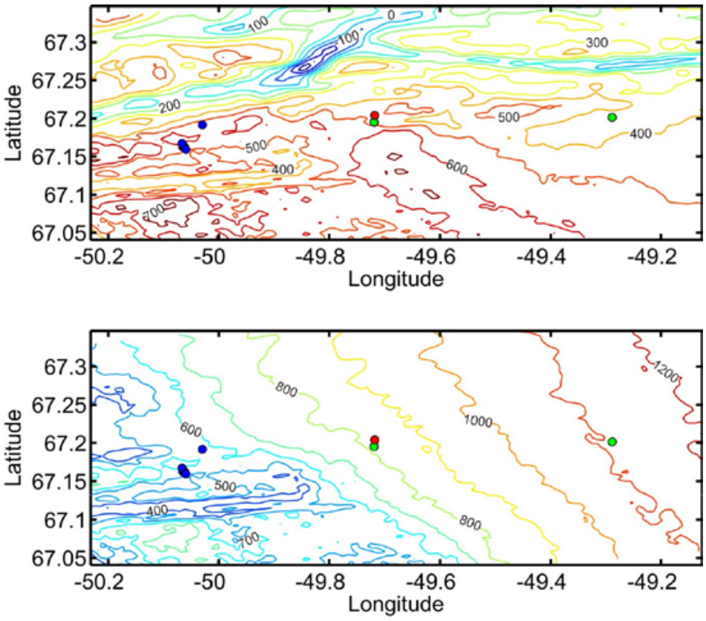

Figure 4-3. Bed (top) and surface (bottom) topography for the GAP study area, highlighting site locations using the same colouring scheme as Figure 4-2. Contours are labelled by elevation and are spaced by 100 m, with mapping done on a 54 × 25 (x, y) km grid.

Data were collected from this case-study region during 2011. Two sites were installed, one located 15 km inland from Point 660 (GL11-1), and one located 30 km inland from Point 660 (GL11-2). Multiple boreholes were installed at each site.

Site GL11-1

This site is located ~ 15 km from the ice margin at Point 660, at an elevation of ~ 850 m above UTM/WGS84 ellipsoid. The surface topography has less of a slope than near the margin, averaging less than 1° when measured over one km, but steeper gradients than farther inland (Figure 4-5). There are numerous crevasses in the area, with very small openings (< 10 cm), several large surface melt streams, and scattered small moulins. The surface melt is on the order of 2.5 m/yr. There is one lake located about 750 m away from the site that formed in June/July of 2012, but did not form in 2011. Ice thickness at the site is ~ 460 m.

A total of 3 boreholes were drilled to bed at this site. Measurements collected include:

- Water pressure,
- Ice temperature,
- Water levels during borehole impulse tests,
- Borehole water samples,
- GPS surface velocity, and
- Meteorological data.

Site GL11-2

This site is located 30 km inland from the ice margin at Point 660, at an elevation of ~ 1190 m above UTM/WGS84 ellipsoid. The surface topography is the flattest of any of the sites (Figure 4-3). The melt rate here is about 2.5 m/yr, which is not substantially lower than at site GL11-1. One large subglacial lake was observed about 1 km away, and numerous lakes exist within 5 km of the site. No crevasses were observed. The area has numerous surface melt streams, and, in 2011, one very large moulin was observed ~ 1 km north of the site. The ice is 825 m thick and the bed is relatively flat (Figure 4-5).

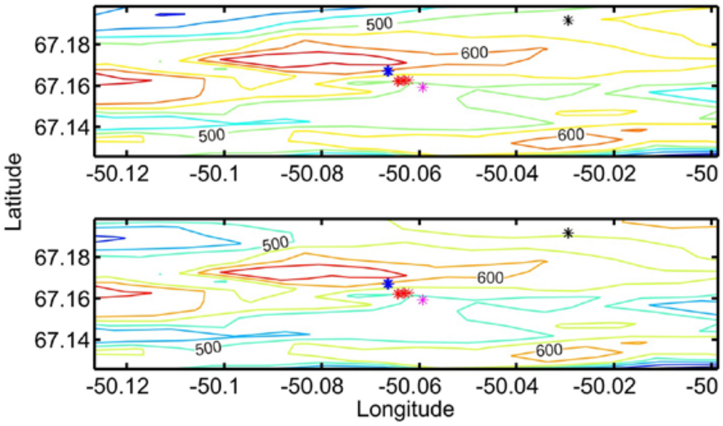

Figure 4-4. Bed (top) and surface (bottom) topography showing boreholes (stars) at margin sites GL10-1 (red), GL10-2 (blue), GL10-3 (black) and GL12-1 (magenta). Contours are labelled by elevation and are spaced by 50 m, with mapping done on a 7 × 7 (x, y) km grid.

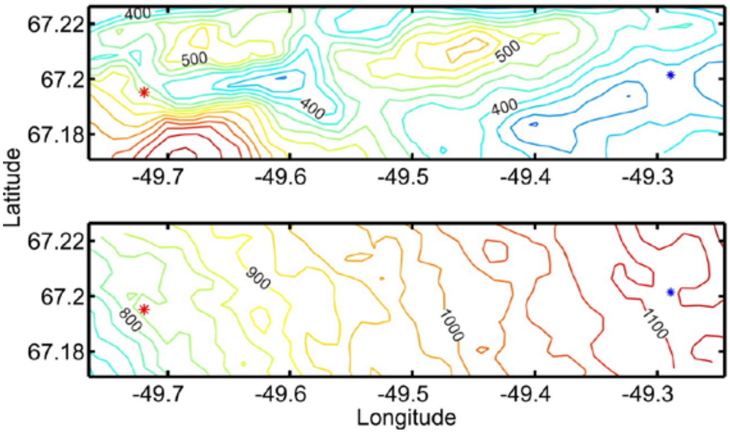

Figure 4-5. Bed (top) and surface (bottom) topography of interior sites GL11-1 (red) and GL11-2 (blue). Contours are labelled by elevation and spacing is 25 m, with mapping done on a 23.5 × 2 (x, y) km grid.

A total of 4 boreholes were drilled at this site, with 3 extending to the bed. Measurements include:

- Water pressure.
- Ice temperature.
- Borehole impulse tests.
- Borehole water sample.
- GPS surface velocity.
- Meteorological data.

4.2.4 Interior trough case-study region: (site GL12-2)

Data were collected in this region in 2012, with just one study site representing the region. The trough site was selected to represent deep basal conditions, where water is potentially routed along the bed to the trough. This region is located 15 km inland from the ice margin at Point 660, and just 1 km north of GL11-1. The trough region is distinctly different than the nearby interior region because it overlies a deep bedrock trough, with ice thickness increasing by > 50 % over the trough. Ice thickness at the trough site is ~ 700 m, while just 1 km south, at the interior site, the ice thickness is only 460 m. Figure 4-6 shows that the trough has relatively steep walls, but the ice surface shows no apparent changes over the trough area. The surface melt is on the order of 2.5 m/yr. The nearest lake is 1.75 km to the south and is the same lake that is 0.75 km south of GL11-1.

A total of 4 boreholes were drilled to the bed at one site within this case-study region. Measurements include:

- Water pressure.
- Ice temperature.
- Borehole impulse tests.
- Borehole water samples.
- GPS surface velocity.
- Meteorological data.

4.2.5 Borehole drilling

All boreholes were drilled using hot water methods (Engelhardt et al. 1990, Humphrey and Echelmeyer 1990, Taylor 1984). A new hot water drill was built specifically for this project. The drill was designed to be capable of drilling to at least 1000 m depth at a relatively high rate, while remaining light weight and breakable into small pieces for easy transport. No single component weighs more than 110 kg. This substantially reduces transportation costs and enables the drill to be moved up to 100 m by a small field team. The penalty for the light weight design is that many components operate at design maximums, thereby increasing the burden of closely monitored drilling due to high risk of drill failure.

Water used for drilling was captured in surface streams using a low pressure submersible pump and was transferred to a storage reservoir (Figure 4-7). In the reservoir, dye tracer was injected into the drilling water. The water was heated and pumped to the drill stem by a mobile ‘power plant’. Two high pressure pumps raised the water pressure to about 7584 kPa and four diesel-fired heaters raised the water temperature to about 80 °C. A 4.5 kW gasoline generator supplied power for the heaters.

The drill was designed to create straight and vertical holes with smooth walls and constant diameter. This was achieved by using a heavy (~ 70 kg) drill stem controlled by an electro-mechanical in-line drive. A load cell on the drill tower monitors the hanging weight of the drill stem with < 1 % error, giving constant input to allow control of the drilling speed. The 200 cm long drill stem has a tapered cross section along its length, from 3.4 to 1.4 cm. The unusually long and narrow stem causes turbulent mixing of hot water in the borehole, ahead of the drill tip and also within upwelling water alongside the drill stem. The thermal decay length of the up-welling water is on the order of metres (Humphrey and Echelmeyer 1990), and the long and narrow end of the drill stem gives turbulent eddies space to grow as they move up the hole. Following drilling, boreholes at the margin case-study region were inspected for smoothness and diameter using a borehole video camera (Harper and Humphrey 1995). Deeper boreholes in other study regions could not be inspected by video camera due to the rapid freezing time of boreholes, but, because identical drilling procedures were followed, those holes are assumed to be straight and vertical also.

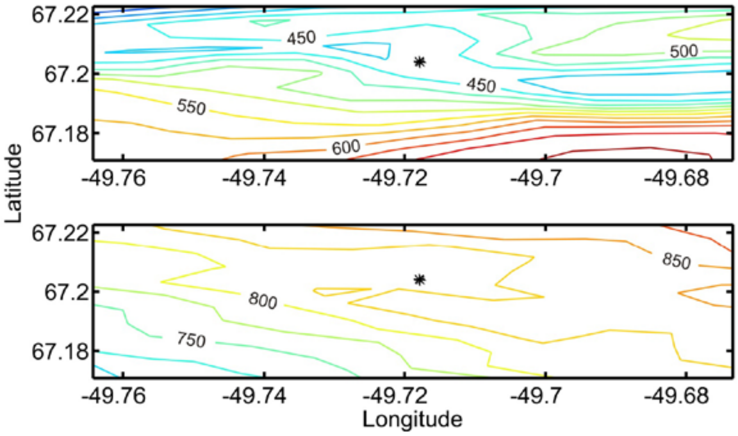

Figure 4-6. *Bed (top) and surface (bottom) topography around trough site GL12-2 (black star). Contours are labeled by elevation and spaced by 25 m, with mapping done on a 5 × 5 km grid.*

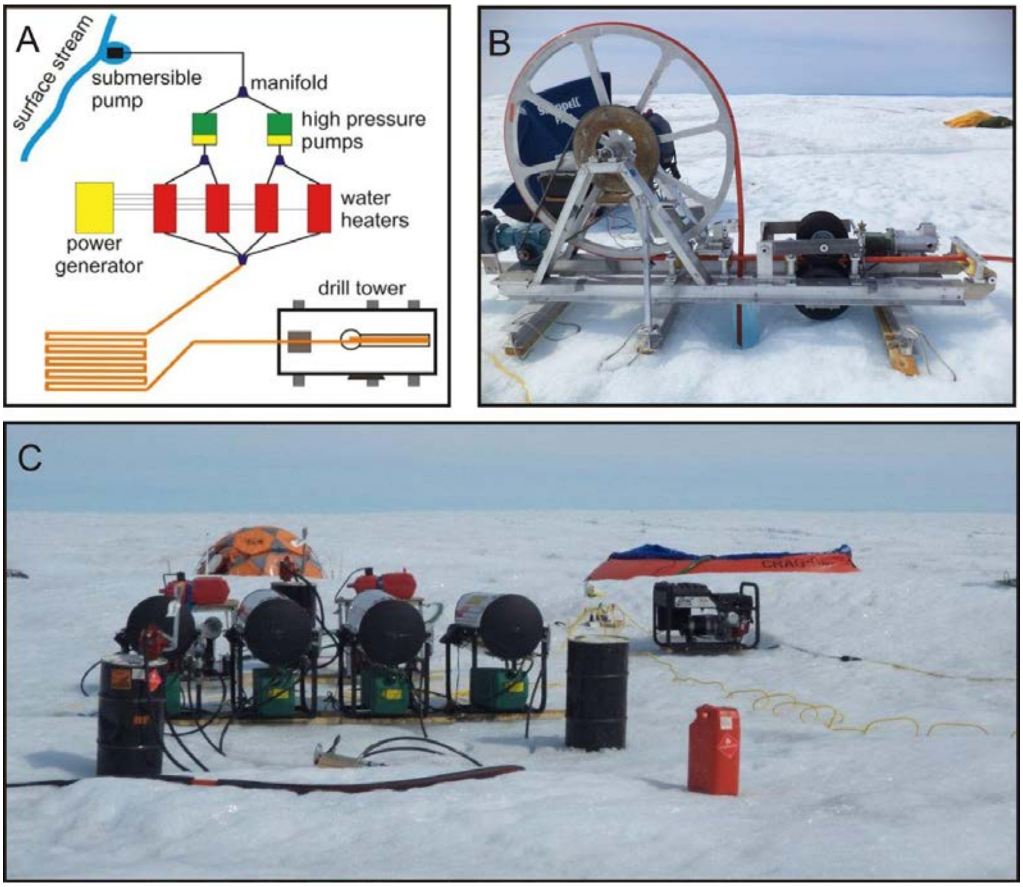

Figure 4-7. A) Schematic of power plant and drill, B) photo of the drill, and C) photo of the power plant. Photos were taken by Arlan Dirkson during the 2012 field season.

4.3 Borehole impulse test experiments

This section presents results and discussion from hydraulic impulse tests performed in boreholes drilled on the GrIS. Specifically, impulse tests were conducted to satisfy four scientific objectives pertinent to building a conceptual model of the GrIS subglacial hydrologic system, as below:

1) Assess hydrologic connectivity along the ice sheet bed at small (hole-to-hole) spatial scale.
2) Investigate the hydraulic capacity of the basal system and time/space variability therein.
3) Elucidate processes by which the basal hydrologic system accommodates flux perturbations.
4) Identify englacial water transport pathways.

Significant spatial heterogeneity at the site scale (tens of metres) was evident in test responses across all drilling sites. These dynamics were manifest in differential connectivity between boreholes in response to testing, and variable capacity to accommodate flux perturbations at the ice sheet bed. This consistent heterogeneity suggests that water flow is concentrated in discrete elements such as linked cavaties or conduits along the ice sheet bed as opposed to flow through a widespread sediment layer. Rapid transient effects, in response to continued perturbation during testing, show that subglacial drainage elements with a reduced hydraulic capacity can rapidly evolve to accommodate variations in flow along the bed. The time scales for such evolution preclude enlargement of existing features by meltback of the overlying ice roof. Instead, rapid readjustment of local drainage elements may take place through mechanical processes. This enlargement of features along the bed enhances flow capacity, facilitates connection with adjacent regions of the basal hydrologic system, and may temporarily increase the fraction of bed in contact with basal water. In this way, active recovery and a drop in basal pressure can accompany basal flow perturbations in the absence of a dominant melting component.

4.3.1 Methods

Borehole impulse tests perturb the basal hydrologic system by artificially raising the borehole water level. Three types of impulse tests were performed in boreholes drilled to the bed, over the course of three field seasons, each of which differs in magnitude and duration.

1) Drilling breakthrough tests: borehole drilling results in a hole which is water-filled to the surface during drilling and introduces a short duration, high magnitude (11 % above overburden pressure) impulse to the basal system upon intersection with the ice sheet bed. Drilling breakthrough tests measure the borehole water level in response to initial intersection with the basal system.
2) Slug tests: repeatable, low magnitude, short duration impulse tests in which a set volume of water is rapidly injected into the borehole and the subsequent water level recovery is documented.
3) Injection tests: long duration impulse tests in which water is pumped into the test hole at a continuous rate for a set period of time.

4.3.1.1 Instrumentation

Borehole water levels were measured using pressure transducers placed at specified depths in boreholes. Voltage output by transducers was converted to metres of water above the sensor following field calibration, as described below. If necessary, depth to water was calculated by subtracting the sensor water level output from the depth of the sensor below the ice surface, which was measured by metre marks on the transducer cable.

In 2010, Omega PX26-015GV pressure transducers with a pressure range of 0–15 pounds per square inch (psi), equivalent to 0–10.54 m of water above the pressure transducer, were used in all impulse experiments. In 2011, Omega PX209-060GI pressure transducers, with a pressure range of 0–60 psi (0–42.18 m of water equivalent above the pressure transducer), were used in the impulse experiments. The same 0–60 psi pressure transducers were used in 2012 also, with one additional 0–200 psi pressure transducer used for the large magnitude (> 100 m) water level changes during drilling breakthrough tests. Pressure transducers logged voltage output in the 0–2000 mV range to a Campbell CR-10X data logger at 4 digit precision, thus the lowest possible output resolution was 1 mV. This corresponds to ~ 0.05 % of the pressure transducer output range, resulting in lowest end-member water level resolutions of 0.005, 0.02, and 0.07 m for the 15, 60, and 200 psi pressure transducers, respectively. Depending on the anticipated time before data download, pressure transducers logged data at either 1 second or 2 second intervals. All pressure transducers were calibrated in the field using a 4–6 point calibration that included lowering sensors to known depths below the water surface and measuring voltage for one minute at each depth. Transducers were kept cold to reduce erroneous fluctuations arising from thermal equilibration.

Pressure transducers were soldered to the ends of 250 m lengths of Cat-5 cable, which was wired to the CR-10X data logger at the ice surface. Cat-5 cable was manually marked at 1 m increments to facilitate depth to water calculations, as described above. To ensure a weather proof connection, the pressure transducer and solder joint were housed in PVC pipe and potted in clear epoxy.

When conditions permitted, water levels were measured in multiple boreholes during impulse experiments. This was achievable in shallow holes near the margin, which remained open for a number of days. However, rapid borehole closure in cold ice at deep sites generally precluded measurement in multiple holes. All pressure transducers output to a central data logger, eliminating timing offsets.

4.3.1.2 Drill breakthrough tests

During drilling, pressure transducers were placed in the borehole to monitor changes in water level occurring from intersection with englacial features and the basal hydrologic system. Water level changes of more than a few cm before the drill reached the ice sheet bed were interpreted to result from intersection with an englacial hydrologic feature. Thus, identification of hydrologic transport or storage features in englacial ice require that water level monitoring be continuous throughout the drilling process.

4.3.1.3 Pumping tests

A set discharge was injected into a test hole during pumping tests by pumping water from nearby surface streams. This was achieved using a single sump pump or combination of pumps in parallel. Injection discharge was measured prior to and after testing by measuring the time to fill a series of 75 L buckets. Discharge varied between 1.26×10^{-3}–4.98×10^{-3} m^3/s between tests but was consistent in pre- and post-test measurements. Borehole water levels were measured prior to testing for as long as possible (but at least 10 minutes) to determine background trends.

4.3.1.4 Slug tests

Borehole slug tests were performed by rapid injection of a set volume of water into the borehole. Test volumes were typically 150–170 L, although some tests were performed using a smaller volume (75 L) to test borehole response to perturbations of varying magnitude. The injection method of rapidly pouring water into the hole from the surface took fewer than 10 seconds. As with pumping tests, background water levels were measured prior to testing.

4.3.1.5 Challenges

Temporary instrument installation for impulse testing was complicated by the propensity for sensors to freeze to borehole sidewalls. While measures were taken to limit sensor freeze-in, some data loss occurred as a result of water levels dropping below the level of sensor placement after freezing.

In addition to sensor freezing, a significant worry in performing the hydraulic tests was the tangling of multiple cables in a single borehole. This concern guided the methodology and protocols for the slug and pumping tests. Such tests are commonly performed by submergence of a sealed cylinder, in the case of slug tests, and by extracting water from the borehole, in the case of pumping tests. However, these methods were not feasible in the field.

4.3.2 Results

Over the course of three field seasons, 41 slug tests, 10 pumping tests and 23 drilling breakthrough tests were conducted at the margin, interior and interior trough sites. Dataset summaries are presented in Table 4-3, Table 4-4 and Table 4-5 for drilling breakthrough, pumping and slug tests, respectively. Results for each of the three impulse test types are reported below. The section concludes with a brief discussion of data synthesis.

4.3.2.1 Drilling breakthrough tests

At the ice sheet margin, six of thirteen holes showed a water level decline when the bed was reached. Water levels declined by as much as 25 % of ice overburden pressure (head drop of 32.6 m) in response to intersection with the bed. Decay times in breakthrough tests at the margin were long, requiring up to 2 hours for complete drawdown. In contrast, all boreholes drilled at inland settings showed a water level drop when the drill intersected the bed. The magnitude and rate of water level decline in boreholes varied between holes and between sites. At inland sites, water levels dropped to levels corresponding to 92–96.5 % of ice overburden pressure (55–124 m). Drilling breakthrough responses at the inland trough site also showed water level drops ranging from 52–72 m, but, in this thicker ice, the borehole water level stabilised near or above ice overburden pressures. Drawdown times at the inland setting were much more rapid than the margin counterparts. The longest response time was 18 minutes, and water levels drew down in as little as 2 minutes before reaching a new equilibrium. Assuming a constant borehole radius of 0.11 m, the subglacial system was able to accommodate up to 4.7 m^3 of water in response to drawdown during a breakthrough event. Peak discharge rates during drawdown reached 0.08 m^3/s.

The spatial variability measured during drilling breakthrough events suggests that the borehole water introduced during intersection with the bed is accommodated by discrete drainage elements within the basal network and not by large scale radial flow. For example, while drilling hole GL11-1C, water levels in holes GL11-1A and GL11-1B were monitored. In response to intersection with the basal system, the water level in GL11-1C drew down 75.4 m over the course of one minute, establishing equilibrium at ~ 92 % of the overburden pressure (Figure 4-8). Coincident with this large impulse, the water level 27 m away in GL11-1B rose by ~ 0.77 m, and exhibited damped oscillations as it recovered to equilibrium. Hole GL11-1A, located 29 m from GL11-1C, showed no response.

Borehole connection with englacial hydrologic features was observed in four boreholes, manifest as water level drops in the drillhole prior to reaching the ice sheet bed. Englacial feature intersection was limited to holes at the ice sheet margin. Figure 4-9 shows borehole water level behaviour during the drilling of GL10-2C. Three separate intersection events at elevations of 485, 483, and 472 m (corresponding to 79, 81, and 92 m below the ice surface) occurred, as evidenced by sharp water level declines. The borehole water level stabilised at 5 m below the surface prior to dropping again when the drill intersected the ice sheet bed, suggesting that at least one of the englacial connections was an active hydrologic pathway. In other instances, intersection of englacial features in the drillhole induced a water level response in an adjacent borehole, indicating that these englacial features are not isolated entities. The presence of englacial hydrologic features provides an additional dimension to the ice sheet hydrologic system. In boreholes that exhibit englacial connection, impulse test responses are a combination of water transport through the basal drainage system as well as through an englacial fracture network. Drilling test results show that impulse tests in boreholes drilled away from the ice sheet margin are uncomplicated by englacial fracture flow. This does not necessarily preclude the existence of such englacial flow features, but it is noted that the persistence of an extensive englacial fracture network in the ice sheet interior is made difficult by the very cold englacial temperatures.

Table 4-3. Drilling breakthrough test results. Asterisks (**) indicate boreholes which were terminated before the ice sheet bed. In boreholes GL11-2D and GL12-2B borehole water level dropped below the sensor which was frozen to the borehole sidewall. Slow draining boreholes (GL10-1D, GL10-2B, GL10-2C, GL10-2D) showed continuing water level decline when the pressure transducer was removed for basal sampling.

Drill Hole	Date DD/MM/YYYY	Ice Thickness (m)	Measured WL decline (m)	Final borehole water column thickness (m)	Final WL (% overburden)	WL decline duration (sec)	Oscillation period (sec)
GL10-1A	6/12/2010	98	0	98	109.9	–	–
GL10-1B	6/13/2010	92.5	0	92.5	109.9	–	–
GL10-1C	6/14/2010	91	0	91	109.9	–	–
GL10-1D	6/14/2010	98.5	15.27	83.23	92.9	> 1385	–
GL10-1E	6/16/2010	91.9	9.07	82.83	99.0	316	–
GL10-1F	6/17/2010	102	0	102	109.9	–	–
GL10-2A	6/20/2010	144	0	144	109.9	–	–
GL10-2B	6/21/2010	148.7	24.5	124.2	91.8	> 6460	–
GL10-2C	6/23/2010	146.3	21.39	124.91	93.8	> 5708	–
GL10-2D	6/23/2010	145.6	24.54	121.06	91.4	> 2458	–
GL10-2E	6/25/2010	148.7	32.63	116.07	85.8	7139	–
GL10-3A	6/30/2010	577.3**	–	–	–	–	–
GL10-3B	7/2/2010	700.4**	–	–	–	–	–
GL11-1A	7/2/2011	457	55.6	401.4	96.5	1090	–
GL11-1B	7/4/2011	466	71.9	394.1	92.9	< 89	–
GL11-1C	7/6/2011	460	75.4	384.6	91.9	70	45.1
GL11-2A	7/13/2011	254.5**	–	–	–	–	–
GL11-2B	7/14/2011	821	104.7	716.3	95.9	< 180	57.8
GL11-2C	7/17/2011	816	124.2	691.8	93.2	245	–
GL11-2D	7/18/2011	815	> 40	–	–	–	–
GL12-1A	6/7/2012	116.6	0	116.6	109.9	–	–
GL12-1B	6/7/2012	114.5	0	114.5	109.9	–	–
GL12-2A	6/13/2012	700	72	628	98.6	1040	–
GL12-2B	6/15/2012	715	> 40	–	–	–	–
GL12-2C	6/17/2012	695	52.8	642.2	101.5	320	–
GL12-2D	6/20/2012	701	52.1	648.9	101.7	950	–

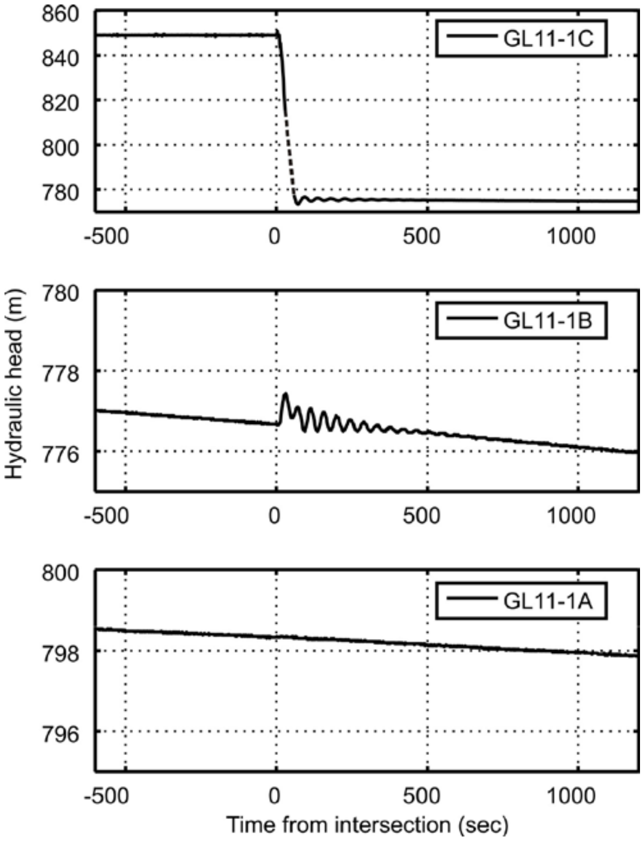

Figure 4-8. *Drill breakthrough response in borehole GL11-1C. In response to the water level drop in GL11-1C, adjacent hole GL11-1B (27 m away), showed a water level rise of ~0.77 m and exhibited damped oscillations towards equilibrium. In contrast, hole GL11-1A, which was located 29 m from the drillhole, showed no response. Note the difference in y-axes between subplots.*

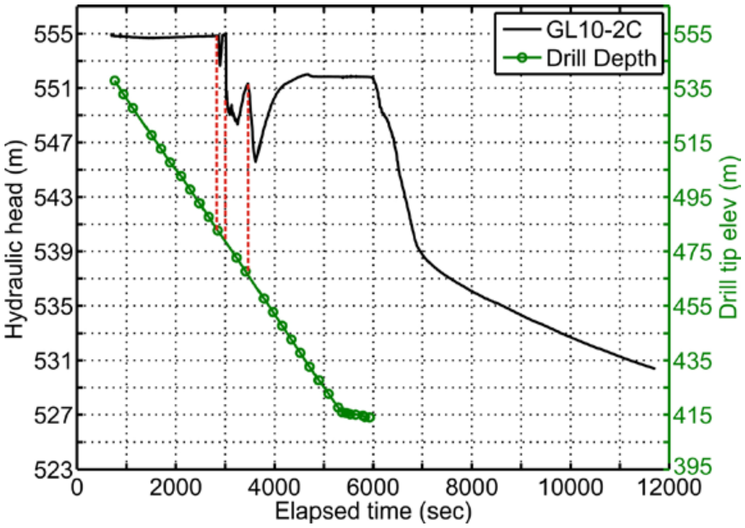

Figure 4-9. *Drilling breakthrough test in borehole GL10-2C. Black line represents the hydraulic head in the drillhole, and corresponds to the left-hand y-axis. Green line corresponds to the elevation of the drill tip, measured at discrete times and represented by green circles. Drill tip elevation corresponds to the right-hand y-axis. Borehole drilling resulted in a drop in drill tip elevation with time until the ice sheet bed was reached at an elevation of 415 m. At elevations of 485, 483, and 472 m (corresponding to 79, 81, and 92 m below the ice surface), the drill tip penetrated an englacial hydrologic feature, triggering a water level drop. Englacial feature intersection events are denoted by red, vertical dashed lines. The drill penetrated the basal hydrologic network after 6000 seconds, prompting a long water level decline that continued after measurements were terminated.*

4.3.2.2 Pumping tests

Two general water level type curves were observed in response to pumping in boreholes. In instances where the hydraulic capacity of the basal system was sufficient to accommodate the pumping perturbation, the borehole response was minor. Water levels rose slightly (less than 2 m) in response to pumping, reaching a plateau until pumping was terminated. This type response is displayed in a pumping test performed in GL12-2B (Figure 4-10a). In response to a pumping perturbation of 3.26×10^{-3} m^3/s, borehole water levels rose 0.8 m and quickly levelled off after less than 2 minutes of pumping. The water level remained ~ static for 24 minutes, after which time pumping was terminated.

Table 4-4. Summary of pumping test results. Response type I corresponds to small magnitude head rise and water level stabilisation in response to pumping. Response type II corresponds to asymmetric type response with larger magnitude head rise and active recovery during pumping.

Test #	Test hole	Ice thickness (m)	Initial water level Depth to water (m)	 % overburden	Pumping rate (m^3 s^{-1})	Duration (min)	Max head rise (m)	 % overburden	Response type
1	GL10-2B	148.7	31.8	0.87	1.26E−03	58	24.5	18.31	II
2	GL10-2B	148.7	34.4	0.85	1.33E−03	106	16.6	12.40	II
3	GL11-1A	457.5	48.4	0.99	1.38E−03	70	5.1	1.24	II
4	GL11-1C	459.5	76.5	0.93	1.38E−03	70	0.6	0.15	I
5	GL12-2B	715	69.7	1.00	1.69E−03	20	0.4	0.06	I
6	GL12-2B	715	69.7	1.00	3.26E−03	24	1.2	0.19	I
7	GL12-2C	695	49.5	1.03	1.89E−03	153	7.2	1.15	II
8	GL12-2C	695	58.0	1.02	4.98E−03	22	10.7	1.71	II
9	GL12-2D	701	54.1	1.03	4.29E−03	635	12.7	2.01	II
10	GL12-2D	701	81.7	0.98	4.98E−03	648	36.3	5.75	II

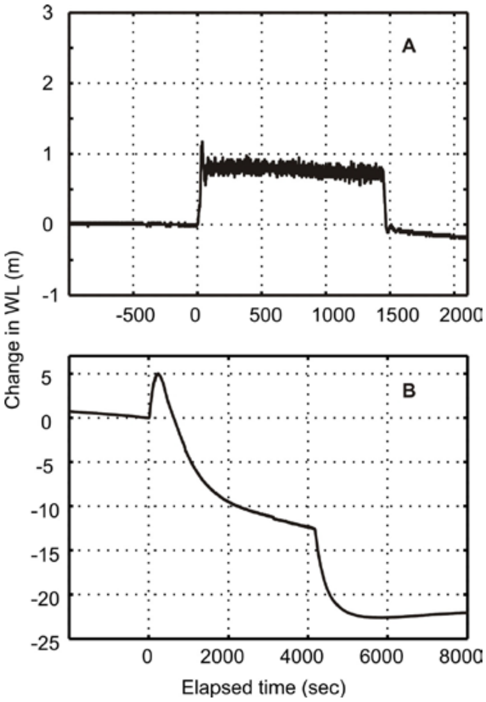

Figure 4-10. Pumping test type responses. A) Efficient type response in which borehole water level showed minor rise and stabilisation in response to pumping. In this example, borehole GL12-2B received 3.26×10^{-3} m^3/s. Pumping was initiated at time $t = 0$ s and continued until time $t = 1440$ s. B) Asymmetric response in which water level exhibited an initially rapid rise, system transmissivity enhancement - forced water level peak, and active recovery while pumping continued. In this example, borehole GL11-1A received 1.38×10^{-3} m^3/s. Pumping began at time $t = 0$ s and continued until $t = 4200$ s. Note the difference in x- and y-axes between subplots.

In contrast, an alternate type curve displayed a larger magnitude water level rise in response to pumping. This rise in borehole water level slowly levelled off and began to recover while pumping continued. The rate of water level recovery was consistently slower than the initial rise, resulting in an asymmetric rise and fall during pumping. In some instances, continued water level recovery resulted in borehole water levels dropping below the pre-test level while pumping continued. This is exemplified in a pumping test performed in GL11-1A (Figure 4-10b). In response to a pumping rate of 1.38×10^{-3} m^3/s, the borehole water level rose 5 m over the first 4 minutes. The water level then levelled off and declined for the remaining 65 minutes of the test. When pumping was terminated, the water level had dropped to over 12.5 m below the pre-test level. Following termination of pumping, the borehole water level continued to decline an additional 10 m over the course of 26 minutes. A small recovery toward a new equilibrium, 22 m below the pre-test pumping level, was apparent over the final 37 minutes of observable recovery.

Table 4-5. Summary of slug test results. Response type UD = underdamped, OD = overdamped, and UD/OD = hybrid type response.

Test #	Test hole	Injection volume (l)	Response type	Day DD/MM/YYYY	Avg. period of oscillation (sec)	Adjacent hole response
1	GL10-1D	132	UD/OD	6/14/2010	15.37	–
2	GL10-1D	151	UD/OD	6/15/2010	12.67	–
3	GL10-1C	132	OD	6/15/2010	–	–
4	GL10-1C	132	OD	6/15/2010	–	–
5	GL10-1D	151	OD	6/16/2010	–	–
6	GL10-1E	151	UD	6/16/2010	31.33	GL10-1D
7	GL10-1E	151	UD/OD	6/17/2010	14.38	GL10-1D
8	GL10-1D	151	UD	6/17/2010	23.34	GL10-1E
9	GL10-1E	151	UD	6/17/2010	25.34	GL10-1D
10	GL10-1D	151	UD	6/18/2010	22	GL10-1E
11	GL10-1E	151	UD/OD	6/19/2010	–	GL10-1D
12	GL10-1D	151	UD/OD	6/19/2010	–	GL10-1E
13	GL10-2C	151	OD	6/23/2010	–	GL10-1D
14	GL10-2B	151	UD/OD	6/24/2010	24.32	GL10-2D, GL10-2C
15	GL10-2D	151	UD/OD	6/24/2010	24.27	GL10-2B, GL10-2C
16	GL10-2C	151	OD	6/24/2010	–	GL10-2B, GL10-2D
17	GL10-2C	151	OD	6/25/2010	–	GL10-2B, GL10-2D
18	GL10-2E	151	UD/OD	6/25/2010	24.31	GL10-2D, GL10-2C
19	GL10-2E	151	UD/OD	6/25/2010	23.93	GL10-2D, GL10-2C
20	GL10-2E	151	UD/OD	6/26/2010	24.04	GL10-2D, GL10-2C
21	GL10-2C	151	OD	6/27/2010	–	GL10-2E
22	GL11-1A	151	OD	7/2/2011	–	–
23	GL11-1A	151	OD	7/4/2011	–	–
24	GL11-1B	151	UD	7/4/2011	43.32	–
25	GL11-1B	151	UD	7/5/2011	44.14	–
26	GL11-1B	75	UD	7/5/2011	43.66	–
27	GL11-1B	75	UD	7/5/2011	45.03	–
28	GL11-1A	75	OD	7/5/2011	–	–
29	GL11-1B	151	UD	7/6/2011	38.04	–
30	GL11-1C	151	UD	7/8/2011	48.3	GL11-1B
31	GL11-2B	151	UD	7/15/2011	58.64	–
32	GL11-2B	151	UD	7/15/2011	55.83	–
33	GL11-2D	151	UD	7/18/2011	63.39	–
34	GL12-2B	170	UD	6/15/2012	54	–
35	GL12-2C	170	UD/OD	6/17/2012	42.9	–
36	GL12-2C	170	UD/OD	6/19/2012	47.6	–
37	GL12-2C	170	UD/OD	6/19/2012	48	–
38	GL12-2C	170	UD/OD	6/19/2012	47.9	–
39	GL12-2C	170	UD/OD	6/19/2012	47.8	–
40	GL12-2C	170	UD/OD	6/20/2012	53.4	–
41	GL12-2D	170	OD	6/21/2012	–	GL12-2C

Consistency in borehole responses was observed, as both type curves described above were measured in pumping tests performed at the inland and inland trough sites. As with drill breakthrough test responses, significant spatial variability was documented at the site scale. At both the inland and inland trough sites, boreholes less than 30 m apart showed both type responses. Heterogeneous connections between holes were also evident in tests, as long term pumping did not guarantee the establishment of connections with adjacent boreholes.

4.3.2.3 Slug tests

Three general types of borehole water level behaviour were observed in response to slug testing:

1) Overdamped water level response characterised by long, gradual water level decay towards equilibrium following injection.
2) Underdamped water level response characterised by oscillatory water level behaviour about the pre-test water level.
3) Hybrid type response characterised by oscillatory water level behaviour imprinted over slow, overdamped recovery.

Examples of the three type responses are presented in Figure 4-11. Of the 14 different boreholes in which slug tests were performed across the three study regions, four boreholes showed consistent overdamped responses, five holes responded in an underdamped manner and five holes displayed hybrid type behaviour. All type responses were measured at each of the three field regions. The period of oscillation in underdamped tests increased through the three study regions, generally following the square root of the ice thickness. In contrast to the rapid recovery of oscillating water levels, recovery times in boreholes that responded to slug tests in an overdamped manner, commonly exceeded one hour. Over these long time scales, the recovery curve was complicated by background water level changes that sometimes exceeded 10 m.

Slug tests in different boreholes at the same site location showed significant spatial variability at the site scale (tens of metres). It was common to measure both underdamped and overdamped responses to slug tests in different boreholes that were less than 30 m apart. This behaviour was consistent in both the margin, inland and inland trough regions. Coincidentally, all boreholes that displayed minor water level rise in pumping tests also responded to slug perturbations in an underdamped fashion. Further, boreholes that exhibited larger magnitude, asymmetric water level response to pumping behaved in an overdamped manner when perturbed with a slug test.

Repeat testing in boreholes suggested that, while a complete mode shift from underdamped to over-damped (or vice versa) was unlikely, the response behaviour was prone to adjustment depending on the background water level at time of testing. This temporal variability is highlighted by three slug tests performed over a four day period in GL11-1A (Figure 4-12). Slug test S1, performed in the borehole shortly after drilling, showed isolated behaviour; 100 minutes after injection, the water level recovered by less than 25 % of the initial slug magnitude (~ 0.85 m). Two days later, a second slug test, S2, in the same borehole showed a rapid recovery in response to the slug. The water level recovered 100 % of the initial slug magnitude and continued to drop below the expected natural water level. In a third slug test, S3, the following day, water level behaviour in the borehole showed a gradual recovery which followed the expected background trend, suggesting an inability of the system to accommodate the injected water package. Background water level at the time of test S2 was 802 m, over 2.5 m greater than test S3, and 15 m greater than test S1. The rapid recovery in test S2 may likely have been facilitated by enhanced connectivity during this period of high water level, which approached overburden level (estimated to range from 795.5–808.5 m).

4.3.3 Summary and discussion of the borehole impulse test experiments

The spatial variability among all three types of impulse tests conducted supports the conceptual model that, at the local scale, water may flow largely through discrete elements in the basal hydrologic network as opposed to more diffusive, laminar flow through a homogenous till layer. Boreholes <30 m apart commonly exhibited opposing type responses during slug testing. Large magnitude pressure pulses associated with drilling breakthrough tests exhibited the capacity to influence water levels in some adjacent boreholes, but not in others. Long duration pumping tests in boreholes showed heterogeneous connectivity to adjacent boreholes. This variability was generally consistent across all drilling sites.

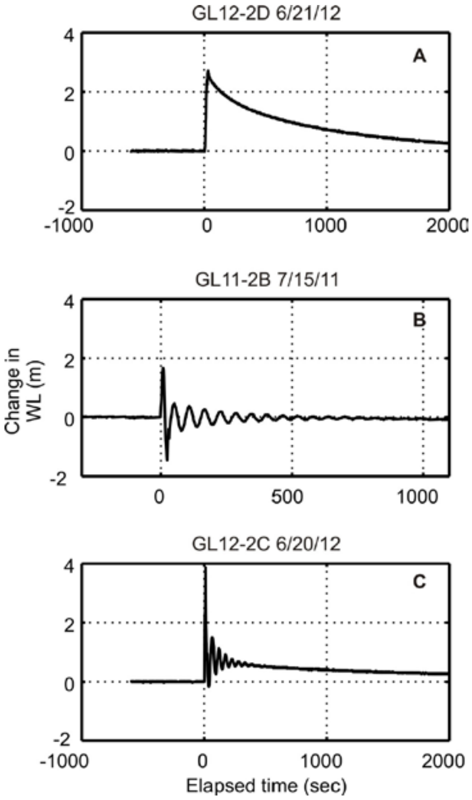

Figure 4-11. Slug test type responses indicating A) overdamped, B) underdamped and C) hybrid type responses. Test borehole and date of slug test are listed above the plots. Note the difference in x-axis among subplots.

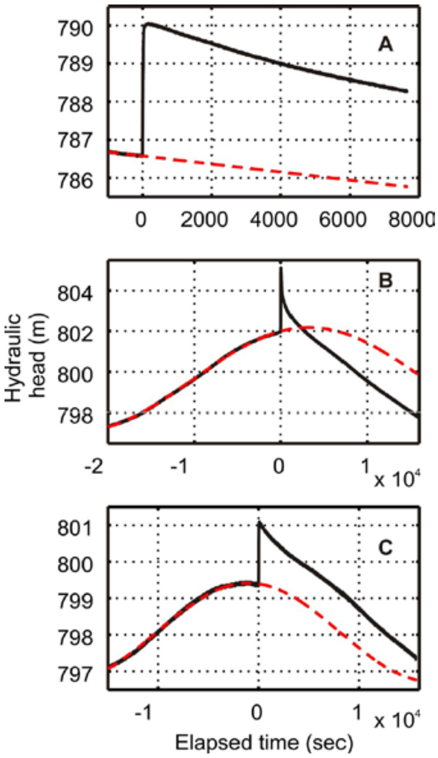

Figure 4-12. Time series of slug tests performed in borehole GL11-1A in 2011 on A) DOY 183, B) DOY 185, C) DOY 186. Expected background water level behaviour in each subplot is fit to pre-test water levels using a first order Fourier fit. The first slug test (A) was performed shortly after drilling was completed, reducing pre-test water level monitoring time. Pre-test water level was highest prior to the slug test performed on DOY 185 (B). Rapid water level recovery followed perturbation and continued beyond expected background trends. The third slug test performed on DOY 186 (C) exhibited behaviour similar to that on DOY 183 (A).

The dynamic nature of connections and rapidly changing background conditions limit the utility of standard hydrogeological transmissivity calculations. Such an analysis assumes steady background conditions, radial and laminar flow, and a homogenous, isotropic medium. These assumptions are all violated on the ice sheet domain. Further, rapid accommodation of pumping perturbations and active recovery during pumping suggests that the system is driven by processes which are not accounted for in standard analytical techniques. This rapid transience means that the effective transmissivity could vary by orders of magnitude over very short time scales (minutes, in the case of pumping tests). As a result of these violations and additional processes, transmissivity values would be subject to considerable uncertainty and would only be representative of a small spatial area for an instant in time. While calculation of transmissivity is of limited utility, borehole response to pumping provides information regarding the flow capacity of basal drainage elements and the processes by which perturbations are accommodated. The minor borehole response to pumping in boreholes GL11-1C and GL12-2B suggests that the background flow through the system to which these holes are connected is likely to be large compared to the injection rate ($1.38–3.26 \times 10^{-3}$ m^3/s). This is also supported by the rapidly recovering underdamped slug test responses in these holes.

Adjacent to transmissive features, other boreholes showed resistant connections, with limited capacity to transmit water, as evidenced by slow draining overdamped slug test responses and gradual water level drops following drilling breakthrough. The hydrologic efficiency of the drainage elements to which these boreholes are connected is quite transient. In response to pumping perturbation, the efficiency of these drainage elements is capable of evolving over short time scales (5–30 minutes) to accommodate the injection, and more, as evidenced by the active recovery while pumping continued. This evolution cannot be explained solely by enlargement of existing connections from meltback of the overlying ice roof. Presumably, a mechanical component may be invoked to increase connectivity at the bed and facilitate increased basal flux. This is supported by repeated slug tests, which showed an enhanced ability to accommodate the perturbation when background water levels were closest to overburden levels. In this setting, the additional head perturbation induced by the slug may act to increase connectivity to other regions of the bed by mechanical separation, facilitating faster water level recovery. In the natural setting, this provides a means of short term expansion of the subglacial network and increased water coverage at the bed during periods when flux overwhelms the existing subglacial system.

Near the ice sheet margin, drilling breakthrough tests and borehole video (not presented here) confirm the presence of englacial features that may act as water storage reservoirs or active transport pathways. While inland boreholes provide a limited sample size, and surface-to-bed water routing moulins are prevalent throughout the ablation zone, no evidence for an extensive englacial fracture network was evident in drill breakthrough tests away from the margin.

4.4 Basal water pressure

4.4.1 Water pressure methods

4.4.1.1 Instrumentation

Bed water pressure was measured by installing a pressure transducer at the base of boreholes drilled to the bed. Borehole sensors and sensor strings were custom fabricated for the project. Sensor strings included both temperature sensors at intervals along the string, and a pressure transducer at the bottom end of the string. The sensors were wired into an eight-conductor cable, with serial communications enabling multiple sensors to share a single conductor.

A 20 cm extension of PVC pipe was placed on the pressure transducer in an effort to prevent the sensor from being in direct contact with basal sediment or bedrock. In addition, attempts were made during installation to lift the sensor an additional 25–50 cm above the base of the borehole to prevent the sensor from being dragged along the bed. Prolonged drilling at the bed produced an enlarged cavity where the borehole intersects the bed, which minimised the risk of isolating the sensor in a closed borehole above the bed.

Pressure transducers manufactured by Omega Engineering were installed on CAT-5e cable of appropriate length. The pressure transducers were potted in epoxy to make them waterproof when submerged at high pressure. The exact model pressure transducer and its accuracy range depended on the depth of the borehole, with a trade-off between pressure range and resolution. The pressure transducers used in all margin-area boreholes, where ice depth was under 300 m, were Omega Engineering model PX-209-300 psi; the pressure transducers used at GL11-S1, where ice depth was ~ 460 m, were Omega Engineering model PX209-2000 psi; and, those used at GL11-S2 and GL12-S2, where ice depth was > 700 m, were Omega Engineering model 3000 psi. All pressure transducers were 4-20 ma output-type. Resolution of the measurements was most dependent on the data logger electronics, and was on the order of 10 cm for the installations of long term pressure measurements at all sites (note that different pressure transducer instrumentation was used for the impulse test experiments described in Section 4.3).

The high bulk and weight of long sensor strings (i.e. up to 850 m in length) prohibited shipping and field transport of fully fabricated strings. Rather, sections of the strings were made in the laboratory and then spliced into a single long string of the appropriate length in the field. The strings were hand lowered into the boreholes immediately after drilling and tied off to a wooden support structure at the surface.

Data loggers, including both hardware and software, were designed and manufactured at the University of Wyoming. The custom-made data loggers were chosen over commercially available equipment because they were designed to operate on ultra-low power, allowing monitoring of the borehole sensors year-round with minimal cost and logistical effort devoted to power supplies. The data loggers were powered for more than a year by just two AA sized lithium batteries and each had a storage capacity of over 24 000 sets of measurements (each set containing 32 measurements). An additional benefit was that custom-made data loggers were inexpensive, allowing deployment of a large number of units at minimal cost. A trade-off was the substantial labour involved in designing and assembling the data loggers.

4.4.1.2 Pressure values

Borehole water pressure data are commonly presented in the literature using several different formats. In this report, the following conventions are used.

1) Hydraulic head is presented in metres DWGS84 ellipsoid. This provides a useful means for comparison to other datasets, such as groundwater head conditions. However, note that errors for head values can be much greater for ice measurements (see details below) than for groundwater measurements.
2) Metres of water equivalent pressure represents the length of a column of water rising above the bed.
3) Absolute pressure is presented in units of kPa and is calculated using a water density of 1000 kg/m^3.
4) Scaled overburden is defined as water pressure divided by ice overburden pressure. Ice pressure is calculated using a density for bulk glacier ice (ice and bubbles) of 900 kg/m^3.
5) Effective pressure is defined as the ice overburden pressure minus the water pressure and is reported in absolute pressure terms (kPa).

Errors:

The reported water pressures have potential errors which arise from a number of sources, as described below.

1) Inaccuracies in estimates of the ice surface elevation from GPS. Hand-held GPS have particularly low resolution in the vertical direction, often in the range of tens of metres. The ice surface near boreholes lowered 3 m or more per year due to ice surface ablation, and the collar of boreholes moved down slope due to ice flow – by hundreds of metres in the horizontal direction and up to 5 m in the vertical direction. Hence, no single-value elevation was necessarily representative of a borehole collar. Most estimates of surface elevation are accurate to far better than 20 m, but the potential for errors on the order of 50 m in select cases cannot be ruled out.

2) Inaccuracies in estimates of ice thickness. Radar imaging has low accuracy and a large footprint, resulting in imprecise estimates of the ice thickness at a particular borehole site (i.e. up to ±25 m). The best estimate of ice thickness is from direct measurement with the borehole drill and sensor strings lowered into the hole. However, the drilling hose has stretch and both the hose and sensor strings have potential length marking errors. These errors are assumed to total not more than about 1 % of the thickness estimate, and are probably less.

3) The borehole and water pressure sensor move over the bed by sliding motion, with local bedrock topography potentially causing uncertainty in the sensor position with respect to the bed. Whether or not the sensor maintains a constant distance over the bed is unknown. This potentially influences the ice thickness measurement and the inferred ice overburden pressure at the bed. These errors are likely very small, on the order of a decimetre, which is unimportant when the ice thickness is many hundreds of metres.

4) Resolution/accuracy of the pressure transducers. The pressure transducers had cm-to-decimetre accuracy, but the location of the pressure transducers had uncertainty of up to 50 cm above the bed. This error also represents a small fraction of the absolute pressure because the ice thickness is many hundreds of metres.

5) Atmospheric pressure changes. No correction is made to the pressure transducer readings to compensate for atmospheric pressure changes. However, these changes are trivial compared to the very high pressures and large pressure changes observed at the ice sheet bed.

4.4.2 Boreholes and records

Margin region (sites GL10-1, GL10-2, GL-3, GL12-1)

2010 boreholes: Water levels were recorded intermittently while the field campaign was being conducted in all 13 boreholes drilled at sites GL10-1 and GL10-2 (Table 4-6). Three holes were selected for continuous water level measurements, with a pressure transducer installed near the borehole base and a data logger on the ice surface (Table 4-7). These data were collected at 5 minute time intervals. Data were retrieved in late September, 2010, yielding records lasting from July–September, 2010. Data loggers were left in-place and continued to collect data for varying periods of time (at minimum, for several more months). Final data were retrieved from these boreholes during the summer of 2011. Communication had been lost with each of the pressure transducers sometime during the winter of 2010–2011, likely due to breakage of the cables from frequent crevassing events in the area. No pressure data were collected from site GL10-3, as the two 720 m deep boreholes drilled in this area did not reach the bed.

Table 4-6. Boreholes with continuous records: site and hole ID, region, day logging began, day logging ended, total number of days logged.

Hole ID	Site	Region	Start Log YYYY-MM-DD	End Log YYYY-MM-DD	Total
1D	GL10	Margin	2010-06-15	2010-09-20	97
2B	GL10	Margin	2010-06-22	2010-09-20	90
2C	GL10	Margin	2010-06-26	2010-09-11	77
1A	GL11	Interior	2011-07-10	2012-07-11	366
1B	GL11	Interior	2011-07-10	2011-09-14	66
1C	GL11	Interior	2011-07-10	2011-09-14	66
2B	GL11	Interior	2011-07-15	2011-09-14	61
2D	GL11	Interior	2011-07-20	2011-09-14	56
2A	GL12	Margin	2012-06-16	2012-09-19	95
2C	GL12	Trough	2012-06-17	2012-09-19	94
2D	GL12	Trough	2012-06-21	2012-09-13	90

Table 4-7. Boreholes from GL10-1 and GL10-2 with manually-measured water level records: Hole ID, day logging began, day logging ended, total number of measurements.

Hole ID	Start Log YYYY-MM-DD	End Log YYYY-MM-DD	Measurements
1A	2010-06-12	2010-06-27	18
1B	2010-06-13	2010-06-27	17
1C	2010-06-14	2010-06-27	28
1D	2010-06-14	2010-06-27	33
1E	2010-06-16	2010-06-27	20
1F	2010-06-17	2010-06-27	14
2A	2010-06-21	2010-06-26	10
2B	2010-06-21	2010-06-27	16
2C	2010-06-23	2010-06-27	14
2D	2010-06-24	2010-06-26	10
2E	2010-06-25	2010-06-27	3

2012 boreholes: Two additional boreholes were installed in the margin region in June of 2012. These holes never connected to an active hydrologic system after reaching the bed (no drainage) and therefore did not demonstrate pressure variations. The water level remained static, with the boreholes filled to the surface throughout the summer. The boreholes were revisited in September of 2012 and were observed to remain full.

Interior region (sites GL11-1, Gl11-2)

Water levels were recorded intermittently in all boreholes while the field campaign was being conducted. At site GL11-1, boreholes GL11-1A, GL11-1B and GL11-1C were selected for continuous monitoring of pressure with a data logger. At Site GL11-2, boreholes GL11-1B and GL11-2D were fitted with data loggers. Data were downloaded in September, 2011, and all boreholes yielded records. Data were downloaded again in June, 2012, but only boreholes from GL11-1A yielded additional data.

Trough region (site GL12-2)

All four boreholes were fitted with data loggers and pressure transducers after drilling. Snowfall and subsequent melting/refreezing during early September encased all data loggers in ice. One of the boreholes, GL12-2B, could not be recovered in September. Therefore, records exist for boreholes GL12-2A, GL12-2C and GL12-2D from mid-June to mid-September only.

4.4.3 Water pressure results

Margin region (sites GL10-1, Gl10-2, Gl10-3, GL12-1)

Most boreholes drilled in this region reveal large seasonal and diurnal water pressure variations (Figure 4-13). On a seasonal basis, pressures were generally high and relatively steady during the winter months. During summer, large diurnal pressure swings occurred. On a diurnal basis, pressures reached values in excess of the ice overburden pressure for short periods of time, and fell to values as low as 25 % of ice overburden for brief periods. During these low pressure events, hydraulic head ranged between about 450 and 510 m. High frequency, but lower magnitude, variations were also observed for several days. However, two boreholes drilled within 150 m of the margin in 2012 showed no pressure variations whatsoever. This demonstrates that patches of the bed are hydraulically isolated. Such a patchwork of hydraulic connectivity can be expected to cause large pressure gradients at the bed.

Interior region (sites GL11-1 and GL11-2)

Measurements show high basal water pressures with diurnal and seasonal variations (Figure 4-14). The water pressure in boreholes at both sites GL11-1 and GL11-2 averaged about 90 % of the overburden ice pressure. This is similar to measurements made at the marginal sites in 2010. GL11-1A, GL11-1B and GL11-1C show hydraulic head values that average around 740, 795, and 760 (m), respectively. At the higher elevation GL11-2 site, hydraulic head averages around 975 (m). The maximum range of pressure changes at site GL11-1 during the period of record was ~ 75 m between DOY 214 and 256. This occurred in borehole GL11-1C and represents about 18 % of the overburden ice pressure, over a range of about 730 to 805 m of hydraulic head. Other boreholes at this site demonstrated lower pressure ranges. Boreholes located at site GL11-2 demonstrated large ranges of water pressures between DOY 197 and 203, when the pressure measurements spanned 78 m between short lived pressure peaks and minimums. This range represents about 10 % of the ice overburden pressure. For GL11-2B, hydraulic head spans between about 925 and 1000 (m) over the entire period, while for GL11-2D the hydraulic head ranges between 960 and 1035 (m).

All boreholes showed changes occurring over a seasonal time scale. Both interior region sites showed irregular water level variations at the start of the measurement interval, lasting until about DOY 205. More regular diurnal variations were then established and continued until DOY 242. On DOY 242 all boreholes at both sites showed a pressure drop followed by a slow increase in pressure that lasted for ~ 2 days. As pressures steadily increased, borehole GL11-2D no longer demonstrated diurnal variations. Other boreholes continued to show diurnal variations, but daily water level swings were subdued and were superimposed on the overall seasonal trend.

During the period with diurnal variations, site GL11-1 demonstrated swings in borehole water level of about 8 m, which is about 1.9 % of the overburden ice pressure. These relatively regular diurnal variations throughout the middle of summer span hydraulic head values between about 735 to 743 m for GL11-1A, 785 to 795 m at GL11-1B, and 738 to 745 m at GL11-1C. Site GL11-2 showed slightly lower relativel pressure swings, with daily changes of about 1.4 % or 10 m in borehole water level. Due to the non-linear decreasing trend in water levels, the 10 m diurnal swings start at 970 m of hydraulic head and drop to 940 m over the period from DOY 207 to DOY 245. Borehole GL11-2D shows a very similar magnitude drop over the same period, ranging between values of 1020 m and 990 m.

Trough region (GL12-2)

Water levels fluctuated on diurnal and seasonal time scales (Figure 4-15). Diurnal variations were present from the start of recording in mid-June. During a one week period in late July, all holes showed synchronous diurnal pressure variations of about 60 m, where borehole GL12-2A spanned between 660 and 730 m of hydraulic head, GL12-2C between 720 and 780 m, and GL12-2D between 720 and 790 m. During all other times, water levels were not identical in each borehole, with implied spatial gradients in bed water pressure of up to 2.5 m/m (before minor corrections for variable bed topography). In late August, all holes showed a marked drop in pressure during a synchronous event, but diurnal pressure variations continued. By mid-August, diurnal pressure variations had terminated in two of the three monitored boreholes. Small diurnal pressure variations continued into September in GL12-2C for intermittent 3–5 day periods, which were superimposed on larger irregular changes in pressure.

During the winter months, the high frequency pressure variations were dampened; each of the boreholes showed steady water pressures relative to the summer months. Borehole GL12-2C demonstrated a sudden rise in pressure of ~ 40 m water equivalent during mid-winter. This increase was not related to surface melt and was not present in the other boreholes. The event is likely a local phenomenon related to the ice sliding over rough bedrock; for example, a water cavity containing the sensor could have been advected into the upstream side of a large bedrock bump, with increased ice pressure. At the end of winter, each of the boreholes then demonstrated simultaneous reestablishment of high frequency (daily) pressure variations. These variations continue through to the end of the monitoring period in mid–July 2013.

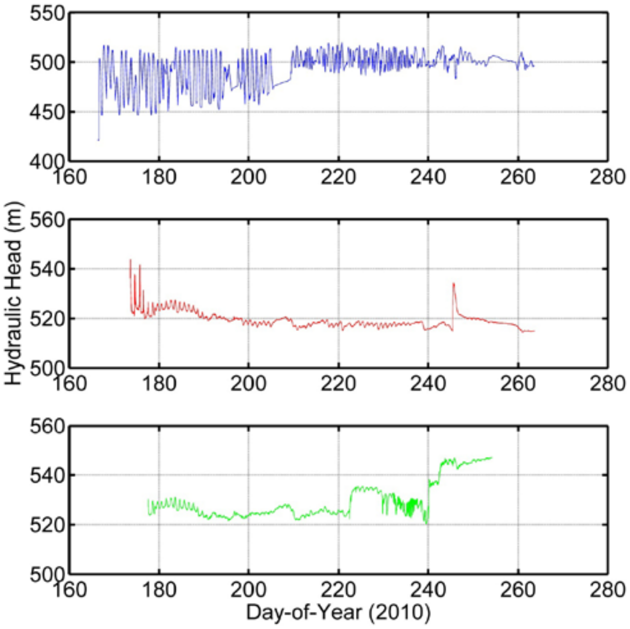

Figure 4-13. *Time series from margin sites GL10-1D (top), GL10-2B (middle) and GL10-2C (bottom), showing pressure variations measured in hydraulic head from the middle of June (2010) to the middle of September (2010).*

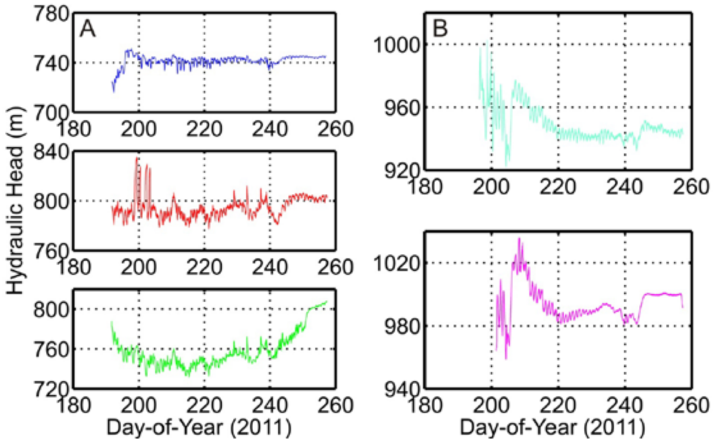

Figure 4-14. *Pressure time series measured in hydraulic head from interior sites GL11-1 and GL11-2. On the left A), although GL11-1A (top) has a full year record, for purposes of comparison, the record is trimmed to match the time period when measurements for GL11-1B (middle) and GL11-1C (bottom) were taken (July (2011) through September (2011)). On the right B), interior site GL11-2 records are shown for boreholes GL11-2B (top) and GL11-2D (bottom).*

4.4.4 Summary and discussion of the basal water pressure

Borehole pressure observations indicate the existence of meltwater flowing in a basal drainage system at the ice/bed interface from the margin to at least 30 km toward the interior of the ice sheet. Flowing water is revealed by basal water pressure variations, which imply the presence of a basal drainage system capable of transmitting relatively high volumes of water. Several other lines of evidence support the inference that a high capacity basal drainage system is present at the study sites: 1) drill breakthrough tests show the drainage system can transport > 3000 L in less than 3 minutes when the drillhole suddenly connects with the bed; 2) pumping tests show the existing basal drainage system has a high capacity for water transmission, as it can accommodate the addition of 300 l/min; 3) diurnal water pressure variations imply fast response to surface melt in a highly connected hydrologic system; and 4) concomitant diurnal velocity variations imply a large fraction of the bed is connected.

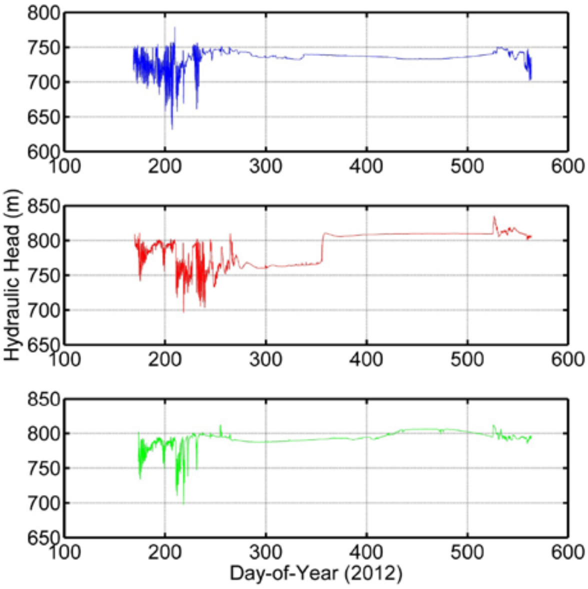

Figure 4-15. Pressure records from the middle of June (2012) through the middle of July (2013) measured in hydraulic head for sites located in the trough region. From top to bottom, records from GL12-2A, GL12-2C and GL12-2D are presented, respectively.

4.4.4.1 High pressures

The highest pressures measured were ~ 110 % of the overburden ice pressure. This high pressure corresponds to a water column equal to the thickness of the ice and was achieved where boreholes were entirely filled with water, from the bed to the surface. This case was observed more than once, and persisted for weeks or more, when boreholes were drilled to the bed and did not drain. Water filling only occurred in boreholes located 1–2 km from the margin – all other boreholes drained below the glacier surface when the borehole intersected the bed. Water pressure equivalent to full ice depth (i.e. 110 % of ice overburden) is perhaps anomalously high because the presence of the borehole itself enables the existence of an artificial water column extending the full ice depth.

In mountain glaciers, pressures exceeding overburden have occasionally been measured and can be attributed to steep surface and bed slopes. The pressure at a given point can reflect the higher head created by the up-glacier elevation potential. In other words, the steep topography creates a ‘water tower’ that pressurises the basal drainage system. Such high pressures are usually limited to temporary events, as the drainage system will adjust to minimise this over-pressure. However, in an ice sheet, the surface slopes are so small relative to the diminishing pressure gradient in the downflow direction that topographically enhanced head, as occasionally seen in steep mountain glaciers, is unlikely, if not impossible.

Without the borehole, could basal water pressure exceeding the ice overburden pressure exist? Two rare, but possible, mechanisms for generating pressures above overburden in an ice sheet do exist, as described below.

1) A moulin, which has water inflow at a rate that exceeds basal outflow, will fill with water to the surface so that the pressure at the base of the moulin is 110 % of the overburden. This is a natural analogy to a filled borehole. Such circumstances are likely rare, especially in summer when a well-developed basal drainage system permits high rates of basal outflow. Moulins are known to occasionally fill to the surface in late fall, when the basal drainage system shuts down, and remain filled throughout the winter. Nevertheless, moulins are sparsely located and the rare water-filled moulin does not likely have widespread influence on basal conditions.

2) During an episode of SGL drainage, the basal pressure in the crevasse/moulin responsible for drainage will reach full ice depth pressure (i.e. 110 %) of overburden. Such events are both temporally and spatially rare.

It is concluded that the maximum possible pressure in the study regions is 110 % of overburden, though this pressure limit is rare in both time and space.

In terms of absolute magnitude, the highest pressures were measured where the ice is the thickest and, therefore, the overburden pressure the greatest. Site GL11-S2, located ~ 30 km from the ice margin and with ice depth of ~ 825 m, demonstrated pressures of up to ~ 7340 kPa. Assuming the bed becomes frozen along the study transect, 90 km inland from the margin (based on the thermo-mechanical ice sheet model used in this study), the ice overburden pressure at this location is 10 650 kPa. This is theoretically the highest pressure at the basal boundary, with all locations well below this value.

4.4.4.2 Low pressures

In terms of overburden ice pressure, the lowest pressure measured was 25 % of overburden. This was observed in more than one borehole, but was limited to boreholes located near the ice margin. Pressures falling to more than 10 % below overburden were never observed inland from the ice margin where the ice thickness is high. Low pressure could occur for a brief instant anywhere. A sudden drop in water input – for example, resulting from surface stream capture, or flash runoff following a rainstorm – would lower the water flux in the basal drainage system and drop the pressure. Such events were not measured and would be expected to be brief.

Atmospheric pressure is the lowest possible pressure along the basal boundary. This pressure was not directly measured in the boreholes, but is theoretically possible in a subglacial drainage tunnel ("R-channel"). Extended periods of atmospheric pressure in R-channels probably only occurs very close (i.e. < 1 km) to the ice margin because ice thickness, and therefore tunnel closure rates, increase quickly inward from the margin. Modelling of the basal drainage system suggests that low pressure in R-channels is not likely to exist for extended periods of time and is limited to a region near the ice sheet margin. For instance, water pressures less than 70 % of ice overburden pressure are likely to be limited to 10–20 km from the ice sheet margin.

4.4.4.3 Time-space variability and averaging

Boreholes from each of the study regions demonstrated variations in basal water pressure, with a seasonal cycle defined by marked differences between summer and winter behaviour. Relatively high water pressure persisted during the winter months, with pressure changing by no more than a few percent of overburden ice pressure over time periods lasting weeks to months. In contrast, summer variations in bed water pressure were rapid and substantial. Pressures changed over time periods as short as hours, and in some cases changed by > 50 % of ice overburden pressure on a repeated daily cycle. During the fall and spring transition periods, the pressure underwent unsystematic pressure variations on time scales of hours to days. The distinct differences between winter and summer behaviour were observed in all study regions despite other important differences between the locations.

This seasonal cycle of basal water pressure is characteristically similar to some observations from mountain glaciers (e.g. Fountain and Walder 1998, Harper et al. 2005, 2007). As with many mountain glaciers, diurnal water pressure swings are the dominant feature of summer water pressure. Boreholes located 1 km, 15 km and 30 km inland from the ice margin have all demonstrated diurnal water pressure swings. An important distinction of the data from the GrIS is that, with increasing distance from the ice margin (toward the interior of the ice sheet), the magnitude of diurnal swings diminished. For example, 1 km inland the swings are up to 83 % of overburden pressure, whereas, at 15 km, the swings are up to just 4 % of overburden pressure, and at 30 km inland the swings are less than 1.5 % of overburden pressure. The interior trough region demonstrated on/off switching of diurnal pressure variations, with diurnal swings on the order of < 10 % of overburden pressure and not persisting for more than a few days at a time.

Another distinction of the GrIS data is that the basal drainage system of the whole ice sheet maintained a high mean pressure, averaging near ice overburden water pressure. Pressures falling below 80 % of overburden ice pressure (on diurnal cycle or during spring and fall seasons) were only observed within a few km of the ice sheet margin. The low pressures in this area were not necessarily uniform across the bed, but were limited to well-connected and highly transmissive areas of the bed, such as those areas influenced by a drainage conduit. Areas between these transmissive areas remain at ice overburden pressure, even areas less than 1 km from the margin. For example, two boreholes were drilled within 200 m of the ice margin that demonstrated no water level variations whatsoever. Other holes drilled a few hundred metres away underwent summer diurnal swings, dropping to as low as 25 % of overburden.

In those sites located within a few km of the margin, relatively low water pressures (in terms of percentage of overburden ice pressure) were not persistent when averaged over the annual seasonal cycle. Low pressures (i.e. < 30 % below overburden) were common on a diurnal cycle during mid-summer or during brief periods of erratic variations in the fall or spring seasonal transitions. Low pressures occurred in the early AM hours, but this was balanced by high pressures in the PM hours. Overburden pressure is most common over time; most of the year, near overburden pressure is present at all study sites.

4.5 Chemistry of basal water and sediment

The chemistry of glacial waters has been analysed frequently over the past four decades, resulting in a wide range of information about subglacial chemistry and processes. Because glacial sediment is typically finely comminuted and transported through glacial systems at relatively high rates (Anderson 2005), the resulting chemistry is often dominated by highly reactive minerals, such as carbonates and sulphides (Tranter et al. 2002), even where such minerals are accessory and silicates are the overwhelming rock components (Raiswell 1984). These processes allow glaciers, in spite of the low temperature inhibition of chemical reactions, to contribute substantially to the global geochemical cycle (Anderson et al. 1997). Because nearly all chemical analyses of glacial waters have been performed on alpine glaciers, it remains to be seen whether or not this paradigm is equally applicable to continental ice masses. Because of their size, ice sheets may be subject to longer residence times both for subglacial waters and sediments. Waters can become progressively enriched in dissolved materials over increased residence times, while sediments may become depleted in reactive accessory minerals. Thus, the measurement of water chemistry in the GrIS allows analysis of the variability in sub-ice water-rock interactions and an assessment of the role of the GrIS in the overall geochemical cycle.

4.5.1 Sampling strategy

To fully assess the balance of chemistry in the subglacial system, rock, sediment and water were sampled. Samples were collected from boreholes and from outlet streams. The analysis of borehole water and sediment chemistry distinguishes this project from much of the previous work on subglacial chemistry. Where outlet streams represent a natural averaging of subglacial conditions, boreholes have the potential to reach a wider range of weathering environments (Tranter et al. 2002). The sampling transect, from marginal to inland (Figure 4-2), allows for the measurement of such environments over a wide range of the ablation zone.

The samples were taken over three field seasons, in June and July of 2010, 2011 and 2012. Due to the need to get other instrumentation down rapidly refreezing holes, only a selection of boreholes were subject to water and sediment sampling. In 2010, water samples were collected from 4 of the 13 holes drilled to the glacial bed. Water samples were also collected from two minor lateral outlets and from the main terminus of Isunnguata Sermia. In 2011, water and sediment samples were collected from 4 of 8 boreholes. Two sets of time series water samples were collected from the terminal outlet of Isunnguata Sermia, along with a representative suite of rock and sediment samples – including suspended sediment samples recovered from the outlet waters. Grab samples from supraglacial streams were also collected in 2011. In 2012, water samples were collected from all 4 boreholes of Site GL12-2 (interior). The 2 boreholes of Site GL12-1 (marginal) were not sampled, as they did not appear to connect with the basal hydraulic system. Sediment samples were collected from 3 out of 6 boreholes. Water samples were also collected from a minor lateral stream and from the main terminus. Sediment was collected from the outwash plain below the main terminus. Additional water samples were also collected by SPC (Chapter 5).

4.5.2 Sampling methods and field measurements

Upon completion of a borehole, sampling typically commenced immediately. For locations where the ice was temperate throughout, or nearly so, holes remained open for hours, or even days, allowing for repeated sampling. Initial samples likely retrieved a mixture of surface water (from the drill) and basal water. Where water levels rose and fell over the course of a day, the boreholes were inferred to be connected to the subglacial drainage network. Where this was the case, it was often possible to collect another water sample while water was rising in the borehole. This second sample likely contains little, if any, drill water. For locations where the ice was cold, holes began to freeze shut as soon as the hose and stem were removed. In these cases, no repeat sampling was possible and fluorescent tracing was employed to determine proportions of drill water, ice melt and basal water in the sample.

Borehole samples were collected using samplers designed to close upon hitting the base of the hole. Though samplers made of steel, aluminium and Teflon were used, comparison of boreholes and outlet streams sampled with differing materials suggests little to no chemical contribution from the samplers (Landowski 2012). The Teflon sampler was designed and fabricated during winter 2010–2011 and is the most inert of the sampler materials, with the least potential for metal transfer. The Teflon sampler was used in 2011 for a few samples before it was lost in GL11-1C. All subsequent samples that year were collected using the steel sampler. A newly fabricated Teflon sampler was employed in 2012.

The use of surface water to drill boreholes presents a mixing problem in the water samples. In 2010, because the ice was temperate (at 0 °C throughout), boreholes stayed open for several days and repeat sampling was possible. Two samples were collected from each of the analysed holes, one shortly after drilling and another ~ 1 day later. In 2011 and 2012, a fluorescent dye (Fluorescein) was added to the drill water as a tracer. This tracer could be measured to part per billion precision with an Optiscience GFP fluorometer. Surface stream water was pumped into a holding tank where dye was added. At ~ 100–200 m above the bed, the pump from stream to tank was shut off, maintaining a constant concentration of dye in the drill water. A concentration of dye of ~ 1 ppm was maintained in the tank. Fluorescein levels in the tank were measured every ten minutes until drilling stopped. To assess the dilution of the drill water by the melting of the borehole walls, fluorescein levels in the returning drill water were measured prior to connection to the basal hydraulic system. The ratio of fluorescein in the sample to fluorescein in the returning drill water is used to estimate the percentage of drill water in the sample.

All water samples were collected and stored in HDPE (Nalgene) bottles that were washed in 10 % HCl and then rinsed three times with ultrapure distilled water before the field season. In general, a 125 ml filtered sample was collected for the analysis of cations, and a 250 ml unfiltered sample was collected for the analysis of anions. In 2010, samples were filtered using Nalgene syringe filters (polyethersulfone) at 0.45 µm. However, not all samples could be filtered in the field in 2010, so the remainder of samples were filtered in the lab using a vacuum filtration system and GE polycarbonate filter membranes. The time elapsed between collection and filtration in these cases was 100–120 days. In 2011, all samples were filtered in the field using a battery-powered vacuum filter and Millipore 0.45 µm membranes. In 2012, samples were again filtered in the field, using both 0.1 and 0.45 µm membranes. All samples, from all three years, were acidified in the lab using ultrapure 12 N HNO_3.

At the terminal and lateral outlet streams, and in superglacial streams, samples were collected by washing the bottle three times with stream water, then submerging the bottle to fill it. Filtration took place immediately, with filtrate eluted into clean bottles (acid washed and rinsed, but not rinsed with stream water). Terminus streams were extremely sediment-laden and required multiple membranes per sample to avoid unreasonably long filtering times. The dry weight of the sediment on these filters was subsequently used to calculate suspended load.

When possible, pH, total dissolved solids (TDS), electric conductivity and ^{222}Rn activity were measured in the field. pH, TDS and conductivity were measured using a Beckman-Coulter Series 460 m. Due to calibration difficulties with the pH metre, Whatman pH indicator strips were alternatively used during most of the 2011 season. With borehole samples, these variables were measured in unfiltered water immediately upon sample retrieval. Otherwise, the variables were measured directly in the stream.

The activity of ^{222}Rn in both borehole and terminus waters was measured with a Durridge Rad7 fitted with an H_2O accessory. The Rad7 circulates air through its detector, where decay energies are converted to an electrical signal, identified, counted and then an activity is calculated from the raw counts. The H_2O accessory bubbles air through a water sample so that gaseous radon leaves solution and circulates through the detector. The Wat250 protocol for the instrument was employed, which is a method of grab sampling. The Wat250 protocol utilises a 250 mL water sample and counts decay emissions over four cycles of five minutes each; an average of the four cycles is the activity of the sample. The only deviation from the recommended settings was to use a large "laboratory drying unit" in place of the small tubes of desiccant. This substitution was done to protect the detector from damage by the high humidity observed at Isunnguata Sermia, and to limit the amount of time required to purge the machine of this humidity (which becomes a concern in the field when the Rad7 runs off its internal battery). The measured activity was doubled to account for the extra air volume in the large column.

Upon sample retrieval, water was transferred from the sampler to the Rad7 glass counting bottle through a funnel rinsed with deionised water before and after each use. The bottle was then immediately sealed. Though there is the possibility for some degassing of radon to occur during transfer from the sampler to the bottle, the partitioning coefficient of radon at 0 °C is sufficiently low that loss should be minimal, and should also be comparable for all borehole samples because the same technique was employed every time. Samples were not filtered before analysis on the Rad7. The counting protocol was initiated immediately following collection, generally within three minutes of sampler return.

In 2011 and 2012, a cast-iron sediment sampler was employed to retrieve sediment from ice-bed interface accessed via boreholes. The sediment sampler works through a suction mechanism that is manually driven by the operator of the winch, pulling a piston set within the sampling tube. Samples were manually extracted from the tube and bagged for future analysis. The tube was subsequently washed with surface water prior to further use. In 2011, sediment was collected from the terminal moraine of Isunnguata Sermia, and from the outwash between the terminal moraine and the ice front. In 2012, sediment was collected from the outwash plain below the terminal moraine. Terminus sediment samples were collected at random locations in the generally homogenous moraines or outwash plains from which they were collected.

Rock samples were selected to be representative of the cobble-sized clasts present on the terminus outwash plain. Several regions of outwash were selected at random, and the lithology of the clasts within an arbitrarily drawn box was briefly assessed. Four principle lithologic types were identified: granodioritic gneiss (A) – 60 %, granitic gneiss (B) – 13 %, weakly foliated granite (C) – 13 % and gabbro (D) – 14 %. These percentages were determined by characterising and counting every clast within the box. Samples of characteristic mineralogy from each of these types were collected for further analysis.

4.5.3 Laboratory analyses

In 2010 and 2011, elemental concentrations in the filtered samples were measured in triplicate on a Perkin-Elmer/Sciex Elan 6000 inductively coupled plasma mass spectrometer and a Perkin-Elmer Optime 3300 DV inductively coupled plasma atomic emission spectrometer at the trace element hydrochemistry analytical lab at the USGS in Boulder, Colorado. Anions were measured using an ion chromatograph. An alkalinity titration was employed to estimate HCO_3^- content. In 2012, samples were analysed by the Geological Survey of Finland using similar instruments and methods.

Sediment samples were dried and weighed. Borehole and some outwash samples were sorted by grain size. Analysis by grain size aliquot addresses grain size bias either due to the sampling method or due to natural sorting by flowing water. Grains were binned into the following ranges: > 0.5 mm, 0.25–0.5 mm, 0.1–0.25 mm, 0.045–0.1 mm, < 0.045 mm. 5–10 g of each grain size aliquot were ground in a ceramic shatter box. The shatter box was cleaned with methanol between samples. Rock samples were cut in two to archive the original sample. One half was crushed in a jaw crusher and then pulverised in the shatter box.

The pulverised rock and sediment samples were prepared for XRF analysis. 0.45–0.6 g of sample were mixed with a lithium metaborate ($LiBO_2$) flux at a ratio of 12 parts flux to 1 part sample. This mixture was heated to a molten state in a platinum crucible, with lithium iodide (LiI) added as an anti-wetting agent, then poured to cool in a platinum mold, resulting in the production of glass beads. 4 g of sample were mixed with 1 g of a cellulose binding product and pressed at 30 tons, resulting in the production of a pressed pellet. Both beads and pellets were analysed on an Axios Panalytic X-ray florescence machine at the University of Wyoming. The beads were analysed for major elements while the pressed pellets were analysed for minor and trace elements.

4.5.4 Results

Field chemistry shows pH values ranging from 5.5 to around 7.75. Low ionic strength samples tend to have slightly acidic pH values. A pH value of 5.5 is expected from the dissolution of atmospheric CO_2 in 0 °C water, and most highly dilute samples are near or at this value. Samples with higher concentrations of dissolved solids tend to be neutral or slightly basic (at 0 °C, neutrality is at pH 7.45), suggesting that dissolution reactions are primarily alkalinizing. A strong correlation between ionic strength and pH is found in the borehole and outlet stream waters (Figure 4-16). The largest components of these waters is alkali metal cations (Na^+ and K^+) and bicarbonate anions (HCO_3^-), with Ca^{2+} abundant in several samples (Figure 4-17). The sampled waters show a wide range of silica concentrations (1–450 µmol/L) with many samples in the range of 30–40 µmol/L. Base cations typically range between 40–400 µmol/L , with Ca, Na and K fairly evenly represented. The geographic distribution of dissolved solids is complex, with variation between adjacent boreholes often comparable to variation across the study region as a whole (Figure 4-18A–C).

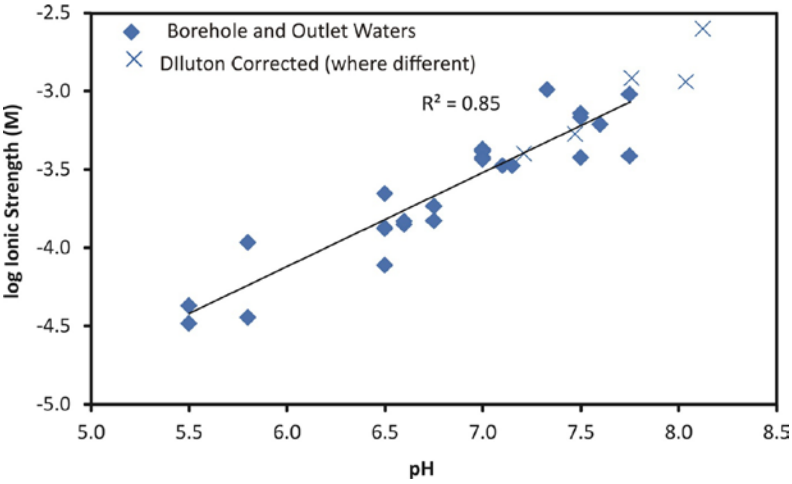

Figure 4-16. *pH vs. ionic strength in selected borehole and outlet stream waters. Dilution corrected values are also shown where fluorescein measurements allow for correction to be made.*

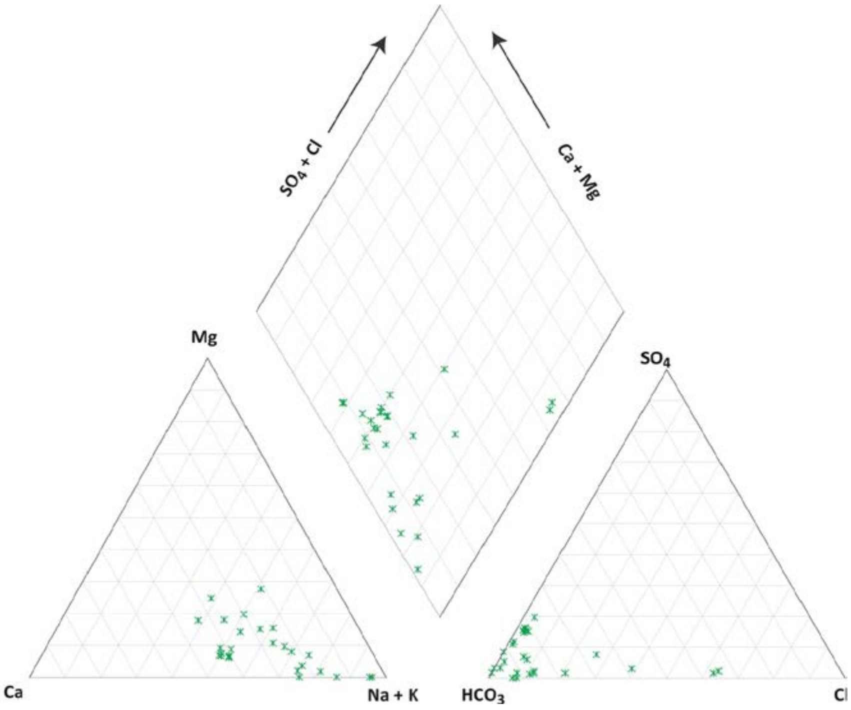

Figure 4-17. *Piper plot of the borehole and outlet water chemistry.*

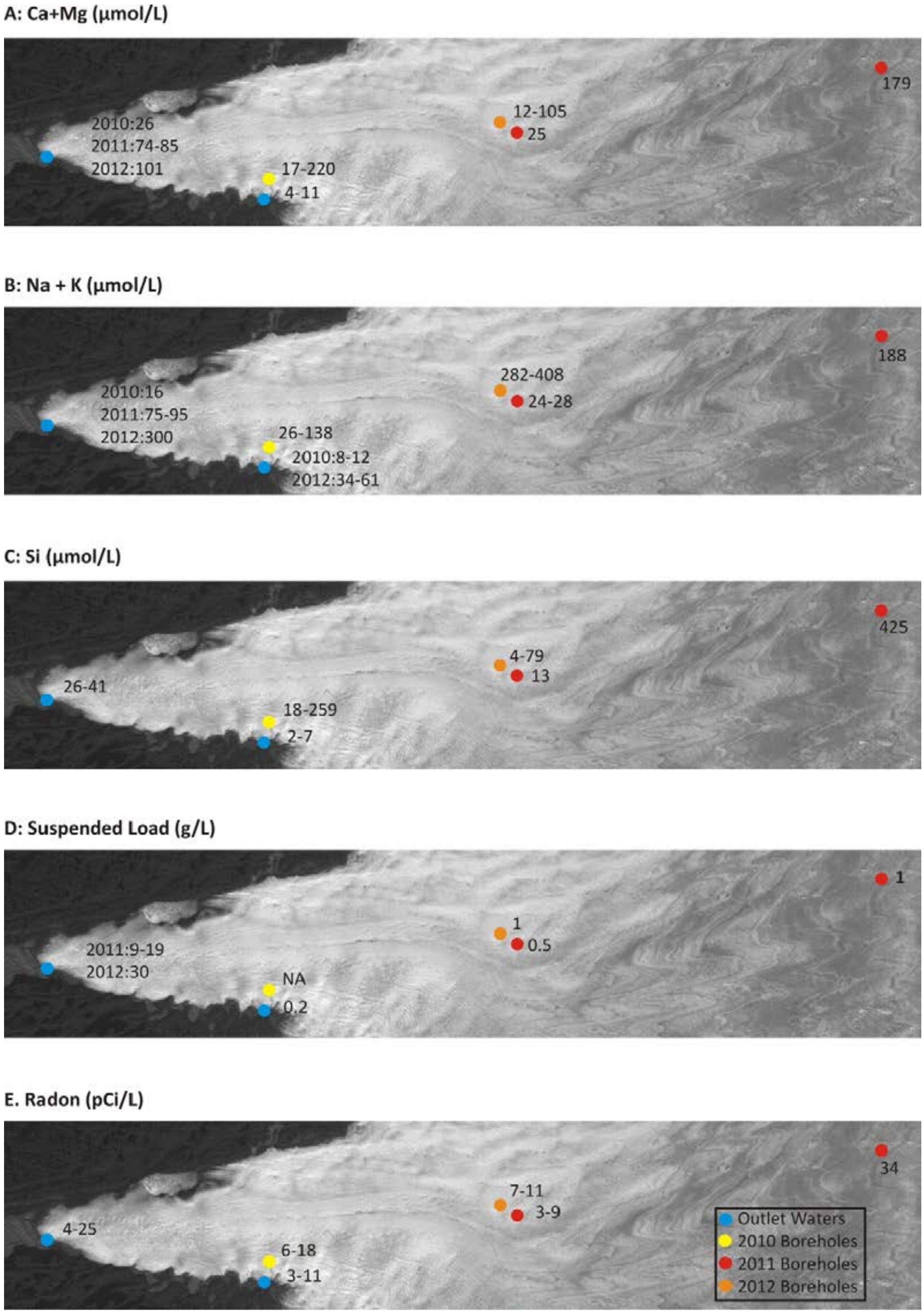

Figure 4-18. *Spatial distribution of A) calcic ions, B) sodic ions, C) dissolved silica, D) suspended sediment, and E) radon in the borehole and outlet waters.*

The terminal outlet waters have an order of magnitude more suspended sediment than the borehole waters, and two orders of magnitude more than the lateral outlets (Figure 4-18D). There is no correlation between dissolved and suspended load, suggesting that the two are controlled by largely unrelated processes.

The ^{222}Rn results are largely equivocal (Figure 4-18E). Most samples generated fewer than 10 counts during the 20-minute sample analysis period, with many recording ^{222}Rn values that may be indistinguishable from background. While a relatively high measurement (34.2 pCi/l) was collected at the most interior site (GL11-2C), correlation between dissolved load and radon activity is weak.

The terminus time series data show cyclic patterns in the various analysed dissolved solids (Figure 4-19). These cycles peak at midday and then decline at night, and display enrichment in dissolved load with an increased flux of meltwater. This is opposite to the results typically found in alpine glaciers, where dissolved load is diluted due to increased meltwater flux (i.e. Mitchell and Brown 2007). Suspended load shows a reverse trend, with the greatest concentrations of suspended sediment found when discharge is lowest (Figure 4-20). The two diurnal patterns are not exact inverses of each other. Maxima in suspended load are found in the early morning (circa 05:00) and minima are found in the late afternoon (circa 20:00). With dissolved load, minima occur circa 05:00, but maxima are circa 12:00.

The minor, trace and rare earth elements show considerable complexity and variability. Al and Fe appear in concentrations comparable to the major elements in several samples, but in trace concentrations in others. Cu and Zn appear to be strongly enriched in several samples, with values of around 1 μmol/L. Arsenic appears to be highly dilute, with most samples containing less than 0.001 μmol/L. The light rare earth elements appear fairly enriched, with values considerably above 0.001 μmol/L in most samples. Redox couples are not in equilibrium in the sampled waters. In slightly basic borehole waters, Fe redox pairs give oxidation potential (Eh) values near 0 volts, Cu redox pairs (Eh values near 0.2 V) and Mn redox pairs (Eh values near 0.55 V) (Figure 4-21).

The bulk chemistry of the rock and sediment samples strongly reflects the granodioritic composition of the underlying bedrock formations. Si and Al are most abundant, with a fairly even balance of elements associated with felsic (Na, K) and mafic (Ca, Mg, Fe) minerals. The analysis of sediment composition shows a strong tendency for mafic minerals to be concentrated in the smallest grain size aliquots (Figure 4-22). Comparison of rock and sediment data shows that base cations (particularly K) have been leached from the sediment. This has led to the enrichment of more conservative elements such as Si. Al does not appear to be strongly conserved in the sediment, which is consistent with the high level of Al found in some water samples.

To determine which of the analysed elements were enriched and depleted in the sediment and water, the proportions of elements were determined in averaged representative rock, water and sediment samples. This analysis shows that elements depleted from the sediment tend to be enriched in the water, and vice versa (Figure 4-23 and Figure 4-24). The sediment is depleted and the water enriched in the alkali metals, Mo, Ni, Cu, Zn, P and S, as well as the light rare earth elements. Si and most of the other transition metals and metalloids are enriched in the sediment and depleted in the water. The alkaline earth metals appear to be depleted from the sediment and enriched in the water, but some cases are ambiguous, particularly when low ionic strength waters are considered.

4.5.5 Summary of chemistry and basal water and sediment

While these results do not directly address the GAP questions about subglacial groundwater at depth, they do provide substantial insight into the chemical processes occurring at the rock-ice interface. The chemistry from boreholes and outlet waters is consistent with an environment where dissolved CO_2 facilitates the weathering of silicate minerals. This differs from many alpine glaciers, where weathering and oxidation of accessory carbonates and sulphides controls most of the aqueous chemistry (i.e. Tranter et al. 2002). A silicate source for most of the dissolved constituents is suggested by the relatively high abundance of Si, K and Na in the water. Bicarbonate is the dominant anion and is present in excess of Ca sourced from carbonate, implying CO_2 as the primary acid.

The measurable depletion of base cations, and the enrichment of silica in the sediment compared to rock, suggests that the bedrock is losing mass to chemical weathering reactions. The general correspondence between such depletion/enrichment patterns, and the distribution of dissolved elements in the water samples, allows the mass loss between rock and sediment to be attributed to presently occurring processes. For such mass loss to occur in a subglacial environment, the residence times of the subglacial sediment are likely to be relatively long.

The results illustrate the variable nature of rock-water interactions in the subglacial environment. Concentrations of dissolved constituents were observed to vary considerably between boreholes drilled tens of metres apart. This small scale variation is of a large enough magnitude that it dampens any larger scale or regional variation in dissolved load. This suggests regions where water is able to cycle very quickly through the basal hydraulic system, as well as regions of far greater water residence times existing in close proximity to each other.

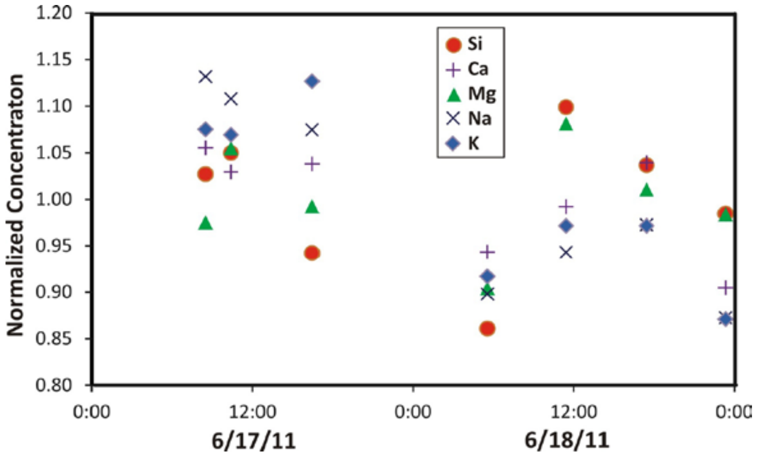

Figure 4-19. *Time series measurements of Si and major cations at the terminus of Isunnguata Sermia, normalised to average value.*

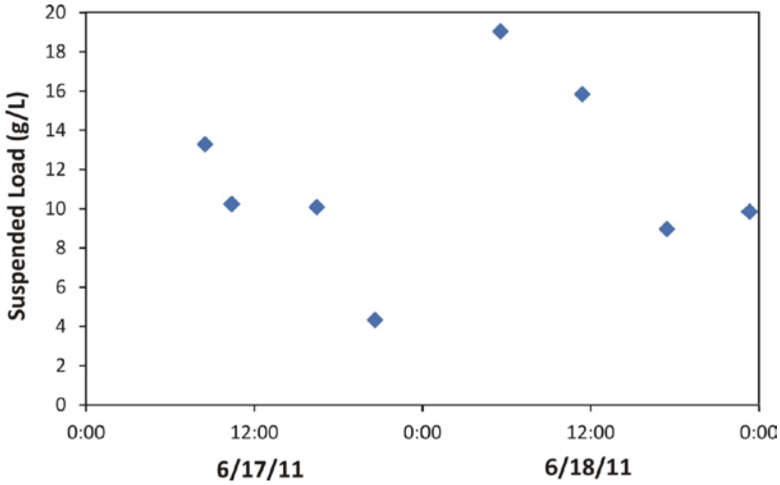

Figure 4-20. *Time series measurements of suspended sediment concentration at the terminus of Isunnguata Sermia.*

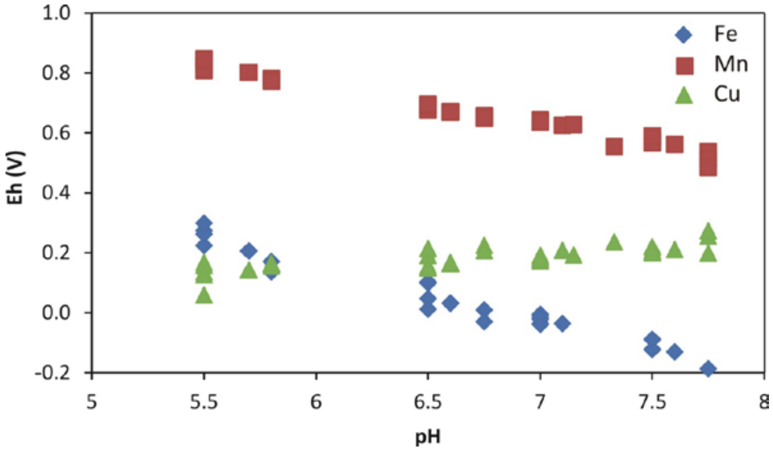

Figure 4-21. *pH vs. Eh relationships in the sampled waters based on redox pairs. All Eh values are calculated from measured pH and element concentrations using the Nernst equation and standard thermodynamic data. The Fe data assume Fe^{2+} equilibrium with Hematite (Fe_2O_3), with samples plotting in Siderite ($FeCO_3$) space excluded. The Mn data take the minimum of the Mn^{2+} / Pyrolusite (MnO_2) equilibrium and Mn^{2+} / Manganite (Mn_2O_3).*

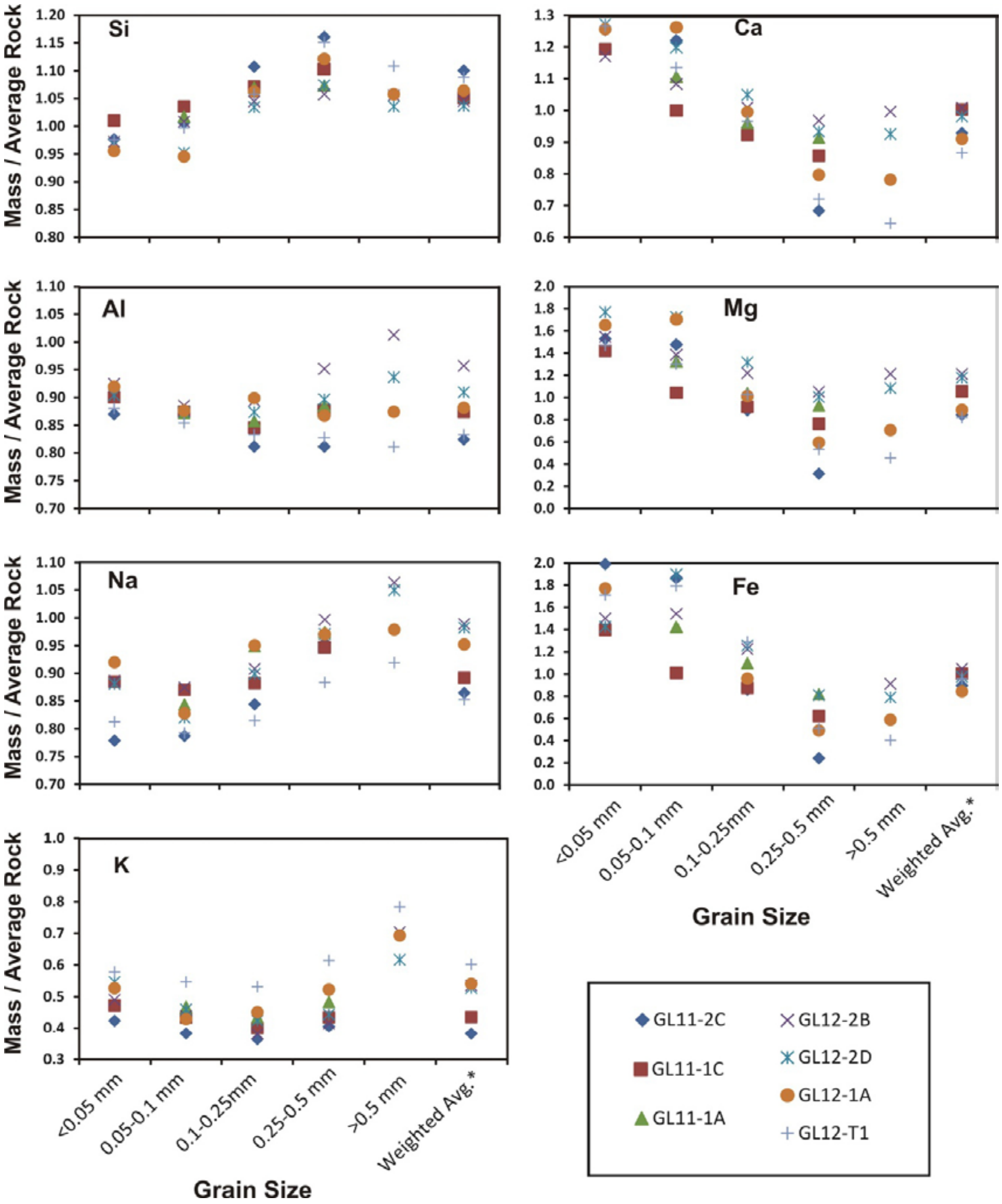

Figure 4-22. *Distribution of major elements by grain size in sediment samples. Data are normalised to the average concentration of the element in the rock samples. The weighted average column reflects the grain size distribution in the sample. Due to bias in the sampling method and natural grain sorting processes, this average may not be representative of the true grain size distribution in subglacial sediment.*

4.6 Ice temperature

4.6.1 Methods

Borehole sensor strings included sensors for measuring temperature at intervals along the length of the borehole. All instrumentation was custom designed and self-manufactured for the project from raw electronic components. The strings utilize temperature-sensing semiconductor chips which are soldered into long strands of CAT-5e cable (signal cable). The sensors were controlled by circuit boards that enable serial transmission of data streams from sensors to a data logger at the surface.

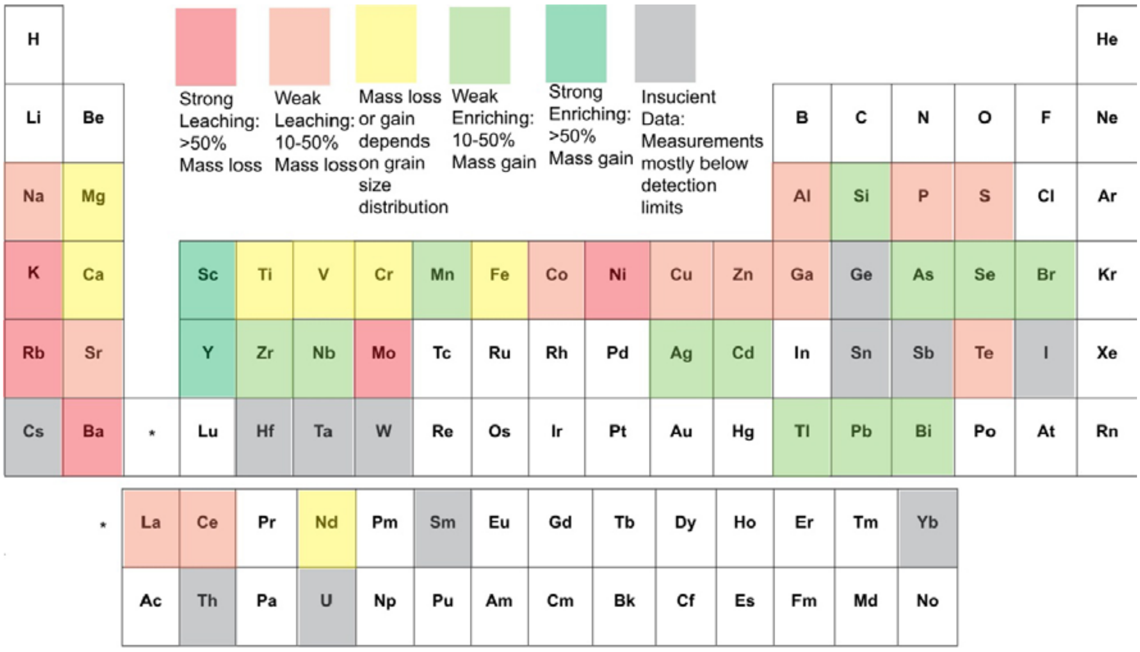

Figure 4-23. *Change in the relative proportion of elements between average rock and average sediment. Analyzed elements are coloured corresponding to the degree to which the element is leached or enriched in the sediment. In yellow marked elements, fine grain sediments are enriched and coarse grained sediments depleted, rendering an assessment of the differences between rock and sediment dependent on an accurate estimate of the grain size distribution.*

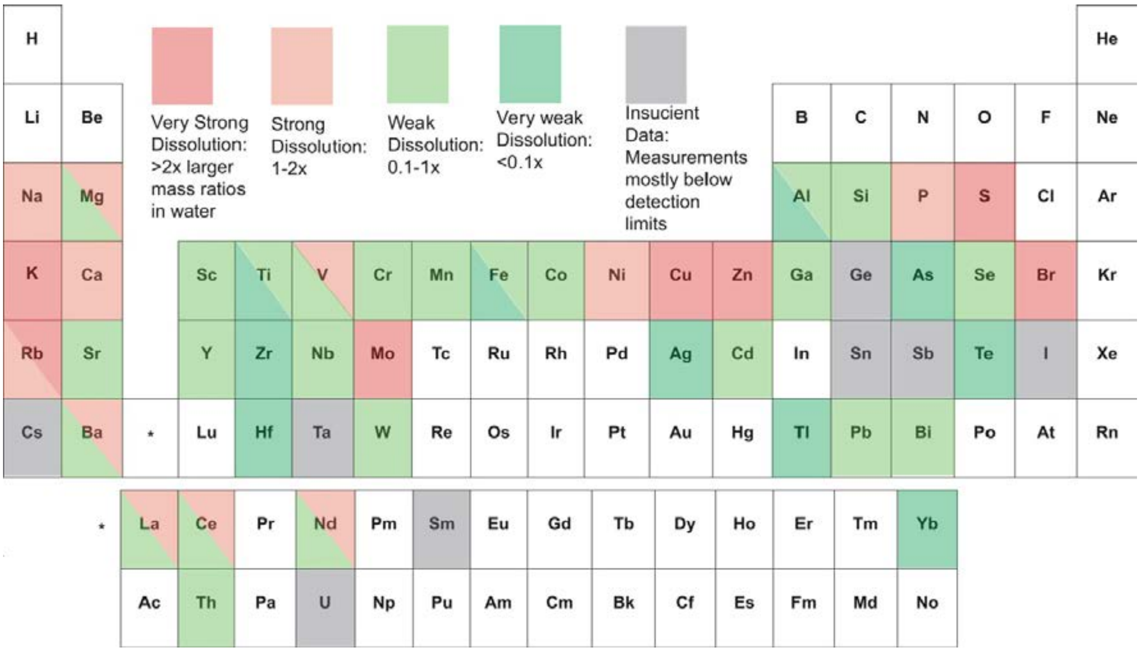

Figure 4-24. *Change in the relative proportion of elements between water and sediment. Analyzed elements are coloured corresponding to the degree to which elements are enriched or depleted in the waters. The colour scheme is reversed from Figure 4-23, so that depletion in the sediment is coloured identically to enrichment in the water. For elements containing more than one colour, the upper right represents conditions in high ionic strength waters and the lower left conditions in low ionic strength waters.*

A single cable with four twisted wire pairs was used to collect data with the temperature sensors spaced every 10 or 20 m along the length of the boreholes. The advantages of these sensors/sensor-strings are that material costs are minimised, they are simple to install in the boreholes, and they have low power requirements for extended data collection. Further, the shared signal line permitted by serial communications enabled > 30 sensors to be placed on the 8 conductor cable, which included power/signal for the pressure transducer. Standard analogue sensors would have required an ~100-conductor cable, which would have been prohibitively large and expensive. However, the disadvantage of this approach is that the custom fabrication requires considerable labour. The sensors and circuit boards were assembled and potted in epoxy to make them waterproof, and then spliced into the cable at the appropriate positions.

The temperature sensors have a resolution of 0.062 °C and are calibrated to ± 1 °C. Each sensor was calibrated to the zero point in an ice bath, and then again in the field while the sensors were submerged in the cold freezing water of the borehole.

Temperature sensors were not installed in every borehole, both due to limited temperature strings and because temperatures at the margin were already estimated to be at melting temperature. The majority of holes were outfitted with temperature strings at each site (Table 4-8). Temperatures were not logged to collect a time series because, typically, ice temperature does not change on time scales of less than many years, except very close to the surface. Due to the thermal disturbance caused by hot water drilling, which takes weeks to months to dissipate, the temperature profile was first measured in the September following drilling. Occasionally, temperatures could not be retrieved from sensor strings in some holes due to time constraints of data collection or sensor malfunction. Temperature profiles were collected again the following year, but showed little difference from the original profile. Seasonal surface temperature variation produces differing near-surface temperatures, depending upon the severity of the winter cold wave at different elevations when the data was collected as well as the depth of the near-surface sensors.

Table 4-8. Boreholes with temperature records.

Hole	Thermistor installation YYYY-MM-DD	Temperature reading YYYY-MM-DD	Difference
GL10-1A	2010-06-12	2010-09-**	**
GL10-2C	2010-06-23	2010-09-**	**
GL10-3A*	2010-06-30	2010-09-**	**
GL11-1A	2011-07-02	2012-06-21	355
GL11-1B	2011-07-04	2012-06-21	353
GL11-1C	2011-07-06	2012-06-21	351
GL11-2B	2011-07-14	2012-06-12	334
GL11-2D	2011-07-18	2012-06-12	330
GL12-2A	2012-06-13	2012-09-12	92
GL12-2C	2012-06-17	2012-09-12	88
GL12-2D	2012-06-20	2012-09-12	85

4.6.2 Results

Margin region (sites GL10-1, GL10-2, GL12-1, GL10-3)

GL10-1, GL10-2, GL12-1

All boreholes drilled within 2 km of the ice margin at the Point 660 area (sites GL10-1, GL10-2, and GL12-1) demonstrated ice temperatures at the pressure melting point (Figure 4-25) throughout the depth of the ice. Because the ice is shallow in this area, the pressure melting point near the bottom of the boreholes remains close to 0 °C. Partial freezing of some boreholes did take place, but this can be attributed to upward movement of water within the boreholes. Water moving upward will eventually freeze due to the decrease in the pressure melting point.

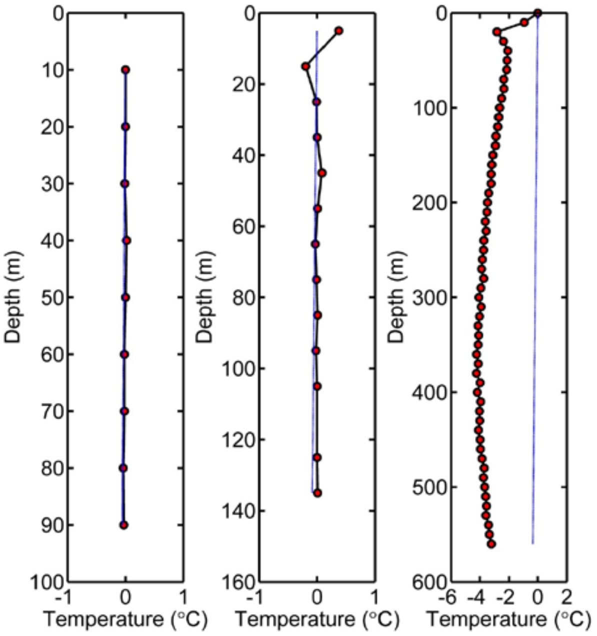

Figure 4-25. Ice temperatures measured (from left to right) for GL10-1 and GL10-2 on the margin, and GL10-3, 3 km from the margin. The blue dashed line represents the pressure melting point as a function of depth. Depth units are relative to the initial ice surface at the top of the borehole.

GL10-3

The ice temperature 3 km inland at site GL10-3, where the ice is > 700 m deep and flows into the deep trough of the Isunnguata Sermia outlet, does have ice below the pressure melting point (Figure 4-25). Here, ice is warm near the surface, cooling with depth to a minimum temperature of about −4.5 °C at 400 m depth, and then warming toward the bed.

Interior region (sites GL11-1, GL11-2)

Temperature measurements for the interior region are summarised in Figure 4-26 and Figure 4-27.

GL11-1

At site GL11-1, about 15 km from the ice sheet margin, the ice temperature reaches a minimum temperature of about −3.75 °C about 150 m below the surface. The ice then warms with depth and reaches the pressure melting point at about 140 m above the bed. Hence, the lowermost 30 % of the ice sheet consists of temperate ice. At about 60 m depth, a brief warming trend is present in the profiles. Additionally, all 3 boreholes at the site exhibit different temperatures despite being located only 20–30 m apart. Temperature offsets between the boreholes are relatively constant throughout the interior of the profiles.

GL11-2

Higher up the ice sheet at site GL11-2, the ice is far colder, reaching a minimum temperature of about −13.8 °C about 500 m below the surface. The ice warms with depth and likely reaches the pressure melting point at some height just above the bed (sensors do not reach bed). The temperate layer will be less than 5 % of the ice thickness.

Trough Region (site GL12-2)

Temperature profiles at GL12-2 (Figure 4-28) exhibit an offset similar to those seen at GL11-1. After a warming trend near the surface, holes A, C and D cool with depth to −4.8 °C, −5.3 °C, and −5.8 °C, respectively, at around 240 m depth. The temperature then warms and reaches the pressure melting point at about 560 m depth; the lowermost 145 m of ice is at the pressure melting point. This shows a similar thickness of temperate basal ice in the trough to GL11-1, just 1 km away, despite the much larger total ice thickness.

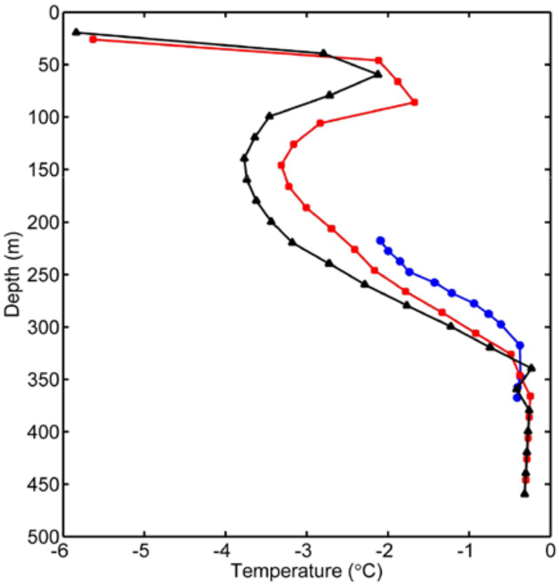

Figure 4-26. *Ice temperatures for GL11-1A (blue), GL11-1B (red) and GL11-1C (black). Data capture from GL11-1A did not yield a full profile. Depth units are relative to the initial ice surface at the top of the borehole.*

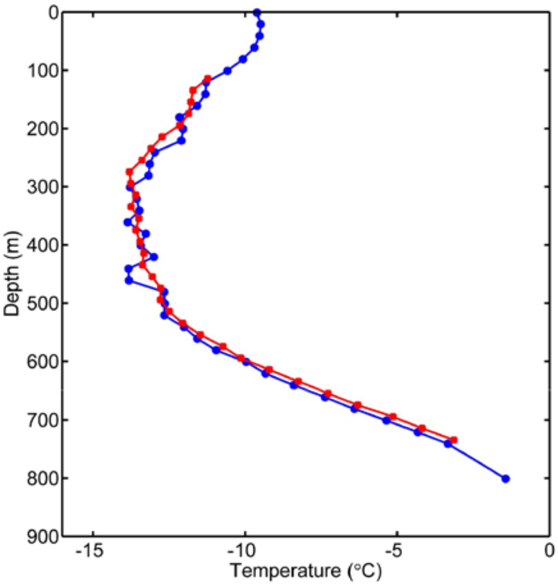

Figure 4-27. *Ice temperatures for GL11-2B (blue) and GL11-2D (red). Depth units are relative to the initial ice surface at the top of the borehole.*

4.6.3 Summary and discussion of ice temperatures

The marginal ice, for several kilometres inland, is approximately isothermal and at the pressure melting point of ice. Farther inland, as far as the deepest holes, the basal ice remains at the pressure melting point and water is present at the bed. The thickness of the warm ice (at the pressure melting point) at the base of the ice sheet decreases up-glacier, going from the full depth near the margin to ~ 140 m thickness (or 30 % of ice depth) at 15 km up-glacier. At the highest site, only 30–40 m of basal ice is warm, which is only a few % of the ice depth. Assuming the thickness of warm basal ice continues to decrease up-glacier, at some point the basal ice will reach below freezing and free water will no longer be present at the bed. Above the bed layer, the ice continuously becomes colder up-glacier and as the ice thickness increases. At the deepest, highest site, the bulk ice temperature drops to −13.8 °C and is expected to get somewhat colder farther up-glacier. Warming surface temperatures at lower elevations, in combination with a warm base, often create the observed cold core at depth, originating from the horizontal advection of cold ice from up-glacier.

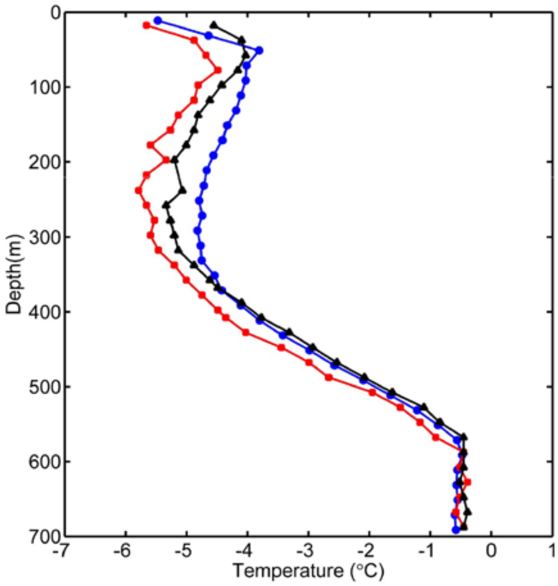

Figure 4-28. *Ice temperatures for GL12-2A (blue), GL12-2C (red) and GL12-2D (black). Depth units are relative to the initial ice surface at the top of the borehole.*

Ice at the margin sites is entirely temperate, providing no thermal barrier to prevent surface melt from making its way to the bed. 15 km up-glacier, the ice temperatures exhibit several atypical features, including a thick temperate layer encompassing the lowermost 30 % of the ice. The site farthest up-glacier, GL11-2, contains a similar thick temperate layer for the lowermost 40 m (< 5 % of ice thickness). All up-glacier sites display a cold core at depth, though it is evident that water is still penetrating to the bed. Generally, these temperature profiles are most useful for input, validation and comparison with numerical models. Additionally, analysis of the anomalous features within the profiles will lead to a better understanding of the impacts that different thermal sources have within this part of the ablation zone.

As a result of the basal thermal structure, where the bed is covered by warm ice, the glacier flow has a large component of basal sliding accompanied by subglacial erosion of the bedrock and other features of glacial sliding. This region extends from well up-glacier of the highest site, all the way to the ice margin. Higher up on the glacier, where the warm basal ice pinches out, and the basal ice temperature drops below the freezing point, glacier motion is restricted to ice deformation and little basal erosion or sliding occurs.

The full depth warm ice at the margin facilitates vertical water motion that drains meltwater from the surface to the bed because less energy is required to melt a pathway when ice is already at the melting point. Although the melt rate near the margin is high, and surface streams abound, the streams tend to be short and small and often disappear into moulins or crevasses before reaching the margin. Farther up-glacier, the cold core of the ice presents a thermal barrier to melt water migration from the surface to the bed. Indeed, up-glacier streams become much larger and travel for considerable distances before flowing into either surface lakes or larger moulins. Based on the presence of moulins, and the drainage of surface lakes, the region of basal water extends up to 50 km up-glacier from the highest drill site; thus, water in this region is freely available at the ice/bedrock interface.

4.6.3.1 Comparison with other measurements

Typical ice sheet temperature profiles exhibit a relatively steady vertical temperature gradient, resulting from the temperate bed and cooling upward to the surface. This is evident in temperatures collected from ice stream B in the West Antarctic Ice Sheet (Figure 4-29) (Engelhardt et al. 1990). The gradient is due to heat generated at the bed, caused by heat of sliding and geothermal heat from the bedrock. Only the base of the ice sheet is temperate. This expected temperature distribution is contrasted by the profiles, which contain anomalous thick layers of temperate basal ice. Nowhere is the bed frozen, suggesting that if ice is frozen to the ground, this must occur farther inland, likely within the accumulation region. The size of these temperate layers grows in thickness from the farthest interior site to the margin. Though the thickness of the temperate layer in the trough, GL12-2, is similar to 1 km away at GL11-1, the relative thickness of GL11-1 is much larger than GL12-2. The origin of the temperate layers in the profiles is likely complex. Potential sources include excessive ice deformation, frictional heating from sliding, basal crevassing and longitudinal ice compression. Analysis of the likelihood and potential interplay of these heat sources will facilitate enhanced understanding of basal processes.

In addition to thick temperate basal layers, profiles from GL11-1 display several other atypical thermal features. All 3 boreholes exhibit different temperatures despite being located only 20–30 m apart. Steep horizontal temperature gradients are generally not expected within ice sheets (Cuffey and Paterson 2010) and, at all other drill-sites the respective boreholes are the same temperature. The consistency of the offset suggests that these profiles must be heated from a vertically uniform source. The previous occupation of a moulin, which transports meltwater from the surface to the bed through a vertical channel and has been shown to have a dense presence in this region, appears to be the only plausible englacial feature capable of providing this uniform heat source. Because multiple boreholes show unusual full-profile temperature offset, a unique opportunity exists to link the thermal effects of water flowing through moulins to actual temperature data. Also under investigation is whether or not the brief warming trend at 60 m depth may represent warming induced by water flowing within crevasses up-glacier, which has been dampened since the ice left the crevasse field. Both the offset and the upper warming trend may be present in the GL12-2 profiles as well, however, further calibrations of the data is required.

Englacial and basal temperature data for the GrIS is sparse. Early temperature measurements were collected in associated with deep core drilling projects. Later, hole-only drilling through hot water drilling methods, to gain access to the ice sheet bed, allowed for additional temperature profile collection. Because the time required to drill to the bed is significantly shorter for hot water drilling, several boreholes are often drilled at a site, allowing for multiple temperature profiles.

Figure 4-30 illustrates the location of all drilling sites on the GrIS at which temperature data have been collected. These temperature profiles provide valuable insight into conditions at the bed and provide useful constraints for application in large-scale ice sheet numerical models. The following paragraphs detail the available temperature information from each site.

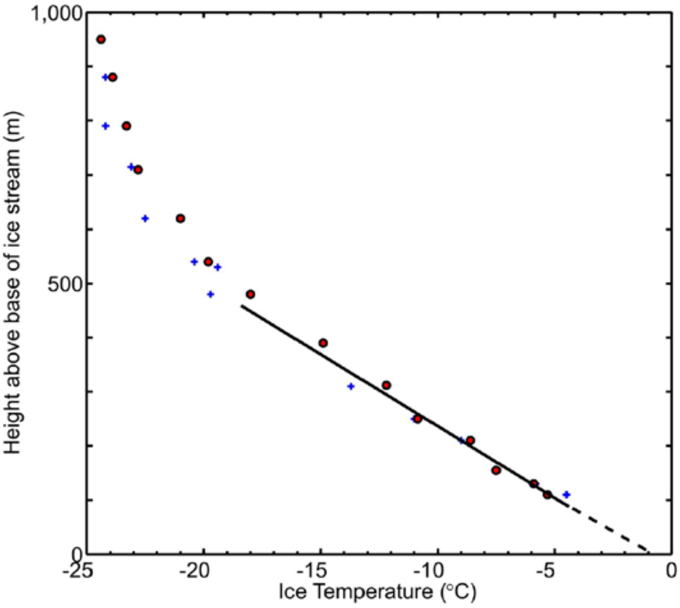

Figure 4-29. *Temperature profile through ice stream B at field station Upstream B in the West Antarctic Ice Sheet (Engelhardt et al. 1990). Circles and crosses represent temperatures obtained by two different data-reduction techniques. The linear black line is a least squares fit to the data points below 400 m, and the dashed line is extrapolation to the bottom.*

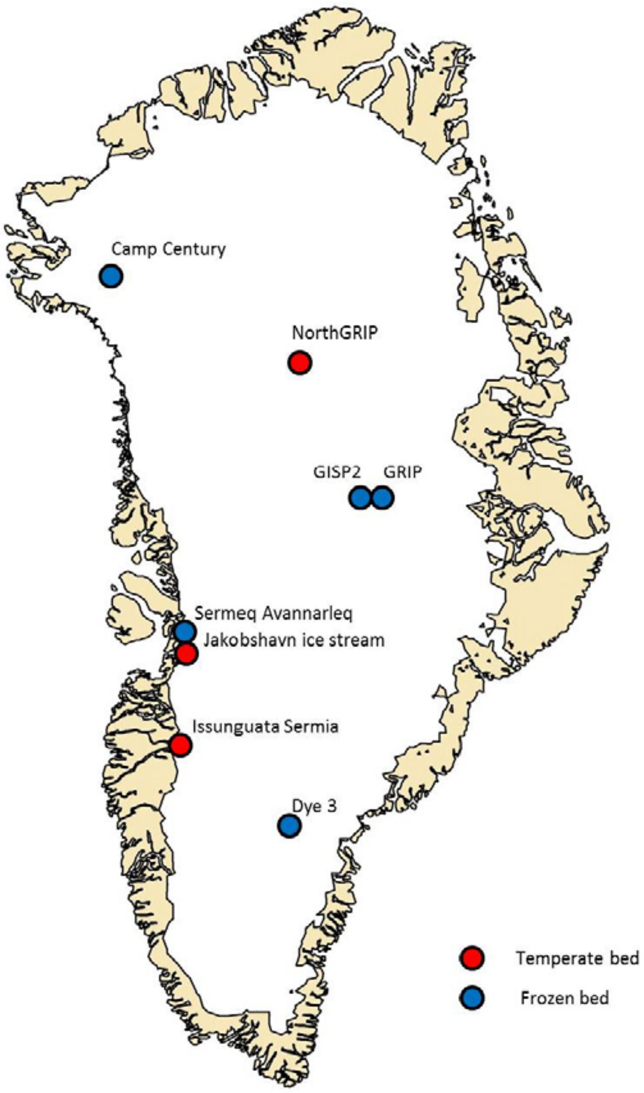

Figure 4-30. *Location map of drill sites with temperature data.*

Camp century

The first full-depth temperature profile for the GrIS was measured in June of 1966 at Camp Century in northwest Greenland (Weertman 1968). The basal temperature was −13.0 °C at a depth of 1387.4 m, indicating that the ice is frozen at the bed. The minimum temperature, −24.6 °C, was measured at 154 m depth. The temperature gradient then increases with depth until it becomes linear for the lower 300 m, suggesting a geothermal heat flow of 41.8 mW/m^2 (Hansen and Langway 1966). The hole was preserved to follow deformational changes, so the upper 280 m of this profile was re-measured in 1989. The two profiles display similar results and slight temperature differences are thought to have been caused by the interpolation equation used for the 1966 profile (Gundestrup et al. 1993a).

Dye 3

A total of 4 temperature profiles were collected at the Dye 3 station in southern Greenland during and after deep core drilling for the GrIS Project (GISP) in a region with mountainous bedrock topography. The first was collected in 1980 over the full depth of the hole at the time (901 m). The others were collected in 1982 and twice in 1983 after the drilling had reached the bed at 2037 m. The basal temperature was −13.22 °C, showing that ice is well below the melting point at the bed (Gundestrup and Hansen 1984). The minimum temperature, around −20.5 °C, was located around 200 m depth (Dahl-Jensen et al. 1998). The temperature gradient for the lower 800 m is lower than the gradient seen at Camp Century (0.012 K/m vs. 0.018 K/m) and the small reduction in gradient near the bottom is from internal friction in the silty basal ice (Gundestrup and Hansen 1984).

Jakobshavns Isbræ

Using hot water drilling methods, boreholes were drilled and outfitted with thermistors at 3 sites (A, B, C) on a transverse section through the Jakobshavns Isbræ ice stream 50 km from the calving front (Iken et al. 1993). Motivations for the temperature measurements were to understand the mechanisms creating the high ice velocities and documenting the basal conditions of the ice stream. Sites A and C, located along the cross-sectional margin of the ice stream, reached the bed (though the Site C thermistor cable only reached a depth of 900 m). Site B, at the centre of the ice stream, reached a depth of 1560 m, 940 m above the bed. The basal temperature at site A reaches the melting point and the temperature minimum is −22 °C at 1100 m depth. The basal temperature gradient is 0.1 K/m. At site B, the temperature minimum is −22.1 °C at 1200 m depth. Near-surface temperatures are warmer for the marginal sites (A and C) than the centre site (B). Though site B does not reach the bed, a large temperate layer (up to 400 m) of ice can be inferred (Funk et al. 1994).

Sermeq Avannarleq

Temperature profiles at 5 locations (TD1–TD5) along the flow line of Sermeq Avannarleq, extending from the margin to the equilibrium line, were collected between 1988 and 1991 (Thomsen 1988, Thomsen et al. 1991). TD1 and TD2 were first measured in 1988, and re-measured in 1989 and 1991. TD1 and TD3 are the only profiles that reach the bed. Neither exhibits a temperate bed, with basal temperatures at −0.9 °C and −0.8 °C, respectively, and a minimum temperature of −2.1 °C. TD2 is relatively uniform, cooling with depth. TD4, located around 20 km inland, warms with depth from around −13 °C at the surface to −2.6 °C at about 500 m depth. TD5 is located at the Swiss field station and cools with depth to a temperature minimum of about −21 °C at 600 m depth. This unpublished data has recently been used to calibrate a dual column thermal model used to simulate the potential effect of the cryo-hydrologic system on ice temperatures (Phillips et al. 2010, Phillips 2010).

GISP2

Two temperature profiles have been collected at the GISP2 ice-coring drill site in central Greenland. The first, collected in 1989, reached a depth of 217 m and exhibited small temperature gradients (< 0.004 K/m) (Alley and Koci 1990). After five seasons of drilling, temperatures were measured from 70 m depth to the bottom of the hole at 3044 m depth (Cuffey et al. 1995). Little temperature variation is present in the upper 1800 m, with values hovering around −32 °C. Below this, the temperature gradient increases and the temperature at the base is −9 °C.

GRIP

Temperatures have been measured in 1993, 1994 and 1995 over the full depth of the GRIP core hole, located 30 km from the GISP2 drill site in central Greenland (Dahl-Jensen et al. 1998, Gundestrup et al. 1993b). The basal temperature was −8.5 °C at a depth of 3028 m, showing that the ice is frozen at the bed. The temperature minimum of around −33 °C is located at about 1600 m depth. The geothermal heat flow at this site has been modelled to be around 51 mW/m^2 (Dahl-Jensen et al. 2003a).

Adjacent to Jakobshavn

To increase understanding of specific ice stream dynamics, multiple boreholes adjacent to the Jakobshavn ice stream were drilled to the bed (830 m depth) and fitted with temperature sensors in 1995 (Luthi et al. 2002). These profiles show the same features as the site A profile from the ice stream margin. The temperature minimum is −22 °C at 520 m depth and the profiles exhibits a large 31 m temperate layer at its base (3.7 % of ice thickness). The temperature gradient above the temperate layers is 0.1 to 0.125 K/m.

NorthGRIP

Temperature measurements were made in 2001 within the 2930 m deep borehole at the North Greenland Ice Core Project drill site. Though the drill had yet to reach the bed (3080 m), the temperature gradient at 2880 m depth of 0.028 K/m predicts a basal temperature of −2.4 °C. This basal temperature suggests that the ice at the base is likely at the pressure melting temperature

(Dahl-Jensen et al. 2003a). In 2003, the hole reached the bed, where subglacial water quickly flooded into the hole (Bentley and Koci 2007). The profile exhibits a similar shape to the GRIP temperature profile; however, below 1500 m depth, the profile exhibits warmer temperatures.

4.6.3.2 GrIS temperature summary

Basal temperatures at the summit in central Greenland (GRIP, GISP2) are well below the melting point, as are basal temperatures from Camp Century and Dye 3. 324 km downstream from the summit sites, NorthGRIP temperature data reveals temperate basal conditions. The basal melt rate is estimated to be 7 mm per year (Dahl-Jensen et al. 2003b). These conditions are thought to be caused by a high local geothermal heat flux (> 55 mW/m^2), illustrating the potential small-scale variability of temperate conditions at the ice sheet bed (Dahl-Jensen et al. 2003a). Along the western margin of the ice sheet, basal conditions for the Jakobshavn ice stream and the Sermeq Avannarleq outlet glacier vary substantially, despite being located less than 60 km apart. Thick temperate layers are documented within and adjacent to the Jakobshavn ice stream, while the melting point is not reached in any of the Sermeq Avannarleq profiles that reach the bed. This data contrasts the usual assumption that beds will be temperate in the ablation zone.

Previous ice temperature measurements within the GrIS, as documented above, provide a useful comparison to the current temperature data along Isunnguata Sermia, and to existing numerical models depicting the thermal state of the bed (Greve 2005, Huybrechts 1996).

4.7 Ice surface velocity

4.7.1 Methods

4.7.1.1 Field installations

GPS stations were installed at selected borehole sites to measure ice surface velocity. Four GPS stations were installed over the course of the GAP, with at least one station within each of the three study regions. The stations were installed at sites GL10-3, GL11-1, GL11-2 and GL12-2 (Figure 4-31). Each GPS system consisted of a Trimble Zephyr antenna, a GPS receiver/data logger (either model Trimble NetRS or NetR9), a waterproof box enclosure, an array of batteries, and a recharging system consisting of a solar panel and a wind turbine.

The station at site GL10-3 consisted of an antenna mounted to a pole drilled into the ice, and a free-floating frame for all other components. This station was only operational during summer/fall of 2010 (Table 4-9). The other stations had an antenna mounted on a pole drilled into the ice also, but the solar panel and wind turbine were secured to a second pole drilled into the ice. A box containing the data logging GPS receiver and the batteries was tethered to the pole, but allowed to 'float' on the ice surface as it melted (Figure 4-32). The poles were drilled ~ 7 m into the ice. The antenna and other components became elevated with time as the ice surface ablated; hence, these items were periodically remounted at lower positions on the pole, and the top of the pole was cut off to avoid vibration from wind.

Table 4-9. Operational time record for sites where GPS stations were installed to track surface ice velocity. Although most sites had gaps in data that lasted fractions of a day, shown here are only days where there is no record for that entire day (last column). The data record (refer to Section 4.10) for sites showing daily averaged velocity only contains gaps for days where there is no data for that entire day.

Site	Start Log YYYY-MM-DD	End Log YYYY-MM-DD	Data Gaps (day of year)
GL10-3	2010-07-03	2010-12-30	265, 270, 350
GL11-1	2010-07-01	2011-10-31	N/A
GL11-2	2010-07-15	2010-09-30	199, 200, 257
GL12-2	2012-06-11	2012-09-14	N/A

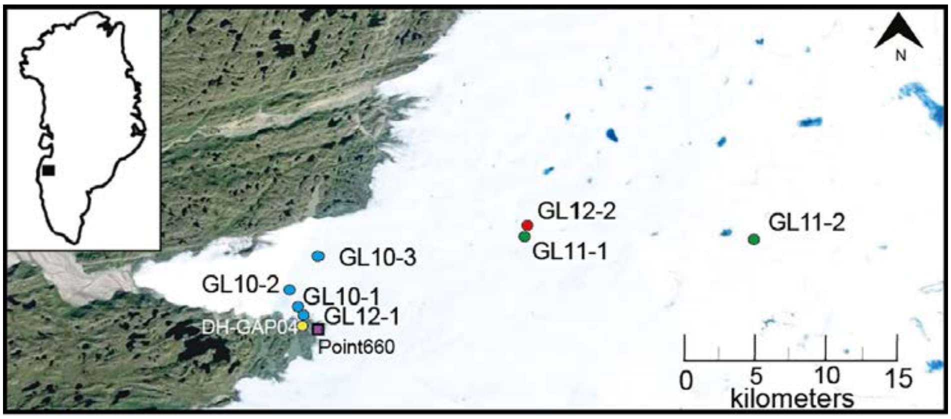

Figure 4-31. Map of the GAP study area with respect to Greenland (inset) showing site locations where GPS stations were installed. Colour of each circle indicate site region: margin = blue, interior = green, trough = red. Yellow circle = location of bedrock borehole DH-GAP04. Purple square = location of Point 660. Dark blue areas show the location of supraglacial lakes (SGL).

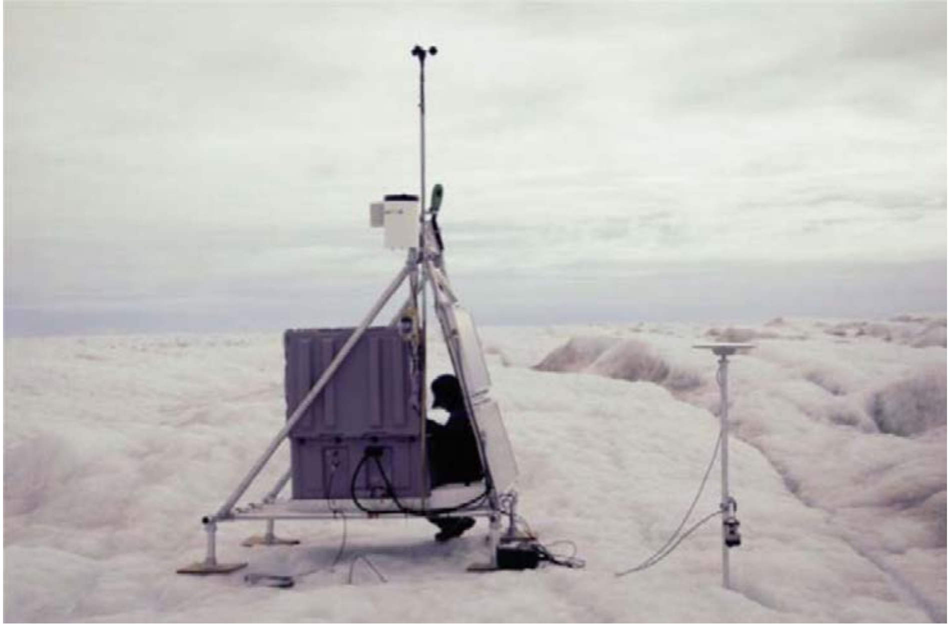

Figure 4-32. Photograph of GPS/meteorological installation. Photo by Joel Harper.

4.7.1.2 Processing

All data were processed using GAMIT/TRACK 1.1.2 geodetic grade GPS software. Each of the stations operated over differing periods due to staggered dates of installation (Table 4-9). Further, each station had unique data gaps caused by ice-melt out, receiver malfunction or poor satellite fixes (Table 4-9). The latter was the most common cause of data gaps. When data availability permitted, GPS stations were processed against Russell Base station GPS which is near the terminus of Russell Glacier and maintained by GAP SPA (see Section 3.4). Other base stations used were RINK and QAAR, each about 100 km north-northwest of Ilulissat, Greenland. Each file was processed as a single day with epochs separated by 30 second intervals. Errors in the positions exist at each epoch. The true position is estimated by smoothing the data over a time interval of six hours for the data processed against the Russell Base station and 48 hours for the other data. Total X/Y motion is calculated for the smoothed solution at each epoch and velocities are calculated from the difference in position divided by the epoch interval.

Due to a lack of close and reliable base station data for processing data from the GPS station at GL10-3, these data were processed against RINK GPS station, which is ~ 520 km from GL10-3. This reduced the accuracy and reliability of the processed point locations. During the time over which data were collected, the receiving antenna tipped over on DOY ~ 240, was reset on DOY 266, fell over again on DOY ~ 344 and needed to be extracted from the ice upon retrieval. The accuracy of the measurements is greatly diminished while the antenna had tipped over.

4.7.1.3 Errors

Approximate errors in GPS locations are highly variable throughout the span of data collection. Error ranges generally are higher for the data processed against RINK or QAAR than the Russell Base station. This is due to the large differences in station/base separation; larger separation leads to larger differences in tropospheric and ionospheric delay times between the satellites and the GPS stations. The error of the position at any epoch is estimated to be equal to the spread of the recorded data around the smoothed data. The error changes as the length of smoothing changes. The data processed against the Russell Base station data are smoothed over a 6 hour Gaussian window, while other data are smoothed over a 48 hour Gaussian window. Position errors for sites processed against Russell Base station are less than 2 cm and velocities errors for these data are less than ~ 50 m/yr. Position errors for the other sites are ~ 3 cm with velocity errors of 40–100 m/yr.

4.7.2 Results

4.7.2.1 GL10-3

Velocities from this station had poor accuracy due to both the long baseline used in processing, and the instability of the station during certain intervals. No diurnal variations in velocity were identifiable in the records, but it is unclear whether or not this is simply due to the poor data accuracy. Nevertheless, several other aspects of longer time period velocity changes were observed (Figure 4-33). From DOY (2010) 185 to 226, the velocity was roughly constant at ~ 130 ± ~ 30 m/yr. On DOY (2010) 226, the velocity began increasing, reaching a peak on DOY (2010) 240 of ~ 250 m/yr. Between DOY (2010) 294–342, the velocity was roughly constant at ~ 85–90 m/yr with a slight sudden (< 1 day) increase in velocity to ~ 100 m/yr around DOY (2010) 333, which linearly decreases to ~ 85–90 m/yr by DOY (2010) 337.

4.7.3 GL11-1

This site showed velocity variations over time periods ranging from daily to seasonal (Figure 4-34). From DOY (2011) 182 to 235, the mean velocity decreased from ~ 125 m/yr to ~ 90 m/yr. There were diurnal variations in velocity, which generally range in amplitude from ~ 40 m/yr to ~ 110 m/yr. The amplitude of these diurnal variations generally decreased between DOY (2011) 215 and 235. Between DOY (2011) 237 and 240, velocity increased from ~ 89 m/yr to ~ 185 m/yr. Starting on DOY (2011) 240, mean daily velocities decrease non-linearly from ~ 185 m/yr on DOY (2011) 240 to ~ 94 m/yr on DOY (2011) 243, and ~ 85–83 m/yr between DOY (2011) 246–253. On DOY (2011) 253–255, the mean velocity was ~ 96 m/yr and dropped about 10 m/yr through the end of the record. Strong diurnal variations in velocity were absent from DOY (2011) 241 onward to the end of the record.

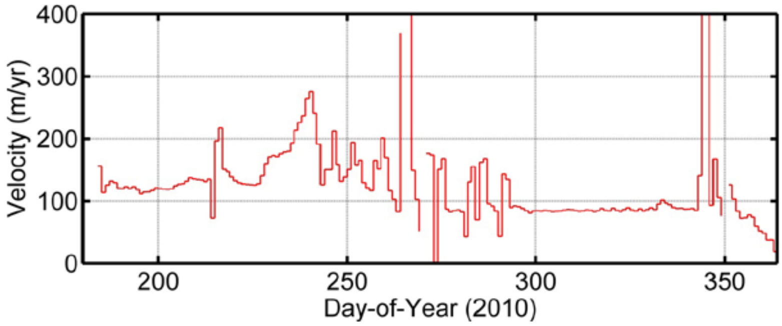

Figure 4-33. *Surface ice velocity averaged over each day for site GL10-3 measured from July 3, 2010 to December 31, 2010. Discontinuities are when no data exist for the whole day. The vertical axis limit is set to 400 m/yr due to uncertainty with respect to the validity and/or cause of large (transient) increases in surface velocity measurements.*

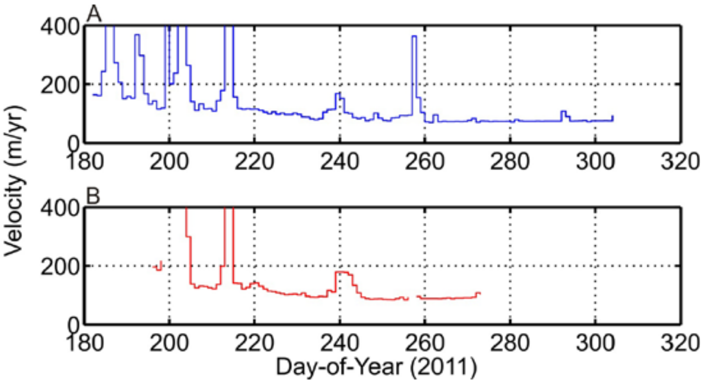

Figure 4-34. *Surface ice velocity averaged over each day for A) site GL11-1 measured from July 1 to October 31, 2011, and for B) site GL11-2 measured from July 15 to September 30, 2011. Gaps are when no data exist for the whole day. The vertical axis limit is set to 400 m/yr due to uncertainty with respect to the validity and/or cause of large (transient) increases in surface velocity measurements.*

4.7.3.1 GL11-2

This site also demonstrated complex velocity variations with both the mean daily velocity and the magnitude of diurnal swings changing at various points during the record (Figure 4-34B). Early in this site's record, from DOY (2011) 196 to 198, the mean daily velocity varied between ~ 187 m/yr and ~ 156 m/yr, but included diurnal swings having amplitude of up to ~ 75 m/yr. Then lasting until about DOY (2011) 215, the mean daily velocity slowed to between 125 m/yr and 150 m/yr. Small diurnal swings (amplitude ~ 37 m/yr) were apparent during DOY (2011) 207–212. Between DOY (2011) 215–222 mean daily velocities were ~ 150 m/yr, but with generally larger amplitude diurnal swings of ~ 30–50 m/yr. On DOY (2011) 222 diurnal swings then diminished to ~ 20 m/yr, as the mean daily velocity also decreased to ~ 100 m/yr by DOY (2011) 226. Between DOY (2011) 229–236 mean daily velocity remained ~ 100 m/yr, but with no definite diurnal swings. Mean daily velocity increased by ~ 20 m/yr between DOY(2011) 237 and 238, but continued to lack diurnal swings. Daily mean velocity increased again to ~ 180 m/yr on DOY (2011) 239 and continued through DOY (2011) 243 with diurnal swings of ~ 60 m/yr present. Velocity dropped to ~ 88 by DOY (2011) 246 and remained constant through the end of the record, and with no strong diurnal swings apparent.

4.7.3.2 GL11-1 and GL11-2 comparison, DOY(2011) 205–256 (July 24, 2011 to September 13, 2011)

Diurnal variations: site GL11-1 generally experienced diurnal variations that were greater amplitude and more consistent across the time period (Figure 4-35). Diurnal variations in velocity were present at site GL11-1 from DOY (2011) 205 to 241, whereas diurnal velocity variations were apparent at site GL11-2 from DOY (2011) 205 to 230; thus, ending or falling below the noise level 11 days earlier.

Speed up event: at both sites GL11-1 and GL11-2, velocity increased by ~ 75 % from ~ 100 m/yr to ~ 175 m/yr on DOY (2011) 239 (Figure 4-35B). The velocity variations are similar between the two sites through the beginning of DOY (2011) 241, after which the velocity at GL11-1 decreases abruptly to ~ 125 m/yr. The velocity at this site continued to slowly decrease to ~ 90 m/yr by DOY (2011) 244. The velocity at GL11-2, however, remained at an average of ~ 175 m/yr with diurnal fluctuations until DOY (2011) 243, when the velocity began decreasing to ~ 90 m/yr by DOY (2011) 246.

4.7.3.3 GL12-2

In Figure 4-36A, daily averaged velocities are shown. Day to day variations range mostly between 100 to 200 m/yr from mid-June, DOY (2012) 163, through the end of the first week of August, DOY(2012) 220, at which point a general decreasing trend is observed in surface velocity – down to daily averaged values of less than 100 m/yr. Diurnal variability in surface velocity (Figure 4-36B) ranges by ~ 80 m/yr. DOY (2012) 218–226, DOY (2012) 239–244 and DOY (2012) 246–255 show smaller diurnal variation of ~ 15 m/yr. From DOY (2012) 218 to 224, during one of the periods of moderated diurnal variability, double diurnal variations were evident. The velocity at this site decreases gradually over the course of the melt season from an average value of ~ 150 m/yr at the beginning of the record (early June) down to ~ 75 m/yr toward the end of the record (mid-September).

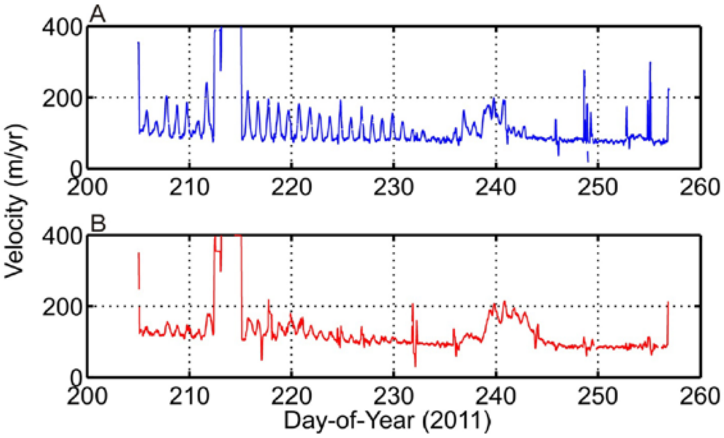

Figure 4-35. *Surface ice velocity for A) GL11-1 and B) GL11-2 showing diurnal variability from July 24, 2011 to September 13, 2011. The vertical axis limit is set to 400 m/yr due to uncertainty with respect to the validity and/or cause of large (transient) increases in surface velocity measurements.*

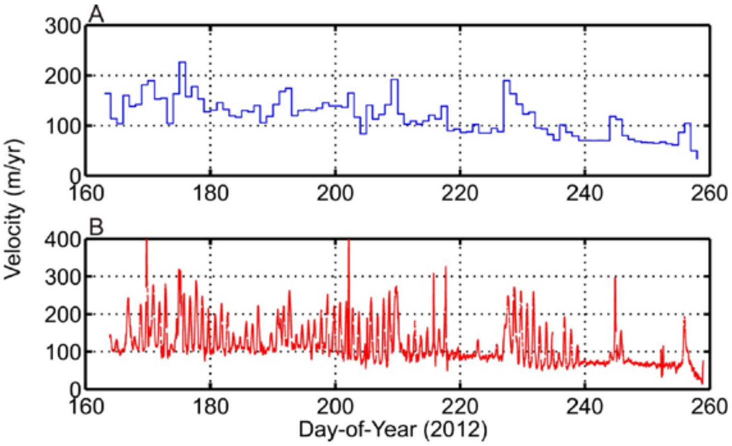

Figure 4-36. *A) Surface ice velocity averaged over each day, and B) surface ice velocity smoothed over a 6 hr period for site GL12-2 measured from June 11, 2011 to September 14, 2012. The vertical axis limit (for B) is set to 400 m/yr due to uncertainty with respect to the validity and/or cause of the large (transient) increases in surface velocity measurements.*

4.7.4 Summary and discussion of ice surface velocity

All GPS stations revealed surface velocities with strong seasonal variably, as evidenced by higher daily average velocities in early summer than in late summer or fall. Diurnal velocities were present at the two interior region stations as well. The diurnal velocity variations were present only during the middle of summer. At the margin region, station GL10-3, which is 3 km inland but located over very thick (>700 m) ice, the GPS measurements did not reveal diurnal velocity variations. However, this could be because variations were below detection limits due to poorer resolution of these data. Nevertheless, diurnal variations in velocity at this site could not have had amplitudes similar to those observed farther inland or they would have been detected. One major speed up event was observed at both interior sites – lasting several days and increasing velocity by up to 75 %.

Surface ice velocity measurements are not direct measurements of conditions at the base of the ice sheet. However, indirect inferences can be made about *change* in subglacial conditions, based on *change* in surface velocity. The simple observation that velocity is time-variable is a fundamental and revealing factor about basal conditions. Because ice deformation rates are related to ice sheet geometry, which does not change over seasonal time scales, daily-to-seasonal variability of surface velocity can only result from changes in the sliding rate at the ice sheet bed. Such changes in sliding rate, in turn, are related to changes in basal hydrologic conditions. The resulting conclusion is that the seasonal changes in velocity are the result of seasonal changes in water input to the bed.

The absolute amount of water input to the bed is not necessarily directly proportional to the magnitude of the sliding velocity (Truffer et al. 2005). This is because, despite increasing water input during the course of the summer, a drainage system develops at the ice/bed interface that becomes more efficient at moving water along the bed over time. Many details about this drainage system remain to be understood, such as whether or not it consists of well-connected cavities behind bedrock bumps, a network of conduits or a combination of both. In addition, the size and bed coverage drainage features are poorly constrained. Nevertheless, the empirical result that the basal drainage system receives surface melt and evolves over the seasonal cycle is clear.

Diurnal changes in ice surface velocity indicate that the drainage system at the bed responds to short time scale (i.e. hours) conditions of surface melt. Water routing pathways must be direct, even at the interior region located 15–30 km inward from the margin. Much remains to be learned about the exact englacial linkages, but because the velocity and pressure (see Section 4.4) were observed to change on diurnal time scales, clear empirical evidence exists for rapid surface-to-bed water transfer. If moulins provide the only access for surface melt to the bed, the water must spread out quickly to a wide area of the bed, because changes in surface velocity from sliding requires large-area decoupling of the ice/bed contact. Both the interior and trough region measurements were km or more away from the nearest moulin or water filled crevasse, implying that water spreads out from access points across large regions of the bed.

Sliding speed has a close association with basal water pressure (Iken and Bindschadler 1986, Iken 1981, Jansson 1995). The physical processes behind a proportionality between pressure and velocity are straightforward; higher basal pressure will a) tend to decouple the bed by floating the ice, and b) cause increased 'jacking', where pressure in a cavity located downstream of a bedrock step in the flow direction pushes the ice forward.

The relationship between velocity and pressure can be complex and not necessarily directly proportional at all times. The change in velocity is most often associated with a change in pressure (Iken and Bindschadler 1986). Correlations between pressure and velocity are not always straightforward and predictable; sometimes pressure correlates with velocity and sometimes it does not (Fountain and Walder 1998). Inconsistencies in the relationship between pressure and velocity result from other driving processes that also play a role in basal sliding, such as the amount of water on the bed and the configuration of the drainage system. For example, very high pressure acting on a very low area drainage system can be expected to result in little velocity change. Other complicating factors are the feedbacks between drainage system geometry and sliding speed. Increasing the sliding speed will cause cavities located behind bedrock bumps to open further through cavitation processes (Iken 1981). The pressure in the cavity will drop because of the added volume, unless new water mass is added to the system. The velocity measurements cannot be directly inverted for pressure measurements, neither in a quantitative nor a qualitative way.

Conclusions relevant to the basal boundary that can be inferred from the ice surface measurements include: 1) surface meltwater reaches the bed of the ice sheet over widespread areas and without substantial delay; 2) this meltwater flux causes the drainage system to undergo evolutionary changes on time scales that vary from diurnal to seasonal; 3) the resulting changes in drainage system geometry lead to changes in ice/bed coupling and sliding speed; and 4) complicated feedbacks between sliding speed, and drainage system geometry and pressure, cause additional change to the drainage system. Each of these results is inferred from surface velocity and are not a direct measurement of the drainage system. Further, the general conclusion that the basal boundary to groundwater flow cannot be considered to be static is robust, as there is no other way to explain the velocity variations.

4.8 Surface meteorological measurements

4.8.1 Methods

4.8.1.1 Instrumentation and setup

Four SPB weather stations were installed on the ice over the course of the project. The sensors were installed on GPS stakes drilled into the ice as part of GPS surface velocity stations. One weather station was mounted at each major study site (GL10-3, GL11-1, GL11-2 and GL12-2). Each weather station was operational for a different time period due to different installation times, and functionality problems during winter resulting from a lack of a power supply fed by solar panels.

Each weather station was designed to measure air temperature, incoming total sun and sky solar radiation, and ice surface melt. The measurements were recorded using a Campbell Scientific CR200 data logger at 15 minute intervals in the summer, and hourly during the winter periods, where data loggers were functional. The data logger received power from a 12 V battery and a 10 W solar panel. Each sensor used was a Campbell Scientific model.

Temperature was measured by a CS-Model 109 temperature probe housed in a radiation shield. Errors in temperature measurements are amplified in cold weather conditions, but at worst, the temperature is measured within a tolerance of ± 0.20 °C (at −40 °C).

Incoming shortwave solar radiation was measured using a CS300 Pyranometer, mounted on a base and stand and attached to a cross-arm so that it was not shaded by the stand or the other sensors. The sensors measure radiation in the spectral range of 300 to 1100 nanometers, which spans most of the shortwave radiation reaching the ice surface. The sensor has an absolute accuracy of ± 5 % for the daily total radiation, and an operating temperature within the ambient temperature experienced at each site (down to −40 °C).

To measure changes in surface height through melting and snow accumulation, a SR50A acoustic sensor (‘sonic ranger’) was installed on a fixed pole drilled several metres into the ice. The sensor was mounted between 0.5 and 1.0 m above the ice surface, with a static beam angle of 30°. This angle decreased (increasing measurement surface area) as the sensor became elevated with time, while the ice surface lowered due to melt and sublimation. Because the two-way travel time of the sensor signal depends on air temperature, temperature compensation was done using the 109 temperature probe. The sonic ranger operates with a resolution of 0.25 mm and down to −45 °C; air temperatures always stayed above −45 °C. Errors with the sensor arise when taking measurements of an uneven surface because the measurement is an average across the circle traced out by the cone radius, which is variable depending on the height of the sensor above the ground.

Prior to each field campaign, the temperature probe and the acoustic sensor were tested in a lab for several days to verify the integrity of the equipment and the measurements. The station was tested outdoors in different conditions as well, and to evaluate the solar sensor in the presence of direct sunlight.

4.8.1.2 Quality control

Temperature and radiation data required no post-processing after collection. Sonic ranger data, however, required removal of erroneous data during quality control. Although not reported in the instrument documentation, large errors found in the sonic ranger apparently were amplified during periods of rapid change in incoming shortwave radiation, such as early or late in the day. The problem was managed by simply removing outlier measurements in post-processing and replacing them with the arithmetic mean of the measurement taken directly prior and subsequent to the erroneous measurement. The minor transient noise from the first source of error was smoothed in post-processing using a Gaussian blur.

4.8.2 Results

4.8.2.1 Margin site (GL10-3)

This station was operational from June 30, 2010 to September 21, 2010. The only alteration to this dataset, besides the post-processing described in Section 4.8.1, was the removal of all SR50A sonic depth measurements taken after August 23, 2010 – due to purely erroneous measurements that could not be replaced by inferring or smoothing.

During the period from June 30, 2010 to September 5, 2010, the temperature stayed above freezing and averaged 3.58 °C, with diurnal swings ranging between ~ 2 and 4 °C (Figure 4-37 and Table 4-10). The average monthly temperature was greatest in August; however, a very warm period occurred at the beginning of September before cooling gradually into the beginning of fall. Solar data show large diurnal swings to zero every night to peak values around noon. Ignoring the outlier measurement on July 2, 2010, the peak radiation on sunny days reaches just over 1000 W/m^2, whereas on overcast days, incoming radiation is obscured and can drop down to about a third of what was experienced on adjacent days with clear skies.

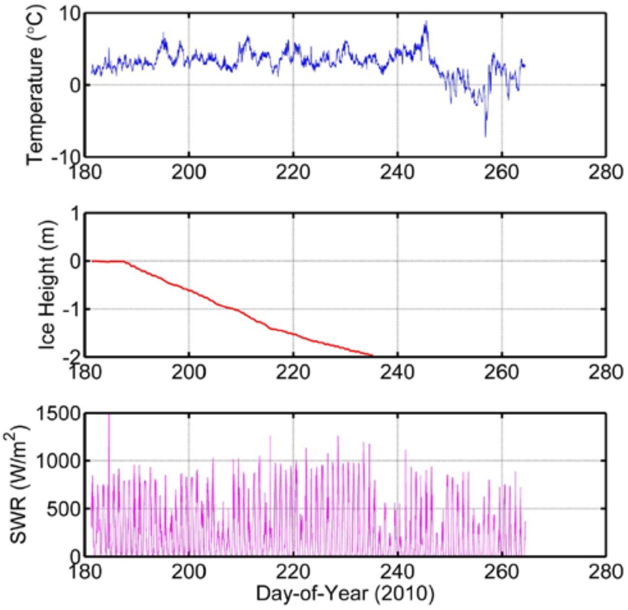

Figure 4-37. *GL10-3 temperature, ice height (relative to height at time of installation) and solar radiation from June 30, 2010 to September 21, 2010.*

Table 4-10. Meteorology station statistics and dates for the station GL10-3.

Measurement Type	Recorded Value	Date(s) YYYY-MM-DD
Min. Temperature	−7.24 °C	2010-09-13
Max. Temperature	8.93 °C	2010-09-02
Avg. Temperature	2.98 °C	2010-06-30 to 2010-09-21
Time Above Freezing	92.2 %	2010-06-30 to 2010-09-21
Ablation	1.96 m	2010-06-30 to 2010-08-23

4.8.2.2 Interior sites

GL11-1: this station was operational from July 19, 2011 to September 19, 2012, with a period of non-functionality from December 18, 2011 to June 11, 2012. This was likely due to a power supply failure to the station during months with little or no sunlight. When the station was maintained in June of 2012, logging was re-initiated.

During the period between July 19, 2011 and September 5, 2011, the temperature stayed above freezing 88 % of the time (Figure 4-38 and Table 4-11). After this period, a gradual decrease in temperature into fall and winter brought temperatures down to an average of −9.0 °C through December 18, 2011. An anomalous warming event occurred on November 13, 2011, when temperatures reached over 5 °C; this event lasted just over seven days before temperatures returned to "on-trend" values. The daily fluctuations in temperature during the colder months are significantly more extreme than those during the summer months. Solar radiation data show diurnal swings (down to zero) with cloudy-day maximum one third of the intensity experienced on adjacent clear days. For the summer months, GL11-1 received ~ 21 % less solar radiation than GL10-3.

Table 4-11. Meteorology station statistics and dates for the station GL11-1.

Measurement Type	Recorded Value	Date(s) YYYY-MM-DD
Min. Temperature	−28.80 °C	2011-11-08
Max. Temperature	6.92 °C	2012-07-27
Avg. Temperature	−0.86 °C	2011-07-01 to 2012-09-19
Time Above Freezing	65.1 %	2011-07-01 to 2010-09-19
Ablation	1.22 m	2011-07-01 to 2011-12-18
Ablation	3.1 m	2012-06-10 to 2012-09-19

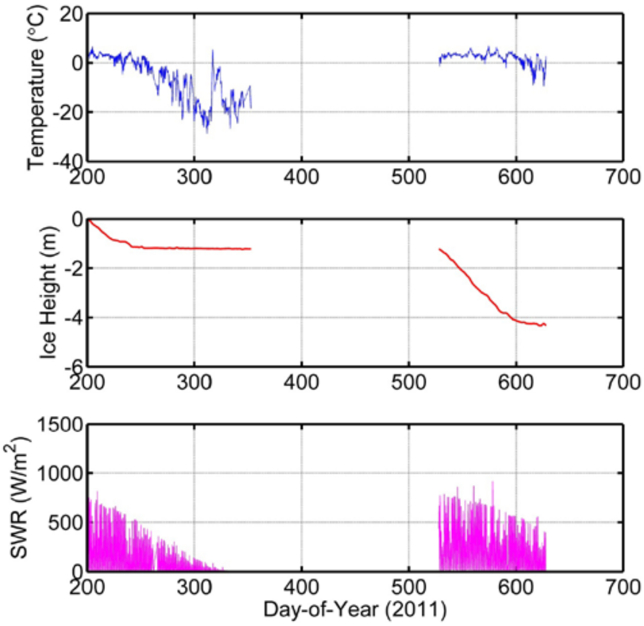

Figure 4-38. *GL11-1 temperature, ice height (relative to height at time of installation) and solar radiation from July 19, 2011 to September 19, 2012. The gap in data is due to instrumentation malfunction.*

GL11-2: this station was operational continuously from July 12, 2011 to September 18, 2012. There were however, instances at the beginning of recording and at the end of the 2012 summer where (only) the sonic ranger did not log. There is no clear explanation for this other than an electronic malfunction.

For comparison with GL11-1, between July 12, 2011 and September 5, 2011, the temperature averaged 1.1 °C and stayed above freezing 80.7 % of the time (Figure 4-39 and Table 4-12). The temperature plot shows a seasonal cool down for the fall and winter months (September 23, 2011 to March 19, 2012), where temperatures averaged −18.4 °C. However, like GL11-1, there was also an anomalous warming event where temperatures peaked at just over 3 °C; this event also lasted just over one week. Sonic ranger data show an impressive ablation trend during the summer from June 20, 2012 to September 18, 2012, where the ice height decreased by ~ 2.6 m. Solar radiation data show the seasonal oscillatory behaviour expected (low in winter, high in summer), with diurnal oscillations similar to the two previous sites. GL11-2 receives ~ 24 % more solar radiation during summer months than GL11-1.

Table 4-12. Meteorology station statistics and dates for the station GL11-2.

Measurement Type	Recorded Value	Date(s) YYYY-MM-DD
Min. Temperature	−40.12 °C	2012-02-28
Max. Temperature	5.24 °C	2012-07-27
Avg. Temperature	−6.32 °C	2011-07-01 to 2012-07-11
Time Above Freezing	45.5 %	2011-07-12 to 2012-09-08
Ablation	1.27 m	2011-07-19 2011-09-19
Ablation	1.70 m	2012-07-19 2012-09-18

4.8.2.3 Interior trough site (GL12-2)

GL12-2 was operational continuously from June 14, 2012 to September 19, 2012.

The hottest months, based on mean monthly air temperature, were June (3.04 °C) and July (3.1 °C), where August cooled down by ~ one degree (2.33 °C). From that time, cooling continued into September (Figure 4-40 and Table 4-13), with a monthly mean temperature of −1.44 °C, but with much more diurnal variability compared to the warmer months. Temperatures for June-July-August remained above freezing ~ 96 % of the time, whereas the cooler month of September only ~ 40 % of the time.

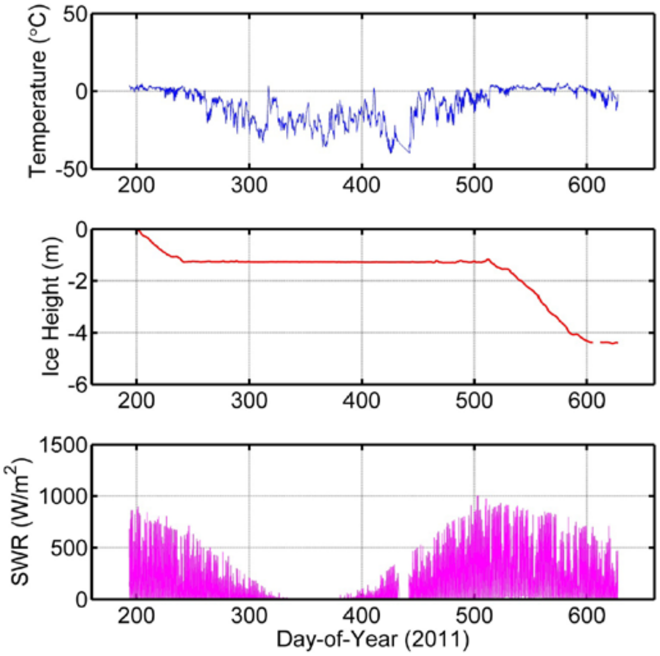

Figure 4-39. *GL11-2 temperature, ice height (relative to height at time of installation), solar radiation from July 12, 2011 to September 18, 2012.*

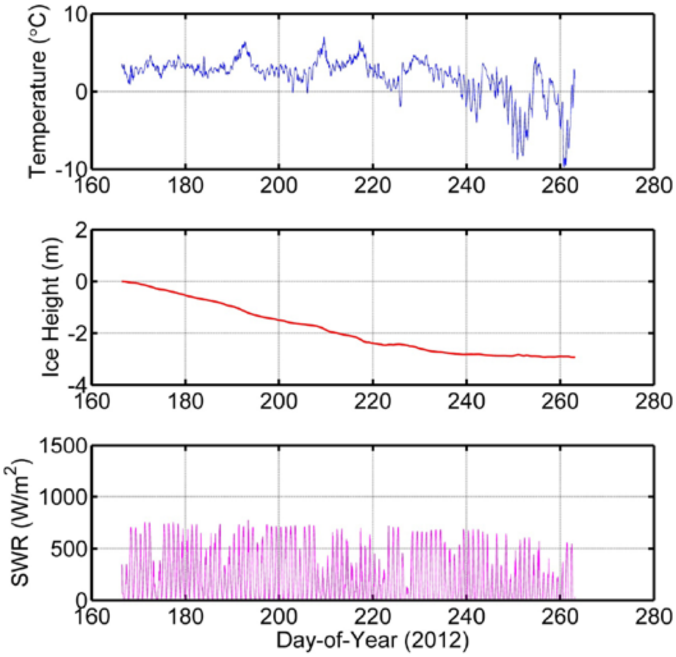

Figure 4-40. *GL12-2 temperature, ice height (relative to height at time of instillation), solar radiation from June 14, 2012 to September 19, 2012.*

The maximum temperature recorded occurred on the same day as the maximum recorded temperature at GL11-2 and GL11-1. Overall, this warm summer resulted in almost 3 m of ablation, as shown by the sonic ranger data. Solar radiation data for GL12-2 show diurnal swings consistent with the other sites, with a gradual decline in peak radiation signals into September. The smallest daily maximum occurred on August 15, 2012, with a peak value 80 % lower than the following clear day. GL12-2 shows a similar solar signature as GL11-1, which is expected because they are only 1 km apart.

Table 4-13. Meteorology station statistics and dates for the station GL12-2.

Measurement Type	Recorded Value	Date(s) (YYYY/MM/DD)
Min. Temperature	−9.74 °C	2012-09-16
Max. Temperature	7.05 °C	2012-07-27
Avg. Temperature	1.93 °C	2012-06-14 2012-09-19
Time Above Freezing	84.7 %	2012-06-14 2012-09-19
Ablation	2.93 m	2012-06-14 2012-09-19

4.8.3 Summary and discussion of surface meterological measurements

Atmospheric conditions and surface melt at all of the sites show strong seasonal influence. Diurnal swings in temperature and solar radiation are also present, which results in diurnal swings in the rate of ice melt at each of the study regions. These results do not differ from expected, and the processes are quantified in much greater detail by SPA (see Section 3.3). The data collected by SPB record local surface conditions at the study sites for a generalised documentation of conditions. The meteorological data collected by SPB does not, on its own provide direct insight into the GAP questions or conceptual models.

4.9 Numerical modelling

4.9.1 Modelling requirements

Understanding the response of the deep subsurface to glacial forcing requires detailed knowledge of processes occurring in the subglacial environment. The subglacial environment can be characterised by a set of variables that act as boundary conditions for models of the geosphere. Examples include temperature, pressure and groundwater recharge rate. Groundwater models with appropriate boundary conditions are capable of tracking the infiltration of basal melt into the groundwater system, and determining if and how it reaches typical repository depths (e.g. ~ 500 m b.g.s. or more).

A fundamental characteristic of the subglacial environment is temperature. Once the bed of the glacier reaches the pressure melting point, it can produce meltwater, and the ice begins to slide on its bed, providing a positive temperature feedback in the form of frictional heating. Temperature is dependent on stresses within the ice, atmospheric temperature, geothermal heat flux and the flow of ice. In the case of the modern GrIS, there is significant melt occurring on the ice sheet surface during the summer months, nearly all of which reaches the bed. For these reasons, an ice sheet model for the GAP must have state-of-the-art energy balances for calculation of temperatures. This energy balance must be coupled to a sophisticated scheme for estimation of ice velocities as well, because the temperature and velocity fields are strongly coupled.

Some features of the subglacial environment are directly measured. However, these often correspond only to those points where boreholes have been drilled. In other cases, such as the bed elevation, a more detailed dataset is known; however, the data are still insufficient to constrain the model. The primary role of the ice sheet model in the GAP is to extend the understanding of the subglacial environment beyond points where measurements exist, and to variables that cannot be directly measured. To do this, a model that can enforce fidelity to data in regions where observations exist is required. Said another way, the model must be capable of estimating important variables where there are no observational data, and honour such data where they do exist.

The focus of the GAP is an approximately 30 by 80 km region of the GrIS. However, there are significant fluxes of water, ice and energy that move into the GAP study area from up-glacier. These fluxes can have a significant impact on modelling results. To accurately model the fluxes into the GAP area, the numerical model has to be nested within a larger model. It is essential that the models span the spatial resolutions being studied, from the 500 m resolution in the GAP area, down to a 25 km resolution deep in the interior of the ice sheet.

The needs of the GAP are rather specialised, and ice sheet modelling remains a developing science. A new ice sheet model was developed to meet the needs of the GAP. Summarising the previous discussion, the key requirements of the ice sheet model are as follows.

1) An advanced treatment of the conservation of energy within the ice.
2) A full or nearly complete balance of forces within the ice that is coupled to the energy balance.
3) The ability to rapidly assimilate new data acquired as part of the GAP and elsewhere.
4) Model nesting to accurately compute the flux of materials into the GAP study area.
5) Variable resolution to allow detailed calculations in areas of interest.

The following section details the model developed to meet these requirements, and follows closely the discussion found in Brinkerhoff and Johnson (2013).

4.9.2 Modelling methods

Variational Glacier Simulator (VarGlaS) can solve for the 3D ice sheet velocity, temperature and geometry through time. All three of these variables are strongly coupled. In the following subsections, the continuum formulation of ice sheet physics is presented, followed by the numerical treatment of each physical component.

4.9.2.1 Conservation of momentum

Development of a variational principle for the momentum balance largely follows Dukowicz (2011). The variational principle for a power law rheology, with linear basal sliding under the constraints of incompressibility and bed impenetrability, is:

$$\begin{aligned}\mathcal{A}[\mathbf{u},P] = &\int_\Omega \underbrace{\frac{2n}{n+1}\eta(\dot{\epsilon}^2)\dot{\epsilon}^2}_{\text{Viscous Dissipation}} + \underbrace{\rho\mathbf{g}\cdot\mathbf{u}}_{\text{Potential}} - \underbrace{P\nabla\cdot\mathbf{u}}_{\text{Incompressibility}}\ \mathrm{d}\Omega \\ &+ \int_{\Gamma_B} \underbrace{\frac{\beta^2}{2}\mathrm{Thk}^r\mathbf{u}\cdot\mathbf{u}}_{\text{Friction}} + \underbrace{P\mathbf{u}\cdot\mathbf{n}}_{\text{Inpenetrability}}\ \mathrm{d}\Gamma\end{aligned} \tag{4-1}$$

where **u** is the ice velocity, ε the rate of strain tensor, P the pressure, $\eta(\varepsilon^2)$ the strain rate dependent ice viscosity, **g** the gravitational vector, β^2 the basal sliding coefficient, *Thk* the ice thickness, r a factor determining the relationship between basal traction and thickness, and **n** is the outward normal vector. The expression is minimised over the ice domain, Ω, with boundaries Γ. Each of the additive terms in Equation (4-1) has a specific meaning. Terms integrated from left to right over Ω are viscous dissipation, gravitational potential energy and the incompressibility constraint, respectively. Terms under the boundary integral are frictional heat dissipation and the impenetrability constraint. The constitutive relationship for ice from Glen (1955) gives a viscosity of:

$$\eta(\dot{\varepsilon}^2) = b(T,\omega)[\dot{\epsilon}]^{\frac{1-n}{2n}}, \tag{4-2}$$

where ε^2 is defined to be the square of the second invariant of the strain rate tensor, and $b(T, w)$ is a temperature and water content dependent rate factor:

$$b(T,\omega) = \left[Ea(T,\omega)e^{-\frac{Q(T)}{RT^*}}\right]^{\frac{-1}{n}} \tag{4-3}$$

Here, E is an enhancement factor; $a(T, \omega)$, $Q(T)$ and R are parameters; and T^* is the temperature corrected for pressure melting point dependence. The traditional momentum balance form of the Stokes' equations can be recovered (in weak form) by taking the variation of Equation (4-1). This is the functional that VarGlaS minimises in order to solve the Stokes' problem.

The Stokes' functional is a relatively complete statement of ice physics (the only assumptions being negligible inertial terms), but it includes four degrees of freedom per computational node (three velocity components and pressure), and is a saddle point problem due to the presence of the Lagrange multiplier pressure terms. A considerable simplification can be made to the Stokes' functional by expressing vertical velocities in terms of horizontal ones through the incompressibility and bed impenetrability constraints:

$$w(\mathbf{u}_{\|}) = -\int_{B}^{z} \nabla_{\|} \cdot \mathbf{u}_{\|} \, \mathrm{d}z' \tag{4-4}$$

with boundary condition:

$$w_b = \mathbf{u}_{\|b} \cdot \nabla_{\|} B. \tag{4-5}$$

Substitution of these expressions into $\mathcal{A}$ yields an unconstrained and positive definite integro-differential functional, which is equivalent to Equation (4-1). However, the integral terms that result from the vertical integration of the mass conservation equation are undesirable. Standard methods for the numerical solution of partial differential equations are not equipped to handle integral terms of this type, so a simplification that eliminates them is sought. In order to derive the functional associated with the so-called 'first order' equations of ice sheet motion (Pattyn 2003), two assumptions must be made. First, bed slopes are small, which is equivalent to assuming cryostatic pressure. Second, horizontal gradients of vertical velocity are small compared to other components of the strain rate tensor. This eliminates vertical velocity terms. After these assumptions and some manipulation, the first order functional is:

$$\begin{aligned} \mathcal{A}_1[\mathbf{u}_{\|}] = & \int_{\Omega} \frac{2n}{n+1} \eta(\dot{\epsilon}_1^2)\dot{\epsilon}_1^2 + \rho g \mathbf{u}_{\|} \cdot \nabla_{\|} S \, \mathrm{d}\Omega \\ & + \int_{\Gamma_S} \frac{\beta^2}{2} H^r \mathbf{u}_{\|} \cdot \mathbf{u}_{\|} \, \mathrm{d}\Gamma \end{aligned} \tag{4-6}$$

where $\mathbf{u}_{\|}$ is the velocity vector in the horizontal directions, S is the elevation of the ice surface, and $\varepsilon^{2}{}_{1}$ is the first order strain rate tensor given by Pattyn (2003) and Dukowicz (2011). Because the first order equations are only associated with horizontal velocity components, this formulation yields a significant computational savings, as well as desirable numerical properties such as guaranteed positive definiteness. Vertical velocity is recovered from the equations for vertical velocity and impenetrability.

4.9.2.2 Enthalpy

VarGlaS uses an enthalpy formulation of the energy balance (Aschwanden et al. 2012). Enthalpy methods track total internal energy, rather than sensible heat, which corresponds objectively to temperature for ice below the pressure melting point and to water content for ice at the pressure melting point. The enthalpy equation is a typical advection-diffusion equation with a non-linear diffusivity:

$$\rho(\partial_t + \mathbf{u} \cdot \nabla)H = \rho \nabla \cdot \kappa(H) \nabla H + Q, \tag{4-7}$$

where H is enthalpy, ρ is ice density and Q is strain heat generated by viscous dissipation, given by the dissipative term in the momentum balance functional. κ is an enthalpy dependent diffusivity given by:

$$\kappa(H) = \begin{cases} \dfrac{k}{\rho C_p} & \text{if cold} \\ \dfrac{\nu}{\rho} & \text{if temperate,} \end{cases} \tag{4-8}$$

where k is the thermal conductivity of cold ice and C_p is heat capacity. ν is the diffusivity of enthalpy in temperate ice and can also be thought of as a parameterisation of the sub-grid scale intraglacial flow of liquid water. It is not clear what the value of ν should be. Both Hutter (1982) and Aschwanden et al. (2012) have suggested that it be a function of both water content and gravity, but intraglacial liquid modelling is beyond the scope of this work, so this value was usually set to either zero or some constant much less than $\frac{\kappa}{C_p}$. This implies that heat does not move diffusively within temperate ice, and that any heat generation immediately goes toward melting. The definitions for cold and temperate ice are as follows:

$$\begin{cases} \text{cold} & \left(H - h_i(P)\right) < 0 \\ \text{temperate} & \left(H - h_i(P)\right) \geq 0 \end{cases} \tag{4-9}$$

where h_i is the pressure melting point expressed in enthalpy,

$$h_i(P) = -L + C_w(T_0 - \gamma P), \tag{4-10}$$

and C_w is the heat capacity of liquid water, γ is the dependence of the melting point on temperature, T_0 is the triple point of water and L is the latent heat of fusion for water.

At the ice surface, a Dirichlet boundary condition is specified corresponding to surface temperature. At the basal boundary, a Neumann boundary condition is applied:

$$\kappa(H)\nabla H \cdot \mathbf{n} = q_g + q_f - M_b \rho L, \tag{4-11}$$

where q_g is geothermal heat flux (assumed known), q_f is frictional heat generated by basal sliding and M_b is the basal melt rate. Frictional heat is given by the frictional term in the momentum balance functional. Note that in temperate ice, where $\kappa(H)$ is zero (no diffusion), this relation defines the basal melt rate. In cold ice, a value must be specified for the basal melt rate (which can be negative). This value is usually taken to be zero.

Enthalpy is uniquely related to temperature and liquid water in the following way:

$$T(H,P) = \begin{cases} C_p^{-1}(H - h_i(P)) + T_m(p) & \text{if cold} \\ T_m & \text{if temperate} \end{cases} \tag{4-12}$$

$$\omega(H,P) = \begin{cases} 0 & \text{if cold} \\ \frac{H - h_i(P)}{L} & \text{if temperate} \end{cases} \tag{4-13}$$

where ω is fractional water content, and h_i and T_m are the pressure melting points expressed in enthalpy and temperature, respectively.

4.9.2.3 Dynamic boundaries

The ice sheet geometry evolves over time according to the kinematic boundary condition:

$$(\partial_t + \mathbf{u}_\parallel \cdot \nabla_\parallel)S = w + a, \tag{4-14}$$

where a is the accumulation rate.

4.9.2.4 Numerical methods

VarGlaS is built upon the finite element package, FEniCS (Logg et al. 2012). FEniCS is a powerful development environment for performing finite element modelling, including strong support for symbolic automatic differentiation, native parallel support and parallel interface with linear algebra solvers such as PETSc (Balay et al. 2013) and Trillinos (Heroux et al. 2005), and automatic code generation/compilation for compiled performance from an interpreted language interface. The Python scripting environment makes the generation and linking of new code straightforward. The Python interface provides a level of extensibility that makes VarGlaS promising for distributed development and rapid prototyping of models for additional components of the cryosphere.

FEniCS has a large library of finite elements available, though only the continuous, linear Lagrange finite element, defined over an unstructured triangular mesh, is used here. This choice of element is unstable for advection-dominated equations, such as the kinematic boundary condition and the enthalpy equation (in most cases), as well as for Stokes' equations due to the pressure term. The following sections cover stabilisation procedures.

The velocity field and enthalpy equations are both non-linear. These are each solved by using a relaxed Newton's method (e.g. Deuflhard 2004), with a Jacobian calculated by automatic differentiation:

$$J[U^n]\Delta U = -F[U^n] \tag{4-15}$$

$$U^{n+1} = U^n + R\Delta U \tag{4-16}$$

where U^n is the solution vector at the nth iteration, ΔU is a solution update, J is the Jacobian matrix and F is the system of non-linear equations. R is a relaxation parameter that arbitrarily shortens the step size in order to improve numerical stability. The amount of damping required is specific to the problem, but a relaxation parameter between 0.7 and 1.0 is typically sufficient to achieve convergence. Both a relative and absolute convergence criteria for Newton's method are defined. The solution is considered converged if the infinity norm (L_∞) of ΔU is less than 10^{-6}, or the L_∞ of the relative tolerance is less than 10^{-9}.

In order to resolve the coupling between enthalpy and velocity, a fixed point (Picard) iteration is used. Each of these non-linear equations is solved independently, and the result is iteratively used as input in calculating the other variable. Convergence is assumed when both the velocity and temperature updates are less than 10^{-3}.

4.9.2.5 Mesh refinement

The model domain is discretized using a tetrahedral mesh that is unstructured in the horizontal dimensions, and structured in the vertical. In order to equidistribute discretization error, the classic anisotropic error metric,

$$\mathbf{e}(c) \propto \max_{i \in E} \mathbf{x}_i^T \mathbf{M} \mathbf{x}_i, \tag{4-17}$$

is used. Here, e(c) is a cellwise error estimate, E a given mesh cell, x_i an edge in E and **M** a metric tensor, in this case defined by:

$$\mathbf{M} = \mathbf{V}^T \,|\Lambda|\, \mathbf{V}. \tag{4-18}$$

V and Λ are the respective eigenvectors and eigenvalues of the Hessian matrix of the field over which error is equidistributed (Habashi et al. 2000). For all the meshes presented forthwith, the Hessian of an observed velocity norm is used for calculating error metrics. A discrete approximation for each component of the Hessian matrix is obtained iteratively for each level of mesh refinement by solving the variational problem:

$$\int_\Omega \mathrm{Hess}_{ij}\, \varphi \; \mathrm{d}\Omega = -\int_\Omega \frac{\partial U}{\partial x_i} \frac{\partial \varphi}{\partial x_j} \; \mathrm{d}\Omega + \int_\Gamma \frac{\partial U}{\partial x_i} \varphi n_{x_i} \; \mathrm{d}\Gamma, \tag{4-19}$$

where Hess_{ij} are the components of the Hessian and U is the surface speed. With error estimates in hand, all cells are isotropic at a specified proportion of the average error. In order to account for the directional nature of the velocity field, anisotropy is incorporated by using Gauss-Seidel iterations to ~ solve an elasticity problem, with computed edge errors as 'spring constants'. This mixed isotropic-anisotropic technique yields high quality and efficient meshes with both the structural simplicity of isotropic refinement, as well as the better-defined error:mesh size ratio of anisotropic techniques.

4.9.2.6 Data Assimilation and regularisation

Many physical quantities of leading order relevance to glacier and ice sheet flow are either practically impossible to collect, or are point measurements which cannot generally be extrapolated to a broader spatial context. Examples of the former include historic variables, such as a detailed record of surface temperature or ice impurity content at deposition. Examples of the latter include basal water pressure, basal temperature, enhancement factors and geothermal heat flux. A particularly important parameter that usually must be estimated is the coefficient of basal traction, which relates basal shear stress to sliding velocity. In many cases, sliding makes up nearly all of the surface velocity of a glacier (e.g. Weis et al. 1999). Any model that aims to reproduce plausible velocity and thermal structures must parameterise traction. The availability of widespread surface velocity data, and the conceptually simple relationship between surface and bed velocities, have made the inversion of surface velocities for basal traction a popular choice for performing this parameterisation (MacAyeal et al. 1995, Goldberg and Sergienko 2011, Larour et al. 2005, Gudmundsson and Raymond 2008, Morlighem et al. 2010, Brinkerhoff et al. 2011).

Basal traction inversion in VarGlaS is implemented using a partial differential equation constrained optimisation. In the following, the method is illustrated using surface velocity in the cost functional and basal traction as the control variable; the procedure is analogous for any choice of objective function of control variable. The fundamental concept behind this method is to define a scalar objective function, to calculate its gradient and to use standard minimisation techniques to find the minimum. A general form for the definition of the cost functional, $\mathcal{J}'$, is employed. Specific examples include a linear cost functional,

$$\mathcal{J}'[\mathbf{u}] = \int_{\Gamma_S} ||\mathbf{u} - \mathbf{u}_{obs}|| \; \mathrm{d}\Gamma, \tag{4-20}$$

or a logarithmic one,

$$\mathcal{I}'[\mathbf{u}] = \int_{\Gamma_S} \left[\log \frac{||\mathbf{u}||}{||\mathbf{u}_{obs}||} \right]^2 \mathrm{d}\Gamma. \tag{4-21}$$

We require the velocity field obtained by this functional to satisfy the equations of motion by imposing the momentum equations via a Lagrange multiplier:

$$\mathcal{J}[\mathbf{u}, \beta^2] = \mathcal{J}' + \delta\mathcal{A}[\mathbf{u}, \beta^2; \lambda], \tag{4-22}$$

where δ implies the first variation operator, and $\mathcal{A}$ is one of the energy functionals defined as part of the momentum balance. λ is a Lagrange multiplier used to enforce the forward model as a constraint. Taking the variation of $\mathcal{J}$ with respect to $\mathbf{u}$, β^2 and λ yields, respectively, a forward model, an adjoint model, and an expression for the gradient of the objective function with respect to β^2 that is expressed in terms of $\mathbf{u}$ and λ. Note that no simplifying assumptions about the nature of the forward model are made. In particular, the full adjoint is calculated via automatic differentiation, rather than making the assumption that the viscosity does not depend on $\mathbf{u}$, as is done in many inversion procedures (e.g. Goldberg and Sergienko 2011, Larour et al. 2012). In the case where strong mismatches between the modeled and surface velocity exist, stability of the inversion numerics necessitates fixing the viscosity and using an incomplete adjoint, as in Goldberg and Sergienko (2011), but only for the first few iterations.

In order to impose a minimum bound on the smoothness of the solution, a Tikhonov regularization term is added to penalise wiggles in the control variable. This regularization is of the form:

$$\mathcal{T} = \alpha \int_{\Gamma_B} ||\nabla\beta^2 \cdot \nabla\beta^2|| \; \mathrm{d}\Gamma, \tag{4-23}$$

where α is a positive weighting tensor. This value is different for different objective functions and different model domains. Note that applying Tikhonov regularization on the gradient in this way is equivalent to applying an anisotropic diffusion operator to the control variable.

With a means of efficiently computing the objective function and its gradient with respect to the control variable in hand, any number of optimisation algorithms can be used to minimise $\mathcal{J}$. The quasi-newton algorithm L_BFGS_B (Nocedal and Wright 1999) is used in this work. Termination criterion for the optimisation routine is essentially heuristic, with the optimisation procedure terminating upon the objective function reaching a valley. The definition of a reliable convergence criterion is a subject of ongoing research, with the methods of Habermann et al. (2012) showing particular promise.

4.9.2.7 Numerical stabilisation

Both the enthalpy and free surface equations are hyperbolic and the standard centered Galerkin finite element method gives rise to numerical instabilities. In order to provide stabilisation, streamline upwind Petrov-Galerkin (SUPG) methods (Brooks and Hughes 1982) are applied. For the enthalpy equation, this consists of adding an additional diffusion term of the form:

$$\rho\nabla \cdot K\nabla H, \tag{4-24}$$

where K is a tensor valued diffusivity defined by:

$$K_{ij} = \frac{\alpha h}{2} \frac{u_i u_j}{||\mathbf{u}||}, \tag{4-25}$$

α is taken equal to unity and h is a cell size metric. Alternatively, the approach can be viewed as stabilisation using skewed finite element test functions,

$$\phi = \varphi + \frac{\alpha h}{2} \frac{\mathbf{u}}{||\mathbf{u}||} \cdot \nabla\varphi, \tag{4-26}$$

to weight the advective portion of the governing equation. Because the time derivative is implicitly defined, there is no need to apply upwind weighting to the time derivative or source terms, and because linear elements are used – applying the weighting to the diffusive component would necessitate second derivatives of test functions, which are always zero for linear elements.

For the Stokes' equations to remain stable, it is necessary to either satisfy or circumvent the Ladyzhenskaya-Babuska-Brezzi (LBB) condition. The typical way of doing this is to use a mixed second-order estimate in velocity, first-order estimate in pressure finite element (the Taylor-Hood element). While VarGlaS has the capacity to use this formulation, it is found that the additional degrees of freedom introduced by the higher order elements leads to an unacceptable loss of computational performance. Instead, this condition is circumvented using a Galerkin-least squares (GLS) formulation of the Stokes' functional:

$$\mathcal{A}'[\mathbf{u}, P] = \mathcal{A} - \int_{\Omega} \tau_{gls} \, (\nabla P - \rho\mathbf{g}) \cdot (\nabla P - \rho\mathbf{g}) \; \mathrm{d}\Omega, \tag{4-27}$$

where τ_{gls} is a stabilisation parameter (Baiocchi et al. 1993). For a linear Stokes' problem, the usual value for τ_{gls} is:

$$\tau_{gls} = \frac{h^2}{12\eta}. \tag{4-28}$$

Because τ_{gls} is a function of the ice viscosity, τ_{gls} should be non-linear. However, experimentation reveals that ignoring the strain rate dependence of the viscosity term yields acceptable results and much better numerical stability. Thus,

$$\tau_{gls} = \frac{h^2}{12\overline{\eta}} \tag{4-29}$$

is used, where $\overline{\eta}$ is some linear estimate of η. $\overline{\eta} = 10^3 \times b(T)$, and *b(T)* is described by Equation (4-3), where the rate factor, *a(T, ω)*, is simplified to a piecewise relation only dependent on *T* (everything else in Equation (4-3) remains unchanged),

$$\mathrm{a(T)} = \begin{cases} 1.733 \times 10^{-3}\ \mathrm{kPa\,s^{-1}}, & T > 263\mathrm{K} \\ 3.613 \times 10^{13}\ \mathrm{kPa\,s^{-1}}, & T \leq 263\mathrm{K}. \end{cases} \tag{4-30}$$

This yields an appropriate blend of fidelity and stabilisation to the governing equations. Note that this has the effect of adding a diffusive term (over pressure) to the conservation of mass equation.

4.9.2.8 Parallelism

VarGlaS has been developed to take full advantage of the innate parallel capabilities of PETSc (Balay et al. 2013) and FEniCS (Logg et al. 2012), from which it was developed. All computationally intensive components of the model are compatible with parallel usage, such as the non-linear solvers, time stepping and optimisation. VarGlaS exhibits good scaling between 1 and 16 cores, the largest cluster to which the authors have access.

4.9.2.9 Numerical experiments

After the numerical model completed a suite of standard experiments to demonstrate that it was functioning correctly, attention was turned toward the GrIS. The strategy was to initialise the model using measured present-day geometry, apply data assimilation tools to obtain an initial estimate of the basal traction field, and then use these results to generate fluxes across boundaries into the GAP field site. All simulations of Greenland were done using the first-order approximation for the momentum balance, as accommodated by VarGlaS.

4.9.2.10 Data

SeaRISE data were used as input data (Bindschadler et al. 2013). Bedrock and surface geometry were from Bamber et al. (2001), with updated basal topography in the Jakobshavn region from CReSIS, surface temperatures from Fausto et al. (2009), basal heat fluxes from Shapiro and Ritzwoller (2004), and surface mass balances from Ettema et al. (2009). InSAR derived 2007–2008 average surface velocities from Joughin et al. (2010), providing a surface velocity target. The Joughin dataset is incomplete and gaps were filled with balance velocities; gradients between the two were reduced by systematically exploring the uncertainties in the accumulation rate.

4.9.2.11 Mesh for Greenland

The boundary of Greenland was digitised using the metre contour of the Bamber, Layberry and Gogineni (Bamber et al. 2001) thickness data. A two-dimensional (planar) mesh was created by imposing a 2 km element size at the margins, grading to a variable, but much coarser, resolution (~ 25 km) at the centre of the ice sheet. This ensured that the mesh captured the complexity of the boundary, while maintaining appropriate coarseness in the interior. The resulting 2D footprint was then extruded over ten vertical layers. Numerical models of Greenland, when more highly resolved in the vertical dimension, demonstrate convergence problems during the Newton's method solution process. This is likely due to the very low aspect ratio elements producing poor conditioning, or due to round-off error in the Jacobian matrix. This is a significant limitation, and attempts to overcome it continue to-date.

4.9.2.12 Data assimilation

Basal traction fields were computed using the techniques described above in 'Data Assimilation and Regularization'. Steady state velocity and enthalpy fields are computed for an arbitrary basal traction, with an initial guess of 4 Pa·yr/m^2 and r equal to unity, implying that basal traction is linearly scaled by thickness, effectively eliminating the dependence of sliding speed on normal force and the covariance between β^2 and H. After achieving steady state, the BFGS algorithm, with a fixed viscosity (and an incomplete adjoint), was used for the first ten iterations, before switching to a full adjoint. The temperature field was also recomputed every fifty evaluations of the objective function in order to maintain thermal equilibrium. After the first ten iterations, the velocity field was visually indistinguishable from that of the data, and the convergence between the temperature and velocity fields became a fixed point iteration on the enthalpy field. The BFGS algorithm was allowed to run for 200 evaluations of the objective function. Convergence of the algorithm is shown in Figure 4-41.

4.9.3 Source of error

Errors in computational modelling are more difficult to track than errors associated with measurement. Verification and validation of models remains a big problem in ice sheet dynamics. Before any datasets are taken into consideration, one must demonstrate that: 1) the model is solving the right equations to represent the physical system (verification), and 2) the equations are being solved correctly (validation). For the most part, the standard has been to simply do intercomparison of model outputs. This is due to the complexity of glaciological systems. Through intercomparison, outliers can be identified and programming errors corrected. More recently (Leng et al. 2012), manufactured solutions have been used to show that ice sheet models are correctly solving the equations describing the conservation of momentum. To-date, a fully coupled thermo-mechanical model has not been validated against a manufactured solution.

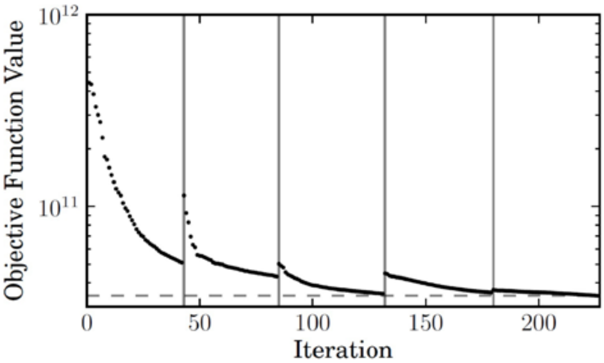

Figure 4-41. Convergence of the BFGS algorithm after 200 iterations. The dotted line tracks the value of the objective function (difference between measured and modelled speed, squared) for each iteration of the optimisation algorithm. The discontinuities in the plot represent places where the model is 'restarted' with a new estimate of the temperature field. Once restarted, the temperature is held fixed and the optimisation algorithm manipulates the mechanical portion of the model.

Errors in the input datasets are also vexing. Ideally, a systematic parameter sweep can be used to identify the sensitivity of the model to its inputs. Unfortunately, the computational costs of such sweeps can be prohibitive. One of the great strengths of VarGlaS is that it includes facilities for adjoint-based data assimilation. These methods allow for estimation of the model inputs that cannot be measured, but are essential to modelling. Parameter sweeps become time consuming when combined with the need for data assimilation.

A final consideration when interpreting the model output is that some real-world physical processes may be inadequately simulated or completely lacking in the modelling scheme. A process that is not yet explicitly treated by any numerical ice sheet flow model is latent heat transfer through all mechanisms of water motion. The results, presented later in this section, demonstrate that this is a particularly important process in the Greenland study. While including these processes is an obvious target for further model development, much remains to be learned about the physical processes moving water (and heat) through the ice sheet.

In spite of the obstacles, the following experiments demonstrate that VarGlas has favourable results for all intercomparisons that it has attempted. In this way, it is shown that the errors associated with using VarGlas are comparable to those arising from other models.

4.9.3.1 ISMIP-HOM

The *Ice Sheet Model Intercomparison Project – Higher Order Model* (ISMIP-HOM) benchmarks are a widely used test of higher order model capabilities (Pattyn et al. 2008). In order to verify model performance, ISMIP-HOM tests A, C and F are run using both the first-order and Stokes' equations for momentum balance.

ISMIP-HOM A simulates steady ice flow with no basal slip over a sinusoidally varying bed with periodic boundary conditions. Figure 4-42 shows the simulated surface velocity for all length scales outlined in the benchmark.

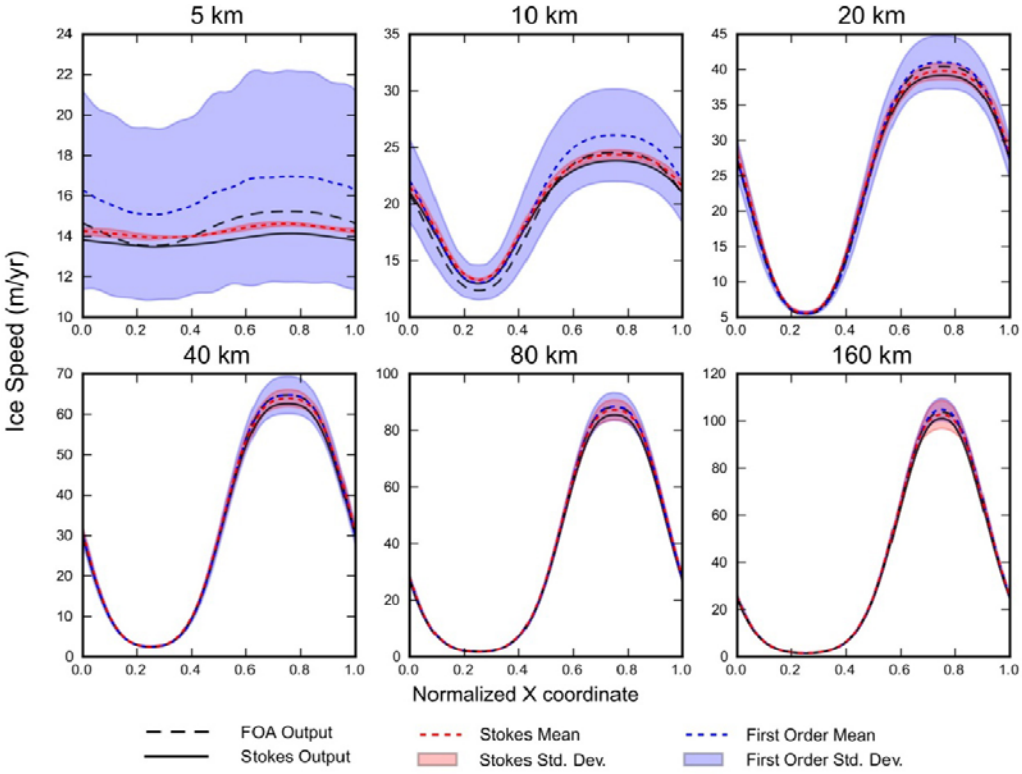

Figure 4-42. *'ISMIP-HOM A' performed using first-order and Stokes' approximations. The FOA is the 'First Order Approximation', also referred to as the 'Blatter-Pattyn Approximation'. Means in this output are assembled from the 28 models that participated in the intercomparison, and have full-Stokes' mechanical balances.*

ISMIP-HOM C simulates steady ice flow, with sinusoidally varying basal traction over a flat bed and periodic boundary conditions. Figure 4-43 shows the simulated surface velocity for all length scales outlined in the benchmark. This experiment specifies that *r* equal zero in the sliding law.

After running the ISMIP-HOM C experiment forward, the velocity field predicted by the model is used to estimate basal traction. This presents an opportunity to test the inverse capabilities of the model, and to invert for a known basal traction. Starting from an initial guess of a uniform basal traction of 1000-1, the inverse model is allowed to predict the basal traction field that produces the velocity field of the forward model (which is known to be a sinusoid). In this case, a length scale of L=80 is used. Figure 4-44A shows the rate of convergence, as well as the 'observed' and modelled basal tractions and surface velocities along the L/4 transect of the ISMIP-HOM model domain (Figure 4-44B).

ISMIP-HOM F simulates unsteady ice flow over a Gaussian bump, with periodic boundary conditions under slip and non-slip conditions, and evaluates the surface geometry and velocity as they relax to steady state. Figure 4-45 shows the simulated surface velocities and elevations for the slip and non-slip cases.

4.9.4 Modelling results

4.9.4.1 Data assimilation

The observed and modelled velocities, along with basal traction and temperature fields, are shown in Figure 4-46. To illustrate some of the fine-scale detail of both the mesh and the data assimilation result, Figure 4-47 shows a close-up of Helheim glacier in eastern Greenland. The velocity field matches the observed velocity closely. For outlet glaciers like Helheim, the surface velocity can be explained by a basal traction composed of both low traction streaming features and sticky pinning points that slow flow. Basal temperature is also related to basal traction, where fast sliding is associated with a melted bed.

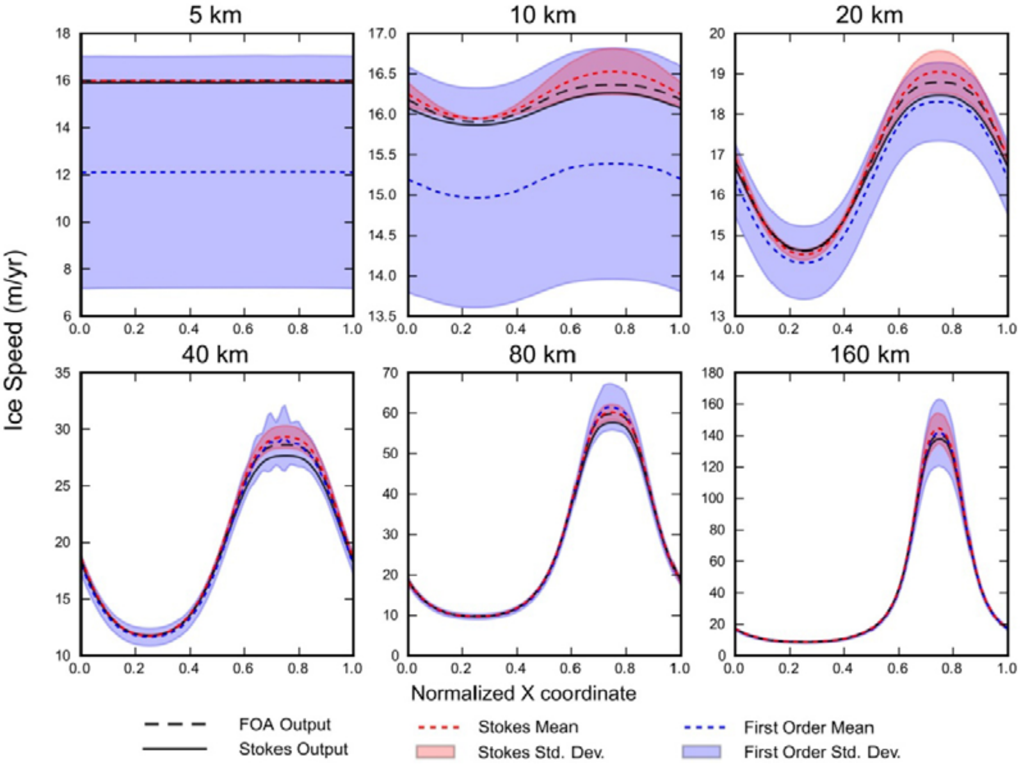

Figure 4-43. *'ISMIP-HOM C' performed using first-order and Stokes' approximations.*

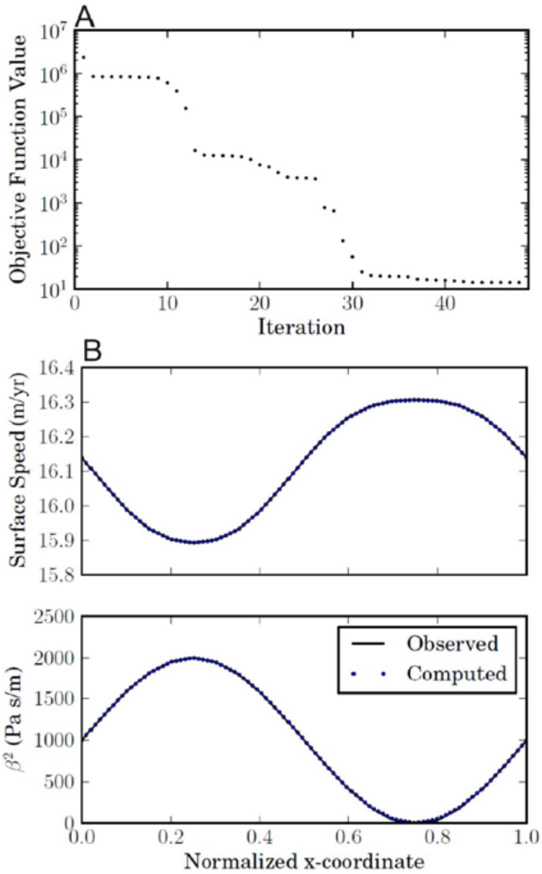

Figure 4-44. *A) 'ISMIP-HOM C' convergence profile; B) 'ISMIP-HOM C' modelled basal traction and velocity.*

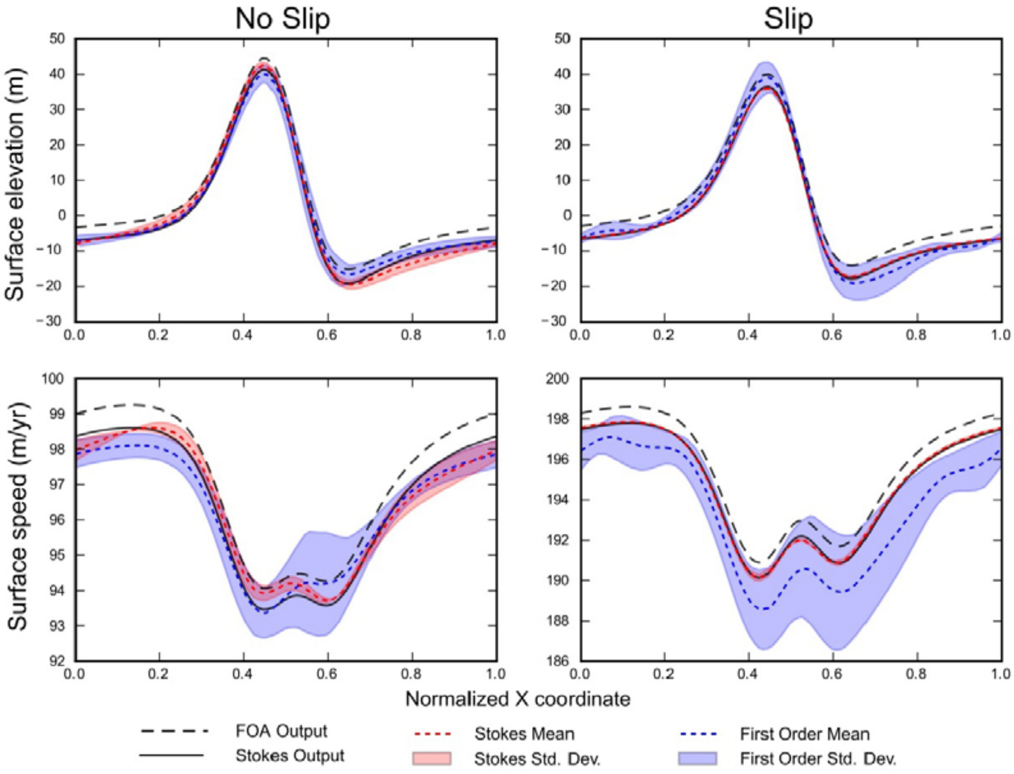

Figure 4-45. *'ISMIP-HOM F' performed using first-order and Stokes' approximations.*

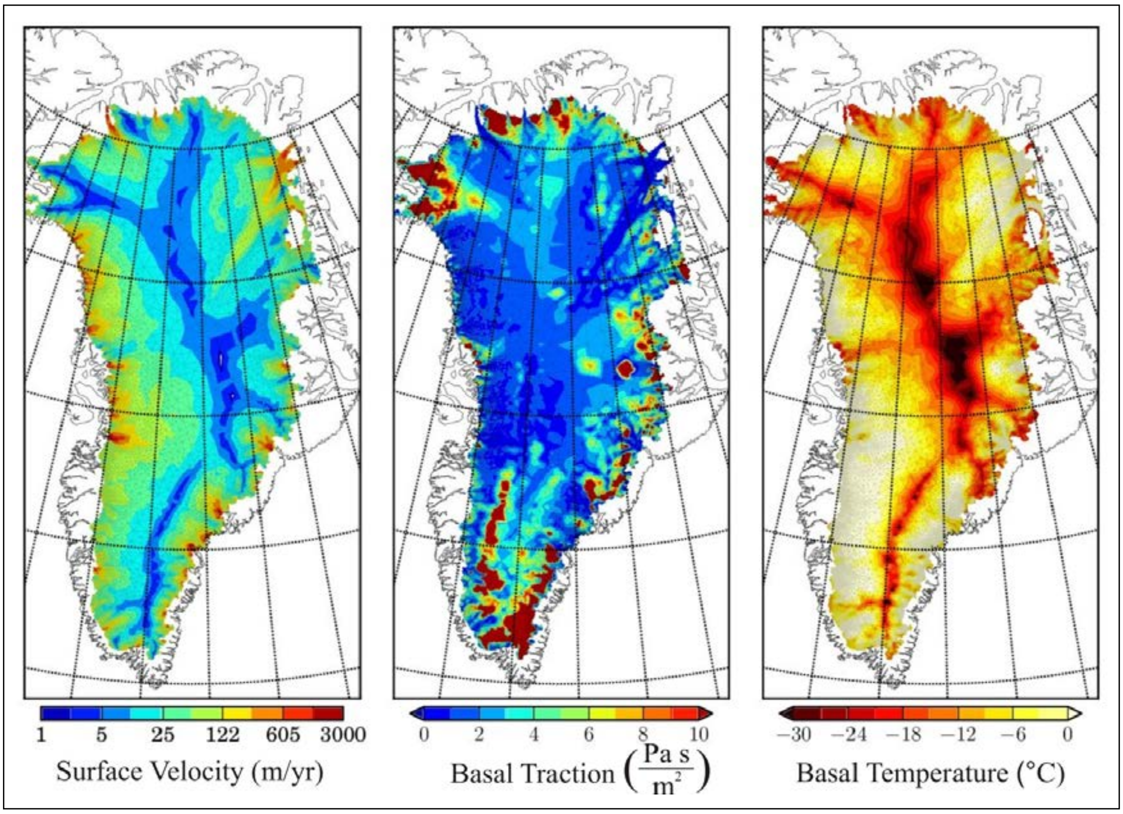

Figure 4-46. *Modelled surface velocity (left), basal traction (middle) and basal temperature with respect to the pressure melting point (right) for the GrIS after the assimilation of surface velocity.*

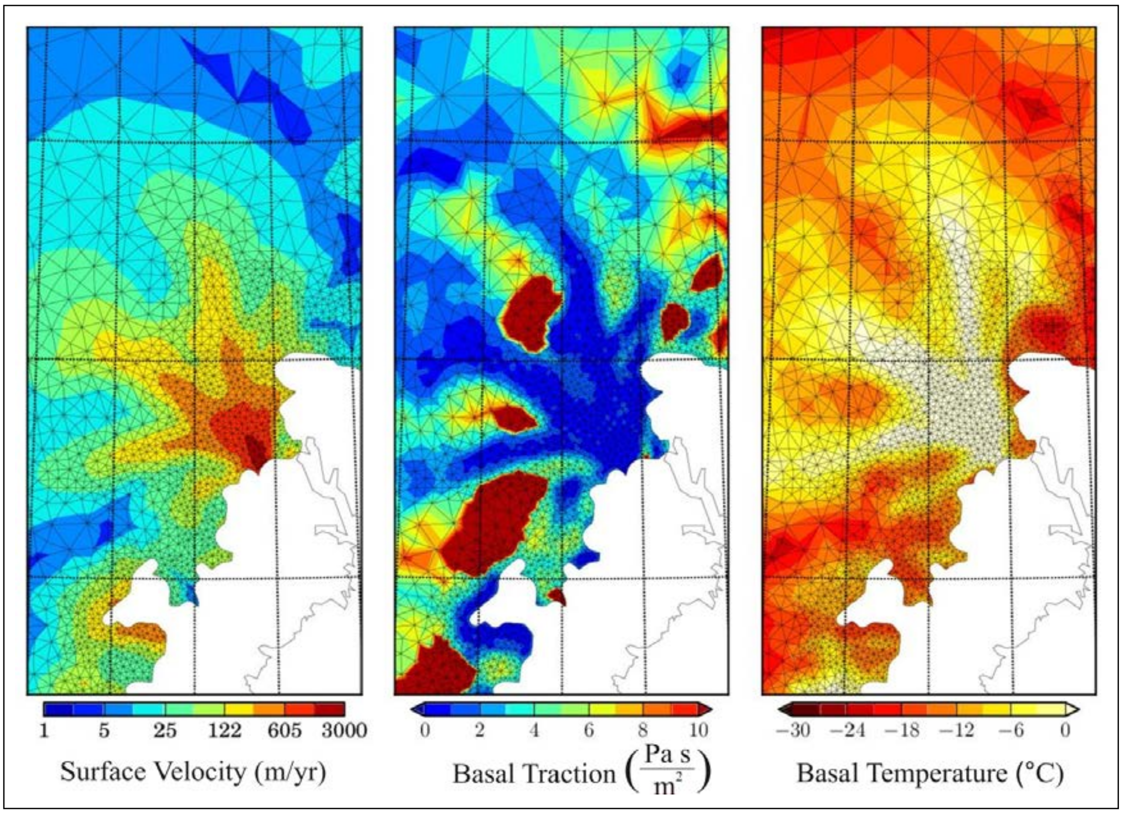

Figure 4-47. *Modelled surface velocity (left), basal traction (middle) and basal temperature with respect to the pressure melting point (right) for Helheim Glacier in eastern Greenland after the assimilation of surface velocity.*

4.9.4.2 GAP field site

Output from model runs done on the whole of the GrIS were collected and applied as boundary conditions to the edges of the GAP study area. The GAP area could be modelled at a much higher resolution, nearly 1 km, due to the bed and surface digital elevation maps assembled by SPA (see Section 3.5). Figure 4-48 shows the domain, and the boundaries that were extracted from the whole GrIS run in order to satisfy the flux boundary conditions.

4.9.4.3 GAP Study area data

All input data for the GAP study area was the same as what was used in the large-scale model, except the following.

- Improved DEM (version 2) from SPA (see Section 3.5) was used.
- To assess sensitivity, a uniform geothermal heat flux was varied from 30 to 42 to 50 mW/m^2.
- The surface temperature pattern was modified to use a lapse rate consistent with data collected as part of the GAP project by Dirk van As (personal communication, and Section 3.3).
- In addition to the two year average of surface velocity provided in Joughin et al. (2010), summer and winter estimates of surface speed from Palmer et al. (2011) were used in the data assimilation process, in order to bracket the amount of basal melt that occurs, assuming steady state conditions.

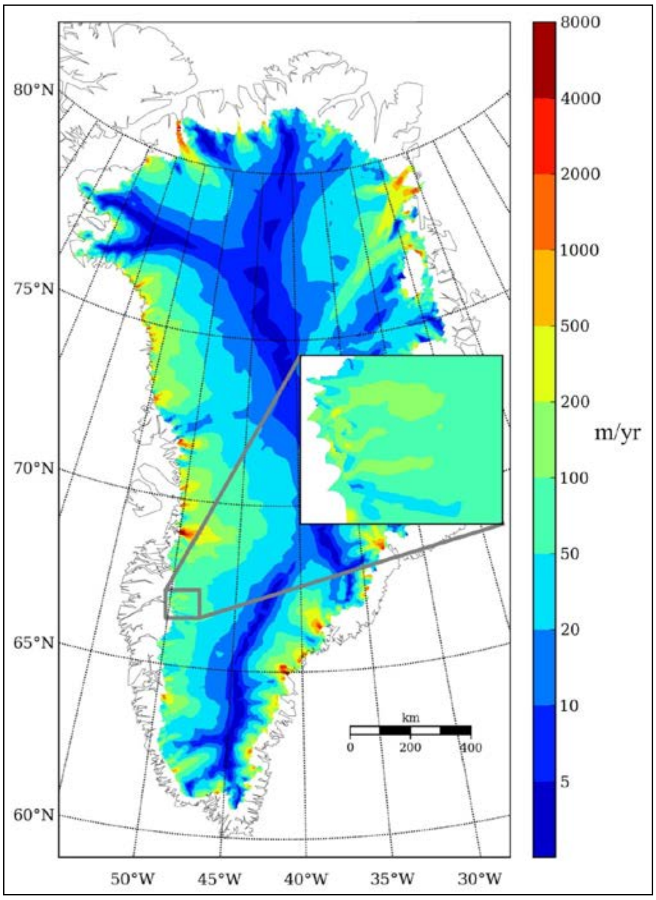

Figure 4-48. *Modelled surface velocity in metres per year for the GrIS, emphasising the results for the GAP study area (inset).*

4.9.4.4 Results

Relatively low surface velocities, less than 20 m/yr, are computed near the centre of the GrIS, while closer to the margin, values increase to around 100–200 m/yr. The area of lower surface velocities is represented by a wide region (~ 200 km) in the northern portion of the GrIS, which narrows to ~ 100 km in the south. This area extends essentially meridionally, with a noticeable split in the contour around 77.5°N. Outside of this region, near the divide, surface velocities generally increase laterally toward to margin, as expected. Near the divide, surface slopes are low and the ice is cold, so much so that the bed is likely frozen, and as a result, the velocities are low. The model has no problem reproducing observations in these areas, although it should be noted that the errors associated with velocity assimilation are highest near the margin.

Closer to the ice sheet margin, the ice sheet is generally more dynamic, with average velocity values around 200 m/yr. In relatively small, isolated areas near the margin, particularly along marine terminating outlet glaciers, surface velocities are orders of magnitude greater, with values reaching values as high as 2–8 km/yr. These very high speed glaciers are likely the result of marine processes and dramatic topographic control on flow; as the ice moves from the interior to the margin, flow becomes confined to narrow fjord-like features, and conservation of mass dictates that the speed must increase dramatically in order to accommodate the high fluxes.

The GAP study area is more typical of marginal behaviour observed away from the most dramatic of the marine terminating ice streams. In this region, ice moves at an average speed of about 100 m/yr, with some locally isolated values rising to between 200–500 m/yr. GPS collected surface velocity data, described in Section 4.7, on seasonally averaged timescales are consistent with these values. Compared to the lower slopes and colder regions deep in the interior, the average values are quite high (5 × greater), but relative to marine terminating outlet glaciers, they are at least ten orders of magnitude lower.

Moving from surface velocity to temperature calculations, Figure 4-49 shows that the model predicts widespread basal melt in the GAP study area. However, there are significant regions with little or no melting predicted by the model. These regions correspond well to the areas where a deep bedrock trough is confining glacial flow. This modelling result is contrary to field data, which indicate that at borehole sites along the Isunnguata Sermia main trough, the bed is melted (Section 4.10). The most likely explanation for this mismatch between model output and observation is that the model neglects the impacts of surface melt and routing on the energy budget. It is now known (Phillips et al. 2010) that significant heat fluxes are generated by the refreezing of surface meltwater that is flowing over and within a glacier. These heat fluxes are missing from this, and every other, ice sheet model. Until they are included, beds in areas of over-deepened ice sheet flow are going to be too cold (due to the tendency for such bedrock features to exert a strong control on the advection of colder ice), drawing cold ice down from up-glacier and pulling it to the bed.

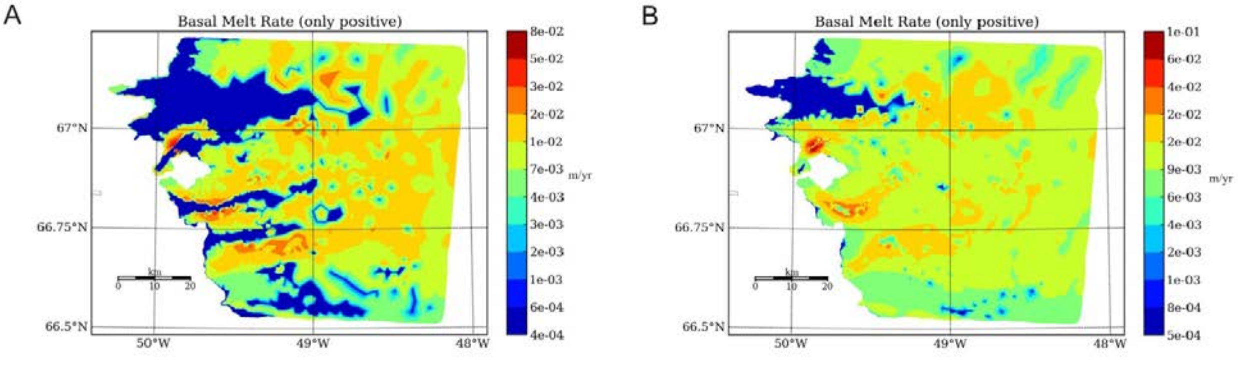

***Figure 4-49.** Presented here are the modelled basal melt rates measured in meters per year for the GAP study area using two different geothermal heat flux values: A) 35 mW/m^2 (best estimate); B) 50 mW/m^2 (increased for sensitivity analysis)*

Basal melt rates for the GAP area for this study are comparable in magnitude with those by Aschwanden et al. (2012), who also uses an enthalpy formulation to track energy; values in both studies average between 10–30 mm/yr. Elsewhere, significant variability of basal melt rates is calculated; typically between 7 and 20 mm/yr, but with local values as high as 30–50 mm/yr. Large spatial gradients in melt rates are indicative of the complexity of bed topography and the basal traction predicted by inversion of surface velocity observations. When the basal boundary condition is at the pressure melting point, κ(H) in (Equation 4-11) becomes zero, and, thus, the basal melt rate is dependent on geothermal heat flux (spatially invariant) and frictional heating from basal sliding only. Therefore, basal sliding either enhances or retards basal melt, depending on the local bed topography and ice flow conditions.

With some interpretation, Figure 4-50 provides a view of likely mechanisms for subglacial routing. High traction areas are those greater than about 10 Pa·yr/m^2. These correspond well to the margins of the ice sheet. This is in agreement with a considerable body of theory that indicates that, as the flux of water routed along the base of an ice sheet increases, the efficiency of the drainage network increases (Section 4.10). At some point, the efficiency of the drainage network becomes so great that all the water exists in a number of well-defined channels, as opposed to a distributed sheet of water. The channels have low pressure and the sheet high pressure. This provides a clear interpretation of the modelled traction field, which shows high traction (low basal water pressure) in regions where one expects channelised drainage, and low traction (high basal water pressure) in areas where there isn't enough water flux to channelise flow. Further, the model results give quantitative insight into where the transition occurs, about 5–10 km from the margin.

Sensitivity studies indicate that the general results do not change appreciably with changes in either the geothermal heat flow or the surface velocity. Increased geothermal heat flow does increase the amount of melting, but produces a more uniform 'shift' in the output results without significantly altering the location of the bed that remains frozen, which still corresponds to the deep trough.

Changes in surface velocity due to the season produce an interesting result in that they provide some insight into where the bed is in a state of higher or lower traction, which, when interpreted as before, can inform understanding of the basal hydrology – in particular, its distributed vs. channelised nature. In the sensitivity study, lower winter velocities have the expected effect and show generally higher traction. Regions of significantly higher traction near the margin remain, regardless of whether winter or summer velocities are selected for assimilation into the model. This indicates that the drainage network may be stable over the course of a year; perhaps, the summer network of channelised features is so robust that it withstands a period of creep closure over the winter.

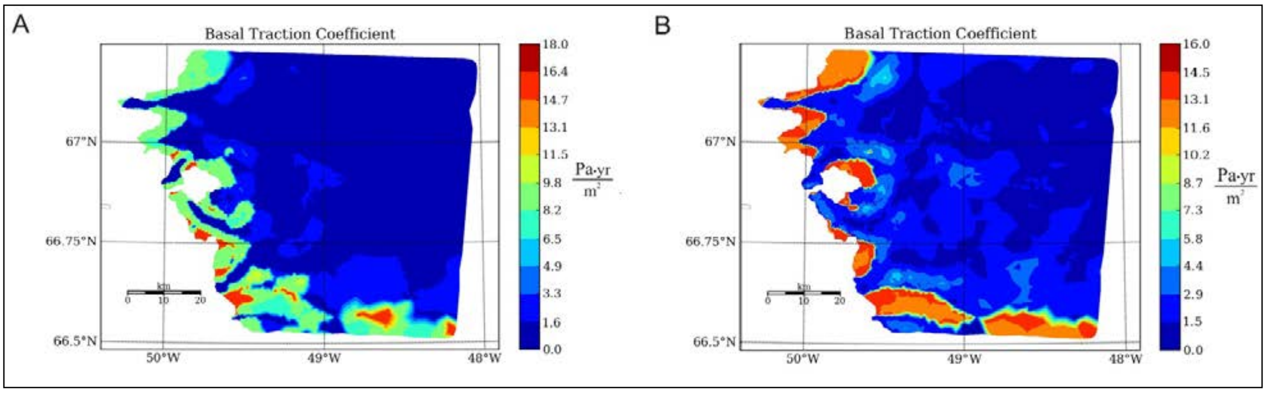

Figure 4-50. *Modelled basal traction coefficient for the GAP study area A) before and B) after decreasing surface velocities.*

4.9.5 Conclusions/findings

The spatial distribution of frozen/melted conditions at the bed of an ice sheet has long been a highly uncertain scientific question. Prior to the GAP, direct measurement of bed conditions along the ice marginal areas were essentially non-existent, and modelling efforts were poorly constrained by observational data. The key factors dictating basal thermal conditions have long been recognised as 1) atmospheric temperature, 2) ice thickness and 3) geothermal heat flux. Basal thermal conditions reflect the balance between geothermal heat sources, the cold atmospheric boundary condition and the ice thickness, which sets the rate of conductive heat transfer away from the bed by dictating the temperature gradient between the warm earth and the cold atmosphere (i.e. the thicker the ice, the lower the temperature gradient). Hence, a warmer atmosphere, thicker ice and higher geothermal heat flux all tend to melt the bed.

The findings here show that these factors, alone, are insufficient for describing basal melt conditions in Greenland; other factors, related to ice flow dynamics, are key drivers in dictating basal thermal conditions. In particular, latent heat transfer is a key process for heat transfer that is not well understood or represented in current models.

A significant (nearly 2 degrees Centigrade) mismatch between model and observed temperature profiles indicates that a stronger role is played by the refreezing of surface meltwater than previously assumed. There are currently no ice sheet models that properly represent this process, and work should occur in this area. Studies should focus on correctly parameterising the bulk hydraulic conductivity of ice, as well as the rate of heating that occurs given the difference in temperatures between ice and meltwater.

The quantity of basal melt being generated annually can be highly variable, depending on local bed topography and basal traction. The mm/yr of basal melt is dwarfed by the m/year of surface melt that is expected to penetrate to the bed; meaning that, for general conceptualisation of summer-time behaviour at the GAP study area, detailed ice energy budgets are unnecessary. However, in winter, it is likely that the basal melt rates are dominated by the ice sheet energy balance, and the modelling is important. Given the known errors in temperature due to the lack of surface meltwater refreezing, it is likely that the overall melting will be considerably large, given a warmer ice sheet.

4.10 Summary of understanding of ice sheet basal boundary developed through SPB

4.10.1 The ice-bed contact

A large range of bed conditions are possible, with one end member being bare bedrock in contact with debris free ice, and the opposite end of the spectrum being a metres thick layer of 'till' with substantial fined-grained materials. The former is commonly called a 'hard' bed, while the latter is referred to as a 'soft' bed. Descriptions of conditions intermediate to these end members should consider: the proportion of the bed covered by sediment; thickness of any sediment cover; the range of grain sizes, including whether fine grained materials are present; and the proportion of debris in the ice.

The structure of the boundary between underlying bedrock and the overlying ice is difficult to determine. Currently, no remote sensing technique can be used to map the debris at the bed, except in cases where the debris is unusually thick, e.g. tens of metres. Here, several direct measures were used to examine the nature of the basal boundary.

1) *Borehole video:* a video camera was lowered to the base of some boreholes to directly observe both the ice sheet bed and the ice near the bed. The video camera images revealed debris entrained in the ice within the lowermost ~ 5 m. The bed was observed to be bedrock with a relatively thin mantle of loose rocks. Where debris existed, it was estimated to be less than 2 dm thick. Importantly, fine-grained sediment was rare, with the bed best described as coarse gravel.
2) *Drill behaviour:* as the hot water drill approached the bed, the behaviour of drilling system revealed information about physical conditions at the bed. Backpressure in the drill-hose/pump system, the weight of the drill hose as it hung in the hole, and the rate of drilling advancement, all revealed information about basal conditions. Drill behaviour implies that debris was typically

present in the ~ 10 m of the ice above the bed. Debris concentration was variable; sometimes debris concentration was very low, implied by limited impact on the drilling system. On other occasions, numerous backpressure events and slow drill advancement suggested substantial debris had accumulated in the borehole. In all cases, however, advancing the borehole was possible, indicating that the debris concentration was probably less than a few tens of percent by volume, assuming that very high concentrations of debris could not be drilled through using hot water. The loss of load on the drill stem implied intersection of the drill with the bed. The load was always lost rather abruptly, and at the same location, when the drill was backed off and re-advanced. This implies that the bed was not a thick layer of sediment that could be drilled through with the high pressure (~ 7000 kPa) jet of water, but instead was a rather thin layer of sediment.

3) *Sediment sampling:* the bed was sampled using a downhole sediment sampler (see Section 4.5). Samples were coarse sand to gravel, and were notably lacking in fine-grained sediment.
4) *Penetrometer:* a devoted bed penetrometer was deployed in boreholes in the margin region, where ice depths were 100–150 m. In deeper boreholes in the interior region, the 2 m long drill stem acted as a penetrometer, with scratches in the drill stem recording sediment interactions. None of the penetrometer observations revealed evidence of a deep and penetrable sediment layer, implying a relatively thin covering of sediment at the bed (if any).
5) *Borehole water level variations:* the rate of change in borehole water levels reveals some information about bed conditions. The higher the transmissivity, the faster the water levels can change. Hence, water flow into the pores of a thick till layer would demonstrate slow changes in water level. However, when the drill intersected the bed, most boreholes drained very quickly (in seconds to 10 s of minutes). Further, the borehole water levels showed rapid responses to surface melt, with strong diurnal pressure variations present in the data. The pressure variations showed sharp trend reversals, implying a lack of diffusive processes. These observations of high transmissivity suggest the bed is not likely to be a thick till layer with substantial fine grains.

Emerging View. Synthesis of the direct measurements of bed conditions suggest that the bed is closest in nature to a ‘hard’ bed, consisting of bedrock covered by a relatively thin veneer of gravel-sized sediment (Figure 4-51). The sediment cover may be patchy, with some bare areas and some areas with sediment cover reaching several decimetres in thickness. Other areas may have ice directly in contact with the bedrock. The ice itself carries debris, located in the lowermost ~ 10 m of ice above the bed. The size of the debris ranges from small particles to very large boulders plucked from the bed, based on observations of glacial erratics (large boulders deposited by ice) at the margin. Other research reported in SPA interpreted seismic data as indicative of a fully sediment covered bed with uncertain thickness. This research was completed tens of kilometres farther inland and south of any of the ice boreholes, implying that bed conditions likely vary in space beneath the ice sheet.

Despite the presence of sediment at the ice/bed interface, the bed in the GAP study area is not classified as a ‘till-covered’ area because the sediment is gravely and patchy. A continuous layer of thick and soft till, holding many fine grains, would have substantially different mechanical and hydrological properties.

A gravel-covered bed is a logical state, based on historical perspectives. This region of the ice sheet has not been covered by marine waters, which would be expected to deposit a thick layer of fine-grained sediment. Further, fine-grained sediment generated *in situ* through basal processes should be flushed from the system over time, because the ablation zone of the ice sheet has long had a vigorously active basal drainage system.

4.10.2 Configuration of the subglacial hydrological system

The GAP field and modelling results enable testing of the conceptual model of Boulton et al. (2007), which depicts different thermal and hydrologic zones at the base of an ice sheet (see Figure 4-1). Understanding of these zones is important in describing ice sheet forcing on the groundwater system. By examination of a real-world study transect on the GrIS, this project moves beyond the purely hypothetical case. The result is that the conceptual model is both altered in some aspects, and refined, with tighter constraints, in other areas.

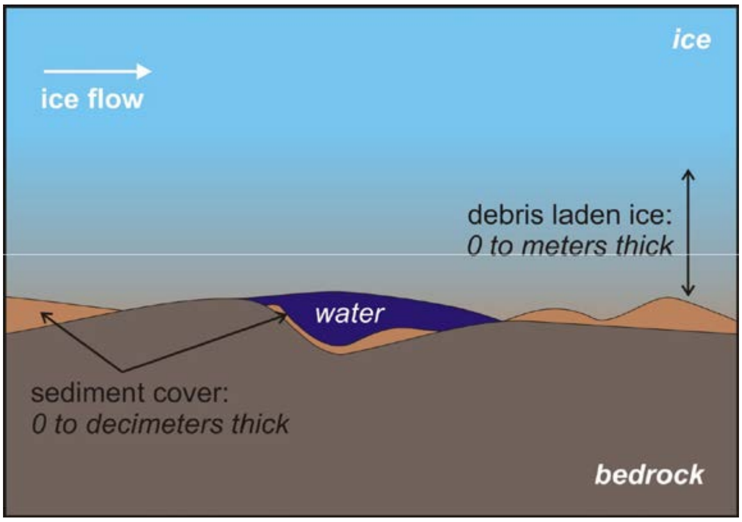

Figure 4-51. *Conceptual view of bed conditions based on several types of observations in boreholes (see text). Note that cartoon is not to scale. Sediment cover on the bed is mostly gravel- and sand-sized grains, and occupies a patchy network with occasional areas of bare bedrock. Entrained sediment in ice is 0 % to perhaps as much as 20 % by volume. High water transmissivity can occur in drainage systems where water cavities are highly linked. Drainage system transmissivity is time variable, and is related to: 1) the water flux, which can open/close connectivity through melting of the ice walls and/or uplift of the ice mass, and 2) the sliding speed of ice over the bed, which can open/close cavities in the lee side of bedrock bumps.*

4.10.2.1 Delineation of zones

Surface zones – the surface of the ice sheet can be classified into three simplified hydrological zones (Figure 4-52).

1) *Surface dry zone*: at the ice surface, the highest elevation zone spanning the region around the ice divide is the dry snow zone. Ice flow in this region is primarily directed downward. During summer, this region receives negligible surface melt or no melt at all. The lowest elevation limit of this region is defined by the long term average highest extent of surface melt. The average yearly maximum position has been determined for the GrIS study transect by satellite backscatter measurements (Abdalati and Steffen 2001).
2) *Surface wet zone*: the wet zone is covered by snow year-round, but this snow experiences some magnitude of melt during summer. This zone extends from the dry zone marking the upper elevation extent to the equilibrium line, which is the lower limit of the surface wet zone. Minor melt occurs at the top of the zone, but melt increases substantially as elevation diminishes across this zone. By the elevation of the equilibrium line, the depth of water equivalent accumulated as snowfall during a given year is equal to the depth of water equivalent melted during summer. Due to the open pore space in the layer of snow and firn, which spans the wet snow zone, a layer that can be up to ~ 100 m thick, surface melt in this zone is generally retained in the surface firn column as either refrozen ice and/or open pore space water (Harper et al. 2012, Humphrey et al. 2012). Hence, the surface melt across this zone does not directly impact the basal conditions.
3) *Surface runoff zone*: the surface runoff zone corresponds to the ice sheet ablation area, which extends from the equilibrium line to the ice sheet margin. A large surface melt gradient extends across the ablation zone, with low albedo ice exposed for longer periods and subjected to warmer temperatures closer to the margin (lower elevation). The equilibrium line is approximately the interior limit, where substantial surface melt has the potential to penetrate to the bed. The amount of melt reaching the bed near the equilibrium line is insignificant compared to farther down glacier, where melt rates are higher and melt accumulates during runoff processes. Closer to the margin, the surface melt rate can be three or more times that near the equilibrium line. The work done by SPA addresses these topics and provides quantitative estimates of meltwater generation and runoff. Much of the surface melt across the ablation zone likely penetrates to the bed because there are no major rivers pouring off the ice sheet, but there are large subglacial outlets discharging water at the margins.

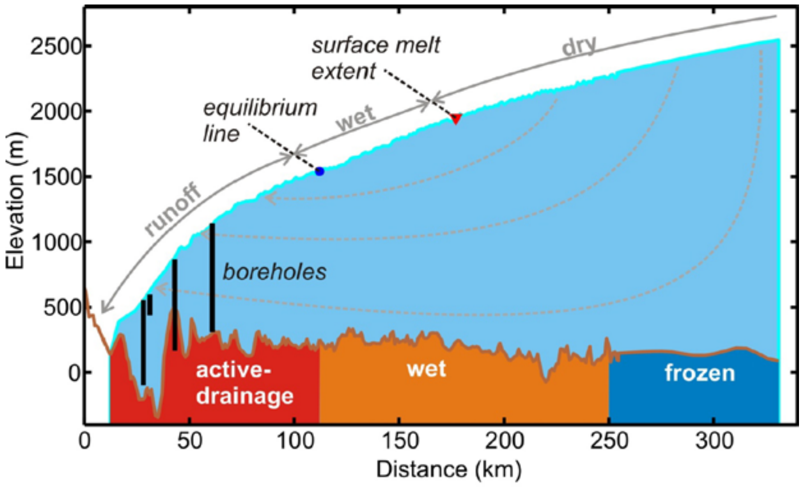

Figure 4-52. *Conceptual view of surface and bed zones along Greenland study transect, extending from ice divide to ice margin. Boreholes are shown as black lines; some boreholes are projected from 1–2 km out of the plane of the transect, giving the false appearance that they do not terminate at the bed. See text for detailed descriptions of the surface and bed zones. Dashed grey lines show idealised internal flow field of the ice sheet.*

Basal zones – the bed can be divided into three zones (Figure 4-52) with contrasting thermo-hydrologic conditions.

1) *Frozen bed zone*: this zone is located beneath a limited portion of the surface dry snow zone at the centre of the ice sheet. Near the ice divide, a large heat deficit is stored in the snowfall accumulating under cold atmospheric conditions. The flow field near the ice divide is nearly vertical so that, as snowfall is transformed to glacial ice, the cold content from the surface is advected toward the bed. For many values of air temperature, snowfall rate and geothermal heat flux, the bed will remain frozen under the conditions present near the ice divide (Brinkerhoff et al. 2011). As the ice near the base of the ice sheet flows away from the divide toward the margins, it slowly warms from the heat supplied by geothermal heat flux. Deformation of the ice causes strain heating, and a small amount of ice sliding across the frozen bed is possible (Cuffey et al. 1999, Echelmeyer and Wang 1987), which adds negligible heat from friction. The bed condition across this zone is a frozen state and no recharge to the groundwater system occurs.

2) *Wet bed zone*: this zone is beneath the entire *surface wet zone*, and likely extends into the lower reaches of the *surface dry zone*. The lower end of the melted zone is located near the ELA. As ice flows away from the divide, the lower depths of the ice sheet are warmed over time by the geothermal heat flux from below. Straining of the ice and small amounts of sliding add additional heat content. Eventually, the ice reaches the pressure melting point temperature and the bed becomes wet and remains wet across the entire *wet bed zone*. As ice moves across the *wet bed zone*, basal sliding is facilitated, which increases the rate of added heat and melting of basal ice from friction. Some water is stored in the pore spaces of the ice grains when heated to the melting point, and then subjected to further heating (e.g. Aschwanden et al. 2012). Water accumulates at the ice/bed interface. The bed in this zone contains liquid water, but with only a few cm per year of melted ice providing this water, the volume of water across this region is small relative to the *surface-drainage bed zone* (see below). Hence, development of a subglacial water drainage system with substantial water flux is unlikely. Water in this region likely exists as thin films and accumulates in cavities on the down-stream side of bedrock bumps. Some cavities may be connected, allowing slow, low-flux water flow. In rare cases, where water is preferentially routed, enough water may accumulate to promote linked cavity water flow. Sliding speeds are low relative to the lower reaches of the ablation zone, so normal feedbacks between sliding speed and drainage system development do not exist. The isolated nature of the water features, coupled with very thick ice, probably renders basal pressure at, or near to, overburden pressure at all times. If fractures and/or permeable bed conditions exist, groundwater may route a substantial portion of the water away from the bed. If transmissivity of bedrock fractures is very high, the recharge rate may be limited by water availability.

3) *Surface-drainage bed zone*: this zone extends from the ice sheet margin for ~ 250 km (see below) to the *wet bed zone*, and lies directly beneath the *surface runoff zone.* This zone is distinct because it receives a substantial input of water from the surface, and because basal sliding rates are high – leading to drainage system/sliding speed interactions. As the surface can generate as much meltwater in one day as is generated in one year at the bed by basal melt, the surface conditions have a substantial impact on bed conditions across this reach. Findings such as borehole pressure (records presented in earlier sections of this report) indicate that water is quite capable of penetrating the km thick ice, at least locally. A very active basal drainage system develops in this zone. The drainage system evolves seasonally in response to changing surface conditions and has spatial/temporal gradients (for a review see, Fountain and Walder 1998). The surface-drainage bed zone has two subregimes, the *transient conduit region*, from the margin to 15–20 km inward, and *the high pressure region*, from 20 km to the ELA. In *the transient conduit region*, water flows through conduits melted into the ice near the margin (within 10 to 20 km of the margin) and through linked cavities farther inward from the margin. The amount of water supplied to the bed far exceeds the amount of water that the groundwater system can accommodate and, so, the vast majority of this water exits to the terminus through a basal drainage system. In the high pressure region, this 'non conduit' view of the drainage system for the interior region implies the bed is covered by water, rather than drained by discrete conduits, with little water in between. Second, the drainage system would not be expected to undergo large pressure drops in response to water input forcing, as hypothesised for a conduit-dominated system that rapidly drains high volumes of water from the bed. Rather, a relatively high pressure can be maintained at all times despite variable water input.

4.10.2.2 Notable refinements and changes

1) *Width of basal zones*: the graphical depiction of basal zones by Boulton et al. (2007; see Figure 4-1) is presented with no scale, and whether or not the relative proportionality of the different zones are intended to be taken literally is unclear. For example, as depicted in the figure, the zone of melted bed with 'groundwater flow only' occupies a small fraction of the total bed of the ice sheet. The work presented in this report provides further information on the conditions and proportionality of the different zones (Figure 4-52 and Figure 4-53).

   The modelling results presented in Section 4.9 suggest that the boundary between frozen and melted bed conditions is likely to be located far inland toward the ice sheet divide. No evidence was found to suggest that the margin regions are frozen at the bed, or that there exists an extensive patchwork of frozen and melted areas between the warm-based and cold-based. The location of the frozen/melted boundary is largely dependent on the thermodynamics of the ice sheet and the geothermal heat flux. However, even though the modelling parameters and geothermal heat flux have uncertainties, they do have constraints; their range of potential values is limited. With standard modelling parameters and a geothermal heat flux of 50 mW/m^2, the frozen/melted transition can be estimated at ~ 250 km inland from the ice margin (Brinkerhoff et al. 2011).

   The modelling results yield a frozen zone that occupies about the inner 30 % of the transect, extending from the ice divide to the margin. The probability of complete melting to the ice divide is low, as implied by modelling results and other ice core temperature measurements reviewed in Section 4.6. The work presented in this report suggests that the melted bed zone (without substantial surface water input) is, in fact, the largest component of the bed, occupying about 40 % of the distance between the ice divide and ice sheet margin. The zone with surface water input occupies approximately the outer 30 % of the transect.

2) *Surface-drainage bed zone*: unlike the conceptual model by Boulton et al. (2007), here it is suggested that conduit-dominated drainage does not extend far inland, except in limited and unusual cases. Rather, widespread conduit-dominated drainage is rare, except near the outer reaches of the ice sheet; the existence of conduits is controlled by topography and water flux, but probably is limited to roughly the outer 5–15 km of the ice sheet. The *in situ* observations reveal basal water pressures unfavourable to development of water-draining conduits extending inland beneath deep ice. This finding is supported by numerical analysis based on realistic ice sheet geometry (Meierbachtol et al. 2013). Slow melt-back of ice walls limits conduit growth, inhibiting the capacity of conduits to transport increased discharge. Hence, key aspects of current conceptual models for Greenland basal hydrology, derived primarily from the study of mountain glaciers, appear inapplicable beyond a limited portion of the ablation zone near the ice sheet margin.

The work presented by Meierbachtol et al. (2013) implies the interior reaches of the *surface-drainage bed zone*, where surface melt does reach the bed, is not predominantly drained by conduit flow. Nevertheless, water flux across a larger portion of this region has been observed to be relatively large and fast flowing (Chandler et al. 2013). If widespread conduits are not likely present, the increased transmissivity at the bed is likely the result of highly enhanced linkages between subglacial cavities. Important distinctions between this type of flow and conduit flow stem from the contrasting physical processes driving drainage system development. Whereas feedbacks from sliding speed and cavity opening are important to linked cavity flow, the rate of ice meltback of conduit walls drives flow through a conduit-dominated system.

While aspects of these findings are a debate for the field of subglacial hydrology, the importance to the GAP science questions is related to the recharge area and pressure conditions at the bed. The 'non conduit' view of the drainage system implies the bed is highly covered by water, rather than drained by discrete conduits, with little water in between. Second, the drainage system would not be expected to undergo large pressure drops in response to water input forcing, as hypothesised for a conduit-dominated system that rapidly drains high volumes of water from the bed. Rather, a relatively high pressure can be maintained at all times despite variable water input.

4.10.2.3 Migration of zones

All of the bed along the marginal area is melted and has a substantial quantity of meltwater derived from both surface and basal melting. A relatively small portion of the interior of the ice sheet is frozen to the bed (see Section 4.9), unless the geothermal heat flux is unusually high. These observations allow for some constraints on the possible thermo-hydrologic conditions at a fixed location as a Greenland-type ice sheet advances and retreats over the location at the ice age time scale. The relevant time scale for the ice age cycles described below, with ice sheets advancing hundreds of kilometres is closer to millennia rather than years.

1) The fixed location will experience wet bed conditions during both the ice sheet advance phase and retreat phases, while the site is overlain by exterior reaches of the ice sheet (i.e. all but the central core). Alternatively, the bed conditions at the site may progress from wet-frozen-wet if the location eventually becomes overridden by the interior of the ice sheet during the peak of the ice age. Hence, the chronology over an ice age cycle for this case is wet-frozen-wet, with the time spent in any one condition being a function of ice sheet advance/retreat rates, but likely millennia rather than years (Figure 4-54).
2) The site would remain wet for the entire advance/retreat episode if no more than the marginal areas cover the site, and the region near the ice divide never advances over the site (Figure 4-54). In addition, the site will remain wet for the entire ice age episode if the ratio of the geothermal heat flux is unusually high relative to vertical ice motion related to the rate of snowfall – so that the region below the ice divide remains melted. While the former is quite probable, the latter is less likely for a Northern hemisphere ice sheet where snowfall rates are high.

4.10.3 Pressure of the subglacial boundary condition

The 'characteristic' pressure at the base of an ice sheet depends on the time-scale and spatial-scale of interest. Further, a definition of characteristic pressure must consider both the magnitude of the pressure and the spatial and temporal gradients in pressure.

4.10.3.1 Long-period and long-length average pressure

The measurements and analysis presented here imply that ice overburden pressure provides an appropriate description of the basal water pressure, as averaged over large distances and long time periods (Figure 4-55). Overburden pressure is typically a slight over-estimate of actual pressure, as the measurements suggest water pressure is most commonly a relatively small fraction below this value. Diurnal and seasonal changes in pressure do occur at all locations within the *surface drainage zone*, with a tendency of fluctuations to drop the pressure below overburden pressure during the summer melt period. However, 1) they occur only during a limited time-fraction of the year, and 2) their magnitude diminishes with distance inward from the margin. Further, where pressure does drop substantially below ice overburden pressure for portions of a day near the ice margin, these low pressure regions are not uniformly distributed over the bed. The low pressure regions are limited to portions of the bed well-connected to high transmissivity drainage features; points only tens of metres away from a location with fluctuating pressure may remain steady at overburden pressure, thereby increasing the spatially averaged pressure.

4.10.3.2 Pressure gradients

Because ice overburden pressure scales with ice thickness, the basal water pressure increases toward the centre of the ice sheet, from atmospheric pressure at the ice margin to > 10 MPa where the ice may become frozen to the bed (Figure 4-55). Hence, a pressure gradient of ~ 115 kPa/km is present in the basal drainage system, when averaged over the distance extending from the margin to interior limit of the study transect. Local gradients in basal water pressure are superimposed on the ice sheet scale pressure gradient, as dictated by local changes in ice thickness and the length scale under consideration (Figure 4-56). Local pressure gradients are substantial near the margin, where the bed has large topographic relief and a steep ice surface.

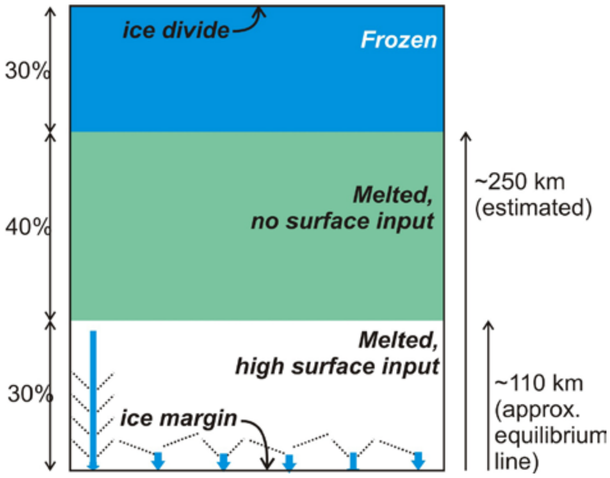

Figure 4-53. *Modified version of the simplified schematic of ice sheet basal conditions by Boulton et al. (2007) (see Figure 4-1). Modifications based on Greenland study transect (Figure 4-52). Percentages on left side indicate fraction of the total distance between margin and divide occupied by each of the three general states of thermo-hydrologic conditions at the bed. Distances on right side are in kilometres; note that the frozen to melted transition zone location is variable (estimated) and is derived from modelling. The position displayed here is estimated using standard values for geothermal heat flux (see Section 4.9).*

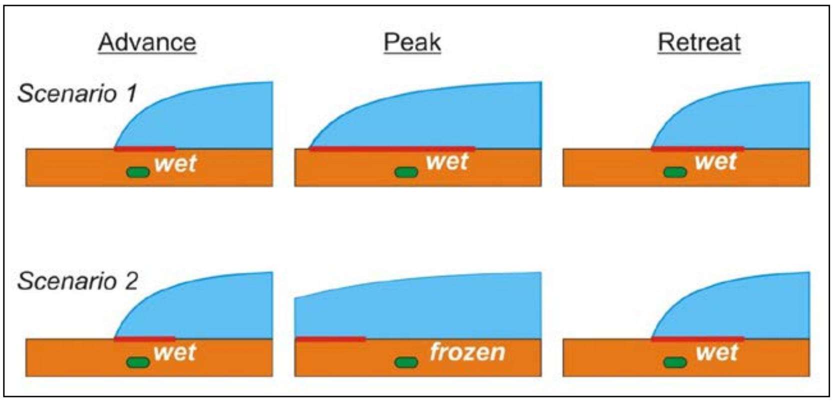

Figure 4-54. *Conceptual overview of two scenarios for ice age cycles based on modern day Greenland analogue. Repository site represented by green oval. Wet and frozen conditions refer to the ice sheet bed and not necessarily the repository itself. In the first scenario, the bed remains wet above the repository for the entire glaciation; in the second scenario the bed becomes frozen at peak glaciation when the advance is so great that the region of the ice sheet near the divide migrates over the site.*

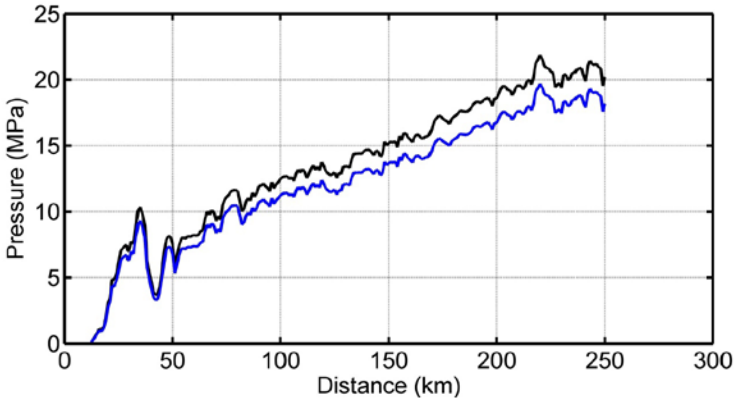

Figure 4-55. *Ice overburden water pressure (blue curve) and water pressure equivalent to a column of water with height of full ice-depth (black curve). Overburden pressure is calculated as 90 % of full ice-depth pressure. Horizontal axis is shown as a function of distance away from the Isunnguata Sermia margin.*

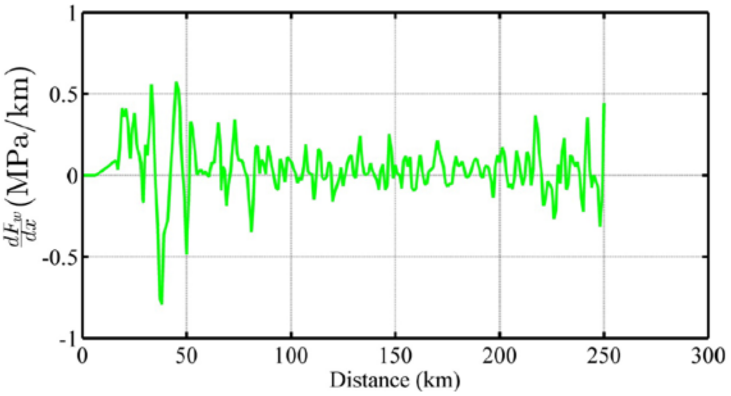

Figure 4-56. *Spatial gradient of ice overburden pressure along the Isunnguata Sermia profile away from the margin. Original pressure data were differentiated against distance, at non-monotonic increments averaging 1.25 km.*

Local pressure gradients are further altered by the basal drainage system, where flowing water can temporarily lead to water pressure drops below overburden pressure, especially during summer months. Hence, temporal gradients in pressure do occur (Figure 4-57). Measurements indicate that these local-scale gradients in pressure do not extend to long distances (i.e. >km) across the ice sheet. Short length scale horizontal gradients in pressure can be expected to be much greater in the *surface-drainage bed zone* than in the *wet bed zone*. This is because of the high flux drainage system that develops, with feedbacks whereby basal sliding opens linked cavities and causes higher transmissivity. In contrast, the wet bed zone has more limited drainage system variability. In addition, spatial gradients in basal water pressure related to drainage system dynamics are likely to be limited to summer months, and not present throughout the rest of the year. In the interior, the fractional pressure drops are small and these gradients are only a small fraction of the higher magnitude pressure.

Very brief but large pressure gradients are theoretically possible where the ice is thick and the drainage system experiences a sudden discharge (pressure) change. Sudden pressure increases are possible, for example, in the case of sudden lake drainage. However, the bed pressure increases associated with these events are dictated by the ice thickness, and, therefore, are limited to a 10 % increase of ice overburden pressure. The maximum likely pressure can be scaled to the ice thickness. In other words, even in cases of sudden pressure increases, the pressure change is likely to be between overburden pressure and 110 % of overburden pressure (equal to ice thickness).

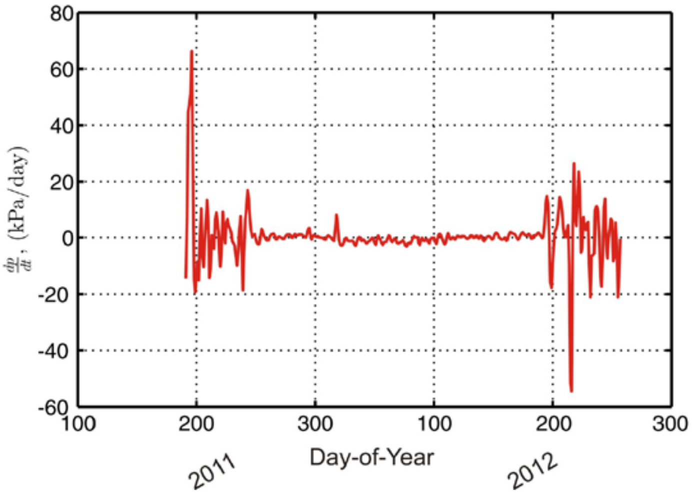

Figure 4-57. *Time derivative of basal water pressure. Original pressure data was averaged over a one day period and the result was then smoothed over a 2-day Gaussian window before being differentiated. The record spans a full year (July 10, 2011 to July 10, 2012).*

Sudden decreases in pressure could occur for very brief periods (i.e. seconds to perhaps minutes) if water input to a high capacity drainage system were suddenly 'shut off'. This might happen when a draining supraglacial stream is suddenly diverted, or during flash flow during a rainstorm. However, such events were never measured, and while they are theoretically possible, are expected to be rare, if they occur at all. Such sudden pressure drops could be severe, from overburden to atmospheric, but such drops would be brief and, as stated previously, would occur rarely. Nevertheless, the impact of such transients may be important to some processes.

4.10.3.3 Summary of constraints

1) **High pressure in the basal drainage system**

   Greater than 110 % of overburden pressure ('ice thickness pressure').

   Not measured, and considered highly unlikely. Perhaps water pressure above 110 % of overburden could be generated in association with freezing processes at the bed, which could potentially develop large transient pressures. However, such effects would be local, and not persistent in time and are purely speculative.

   Equal to 110 % of overburden pressure ('ice thickness pressure').

   Not directly measured, but expected in cases of supraglacial lake drainage. However, lake drainage events are isolated in time and space, and therefore do not depict mean conditions across the bed.

2) **Low pressure in the basal drainage system**

   Atmospheric.

   Not measured, but expected to occur in outlet streams very close to the ice sheet margin (i.e. within hundreds of metres). In other locations, very low pressures are theoretically possible in circumstances where water input undergoes a sudden and large discharge drop, but never for sustained periods of time.

3) **Time and space average pressure of the basal drainage system**

   Near overburden.

   All measurements indicated pressures near overburden occurred for the majority of the year. Pressures fell below overburden by no more than 10–15 % at locations farther than 2 km from the ice sheet margin. Pressures fell below overburden pressure, by up to 70 %, at locations close to the margin, but only during summer months and for a portion of each day. Overburden pressure represents a relatively small over-estimate of the time/space average of pressure.

4.10.3.4 Important considerations

Water pressure at the bed of the ice sheet can be characterised by several different metrics. Any analysis that includes the water pressure of the basal boundary should take into consideration the form of basal water pressure that is most relevant to the problem. Important considerations include an assessment of:

1) The significance of points in time (transient events) relative to time-averaged pressure.
2) The significance of points in the field (localised events) relative to space-averaged pressure, and
3) the relative significance of pressure absolute magnitudes to time and/or space gradients in pressure.

5 Subproject C – Hydrogeology and hydrogeochemisty

5.1 Introduction and objectives of SPC

5.1.1 Aims and background of SPC

The aim of the investigations conducted by Subproject C (SPC) was to increase the understanding of hydrogeochemical and hydrogeological conditions in subglacial and periglacial environments. Special interest was focused on the fate of recharging meltwater. Data collected by SPC contributed to addressing the following GAP questions i.e. *Question 2) What is the hydraulic pressure situation under an ice sheet, driving groundwater flow?; 3) to what depth does glacial meltwater penetrate into the bedrock?; 4) what is the chemical composition of glacial meltwater if, and when, it reaches typical repository depths (500–1000 m)?; and 6) what is the role of taliks in the proglacial hydrogeology?* Drilling of deep bedrock boreholes, including an inclined borehole under the margin of the GrIS, was the focus of SPC field activities in order to facilitate the research and monitoring of groundwaters.

Exchange of information with the other two subprojects, SPA and SPB, was important in developing an understanding of the deep system and its coupling to the ice sheet. Knowledge of thermal state of the ice sheet, wet-based areas, bed topography and general glacial hydrology have been used as guides in selection of the bedrock drilling sites and in the interpretation of hydraulic downhole data. Co-operation with the *Greenland Analogue Surface Project* (GRASP) in terms of talik hydrology was established during 2010.

Before attempting to collect new data in order to address the above GAP questions, it was necessary to gain sufficient understanding of the general geology, surface hydrogeochemistry and the periglacial conditions, especially the depth of permafrost, in the GAP study area. All of this information is part of the site characterisation and conceptualisation, and also provides necessary background information for the planning and implementation of the research of the deep system. Although the Kangerlussuaq area has been the focus of vast number of research projects during the past decades, all reported investigations (ecology, limnology, Quaternary deposits, etc.) are related to features and processes at the surface. They provide an excellent set of useful background information, but little, if any, information was available from the deep systems.

No other published studies have dealt with the deep groundwaters in Greenland. The lack of reference data and the general understanding of the groundwater systems in Greenland (and specifically in the GAP research area), complicate the evaluation of the impact of glacial meltwaters on the evolution of local groundwaters. Prior to the GAP, it was not clear as to what kind of deep seated groundwater system any recharging meltwaters would be mixing with, which would make it difficult to establish mixing scenarios that are valid for both qualitative and quantitative considerations.

The literature review by Jansson (2010) also identified a shortage of information related to permafrost conditions in the area. In addition to its essential impact on the hydrogeology of the area, information on permafrost depth and distribution was of practical importance for the SPC work. Some knowledge of permafrost depth was required in order to plan and successfully drill the deep borehole and design the downhole instrumentation.

The necessity of extended field investigations prior to the drilling of the deep borehole resulted in a delay in drilling of the borehole until 2011. As a consequence, the recovery time from the drilling disturbance and the monitoring period, in terms of hydrogeochemical sampling and physico-chemical parameters, was short. By the end of 2012, when the GAP field activities officially ended, groundwater samples uncontaminated by drilling fluid could not yet be obtained from the deep research hole (DH-GAP04). The *pressure* (P), *temperature* (T) and *electrical conductivity* (EC) in the borehole were still in a transient stage, possibly related to seasonal variations or subglacial events, which hampered the identification of cyclic patterns. Thus, some of the datasets presented in this report are incomplete and post-GAP monitoring is ongoing in order to improve and confirm the conclusions presented.

5.1.2 Implementation of SPC work

The research work has been grouped into five main themes, each of which includes several lines of research, as follows.

Geology:

- Geological surface mapping, including lithologies and structures, at different scales;
- Drill core logging of lithologies, fractures and fracture infillings, orientation of the planar structural features;
- Petrophysical measurements from drill cores; and
- Aeromagnetic interpretation of lineaments and ground-truthing/characterisation of lineament sets.

Permafrost:

- Temperature profiling of boreholes and of the 'Talik lake' (Figure 5-2);
- Geophysical soundings; and
- Geothermal modelling.

Hydrogeochemistry:

- Surface water studies, including lakes, springs, rivers and glacial meltwaters;
- Groundwater studies, including sampling of DH-GAP01 and DH-GAP04 (Figure 5-2) and the Leverett Spring (Figure 5-65);
- Monitoring of pressure, temperature and electrical conductivity in DH-GAP01 and DH-GAP04;
- Matrix porewater studies – crush and leach of core samples and porewater extraction from preserved core samples; and
- Microbial investigations of borehole and lake water.

Mineralogical studies:

- Fracture infillings and drill core observations;
- Stable isotopes and fluid inclusions in calcites;
- Mineralogical and isotope geochemical studies on sulphur and sulphate phases; and
- Observation of redox conditions based on fracture infillings.

Hydrogeology:

- Hydraulic testing of DH-GAP04;
- Slug tests of DH-GAP01; and
- Pressure and electrical conductivity monitoring in DH-GAP01 and DH-GAP04.

5.2 Geological setting

Topography and Quaternary geology of the GAP study area are described in Chapter 2. The GAP study area is located in the southern part of the Nagssugtoqidian Orogen, formed circa 1.88–1.83 Ga due to the collision between two large rifted Archaean continents (van Gool et al. 2002). The rocks in the Nagssugtoqidian orogen are dominated by Archaean orthogneiss, with minor components of Palaeoproterozoic amphibolite and metasedimentary rocks that were deformed under high grade metamorphic conditions in the Palaeoproterozoic (Figure 5-1). The Nagssugtoqidian structures reflect the ductile nature of regional deformation in the area and include a penetrative gneissic fabric, macro-scale folds and evidence of shearing in pronounced shear zones. Deformed mafic dykes are observed occasionally in the area, including the Kangâmiut Dyke Swarm (Mayborn and Lesher 2006). The GAP study area is useful as an anologue site, in part because of some similarities to crystalline environments in Finland, Sweden and Canada. Brittle structures, such as faults and fractures, are abundant in the GAP study area and probably formed in a shallow, younger, colder, and, hence, more rigid environment.

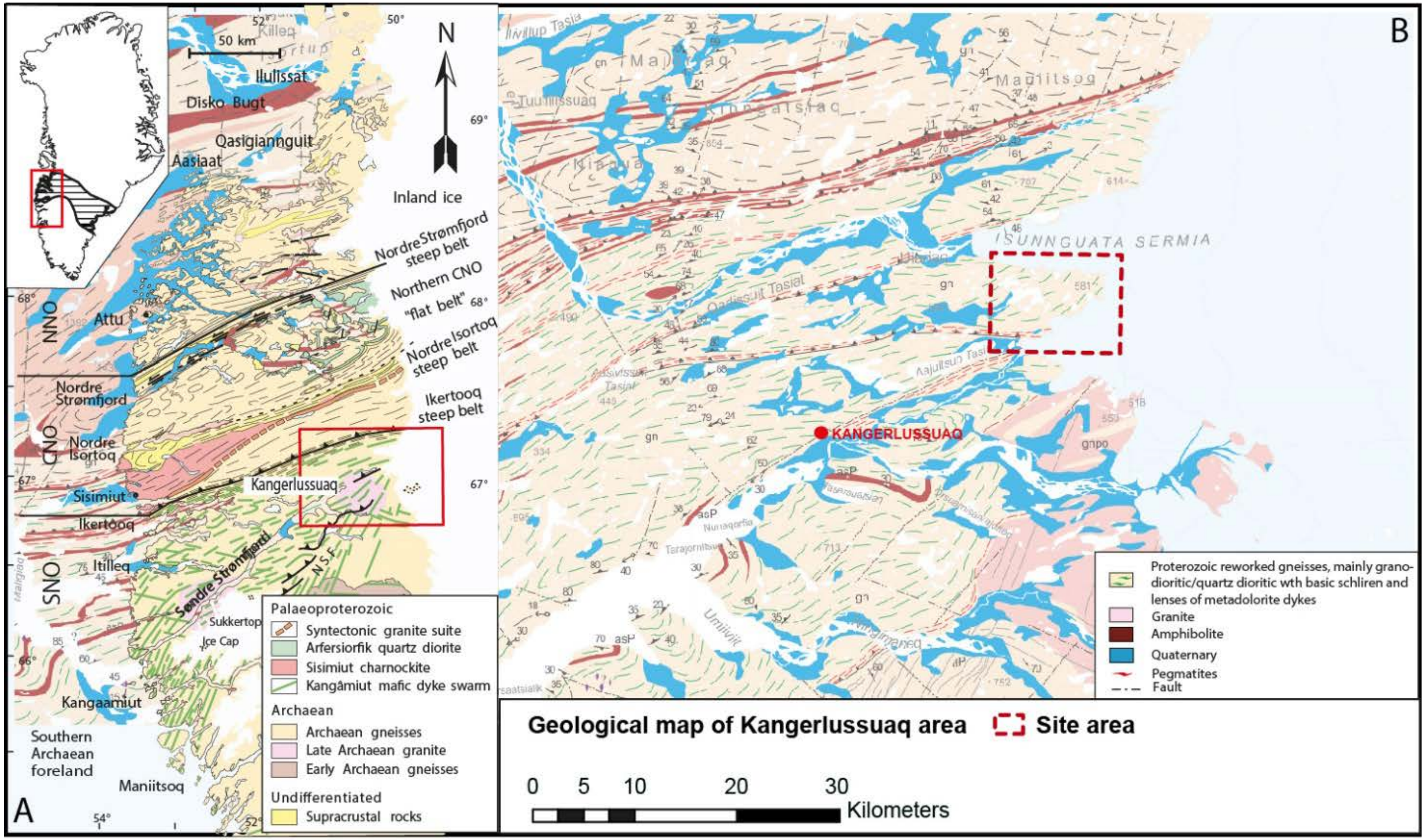

Figure 5-1. A) Geology beween the GrIS and the sea and, B) the regional field area. (Map modified from Garde and Marker 2010, and Garde and Hollis 2010).

5.3 Drilling and instrumentation of research boreholes

5.3.1 Purpose of drilling bedrock boreholes in GAP study area

The goal of SPC was to increase hydrogeochemical and hydrogeological knowledge about the periglacial and subglacial environment in the GAP study area, especially in relation to meltwater recharge. An essential part of the investigations involved the drilling of a deep inclined borehole to allow for multilevel sampling and monitoring of groundwaters down to typical repository depths (i.e. ~ 500 m vertical depth).

Early field trip and literature review not only provided a basic understanding of the present geological and periglacial conditions at the site, but also revealed some critical knowledge gaps. Poor understanding of permafrost conditions, the lack of fracture information in 3-dimensions, and a lack of reference data for groundwater chemistry and prevailing hydrogeological conditions, were identified as such data gaps. The planning of the deep research borehole (DH-GAP04) and the associated instrumentation was considered to be high risk without additional information. To fill these data gaps, it was necessary to conduct field investigations, which required diamond drilling to obtain drill core and to facilitate downhole monitoring. Therefore, within a four week period in 2009, three boreholes, DH-GAP01, 02 and 03 were drilled and two of them (DH-GAP01 and DH-GAP04) were instrumented for monitoring purposes (DH-GAP02 was abandoned during drilling due to technical issues). The aims of these drillings were: 1) to obtain bedrock temperature profiles in order to define the (maximum) depth of permafrost at the ice sheet margin; 2) to demonstrate the presence of a talik structure beneath a lake; 3) to collect core material for geological and structural studies; and 4) to provide groundwater sampling and hydraulic testing opportunities.

After analysing the data obtained from the three boreholes, planning of the deep borehole and its instrumentation began late in 2009. Amongst all of the achieved knowledge and experience in preparation for drilling of DH-GAP04, the depth of permafrost was probably the most important single piece of information. The depth of permafrost in the area largely defined the drilling technique, minimum drilling depth and the design of the downhole instrumentation, including the length of heating cable to be applied through the frozen bedrock. The deep inclined borehole was drilled, tested and instrumented in 2011.

In addition to the general aims, each of the GAP boreholes had specific scientific targets, as described in Sections 5.3.1.1, 5.3.1.2 and 5.3.1.3 which defined their locations (Figure 5-2). Additionally, logistical reasons, environmental aspects, safety issues related to personnel and material, and accidental or intentional human actions, were taken into consideration. Drilling permits were obtained from the Greenland Bureau of Minerals and Petroleum.

A standard drilling technique was used for all drillings. However, the thick permafrost and consequent freezing risk required the use of heated drilling water (up to 60 °C) and limited the time available for borehole testing and instrumentation. A local, geochemically well-characterised water source (see Sections 5.3.1.1, 5.3.1.2 and Harper et al. 2011) was used and the drilling water was spiked with sodium fluorescein dye ($C_{20}H_{10}Na_2O_5$) to allow for the evaluation of the drilling water contamination in subsequent geochemical sampling. The consumption of drilling water was monitored, but the amount of return water was not measured. Upon retrieval, all of the drill cores were shipped to Olkiluoto, Finland, and are stored at Posiva's drill core facility (SKB 2010b, Harper et al. 2011). Detailed core logging, and subsequent core sampling, was conducted at Posiva (Pere 2014).

The specific aims and technical details for each borehole, as well as a description of downhole instrumentation are given in the following sections. The obtained data and other research outcomes are discussed in the topical sections.

5.3.1.1 Borehole DH-GAP01

Taliks are assumed to have an important role in periglacial hydrogeology, potentially allowing vertical water flow, which is prevented elsewhere by the frozen ground. DH-GAP01 was drilled to confirm the existence of, and to allow for the study of, a talik structure (unfrozen zone in the permafrost) under a lake. Selection of the lake for talik investigations was based on the general knowledge of the formation of taliks, the experience gained in the Canadian Arctic by the Permafrost Project (e.g. Stotler et al. 2009), as well as the preliminary field investigations carried out in 2008 (Aaltonen

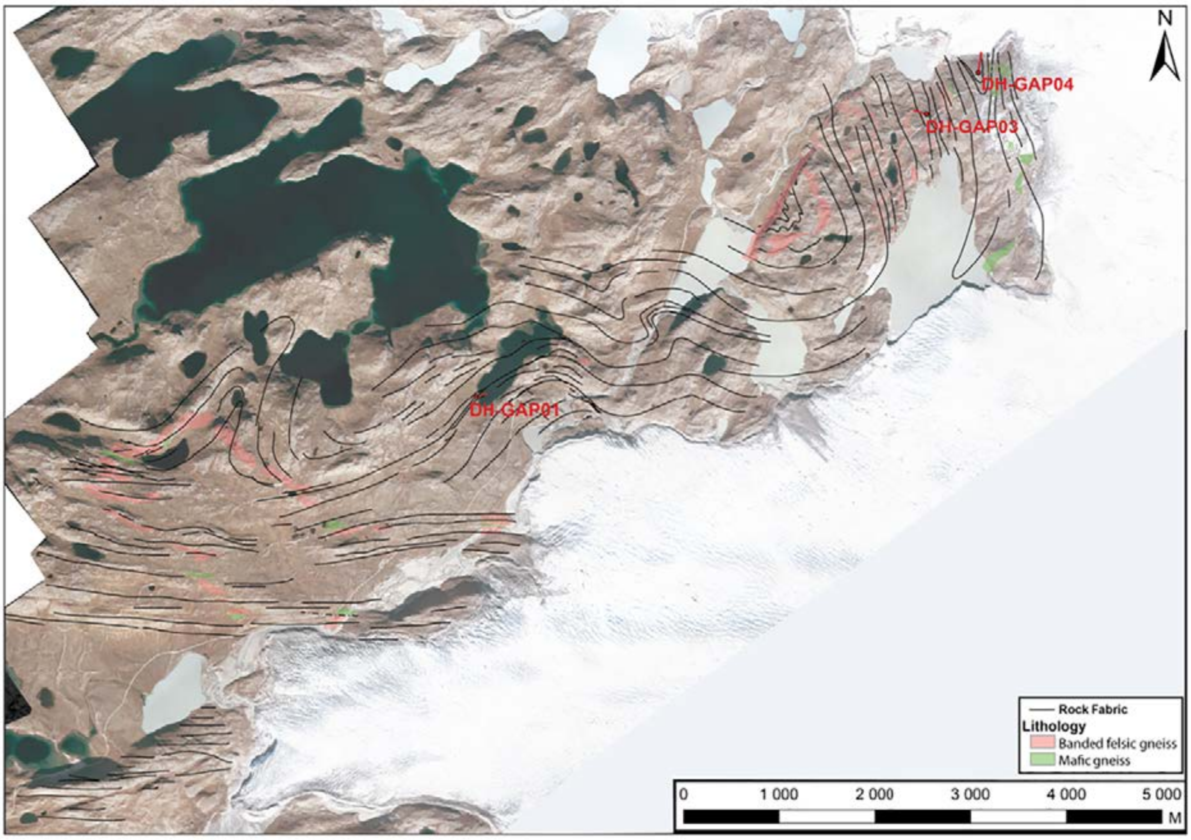

Figure 5-2. *Map of the GAP boreholes superimposed on an aerial photo together with the interpreted outlines of geological structures. DH-GAP01 is drilled under a lake called 'Talik lake'. Aerial photo is from 2006.*

et al. 2010). The main criteria for selection of a drill site for DH-GAP01 were that the water body should be large and deep enough not to freeze down to bottom during winter and that it should be located in a lineament or fault. The first criterion is the thermal precondition for the existence of an unfrozen zone, and the second aims to increase the probability of a higher hydraulic conductivity of the bedrock within the talik. The selected lake, referred to as the Talik lake in this report (called also the Two Boat Lake and SS903 by other research teams), is 1200 m long, 300–400 m wide and the greatest depth is ~ 30 m (SKB 2010b).

Drilling

DH-GAP01 was drilled beneath the lake basin ~ 20 m from the lake shoreline (Figure 5-3) using Talik lake water as drilling water. Drilling orientation was towards NNE at a 60° angle. The length of the 56.8 mm (BQ) borehole is 221.50 m, which equals 191 m vertical depth (Table 5-1). After the hole was drilled, it was flushed for an hour and a deviation measurement was conducted. In total 40 m^3 of flushing water taken from the Talik lake was used. The temperature of the inflow was 30–40 °C (SKB 2010b).

It was not possible to carry out hydraulic testing in DH-GAP01, but the decrease of returning drilling water after 20 m depth, and the significant drop in flushing water pressure at around 204 m, provided evidence of hydraulic conductivity within the unfrozen part of the borehole. Additionally, the temperature profile in the upper 140 m of the hole revealed peaks of positive temperatures at certain locations for an extended period after drilling. These anomalies were interpreted to indicate fractures slowly delivering warm drilling water back into the borehole. Although there is no certainty as to how these fractures contribute to groundwater flow, they tend to support a model of sparsely fractured bedrock with a small number of hydraulic zones.

***Figure 5-3.** Drilling of DH-GAP01 to investigate the talik beneath the lake. The drilling direction is towards the lake. Photo by Timo Ruskeeniemi.*

5.3.1.2 Boreholes DH-GAP02 and DH-GAP03

Boreholes DH-GAP02 and 03 were drilled close to the margin of Isunnguata Sermia, about 6 km NE of the Talik lake and DH-GAP01 (see Figure 5-2). The aim of these boreholes was to determine the maximum depth of permafrost in the area, and it was assumed that the mean average air temperature would be lowest near the ice margin at a high elevation, where the snow cover, vegetation or other potentially insulating factors would be minimised (Figure 5-4). Additional considerations for siting the permafrost boreholes included the presence of sparsely fractured bedrock, which would best represent the preferred conditions for a deep geologic repository, balanced with a proximity to zones of increased fracturing if possible (SKB 2010b).

***Figure 5-4.** Drilling of DH-GAP03. The drilling direction is to the left towards the lowland. Photo by Timo Ruskeeniemi.*

At the time of the 2009 GAP borehole drillings there was no clear understanding as to how deep the permafrost would be in the ice marginal area. A borehole at Paaqitsok, 275 km north from Kangerlussuaq was reported to have 220–230 m of permafrost (Kern-Hansen 1990). The target depth for the GAP borehole was set to about 400 m of borehole length, which would equal about 370 m vertical depth with a drilling dip of 70°.

Drilling

The borehole DH-GAP02 was orientated towards NWW with a 70° angle of inclination. The orientation was determined by the orientation of geological structures. The diameter of the borehole is 56.8 mm (BQ), the same as DH-GAP01 (Table 5-1). Drilling of DH-GAP02 began 2009-06-29. Drilling was terminated at 128.30 m the following evening due to technical problems – the drilling string was jammed and 30 m of rods were lost in the hole. The rig was moved a metre backwards and the drilling was re-initiated. The new hole was coded as DH-GAP03 and it had the same orientation and dip as DH-GAP02. DH-GAP02 was neither instrumented nor was the core logged. However, the core is stored at the Posiva core shed and can be used, if necessary, to collect supplemental material for DH-GAP03. DH-GAP02 is not discussed further in this report.

Table 5-1. Technical details of boreholes DH-GAP01, DH-GAP02 and DH-GAP03. Coordinates and elevations are provided in both latitude and longitude (UTM/WGS84 ellipsoid) and x-easting and y-northing (UTM/WGS84 ellipsoid, UTM zone 22N) systems.

Hole ID	DH-GAP01	DH-GAP02	DH-GAP03
Latitude (y-Northing)	67.125526 (7445607)	67.151396 (7448557)	67.151396 (7448557)
Longitude (x-Easting)	−50.181777 (535491)	−50.072708 (540179)	−50.072708 (540179)
Elevation (ellipsoidal)	374.13	484.45	484.45
Length	221.50	128.30	341.20
Hole Path	Linear	Linear	Linear
Azimuth	083	288	288
Dip	60	70	70
DH survey dip	−59.96		−70.5
Project	Greenland Analogue Project	Greenland Analogue Project	Greenland Analogue Project
Location	Kangerlussuaq/Greenland	Kangerlussuaq/Greenland	Kangerlussuaq/Greenland
Date drilled	26–28.6.2009	29–30.6.2009	30.6–3.7.2009
Remark		Hole terminated, drill string stuck	Drilling terminated due to a severe deformation zone
Name hole	GAP	GAP	GAP
Name number	1	2	3
Survey type	GPS	Estimated	GPS
Grid ID	UTM zone 22, WGS84	UTM zone 22, WGS84	UTM zone 22, WGS84
Survey note			
Overburden (m)	2.70	1.40	1.50
Top of casing (TOC), (ellipsoidal)	374.68 m	c. 484.60 m	484.87 m
Casing above ground level (m)	0.63 (0.55 vertical)	0.25 (0.24 vertical)	0.45 (0.42 vertical)
Storage	Olkiluoto	Olkiluoto	Olkiluoto
No of core boxes	42	23	63
Casing (mm)	74/57 steel	74/57 steel	74/57 steel
Hole diameter (mm)	56.8	56.8	56.8
Sample diameter (mm)	39	39	39
Equipment	WL-56	WL-56	WL-56
Deviation survey			
- Hole ID	GAP1	GAP2	GAP3
- Method	DeviFlex		DeviFlex
- Surveyor	Oy Kati Ab		Oy Kati Ab
- Survey date	27.6.2009		3.7.2009

Note that the coordinates and elevations differ from the hand-held GPS coordinates reported in SKB (2010b). More precise locations were measured in 2011.

The drilling of DH-GAP03 advanced quickly down to 330 m borehole length. At that depth, a highly fractured and altered zone was encountered – runs were shortened to few tens of centimetres and core was lost. Drilling continued slowly to 341.20 m borehole length, until the fault started to cave and there was a risk of borehole collapse. Although the target length of 400 m b.g.s. was not yet reached, drilling was terminated. The drilling of DH-GAP03 took ~ 65 h. The borehole extended down to 320 m vertical depth. Total flushing water consumption was 65 m^3 and the temperature of the inflow varied from 30 to 60 °C. The drilling water source was a small lake/pond (L25) about 500 m SW from the drilling site. The lake water was analysed both for chemistry and isotopic analysis (SKB 2010b).

5.3.1.3 Borehole DH-GAP04

The aim of the deep research borehole DH-GAP04 was to provide groundwater sampling and monitoring opportunities down to, or below, typical repository depths of 500 m b.g.s. and greater. Preferentially, the hole would extend beneath the margin of the ice sheet, and would intersect geological units of interest for potential crystalline repository sites (Harper et al. 2011).

After evaluating the gathered information and considering logistical, environmental and safety aspects, the area called 'Caribou' was selected as the site for DH-GAP04 (see Figure 5-2 and Figure 5-5). Additional fieldwork and structural analyses focused around the Caribou area in 2010 did not find indications of major faults or other features disadvantageous for drilling. In 2010, GAP SPB drilled two ice holes close to the ice margin (Section 4.2.2, Harper et al. 2011) to provide information about the ice thickness, basal temperatures and pressures from the marginal region next to the Caribou area. The outcome of the ice boreholes showed that the marginal region is warm-based, which is the first prerequisite for the recharge of meltwater.

Figure 5-5. *Drilling of DH-GAP04. The site was selected as close to the ice margin as possible in terms of safety and logistics. Photo from June 2011, by Anne Lehtinen.*

Drilling

The drilling of DH-GAP04 was done using double tube WL-75 (NQ-2) equipment, providing a 75.7 mm diameter hole and 50.5 mm diameter core (Table 5-2). After every third run, the core was oriented using an Ezy-Mark™ system. A bottom orientation line is drawn based on these marks, and it serves as a reference for the true orientation measurements (e.g. foliation, fractures). After completing the drilling a deviation measurement was done using a GyroSmart instrument. The final drilling length of the hole is 687 m. Drilling started with the dip of 69.6°, but the hole began to steepen and reached 71.3° at 400 m. The dip at the end of the hole is 70.4°. Possibly, the same geological feature that initiated steepening is responsible also for turning the hole to the right from the original orientation of 010°. DH-GAP04 reached a vertical depth of ~ 645 m relative to the drilling site, and 600 m relative to the ice margin elevation, and advanced slightly beyond (~ 20 m) the ice margin (Figure 5-6).

The same lake/pond (L25) that was used for drilling of DH-GAP03 was used as a source of drilling water for DH-GAP04. Analyses for chemistry and isotopes showed that the water quality, generally, had remained unchanged. The total water consumption was 535 m^3, where 301 m^3 was used for actual drilling and 234 m^3 for keeping the borehole warm until instrumentation. There were two warming periods, where hot water was circulated in the hole. Drilling was completed earlier than estimated, and an ~ 45 h warming was done prior to hydraulic testing. The second, 87 h warming period, occurred between testing and the installation of the downhole equipment (Harper et al. 2011).

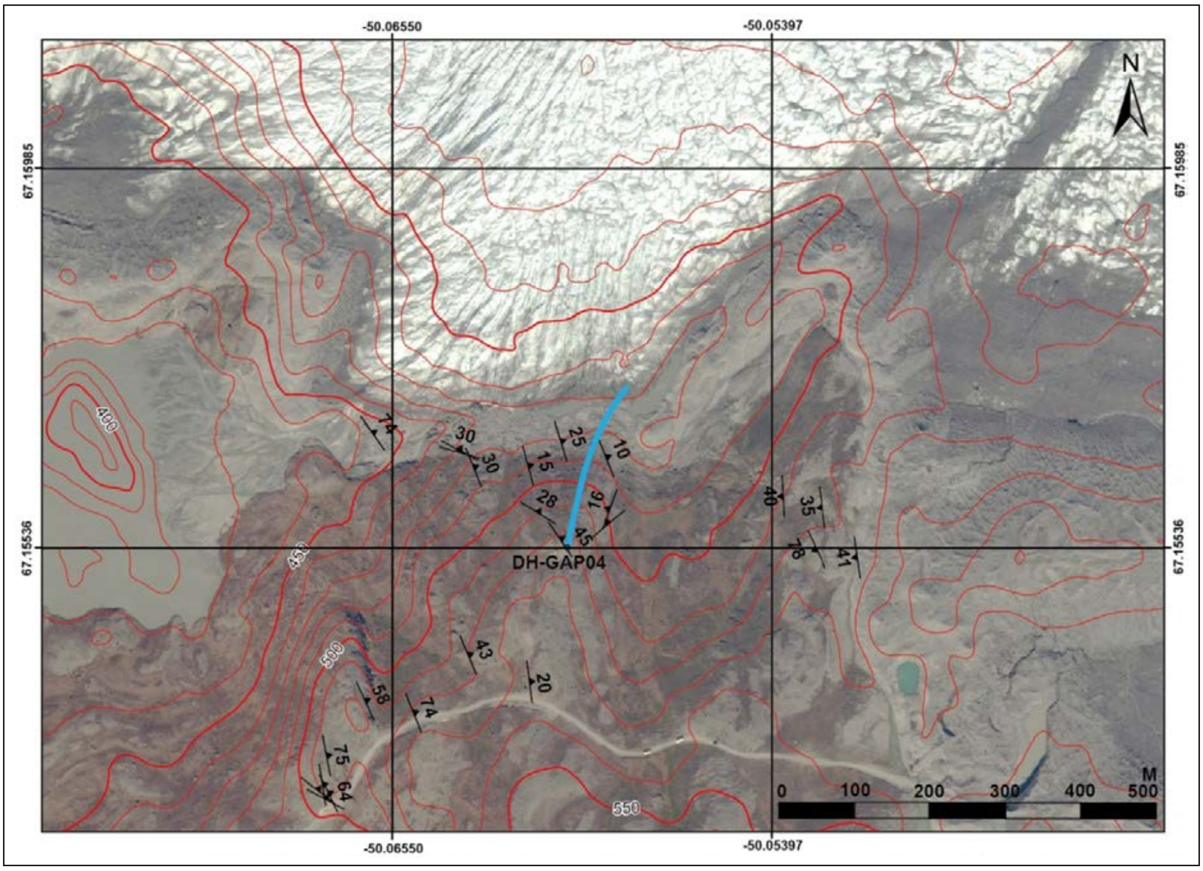

Figure 5-6. Location of DH-GAP04 drilling site with the trace of the hole. Note the bending of the borehole to the right. Also, foliation measurements are given, indicating the strike, dip direction and dip angle. Background image is a Quickbird satellite image acquired July 4, 2011.

Hydraulic testing

After the drilling of DH-GAP04, the hole was tested for hydraulic parameters, transmissivity, hydraulic heads and fracture flow rates using *Posiva Flow Log* (PFL) (see Section 5.6.3.1). The goal of the testing was to locate the flowing fractures so that the downhole instrumentation could be installed in an optimal way (Harper et al. 2011, Pöllänen et al. 2012). Due to time constraints related to freezing conditions at the DH-GAP04 site, the testing program was designed to optimise the critical data needs and time. A 10 m test section, isolated with rubber discs, was used with a two metre step – which allows for better than ± 3 m accuracy. Combined with core observations, this was considered to be sufficient to identify flowing fractures for the purposes of GAP research. It was inferred from the hydraulic testing results that the base of permafrost is at around 400 m of borehole length because all water-conducting features were observed at depths greater than this. Several flowing hydraulic zones were observed between 540–640 m. The results are discussed in Section 5.6.3.

Table 5-2. Technical details of the borehole DH-GAP04. Coordinates and elevations are provided in both latitude and longitude (UTM/WGS84 ellipsoid) and x-easting and y-northing (UTM/WGS84 ellipsoid, UTM zone 22N) systems.

Hole ID	DH-GAP04
Latitude (y-Northing)	67.155330 (7449004)
Longitude (x-Easting)	−50.059795 (540732)
Elevation	525.64
Length	687.00
Hole Path	Linear
Azimuth	010
Dip	70
DH survey dip	−69.58
Project	Greenland Analogue Project
Location	Kangerlussuaq/Greenland
Date drilled	18–28.6.2011
Name hole	GAP
Name number	4
Survey type	GPS
Grid ID	UTM zone 22, WGS84
Survey note	
Overburden (m)	0.65
Top of casing (m)	526.17
Casing above ground level (m)	0.56 (0.53 vertical)
Storage	Olkiluoto
No of core boxes	152
Casing	90/77 steel
Hole diameter	75.7
Sample diameter	50.5
Equipment	WL-76
Deviation survey	
- Hole ID	DH-GAP04
- Method	GyroSmart
- Surveyor	Oy Kati Ab
- Survey date	29.6.2011

5.3.2 Instrumentation of the boreholes

5.3.2.1 DH-GAP01

DH-GAP01 was equipped with a U-tube sampling device (Freifeld et al. 2005), which includes one inflatable packer, a water sampling unit and an In-Situ Inc. Aqua TROLL® 200 to monitor in situ pressure (P in kPa), temperature (T in °C) and electrical conductivity (EC in µS/cm) of the water (for a detailed description of the installation, see SKB 2010b). The entire length of the device is 12 m. The packer, which is located above the device, was placed at 150 m borehole length (130 m b.g.s) in an intact bedrock section. Because hydraulic testing data was not done, the only indication of hydraulic conductivity was the drop of flushing water pressure at 204 m borehole length. In order to ensure the potential for groundwater monitoring and groundwater sampling, the packed-off section was extended to include some other 'potential' fracture zones (Figure 5-7). The sample intake and the sensors are located at 161 m borehole length (138.57 m below TOC) (Figure 5-7 and Figure 5-62). The section length between the packer and the bottom of the hole is 71 m and its volume is 174 L. A heating cable, which keeps the system operational under freezing conditions, is installed down to the depth of the packer (150 m borehole length).

Groundwater sampling is achieved by applying nitrogen gas pressure in a tube running down to the sampler. Increased pressure closes a check valve at the lower end of the sample reservoir and forces water up along another tube line branching from the U-bend. The sample remains isolated from atmosphere all the way up to the surface.

A fiber optical *Distributed Temperature Sensing* (DTS) cable (see Section 5.5.1) provides a continuous temperature profile extending from surface down to the packer.

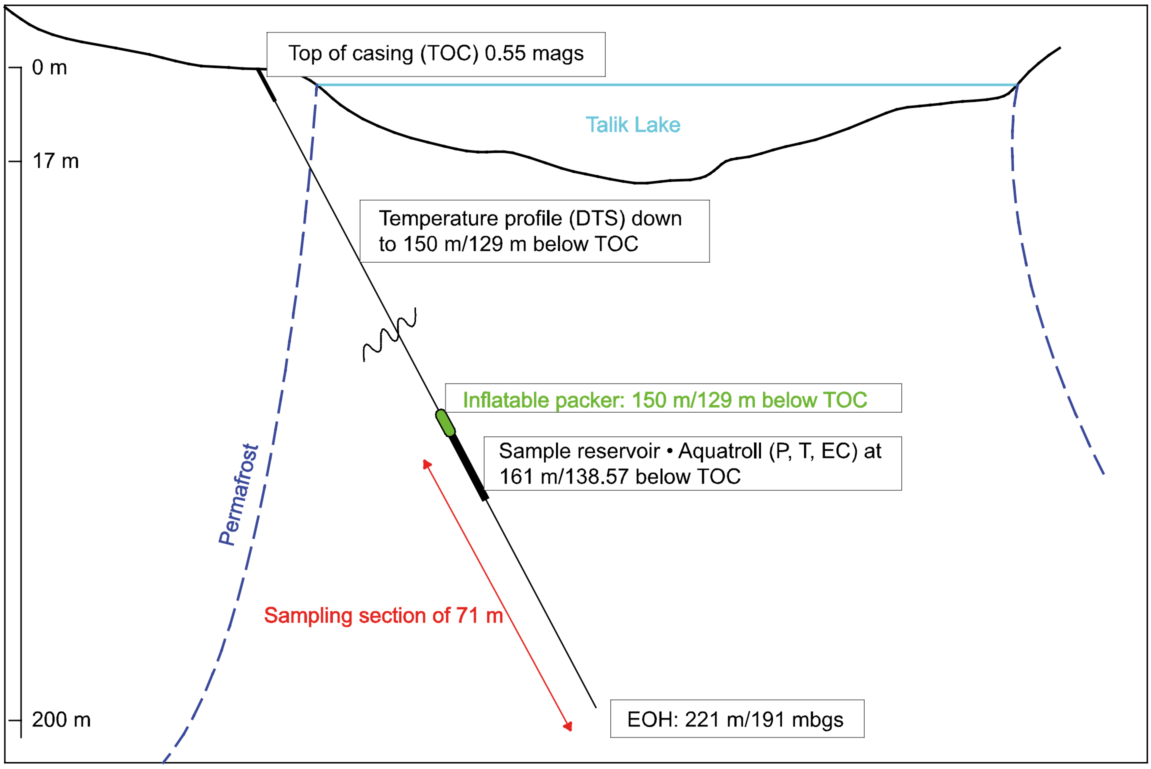

Figure 5-7. *Schematic plan of the borehole DH-GAP01, the instrumentation and the hydrogeological context. The top of casing (TOC) is 0.55 m above the ground surface (mags) and serves as the reference for depth measurements; m b.g.s. = meters below ground surface; EOH = end of the hole.*

5.3.2.2 DH-GAP03

Although the main reason for drilling DH-GAP03 was to obtain information on the permafrost depth, instrumentation such as that installed in DH-GAP01 was planned for this borehole too. During packer installation in DH-GAP01, a great deal of friction between the instrumentation string and the wall of the borehole was observed. In DH-GAP03, the observed friction became too high by ~ 120 m depth that the installation had to be terminated. Instead of full-scale instrumentation, an Aqua TROLL® 200, together with a DTS cable and two heating cables, was lowered to a depth of 329 m (309 m vertical depth). The expected physico-chemical data from this borehole included continuous temperature profile from surface down to 309 m vertical depth, as well as P, T and EC data from this depth. The Aqua TROLL sensors failed soon after installation, propably due to freezing of the hole, and no data was retrieved. The DTS cable is intact, however, and can provide temperature data whenever the DTS unit is operated.

5.3.2.3 DH-GAP04

Instrumentation of the deep research borehole DH-GAP04 was a challenging task and preparations began in 2009. During the pre-studies, emphasis was placed on ensuring that the design of the downhole equipment allowed simple and quick installation. These requirements necessitated that all of the components of the downhole equipment had to be prepared in advance, with only final assembly remaining to be done in the field. The installation depth of the whole package could be selected in the field, but everything with respect to instrument length and arrangement was fixed.

The downhole set-up includes two inflatable packers, which isolate a section with a fixed 10 m separation (Figure 5-8). Thus, the borehole is divided into three parts: the **upper section** (Sect-up), the **mid section** (Sect-mid) and the l**ower section** (Sect-low). All measures are referenced to the TOC (Table 5-3, Figure 5-37 and Figure 5-63). All three sections are equipped with Druck PTX 1830 pressure sensors and AMT 7-pole-cell (serial no. 125) conductivity sensors. The mid section contains an INOR 66 RKM 06876 temperature transmitter also. The design of the instrumentation and its components are described in detail in Appendix B. Information about the drilling and instrumentation of this borehole can also be found in Harper et al. (2016).

After carefully checking the quality of the drill core, the section around the fracture at 600.2 m borehole length was concluded to be suitable for positioning of the packer assembly (Table 5-3 and Figure 5-63). This zone would serve as the **mid section** (Sect-mid). A weaker feature at 604.0 m borehole length was also included within the fixed 10-m sampling section. The top of the upper packer is at 593.5 m borehole length and the end of the lower packer is at 605.5 m borehole length. The volume of the mid section is ~ 44 L.

The **upper section** (Sect-up) extends from the base of permafrost (around 400 m) down to the uppermost packer. The length of the upper section is about 190 m and the volume is 840 L. Sample intake and the EC sensor are located at 541 m, while the pressure transducer is right above the upper packer at about 593 m borehole length (Table 5-3). Groundwater flows into the section from three fractures/fracture systems located at 548 m, 551 m and 584 m, with transmissivities between 10^{-7} and 10^{-6} m^2/s. A feature at 415 m is so weak that it does not have any significance in the context of groundwater inflow (Figure 5-63).

The **lower section** (Sect-low) is located below the lowermost packer and the bottom of the hole. It is about 80 m long, with a volume of 350 L. There are only three rather weak features in this section, at 638.4 m, 670.0 m and at 682.0 m borehole length. The transmissivity of the first is on the order of 10^{-8} m^2/s and the others are even weaker features. Sample intake, the EC and P sensors are located less than two metres below the lower packer (Table 5-3).

Each sampling section has a pressure sensor and an electrical conductivity sensor. In addition, the fixed section has a temperature sensor (Figure 5-8). All sensors can be programmed to collect data on preset frequencies. Data is collected on a data logger at the surface in the wellhead container (Figure 5-9). Collected data is transmitted via a satellite modem to a server once a week. The system is powered by batteries, which can be recharged with the generator and their capacity was designed to cover nine months of logging. However, due to the extended powering times of the sensors, a wind turbine was added to the system in 2012. Gas pressure in the cylinder and packers, as well as the voltage of the batteries, can be monitored via the satellite link, allowing for early detection of potential problems.

Table 5-3. Coordinates, lengths, and depths to the different components in the borehole DH-GAP04 instrumentation. The components located within the mid section are highlighted with blue colour. Note that the coordinates and elevations are provided in Easting and Northing (UTM/WGS84 ellipsoid, UTM zone 22N) and that measures are referenced to the TOC and coordinates (for more details see Appendix B). Table 5-2 provides the coordinates of the location of DH-GAP04 in latitude and longitude.

	Borehole length (m)	Northing (m)	Easting (m)	Elevation UTM/D_WGS84 (m)	Depth below TOC (m)
Top of casing	0.00	7 449 003.90	540 732.20	526.17	0.00
Ground surface	0.56	7 559 004.09	570 732.23	525.62	0.48
U-bender, heating cable	479.75	7 449 155.95	540 774.42	73.29	−452.88
Esect-up	541.32	7 449 173.87	540 783.64	15.10	−511.07
Filter sect-up.	541.70	7 449 173.98	540 783.70	14.74	−511.43
Psect-up	592.01	7 449 188.27	540 792.13	−32.75	−558.92
Sect-mid upper limit	594.50	7 449 188.97	540 792.56	−35.10	−561.27
Esect-mid	595.70	7 449 189.30	540 792.77	−36.23	−562.40
Filter sect-mid	596.08	7 449 189.40	540 792.84	−36.59	−562.76
Psect-mid	596.74	7 449 189.58	540 792.96	−37.21	−563.38
Tsect-mid	597.47	7 449 189.78	540 793.09	−37.90	−564.07
Sect-mid_lower limit	604.50	7 449 191.72	540 794.36	−44.54	−570.71
U-bender, optical fibres	605.52	7 449 192.00	540 794.54	−45.50	571.67
Psect-low	606.90	7 449 192.38	540 794.80	−46.81	−572.98
Esect-low	607.52	7 449 192.54	540 794.92	−47.39	−573.56
Filter Sect-low	607.60	7 449 192.57	540 794.92	−47.47	−573.64
Deepest, deviation measurement	687.56	7 449 213.83	540 810.77	−122.9	−649.07

A heating cable was installed in the hole to facilitate thawing of the sampling lines in the permafrost section in order to obtain groundwater samples. The cable was installed well beyond the base of permafrost (i.e. to 479 m borehole length), but not to a depth that could disturb water sampling activities or the monitoring of pressure, temperature and electrical conductivity.

Using the DTS technique, a continuous temperature profile from the surface through permafrost and down to the fixed section is enabled. The cable forms two loops, which allows failure in one loop without disturbing the use of the other. The bend of the loop (i.e. the lower end of the cable) is mounted inside the lowermost packer at 605.5 m borehole length.

Water sampling is based on the same principle as the equipment installed in DH-GAP01: a U-coupling-check valve combination, which allows purging of samples using nitrogen gas. Each purge provides 5–7 L of water (depending on the section from which the sample is collected) and samples can be collected from all three sections. The purge can be repeated as soon as the pressure sensor shows that sampling section has recovered, which takes ~ 20–30 minutes.

Water samples are isolated from atmosphere at all times, but the in situ pressure is not maintained during a standard sampling cycle. It is possible, however, to take pressurised samples using vacuumed cylinders attached to the sampling line, which is the only way to collect gas samples as well. The sampling procedure is managed from a valve and control panel installed in the container, and the behaviour of P, T and EC in the sampling sections can be monitored on-line. It is possible to transmit the monitored data using an Iridium® satellite modem set up.

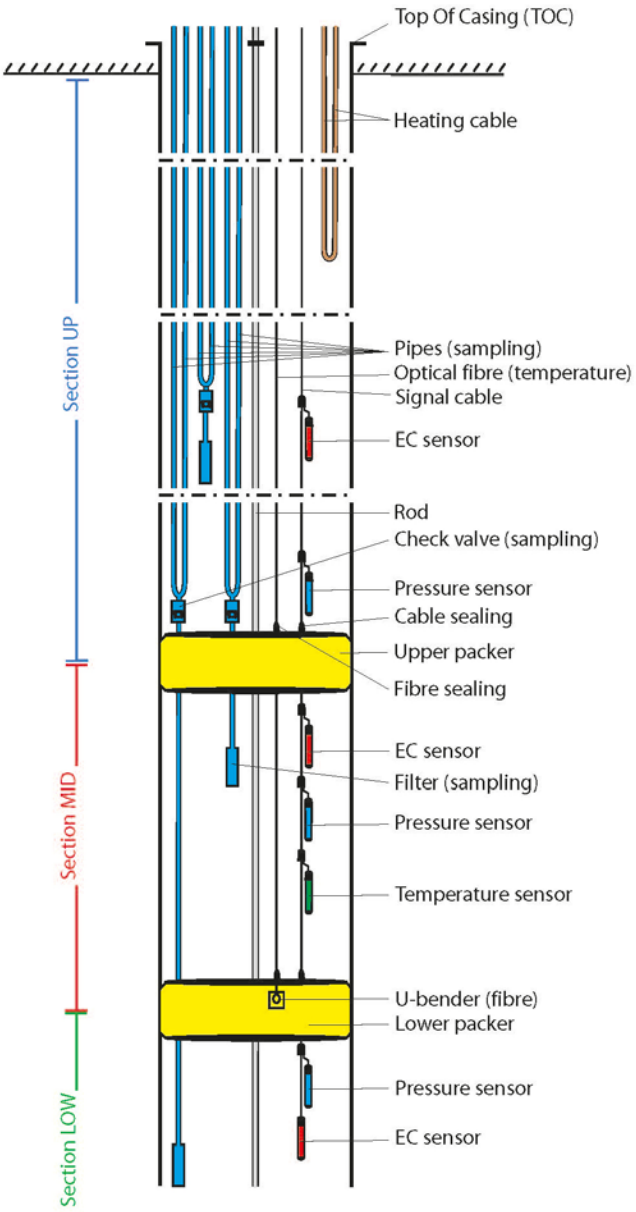

Figure 5-8. *Equipment in borehole DH-GAP04. Sect-up is ~ 190 m and extends from the base of the permafrost to the uppermost packer. Sect-mid is isolated by the two packers and is 10 m long. Sect-low is 80 m long and extends from the lowermost packer to the bottom of the hole.*

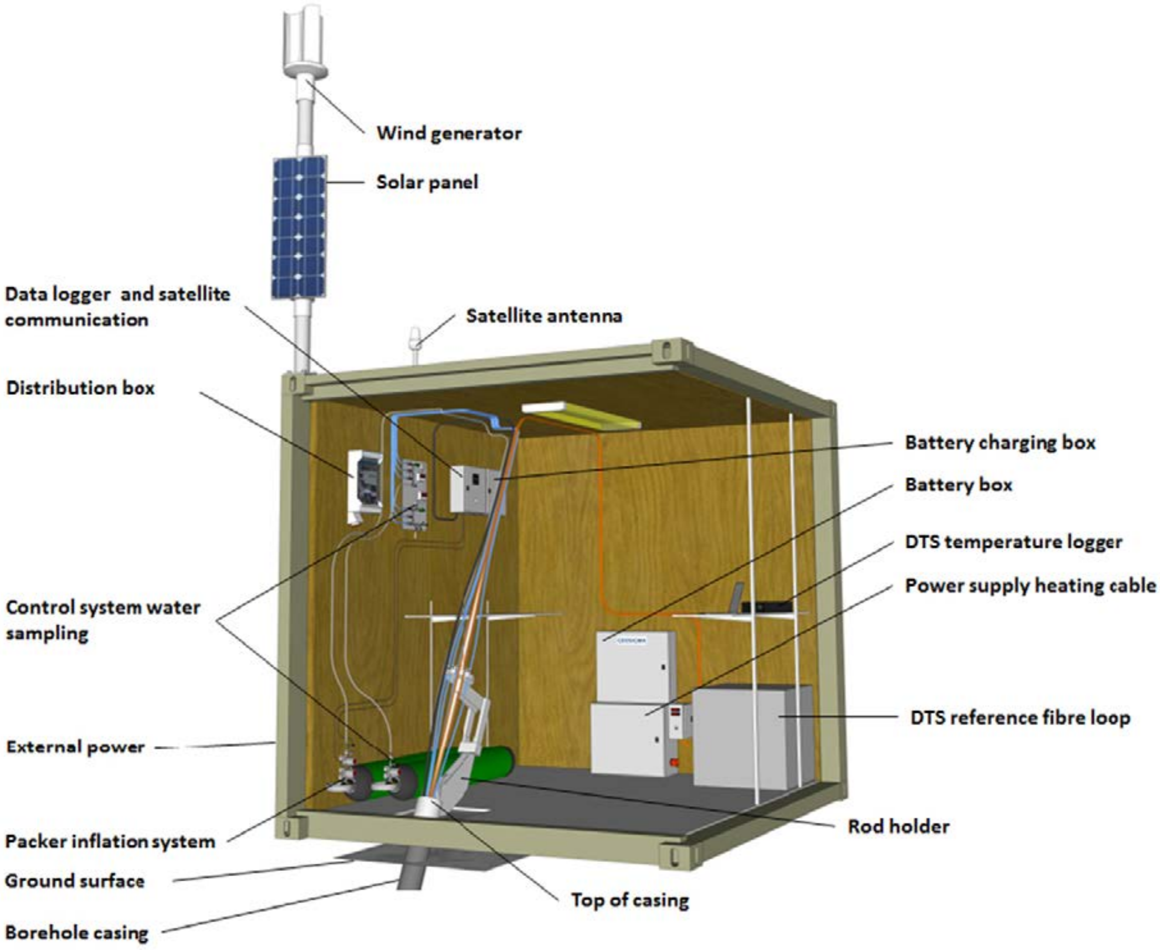

Figure 5-9. *Container and surface equipment (for details see Appendix B). The container is located on a bedrock terrace and replaced the drilling rig shown in Figure 5-5.*

5.4 Geological investigations in the GAP study area

5.4.1 Overall mapping and logging

Geological mapping of the region was conducted from 2008–2013 in order to enhance the geological and structural understanding of the GAP study area. In 2008, detailed geological investigations were conducted at 7 different key locations, which included scanline mapping of fractures and faults, together with characterisation of the foliation and main rock types (Aaltonen et al. 2010). In 2009 and 2010, the mapping was focused around the sites selected for the drilling of DH-GAP01, DH-GAP03 and DH-GAP04 (SKB 2010b, Harper et al. 2011). The mapping campaign undertaken during the 2011 field season aimed to increase the general understanding of the complex geology of the area and provided enough new data to generate a complete map of the drilling sites and intermediate areas (Harper et al. 2011). However, during the summer 2013 some additional mapping was done close to DH-GAP04 in order to achieve more detailed structural geological description of the borehole area (Engström and Klint 2014).

Drill cores DH-GAP01, DH-GAP03 and DH-GAP04 provided detailed information, which helped to expand the 2D mapping information to 3D. Drill core investigations included detailed fracture characterisation, lithological mapping, and mapping of foliations and deformation zones. In addition, material for the measurements of petrophysical properties and for fracture infilling studies was provided. The drill core logging procedure and the observations are reported in Pere (2014).

In order to create a link between the geology and hydrological modelling, a regional geological model was constructed for the GAP study area that included a deformation zone model for the needs of groundwater modelling groups. Engström et al. (2012) presents a 2D model, which describe the geological structures and lineaments occurring in the Kangerlussuaq area and which forms the basis for the GAP Geomodel version 1, produced by that same team. Using modelling tools and data from Forsmark and Olkiluoto, the 2D model was developed into 3D. The mapped lineaments were given hydraulic properties adapted from Forsmark, Laxemar and Olkiluoto (see Follin et al. 2011) and the model was adapted into a regional area and a site area (Figure 5-10). The model of the regional area was produced for hydrological modelling, while the site area is where most of the SPC research was conducted.

5.4.2 Bedrock geology

Most of West Greenland is part of a denuded Precambrian shield, with mainly Archaean and Proterozoic rocks (Henriksen et al. 2000), Figure 5-11. According to the regional lineament studies by Wilson et al. (2006), which focused on the on-shore expression of continental break-up and sea-floor spreading in central West Greenland, five main lineament systems could be identified: N–S, NNE–SSW, ENE–WSW, ESE–WNW and NNW–SSE.

The overall GAP geological study area covers a 100 × 50 km modelling domain, including a substantial area in front of, and covered by, the GrIS (Figure 5-10). Detailed geological mapping focused on a transect ranging from Kangerlussuaq to the ice-margin, as well as a smaller sub-area surrounding the sites selected for the drilling of the three boreholes, DH-GAP01, 03 and 04 (Figure 5-11). The site area (in close proximity of the three boreholes) shows a complex geology due to folding of the bedrock during several geologic events (e.g. Engströn and Klint 2014). On Figure 5-12, high resolution aerial images are overlain by the interpreted structural form lines (foliation, fold hingeline, fault and shear zone traces) to provide an overview of the geological framework of the GAP study area. This compilation shows the curvilinear nature of the foliation trace, and highlights 1) the superposition of two stages of folding (F1 and F2), 2) a well-developed E-W trending shear zone fabric, and 3) a later brittle fault overprint.

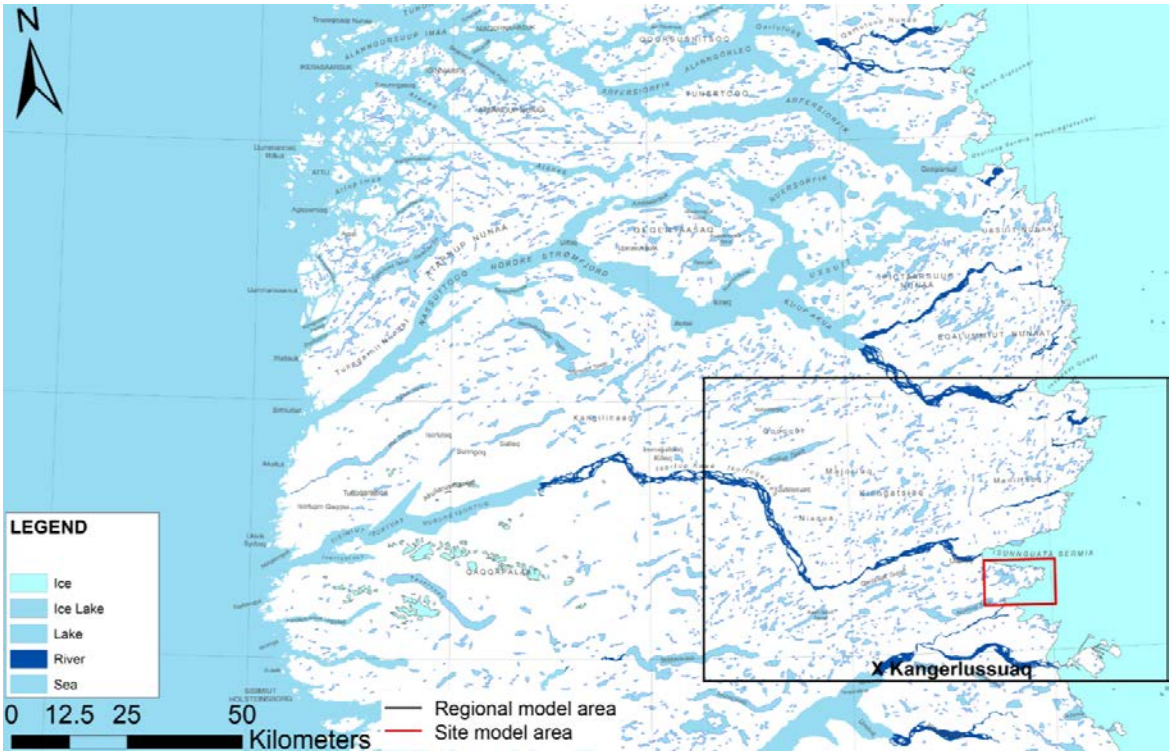

__Figure 5-10.__ General overview over GAP modelling area. The GAP Geomodel area is outlined in black (large box) and the site scale area in red (small box). The map is modified from GEUS (Geological Survey of Denmark and Greenland) geological map 2010 (from Garde and Marker 2010).

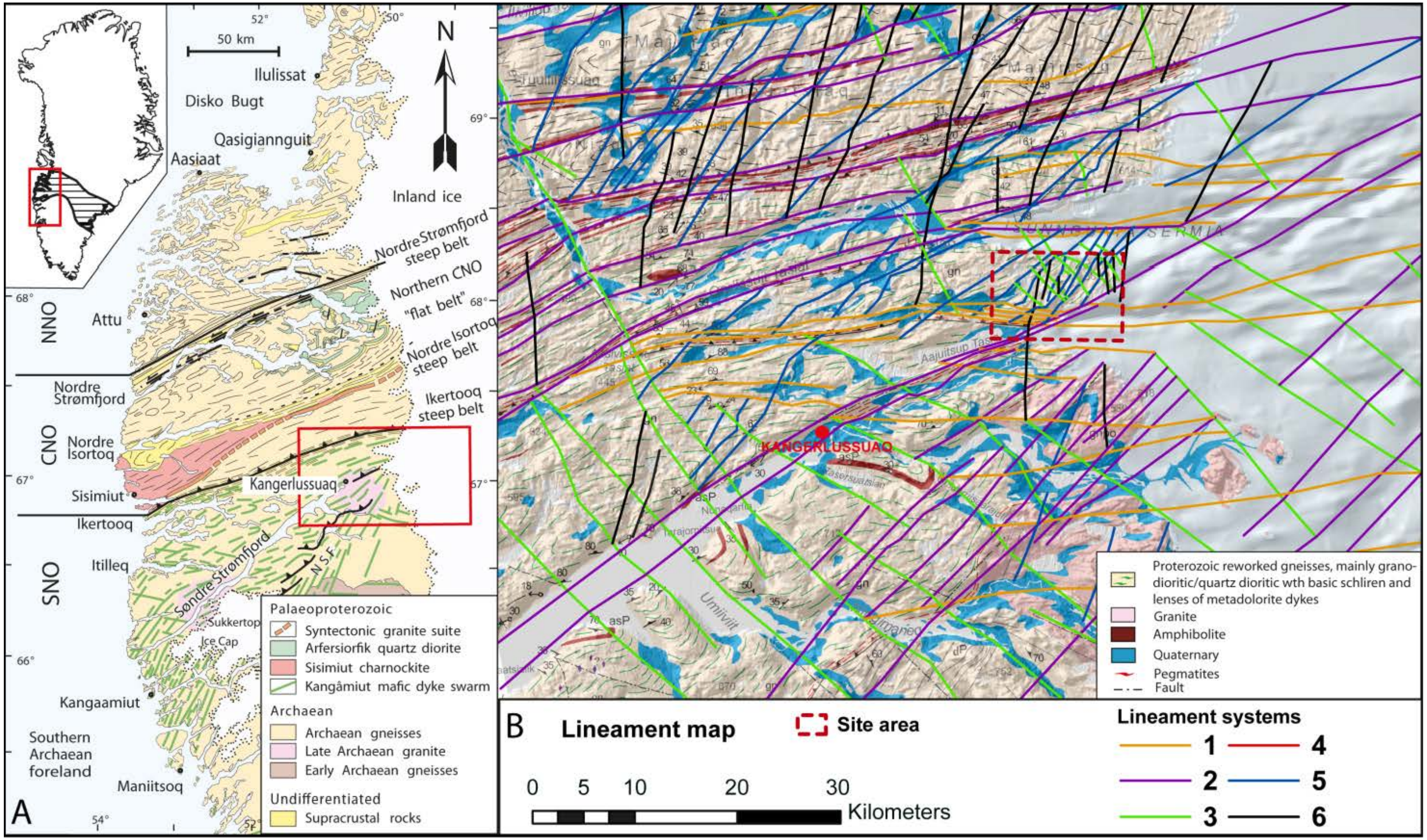

Figure 5-11. *A) Regional geology and B) lineament map of the regional field area. The nature and relationship between the lineaments were investigated during the fieldwork. Selected sites in area A (red rectangle) and area B (red dashed rectangle), where the three boreholes are located, were mapped in more detail. A more detailed view of area B is provided in Figure 5-12 (map modified from Garde and Marker 2010, and Garde and Hollis 2010).*

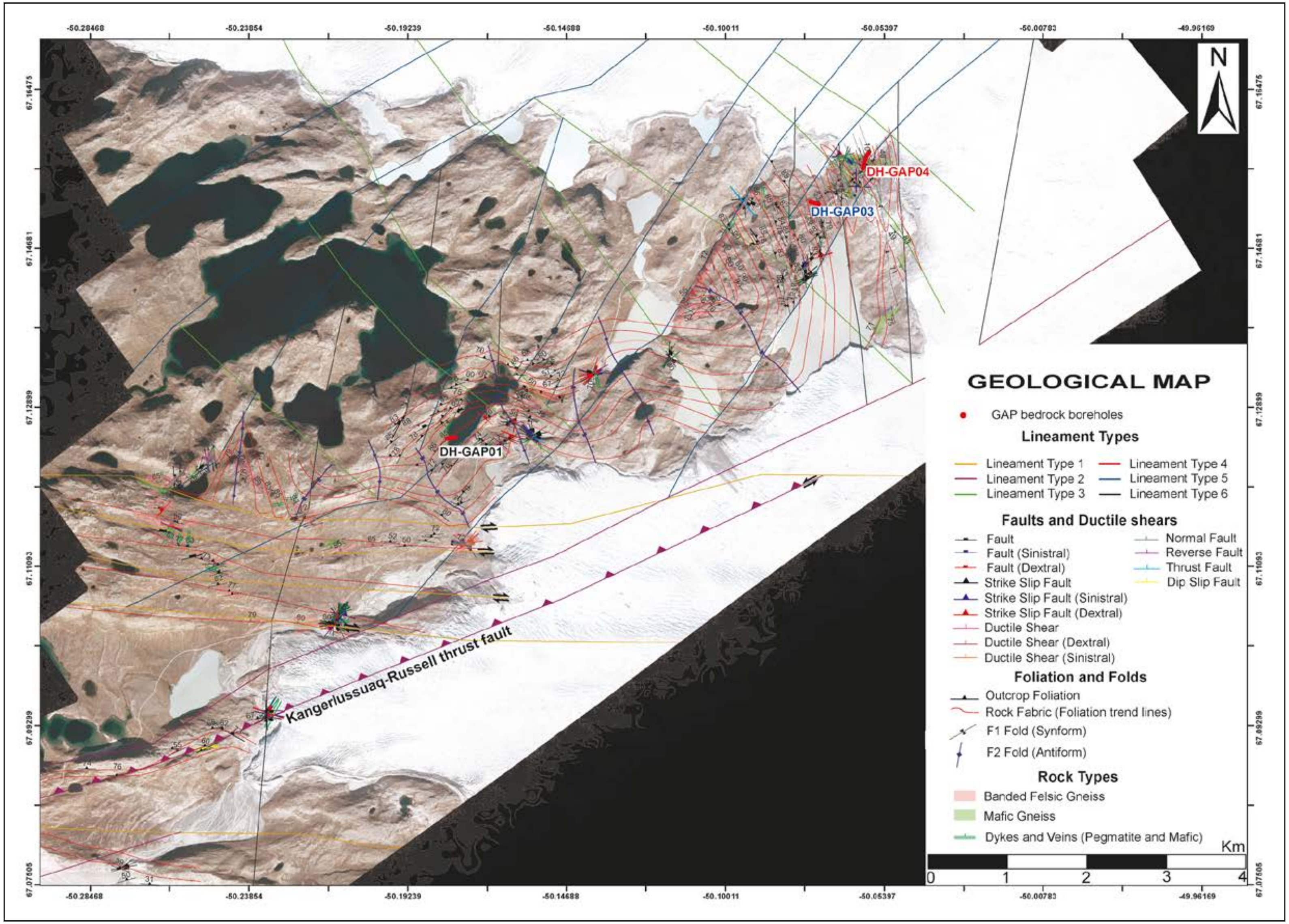

Figure 5-12. *Aerial image overlain by the mapped and inferred rock fabric (foliation), rock types and structural elements. The macro scale structure outlines large scale folding overprinted by various shear zones and more brittle fault zones. The three deep boreholes are also displayed as DH-GAP01, DH-GAP03, and DH-GAP04.*

5.4.3 Drill core observations

The three boreholes, DH-GAP01, 03 and 04, were drilled into different geological settings. The rock types in the boreholes can be divided into four main types: felsic gneiss, mafic gneiss, *intermediate gneiss* (IGN) and granitic pegmatite (Figure 5-13, see also Figure 5-22, Figure 5-23 and Figure 5-24). The relative amount of mafic/felsic minerals have been used as a guideline when defining the rock types. The *felsic gneisses* (FGN) consist typically of K-feldspar, quartz and plagioclase with some biotite. The mafic gneisses typically are massive or slightly foliated and contain large amounts of garnet with amphibole and pyroxene. The intermediate gneisses resemble mafic gneisses but contain more plagioclase and biotite instead of amphibole and pyroxene.

DH-GAP01 is situated in foliated felsic gneiss which has both mafic and intermediate layers. In DH-GAP03 alternating layers of felsic and mafic gneisses dominate. DH-GAP04 is situated in lithologically and structurally different geological setting compared to the other boreholes. It was drilled in a shallowly plunging open fold structure. The borehole is dominated by mafic garnet gneiss in the upper 300 m, with more foliated intermediate to felsic gneiss below.

A short review of the lithological core loggings is given below. The comprehensive logging tables are provided in Pere (2014).

5.4.3.1 DH-GAP01

DH-GAP01 core consists mainly of feldspar-rich felsic gneisses, interlayered with shorter sections of mafic, amphibole-rich gneisses; intermediate composition occurs as well. The rock is foliated almost throughout the borehole length.

Fracturing occurs sporadically along the entire length of the core, except for a relatively unfractured section around the borehole depth of 50 m. The number of slickenside fractures is highest in the middle parts of the core and at the lower levels they occur at rather regular intervals. The shallow fractures are filled primarily with drill cuttings and only thin fracture fillings occur. Single fractures with thicker clay-fillings were observed sporadically at deeper levels. A few distinct, randomly distributed, fracture zones and fault zones were mapped from the core. These zones are slightly altered and the fault zones contain both cohesive breccia and alteration on the fracture surfaces evidenced by the presence of chlorite, calcite and clays (Pere 2014).

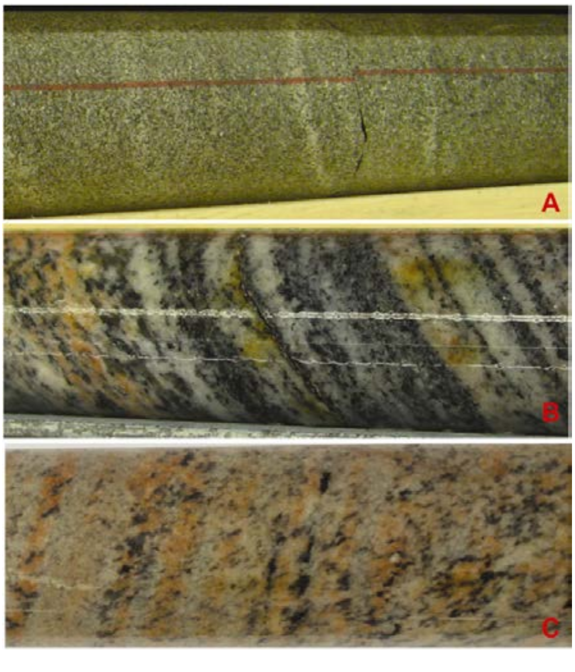

***Figure 5-13.** Examples of the typical rock types observed in the GAP boreholes. A) Homogeneous and weakly oriented mafic gneiss (DH-GAP04, 259 m), B) Banded intermediate gneiss (DH-GAP04, 433 m), and C) Banded felsic gneiss (DH-GAP04, 307 m). Photos by Tuomas Pere.*

5.4.3.2 DH-GAP03

DH-GAP03 core consists of interlayered mafic and felsic gneisses with sections of intermediate, amphibole-rich gneisses. Banded foliation is common for all these gneissic rocks. Single pegmatite veins were logged in the drill core as well. Iron hydroxides and oxides occur on the fracture surfaces close to the ground level and are visible to ~ 40 m borehole depth. These "rusty" fractures were interpreted as open fractures that have been subjected to surface water circulation during permafrost-free periods in the past.

The fracture frequency is relatively high through the entire length of the borehole. The most intense fracturing is concentrated in the mafic sections, while felsic gneisses typically are intact and relatively unfractured. The lowest 100 m of core is very densely fractured and the section contains three fault/deformation zones. In many places, marker horizons indicate that slip has occurred, though it was not possible to determine the exact amount of slip (Pere 2014).

5.4.3.3 DH-GAP04

DH-GAP04 core consists of four main rock types. These are mafic, intermediate and felsic gneiss, as well as pegmatites. All of these, except pegmatite and some sections of massive mafic gneiss, appear to belong to the same series of originally layered rocks, which were later recrystallised and metamorphosed. In some cases, the classification of the rock types is ambiguous because the contacts between different lithological units are gradual and the units contain other rock types as interlayers. This applies to all the three drill cores. It should be noted that the homogeneous and weakly oriented garnet-bearing mafic gneiss in DH-GAP04 differs texturally and mineralogically from the mafic variants reported from the other two drill cores.

Mafic gneisses typically are crosscut by narrow (< 1 cm) veins of felsic material. These veins sharply crosscut the foliation and appear to be younger features than the foliation of the gneiss. The veins seem to be orientated in a more or less uniform direction. In some locations, semi-ductile deformation can be seen to be related to the veining. Garnet was detected from each of these three rock types and is most abundant in mafic gneisses. The gneissic rocks are also crosscut by coarse veins of massive, non-foliated pegmatite. In addition, one section of irregularly deformed rock was mapped, which was classified as diatexitic gneiss. A third vein type, sharply cross-cutting the gneisses, are narrow mafic veins that have brecciated the wall rock while intruding (Figure 5-14). These veins are recrystallised to some degree, but do not show evidence of significant deformation following crystallisation. The sharp contacts and angular wall rock clasts indicate intrusion along fractures in a brittle environment, probably in connection with shear. In DH-GAP04, some millimetre-wide, black and hard fracture/vein fillings composed of extremely fine-grained pseudotachylitic material were observed (Pere 2014).

5.4.4 Structural geology

The structural geological mapping within the GAP can be divided into three entities based on the scales: (1) the lineament mapping, (2) surface mapping and (3) drill core studies. In the following section, the studies are described, beginning with the larger scale (100 km wide) lineament mapping, then the intermediate scale (5 km wide) surface mapping, and finally the fine scale (200–700 m borehole length) drill core studies.

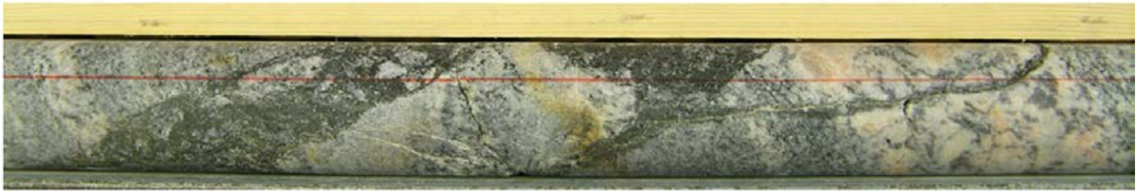

Figure 5-14. *Narrow mafic vein, which has intruded the gneiss in a semi-brittle environment. DH-GAP04, 416 m borehole length. Photo by Tuomas Pere.*

5.4.4.1 Lineaments

Most lineaments in crystalline rocks represent (1) structural features like fault and shear zones, (2) the pre-existing rock fabric, or (3) mineralogical variations affecting the competence of the basement rocks. Lineament mapping generally consists of three steps: (1) identification of lineaments using remotely-sensed GIS data, primarily combining aerial imagery with topographical, geological and geophysical data; (2) verification of the nature of the individual lineaments in the field in terms of their character (e.g. intrusion, fault/fracture zone, rock fabric, etc.), orientation, scale (width, length) and kinematic (movement) history; and (3) construction of a regional event stratigraphic model by determination of relative lineament ages (older/younger) using cross cutting relationships based on the interpretations made during steps 1 and 2. Finally, a tectonic model may be developed by integration of the results from step 3 into the known geological framework of the area under investigation, and possibly by dating of selected rock types.

The original lineament map for the GAP study area (Engström et al. 2012) was produced early in 2011. During the 2011 summer field season, detailed mapping was carried out with a focus on confirming the lineaments identified in the original version. The mapping was focused on the site area (red square in Figure 5-10) around the three boreholes, but also along a prominent lineament extending from Kangerlussuaq harbour all the way to Russell Glacier, known as the Kangerlussuaq-Russell fault zone. The fieldwork in a number of key locations focused on ascertaining the nature of the various lineaments, including their kinematic history and cross cutting relationships, in order to establish an event stratigraphic model.

The use of geophysical data allowed the lineament interpretation to extend farther east into the ice covered area by providing support for the basic assumption that the features and patterns seen in the foreground will be detected under the ice as well. During the fall of 2012, the eastern part of the lineament model was evaluated using the subglacial topography model produced by SPA (Section 3.5). The original interpretation received confirmation and several pronounced lineaments could be traced under the ice for long distances (Figure 5-11 and Figure 5-15).

With the new data collected during 2011 and 2012, the original lineament model (Engström et al. 2012) was updated and improved (Engström and Klint 2014). The lineament interpretation for the regional area includes six types of lineaments (Figure 5-11). This interpretation differs slightly from the original interpretation of four different types (Engström et al. 2012). In the updated model, a ductile shear zones is introduced (orange colour; Type 1) with the same orientation as the type brittle features (lilac colour; Type 2). Type 4 (red colour) is acknowledged as a sub-horizontal lineament with a shallow dip toward the SE. This set is not shown in the 2D surface map in Figure 5-15.

The updated lineament model includes five general lineament systems outlined from the GIS analysis, and a sixth sub-horizontal system identified during fieldwork. The system 1 shear zones are ductile type shear zones showing a dextral type of shearing. The system 2 (e.g. Kangerlussuaq-Russell fault zone) is a thrust fault system that locally has been reactivated with sinistral strike slip movement. The system 3 lineaments are clearly overprinting system 1 and the F2 folds. The system 4 normal faulting and NNE trending pegmatites indicate either a general extensional stress regime or local transtension during strike slip movements; however, the timing of occurrence is highly speculative. Finally, the youngest geological events are related to the type 5 and 6 lineaments, forming two generally brittle strike slip fault systems that, together with the Type 4 (sub-horizontal) normal fault system, are interpreted to be responsible for the primary hydraulically conductive zones in the area (Engström and Klint 2014).

The absolute ages of the different types of ductile and brittle deformations are uncertain because of a lack of radiometric dating. However, in relative terms, it is suggested that the ductile shear zones and the Kangerlussuaq-Russell thrust fault, and most other semi-ductile shear zones, are ancient features related to the Nagssugtoqidian orogeny (Engström and Klint 2014, van Gool et al. 2002). Type 3 and 4 semibrittle lineaments may be of intermediate age and related to tectonic events taking place after the orogeny. The youngest and most brittle deformations may be related to the opening of the North Atlantic Ocean, the Labrador Sea and Baffin Bay over the last 100 Ma (Engström and Klint 2014, Wilson et al. 2006).

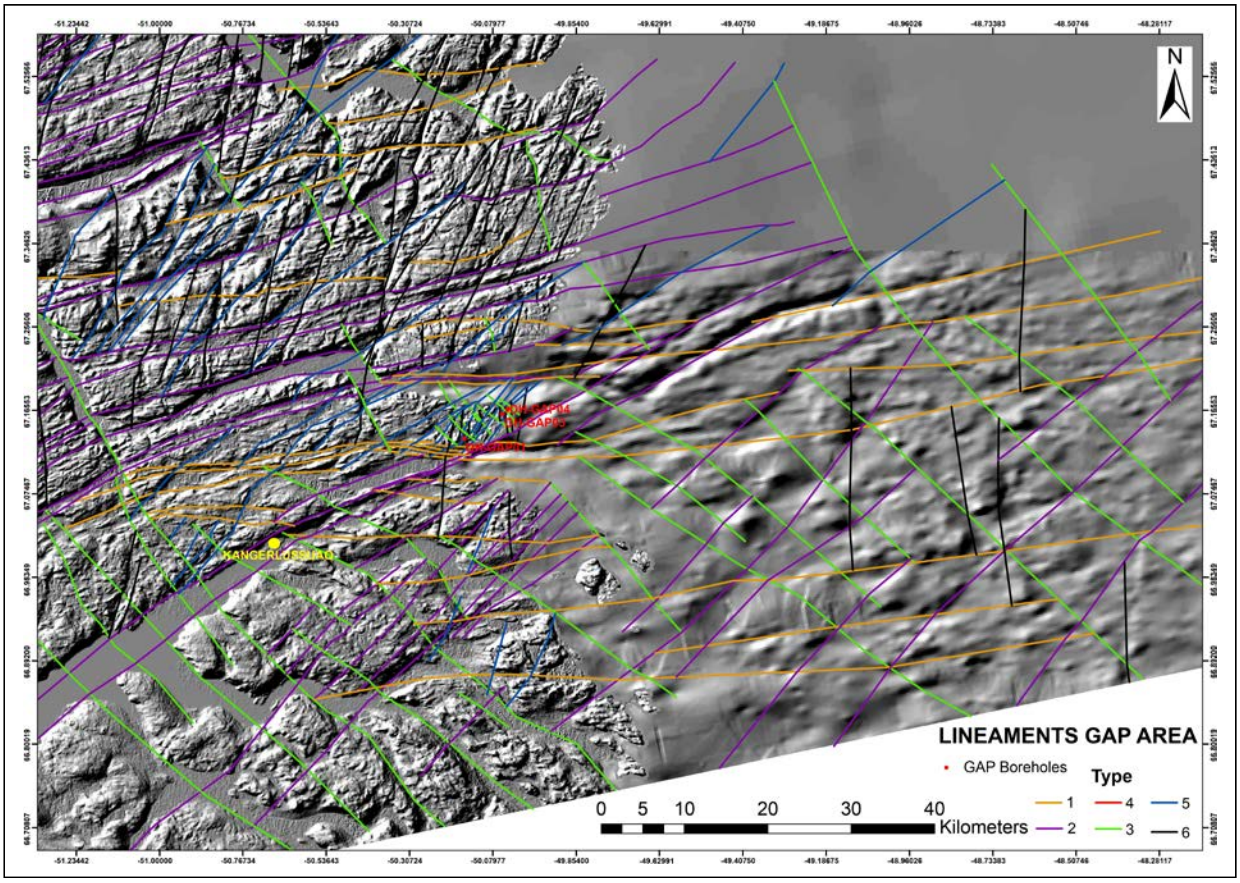

Figure 5-15. The different lineament types are indicated with colours overlying the DEM. Note that the sub-horizontal Type 4 lineament is not shown. The DEM of the ice covered area was provided by SPA (see Section 3.5).

5.4.4.2 Fracturing based on surface mappings

The surface mappings were performed at various occasions throughout the GAP, each with different aims. The scanline mapping during 2008 (Aaltonen et al. 2010) gave valuable input about rock types and fracture characteristics in the area. The main purpose of the scanline study was to verify the primary lineaments and to collect systematic data on fracture populations. The focus was directed at major fractures and fault systems. Fractures were mapped and measured along traverses, typically inside lineaments that were selected from aerial photos. Complementary mapping was done along scanlines (perpendicular to each other) at each selected location. In total, 343 measurements were made on major structures: faults, major fractures, foliations, folds, contacts and intrusions. In addition, more than 1000 measurements were made on structures along fixed scanlines. Fracture densities in the 17 scanlines varied between 0.88/m and 3.60/m, and the average density is 1.92/m. The fracture densities in selected investigation trenches in Olkiluoto, Finland, are 1.44/m on average (Aaltonen et al. 2010). The average fracture densities from the Swedish investigation sites are generally a bit higher than at Olkiluoto, i.e. 3.23/m in Oskarshamn (Wahlgren et al. 2008) and 2.84/m in Forsmark (Stephens et al. 2007).

During 2009 and 2010, mapping was focused around the sites planned for the drilling of boreholes DH-GAP01, DH-GAP03 and DH-GAP04. The main emphasis of these studies was to obtain detailed information about foliation and fracturing in order to orientate and perform the drilling of the boreholes. In addition, this provided valuable input about the complex nature of the geology in the site area, indicating that a detailed mapping campaign would be beneficial to resolve the structural geology of the area.

The mapping campaign during the field season of 2011 provided information to link together the previously mapped areas. Nine sub-areas were mapped in the vicinity of the three boreholes, and also along the Kangerlussuaq-Russell fault zone (Figure 5-11), in order to improve the original understanding of the area. The mapping produced detailed data on ductile deformation, fractures and faults.

5.4.4.3 Drill core observations

The structural geological investigation of the drill cores confirmed the complex nature of the bedrock in the site area. The three drill cores differ from each other in terms of both foliation and fracturing. The foliation in DH-GAP01 is striking predominantly NE-SW, with a rather steep dip toward the NW, whereas the foliation in DH-GAP03 is striking almost NNW-SSE, with a steep dip toward the NNE. DH-GAP04 is situated in a totally different geological setting, because it was drilled in an open fold with a NNW-trending and shallowly plunging (~ 14°) synform. The foliations measured in the drill core are gently dipping toward the NW/NE (Figure 5-16).

Information on planar features (e.g. fractures, foliation) in 1D is extracted from the borehole drilling record and core. Thus, some features oriented subparallel to the drilling orientation are likely missed. This is especially relevant for small-scale (i.e. short) fracture features. A Terzaghi correction is commonly used to adjust fracture orientations to reduce bias caused by the sampling orientation (Terzaghi 1965), and this method was used to assess DH-GAP04 fracture data to determine the potential for hydrogeologically relevant fracturing, trending towards Isunnguata Sermia, to be underestimated due to the drilling orientation.

For this purpose the data was divided in two sets: 1) fracturing in permafrost (0–400 m of borehole length) and 2) fracturing below permafrost (400–687 m of borehole length). The outcome is presented in Figure 5-17A and Figure 5-17B. The upper part of the borehole exhibits more sub-vertical fractures/faults and a NW-SE trending set dipping steeply towards SW can be observed (Figure 5-17A). It becomes more pronounced when Terzaghi correction is applied (Figure 5-17B). However, when examining the fracturing below permafrost (i.e. the hydraulically interesting part) this NW-SE trending set of fractures/faults disappears and the horizontal and sub-horizontal fracturing/faulting becomes more dominant (Figure 5-17C). One set of vertical N-S trending fractures/faults is slightly intensified when Terzaghi correction is applied (Figure 5-17D). However, the difference is not significant and the hydraulic conductivity in this borehole is known to be related to subhorizontal fracturing (see Section 5.6), which was not affected by the correction. Therefore, the fracture data discussed later in this report and shown in Figure 5-20, Figure 5-21 and Figure 5-46 is based on the primary data measured from the drill core (i.e. are not Terzaghi corrected).

The fracturing in DH-GAP01 and DH-GAP03 show moderate to sub-vertically dipping fractures, while DH-GAP04 primarily shows sub-horizontal fracturing. It is well known that the foliation controls fracturing and, typically, one of the main fracture sets is parallel to the foliation. This is also the case in the SPC study area (Figure 5-18 and Figure 5-21).

When examining the fracturing with depth it is evident that the boreholes differ from each other. DH-GAP01 is unevenly fractured, having narrow highly fractured zones, but also totally intact sections and an average fracture frequency of 2.23 m (Figure 5-19). DH-GAP03 and DH-GAP04 are fractured throughout the entire borehole length, with an average fracture frequency of 3.36/m (DH-GAP03) and 1.97/m (DH-GAP04), respectively. DH-GAP03 is intensely fractured at the end of the hole due to a main fault zone, which was responsible for the termination of drilling of the borehole in 2009 (Figure 5-19). DH-GAP04 is rather evenly fractured throughout, but increased fracturing is observed around 500–600 m borehole length, which is also where most of the water-conductive fractures occur (see Figure 5-63). The highest fracture density in DH-GAP04 is 22/m, while DH-GAP-01 and DH-GAP03 have highest fracture densities of 31/m and 33/m, respectively (Figure 5-19). Note that the fracture frequencies are not corrected for the possible bias due to the drilling orientation.

The fracturing in DH-GAP04 is interesting because the orientation of fractures differs significantly with depth, whereas the foliation shows a subhorizontal dip generally towards north. In the upper 100 m, sub-vertical fracturing, of variable orientation, is dominant (Figure 5-20) From 100 m to 300 m depth, the fracture orientations change. Eastward dipping fracturing disappears and sub-horizontal fracture sets become more common. Sub-vertical fracturing dips toward the south and SW (Figure 5-20). The sub-vertical fracturing further decreases between 300 m and 500 m depth, while the sub-horizontal NW dipping fracturing, parallel to foliation, increases (Figure 5-21). The fracture frequency increases significantly between 500 m and 600 m depth, showing sub-horizontal fracturing (mainly parallel to foliation); fractures with a moderate dip to NW, striking NE-SW (Figure 5-21), also occur. From 600 m depth to the end of the hole, the fracturing decreases and the sub-horizontal north-dipping fracturing dominates (Figure 5-21).

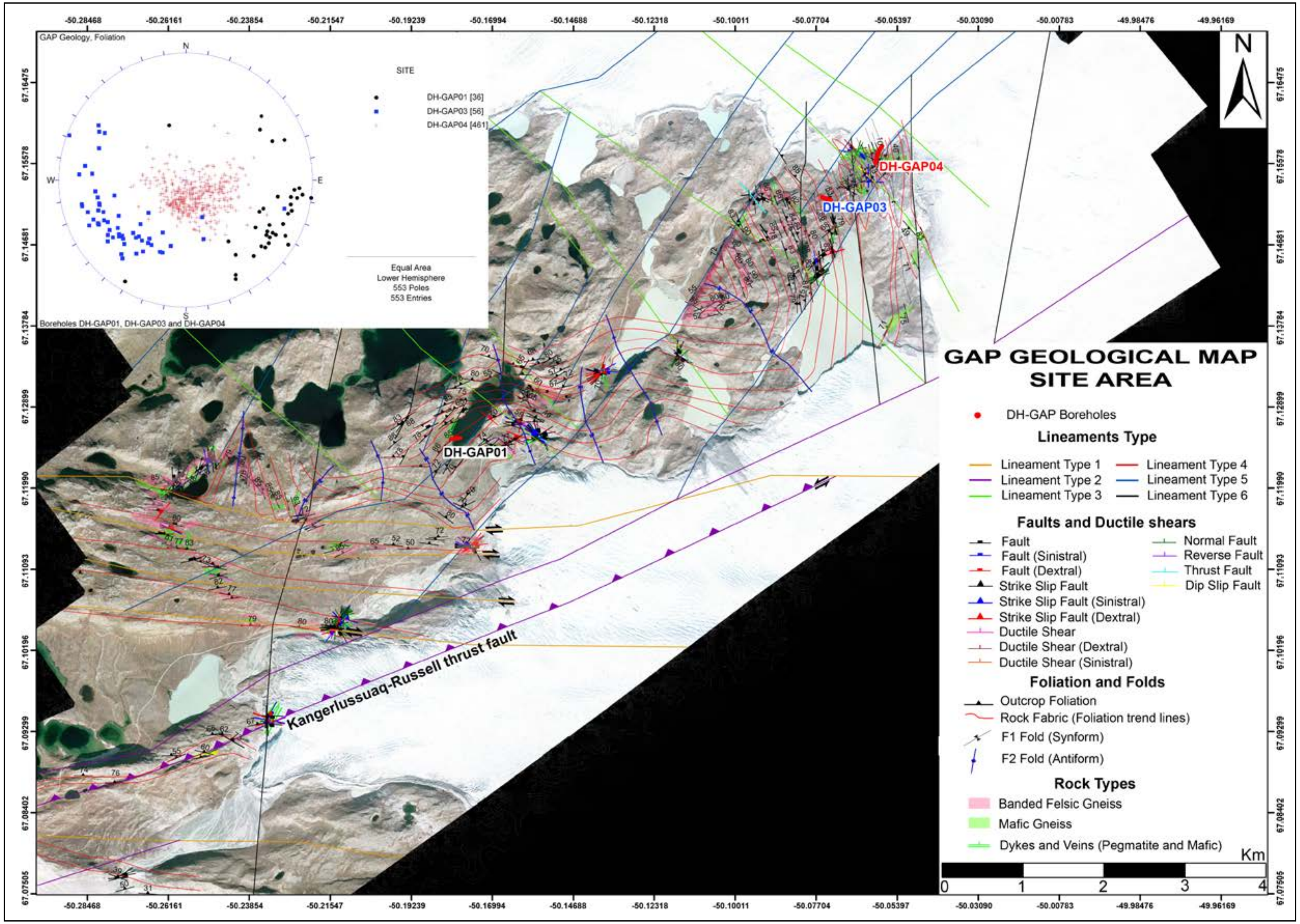

Figure 5-16. *Foliation measurements from the GAP drill cores and the inferred foliation traces and ductile shear zones based on geological mapping. The three boreholes are displayed as DH-GAP01 (Black), DH-GAP03 (Blue), and DH-GA04 (Red). The same colours are utilized in the stereographic projection (Equal area, Fisher projection).*

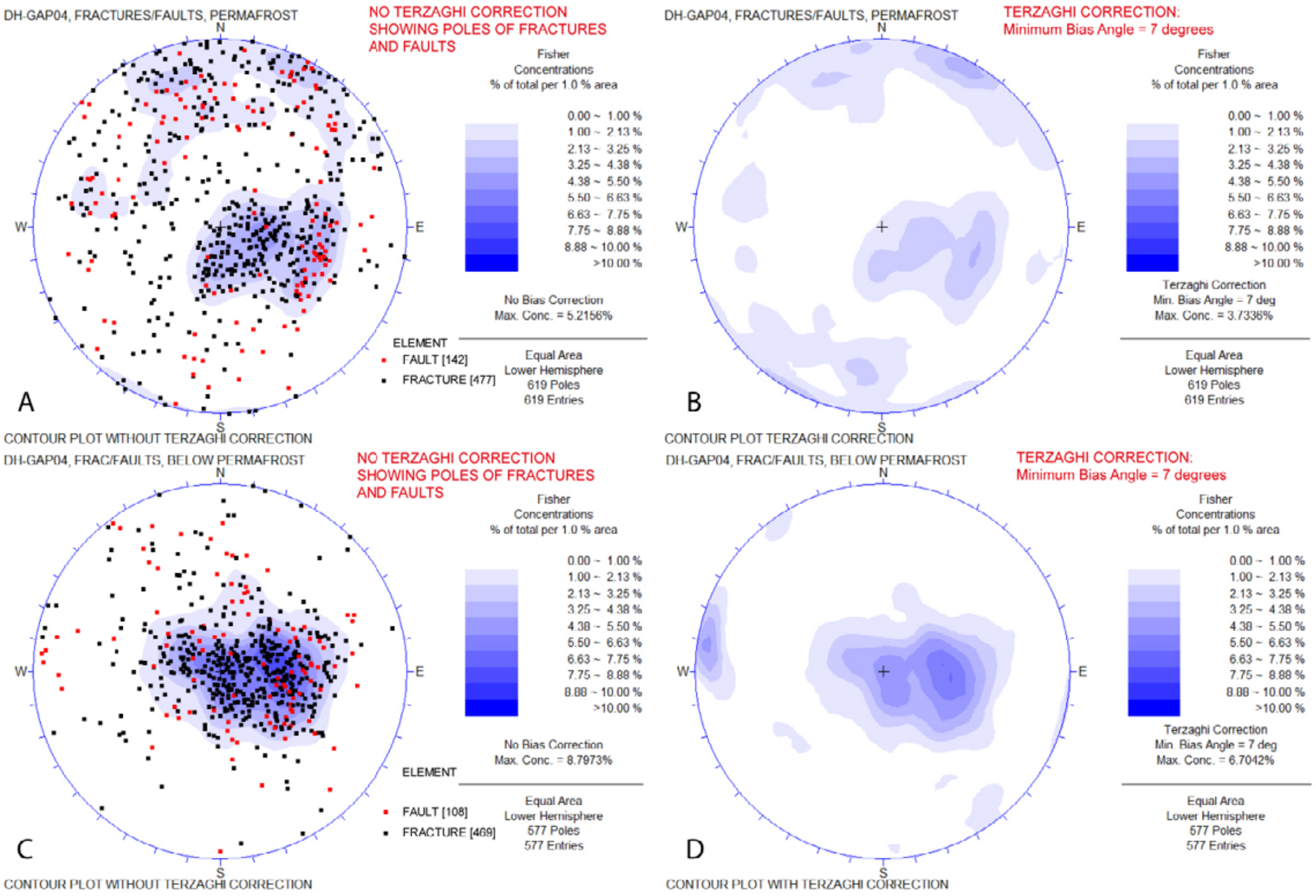

Figure 5-17. *A) Orientation of fractures/faults within permafrost (0–400 m borehole length) in DH-GAP04 and B) the same data with Terzaghi correction. C) Orientation of fractures/faults below permafrost (400–687 m borehole length) and D) the same data with Terzaghi correction. A 7-degree minimum bias angle was applied for the correction.*

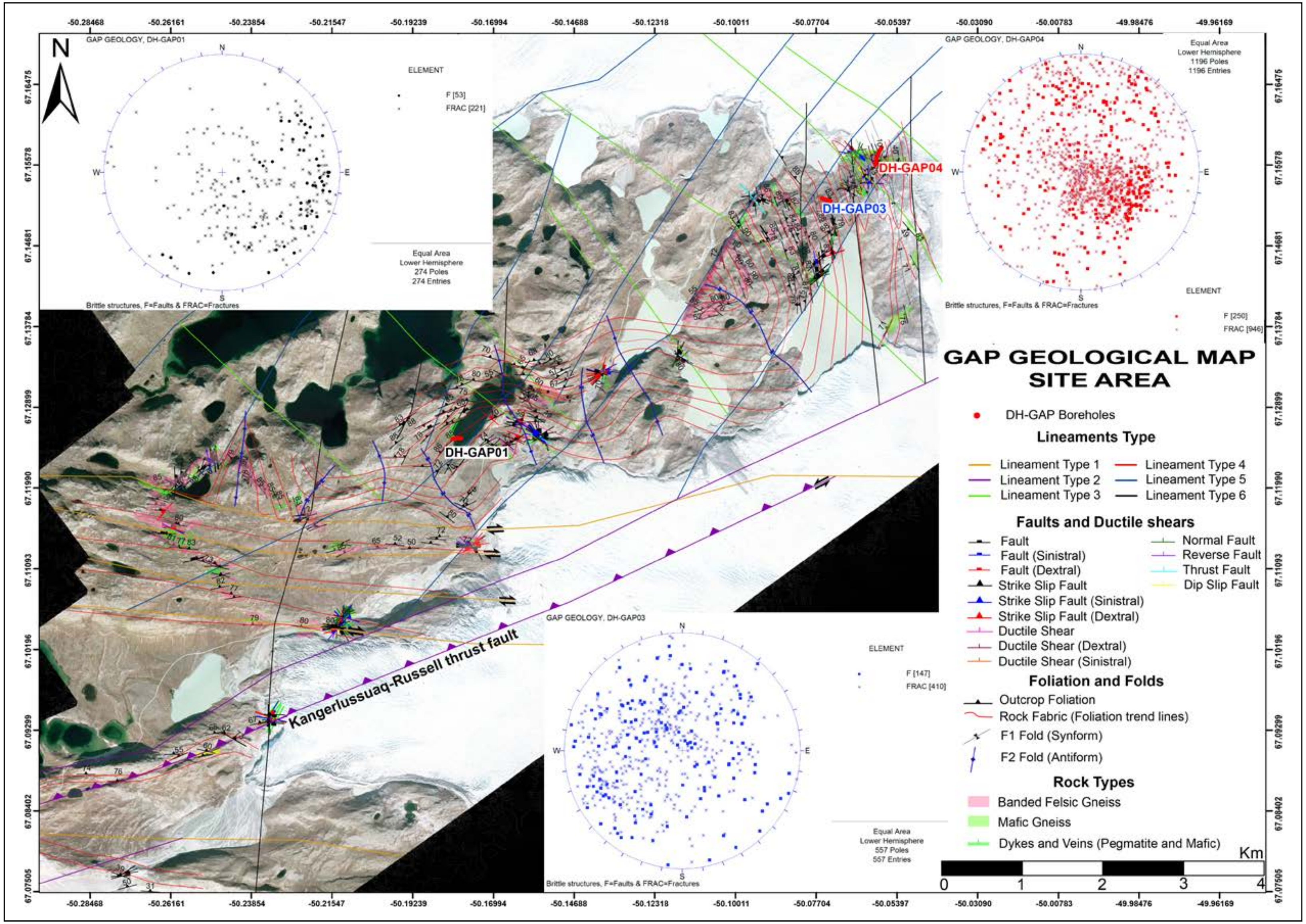

Figure 5-18. *Fracture measurements from the GAP drill cores. Aerial image overlain by the foliation, inferred foliation traces and ductile shear zones. The three boreholes are displayed as DH-GAP01 (Black), DH-GAP03 (Blue), and DH-GA04 (Red). The same colours are utilized in the sterographic projection (Equal area, Fisher projection).*

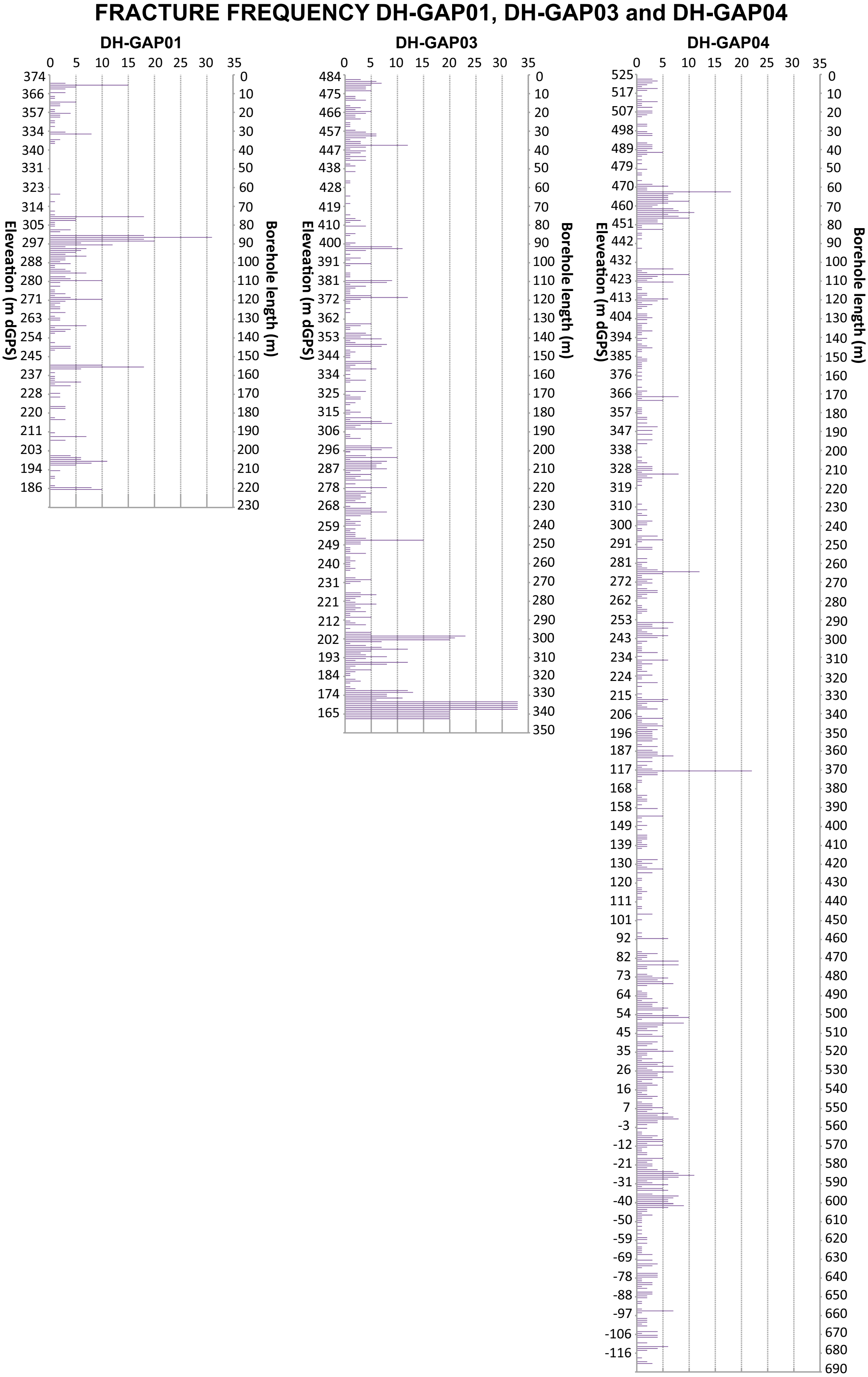

Figure 5-19. *Fracture frequency histogram (fractures/m) for DH-GAP01, DH-GAP03 and DH-GAP04, displayed as borehole length. The average fracture frequency and amount of fracturing per 100 m is shown.*

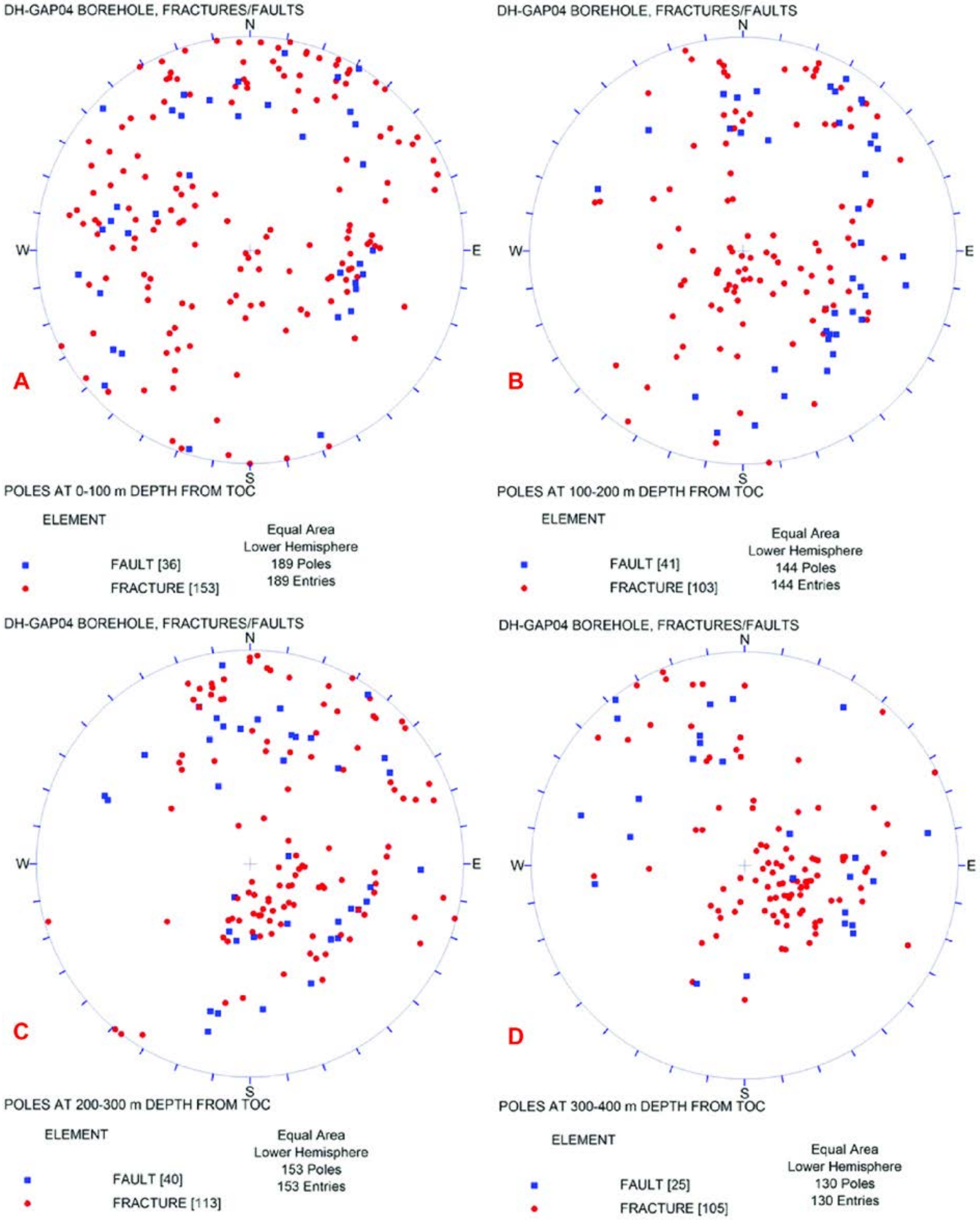

Figure 5-20. *Fracture orientations vs. vertical depth for every 100 m section in DH-GAP04 from 0 to 400 m depth. Terzaghi correction is not applied for fracture orientations.*

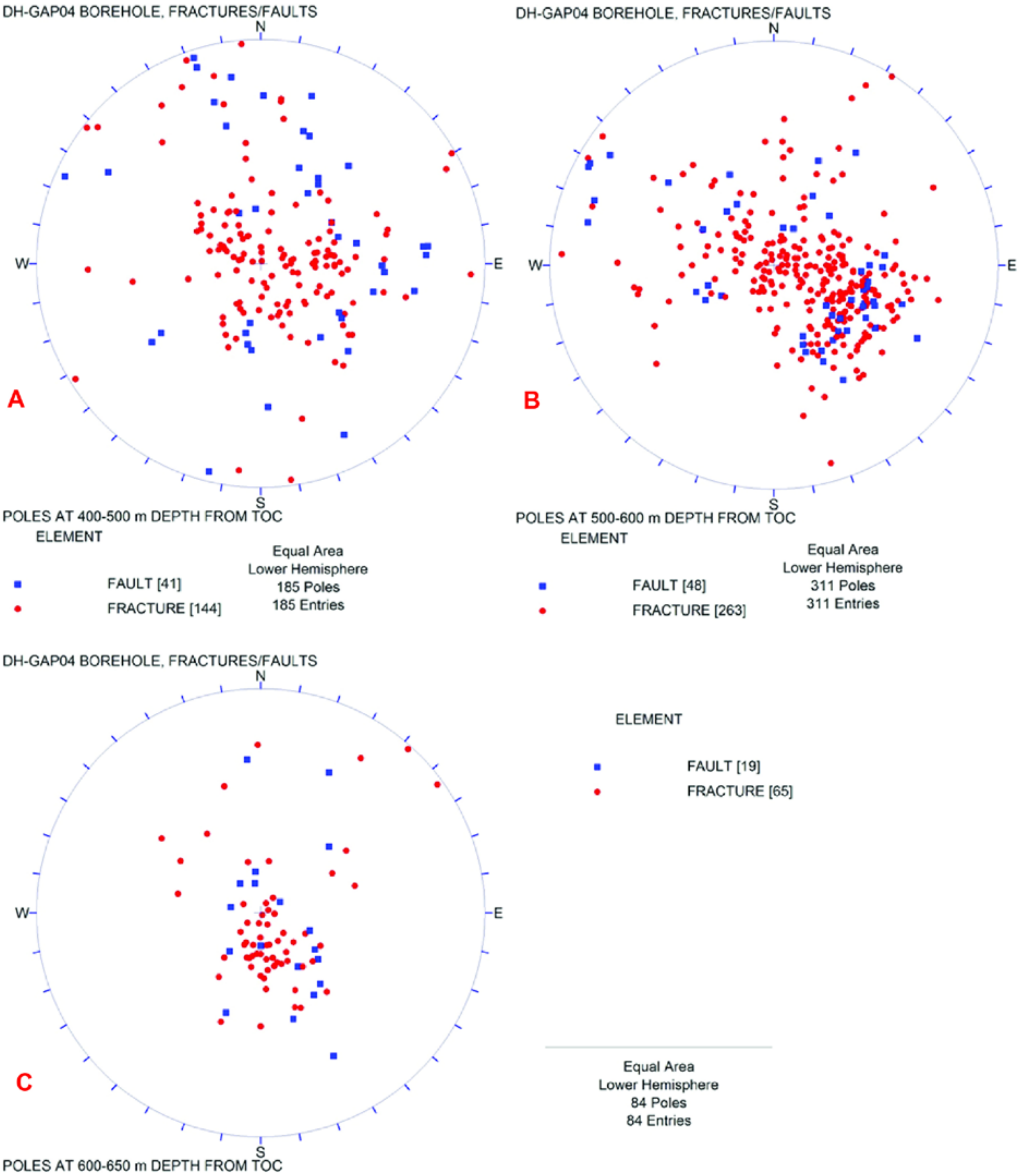

Figure 5-21. *Fracture orientations vs. vertical depth for every 100 m section in DH-GAP04 from 400 to 600 m depth. Terzaghi correction is not applied for fracture orientations.*

Comparable correlation between depth and fracture orientation is not observed in the other two boreholes (Figure 5-22, Figure 5-23 and Figure 5-24).

The geological analysis of the hydraulic zones is discussed in Section 5.6.3.3 and the fracture logging data is given in Pere (2014). Composite plots summarising the geological data from all three boreholes are given in Figure 5-22, Figure 5-23 and Figure 5-24. Composite plots focusing on the hydrogeological features in DH-GAP01 and DH-GAP04 can be found in Section 5.6.2 and 5.6.3 (Figure 5-62 and Figure 5-63).

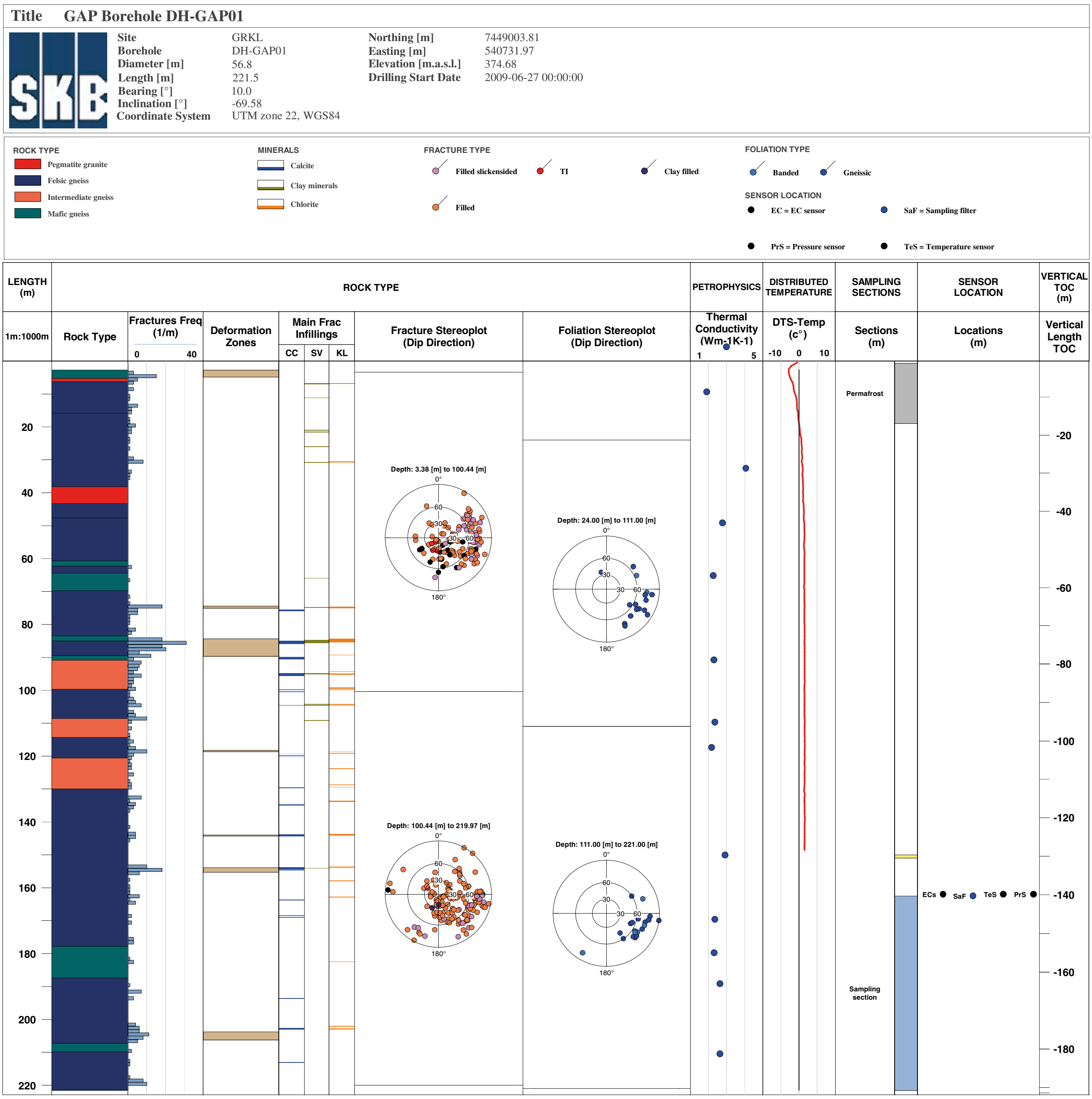

Figure 5-22. WellCad plot from borehole DH-GAP01 showing geological and petrophysical parameters vs. vertical depth. The location of downhole instrumentation is shown.

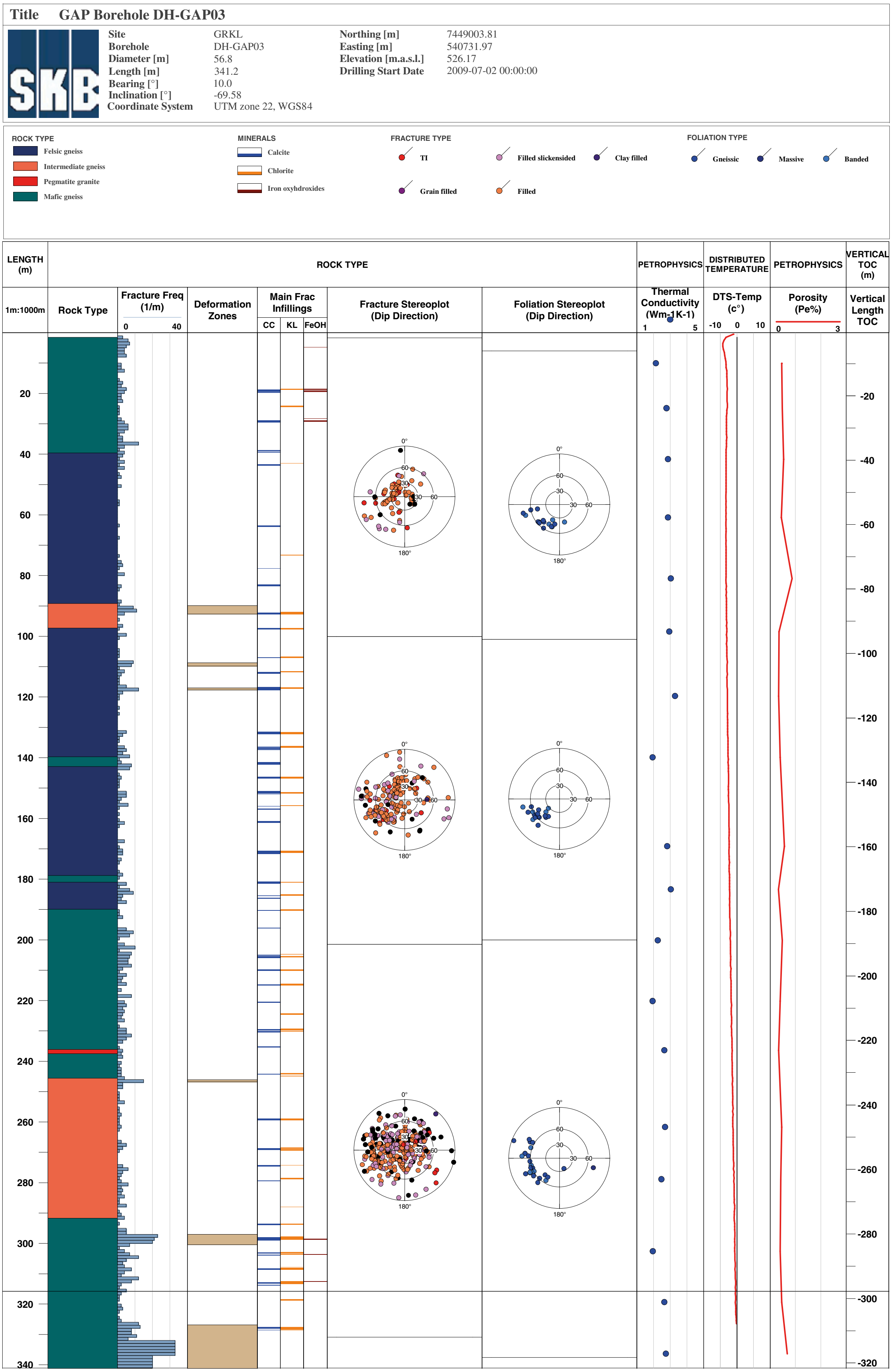

Figure 5-23. *WellCad plot of borehole DH-GAP03 showing geological and petrophysical parameters vs. vertical depth. Note that there are no downhole sensors (except the optical fiber for DTS) in DH-GAP03.*

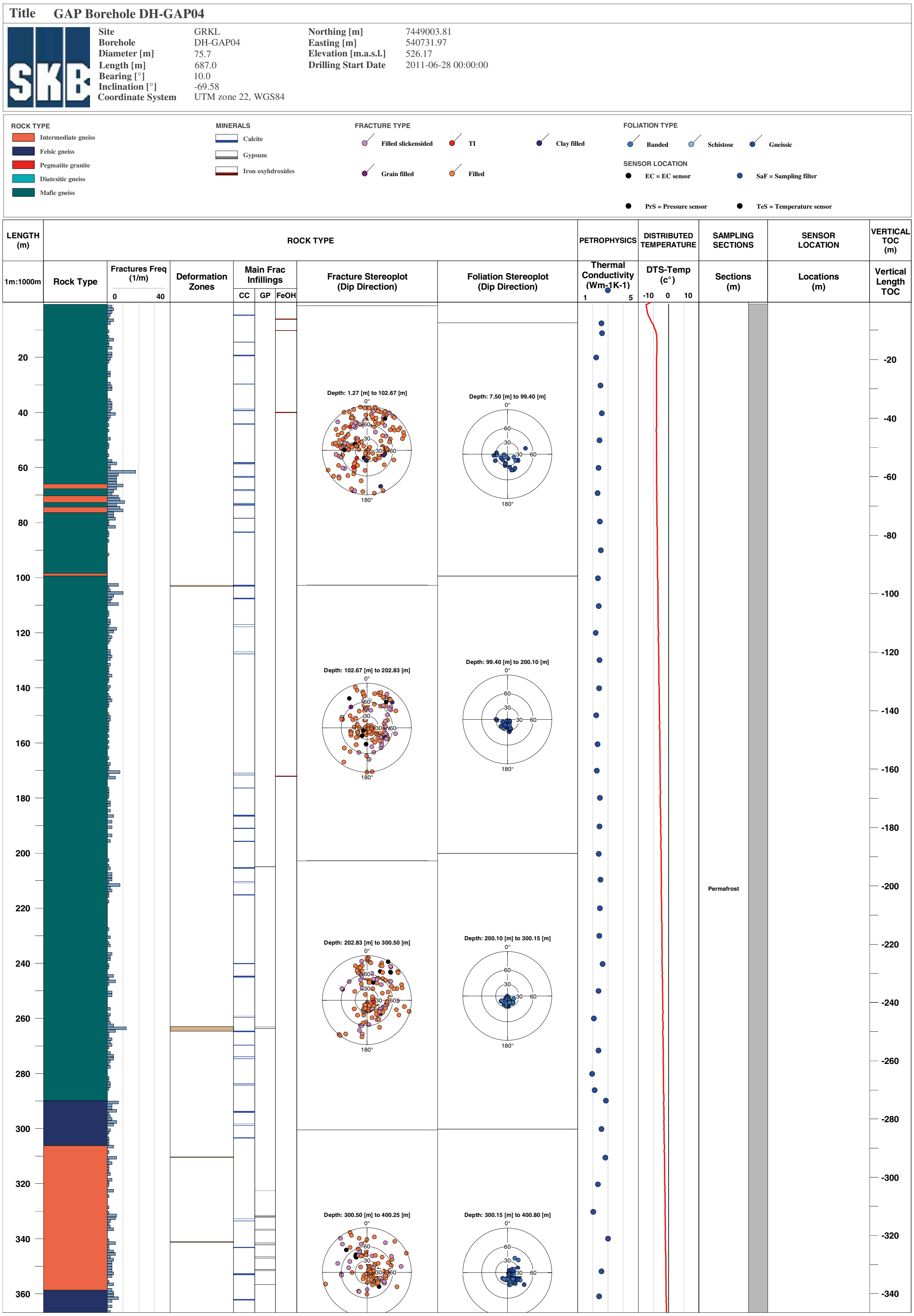

Title GAP Borehole DH-GAP04

Site	GRKL	**Northing [m]**	7449003.81
Borehole	DH-GAP04	**Easting [m]**	540731.97
Diameter [m]	75.7	**Elevation [m.a.s.l.]**	526.17
Length [m]	687.0	**Drilling Start Date**	2011-06-28 00:00:00
Bearing [°]	10.0		
Inclination [°]	-69.58		
Coordinate System	UTM zone 22, WGS84		

Figure 5-24. *WellCad plot of borehole DH-GAP04 showing geological and petrophysical parameters vs. vertical depth. Also the groundwater monitoring sections, together with the positions of the downhole instrumentation, are shown.*

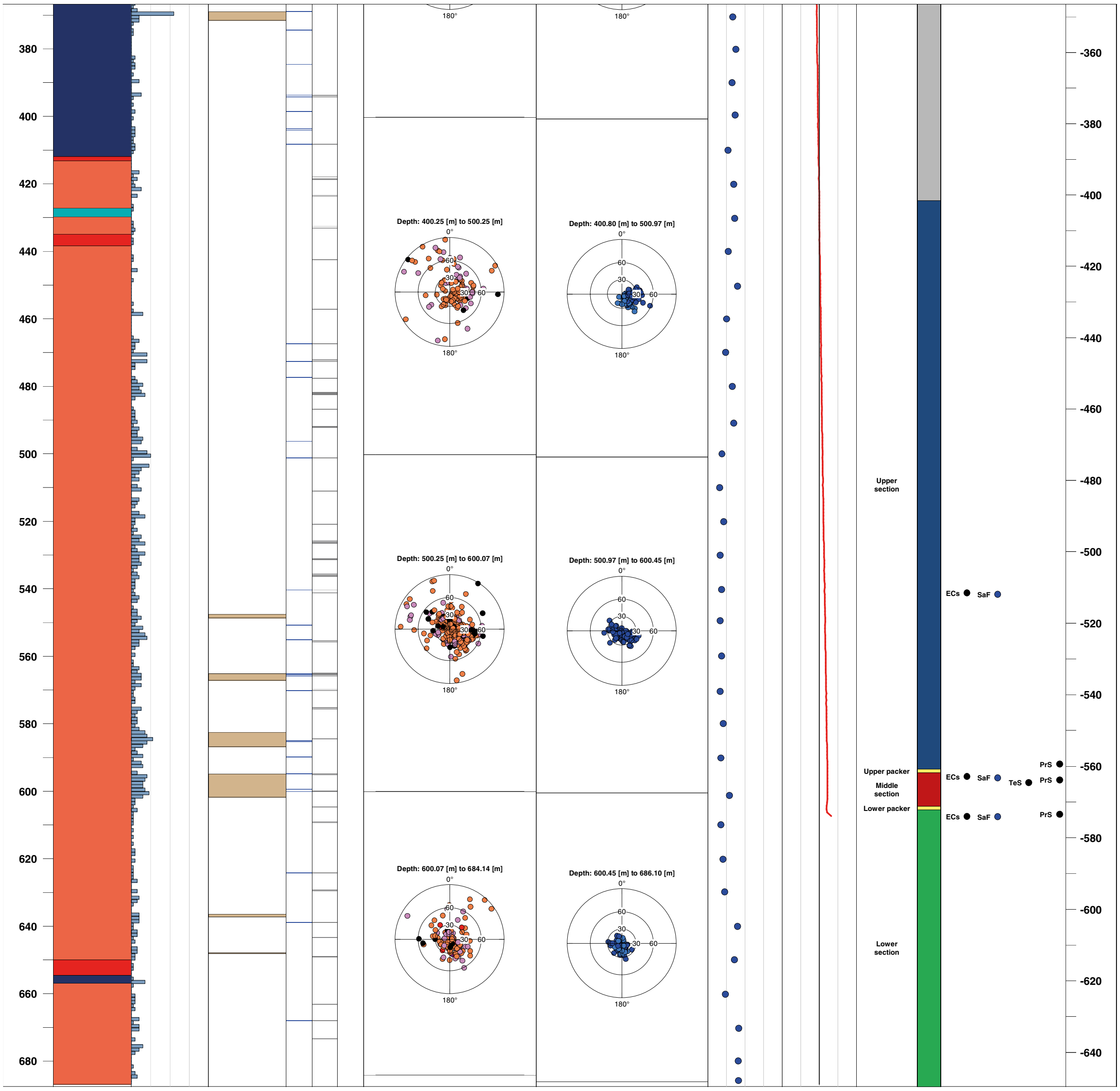

Figure 5-24. Continued.

5.4.4.4 Main conclusions from geological investigations

The bedrock geology in the GAP study area is complex and several episodes of deformation have reworked the rocks in the area. The complexity is well illustrated by the different structural geology of the three boreholes. DH-GAP01 and DH-GAP03 have the same type of lithology, but they differ structurally, while DH-GAP04 differs both in structure and lithology from the two others. The lineament model and the fieldwork confirmed that six different types of lineaments are found within the GAP study area. The lineaments can be expanded to a larger area that extends significant distances and covers areas currently beneath the ice sheet. The lineaments represent different structural features and all except the Type 1 lineaments represent typical brittle structures.

The bedrock in the GAP study area has comparable general appearance with the sites chosen for deep repositories in Fennoscandia. Observations both at surface and from drill cores (see Figure 5-22, Figure 5-23 and Figure 5-24) indicate that the fracture network (frequency, spacing and geometry) bears similarities with the fracturing observed in Fennoscandia. There is no obvious increase in fracturing in the upper part of the bedrock, which could occur as a result of cyclic freezing/thawing. All of the high fracture densities can be explained by tectonic events.

One of the fracture sets in all drill cores is parallel to the foliation. Because the three boreholes intersect different parts of large folds, the geometry of fracturing is different. A steeply dipping fracture set is dominant in DH-GAP01 and DH-GAP03, whereas sub-horizontal fracturing is characteristic for DH-GAP04. There are zones of intense fracturing in all drill cores, but they are usually relatively narrow and lack characteristic features, such as abundant fault gouges, which would help to trace the zone from one borehole to another.

An interesting feature in DH-GAP04 is that the fracture orientations change with depth, whereas the foliation remains constant along the length of the borehole. Vertical fractures are common in the upper 300 m of the bedrock. Below 300 m, vertical fractures become rare and sub-horizontal fractures dominate.

The fracture network is well developed, at least down to the observation depth of 600 m. Permafrost, fracture infillings and the geometry of the fracturing define which part of the fracture network is currently available for water flow. Fracturing in the water-conducting zones in DH-GAP04 is discussed in Section 5.6.3.

There is no information available about the hydraulic properties of the regional deformation zones. Based on the fracture observations at surface, and the multi-phase deformation history of the region, it is plausible that brittle reactivation of the zones has occurred on several occasions, providing pathways for water flow. No signs of postglacial faulting have been observed, although such faulting could be expected in an area of oscillating ice margin. The depth and length extension of the deformation zones define them as regional hydrogeological features, which have been active below the thick confining permafrost as well. The fact that they extend beneath the ice sheet, forming deep subglacial and possibly sediment filled valleys (see Section 3.5), increases their importance as potential zones for meltwater recharge and flow.

5.4.5 Petrophysical properties

Variations in rock type and in rock physical properties have impacts on many of the features investigated in the GAP. For example, the growth of permafrost and the development of active layers are linked to the thermal properties of the rock and, to a lesser extent, to the porosity of the rock. Matrix waters and fracture waters are interacting and the amount of pore volume determines the significance of such interaction. Geophysical interpretation is based on the contrasts, for example, in magnetic properties or density. If site-specific data is missing, literature values can be used, but that is not ideal. The essential parameters required in thermal modelling and in geophysical investigations can be readily measured from rock samples.

5.4.5.1 Methods and data produced

Measurement of petrophysical properties ideally is performed on fresh, non weathered rock samples, and in sufficient amounts, to achieve statistical significance over the natural variability within the sample set. Drill cores are optimal sample material for petrophysical measurements. Petrophysical analyses were performed twice over the course of the project. The work was conducted in the Geophysical Laboratory of the Geological Survey of Finland.

In 2010, 12 samples were taken from the core DH-GAP01 and 18 from DH-GAP03. This was roughly one sample for every 20 m of drill core. The aim was to investigate properties of the main rock types, as distinguished by their mineralogical and textural characteristics. A 10 cm sample was cut from the core using a diamond saw. In addition, two hand specimens from the proposed Caribou drilling site were analysed because they were considered representative of the rock type assumed to be dominant in DH-GAP04. In total, 10 sub-samples were cored from the two hand specimens for measurement. The measurements included: density (kg/m^3), matrix porosity (%), thermal conductivity (W/mK), magnetic susceptibility (10^{-6}SI), remanent magnetisation (A/m), seismic P-wave velocity (m/s) and specific resistivity (Ωm).

In 2012, a more comprehensive sample set was collected from DH-GAP04. The main focus was to obtain parameters for geothermal modelling and, therefore, the spectrum of determined parameters was expanded to include specific heat capacity, radiogenic heat production and the anisotropy of thermal conductivity. Samples from the DH-GAP04 core were collected every 10 metres, avoiding specimens with apparent fracturing, without specific attention paid to rock type. In this way, the intent was to obtain a statistically representative dataset. Each sample was 12–15 cm long and was terminating either at a fresh break or by cut with a diamond saw. In total, 71 samples were collected.

The measurements for 71 samples included: density (kg/m^3), magnetic susceptibility (10^{-6} SI), remanent magnetisation (mA/m), matrix porosity (%), inductive resistivity (Ωm), galvanic resistivity (IP, Ωm), seismic P-wave velocity (m/s), thermal conductivity (W/mK) and specific heat capacity (J/kgK). In addition, the anisotropy of thermal conductivity was measured on 10 samples and radiogenic heat production (U, Th and K) on 30 samples.

5.4.5.2 Main conclusions from petrophysical measurements

As expected, the felsic and mafic rock types have different densities. The average density for the felsic to intemediate rocks is 2600–2700 kg/m^3, depending on the borehole. Mafic rocks in DH-GAP01 and DH-GAP03 are in the minority compared to felsic varieties, and their mineralogical composition is variable. In DH-GAP04, homogeneous mafic rock dominates in the upper 300 m borehole length. The average density of the garnet-pyroxene-amphibole gneisses is 3208 kg/m^3.

In general, the felsic and mafic rocks have similar matrix porosities, ranging from 0.2 to 0.6 %, and averaging around 0.45 % (Figure 5-25). There are two groups that stand out from the average range. All boreholes have samples that plot in the range 0.7–0.9 %, regardless of depth. Another distinct group of felsic rocks, occurring between 500 and 650 m borehole length in DH-GAP04, have matrix porosities ranging from 0.9 % to 1.32 %. Currently, there is no explanation for this anomaly. The rock type is not particularly deformed, and lacks other apparent features that would explain the higher porosities. All of the known hydraulic zones are located within this depth interval (see Figure 5-63).

The range of porosities for intact rock is relatively wide (0.2–1.32 %). Porosity generally does not correlate with depth or lithology, but the highest porosity is characteristic of the deep seated, 150 m thick felsic rock unit. Because this is the same geological unit where high hydraulic conductivity was observed (see Section 5.6.3), it is reasonable to assume that there is a chance for enhanced water-rock interaction and porewaters may retain chemical signatures of former groundwater.

Although only little information on the mineralogy or the geochemistry of the rocks in the research area exists, it can be assumed that the mineralogical compositions of the main rock types differ, which contributes to their thermal properties. Felsic and quartz-feldspar-plagioclase-biotite rocks have higher concentrations of U-, Th- and K-bearing minerals compared to mafic rocks, which are predominantly composed of Fe-Mg minerals and, therefore, their radiogenic heat production is slightly higher. The average radiogenic heat production for felsic rocks in DH-GAP04 is 0.36 μW/m^3, while the average for the mafic rocks is 0.22 μW/m^3.

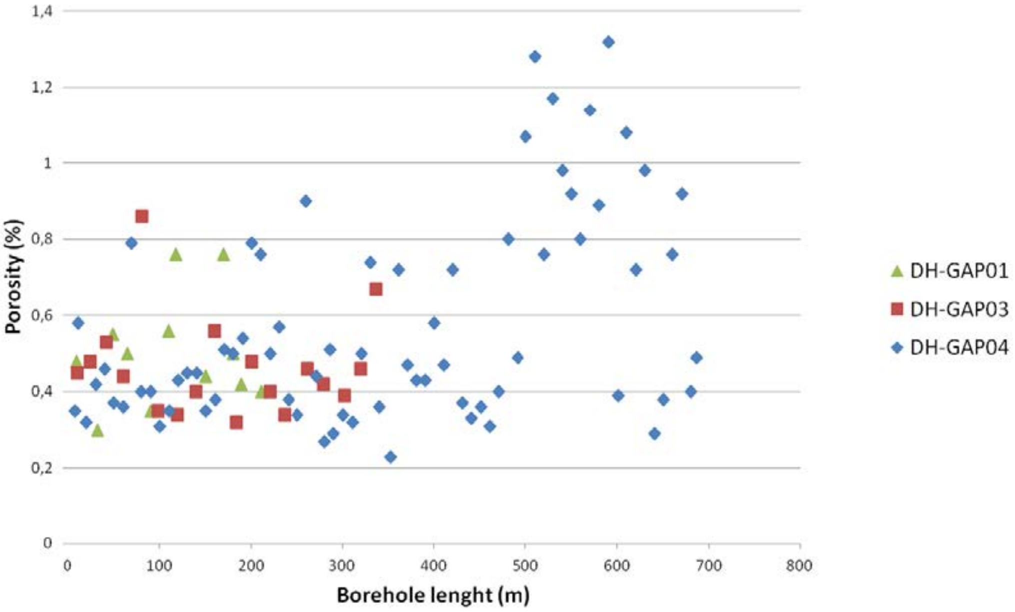

Figure 5-25. *Porosity vs. borehole length for all measured GAP borehole samples. Increased porosity at 500–650 m is related to a specific felsic rock type in DH-GAP04.*

The thermal conductivity does not correlate with rock type (Figure 5-26). There is scatter in the data for the felsic rocks, but the calculated average 2.50 W/mK for all three drill cores is considered to be representative of bedrock in the research area. The more porous felsic rocks in DH-GAP04, at 500 to 650 m depth, plot between 1.50 and 2.00 W/mK, reducing the DH-GAP04 average to 2.28 W/mK. The average for DH-GAP01 samples is 2.59 W/mK and 2.62 W/mK for DH-GAP03 samples. Specific heat capacity was measured only for DH-GAP04 samples. The average is 679 J/kgK and is not dependent on rock type. The results suggest that geology in the research area has only a minor impact on permafrost thickness due to its relatively uniform thermal properties.

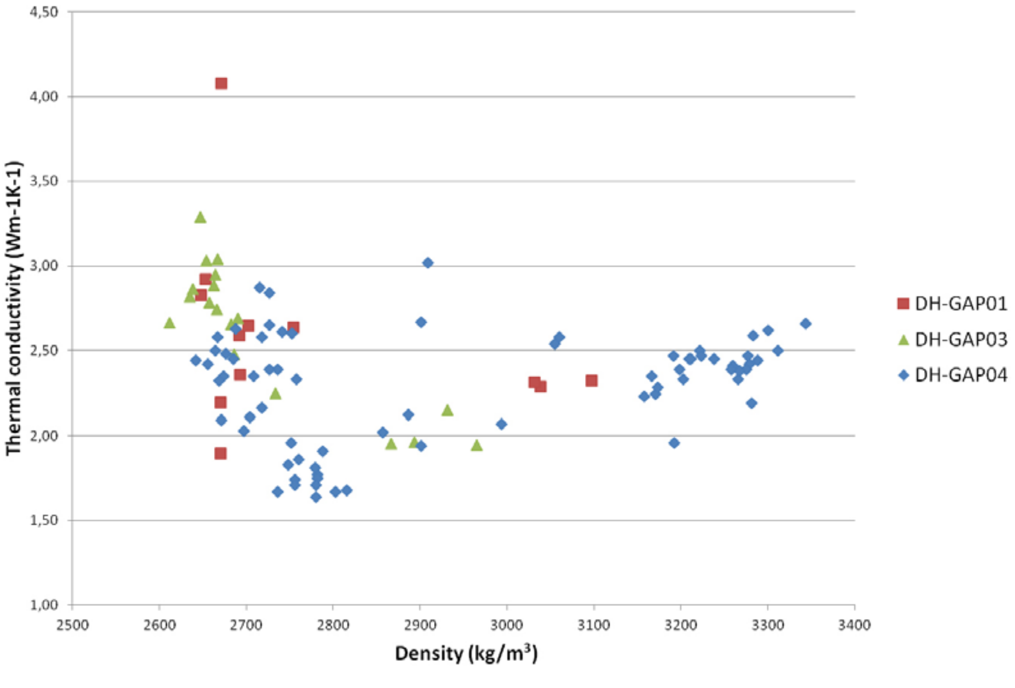

Figure 5-26. *Thermal conductivity versus density for all measured GAP borehole samples. Felsic to intermediate gneisses (densities 2600–2800 kg/m^3) have a wider range in thermal conductivity than the mafic rock types. The cluster of low thermal conductivities between 1.50 and 2.00 W/mK is related to a porous felsic rock unit observed in DH-GAP04. The calculated average for all samples is 2.50 W/mK.*

5.5 Permafrost

Permafrost is, by definition, ground that remains at or below 0 °C for at least two consecutive years. There is a general relation between the MAAT and the mean MAGT. The ground temperature increases with depth due to heat input from the interior of the earth, and, at the surface, heat exchange with the atmosphere takes place. Winter snow cover, vegetation and other features buffer the ground from cold air temperatures and the MAGT is commonly 2 to 4 °C warmer than the MAAT (e.g. Brown and Pewe 1973). Therefore, the MAAT must be lower than −2 °C before permafrost can exist.

Permafrost is normally classified as continuous or discontinuous. In areas with continuous permafrost, permafrost occurs everywhere beneath the exposed land surface. Zones of unfrozen ground – taliks – only occur beneath large lakes, rivers and arms of the sea. In areas with discontinuous permafrost, areas of unfrozen ground separate bodies of permafrost. In the transition to boreal conditions, the occurrence of permafrost becomes increasingly sporadic (Figure 5-27).

The uppermost layer of the ground thaws and refreezes annually. The layer of ground that is subject to annual thawing and freezing is called the active layer. The permafrost and the seasonally frozen active layer restrict infiltration and groundwater recharge. Most of the annual precipitation contributes to surface runoff, and stream flow rates vary widely over the year.

In Arctic regions, it is important to know the lateral and vertical distribution of permafrost because frozen ground has a major impact on the local hydrology, both at surface and in deep systems (White et al. 2007). Melting of ground ice in the watershed area is assumed to be one of the major sources providing water into the lakes found in periglacial areas. Recharge of meteoric waters is limited to the active layer; thus, surface runoff is the principle hydrological process, while mixing with groundwater is generally restricted. Through taliks existing beneath lakes, however, can provide potential pathways for vertical flow, allowing both recharge and discharge.

Growth and extent of permafrost is related to climatic conditions. The main source for the temperature records in the Kangerlussuaq area is the DMI weather station at the Kangerlussuaq airport (50 m a.s.l.). The long term records (1977–2011) indicate −5.1 °C as the MAAT (Cappelen 2012). Shallow boreholes (maximum 14 m) at the airport show that the MAGT in the proximity of the airport is around –2 °C. Based on this data, the permafrost at the airport is modelled to be 100–160 m thick (van Tatenhove and Olesen 1994).

Prior to the GAP, there was no information about the permafrost close to the ice margin, which is situated at considerably higher elevation, around 300–500 m a.s.l. Therefore, early on, the GAP had to obtain bedrock temperature information. The thickness of frozen ground, the minimum temperatures in the bedrock, and whether or not taliks exist in the area, were key questions. Utilisation of downhole fiber optical cable(s) to allow for continuous temperature profiling in deep boreholes made it possible to investigate these features despite freezing conditions.

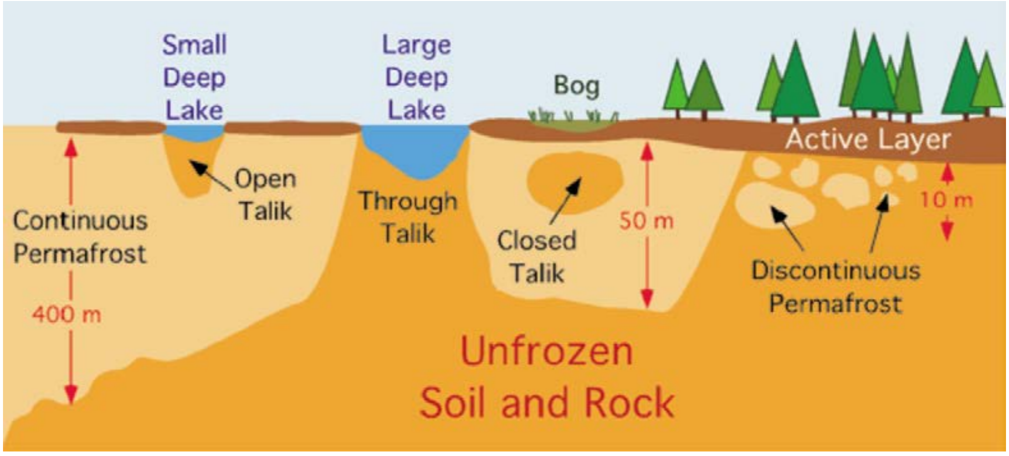

Figure 5-27. Vertical cross section of the transition zone between continuous and discontinuous permafrost and schematic representation of typical features (Pidwirny 2006). Figure reprinted with permission from Jones Scott.

The primary reason for temperature profiling in DH-GAP01 was to investigate the question of whether or not a talik exists underneath the lake. DH-GAP03 was profiled to investigate permafrost depth and bedrock temperatures near the ice margin. This information was also needed to design the drill plan for DH-GAP04, and for the design and installation of the borehole instrumentation. The high resolution temperature data provides opportunity to investigate the geothermal properties of the bedrock, the growth of permafrost and to observe the movement of groundwater (e.g. Freifeld et al. 2008, Lowry et al. 2007, Tyler et al. 2009).

In order to evaluate the site scale hydrogeology, the permafrost information obtained from the boreholes was extrapolated to a broader area. Because it is typically not possible to increase the number of direct observations, a wide range of geophysical methods have been used in other studies to map the distribution of permafrost (e.g. see the review by Scott et al. 1990). Geophysics is generally considered the only practical method to obtain information about subglacial permafrost. The applicability of an electromagnetic method (SAMPO) was tested in the Kangerlussuaq area from September 20, 2012 to September 28, 2012. The campaign was planned to cover different geological and hydrogeological settings. The main questions related to the SAMPO methodology were to determine: 1) if the low salinity groundwaters in the GAP study area give enough contrast at the base of permafrost, and 2) how the temperate ice and basal meltwater affect the geophysical soundings through the ice. The outcome of the metholodogy testing in 2012 was promising, and so the soundings were continued in 2013. The second campaign was conducted between August 26 to September 9, 2013. For the second campaign, the focus was on soundings on the ice and on obtaining information on subglacial conditions.

5.5.1 Temperature profiling in GAP boreholes

5.5.1.1 Distributed temperature sensing (DTS)

Three bedrock boreholes (DH-GAP01, DH-GAP03 and DH-GAP04) are equipped with optical fibers, which allows for accurate, high-resolution temperature monitoring utilising the DTS technique. This technique measures temperature by means of optical fibres functioning as linear sensors. Temperatures are recorded along the optical fibres as a continuous profile, not at individual points. Typically, the DTS systems can locate the temperature to a spatial resolution of 1 m, with accuracy to within ± 1 °C at a resolution of 0.01 °C (Selker et al. 2006). The DTS technique is based on the proven Raman-Optical Time-Domain-Reflectometry technique (Selker et al. 2006, Tyler et al. 2009), where a pulsed laser is coupled to an optical fibre through a directional coupler (Figure 5-28). Light is backscattered as the pulse propagates through the fibre, owing to changes in density and composition as well as to molecular and bulk vibrations. In a homogenous fibre, the intensity of the backscattered light decays exponentially over time. By accurately measuring the difference in the signal intensity of the backscattered light, in combination with distance measurement through time-of-flight of light, accurate temperature measurements are provided along the entire fibre length.

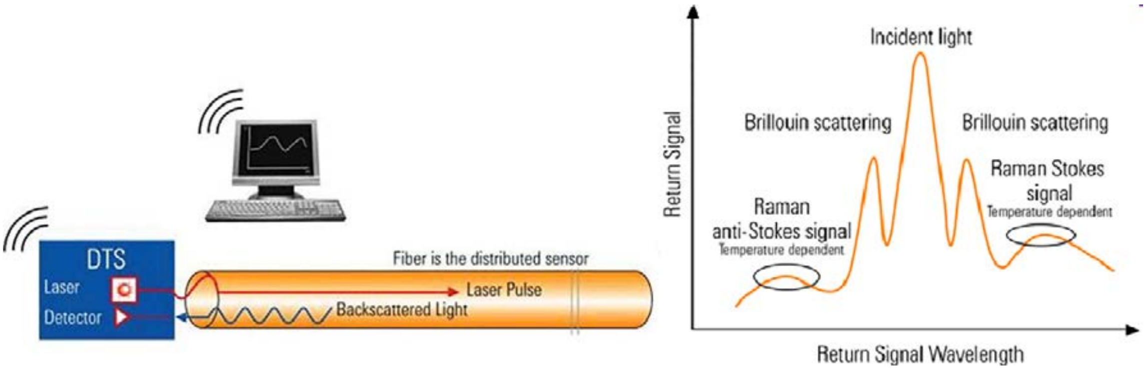

Figure 5-28. The DTS-technique is based on the Raman-Optical Time-Domain-Reflectometry technique, where an optical laser pulse is propagated through an optical fibre and scattered light is received at the transmitting end, where it is analysed (© AP Sensing).

5.5.1.2 DTS investigations in DH-GAP01 and in DH-GAP03

Two different DTS instruments were used for the temperature monitoring in DH-GAP01 and DH-GAP03: an Agilent from AP Sensing, and an ORYX from Sensornet. The accuracy is dependent on the calibration with a known external temperature source (e.g. an ice bath) and length of the measurement time. Based on these criteria, the accuracy of the DTS measurements presented here is better than ± 0.2 °C.

Both boreholes were equipped with steel-coated optical BRUsteel FRNC cables designed for harsh environments immediately following drilling in 2009. DH-GAP01 reached a vertical depth of ~ 191 m and the DTS cable extends from the surface down to the packer, terminating at a vertical depth of 130 m. The AquaTROLL, providing an independent temperature reference, is located at a vertical depth of 138.6 m. DH-GAP03 reached a vertical depth of ~ 321 m and the DTS cable was lowered together with the AquaTROLL down to a depth of 309 m. Unfortunately, the AquaTROLL failed after a few months and could not provide any additional temperature data for referencing; thus, all measurements are referenced to an ice-bath at surface (SKB 2010b).

During 2010, DTS measurements were performed in May and September in DH-GAP01, whereas DH-GAP03 was measured in May only. The aim was to observe if the 2009 measurements show evidence of still being affected by the hot water drilling. Once steady state temperatures are reached, it is not expected that the bedrock temperatures would vary much below the upper 10–15 m of seasonally disturbed bedrock.

DH-GAP01 was drilled under a lake to investigate the assumed talik and to observe the hydrogeochemical and physical conditions in such a structure (Section 5.3.1.1; SKB 2010b). Temperature profiling of the borehole shows that as soon the borehole advances beneath the lake basin, the bedrock temperature increases (above zero) and stabilises quickly at ~ 1.3 °C. This temperature is maintained along the profile, down to the depth of 140 m, which is the deepest monitoring point (Figure 5-29). DTS measurements were performed on several occasions following installation. The first measurement was conducted one day after installation and this measurement revealed distinct temperature peaks at several locations along the profile (Figure 5-30). It is assumed that the backflow of hot drilling water from conductive fractures induced the temperature peaks. This theory is consistent with fracture logging data – all temperature anomalies are located at or close to natural fractures, while none are observed in the non-fractured section between 35 and 60 m borehole length.

In DH-GAP03, the temperature stays below zero along the entire length of the DTS fibre, suggesting that the end of the borehole is probably in permafrost. In both DH-GAP01 and DH-GAP03, the seasonal variation is noticeable and extends down to a depth of about 10 m (Figure 5-29). In May 2010, the coldest temperature in DH-GAP01 was −3.0 °C at 3.5 m depth, while at the same depth in DH-GAP03 the temperature was −4.2 °C ± 0.1 °C. The difference in temperature is likely due to a combination of the difference in both the elevation and the location of the boreholes. DH-GAP01 is situated next to a talik at 374 m elevation, while DH-GAP03 is in a permafrost region at 484 m elevation. The soil cover and vegetation are somewhat different at these respective locations as well. If the temperature curve is extrapolated for DH-GAP03, the base of the permafrost is expected to be at 335 ± 14 m depth below TOC, based on the measurements from 2010.

5.5.1.3 DTS investigations in DH-GAP04

DH-GAP04 was instrumented with a DTS cable of double steel tube type, containing four multimode fibres for temperature measurements. The use of several fibres provides better monitoring flexibility and redundancy. In this case, two loops were made using a minibend, which allows the light to turn back with acceptable signal losses. The cable has a total length of 792.5 m, including optical connectors (patch cords). The advantage in using two loops is that failure in one loop does not disturb use of the other, as both loops can be measured independently. Laser light pulses sent from the DTS instrument first travel through a reference coil located in an insulated box (with several external temperature sensors), which is placed inside the borehole container, before the pulse enters the borehole. Subsequently, the pulses travel twice through 608.74 metres of cable located inside the borehole, after passing the TOC. A minibend (i.e. where fibres are connected in pairs, forming a loop) is placed in the lowermost packer (at a vertical depth of 571.57 m). The minibend provides redundant data as laser light travels down and up along the fibre.

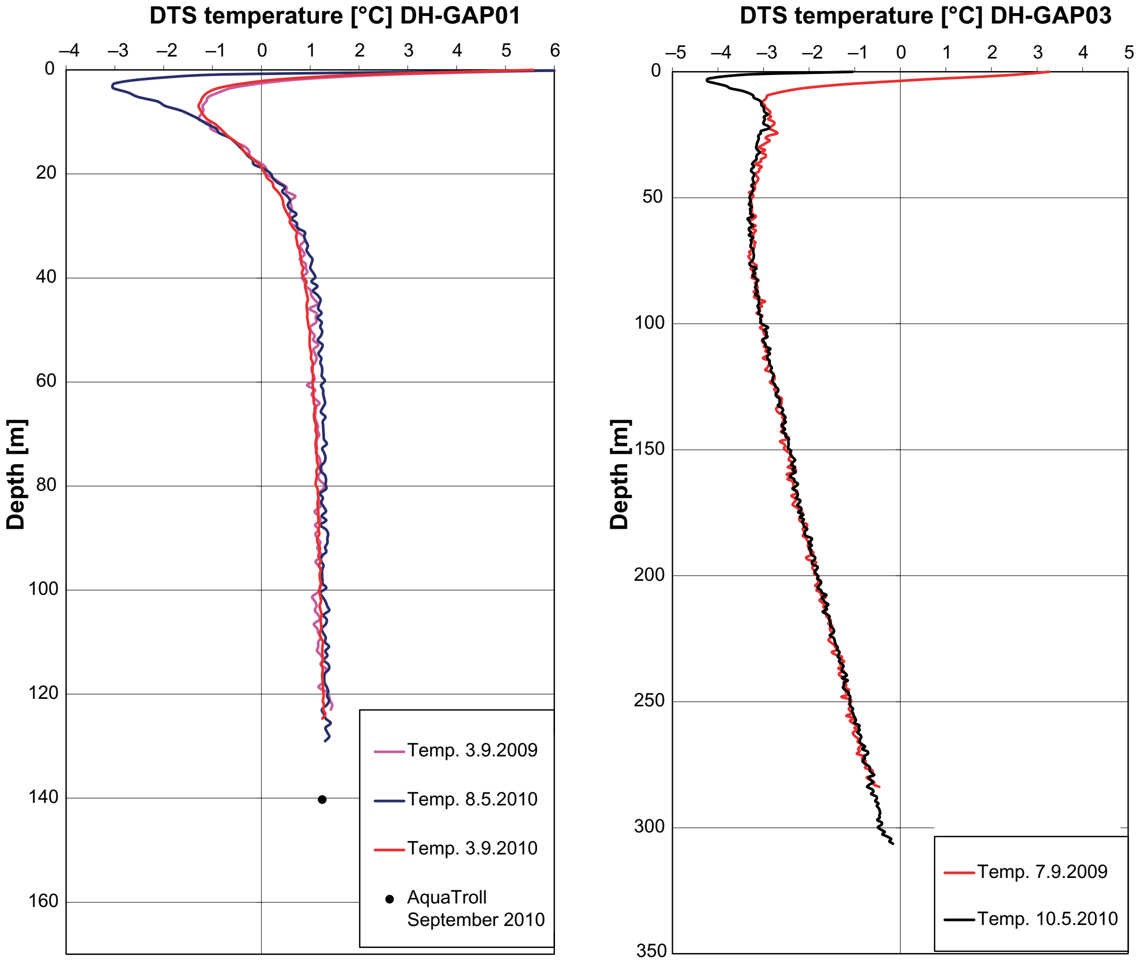

Figure 5-29. *Temperature profiles in DH-GAP01 (left) and DH-GAP03 (right) calculated for vertical depths. AquaTroll provides an independent reference temperature at 162 m (139 m vertical depth) in DH-GAP01. Note that the vertical depth extension is not the same in the two figures.*

Two temperature readout instruments were used for temperature measurements in DH-GAP04. An ORYX DTS (Sensornet), with a sampling resolution of 1 m (i.e. temperatures are simultaneously measured along one metre sections), is installed in the DH-GAP04 container (see Figure 5-9). In order to obtain better resolution, and to be able to adjust data, an ULTIMA temperature readout instrument (Silixa Ltd.), with a sampling resolution of 12.5 cm, was used over a shorter period of time. Correction of the temperature data (offset and length calibration) is necessary, especially when surface temperatures are very cold (i.e. less than −30 °C). After all of the corrections are applied, the precision of the absolute temperature along the profile is ± 0.1K.

Temperatures have been measured continuously since July 2011, with different measurement intervals depending on the purpose of the monitoring – ranging from several measurements per hour to about 10 measurements per month. The integration time is 7.5 minutes.

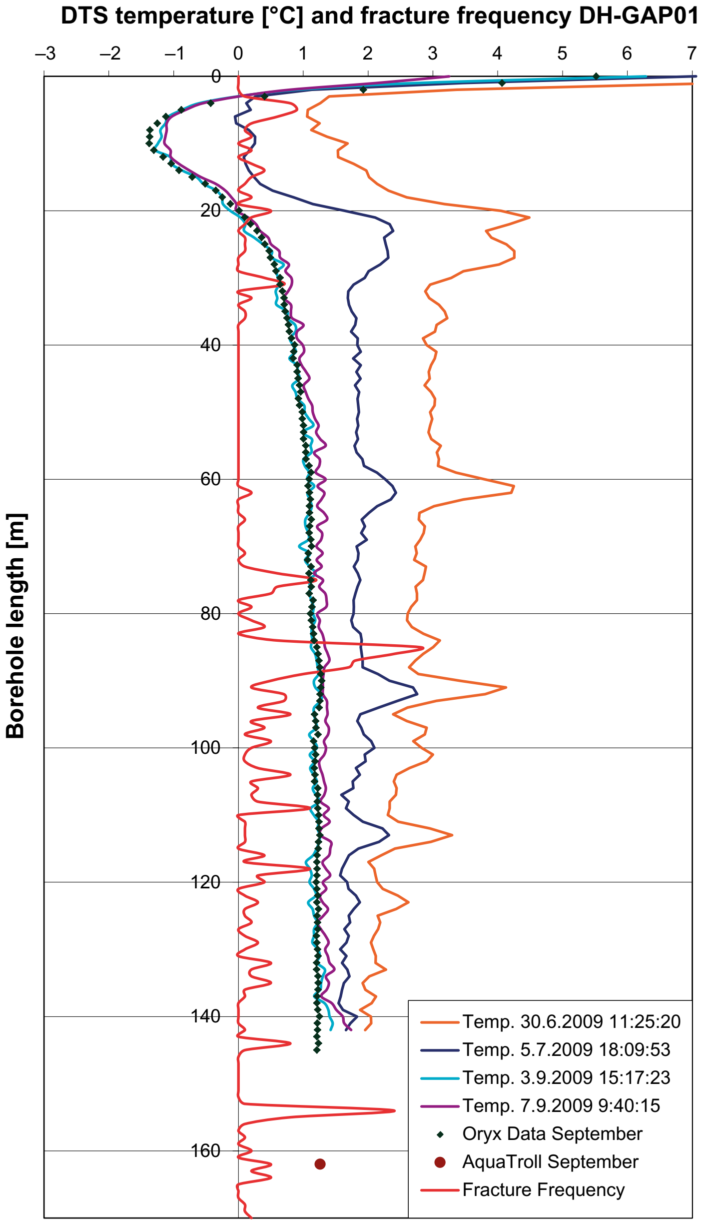

Figure 5-30. *Chart showing temperature profiles in DH-GAP01. The orange and blue lines demonstrate the process of cooling after hot water drilling. Heterogeneous cooling is evident and it is assumed that the peaks are related to flowing fractures. The steady state was reached in September 2009. The red line gives the fracture frequency per meter (not in scale). The highest peak indicates > 25 fractures/m (SKB 2010b).*

The temperatures in the borehole decreased after drilling (June – July 2011) until November 2011 (Figure 5-31). More stable temperature profiles were observed after December 2012 (Figure 5-32), when the effect of the drilling had decreased to a minimum. The measured raw temperatures were similar, but varied within a range of ± 0.2K due to the drastic temperature changes of the measurement instrument (located in the DH-GAP04 container, which is exposed to air temperatures ranging from about −30 to 10 °C) and its start up process. Based on several constant observations and on changes to the measurement protocol, it has been possible to systematically improve the data quality during the monitoring period.

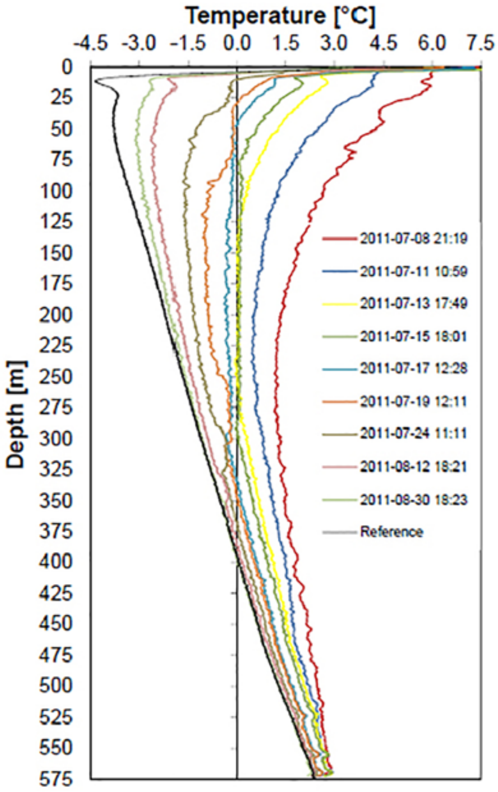

Figure 5-31. *Measured temperatures during the initial thermal recovery of DH-GAP04 following drilling. The reference curve is the temperature obtained in August 2012. Figure 5-32 shows the latest obtained temperature curves (from June and August 2013).*

The ground thermal response and recovery of the borehole was calculated using line source theory (Ingersoll and Plass 1948), assuming a thermal conductivity of 2.4 W/mK and taking into account the heat loads caused by drilling and circulation of hot water, as well as any heat added during sampling. The results show that the borehole is still 0.2K from being completely thermally recovered. The current 0-isotherm, as obtained in June 2013, is located at a depth of 405 ± 10 m (Figure 5-32). Taking into account the ± 0.1K temperature uncertainty of the ORYX, the 0-isotherm is located between 395 and 415 m depth, based on the 2013 measurements. The form of the temperature curve, and the lowest bedrock temperatures in DH-GAP03 and DH-GAP04, are comparable (Figure 5-33).

5.5.1.4 Thickness of permafrost

The two boreholes (DH-GAP03 and DH-GAP04) providing temperature information relevant for the interpretation of e.g. the permafrost thickness are located 500–600 m apart. They are located on an elevated, fairly well exposed bedrock ridge, where the soil cover is thin and the snow cover during winter is known to be thin as well. The drilling orientation of both holes is roughly northward, toward a valley between the ridge and the ice margin (i.e. the terrain slopes to the north). In practice, this means that a topographic correction needs to be made for the borehole temperature measurements when the thickness of permafrost is considered. Based on the elevation model, the correction for DH-GAP03 is 14 m and for DH-GAP04 is 51 m.

The base of the permafrost (0 °C isotherm) was measured at a vertical depth of 335 ± 14 m in DH-GAP03 (based on 2010 measurements) and at 405 ± 10 m in DH-GAP04 (based on 2013 measurements). To account for differences in the ground surface topography between the two drill sites, the elevation of a point on the ice margin directly north of DH-GAP04 was determined and used as a reference point to calculate permafrost thickness at each location. Using this approach, permafrost thickness is ~ 315 m at DH-GAP03 and ~ 350 m at DH-GAP04. The small, observed difference in permafrost thickness between the two borehole sites may be related to differences in geology, differences in local surface conditions over time, slight differences in instrument calibration procedures, or a combination of these factors.

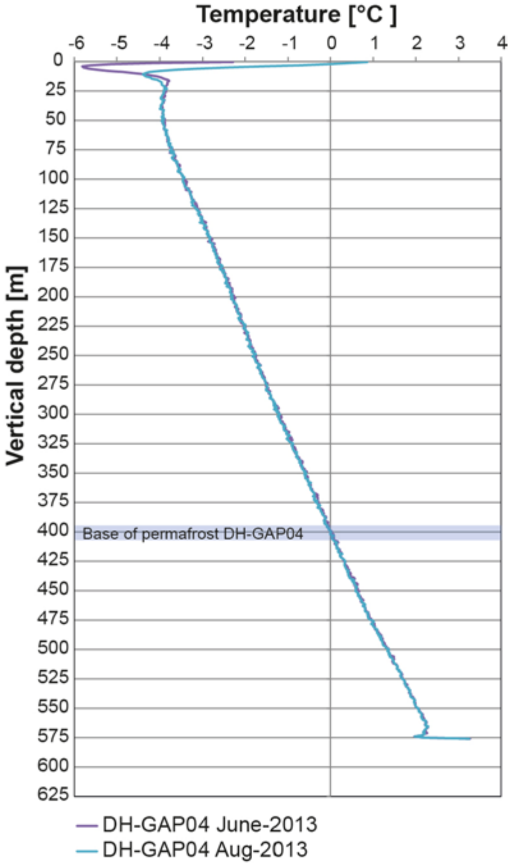

***Figure 5-32.** Temperature curve(s) from DH-GAP04 showing temperature profiles obtained in June and August 2013, respectively. The 0-degree isotherm is reached at a borehole depth of 395 to 415 m, here indicated as 'base of permafrost'.*

The temperature data from the boreholes indicates that the permafrost has grown during a period when the climate was cooler than at present (Figure 5-33). The long term records from Kangerlussuaq give a MAAT of −5.1 °C for the period 1977–2011 (Cappelen 2012). Based on the temperature profiles, present ground temperature (not affected by annual variations) is about −3 °C, while the value extrapolated from the deep permafrost is −4.4 °C. The sub-permafrost gradient in DH-GAP04 reflects even lower values, approaching −6 °C. Warming of the climate during the past decades is evident from the upper part of the curves.

5.5.2 Electromagnetic soundings for permafrost investigations

5.5.2.1 Method

The applicability of geophysical methods to permafrost investigations is based on the cryogenic contrast in the relevant physical parameters between the frozen and unfrozen ground (e.g. Scott et al. 1990). Ideally, the electrical contrast should be larger than an order of a magnitude. The formation resistivity is the result of two components: dry rock/soil resistivity, and the resistivity of the pore-water weighted by the matrix porosity (e.g. Paananen and Ruskeeniemi 2003). In groundwater and permafrost investigations of crystalline bedrock, the electrical contrasts are weak due to the low porosities. Unless the water is brine, the small amount of water present is not able to increase the electrical conductivity of the rock significantly. For the same reason, the reduction of the electrical conductivity during freezing is rather small. Nevertheless, under favourable conditions, weak contrasts can be observed, although the interpretation may be quantitatively less accurate. Favourable conditions imply that disturbances as a result of anthropogenic (power lines, buildings) or natural (mineral conductors, saline soil) reasons are minor, and that the data quality is good. The soundness of the interpretation can be improved by site-specific information on the material properties of the rock. The degree of success can be increased if there is a hypothesis to test (i.e. a defined target for the soundings).

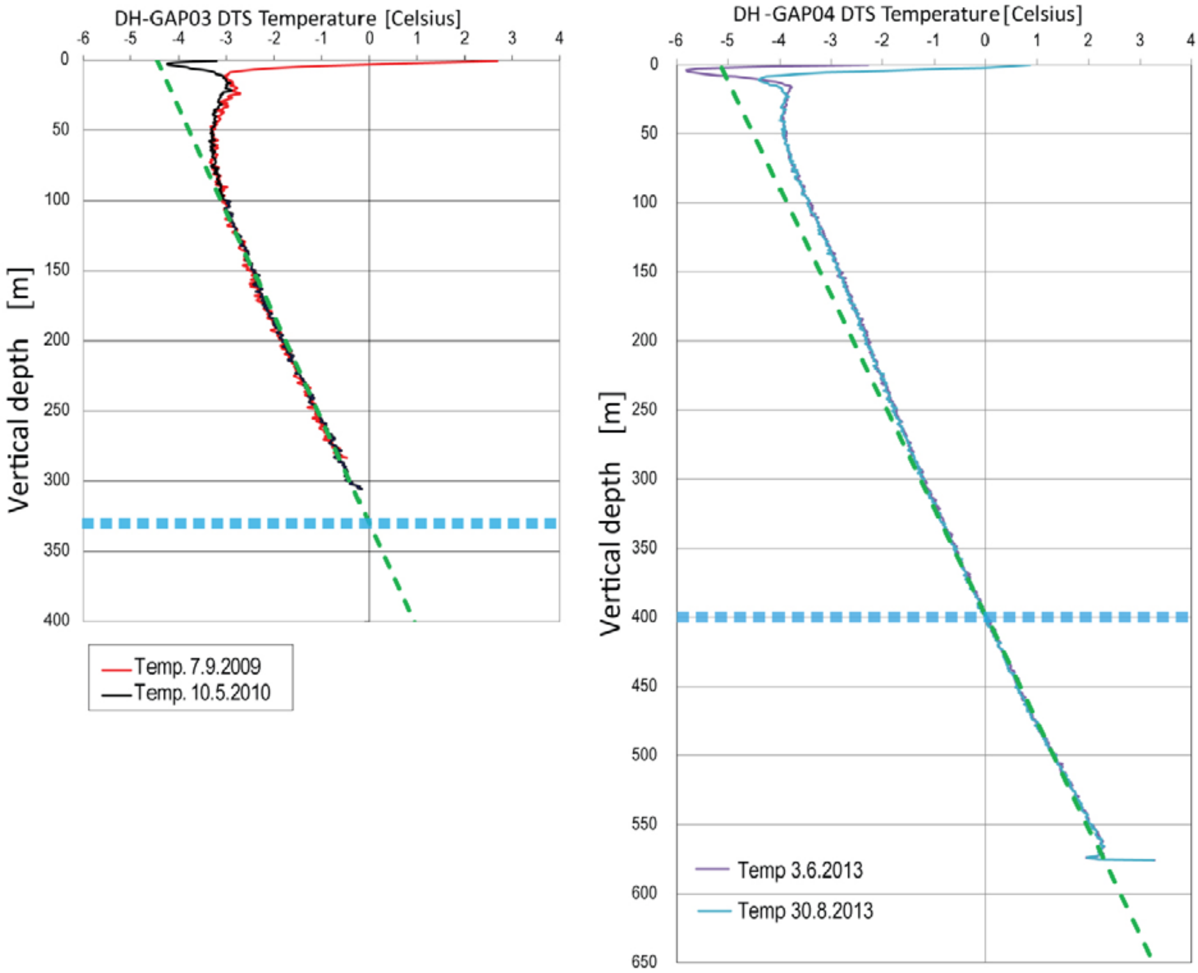

Figure 5-33. *DTS temperature profiles from DH-GAP03 (left) and DH-GAP04 (right) suggest that the initial ground surface temperature has been significantly colder than present during the growth of the deep permafrost. The present day MAGT is about −3 °C as indicated by the two DTS profiles from DH-GAP03 measured at different times of the year. The blue dashed line marks the base of permafrost.*

The SAMPO wide-band frequency-domain electromagnetic sounding system consists of a horizontal transmitter loop and a receiver made up of three perpendicular coils (Soininen and Jokinen 1991, Korhonen et al. 2009). The transmitter loop is used to generate a magnetic primary field at 82 discrete frequencies between 2 Hz and 20 kHz. The primary field induces secondary magnetic fields in subsurface conductors. The receiver coils are used to measure the radial, tangential and vertical components of the superposition of the primary and secondary magnetic fields (the total magnetic field) at a distance from the transmitter. For qualitative interpretation, the measured vertical-to-radial electromagnetic field component ratios are transformed into curves of apparent resistivity as a function of depth (ARD curves).

The electromagnetic soundings are typically carried out at regularly spaced measurement stations along straight measurement lines, keeping the transmitter-receiver distance (the coil separation) fixed. The coil separation is chosen according to the desired depth of investigation. Larger coil separations are used for greater depths of investigation and require large loops with higher magnetic moments. Additionally, the investigation depth depends on the frequencies employed and the electrical properties of the ground. In favorable environments, the depth of investigation can be in excess of one kilometre.

SAMPO soundings are interpreted using software, which calculates a layer model yielding the best fit for the measured resistivity curve. The method identifies if the sounding target is homogeneous or if it is composed of contrasting resistivity layers. It should be noted that interpretation is not a unique solution; the presented layer resistivities, depths and thicknesses should not be considered absolute values. However, if there is a hypothesis of an existing conductor structure and some reference information on the site-specific material properties, the most realistic solutions can be selected with high reliability.

5.5.2.2 Interpretation of the electromagnetic soundings

SAMPO soundings were conducted in the GAP study area to obtain information on permafrost in the area. Eight profiles and 60 sounding points were measured in 2012, and 17 profiles with ~ 200 sounding points were measured in 2013 (Figure 5-34).

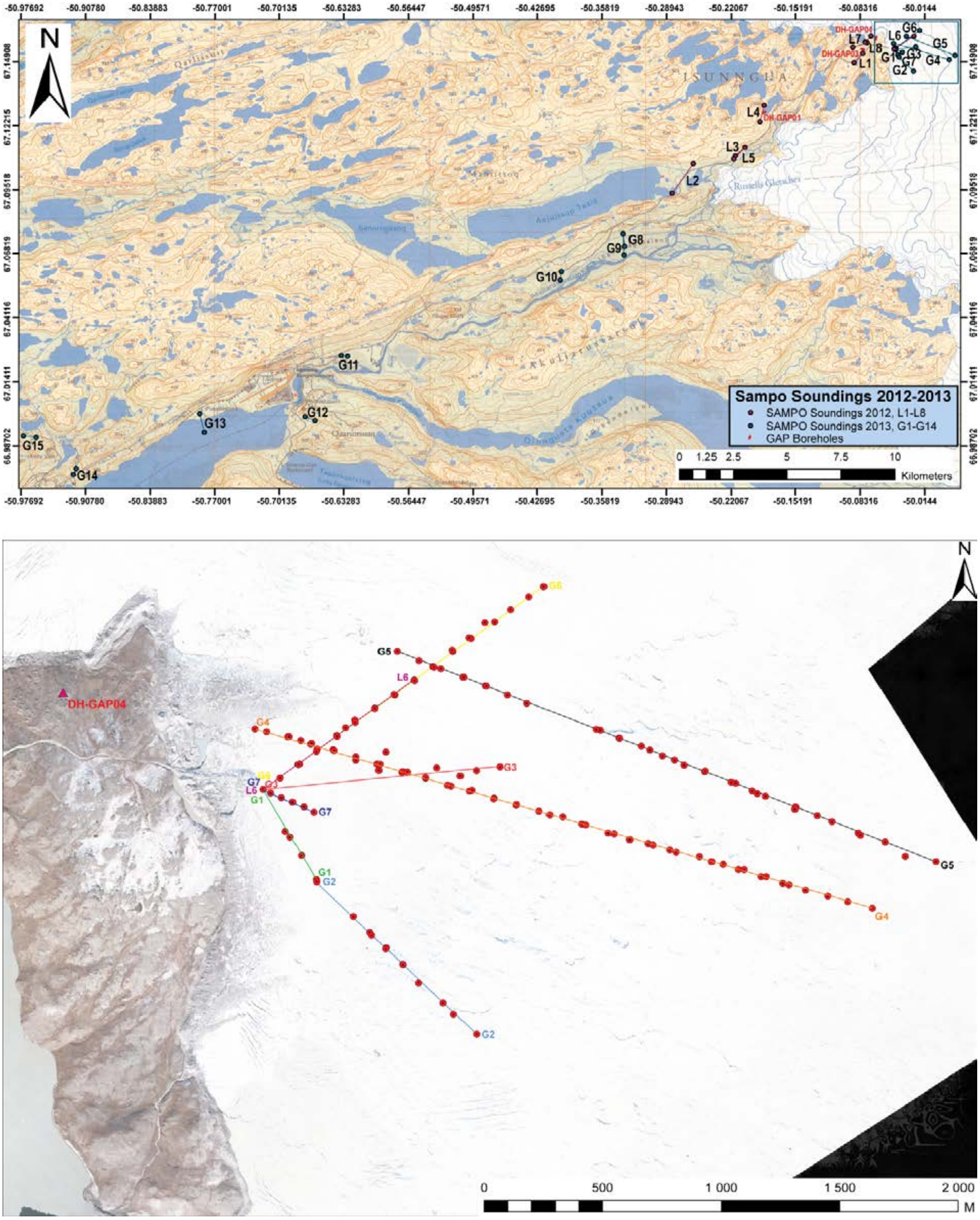

Figure 5-34. Electromagnetic sounding profiles measured in 2012-2013. The blue rectangle (upper panel) shows the area investigated in August-September 2013. Detailed locations of the on-ice soundings from 2013 are shown in the lower panel.

The SAMPO profiles from Kangerlussuaq provided a consistent cryogenic structure for the soil and crystalline bedrock at the ice margin, which included: 1) a low resistivity active layer, 2) highly resistive permafrost, and 3) lower resistivity bedrock beneath. In the ice covered area, four layers can be distinguished: 1) ice, 2) an unfrozen layer, 3) permafrost, and 4) a low resistivity feature at depth in the ice-free areas.

The first field campaign took place September 2012. The second field campaign took place in August/September 2013. The soundings were focused on ice profiles in order to obtain confirmation of the electromagnetic layering observed in 2012, and to gain a better spatial understanding about how the layering develops under thicker ice.

5.5.2.3 Soundings at the foreground of the ice sheet

All of the SAMPO profiles done at the foreground of the GrIS reveal a thin active layer (< 1 m), with a relatively high electrical conductivity (low resistivity). The modelled resistivities (20–300 Ωm) correspond with electrical conductivity ranging from 30 to 500 µS/cm. These values are consistent with measured values from Finnish clays and tills (Peltoniemi 1988).

The underlying frozen bedrock is highly resistive (≥ 10 000 Ωm). The range of resistivities of common non-mineralised crystalline rock types is rather narrow, largely because of comparable mineralogy and porosities. In theory, the fluid evolution of the site, resulting in variously saline groundwaters, together with irregular bedrock deformation, could generate considerable variations in electromagnetic properties. Increased effective porosity and/or increased salinity of the porewater reduces the resistivity. Porosity may increase due to brittle deformation or weathering. The impact of matrix salinity is not completely eliminated, even during freezing. It is typical that saline water films are forming around mineral grains, generating a network that supports electrical conductivity. As a result, the resistivity difference between unfrozen and frozen rock is not necessarily very large, although most of the existing water is transformed into ice. An often cited concept with respect to the enrichment of salts in cryopegs is the freeze-out process, which could enhance the contrast at the base of the permafrost, but both experimental and field investigations have failed to confirm the importance of freeze out in crystalline rocks (e.g. Stotler et al. 2009, 2012, Zhang and Frape 2002).

The weak conductor seen in almost all of the GAP permafrost profiles at 550–750 m depth could possibly indicate the base of permafrost. However, based on the temperature profiling of the GAP boreholes, it is known that the permafrost in the GAP study area extends to depths of 350–400 m. The most likely explanation of the weak conductor seen at 550–750 m depth is that the salinity of groundwater exceeds a certain threshold level and becomes observable.

The resistivity of the conductor is modelled to be in the range of 200–5000 Ωm. Assuming that the porosity in the rock is 0.5 % and the temperature is 2–4 °C at the depth of the conductor, then the salinity of the groundwater can be roughly estimated. The result of this examination strongly depends on the porosity model used. Paananen and Ruskeeniemi (2003) tested two different models based on 1) Archie's law applied for igneous and metamorphic rocks (Parkhomenko 1967) and 2) a fracture porosity equation (Grant and West 1965), taking into account the resistivity of the dry rock matrix. From these two models, the latter proved to provide more realistic water resistivities. Using 30 000 Ωm as the dry rock resistivity, as well as the values above, the calculated water resistivities are 1–30 Ωm. At standard temperature (25 °C), this corresponds to resistivity range of ~ 0.5–15 Ωm (20 000–700 µS/cm). Applying the linear correlation of conductivity and salinity, based on hydrogeochemical samples from Lupin mine, Canada (Ruskeeniemi et al. 2002), total dissolved solid (TDS) values of 400–12 000 mg/L are estimated. The groundwaters in DH-GAP04 fit within this range. Taking into account the corrections due to the known drilling water contamination (see Section 5.7.4), the electrical conductivity of the groundwater at the depth of around 600 m is in the range of 3000–4000 µS/cm, corresponding to TDS 2000–3000 mg/L.

The fact that this conductor is seen in the GAP study area in different geological environments almost 15 km apart, even below the ice sheet, suggests that it is related to a regional feature. As in the permafrost investigation, the present conclusion is that it is not possible to determine the permafrost thickness from the electromagnetic data.

5.5.2.4 Soundings on ice-covered area

At the time of the soundings in 2012, the ice was saturated with water, while the late summer in 2013 was cool and surface melting was slight. During the melting season, the water in the upper part of the ice is a mixture of meltwater and rain water. Both are distilled waters containing extremely low amounts of solutes. Thus, the electrical conductivity of the saturated ice layer is not significantly higher than that of dry ice (i.e. the ice is resistive). The area covered with the soundings is 3 km by 3 km and the longest profiles provide information about three kilometres inland from the margin. The applied method does not provide an accurate estimate of ice thickness, but the GPR soundings suggest that the ice thickness varies from 100 m to about 300 m farther inland. There is significant relief at the marginal ice field due to ice flow deformation and metwater action (channels, moulins, meltwater lakes), yielding considerable thickness variation along each profile.

An interesting finding of the SAMPO soundings is the low resistivity layer beneath the ice. Because it is electrically so distinct from the resistive ice and permafrost, it seems to indicate that it may be due to unfrozen conditions. The layer is rather thin (modelled 5–10 m) and not observed in all soundings, but, in general, it seems to extend more than a kilometre underneath the ice. It is not quite certain if this potentially unfrozen layer is in sediment or bedrock, but the high conductivity/low resistivity would suggest porous media because it is highly unlikely that saline water would exist so close to the base of melting ice sheet. High solid/water ratios in sediments with abundant silty or clay-size material would increase the electrical conductivity. The model resistivity of the layer is 300–700 Ωm, corresponding to 10–30 µS/cm, which is within the range measured for water saturated till (Peltoniemi 1988). Ice saturated with meltwater has significantly higher resistivity (> 10 000 Ωm) than this, so wet ice cannot explain the observation.

Regardless of the media, this section probably allows subglacial flow. This may also be the reason why the layer exists. Flowing water transports energy and prevents freezing. It is uncertain if the flow could be maintained during the cold winter, when the cold from both the surface and the permafrost limits flow.

The characteristics of the permafrost are the same as in ice-free areas. The rock is highly resistive, which is indicative of frozen rock, but it is not possible to define the exact depth to the base of permafrost. The soundings in 2013 indicate that permafrost beneath the ice extends at least two kilometres from the ice margin towards the ice divide in the study area. The sounding points located farther away from the ice margin suggest that the bedrock is probably unfrozen.

The deep conductor discussed above (possibly saline groundwater) below 550 m depth is observed beneath the ice as well.

5.5.3 Taliks and their development

Repeated temperature profiling of borehole DH-GAP01, which was drilled to intersect a talik, shows that as soon as the borehole advances beneath the lake basin, the bedrock temperature increases above zero degrees Celsius. The temperature stabilises quickly to about 1.3 °C and is maintained along the profile down to the deepest monitoring point at the depth of 136.57 m (Figure 5-29).

Geothermal modelling was applied to investigate the nature of the talik and determine whether or not it extends through the permafrost or whether it is an open talik that closes deeper down. The constraints for talik formation were of interest as well, such as: 1) how large must the lake be in order to form a talik, 2) how long does it take for the lake to develop into a talik, and 3) how do the chosen boundary conditions affect the results (Harper et al. 2011). The heat transfer in bedrock was studied by 2D conductive models using the simulation code, Processing Shemat (Clauser 2003). The steady state temperature at the lake bottom is a critical boundary condition for talik formation.

In order to evaluate this boundary condition, the lake bottom temperatures were measured from the lake ice in May 2010. It was presumed that the temperatures would be at an annual minimum after the cold winter just before the onset of the melting season. An Antares (0.001 °C resolution) temperature probe was lowered at regular intervals on a measuring tape, allowing the temperature probe time to calibrate at each measuring depth. The data was then processed to create temperature profiles with depth. The results show that the minimum temperatures in the lake bottom are above +3.4 °C year round, confirming that the temperature conditions necessary to result in talik formation exist (Harper et al. 2011).

In the talik simulations performed, the basal heat flow was set to a value of 38 mW/m^2, which was calculated based on the data from borehole DH-GAP03 (see below), −4.4 °C was taken as the initial ground surface temperature and +4 °C was used as the upper boundary condition (lake bottom temperature) for the talik. Latent heat of porewater is ignored due to the very low porosity (average 0.48 %) measured from the drill core samples (Harper et al. 2011).

The main conclusion regarding the development of taliks was that under steady state conditions, as defined above, through taliks are likely to form through a 300 m deep layer of permafrost, if the lake is wider than about 200 m (Harper et al. 2011). Open taliks (open to surface, confined by frozen ground beneath) are forming beneath lakes that are about 100 m wide. It is noteworthy that, according to our model, taliks form rather quickly in low-porosity crystalline rocks. If a large enough lake basin is formed on frozen ground, an open talik can be observed in less than 100 years, and a through taliks can form in less than 500 years (Figure 5-35).

Another possible cause for talik formation in the research area could be that the lake basins were present already when the climate began to deteriorate. This is a more plausible scenario than the thawing through concept, based on the deglaciation history of the area. Retreat of the ice margin farther to the east (relative to the present location) during the Holocene Climate Optimum (see Section 2.3), and the cooling of the climate and re-advance of the ice sheet after 5000 years BP, suggest that the permafrost may be younger than the lakes. In this case, the lakes insulated the bedrock from the cold air resulting in the bedrock beneath remaining unfrozen, while the ground surrounding the lakes froze.

In either case, what is most relevant is that surface water bodies influence the distribution of permafrost and the talik-related recharge-discharge areas, and changes in these can be very rapid in comparison to geological time scales (Harper et al. 2011). Considering the following observations: 1) permafrost in the area is about 350 m thick; 2) stable positive temperatures, above 1 °C, are measured at 140 m depth (Section 5.5.1); 3) geochemically more mature groundwater is observed in the deeper part of the borehole (Section 5.7.4); 4) geothermal modelling results, 5) hydraulic gradient exists with depth below the lake (Section 5.6.2); and 6) glacial history of the site, all data suggest the presence of a through talik under the Talik lake, and others may exist under other comparable water bodies.

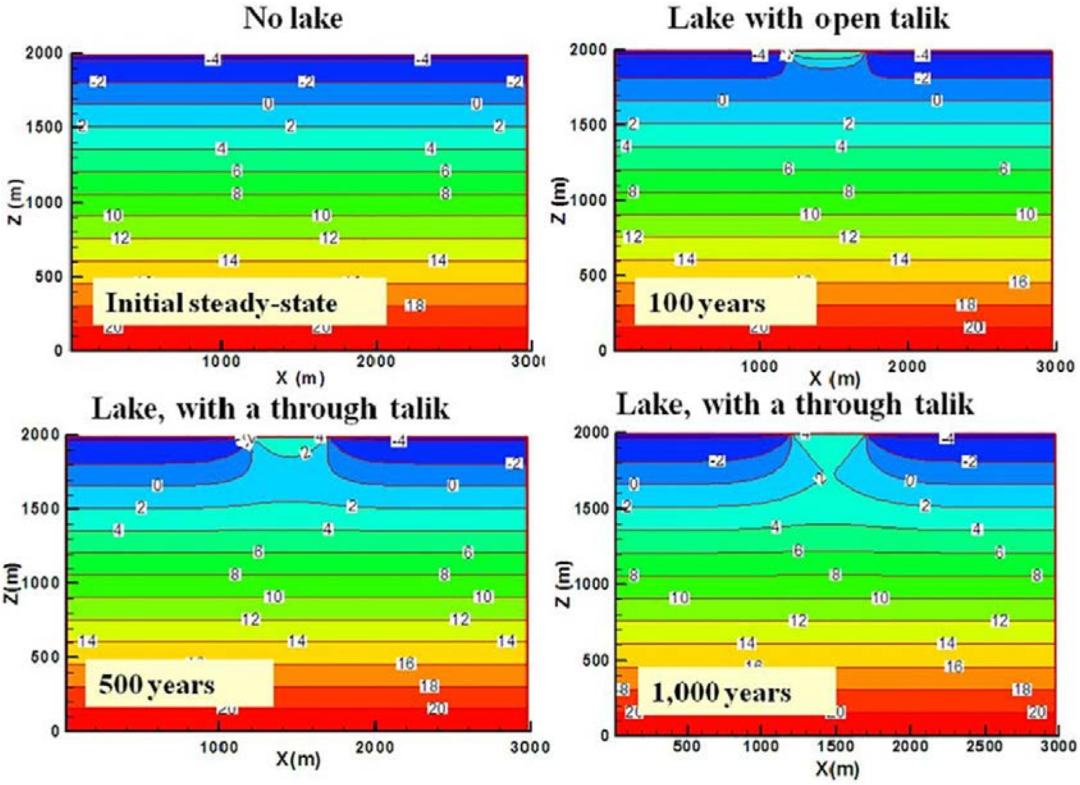

Figure 5-35. Development of a talik through a 300 m deep layer of permafrost. Initial ground surface temperature is assumed to be –4.4 °C and the lake bottom temperature +4 °C appears at year zero. Basal heat flow of 38 mW/m^2, thermal conductivity of 3 W/mK and porosity 0 % (i.e. porosity was neglected) were applied for the simulation (Harper et al. 2011).

The GAP was also able to obtain some information about the hydrogeological nature of the talik beneath the Talik lake. The co-varying pressures in the lake and the lower part of DH-GAP01 indicate good hydraulic connection. The lower hydraulic heads in the borehole compared to the lake, and the continuous downward gradient, suggest that processes in the lake influence the hydraulic conditions at depth, and that the talik might be currently recharging (Section 5.6.2, Johansson et al. 2015a).

Geochemical observations do not provide direct answers to the question of whether the talik is discharging or recharging. Both the chemical and isotopic compositions of the lake water and borehole water are distinctly different (e.g. Section 5.7.4 Harper et al. 2011 and Harper et al. 2016). The significant difference in the $\delta^{18}O$ fingerprint (−12 ‰ vs. −21 ‰, respectively) suggests that mixing has not been extensive. There is no tritium in the borehole water, indicating that there has been no mixing with meteoric waters during the past 60 years. However, the calculated travel time (66–160 years) from surface down to the borehole section is long compared to tritium's half-life (12.3 years), making the observation inconclusive in terms of recharge/discharge speculation. The $^{87}Sr/^{86}Sr$ signature in the borehole water is 0.7075, while the value for Talik lake water is higher (0.7385). It is noteworthy that the Talik lake $^{87}Sr/^{86}Sr$ value is lower than other lakes sampled in the area (Section 5.7.4.2).

More field work would be required to fully understand the hydrogeological system in the talik. Complications arise from complex hydrogeological routing (shallow circulation), long travel distances and small volumes of water involved in flow. Additionally, changes in hydrogeological conditions (e.g. due to the oscillation of the ice sheet and subsequent bedrock movements) may change the direction of the vertical gradient, resulting in alternating recharge and discharge conditions. Shallow and deep waters may represent the results of temporally different mixing regimes. Theoretically, it is possible that part of a lake basin is discharging, while recharge is observed in some other part (Bosson et al. 2010, Vidstrand 2015)[1].

The Leverett Spring (also refered as Pingo Spring), in front of the Leverett Glacier (for location see Figure 5-65), represents another type of talik structure. van Everdingen (1998) defined the term hydrothermal talik for a structure where pressurised flow forces water (temperature > 0 °C) through permafrost and ensures flow is on-going year round. Note that the term does not necessarily imply that hydrothermal waters would be involved, but that the talik formation is based on the heat supply of the flow. This seems to be the case with respect to Leverett Spring. The spring is located in the center of a rounded cone shaped formation with a diameter of about 70 m (Figure 5-74; Aaltonen et al. 2010). The shape has been described by Scholz and Baumann (1997) as a collapsed pingo. In May 2010, it was discovered that the spring continued flowing throughout the winter, resulting in the build up of a large ice mound over the outlet and indicating that the water was under pressure (Harper et al. 2011). The area is in a valley and most likely underlain by a major lineament. The origin of the water is unclear. It is not meltwater or groundwater with hydrothermal finger printing, but may be a mixture of these (see Section 5.7.4). No other similar springs have been observed in the GAP research area.

5.5.4 Geothermal properties of the bedrock

Model calculations, DTS temperature profiling and petrophysical data from DH-GAP03 were used to obtain the first estimate for the steady state *Heat Flow Density* (HFD). The upper 150 m of the temperature data was omitted to reduce the influence of the recent (past 15 years) warming observed in the upper part of the profile (Figure 5-36). Using the temperature gradient, 13.9 mK/m, determined at 150–300 m, and the average measured thermal conductivity values (9 determinations) for the rocks in the test section of 2.50 ± 0.13 W/mK, resulted in a HFD value of 34.8 ± 1.9 mW/m^2 (Harper et al. 2011).

It should be noted that this value is not the deep undisturbed steady state heat flow value and is still affected by the temperature fluctuation induced by past glacial stages and Holocene variations (extends down to 1–2 km). The average HFD (apparent heat flow, not corrected for climatic effects) from the deeper DH-GAP04 borehole, calculated between 100–650 m, is 27.2 ± 1.8 mW/m^2.

---

[1] Vidstrand P, in prep. Concept testing and site-scale groundwater flow modelling of the ice sheet marginal-area of the Kangerlussuaq region, Western Greenland. SKB R-15-01, Svensk Kärnbränslehantering AB.

The calculated HFD values are considerably lower than previous HFD estimates for this part of Greenland, e.g. the 58 mW/m^2 estimate by Shapiro and Ritzwoller (2004) and the 75 mW/m^2 value calculated by Fox Maule et al. (2009).

The HFD values from DH-GAP03 and DH-GAP04 are not corrected for climatic effects, i.e. the long term palaeoclimatic variations have not been considered. If a climate correction were to be made, the values would be somewhat higher, but still not as high as previous estimates. Furthermore, the difference between the new and old values is well within the large expected variability of HFD values in this type of geologic setting (cf. Näslund et al. 2005, Maule et al. 2009).

5.5.5 Main conclusions from the permafrost investigations

Temperature profiling in the GAP bedrock drillholes shows that close to the ice margin, and at higher elevations, the permafrost thickness reaches ~ 350–400 m. The thick permafrost probably continues below the ice sheet. Electromagnetic soundings suggest that, east of DH-GAP04, permafrost in the bedrock extends two kilometres inward from the margin of the ice. Because the method is not able to observe the base of permafrost, however, it is not known if the permafrost thickness changes. It is likely that the permafrost gets thinner farther in under the ice sheet since areas far away from the present margin have been subject to a shorter time of permafrost development, and hence development of thinner permafrost because they experienced shorter duration of ice free conditions compared to areas close to the present margin. In addition, areas farther in from the margin have experienced the longest time of melting of subglacial permafrost from below by geothermal heat without potential for permafrost growth (i.e. the present period of warm-based ice coverage).

A thin unfrozen layer, detected with SAMPO, between the ice and the permafrost seems to extend at least a kilometre inland from the margin. This is consistent with temperature profiles collected from ice holes, which show that the temperature at the ice sheet bed is 0 °C, both close to the ice margin and farther in on the ice sheet (Section 4.6). The warm-based conditions are caused by heat generated within the ice sheet (from internal deformation and from basal sliding) and by the geothermal heat flux. In addition, meltwater flow in a porous sediment layer may assist in the thawing. More electromagnetic soundings are required before conclusions can be made about the spatial coverage of these features, for example, in areas farther up-glacier. Even if a melted layer below the ice sheet is limited to sediment covered ice marginal areas, it provides hydrogeologically important pathways for meltwater, possibly with subsurface continuations in the sediment-filled river valleys.

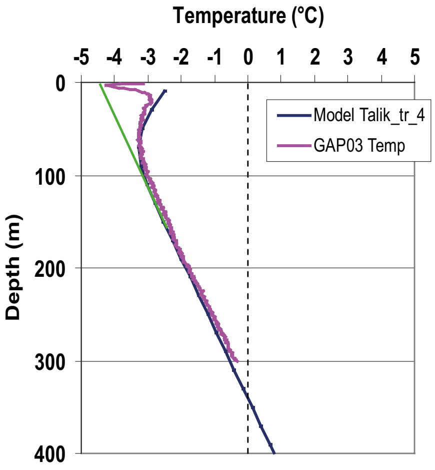

Figure 5-36. *DTS temperature profile from DH-GAP03 (pink) and a model curve fitting (blue) used for HFD calculation. The green dashed line suggests that initial ground surface temperature has been about −4.4 °C during the growth of deep permafrost.*

Through taliks are common in the area. All larger (i.e. a diameter > 400 m) non-meltwater lakes are assumed to maintain a talik. How they contribute to the hydrogeology depends on the properties of the lake bottom sediments, the underlying bedrock, and the ambient hydraulic gradients. Taliks in fractured bedrock (e.g. along deformation zones) are more likely to be hydrogeologically active than taliks in sparsely fractured rock.

The role of taliks in the periglacial hydrogeology currently is unclear. Based on the various studies related to the Talik lake, it is known that through taliks occur in the area. Potential taliks are located at different elevations along the entire drainage transect from the ice margin down to Kangerlussuaq fjord. It is reasonable to assume that many of them are located in fractured bedrock, or even in deformation zones providing pathways for vertical flow (i.e. discharge and recharge). It is difficult to assess the nature of the taliks (i.e. whether they are discharing or recharging). Presently, there is no field information from other potential taliks, and hydraulic gradients in the area are difficult to interpret. Topography suggests that flow is westward toward the Kangerlussuaq fjord, and also northward under the Isunnguata Sermia outlet glacier, where the ice bed is considerably depressed. Further, fluctuations, or reversals in the hydraulic gradient at local and/or regional scales over the course of the annual melting cycle, or in relation to the past movement of the ice margin, are likely. Thus, the taliks, and talik related waters, may indicate different hydraulic systems depending on the timing of the investigations and the part/depth of the system studied.

5.6 Hydrogeology

5.6.1 Hydrogeology in the glacial-periglacial system

The hydrologic cycle in cold areas is greatly affected by the presence of permafrost (White et al. 2007), which has a low hydraulic conductivity, and hence reduces both groundwater recharge and discharge. In areas with continuous permafrost, groundwater recharge and discharge are restricted to taliks (e.g. French 2007, Lemieux et al. 2008, Bense et al. 2009, Frampton et al. 2011, Kane et al. 2012, Weaver 2003, Bosson et al. 2013). Very few studies of sub-permafrost groundwater flow have been performed and the conditions for groundwater flow below permafrost are, consequently, poorly understood.

The Kangerlussuaq area has been characterised reasonably well from a glacial hydrological point of view (e.g. Mernild et al. 2012, van As et al. 2012). The permafrost hydrology and sub-permafrost groundwater system are more difficult to characterise. SPC has drilled two bedrock boreholes, DH-GAP01 and DH-GAP04, in order to determine hydraulic properties, groundwater levels and water chemistry. DH-GAP01 is assumed to be a through talik and DH-GAP04 extends below the thick permafrost layer adjacent to the ice sheet margin of the Isunnguata Sermia Glacier. Ambitious efforts have been made to look for indicators of discharge of deep groundwater in the through talik and for indicators of recharge of glacial meltwater below the thick permafrost in order to characterise system dynamics.

5.6.2 Evaluation of hydraulic tests in DH-GAP01

5.6.2.1 Pressure responses during water sampling

Two pressure response tests were performed in borehole DH-GAP01 in September, 2010 (Harper et al. 2011). The tests were run in conjuction with pumping and sampling for water chemistry analysis. The objective was to obtain pressure data for evaluation of transmissivity, T (m^2/s), and hydraulic conductivity, K (m/s), of the rock surrounding the borehole. The tested interval in DH-GAP01 was 130–191 m vertical depth, i.e. the 71 m long section between the packer and the bottom of the borehole; see Section 5.3.2 for the instrumentation.

When water was pumped from the borehole for water sampling, the downhole pressure responses were monitored with a pressure sensor. The pressure recovery following the termination of the water removal was evaluated, which allowed calculation of transmissivity and hydraulic conductivity using evaluation methods for so-called slug tests. That is, the pumping had short durations and involved small water volumes, implying that the evaluated parameters relate directly to the rock immediately surrounding the borehole.

The recovery data were evaluated using AQTESOLV ver. 4.50 professional software (http://www.aqtesolv.com/) and the following commonly employed methods: Cooper-Bredehoeft-Papadopulos (Cooper et al. 1967), Bouwer-Rice (Bouwer and Rice 1976) and Hvorslev (1951). Potential influence of borehole skin was tested using the KGS method (Hyder et al. 1994), whereas the Barker-Black method (Barker and Black 1983) was used to evaluate the transmissivity of fractures and the hydraulic conductivity of the rock mass between fractures. Measured pressures, p (Pa), were converted to fresh water pressure heads, h_p (m), by assuming a water density (ρ) of 1000 kg/m^3 and a gravitational acceleration (g) of 9.81 m/s^2:

$$h_p = \frac{p}{\rho g}$$

The results of the evaluation of the two pressure response tests suggest a total transmissivity of ~ 10^{-6} m^2/s and a rock-mass hydraulic conductivity of ~ 10^{-8} m/s (Harper et al. 2011).

5.6.3 Evaluation of hydraulic tests in DH-GAP04

5.6.3.1 Posiva flow logging

Information on the location of water-conducting fractures was a prerequisite for a successful placement of the downhole packers and the associated instrumentation (sensors) for pressure, electrical conductivity and temperature measurements, see Section 5.3.2.3. Therefore, flow logging was done in DH-GAP04 prior to the instrumentation of the borehole (Harper et al. 2011).

The flow logging was done using the PFL (Pöllänen et al. 2012), which provides a flexible and relatively quick method to identify the positions of water-conducting fractures (Ludvigson et al. 2002). Although the motivation to do the PFL testing was to find the best location of the packers for water sampling, the data from the PFL survey may also be useful for hydrogeological characterisation of the tested bedrock volume, in particular the specific capacity (flow rate per unit head change, $Q/\Delta h$, m^3/s) of each water-conducting fracture intersecting the borehole, (see below).

PFL measures the flow of water into or out of a defined test section and observes simultaneously a number of other parameters. Besides specific capacity of intersected flowing fractures, the PFL method also measures the hydraulic head in these fractures, the electrical conductivity of the water (both borehole water and the fracture-specific water), the single point resistance of the borehole wall, and the temperature of the borehole water. The specifications for the sensors used are given in Table 5-4. The PFL method is based on tracking of both the dilution (cooling) of an electronically generated thermal pulse and transfer of the pulse by the moving water (Pöllänen et al. 2012). During measurement, the test section of interest is isolated with rubber disks, which improves the detection of poorly flowing fractures. With the PFL flow meter, it is theoretically possible to measure flow rates between 0.5 to 5000 mL/min, corresponding to 8.3×10^{-10} to 10^{-5} m^2/s for a head change of 10 m.

The interpretation of PFL fracture transmissivity T_{PFL} (m^2/s) assumes that the well equation by Thiem (1906) is applicable, which postulates confined steady state flow to a line sink. As described in Pöllänen et al. (2012), T_{PFL} (or just T) was evaluated as the specific capacity of each fracture (cf. above).

Table 5-4. Range and accuracy of PFL sensors (Pöllänen et al. 2012).

Sensor	Range	Accuracy
Flow	30–300 000 mL/h	± 10 % of curr.value
Temperature (central thermistor)	0–50 °C	0.1 °C
Temperature difference (between outer thermistors)	−2 – (+2) °C	0.0001 °C
Electrical conductivity of water (EC)	0.02–11 S/m	± 5 % of curr.value
Single point resistance	5–500 000 W	± 10 % of curr.value
Groundwater level sensor	0–0.1 MPa	± 1 % full-scale
Air pressure sensor	800–1 060 hPa	± 5 hPa
Absolute pressure sensor	0–20 MPa	± 0.01 % full-scale

Due to the likelihood of freezing there was no time to await steady state flow conditions, and hence the PFL measurements were done only two days after the completion of drilling. This implies that the PFL-measurements were carried out during transient flow conditions.

Before the downhole measurements with the PFL method started, the ambient pressure head in the fully open borehole was measured at the top of casing (TOC) together with the flow of water out of the borehole. However, as the initial ambient pressure head was artesian due to the backflow of water forced into the bedrock fractures during drilling, the measurement of the pressure head was achieved by extending the casing by attaching a nylon tube to the casing. The recorded water level in the tube was ~ 3.52 m above ground surface (2.99 m above TOC). The flow at the TOC was estimated to be about 2.85 L/min. The ratio of these values suggests a gross value of the total transmissivity at the completion of the drilling of ~ 9×10^{-5} m^2/s for the unfrozen parts of DH-GAP04.

Based on the temperature data from the nearby DH-GAP03, it was assumed that the frozen ground conditions would extend down to ~ 300 m vertical depth in DH-GAP04 (SKB 2010b, Harper et al. 2011). As a precaution, a few short test measurements were carried out high up in the borehole starting at 184 m borehole length. Survey data obtained from these measurements confirmed that there was no measurable flow of water to or from the borehole between 184 and 400 m borehole length.

For the actual logging, a head change (drawdown) of 12 m below the TOC was generated with a submersible pump. The pumping rate varied from 16.5 L/min to 10.0 L/min (Pöllänen et al. 2012) and the testing started well above the assumed base of permafrost, from 274 m borehole length downward. The lowest test section was 675–685 m borehole length, leaving two metres from the bottom of the borehole untested. A 10 m long test section was used with sequential measurements every two metres (i.e. a two metre overlap). The total error in position, including the strain of the cable, was ± 3.3 m for this testing geometry.

Table 5-5 shows PFL the calculated transmissivities (T_{PFL}, or T) and hydraulic heads (given as fresh water head) of nine 2 m test sections with measurable flow. Figure 5-37 provides a schematic presentation of the relevant hydrogeological units in the surroundings and their locations in the borehole. More detailed information is given in the hydrogeological composite plot (Figure 5-63).

The following is noted in particular:

- All calculated fracture-heads, except for the test section at the bottom of the borehole, are higher than the ambient head in borehole (Table 5-5). The highest fracture-head (537.20 m) was encountered for the fracture at 600.20 m borehole length. Borehole-head at the same depth is 527.83 m. For comparison, the ellipsoidal elevation of the drill site where the TOC of DH-GAP04 is situated is 525.66 m and the vertical depth from the fracture at 600.20 m borehole length to the ground surface at the nearby margin of Isunnguata Sermia is about 40 m less, i.e. ~ 485 m elevation.
- The sum of all measured positive downhole flows (flows to the borehole) during ambient conditions, i.e. without pumping, was ~ 3.5 L/min. At the same time, the measured flow out of the TOC was 2.85 L/min. Thus, there is a flow difference of 0.65 L/min or 39 000 mL/h. The reason for this imbalance is not resolved. The only negative flow (flow out from the bore borehole) is 179 mL/h, located at 682 m. Potentially, there could be more outflow in the unmeasured bottom part of the borehole.
- The pumping rate during the measuring period varied between about 10 and 16.5 L/min. However, the sum of all measured downhole flows with the PFL tool during pumping was 8.4 L/min. The difference may result because flows in the individual sections along the borehole vary in time. Again, another explanation is that there may be flowing fractures in the unmeasured bottom part (two metres) of the borehole.

Table 5-5. Summary of the hydraulic testing results from DH-GAP04 (Pöllänen et al. 2012). The reference elevation for the measurements was the TOC. Fractures highlighted by yellow shading are located within the mid-section.

Length (m)	Head0 (m)	Flow0 (mL/h)	Head1 (m)	Flow1 (mL/h)	T_{PFL} (m^2/s)	Head of fracture (m)	Comments
415.70	526.41	–	514.35	103	2.35E−09	–	*
548.00	527.00	3340	515.05	8390	1.16E−07	534.90	
551.60	526.98	16 300	515.01	50 500	7.86E−07	532.69	
584.60	527.09	73 500	515.20	182 000	2.51E−06	535.14	
600.20	527.23	119 000	515.67	257 000	3.29E−06	537.20	
604.00	527.18	1040	515.25	3570	5.82E−08	532.08	*
638.40	527.34	214	515.43	653	1.01E−08	533.15	
670.00	527.53	–	515.61	68	1.57E−09	–	*
682.00	528.10	−179**	516.25	140	7.40E−09	521.45	*

* Uncertain fracture. The flow rate is less than 30 mL/h or the flow anomalies are overlapping or they are unclear because of noise.

** Negative flow means flow out from the borehole.

Length = Length along the borehole from reference length to the fracture (m) = borehole length
Head0 = Fresh water head in the borehole without pumping (metre above sea level)
Flow0 = Flow from the fracture to the borehole without pumping (mL/ h)
Head2 = Fresh water head in the borehole with pumping (metre above sea level)
Flow2 = Flow from the fracture to the borehole with pumping (mL/ h)
T_{PFL} = PFL Transmissivity of the fracture (m^2/s)
Head of fracture = Fresh water head in the fracture (m)
Comments = Additional information

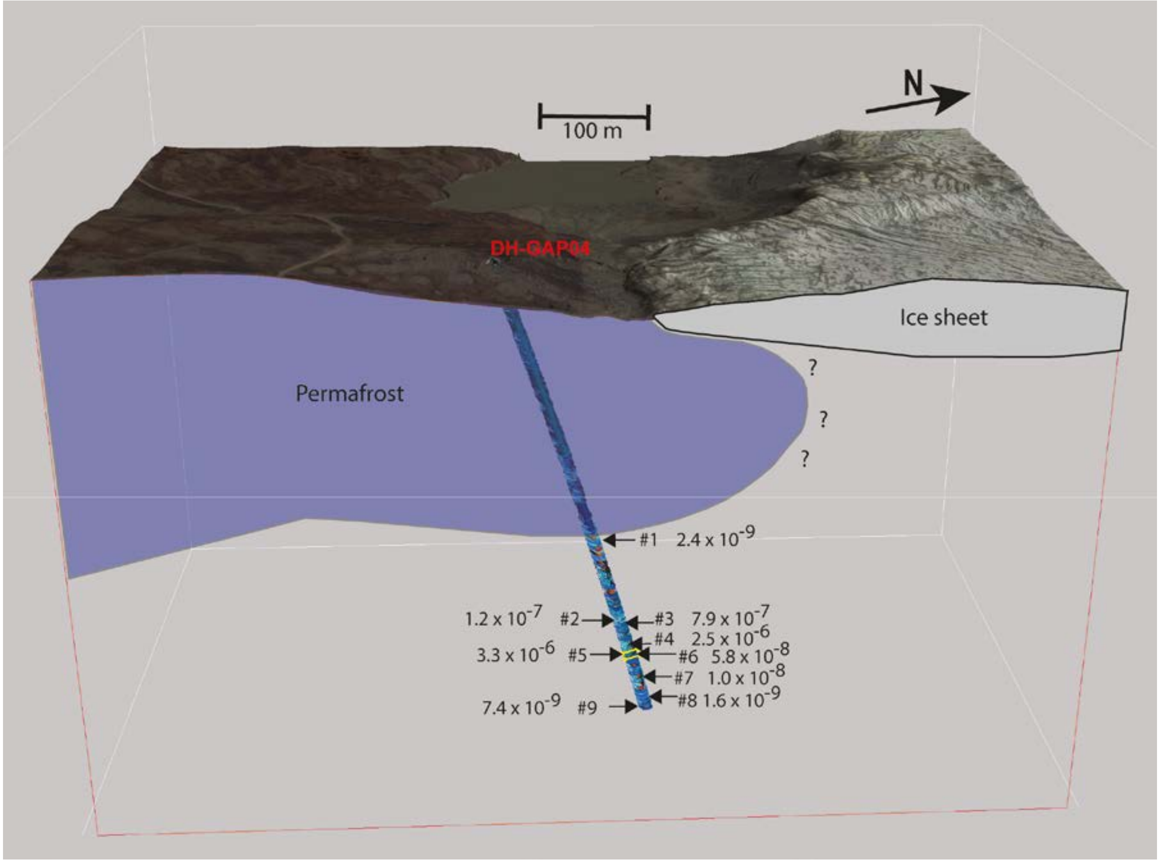

Figure 5-37. *Schematic presentation of the topography and the nine water-conducting features (indicated by arrows) with measured specific capacities (flow rate in m^3/s per metre of drawdown) in DH-GAP04. The two yellow lines at ~ 600 m borehole length indicate the location of packers. Purple area denotes permafrost. The base of the permafrost is defined as the 0-degree isotherm.*

5.6.3.2 Pressure responses during water sampling

The lack of measurable water conductivity between 184 and 415 m borehole length, combined with the permafrost information from the nearby DH-GAP03 (SKB 2010b, Harper et al. 2011), indicate that permafrost may extend down to ~ 400 m borehole length in DH-GAP04. This was later confirmed by temperature profiling (see Section 5.5.1.3. The fracture zone at 600.20 m was selected as the main target for the hydrogeochemical investigations, i.e. this section was chosen as the primary water sampling section. The section was isolated with two packers, resulting in three monitoring sections Sect-up, Sect-mid and Sect-low, see Section 5.3.2.3.

Although the downhole instrumentation designed for water sampling was not optimal for the evaluation of the hydraulic properties of the bedrock, hydraulic evaluation of pressure data collected during the water sampling campaigns in September 2011 and September 2013, was carried out.

During the sampling campaign in September 2011, a total of 68 pumping cycles were performed in the three monitoring sections. The water volume removed during each cycle was ~ 5 L and the duration of one pumping cycle ranged between 25 and 30 minutes, including five minutes to pump the water sample to the surface.

Due to the long scanning time (5 minutes) for pressure recordings during water sampling, it was not possible to evaluate each pumping cycle separately (e.g. by slug test analysis). Pressure responses in the sections during water sampling in 2011 are shown in Figure 5-38, Figure 5-39 and Figure 5-40.

During the sampling campaign in September 2013, a total of 526 pumping cycles were performed. For the hydraulic evaluation, five pumping cycles were performed in each section before water sampling occurred. Although the scanning time was shortened to 6 seconds between recordings, it was not possible to evaluate each pumping cycle separately (e.g. by slug test analysis). The head variations in the sections during pumping are shown in Figure 5-41, Figure 5-42 and Figure 5-43.

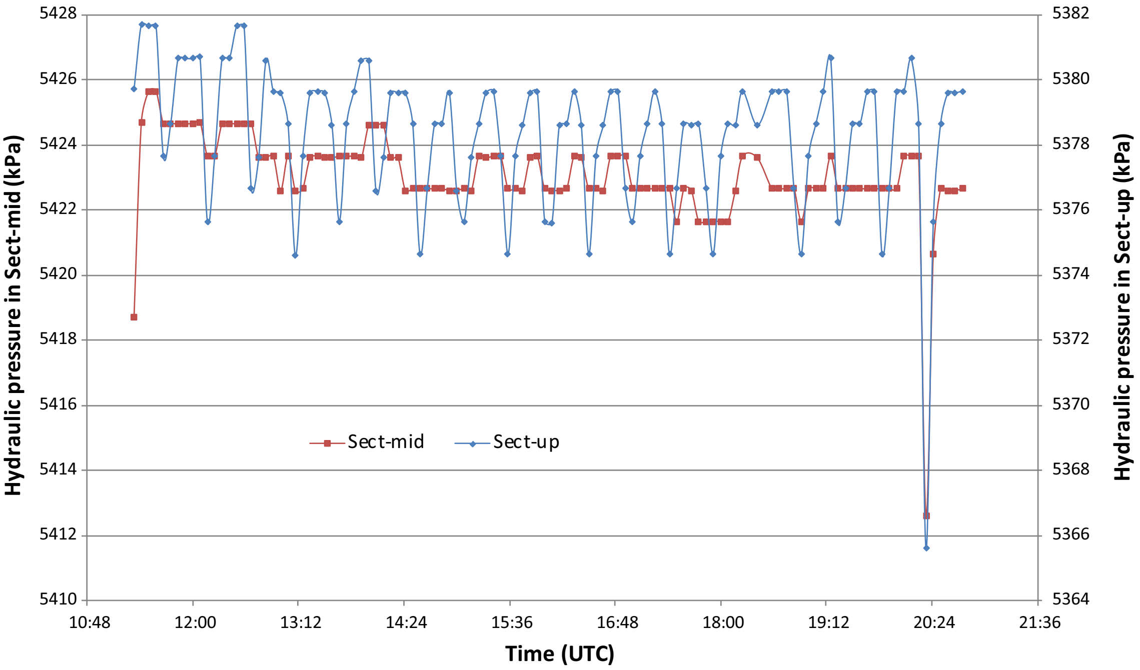

***Figure 5-38.** Pressure responses in DH-GAP04 Sect-up and Sect-mid during pumping in Sect-up, September 10, 2011.*

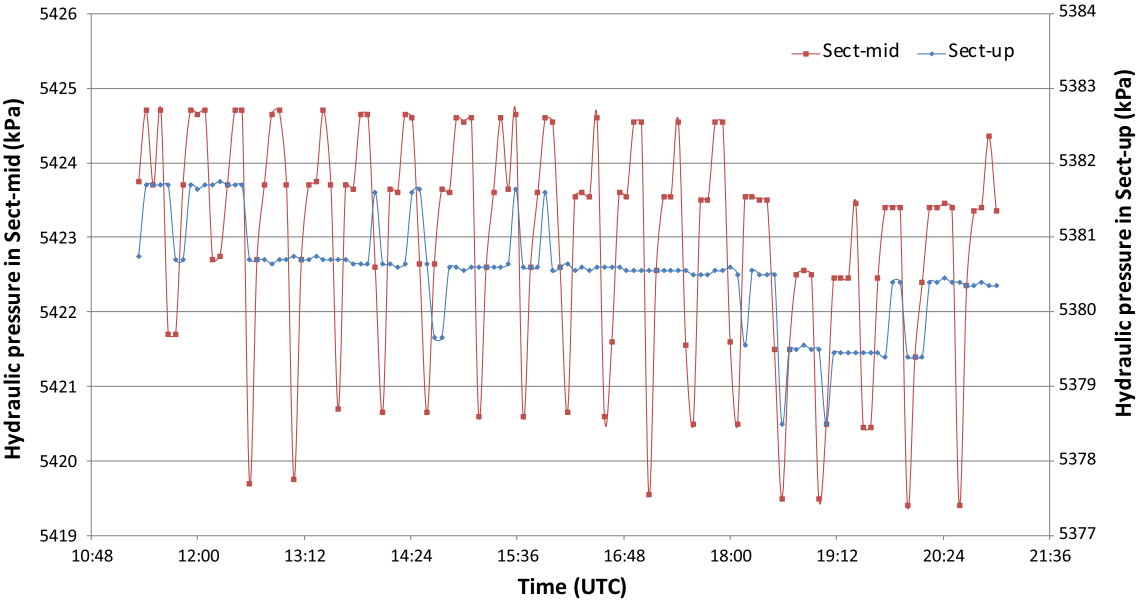

Figure 5-39. *Pressure responses in DH-GAP04 Sect-up and Sect-mid during pumping in Sect-mid, September 9, 2011.*

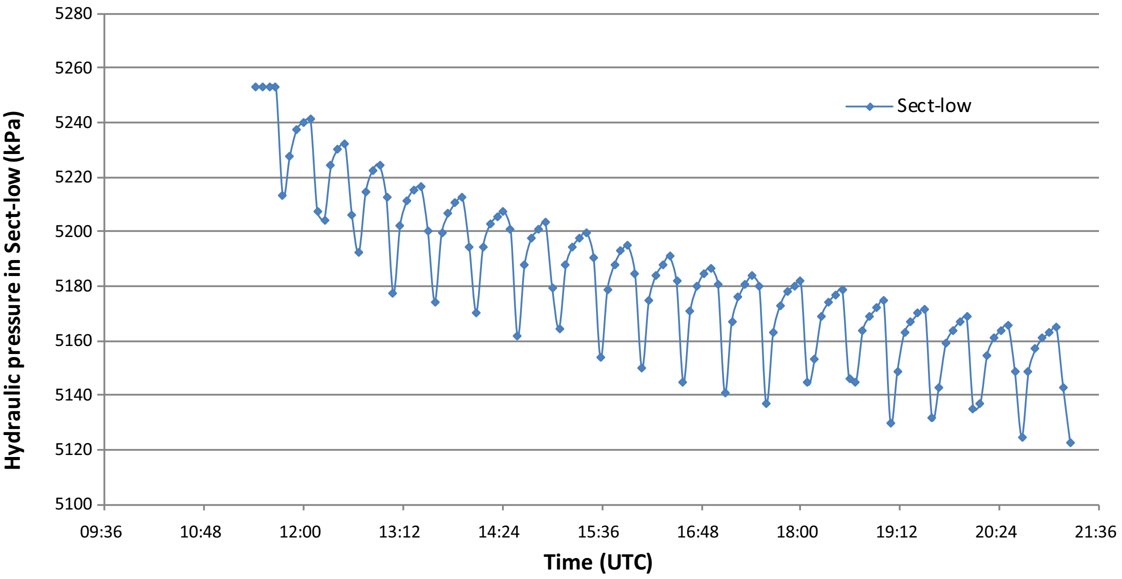

Figure 5-40. *Pressure responses in DH-GAP04 Sect-low during pumping in Sect-low, September 8, 2011.*

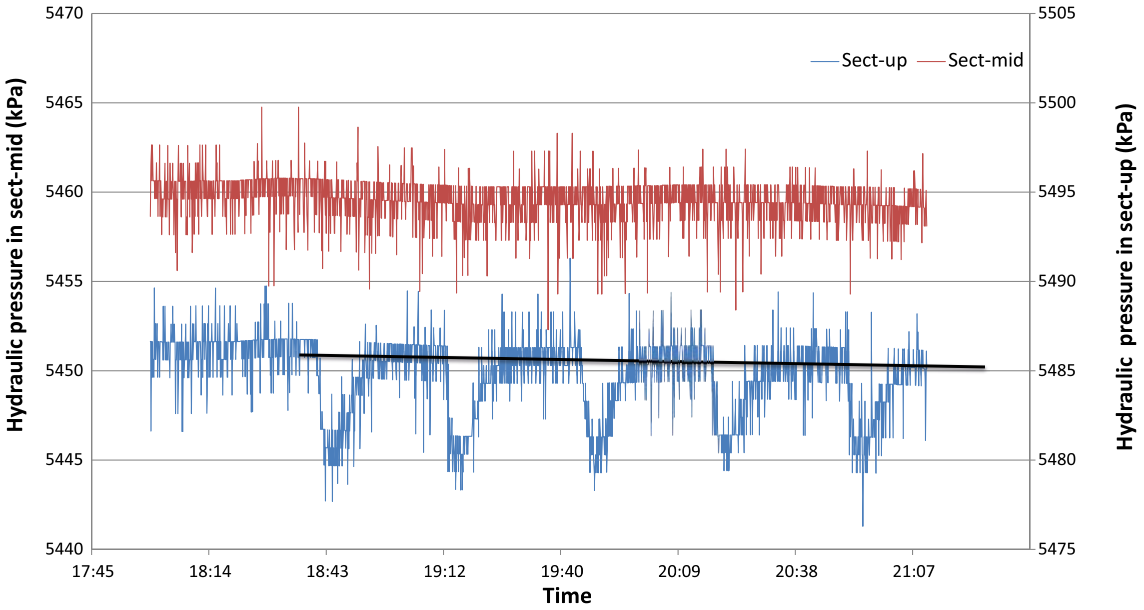

Figure 5-41. *Pressure responses in DH-GAP04 Sect-up and Sect-mid during pumping in Sect-up, September 4, 2013. Black line represents the pressure decrease during pumping.*

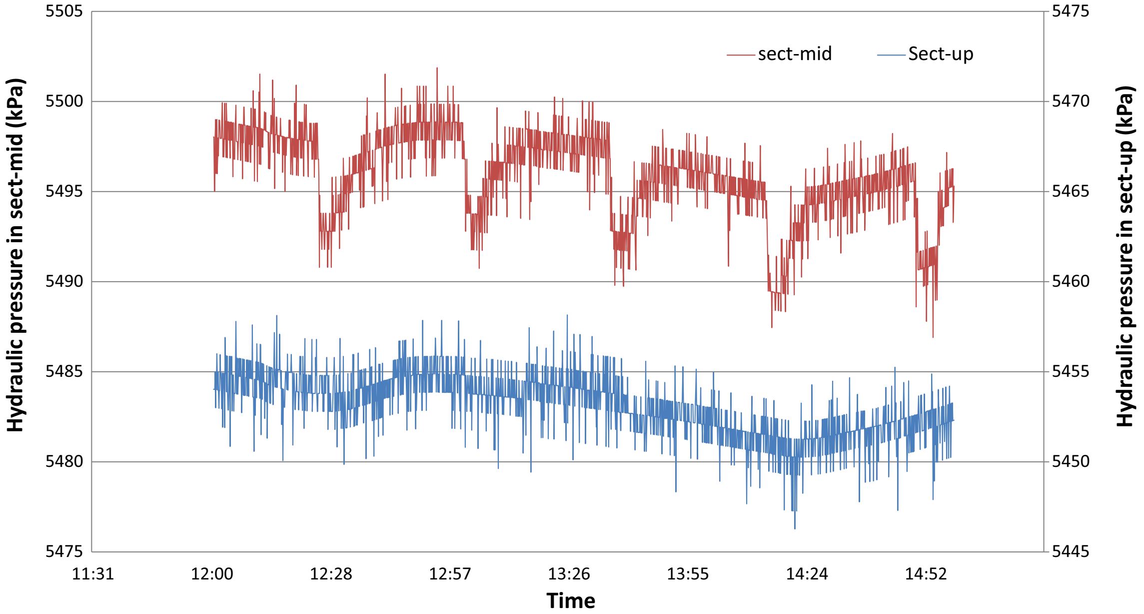

Figure 5-42. *Pressure responses in DH-GAP04 Sect-up and Sect-mid during pumping in Sect-mid, September 4, 2013. Pumping seems to be affected by some other external pressure disturbance. The air pressure is only decreasing about 0.5 kPa during the pumping period.*

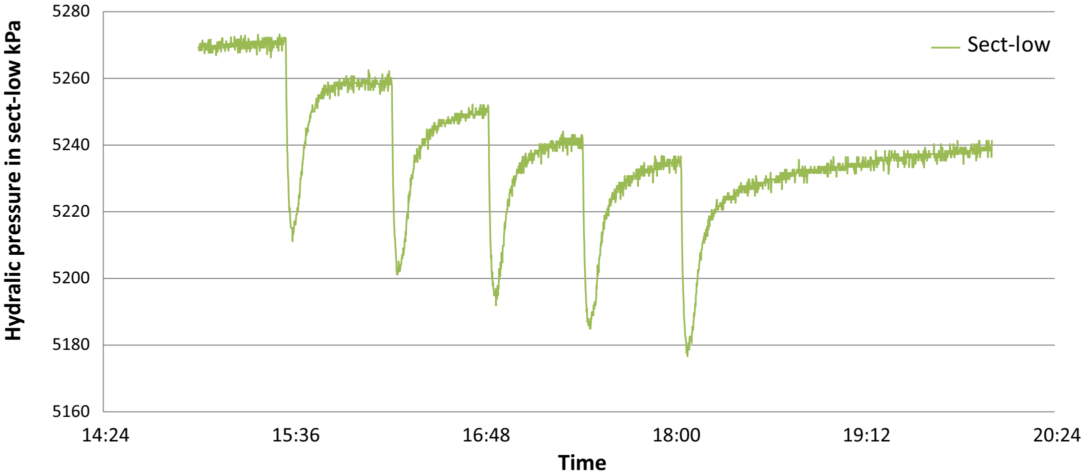

***Figure 5-43.** Pressure responses in DH-GAP04 Sect-low during pumping in Sect-low, September 4, 2013.*

The estimation of the specific capacity (transmissivity) of each monitoring section from the water sampling in September 2011 is shown in Table 5-6. The values of the specific capacities assume steady state flow conditions.

In addition, a transient estimation was carried out for Sect-low, rendering a transmissivity value of ~ 1.7×10^{-7} m^2/s (see Figure 5-44). The recovery data evaluation was made according to Dougherty-Babu's solution in AQTESOLV software.

Table 5-7 shows the corresponding results for the upper and lower monitoring sections from the water sampling in September 2013.

Table 5-6. Specific capacity Q/Dh in the DH-GAP04 monitoring sections during the September 2011 assuming steady state flow conditions.

Section	Head change (m)	Average flow rate (m^3/s)	Specific capacity (m^2/s)
Sect-up	Approx 0.1	2.90×10^{-6}	3×10^{-5}
Sect-mid	Approx 0.15	3.03×10^{-6}	2.0×10^{-5} *
Sect-low	9.0	2.86×10^{-6}	3.2×10^{-7}

* Estimated values of specific capacity are too high due to the hydraulic contact between Sect-up and Sect-mid and also uncertain due to the uncertain values of the actual drawdown.

Table 5-7. Specific capacity Q/Dh in the DH-GAP04 monitoring sections sections during the September 2013 assuming steady state flow conditions.

Section	Head change (m)	Average flow rate (m^3/s)	Specific capacity (m^2/s)
Sect-up	Approx 0.17	3.1×10^{-6}	2×10^{-5}*
Sect-mid	–	–	– **
Sect-low	3.6	2.8×10^{-6}	7.8×10^{-7}

* Estimated values of the specific capacities are probably too high as it can be assumed that there is a hydraulic contact between Sect-up and Sect-mid and due to the uncertain values of the actual drawdown, which is very small.

**The values from the section are not evaluated because of uncertainties regarding impact of other factors than pumping.

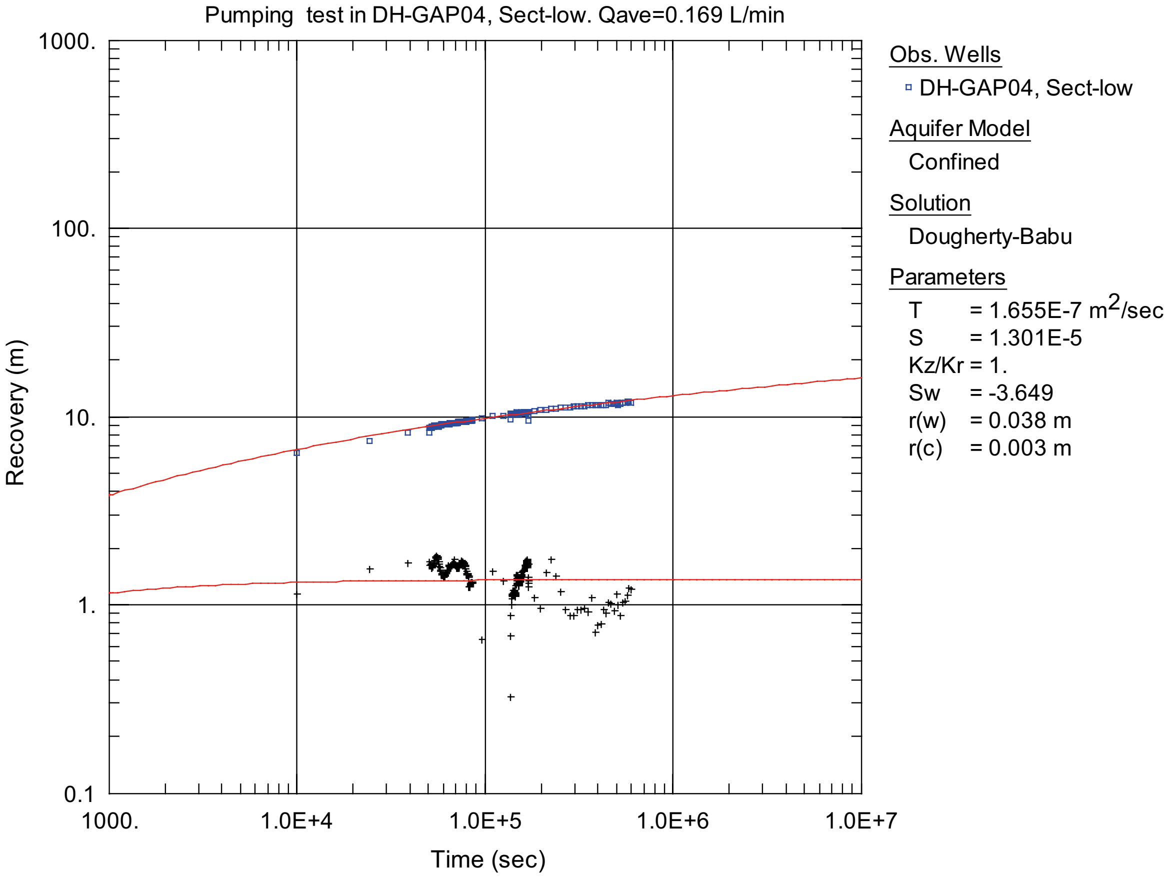

Figure 5-44. *Evaluation curves from DH-GAP04 Sect-low, recovery phase. □=Pressure. +=Pressure derivative.*

The estimated transmissivity from a transient analysis of the recovery phase in Sect-low is ~ 1.9×10^{-7} m^2/s (see Figure 5-45). Again, the recovery data evaluation was made according to Dougherty-Babu's solution in AQTESOLV software.

5.6.3.3 Structural-hydraulic analysis of DH-GAP04

The hydraulic testing of borehole DH-GAP04 revealed nine water-conducting intervals below the permafrost (Table 5-5 and Figure 5-37). The length inaccuracy of the applied PFL testing makes the tracing of single fractures rather challenging. However, when analysing the fracturing within the potential sectors, it was observed that, in some cases, the water-conducting intervals could be linked to increased fracture density, while, in other intervals, the only candidates were discrete fractures. The water-conducting intervals are separated by 4–35 m long non-conducting drill core sections.

As a visual inspection of the fracture surfaces in the drill cores could not reveal which fractures were the most water-conducting, a statistical approach was applied where all fractures and faults within ± 3.3 m around the water-conducting intervals were included. Following this concept, 78 potentially water-conducting fractures and 11 faults were included within the upper sampling section (Sect-up), and 35 fractures and 8 faults were included in both the middle (Sect-mid) and the lower (Sect-low) sections. The reasoning for this division was that the faults are assumed to have a longer extent than fractures. Despite the scatter in the data, some differences are apparent.

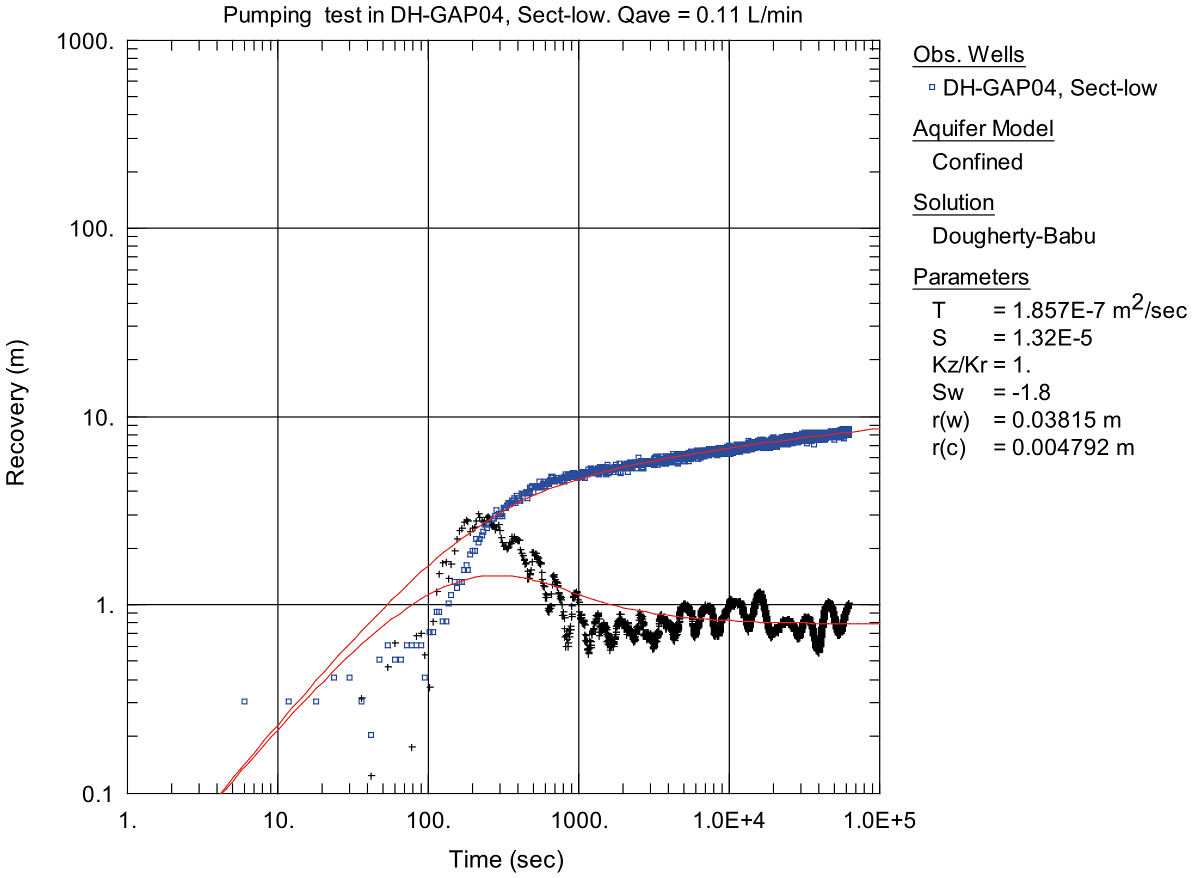

Figure 5-45. *Evaluation curves from DH-GAP04 Sect-low, recovery phase. □=Pressure. += Pressure derivate. Q_{ave} is calculated as total pump volume divided with total pump time.*

In Figure 5-46A, all fractures in DH-GAP04 (crosses) are shown together with potentially water-conducting fractures in the upper (blue), middle (red) and lower (green) sections. Figure 5-46B gives the corresponding information about faults. It is obvious that the water conductivity in this borehole is related to sub-horizontal features, i.e. fractures with a dip less than 45°.

In Sect-up and Sect-low, the fracturing seems to be predominantly parallel to the prevailing foliation (i.e. dipping gently toward NW), while in Sect-mid many fractures dip to the opposite direction and cut the foliation at an ~ 30–40 degree angle (Figure 5-46C and Figure 5-46D). These SE and NW dipping fracture sets may be related to the Type 5 faults in the Geomodel (see Figure 5-15). It is interesting that at a larger scale the Type 5 lineaments, despite having the same trend, are seen to dip in opposite directions. The lineament intersecting DH-GAP03 is dipping SE, while the lineament running through the upper part of DH-GAP04 is dipping NW. This is implying that the same brittle feature can be seen at different scales and the related conjugate fracture sets may explain the connection between Sect-up and Sect-mid and also to larger structures in the vicinity of DH-GAP04.

The measured fluid pressures, electrical conductivity (Section 5.6.5.2) and the chemistry (Section 5.7.4.3) show that Sect-low is hydraulically isolated from the upper levels. The ~ 30 m bedrock section immediately below the lower packer contains only a few fractures and is considered intact (Figure 5-47). The fracturing deeper down in Sect-low is mainly sub-horizontal and lacks steeply dipping fractures. It seems that the intact bedrock section is laterally extensive enough to prevent vertical flow in the vicinity of the borehole.

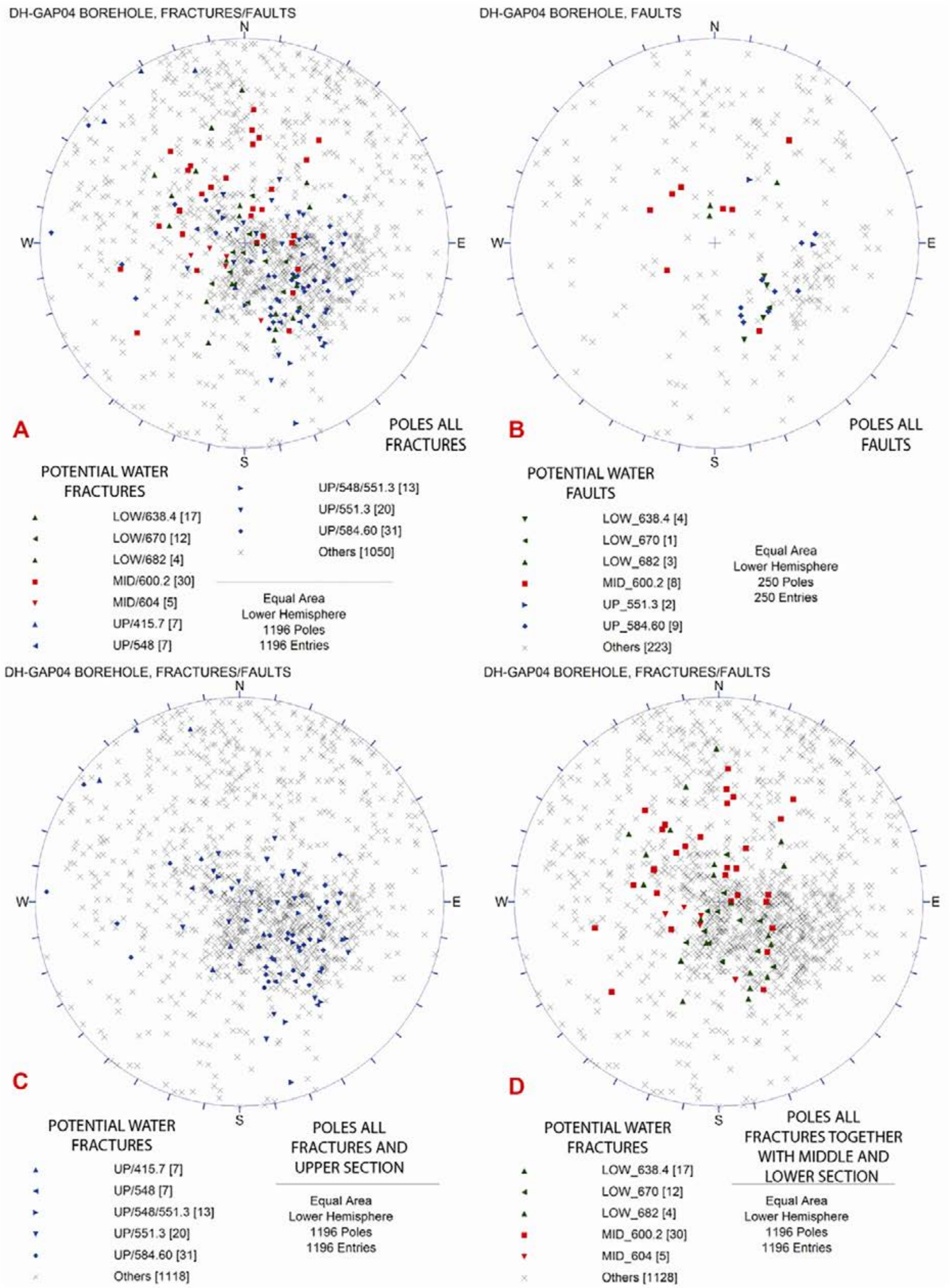

Figure 5-46. *Sterographic projections from DH-GAP04 showing potential water bearing fractures and faults (equal area, lower hemisphere projection): A) all potential water-conductive fractures and faults in DH-GAP04, B) possible water-conductive faults in DH-GAP04, C) possible water-conductive fractures and faults in Sect-up, and D) possible water-conductive fractures and faults in Sect-mid and Sect-low. Terzaghi correction is not applied for fracture orientations.*

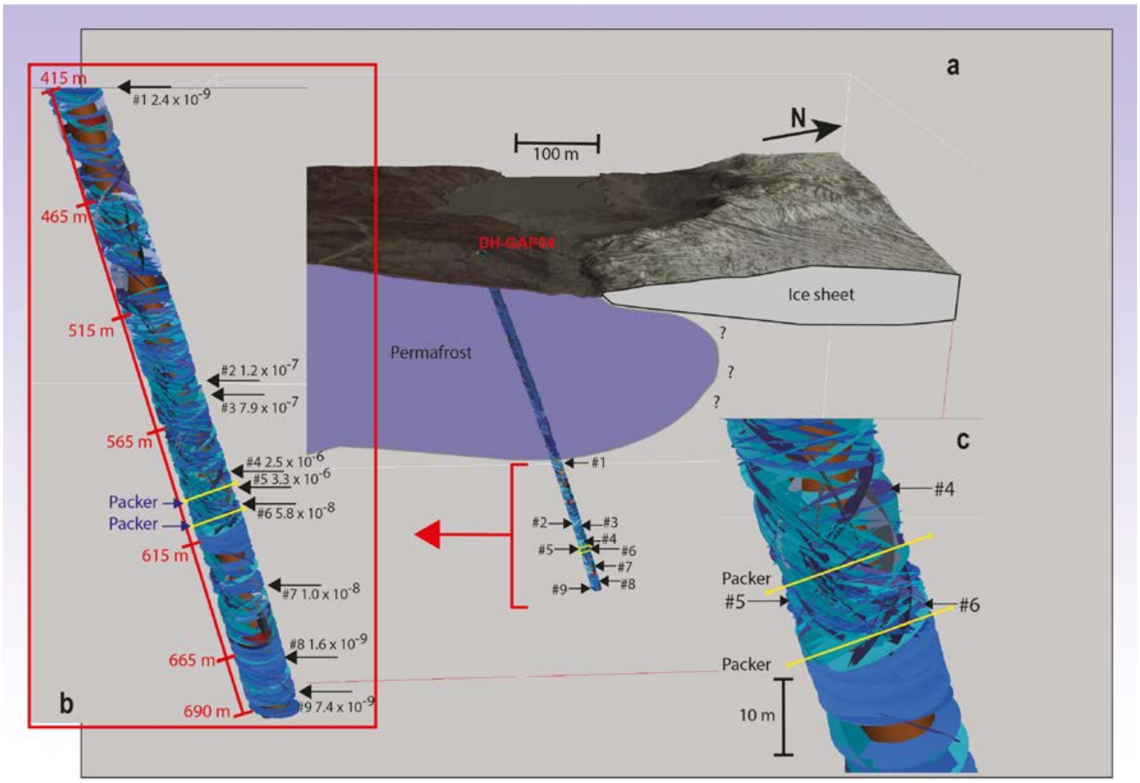

Figure 5-47. *a) Location and orientation of all fractures in DH-GAP04. b) shows the fracture characteristics below the permafrost (purple). The given depths are borehole lengths. Fracture frequency is lower in the upper part of the core and increases downward. At the same time, the subhorizontal fracturing (blue) becomes more common and dominates at the end of the borehole. It is noteworthy that the observed water conductivity is within the intensly fractured part of the core, i.e. in the lower third of the borehole. c) gives a detailed view of the fracturing around the packed-off section (Sect-mid). The cross-cutting fracturing within Sect-mid and in the lower part of Sect-up explains why these sections are hydraulically well connected. Immediately below the packers is a 30–40 m thick unit where the fracture orientations become uniformly subhorizontal and the fracture frequency distinctly reduces. This unit seems to isolate Sect-low from the rest of the borehole.*

In terms of hydrogeology, DH-GAP04 can be devided in three units, or four, if the permafrost is considered. The subpermafrost units are as follows.

- Unit A: bedrock section between 548–604 m borehole length, including the fractures with the highest transmissivities. The well-connected water-conducting internal facturing within this unit is sub-horizontal and either parallel to the foliation or cutting it. Sect-up and Sect-mid are in this unit.
- Unit B: a 34 m thick intact unit, which separates unit A from the lower part of the borehole and acts as a hydraulic barrier.
- Unit C: bedrock section at borehole length 638–687 m. Observed PFL transmissivities are significantly lower than in unit A and water conductivity is strongly controlled by fracturing parallel to the foliation. This unit includes Sect-low.

DH-GAP04 intersects a large fold with a fold axis dipping gently toward the NW (e.g. Section 5.4.4.3 and Figure 5-15). This implies that at the hinge area of the fold the hydrogeological units dip gently to NW, i.e. in under the ice tongue of the Isunnguata Sermia Glacier (Figure 5-95).

5.6.4 Fluid pressure, density and hydraulic head

The boreholes are equipped with absolute (total) pressure transducers located between packers, meaning that acquired data represent changes in absolute pressure within the saturated bedrock fractures intersecting the monitored borehole sections. The only time the fluid in the borehole may be in contact with atmosheric pressure is when the frozen upper parts of the boreholes are heated to facilitate water sampling; at all other times the upper parts of both boreholes are frozen. Measured downhole pressures were transformed to fluid pressures by subtracting 100 % of the barometric pressure changes measured at a nearby weather station. This was required because the pressure transducers measure the total pressure.

Table 5-8 and Figure 5-48 show measured densities of water samples acquired in DH-GAP04 at different temperatures, as determined in the laboratory (Teollisuuden Voima Oyj). The density of the water sample acquired in Sect-up is just below 1001 kg/m^3 in the interval 2–2.5 °C, which is similar to the density in Sect-mid and is lower than the density in Sect-low, which is just below 1002 kg/m^3 in the temperature interval 2–2.5 °C. The measured values suggest slightly more dense water than pure water, with highest density observed in water from the bottom of the borehole. However, of all practical applications, the density of pure water could be used to transform pressures to hydraulic heads. Thus, the fluid pressures, p (Pa), discussed in this report are transformed to hydraulic heads, h (m), assuming a constant density of pure water at +2 °C of 999.968 kg/m^3 (http://www.csgnetwork.com/h2odenscalc.html) and the WGS-84 ellipsoid as a reference elevation datum for z_{ref}:

$$h = \frac{p}{\rho g} + z_{ref}$$

Table 5-8. Density (kg/m^3) of water samples acquired in DH-GAP04 on September 22, 2013 (Sect-up), September 23, 2013 (Sect-mid) and September 24, 2013 (Sect-low).

	Borehole section and laboratory ID			
	Sect-up	**Sect-mid**	**Sect-low**	
Temperature	**GAP13-26**	**GAP13-22**	**GAP13-24**	**Pure water**
1 °C	1000.6	999.7	1001.4	999.927
2 °C	1000.9	1000.9	1001.9	999.968
5 °C	1000.9	N/A*	1001.8	999.992
10 °C	1000.7	1000.7	1001.8	999.728
15 °C	1000.2	1000.1	1001.2	999.129
20 °C	998.1	999.3	1000.2	998.234
25 °C	996.7	996.1	997.7	997.075

* Laboratory was not able to get the stable result for the sample at this temperature

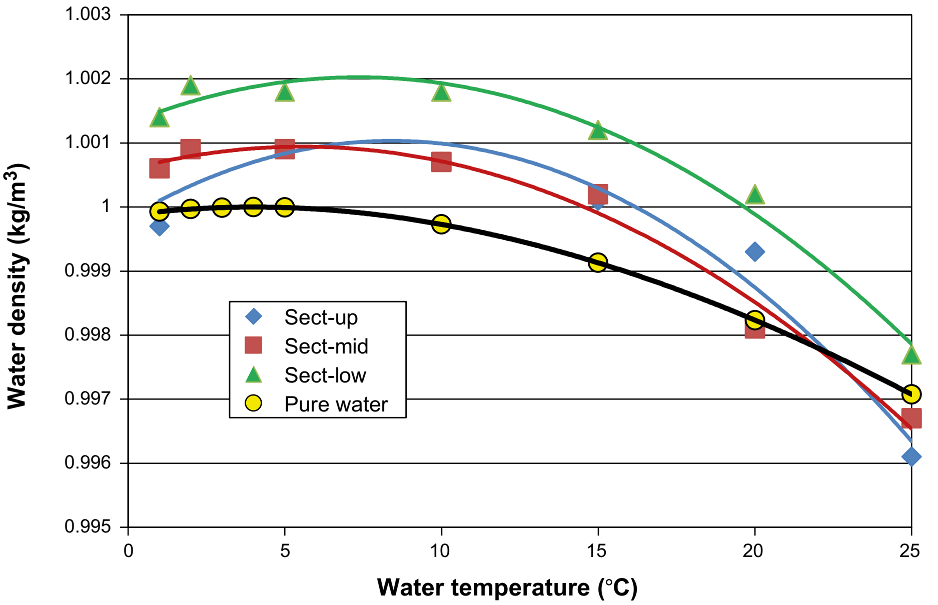

Figure 5-48. *Density (kg/m^3) of water samples acquired in DH-GAP04 in September 2013 and of pure water (http://www.csgnetwork.com/h2odenscalc.html). The curves are only inserted to help the comparison of the four datasets.*

5.6.5 Downhole long term monitoring of boreholes DH-GAP01 and DH-GAP04

Boreholes DH-GAP01 and DH-GAP04 are both instrumented with downhole sensors (see Section 5.3.2.1 and 5.3.2.3), allowing monitoring of fluid pressure (p in kPa), temperature (T in °C) and electrical conductivity (EC in µS/cm). The aim of the installations was to obtain continuous long term monitoring records of the hydraulic and hydrogeochemical behaviour of 1) the presumed through talik (data from borehole DH-GAP01), and 2) groundwater below the permafrost (data from borehole DH-GAP04). It was deemed particularly important to cover the onset of melting during spring and freezing during the fall, when the most significant changes in hydraulic gradients are expected. Meltwater runoff responses on pressure recordings at depth in crystalline bedrock have, for example, been observed at Forsmark, Sweden (Follin et al. 2007) and at Olkiluoto, Finland (Vaittinen et al. 2014).

5.6.5.1 Data from DH-GAP01 (June 2009 to August 2013)

DH-GAP01 (azimuth: 083; dip: 60) is drilled ~ 20 m from the shoreline of the Talik lake (also referred to as Two Boat Lake by Johansson et al. 2015a, b.). The elevation difference between the TOC and the lake level is ~ 5.2 m. Lake level variations have been monitored since 2010 (see Johansson et al. 2015b and Figure 5-51) and borehole pressure has been monitored since June 2009.

The U-tube sampler in DH-GAP01 is equipped with downhole sensors, allowing for water sampling and P, T and EC monitoring (Figure 5-7). The packer and sampling system is located at a vertical depth interval of 130–140 m below TOC. The sensors are located below the inflatable packer at a vertical depth of 138.57 m, and are connected to the surface via a non-vented cable, which means that the measured pressures are total pressures (i.e. fluid pressures plus atmospheric). The section below the packer is 71 m long, with a diameter of 56 mm, giving a section volume of 175 L. A detailed description of the installation of the U-tube sampler and downhole sensors is presented in the GAP 2009 yearly report (SKB 2010b).

As the logged pressure data originates from a non-vented pressure sensor, all pressure forces exerted on the strain gauge, including atmospheric pressure, are included. To account for the effects of changes in barometric pressure, post-corrections of absolute (non-vented) variations are necessary in order to obtain the real (gauge) fluid (pore) pressure at depth. Barometric correction of the pressure data from DH-GAP01 was done using barometric pressure from two AWS: KAN_L (from June 2009 to April 2010) and KAN_B (from April 2010 to August 2013). The KAN_B station is located next to borehole DH-GAP01, however, this station has not been operating for the entire time period that pressure has been monitored in DH-GAP01. The KAN_B station has been in operation since April 2010. Data from the KAN_L station, situated on the ice sheet at an altitude of 680 m and a distance of ~ 11 km from DH-GAP01, was used for correction between June 2009 and April 2010. During this time period, the KAN_L barometric pressure is converted to the equivalent barometric pressure for the DH-GAP01 altitude.

Pressure and hydraulic head

The downhole P, EC and T data and the calculated hydraulic head is monitored for the period June 2009 to August 2013 (Figure 5-49 and Figure 5-50). The undisturbed (i.e. sampling events removed) hydraulic head, temperature and EC is monitored from June 2009 to August 2013 (Figure 5-51). Drilling recovery, however, is still included.

The hydraulic head, temperature and EC for the initial monitoring period following drilling and instrumentation is monitored from June to October, 2009 (Figure 5-52). Before packer inflation, the head was 5.3 m below TOC. Immediately after deployment and packer inflation, the U-tube system was operated 28 times over a span of 4 days (June 28 to July 1, 2009), recovering ~ 310 L of water. During this time, the head decreased from 5 m to ~ 8 m below TOC. From July 2009 to June 2010, the head increased from ~ 8 to 6.8 m below TOC (Figure 5-51), after which time the head began to decrease, reaching the lowest head in January 2012 (8.2 m below TOC). From February to May 2012, the head increased, reaching ~ 7.5 m below TOC before beginning to decrease again. By the time the connection to the logger was lost on July 29, 2012, the head had reached 7.9 m below TOC. In April, 2013 the connection was re-established. At that time, the head was 8.4 m below TOC. From the end of April to mid June, 2013, the head increased to 7.6 m below TOC before beginning to drop, reaching 8.2 m below TOC in mid August, 2013. The sampling events during the monitoring period took place in: June/July 2009, September 2009, May 2010, September 2010 and September 2011.

During the entire monitoring period, a total 696 L of water (59 purges, yielding ~ 11.8 L per purge) was recovered from DH-GAP01, meaning that approximately four flushing cycles of the section below the packer (the section volume is 175 L) were extracted.

The initial head drop in 2009 (Figure 5-52) is likely related to stabilisation of the borehole because large volumes of hot drilling water were injected into the bedrock during drilling. In total, 40 m^3 of hot flushing water (with an average EC of ~ 171 µS/cm (± 0.5 %)) was injected. After about 20 m of drilling (i.e. when entering the bedrock beneath the Talik lake), the amount of return water decreased considerably. Flushing water discharged only when the core barrel was retrieved. There was no means to measure how much water was forced into the bedrock, but judging from the relatively quick cleaning of the sampling section, the volume at the deeper levels was considered small (SKB 2010b). The stabilisation effect is observed in the temperature and EC data as well (Figure 5-50) and is explained below.

The purging of water from the borehole is depicted by significant head drops and synchronous shifts in specific conductivity, as well as slight changes in temperature in June 2009, September 2009, May 2010, September 2010 and September 2011 (see Figure 5-50). A small head drop and recovery (~ 0.3 m drop relative to TOC) that was not associated with purging occurred from April 15 to May 13, 2011 (see Figure 5-51). This drop is not associated with changes in EC or temperature. Another hydraulic head drop and recovery unrelated to purging occurred from July 25 to August 1, 2011. The drop was equivalent to 1.2 m (from 7.5 m to 8.7 m below TOC), after which the head recovered to 7.8 m below TOC. A slight, but still within the measuring accuracy, synchronous temperature increase occurs over the same time period (Figure 5-53). Electrical conductivity changes were not observed during this event.

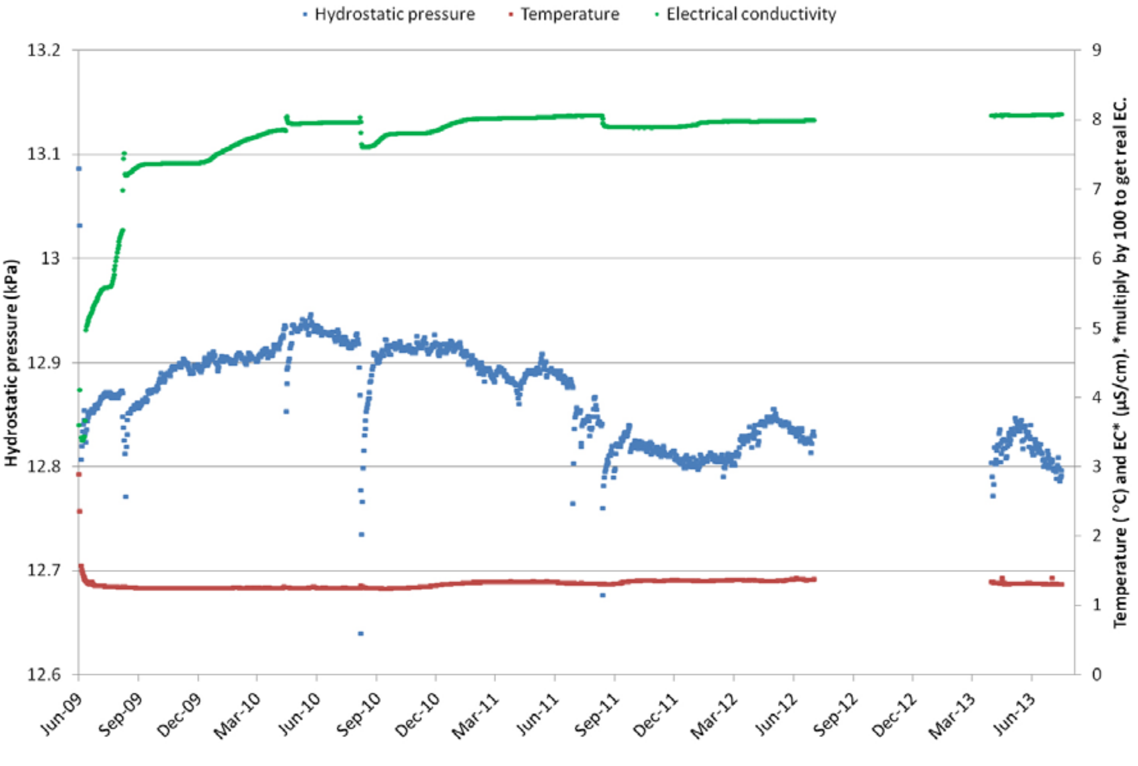

Figure 5-49. *Downhole P and EC (presented as µS/cm divided by 100, i.e. to get electrical conductivity in µS/cm multiply by 100) and temperature as daily averages over time (June, 2009 to August, 2013) in DH-GAP01. Due to powering problems, data is missing from July, 2012, to April, 2013. The fluid pressure is corrected for barometric variations. The purging of the borehole is seen as significant pressure drops (June 2009, September 2009, May 2010, September 2010 and September 2011). The logging frequency has not been constant over time. From June 28 to September 6, 2009, the frequency was 15 minutes. From the September 7, 2009, to September 6, 2010, the frequency was 6 hours. From September 7, 2010, onward, the logging frequency has been 12 hours. During short intervals (i.e. during purging of the borehole), the frequency has been set to 1–10 minutes.*

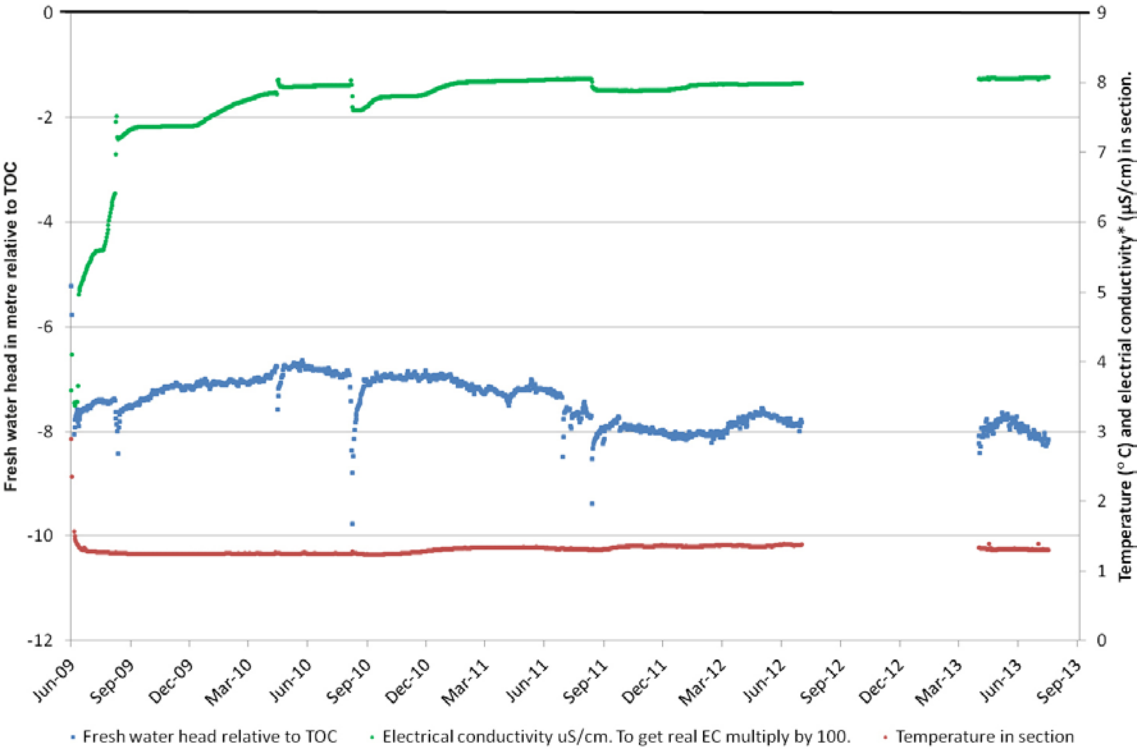

Figure 5-50. *Daily average EC, calculated hydraulic head and downhole temperature in DH-GAP01 from June, 2009, to August, 2013. Due to powering problems data is missing from July, 2012, to April, 2013. Calculation of head uses the TOC of DH-GAP01 (374.68 m) as the 0 reference (highlighted as a black horisontal line) and assumes 1 kPa = 0.1019 m of water.*

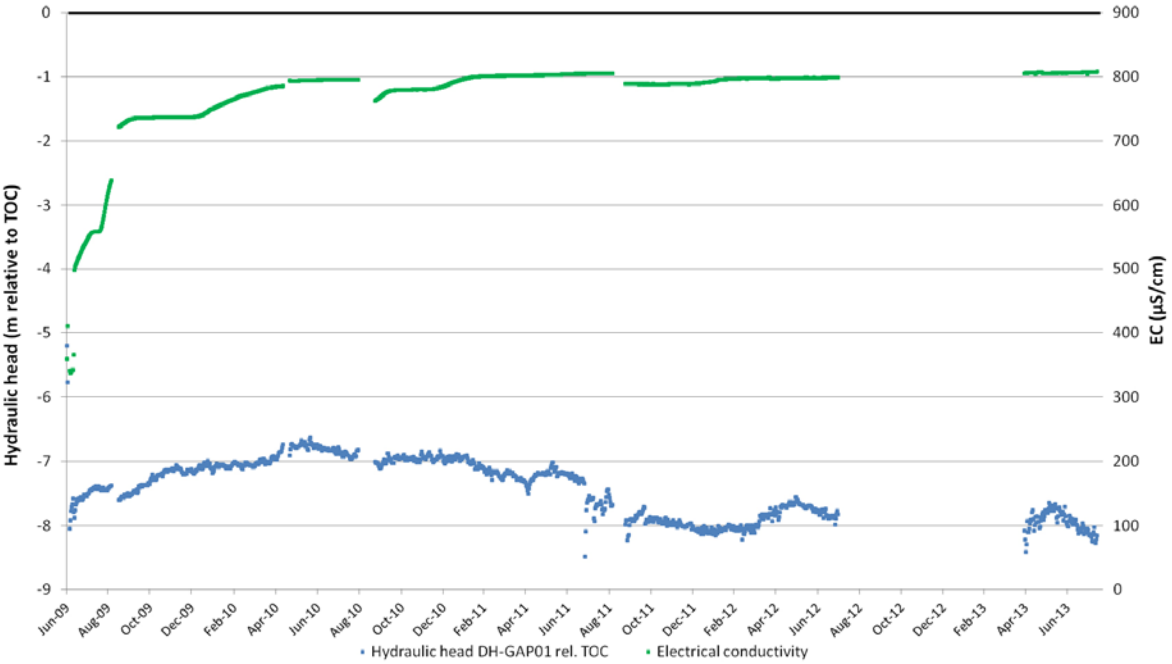

Figure 5-51. *Undisturbed *daily average EC and calculated hydraulic head in DH-GAP01 from June, 2009, to August, 2013. Due to powering problems data is missing from July, 2012, to April, 2013. Calculation of head uses the TOC of DH-GAP01 (374.68 m) as the 0 reference (highligted as a black horisontal line) and assumes 1 kPa = 0.1019 m of water. *In order to estimate natural (undisturbed) hydraulic head and EC, periods with hydraulic disturbances (i.e. sampling or hydraulic testing) were removed. Calculation of head uses the TOC of DH-GAP01 (374.68 m) as the elevation datum. The drilling recovery period is not removed from the dataset. Note that the pressure drop in July, 2011, is not associated with purging events.*

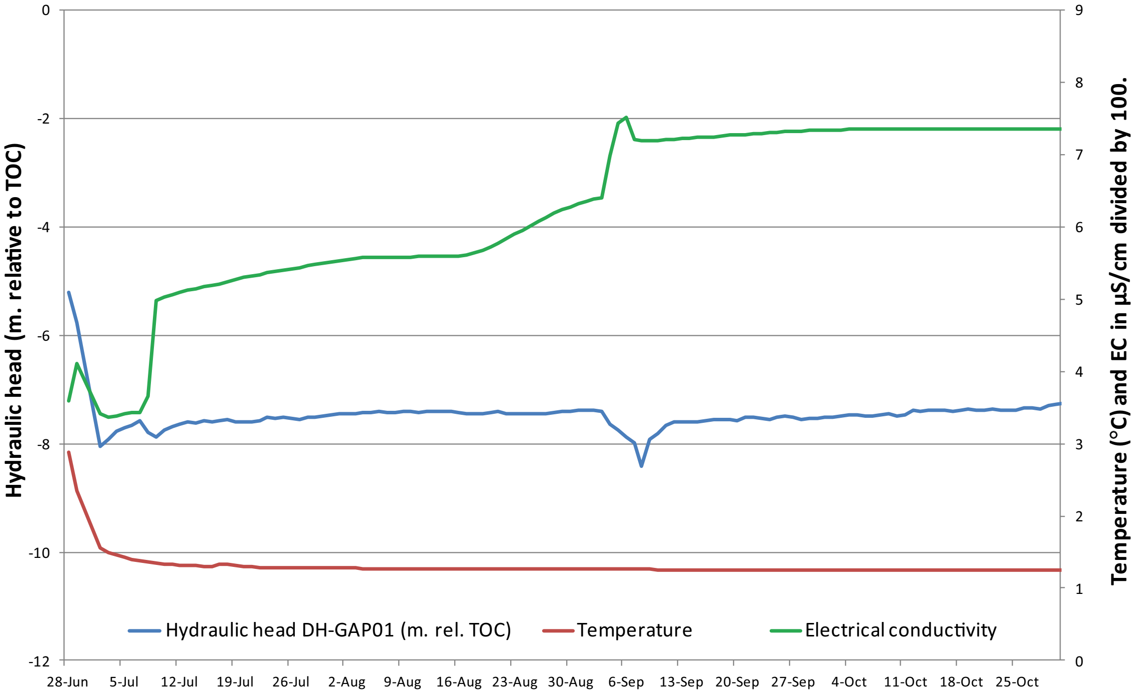

Figure 5-52. *Hydraulic head, temperature and electrical conductivity in DH-GAP01 (presented as µS/cm divided by 100, i.e. to get electrical conductivity in µS/cm multiply by 100) during the initial monitoring period (June to October, 2009).*

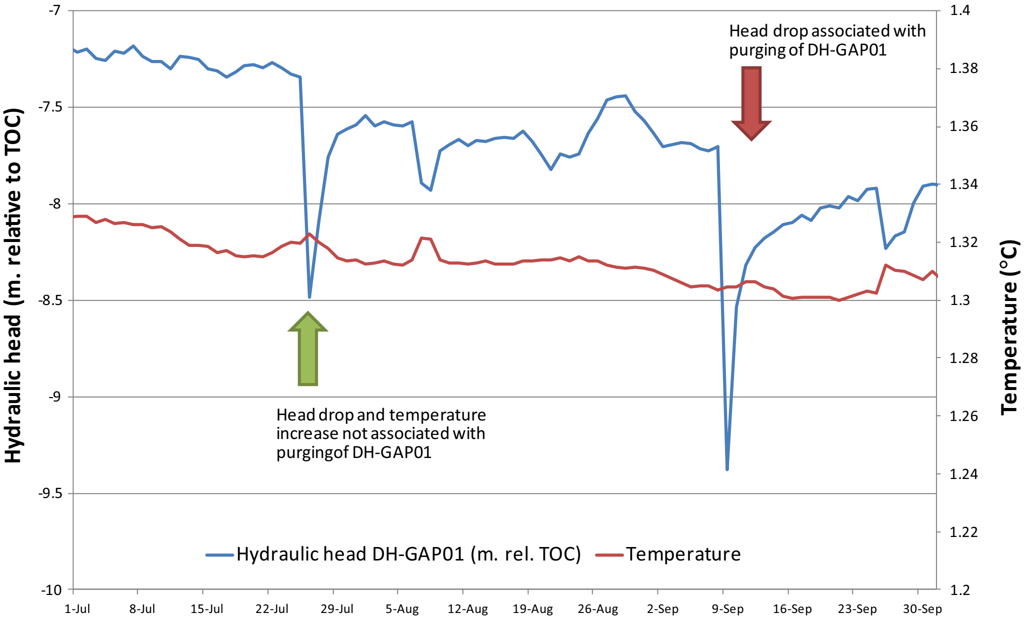

Figure 5-53. *Hydraulic head and temperature in DH-GAP01 from July 1, 2011, to October 1, 2011. The head drop and small temperature increase in July is not associated with purging of the borehole, whereas the head drop in September coincides with purging (a total of 59 L was extracted during this sampling campaign). One possible explanation for the head drop in July is that it is a response to a significant drop in lake level (see Figure 5-54).*

Seasonal variations cannot be readily derived from the dataset (Figure 5-51). Head increased by ~ 1.2 m from June 2009 to June, 2010, after which it decreased ~ 1.5 m over the next 1.5 years. A slight increase and decrease occurred from February to July, 2012. If any cyclic pattern does exist, the cycle is longer than the present monitoring period.

Figure 5-51 shows the head in DH-GAP01, co-plotted with the head in the lake. Over the course of the monitoring period, the lake level varied from a minimum of −5.6 m (during winter 2011–2012) to a maximum of −5.3 m (in June, 2013) relative to TOC. During the same time period, the level in the borehole varied from a minimum of −8.5 m (in July, 2011) to a maximum of −6.6 m (in June, 2010) relative to TOC. The groundwater level in the monitoring section (h = ~ 367 m) is lower than the elevation of the TOC, and it is lower than the lake level (h = ~ 369 m) as well. This could indicate a downward gradient from the part of the lake where DH-GAP01 is drilled. It is noted that the lake level and groundwater level in DH-GAP01 are co-varying (see Figure 5-54), i.e. when the lake level drops and increases, so does the borehole level, which indicates a hydraulic connection between the lake and the borehole. A downward gradient between the lake and the groundwater in the talik indicates recharging conditions, i.e. the lake recharges the talik beneath it (Johansson et al. 2015a). It should be noted that this observation is based on hydrological data only. The chemical and isotopic composition of the talik is discussed in Section 5.7.4.2.

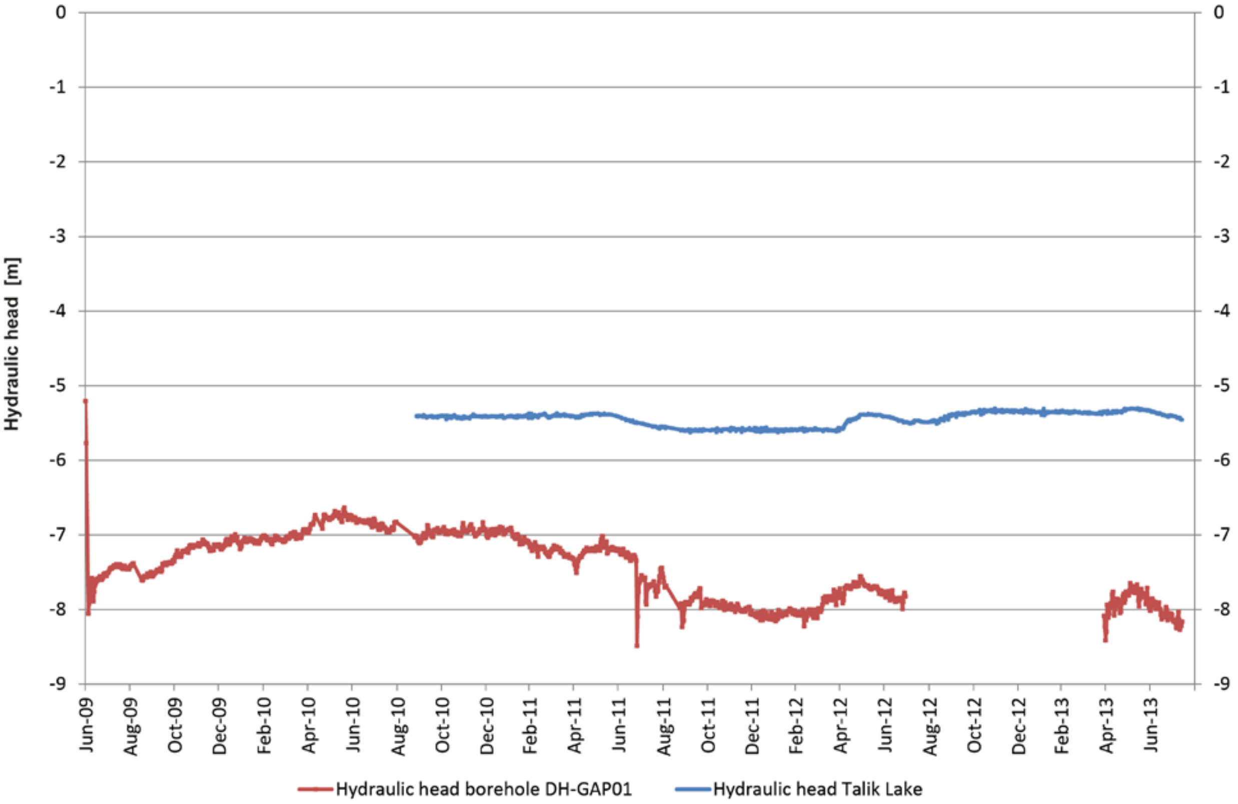

Figure 5-54. *Undisturbed *daily average calculated hydraulic head for DH-GAP01 and the Talik lake from September, 2010, to August, 2013 (lake level data provided by E. Johansson). Due to powering problems data from borehole DH-GAP01 is missing from July, 2012, to April, 2013. Calculation of head uses the TOC of DH-GAP01 (374.68 m) as the 0 reference (highlighted as a black horisontal line) and assumes 1 kPa = 0.1019 m of water. *In order to estimate natural (undisturbed) hydraulic head, periods with hydraulic disturbances (i.e. sampling or hydraulic testing) were removed; however, the drilling recovery period is not removed from the dataset. Note that the pressure drop in July, 2011, is not associated with purging events, but it is suggested to possibly be an effect associated with significant lake level lowering.*

Electrical conductivity

The EC of the borehole water, measured directly after drilling was completed in June, 2009, was ~ 265 µS/cm (obtained from downhole sensor), which is compared to the EC of the drilling water (171 µS/cm). During the summer of 2010, the EC increased to about 800 µS/cm and has remained fairly constant since. There is a significant difference in EC between the borehole and the lake. The values suggest that the borehole recovered from drilling contamination during the spring of 2010. During the first year after drilling, purging of the borehole resulted in a rapid increase in EC, followed by post-purging decreases (Figure 5-49 to 5-53). Conversely, from July, 2010 and onward, purging resulted in simultaneous EC drops, followed by post-purging EC recovery. The purging-associated variations in EC are probably explained by a pumping effect where 1) the EC increase is a result of an increased portion of fracture water/groundwater (with a long residence time) re-entering the hole and 2) the EC decrease is a result of fracture water from a more dilute source (possibly fractures situated closer to surface) entering the hole. One way to interpret this is that following the EC stabilisation in the borehole, less saline, and likely shallower, water enters the hole during purging. This is supported by the groundwater analyses performed in 2010, which indicated only a small percentage of drill water contamination (see Section 5.7.4.2).

Temperature

Immediately following drilling and instrumentation, the initial downhole T was ~ 2.9 °C (Figure 5-52). A considerable T drop occurred during the first weeks following hot water drilling (the drilling water had an average T of 30–40 °C) and instrumentation, and is related to cooling of the borehole. By the end of July, 2009, the T stabilised at around 1.25 °C. Except for minor T increases coinciding with purging of the borehole (i.e. in June 2009, September 2009, May 2010, September 2010 and September 2011), the T remained at around 1.25 °C until October, 2010, when it began to increase slightly. In March, 2011, the T reached 1.33 °C. During the sampling in September, 2011, the T decreased slightly, after which it returned to 1.36 °C during the early winter of 2012. Although all T changes are within the accuracy of the T sensor, they indicate that slightly warmer water enters the hole during purging. From spring 2010, purging of the borehole resulted in the entrance of less saline water into the borehole. This is supported by the observed EC decrease and slight T changes associated with purging events. Because salinity of water normally increases with depth, it is possible that the less saline water entering the hole comes from shallower depth.

5.6.5.2 Data from DH-GAP04 (July, 2011 to December, 2013)

After the drilling of DH-GAP04 (azimuth: 288; dip: 70) was completed, the hole was instrumented with a two packer system isolating a 10 m long section between 561.27 and 570.71 m vertical depth, dividing the hole into three sections (Harper et al. 2016). DH-GAP04 and its instrumentation were intended to provide information about the geological, hydrogeological and hydrogeochemical conditions (i.e. lithology, fracture frequency, fracture mineralisation, flow conditions, thermal conditions, and chemical properties of the groundwater) at a depth corresponding to typical repository depth (i.e. ~ 500 m b.g.s.). Sect-up is ~ 190 m long, extending from the base of the permafrost to the uppermost packer, and its volume is 840 L. Sect-mid is straddled by the two packers and is about 10 m long, with a volume of 44 L. Sect-low is 80 m long, extending from the lowermost packer to the bottom of the hole, and has a volume of 350 L. With the downhole instrumentation it is possible to:

- Monitor the temperature (T in °C) along the borehole using the DTS technique,
- Monitor the electrical conductivity (EC in µS/cm) of water in each section,
- Monitor pressure (P in kPa) in each section,
- Monitor the temperature (T in °C) in the middle section,
- Melt the ice in the permafrost part of the hole, enabling water sampling, and
- Collect water samples (both pressurised and non-pressurised) in all sections.

Instrument specifications

The monitoring data were transmitted once a week via the Iridium satellite network. A total of 12 parameters are monitored and logged (Table 5-9). Appendix B provides a detailed description of the parameters being monitored and the different program set ups that are used for monitoring fluid pressure, temperature and electrical conductivity, as well as a description of the the installation. The downhole instrumentation and position of sensors can be found in Section 5.3.2.

Table 5-9. Parameters logged in DH-GAP04.

Parameter	Name on the logger	Unit
Air pressure *	Pair	kPa
Air temperature (inside the logger box)	Tair	° C
Pressure in gas bottle *	Pgasbottle	kPa
Packer pressure *	Ppack	kPa
Section pressure (upper section) *	Psect-up	kPa
Section pressure (middle section) *	Psect-mid	kPa
Section pressure (lower section) *	Psect-low	kPa
Temperature (Middle Section)	Tsect-mid	° C
Electrical conductivity (upper section)	Esect-up	µS/cm
Electrical conductivity (middle section)	Esect-mid	µS/cm
Electrical conductivity (lower section)	Esect-low	µS/cm
Battery capacity	Bat	Volt

* Absolute pressure.

Pressure measurements and hydraulic head

Figure 5-55 shows the fluid pressure and temperature data from DH-GAP04 from July 2011 to December 2013. Figure 5-56 shows the hydraulic heads in the three sections during the initial monitoring period following instrumentation.

- Before the packers were inflated, water flowed above the TOC. When the packers were inflated, head dropped relatively quickly and substantially in Sect-low (~ 23 m during the week following inflation).
- In Sect-mid, the head remained above the top of casing for a short period of time before it started to decline. The excess head is caused by the drilling, and is an expected phenomenon related to the large volume of drilling water injected into the bedrock – generates a transiently over-pressured system. The over-pressure falls off in time as water dissipates into the formation. According to the PFL results, the hydraulically active fractures are variably over-pressured, suggesting that they have different transmissivities (see Section 5.6.3).
- The water from Sect-up flowed above the TOC until the upper part of the borehole was completely frozen, which occurred around July 14–15, 2011. Since this freezing event, the heads in Sect-up and Sect-mid have mimicked each other.

It is noted that the head in Sect-low is substantially lower than in Sect-up and Sect-mid. In order for the calculated head in Sect-low to be equal to, or greater than, the calculated head in Sect-up and Sect-mid, the fluid pressure in Sect-low must be significantly greater than the actual measurements indicate. Potential uncertainties related to the determination of elevation, head, fluid density, instrument limitations and barometric correction have been evaluated and none could explain the observed head differences between Sect-mid and Sect-low. The remaining explanation is that the head in Sect-low is real and is caused by specific hydrogeological or structural geological conditions at the drilling site (see below).

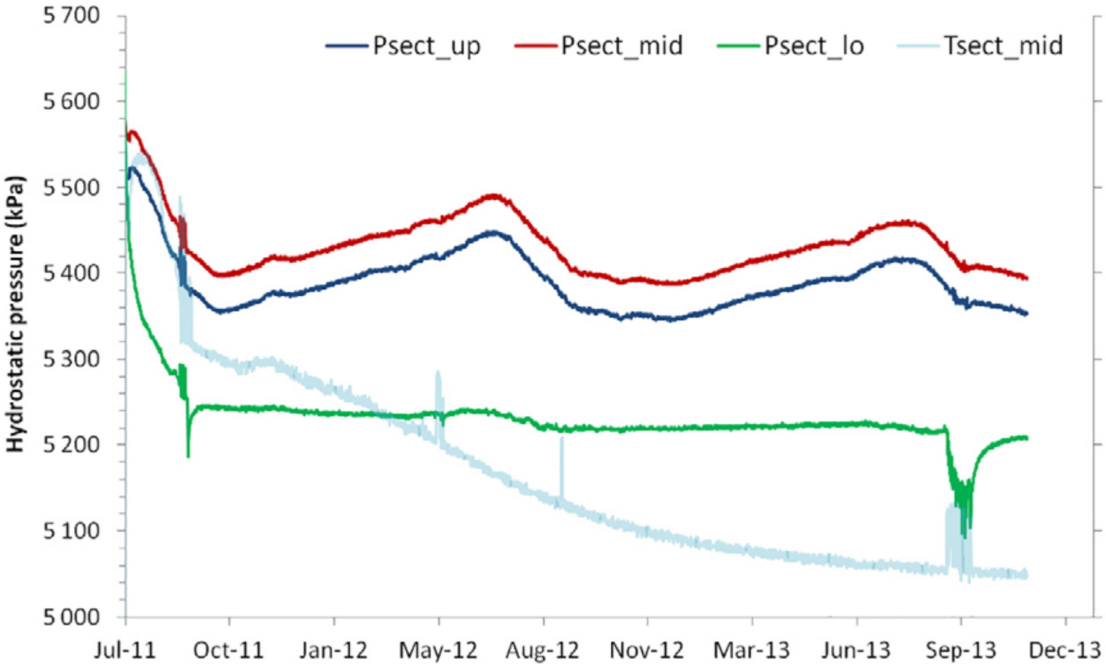

Figure 5-55. *Fluid pressures in DH-GAP04 Sect-up, Sect-mid and Sect-low, and temperature in Sect-mid plotted against time. Pressure is barometrically corrected. The scatter occurring in September, 2011, May, 2012, September, 2012, and September, 2013 is related to water sampling campaigns. Two successful campaigns have been carried out (September 2011 and September 2013). During these campaigns, all three sections were purged and water samples obtained.*

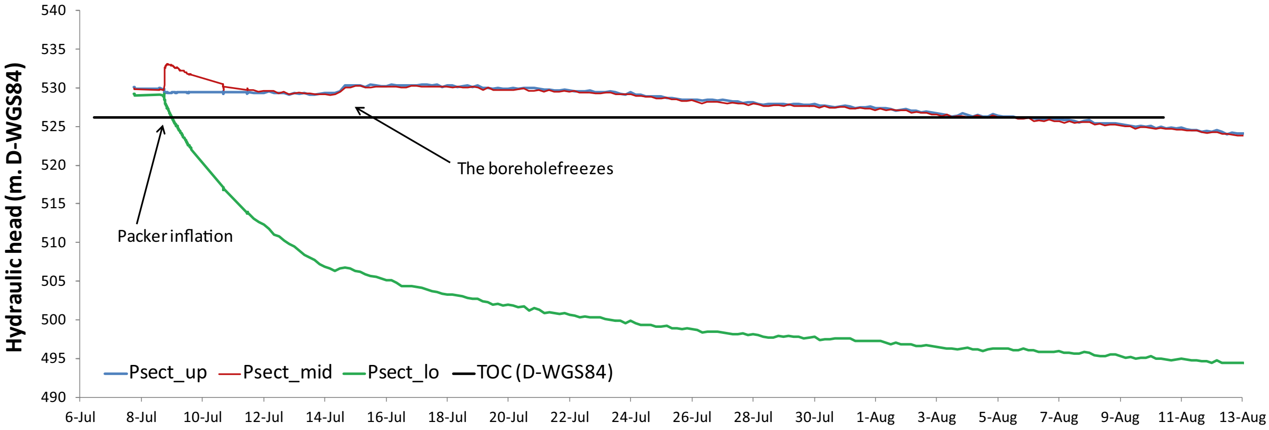

Figure 5-56. *Hydraulic head in DH-GAP04 Sect-up, Sect-mid and Sect-low during the initial monitoring period (July 7, 2011, to August 13, 2011). The elevation of the TOC of DH-GAP04 (526.17 m, D-WGS84) is indicated as a black horizontal line. The calculation of hydraulic head assumes 1 kPa = 0.10196 m of water.*

Figure 5-57 shows calculated head in Sect-up, Sect-mid and Sect-low together with the temperature in Sect-mid for the period July, 2011, to November, 2013. Two successful sampling campaigns have been completed during this period. In September, 2011, a total of 60 pumping cycles were performed (19 cycles from Sect-up, 21 cycles from Sect-mid and 20 cycles from Sect-low). In total, 300 L of water were removed, which is about 1/3 of the water volume present in the borehole below the permafrost. In relative terms, the most effective pumping was achieved in Sect-mid, where the water volume in the section was exchanged 3–4 times. In September, 2013, a total of 475 pumping cycles were performed (131 cycles from Sect-up, 216 cycles from Sect-mid and 128 cycles from Sect-low). During this campaign 2 295 L of water were removed. In total, 751 L of water has been removed from Sect-up, 1 203 L of water from Sect-mid and 676 L of water from Sect-low. This means that Sect-up has been flushed 0.9 times, whereas Sect-mid has been flushed 27 times, and Sect-low has been flushed 1.9 times. Results of the water analyses from the sampling campaign are described in Section 5.7.4.

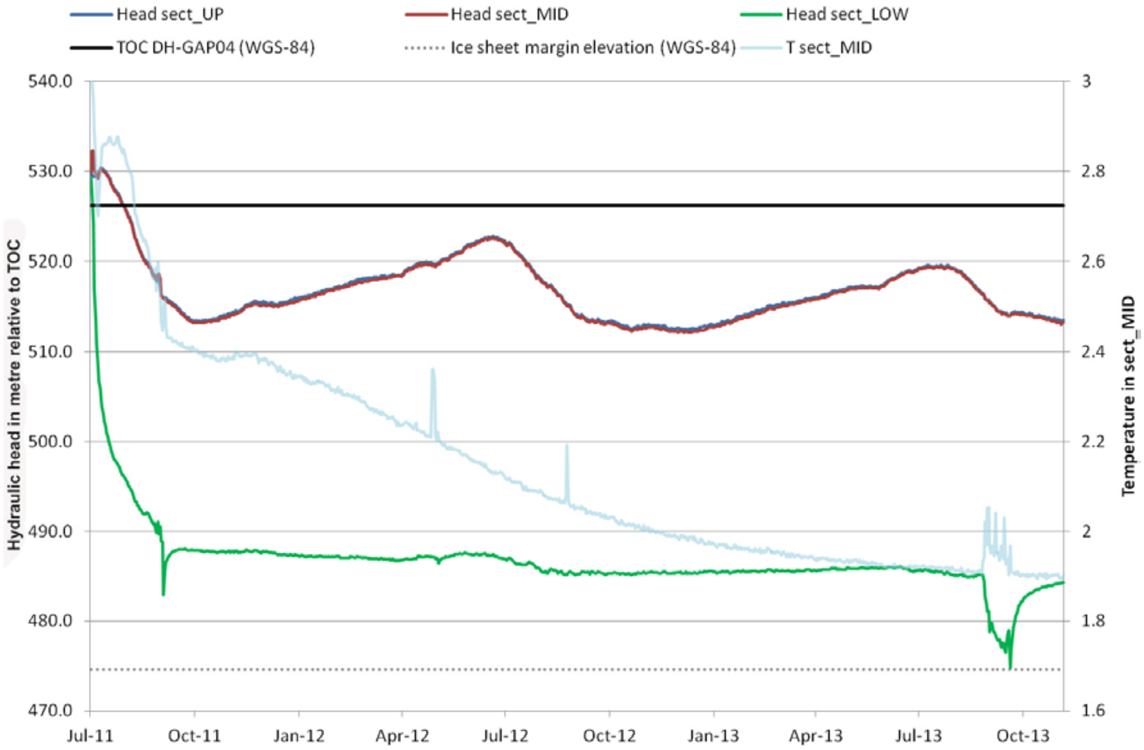

Figure 5-57. *Daily average hydraulic heads in DH-GAP04 Sect-up, Sect-mid and Sect-low, and temperature in Sect-mid plotted against time (July, 2011, to November, 2013). The elevation of the TOC of DH-GAP04 (526.17 m, D-WGS84) is indicated as a black horizontal line. The calculation of hydraulic heads assumes 1 kPa = 0.10196 m of water. The dotted line represents the elevation of the ice sheet margin.*

Head variations in Sect-up and Sect-mid

The heads in Sect-up and Sect-mid dropped when the packers were sealed, but not to the same magnitude as in Sect-low. From July to October, 2011, the heads dropped by ~ 17 m, reaching ~ 15 m below TOC (h = 513 m). From October, 2011, to June, 2012, the heads increased by 10 m, reaching a level of about 5 m below TOC. From June to October, 2012, the heads dropped by ~ 10 m, and from December, 2012, to July, 2013, there were a significant head increase in both sections, after which they begin to drop again – at the same rate as that observed in 2012. The heads in these sections reached their lowest level, which were about 15 m below TOC, in October, 2011, and December, 2012, and reached their highest level, about 5 m below TOC (h = 521 m), in June, 2011, and July, 2012.

The shapes of the head curves indicate that there is seasonal variation, and that there may be a coupling to the basal drainage system; this is discussed further below.

Head variations in Sect-low

It can be seen that the head in Sect-low decreased to about 40 m below TOC (h = 486 m) during the three months following drilling and instrumentation (Figure 5-55 and Figure 5-56). Following the drilling recovery, the head variations in the lower section are small throughout the monitoring period. A head increase of about one metre occurs in April–June, 2012, before the head dropped about two metres between June and mid-August, 2012. This drop coincides with head drops in Sect-up and Sect-mid as well. From August, 2012, to June, 2013, the head slightly increases in Sect-low, and then begins to drop. In September, 2013, the head was greatly disturbed due to pumping of the borehole. The slow head recovery following pumping indicates that the transmissivity of this section is lower than those of Sect-up and Sect-mid – which is indicated also by PFL measurements (see Section 5.6.3.1) and the evaluation of the hydraulic recovery. The shape of the head curve indicates that there is seasonal variation although not as pronounced as in Sect-up and Sect-mid (see above).

Electrical conductivity in Sect-up, Sect-mid and Sect-low

Figure 5-58 shows EC and T in Sect-mid from April, 2012, until November, 2013. Due to technical issues associated with reception of signal from the EC loggers, the EC values prior to this date are unreliable. The EC values in Figure 5-58 correspond well to the EC values measured with the field probe on water collected during the sampling campaigns (September 2011 and 2013). Because the water is still contaminated by drilling water, and because the monitored EC is an *in situ* value, a slight difference between the monitored and the measured EC on purged water samples will exist. EC values in Sect-mid and Sect-low are similar and mirror each other from April to October, 2012, during which they increased from ~ 1500 to 1800 μS/cm. In October, 2012, the EC in Sect-low surpassed the EC in Sect-mid and has continued to increase linearly until the pumping campaign in September, 2013, when the EC increased significantly, reaching values > 4000 μS/cm. During this sampling, the electrical conductivity dropped slightly, and now is slowly increasing again. EC in Sect-mid increased during the monitoring period and reached 1900 μS/cm before the sampling in 2013. During the pumping in September, 2013, the EC varied quite a bit and was slightly lower after pumping was completed than it was when pumping began. EC in Sect-up has been higher than in Sect-mid and Sect-low for the majority of the monitoring period. In October, 2012, it levelled off at around 2200 μS/cm. From November, 2012, to September, 2013 the EC remained at ~ 2350 μS/cm in this section. The EC dropped slightly in Sect-up during the pumping in September, 2013, and is increasing slightly at the time when this report is written. It is noted that step changes in the electrical conductivity occur in Sect-up at the beginning of June, 2012, and in September, 2012. These changes are not associated with changes in hydraulic head or temperature, or any sampling activity in the borehole, but have not been further analysed.

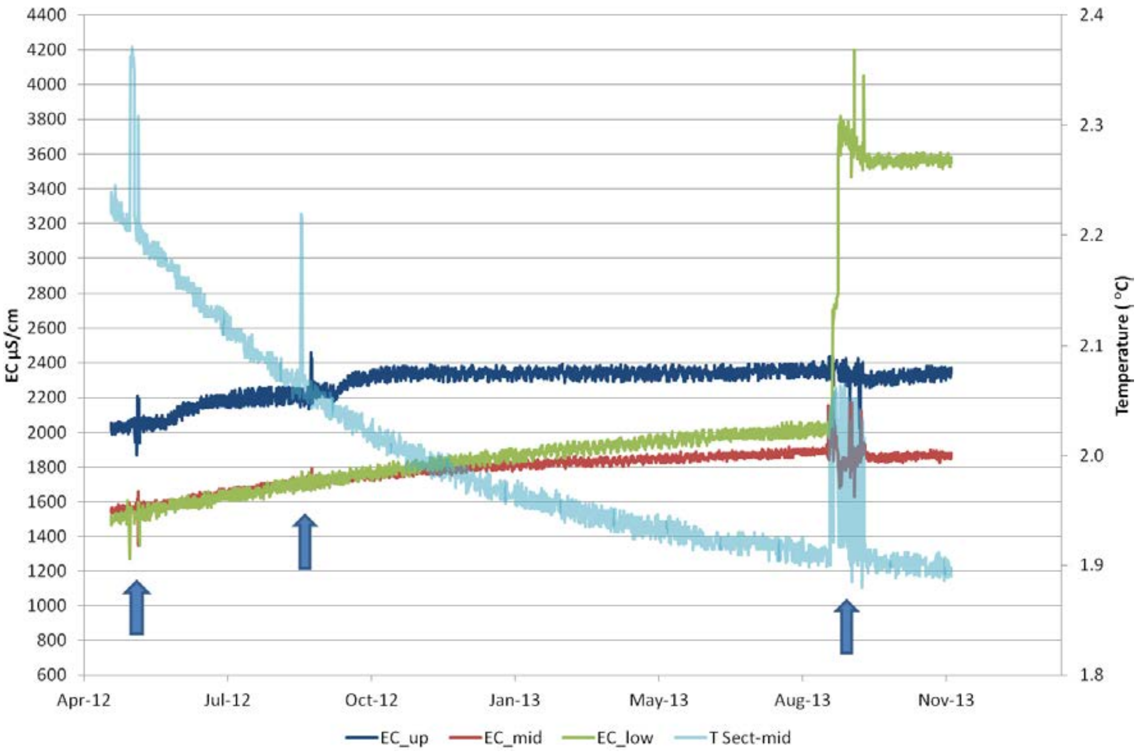

Figure 5-58. *T in DH-GAP04 Sect-mid, and temperature corrected (to 25 °C) EC in Sect-up, Sect-mid and Sect-low from April, 2012, to November, 2013. The logging frequency was every 4 h. The EC and temperature drops and increases occurring in May, 2012 (in all three sections), in September, 2012 (in Sect-up and in Sect-mid), and in September, 2013 (in all three sections), are associated with water sampling attempts. A total of 10 L was recovered from Sect-low in May, 2012, whereas no water was recovered from Sect-mid or Sect-up. During the sampling attempt in September, 2012, no water was recovered from any of the sections, but an increase in temperature in Sect-mid and electrical conductivity in Sect-up were observed. During the sampling in September, 2013, from the three sections, 651 L were extracted from Sect-up, 1068 L were extracted from Sect-mid and 576 L were extracted from Sect-low.*

The salinity, and hence EC, usually increase with depth in crystalline bedrock (e.g. Laaksoharju et al. 2009). Prior to the sampling campaign in September, 2013, this was not the case in DH-GAP04. However, following the extensive pumping of DH-GAP04, the EC is now highest in Sect-low. According to hydraulic tests (see Section 5.6.3) and pressure monitoring, it appears that Sect-up and Sect-mid are in good hydraulic contact, however, the EC-values between these sections differ by ~ 300 µS/cm. The water chemistry and isotopic composition of these sections are described in Section 5.7.4.

Temperature in Sect-mid

Figure 5-57 shows the calculated hydraulic head in all three sections, together with the T, in Sect-mid throughout the monitoring period. Following installation, the T in the hole dropped from about 3 to 2.8 °C between July and October, 2011. The initial monitoring period is greatly affected by the hot drilling water (average T of drilling water ~ 60 °C) injected into the hole. Between October, 2011, and June, 2013, the T dropped another 0.5 °C. Temperature is, more or less, following an exponential decay curve from mid-September, 2011, onward, and analysis of T data from the DTS-monitoring (see Section 5.5.1) confirms that the borehole is still cooling and recovering from drilling. Figure 5-58 shows EC and T from April, 2012, to November, 2013. During the water sampling attempts in May and September, 2012, and in September, 2013, changes in both electrical conductivity and T are observed. While T increases during purging, EC displays both increases and decreases, which likely is related to the fact that water is being "pushed" back and forth through the check valve downhole during purging events. It is noted that the T increase in Sect-mid during both sampling and the sampling attempts are roughly the same, irrelevant of the amount of water pumped out from the section.

Discussion on results from hydrogeological investigations in DH-GAP04

The shapes of the head curves in DH-GAP04 reveal a seasonal variation where the heads peak in June–July and reach their lowest levels in October–December, which roughly coincides with times when the ice sheet is the most and least active, respectively, suggesting that there may be a coupling to the hydrological conditions in the basal drainage system. This seasonality is particularly pronounced in the upper and mid sections, whereas it is much reduced in Sect-low (Figure 5-59).

By comparing the DH-GAP04 borehole heads with the calculated regional runoff from the ice sheet (see Figure 5-59, Figure 5-60 and Figure 5-61) the following is noted:

- The head changes in both Sect-up and Sect-mid roughly coincide with the changes in the calculated runoff. The correlation between the head in Sect-low and runoff appears less pronounced (Figure 5-59).
- The peak heads in Sect-up and Sect-mid and peak runoff correlation is prominent. However, a closer examination of the timing of the bulk surface meltwater runoff and maximum heads reveal a phase offset between the two, where the heads in Sect-up and Sect-mid peak approximately one week before runoff, after which both the heads and runoff drop (Figure 5-60).
- The head amplitude appears to correlate with the runoff magnitude, i.e. the highest heads in the borehole occurred in 2012 when also the runoff was considerably larger than in 2013 (Figure 5-60).
- Borehole heads seem to react instantaneously to runoff initiation (Figure 5-60 and Figure 5-61).

In Figure 5-51, lines are inserted to illustrate the similarities between different years in terms of head increase and decrease rates, as well as increased/decreased magnitudes. The head increase rates in 2011/2012 and in 2012/2013 (green dashed lines) are the same. As soon as the ice sheet starts melting substantially in April–May and runoff initiates, head increases at elevated rates (orange dotted lines). The head decrease rates in 2012 and 2013 (blue dashed lines) are the same, though runoff is significantly different between these years. Although the groundwater system was disturbed by drilling, because huge volumes of water were injected into the bedrock, the head drop rate is the same from September to October, 2011 as the head drop rates observed in 2012 and 2013 (a blue dashed line was superimposed on the head curves in 2011). The head increase from the lowest levels in 2011 and 2012 are the same until runoff begins, i.e. the pressure increase during winter is the same (indicated by red arrows in Figure 5-61). Once runoff initiates and the head increase rate speeds up, the magnitude by which heads increase in 2012 and 2013 differ (blue arrows). In 2012, the maximum head is approximately three metres higher than in 2013.

In conclusion, the head changes in both Sect-up and Sect-mid roughly coincide with the changes in the calculated runoff. The synchronised responses of Sect-up and Sect-mid imply that the flowing fractures intersecting these two monitoring sections are interconnected and are part of, or connect to, the fracturing along geological structures that potentially outcrop at locations where melting conditions prevail below the Isunnguata Sermia Glacier. The cross-cutting fracturing within Sect-mid and in the lower part of Sect-up probably explains why these sections appear to be hydraulically well connected.

In comparison, the time series showing a consistently lower head in Sect-low in Figure 5-59 reveals significantly weaker correlation to the seasonal changes in the regional runoff envelope. This difference is attributed to the almost complete lack of steeply dipping fractures intersecting Sect-low and by the generally lower specific capacity values at depth in DH-GAP04. Together, these conditions probably explain why the head values in Sect-low are considerably lower and less sensitive to pressure changes associated with seasonal changes in regional runoff. To conclude, the significantly higher (artesian) heads in Sect-up and Sect-mid are likely due to a better connection at these elevations to the surface in combination with their ‘confined location’ between the upper ‘sealing’ permafrost boundary and the lower sealing intact 30 m thick bedrock unit.

5.6.6 Summary of downhole monitoring observations

Figure 5-62 and Figure 5-63 show WellCad plots of the geological and hydrogeological parameters vs. vertical depth in DH-GAP01 and DH-GAP04, respectively. Information on downhole instrumentation is also given.

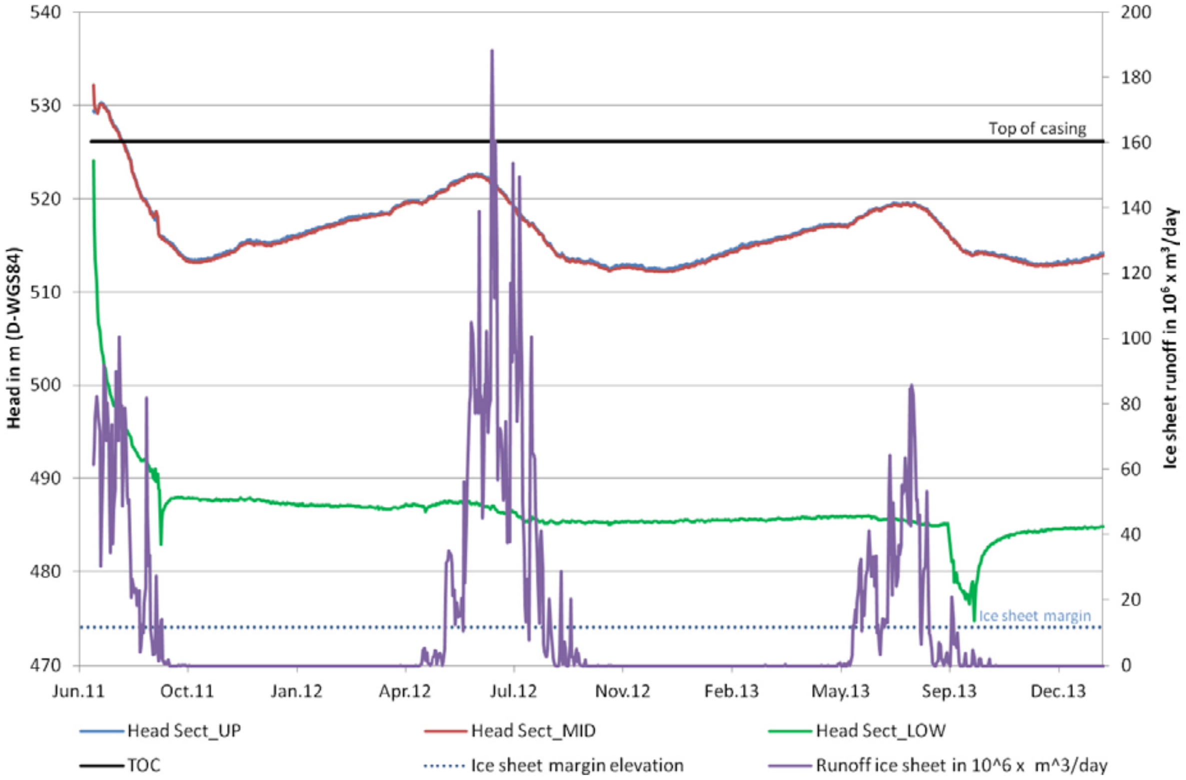

***Figure 5-59.** Daily average heads in Sect-up, Sect-mid and Sect-low in borehole DH-GAP04 and surface meltwater runoff from the Kangerlussuaq sector of the GrIS. The elevation of the TOC of DH-GAP04 (526.17 m, D-WGS84) is indicated as a black horizontal line. The calculation of hydraulic heads assumes 1 kPa = 0.10196 m of water.*

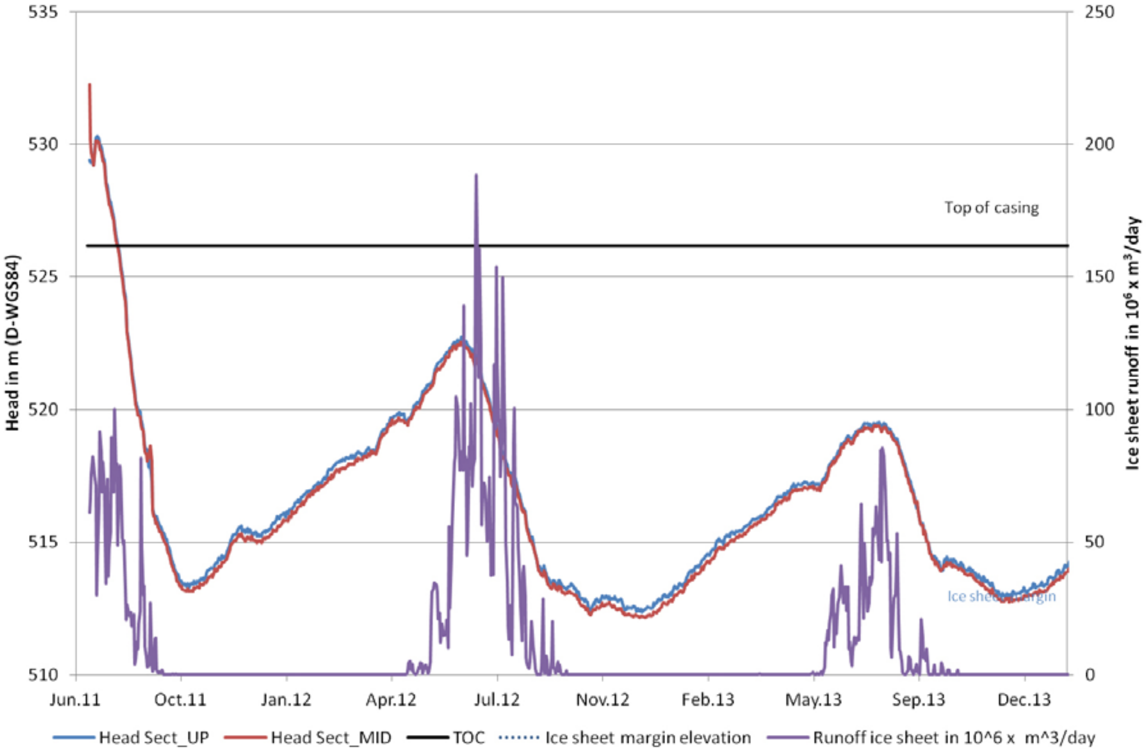

***Figure 5-60.** Daily average heads in Sect-up and Sect-mid of borehole DH-GAP04 and surface meltwater runoff from the Kangerlussuaq sector of the GrIS. The elevation of the TOC of DH-GAP04 (526.17 m, D-WGS84) is indicated as a black horizontal line. The calculation of hydraulic heads assumes 1 kPa = 0.10196 m of water.*

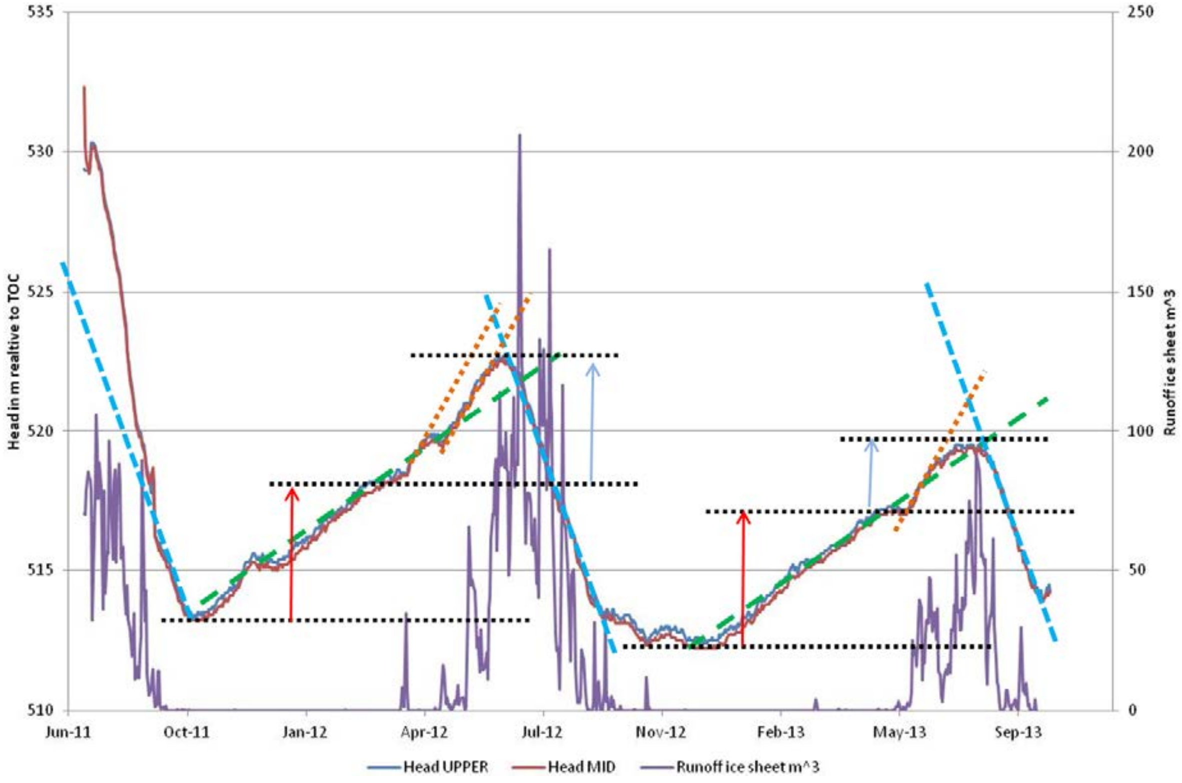

***Figure 5-61.** Daily average heads in Sect-up and Sect-mid of borehole DH-GAP04 and surface meltwater runoff from the Kangerlussuaq sector of the GrIS.*

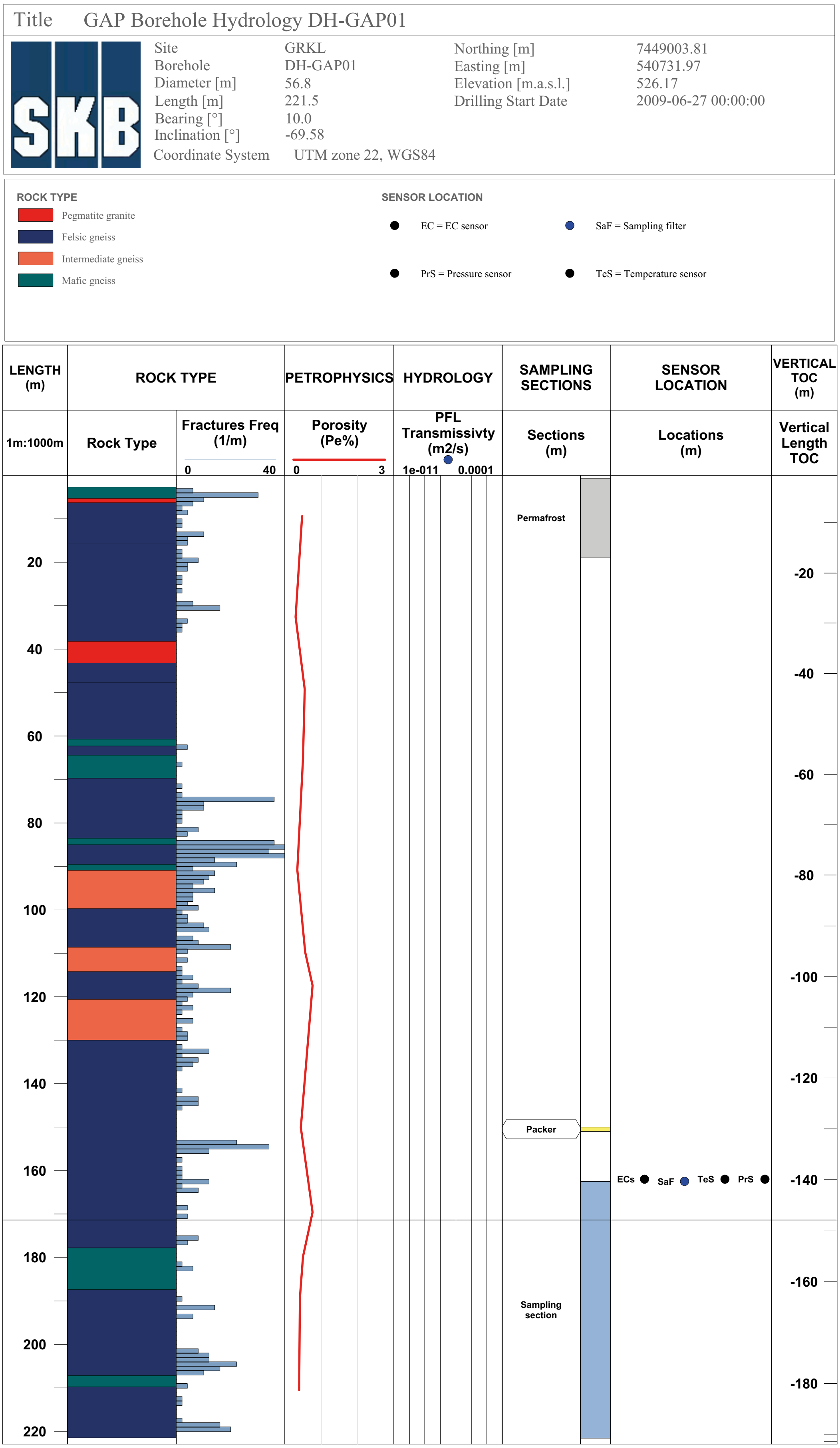

Title GAP Borehole Hydrology DH-GAP01

Site	GRKL	Northing [m]	7449003.81
Borehole	DH-GAP01	Easting [m]	540731.97
Diameter [m]	56.8	Elevation [m.a.s.l.]	526.17
Length [m]	221.5	Drilling Start Date	2009-06-27 00:00:00
Bearing [°]	10.0		
Inclination [°]	-69.58		
Coordinate System	UTM zone 22, WGS84		

Figure 5-62. WellCad plot of the geological and hydrogeological parameters vs. vertical depth in DH-GAP01. Information on downhole instrumentation is given.

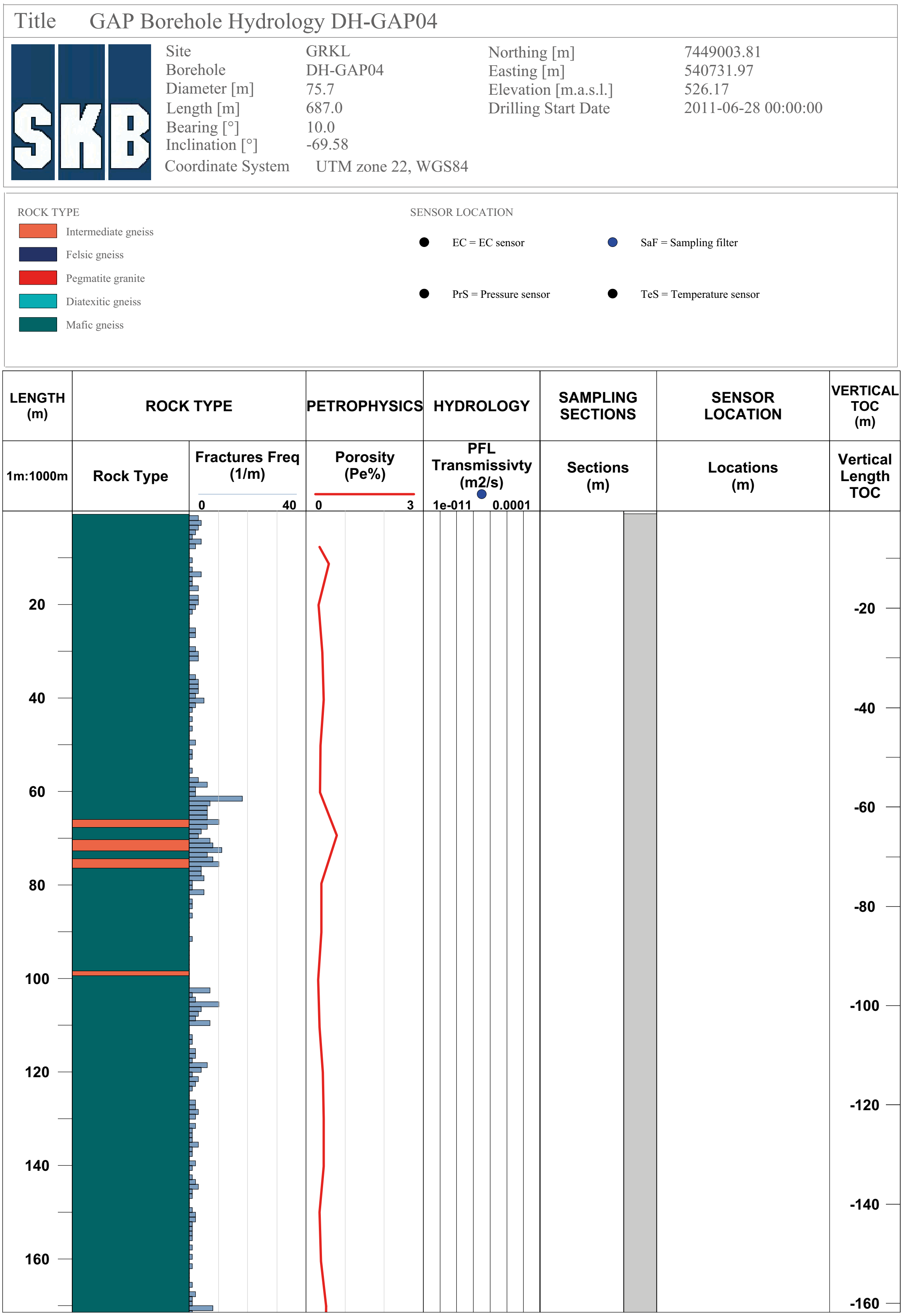

Title GAP Borehole Hydrology DH-GAP04

Site	GRKL	Northing [m]	7449003.81
Borehole	DH-GAP04	Easting [m]	540731.97
Diameter [m]	75.7	Elevation [m.a.s.l.]	526.17
Length [m]	687.0	Drilling Start Date	2011-06-28 00:00:00
Bearing [°]	10.0		
Inclination [°]	-69.58		
Coordinate System	UTM zone 22, WGS84		

Figure 5-63. *WellCad plot of the geological and hydrogeological parameters vs. vertical depth in DH-GAP04. Locations of the groundwater monitoring sections are indicated together with the positions of the downhole instrumentation. Permafrost confining the upper section is highlighted in grey.*

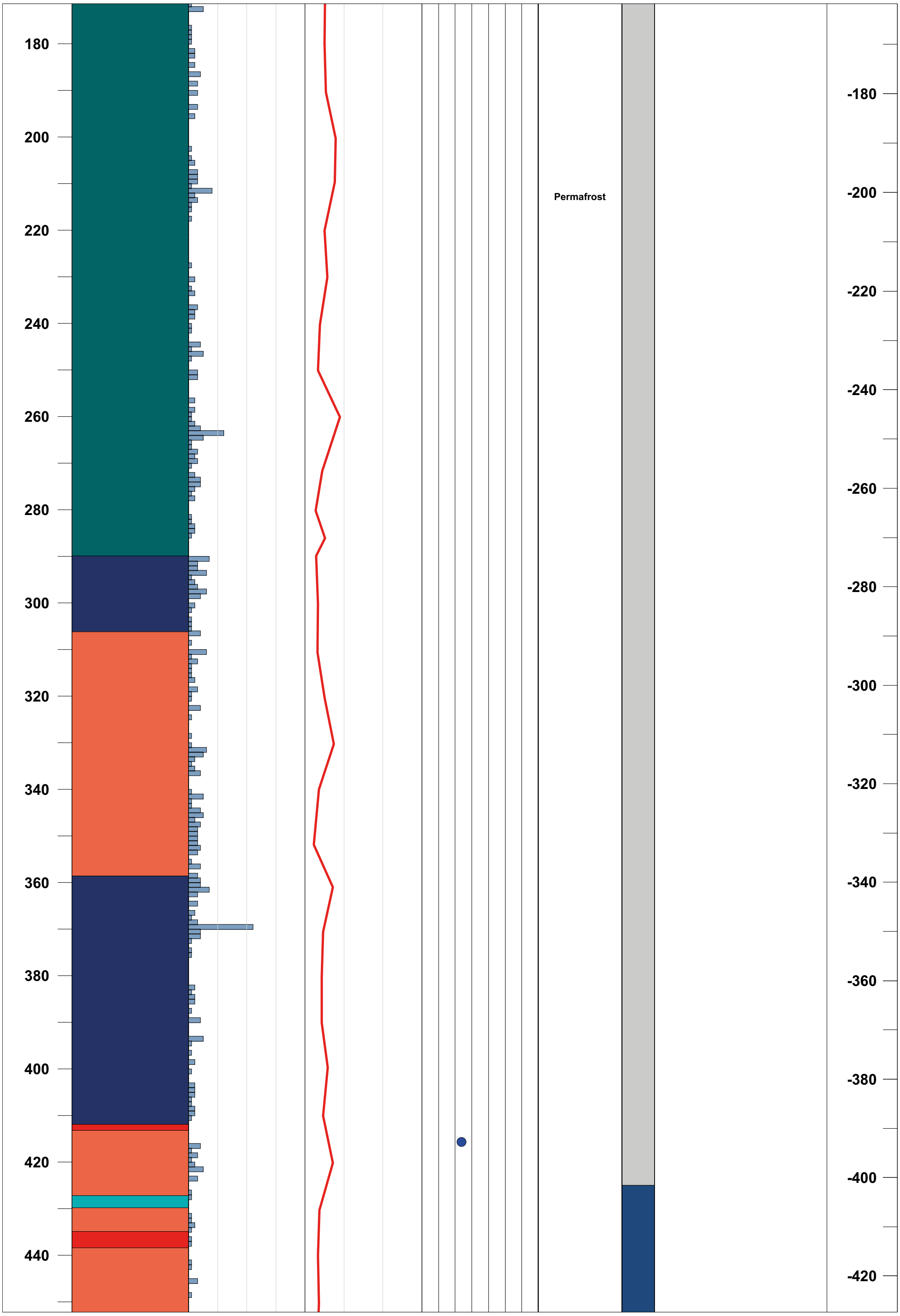

Figure 5-63. *Continued.*

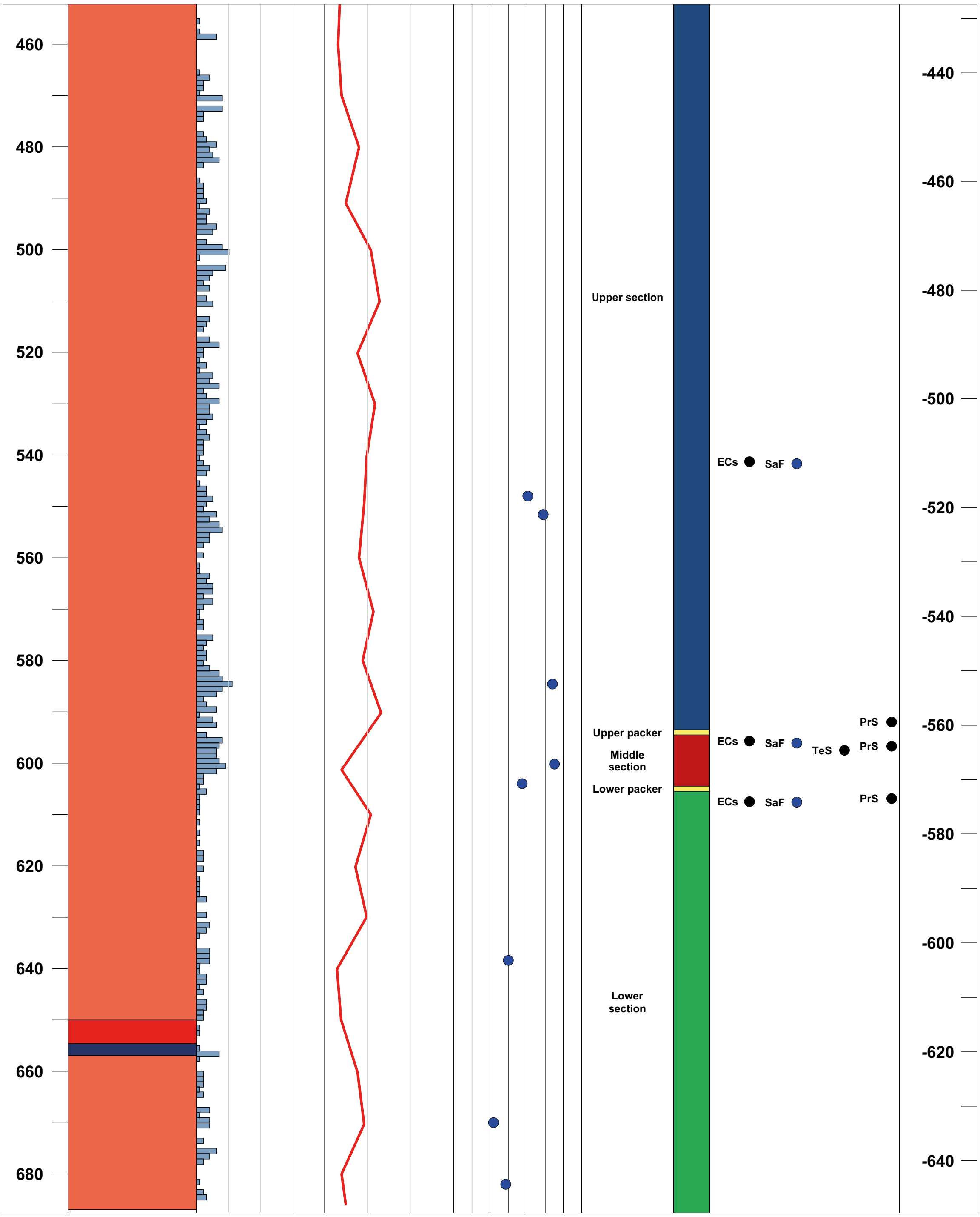

Figure 5-63. *Continued.*

Figure 5-64 gives the hydraulic heads in DH-GAP01 and DH-GAP04 for their entire monitoring periods with respect to the TOC of each borehole. The water level in DH-GAP01 is ~ 7–8 metres below TOC during the monitoring period, whereas the level in DH-GAP04 is ~ 40 m below the TOC in Sect-low (~ 486 m) and between 5 to 14 m below TOC in Sect-up and Sect-mid (~ 521 m and 512 m) below the TOC during the monitoring period. Generally speaking, because drilling water is forced into the formation during drilling, the pressures increase temporarily in response. Following cessation of drilling, recovery initiates and pressures in the formations decline. This is observed in both boreholes.

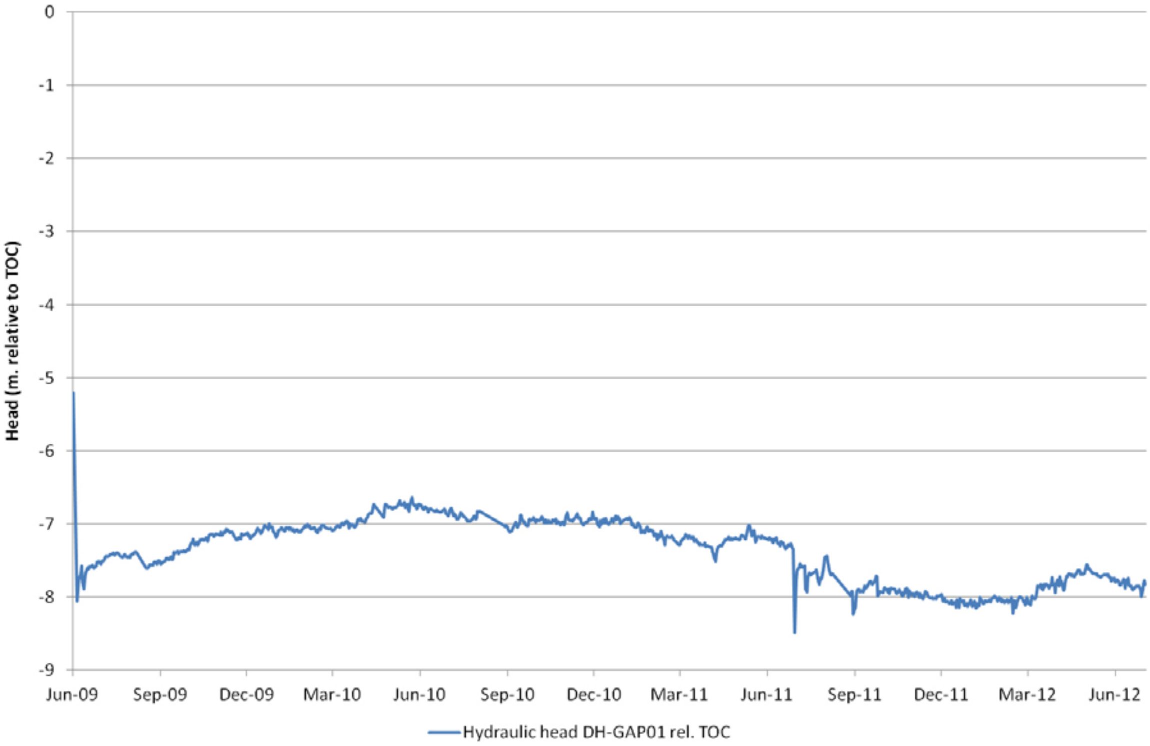

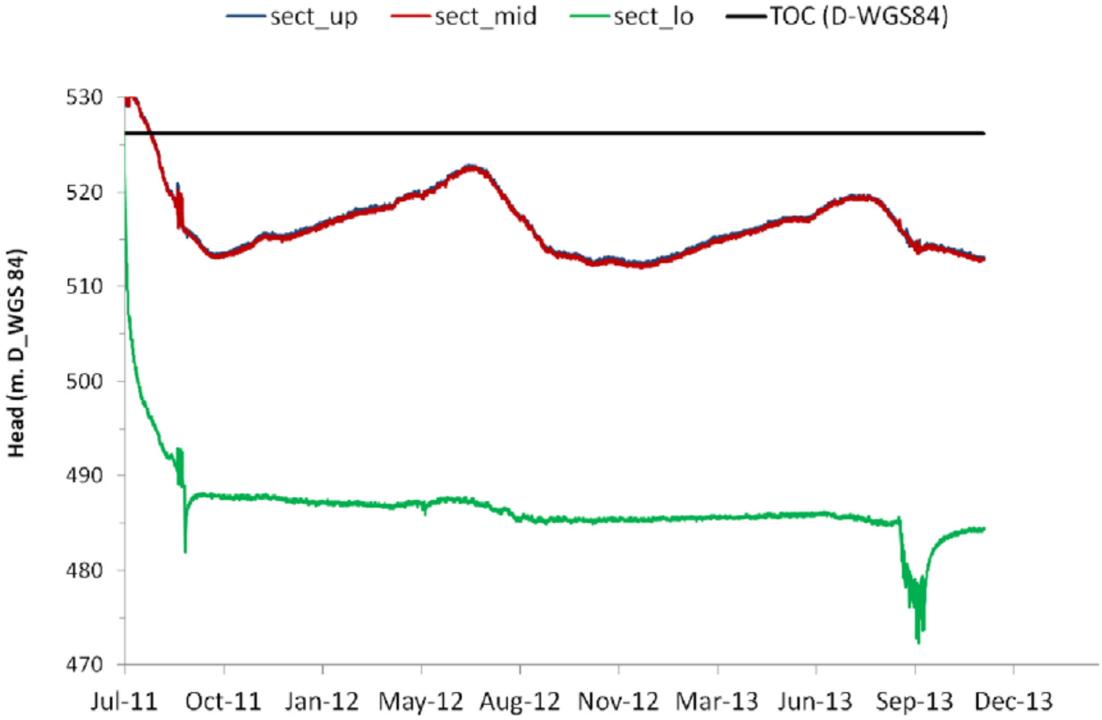

Figure 5-64. *Daily mean hydraulic heads in DH-GAP01 (upper chart) and DH-GAP04 (lower chart). Note the different scales on the y-axis in the two charts. The reference datum in the upper chart is the TOC of DH-GAP01, whereas the reference datum in the lower chart is D-WGS84.*

The presence of seasonal head variation, as observed in DH-GAP04, is not observed in borehole DH-GAP01. This is in agreement with the interpretation by Johansson et al. (2015a), suggesting that the groundwater in the Talik lake is governed by local surface hydrological processes (i.e. lake processes) rather than being coupled to the ice sheet system. The observations from DH-GAP04 show that the heads at 500 m depth, i.e. Sect-up and Sect-mid, are clearly affected by the ice sheet and glaciohydrological processes, and a dynamic coupling between the bedrock and ice sheet is evident.

In contrast, the time series from DH-GAP04 show a consistently lower head in Sect-low and also reveals a significantly weaker correlation to the seasonal changes in the regional runoff. This difference is attributed to the almost complete lack of steeply dipping fractures intersecting Sect-low, and by the generally lower specific capacity values at depth in DH-GAP04. Together, these conditions probably explain why the head values in Sect-low are considerably lower and less sensitive to pressure changes associated with seasonal changes in regional runoff. To conclude, the significantly higher artesian heads in Sect-up and Sect-mid are likely due to a better connection at these elevations to the surface below the ice sheet in combination with their 'confined location' between the upper 'sealing' permafrost boundary and the lower sealing intact 30 m thick bedrock unit.

5.7 Hydrogeochemistry

Hydrogeochemistry studies during SPC field work were focused on two main areas: surface waters and groundwaters. DH-GAP04 was a key source of data, around which other studies have provided complementary information and increased understanding of hydrogeochemistry in a glacial environment. DH-GAP04 has provided pressure, chemistry, and temperature data for groundwaters beneath the ice sheet. DH-GAP01 has provided over 3 years of pressure, temperature, and conductivity monitoring data, as well as samples of groundwater from within a talik. Surface water studies provide background information on geochemical processes in the study area.

Surface water studies began in 2008 during initial evaluation of the Kangerlussuaq region for its suitability to host the GAP. Overall, 44 lakes in the area were sampled for main chemical and isotopic analyses, including $\delta^{18}O$, $\delta^{2}H$, ^{3}H, $\delta^{37}Cl$, ^{87}Sr, and $\delta^{34}S$ and $\delta^{18}O$ of SO_4. Meltwaters were sampled in several locations at Leverett Glacier and Isunnguata Sermia for chemical and isotopic analyses. Also ice samples were analysed for $\delta^{18}O$, $\delta^{2}H$ and tritium. Locations of sampled lakes, boreholes and ice samples are shown in Figure 5-65.

Waters from DH-GAP01 and DH-GAP04 were analysed for a full suite of chemical parameters, as well as $\delta^{18}O$, $\delta^{2}H$, ^{3}H, ^{36}Cl, $\delta^{37}Cl$, ^{87}Sr, and $\delta^{34}S$ and $\delta^{18}O$ of SO_4.

5.7.1 General methods for hydrogeochemical samples

The following section outlines the sampling procedures and treatments used for both surface and groundwater samples, as well as the laboratory methods used in the analyses of these samples. Any additional clarifications of methods, specific to a sampling location, are outlined in the appropriate subsection.

Lake and river samples were generally collected from the shoreline, near the surface, with shallow or partially enclosed areas avoided. A portable Oakton pH, conductivity and temperature meter (pH/Con 10 series, Vernon Hills, Illinois, USA), a YSI 6600 multi-parameter meter or an In-Situ Inc. ® Troll 9500 multi-parameter meter was used to measure field parameters at sampling locations. In some cases, as indicated in the sample name by a depth measurement in metres (e.g. Talik lake, 25 m), a grab sampler, such as a kemmera bottle, was used to obtain samples at depth. Meltwater samples were taken from sub- or supra-glacial flow at the ice sheet margins.

Water samples from boreholes DH-GAP01 and DH-GAP04 were acquired using the systems described in Section 5.3.2. Microbial samples were acquired from DH-GAP01, in July, 2009, and in September, 2010. In addition, two gas samples from DH-GAP04 (Sect-up) were taken with pressurised water sampling equipment (PAVE) (Öhberg 2006) in September, 2013. Sect-up was chosen for gas sampling due to the visible existence of gas bubbles during groundwater sampling. While collecting the gas samples, the dissolved oxygen measurement was monitored with an optical dissolved oxygen measurement probe (Mettler Toledo, SG9 SevenGo pro™). Groundwater samples acquired from the Leverett Spring were collected where water was flowing into the spring from the subsurface.

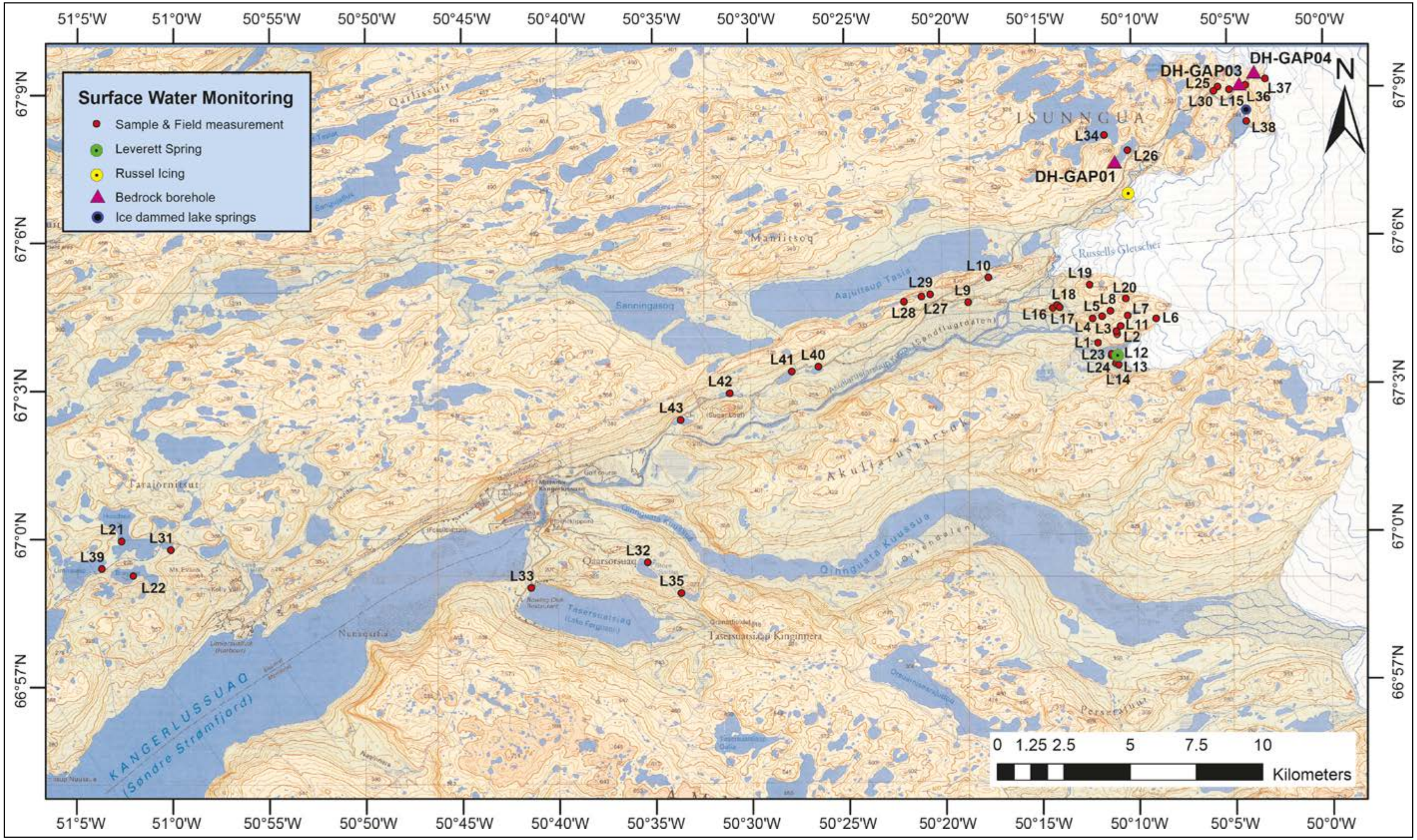

Figure 5-65. Locations for surface and groundwater hydrogeochemical sampling.

Gas samples were acquired from the Leverett Spring at the same location. In the summer of 2009, four drive-point piezometers were installed at several locations and depths in the Leverett Spring pool. Because the piezometers were destroyed during the following winter due to ice build-up, only one sampling period was possible.

Water samples for isotopic and anion analyses were collected in plastic Nalgene bottles and were not filtered or otherwise treated. Cation samples were filtered with 0.45 µm filters and acidified with ultra-pure nitric acid (HNO_3). Samples collected for analysis of the tracer, sodium fluorescein, were wrapped in aluminum foil to prevent deterioration of the tracer from exposure to light.

Bubbling can be observed at the Leverett Spring, focused around the spring outlet. Samples of this gas have been collected since 2008. In general, samples were collected for composition and isotopic analyses. A large funnel was inverted and held underwater where it feeds into an inverted glass bottle that has been filled with water from the spring pond. Water is displaced as the gas sample is collected and the bottle is capped underwater with a teflon septum-equipped cap, while some water remains in the inverted bottle to help seal the gas sample. Following sampling, bottles were transported in an inverted position to help prevent atmospheric gases from mixing with the sample. Further refinement of the sampling method was employed in 2011 – the samples were transported with the caps positioned underneath a layer of water and the samples were kept cool during transport and storage. Results believed to be more representative were achieved in 2011 due to these improved methods.

Water and gas isotope analyses were performed at the University of Waterloo Environmental Isotope Laboratory. Geochemical samples were analysed at Labtium Oy or at *Teollisuuden Voima* (TVO) laboratory in Finland. Gas samples were analysed for composition at the University of Waterloo Organic Geochemistry Laboratory (Waterloo, Ontario, Canada) or at the Microbial Analytics Sweden AB laboratory. Microbial samples were analysed at the Microbial Analytics Sweden AB laboratory.

5.7.1.1 Geochemical analyses

Geochemistry samples were analysed at Labtium Oy, Finland, in 2008 and 2010–2012, and the TVO laboratory in Finland in 2009. Geochemical analyses were performed using the following methods at Labtium Oy. Alkalinity was measured using a titrimetric determination. Anions were measured by *Ion Chromatography* (IC) and cation multi-element determination was performed by a combination of *Inductively Coupled Plasma Mass Spectrometry* (ICP-MS) and *Inductively Coupled Plasma Atomic Emission Spectroscopy* (ICP-AES). At TVO, multi-element analysis was done using *Inductively Coupled Plasma Optical Emission Spectrometry* (ICP-OES) and ICP-MS. Analysing methods are presented in Table 5-10.

Table 5-10. Analysing methods at Labtium Oy and TVO laboratory.

Lab	Analysis	Method
Labtium Oy (2008; 2010–2012)	Alkalinity	Titrimetric determination
	Anions	Ion Chromatography
	Cations	ICP-MS and ICP-AES
Teollisuuden Voima Oyj (2009)	Multi-element analysis	ICP-OES and ICP-MS

5.7.1.2 Isotope analyses

Tritium pre-analysis was determined using the electrolytic enrichment method of Taylor (1977). After enrichment, samples were counted in a LKB Wallac 1220 Quantalus liquid scintillation counter with a detection limit of 0.6 ± 0.8 TU. Deuterium determinations were made following the Cr reduction method, outlined by Morrison et al. (2001), and analysed on an Isoprime *isotope ratio mass spectrometer* (IRMS) coupled to a Eurolectron elemental analyser. Oxygen isotope analysis was performed on an IsoPrime *continuous flow isotope ratio mass spectrometer* (CF-IRMS) using the preparation procedures of Epstein and Mayeda (1953) with Moser's modification (Moser 1978).

Results for $\delta^{18}O$ and $\delta^{2}H$ are reported based on standard corrections to *Vienna Standard Mean Ocean Water* (VSMOW) and *Vienna Standard Light Antarctic Precipitation* (VSLAP) from the *International Atomic Energy Agency* (IAEA). Analytical reproducibility of $\delta^{18}O$ and $\delta^{2}H$ are ± 0.2 ‰ and ± 0.8 ‰, respectively. After the September, 2013, sampling campaign at DH-GAP04, preliminary results for $\delta^{18}O$ and $\delta^{2}H$ were determined using the Los Gatos *off-axis integrated cavity output spectroscopy* (OA-ICOS) (Berman et al. 2013). Results are comparable to the IsoPrime analyses.

Sulphate is extracted using $BaCl_2$ and converted to SO_2 by combustion with N_2O_5 and analysed on a Micromass IsoChrom-IRMS (± 0.3 ‰) (Rees and Holt 1991, Morrison et al. 1996). For analysis of ^{18}O in SO_4, the $BaSO_4$ is combusted to produce CO and analysed in a GVI IsoPrime-IRMS (± 0.5 ‰). ^{18}O and ^{34}S are corrected to $BaSO_4$ IAEA-SO-5, IAEA-SO-6 and NBS-127. Analysis for ^{37}Cl is carried out after conversion of precipitated Cl as AgCl to CH_3Cl and is anlaysed using continuous flow technology on a Micromass IsoPrime IRMS (± 0.2 ‰) (Kaufman et al. 1984, Eggenkamp et al. 1995, Shouakar-Stash et al. 2005a). ^{81}Br was determined following the method described in Shouakar-Stash et al. (2005b) using continuous flow IRMS. Analyses of the ratio of ^{87}Sr to ^{86}Sr was done using *thermal ionization mass spectrometry* (TIMS), using a method modified from Dickin (2005). ^{36}Cl was analysed by *accelerator mass spectrometry* (AMS) using the 6 MV EN-Tandem accelerator (blank level $^{36}Cl/^{35}Cl=1-2\times10^{-15}$) at the Laboratory of Ion Beam Physics at ETH Zurich (Christl et al. 2013).

A summary of the analysis methods is presented in Table 5-11.

Table 5-11. Analysing methods for isotopic analyses.

Analysis	Laboratory	Instruments	References
Tritium (^{3}H) Tritium Units (TU)	University of Waterloo Environmental Isotope Laboratory	LKB Wallac 1220 Quantalus liquid scintillation counter (± 0.8 TU)	Taylor (1977)
Deuterium ($\delta^{2}H$) ‰VSMOW	University of Waterloo Environmental Isotope Laboratory	IsoPrime IRMS, Euroelectron element analyser (± 0.8 ‰)	Morrison et al. (2001)
Oxygen-18 ($\delta^{18}O$) ‰VSMOW	University of Waterloo Environmental Isotope Laboratory	IsoPrime IRMS (± 0.2 ‰)	Epstein and Mayeda (1953), Moser (1977)
Sulphur-34 ($\delta^{34}S–SO_4$) ‰ CDT	University of Waterloo Environmental Isotope Laboratory	Micromass IsoChrom-IRMS (± 0.3 ‰)	Rees (1984), Morrison et al. (1996)
Oxygen-18 ($\delta^{18}O–SO_4$) ‰VSMOW	University of Waterloo Environmental Isotope Laboratory	GVI IsoPrime-IRMS (± 0.5 ‰)	Morrison (1997)
Chlorine-37 ($\delta^{37}Cl$) ‰VSMOC	University of Waterloo Environmental Isotope Laboratory	Micromass IsoPrime-IRMS (± 0.2 ‰)	Kaufman et al. (1984), Eggenkamp et al. (1995), Shouakar-Stash et al. (2005a)
Bromine-81 ($\delta^{81}Br$) ‰VSMOB	University of Waterloo Environmental Isotope Laboratory	Continues flow IsoPrime-IRMS (± 0.2 ‰)	Shouakar-Stash et al. (2005b)
Strontium-87 $^{87/86}Sr$ ratio	University of Waterloo Environmental Isotope Laboratory	TIMS	Dickin (2005)
Chlorine-36 $^{36}Cl/Cl$	ETH Zurich	AMS	Christl et al. (2013)

5.7.1.3 Gas Sample Analyses

Gas samples from DH-GAP04 (Sect-up) were analysed at the Microbial Analytics Sweden AB laboratory and the analysis method is described in Pedersen (2008). Air contamination may happen during sampling and Pedersen (2008) notes that minor air contamination can happen during extraction of the gas. Therefore, the air contamination corrected results are used as final results. Gas samples from the Leverett Spring were analysed at the University of Waterloo Organic Geochemistry Laboratory on a Fisher/Hamilton Model 29 gas chromatograph for oxygen, nitrogen, carbon dioxide and methane.

5.7.2 Surface water geochemistry

There were several goals to the surface water investigations that took place as a part of the GAP SPC work. These include the following:

1. Providing end members for various geochemical parameters (compositional and isotopic) for lakes and meltwaters. Groundwater values could then be compared as part of a dynamic system. This was particularly important for meltwaters – to help determine the depth to which meltwater penetrates into the subsurface.
2. Understanding possible interaction between groundwaters and surface waters and determining whether there were geochemical indicators for groundwater upwelling into lakes through taliks.
3. Determining the cause of salinity in the lakes so that the cryogenic concentrations model of salinity development in front of ice sheets (Herut et al. 1990, Starinsky and Katz 2003) could be evaluated.
4. To be able to compare and distinguish the chemical and isotopic similarities and differences between suspected glacial recharge and surface meteoric recharge from lakes.
5. To provide understanding of the geochemical systems for key elements, such as sulphur and strontium, which can help to determine flow paths and interpret the geochemical evolution of groundwaters.

In the following sections, data and conclusions are broken down into individual subsections for each of the surface water categories.

5.7.2.1 Precipitation and spring runoff

Only one precipitation sample was gathered during the course of the study for the purpose of isotopic analyses. This sample was gathered as snow at the camp near DH-GAP03 and had a $\delta^{18}O$ value of −20 ‰ which is similar to the −19 ‰ given in Leng and Anderson (2003), and corresponds well with the intersection of the local evaporation line described by the lakes (Figure 5-66). Tritium in the snow sample was measured at 13.8 TU, much higher than values found in any lakes in the study area, except for the most evaporated. Tritium values for arctic areas are less readily available than $\delta^{18}O/\delta^{2}H$ data.

Spring runoff samples were collected in 2012 from runoff streams during snow melt. Runoff is similar to precipitation values and plots (Figure 5-66B) along the local meteoric water line described by precipitation in Thule, the closest town with historical IAEA precipitation monitoring. Tritium values in spring runoff (9–10 TU) are lower than that found in precipitation (13.8 TU) and are more similar to those found in many lakes. Dilution due to the addition of old ground ice, or storage of water in the active layer, is likely contributing to the large scatter in tritium values between the lakes and precipitation. Leng and Anderson (2003) mention storage in the active layer as a process that causes scatter in the $\delta^{18}O$ values of lakes. Bursey (1990) noted that poor mixing of shallow groundwaters, due to heterogeneities in the till active layer, and the contribution of melting of isotopically depleted ground ice contribute to a large variation in isotopic signatures.

5.7.2.2 Lake waters

Lakes are subdivided into saline and dilute based on the categorisation of Anderson et al. (2001), where dilute lakes have an EC < 800 µS/cm and saline lakes > 800 µS/cm. Anderson et al. (2001) observed that lakes with conductivities above 800 µS/cm had chemistries that differed from the more dilute lakes, an observation made also in the lakes sampled by SPC. Locations of sampled lakes are shown in Figure 5-65. More information about lake investigations are provided in Aaltonen et al. (2010), SKB (2010b), Harper et al. (2011, 2016) and Henkemans (2016). Lakes analysed as part of SPC are subdivided into several categories in the following data tables and figures, in order to allow for ease of comparison.

Lake chemistry and isotopic composition is heavily influenced by evaporation. Lake waters fall along a *local evaporation line* (LEL) defined by the progressive enrichment in the heavy isotopes, oxygen-18 and deuterium, as the light isotopes of water are removed through evaporation (Figure 5-66). The proglacial lakes located in front of Leverett Glacier fall below the LEL. It is most likely that this is due to the influence of isotopically depleted ice melting from the frozen moraine in which these lakes are located. The ice can have a substantial component of old glacial precipitation (snow/ice), which most likely represents different paleoclimatic conditions of the past.

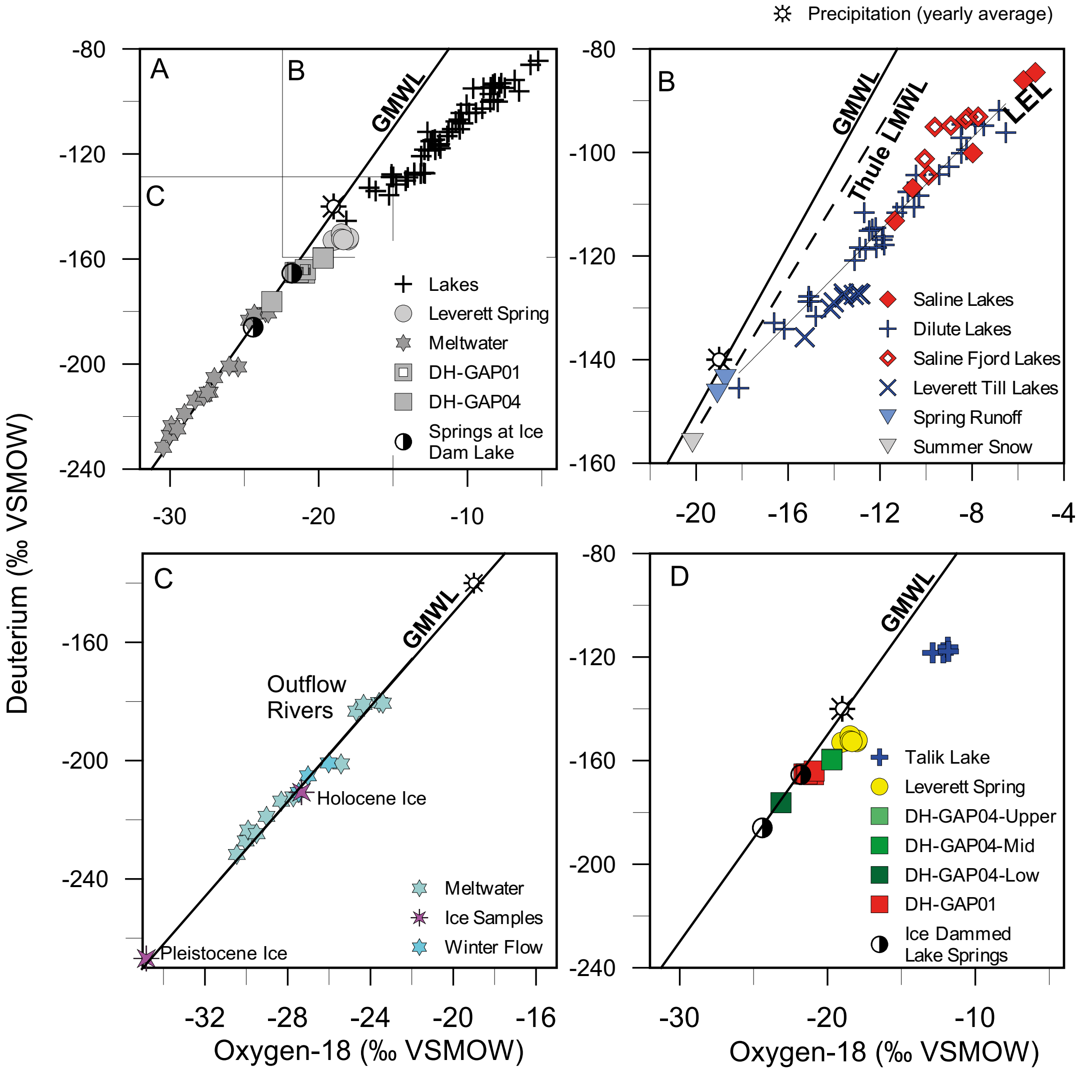

Figure 5-66. *Oxygen-18 and deuterium (^2H) results for A) all surface water and groundwater samples, B) lake samples, C) meltwater samples and D) groundwater samples. Note that, in the case of DH-GAP04, the given values are non-corrected samples from September 2013 (i.e. Sect-up and Sect-mid are affected by drilling water contamination). Sect-up and Sect-mid of DH-GAP04 overlap closely. Yearly average precipitation is marked on all plots with the symbol indicated at the top right of the figure. GMWL depicts the linear relationship between oxygen-18 and ^2H in precipitation around the globe, whereas the Thule LMWL depicts this relationship based on local precipitation. The LEL describes the linear relationship between $\delta^{18}O$ and δ^2H in waters evaporating under local temperature and humidity conditions.*

Lakes in the immediate proglacial area are dominated by Ca^{2+}, whereas lakes farther from the current ice margin, which underwent deglaciation less recently, may be dominated by $Ca^{2+,}$ Mg^{2+} or Na^+. Generally, lakes dominated by Na^+ are saline lakes. These findings are similar to those observed by Anderson et al. (2001). The influence of progressive evaporation can be observed in plots of various elements versus chloride as well, where the more saline lakes represent concentrated end members (Figure 5-67 and Figure 5-68). In Figure 5-67, where sulphate is plotted against chloride, it can be seen that lakes around the fjord tend to be chloride dominated compared to the more saline lakes between the fjord and the ice, where sulphate dominates. This is likely due to the presence of sea salt aerosols in the vicinity of the fjord.

Lake salinity may be influenced by the precipitation and dissolution of efflorescent salts, as has been suggested by Cooper et al. (2002) for arid, polar climates. The observation of gypsum- and halite-dominated salt crusts around many of the saline lakes supports this theory (Henkemans 2016).

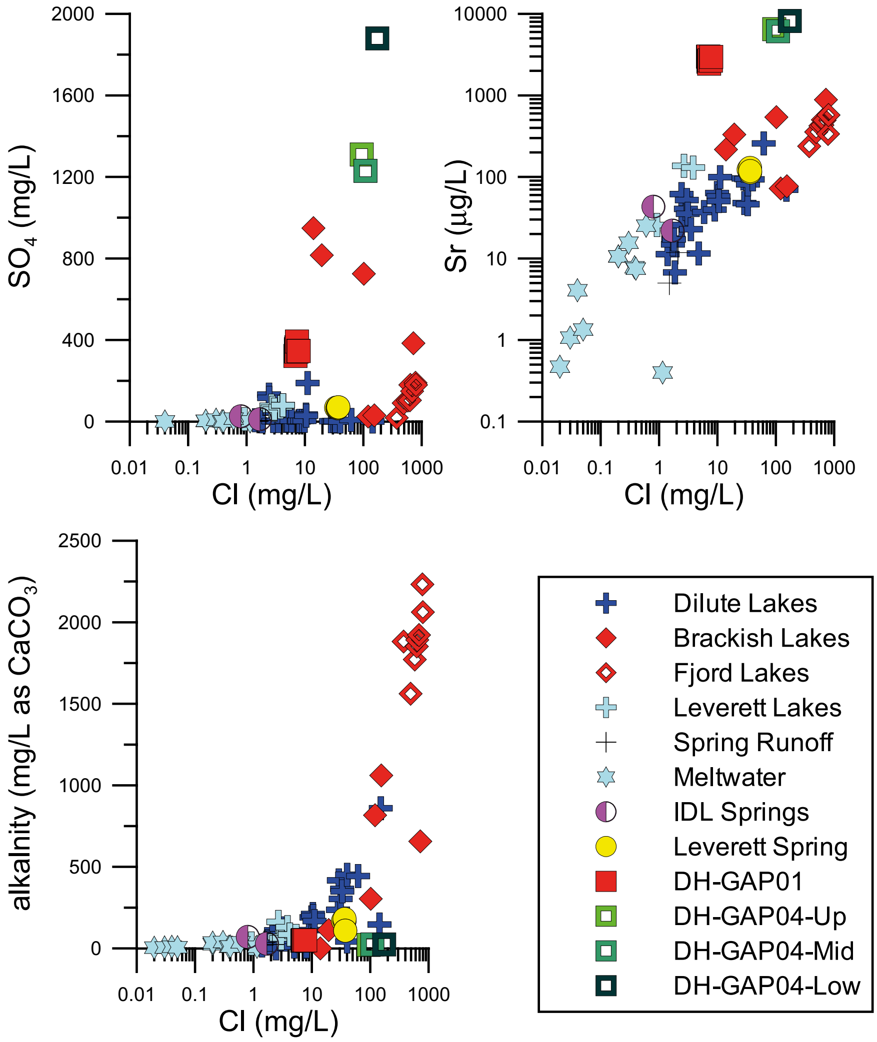

Figure 5-67. *Sulphate, strontium and alkalinity plotted against chloride. Note that DH-GAP04 concentrations for the Sect-up and Sect-mid are based on samples that are still moderately contaminated with drilling fluid (38 and 33 % respectively). Meltwater samples are shown, but often contain large charge imbalances. IDL springs refer to Ice dammed lake springs.*

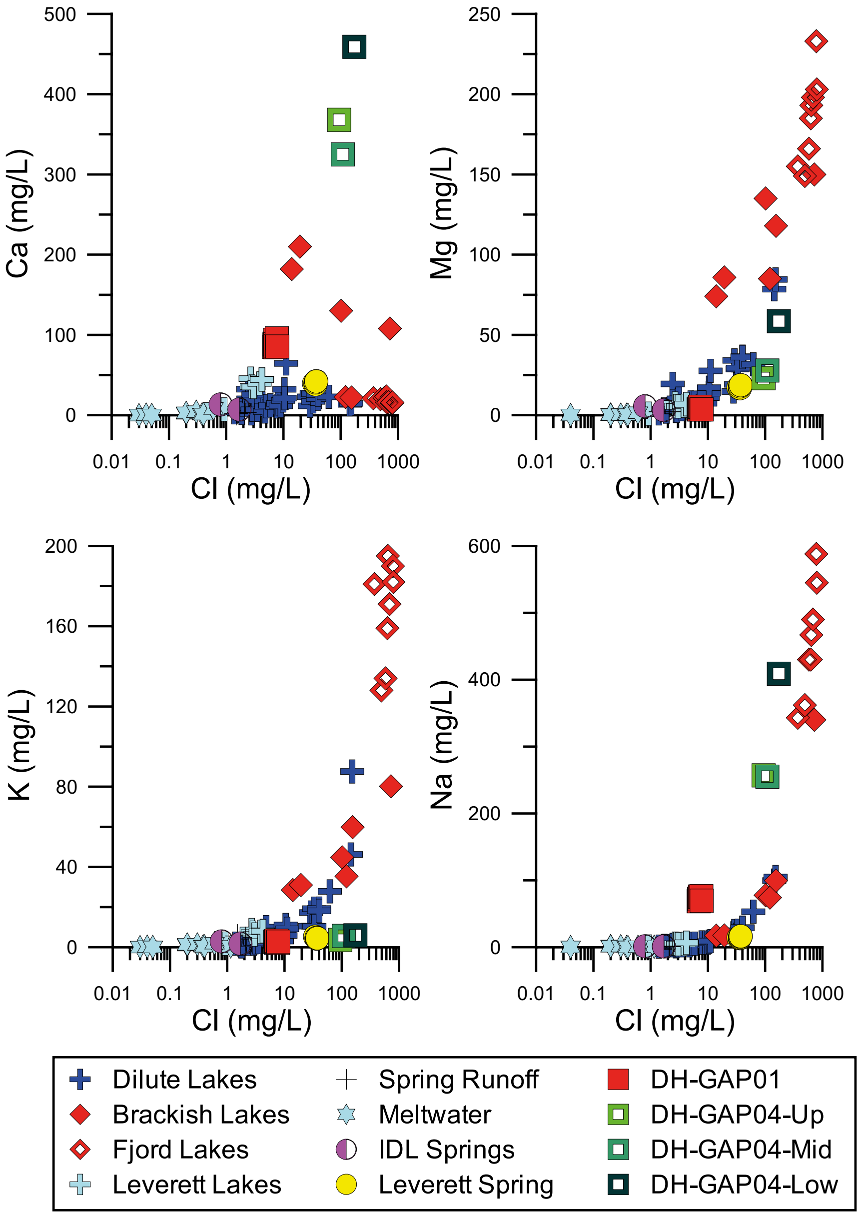

***Figure 5-68.** Major cations (Ca, Na, Mg and K) plotted against chloride concentration. Note that DH-GAP04 concentrations for Sect-up and Sect-mid are based on samples moderately contaminated with drilling fluid (38 % for Sect-up and 33 % for Sect-mid). Meltwater samples are shown, but often contain large charge imbalances. IDL springs refer to Ice dammed lake springs.*

Lakes located between the fjord and the ice have waters with high ^{87}Sr/^{86}Sr signatures, ranging from 0.7347 to 0.7574 (Figure 5-69). This is consistent with other studies in glacial sediments, and has been attributed to the rapid weathering of biotite when glacially commuted material is exposed at the surface (McNutt et al. 1990, Blum and Erel 1997). Lakes located closer to the fjord, such as the Kellyville Basin lakes and Lake Ferguson (L33) (Figure 5-65), in earlier deglaciated areas, have a lower ^{87}Sr/^{86}Sr ratio (0.7187 to 0.7540, with the majority below 0.73) (Figure 5-69). This may be attributed to a more mature weathering profile, where biotite weathering is less influential, or may be influenced by sea salt aerosols as well, which would have a strontium ratio of 0.709. The outlier of the lakes, located around the fjord at ^{87}Sr/^{86}Sr of 0.7540, is Store Saltsø, a closed basin lake marked L32 in Figure 5-65. It is unknown why L32 would have a much more radiogenic signature than Lake Ferguson (L33) due to their close proximity (Figure 5-65), but it may be a local geological effect.

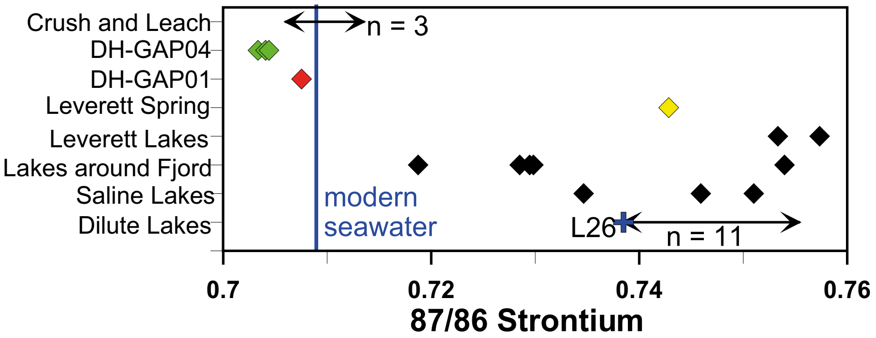

Figure 5-69. Strontium isotope ratios for surface waters and groundwaters. The "Talik lake", L26, is indicated separately within the dilute lakes category. Lakes around the fjord include the Kellyville Basin lakes, L32 (Store Saltsö) and L33 (Lake Ferguson) (see Figure 5-65).

Br/Cl ratios do not indicate cryogenic concentration of sea water as a potential source of salinity. Br/Cl and Na/Cl ratios in the study area (Figure 5-70) are greater than those of sea water, and greater than those predicted by Starinsky and Katz (2003) and Herut et al. (1990) to describe cryogenic concentrations of sea water. The model proposed by Starinsky and Katz (2003) suggests that the upwelling of highly saline water, created through cryogenic concentration of sea water, would occur at the forefront of continental ice sheets. There is no indication that this is occurring in the study area. Saline waters, similar to those observed in the Canadian and Fennoscandian shield regions (Frape et al. 1984), were not observed in the study area, and Br/Cl vs. Na/Cl values are different from those observed in the Canadian or Fennoscandian shields.

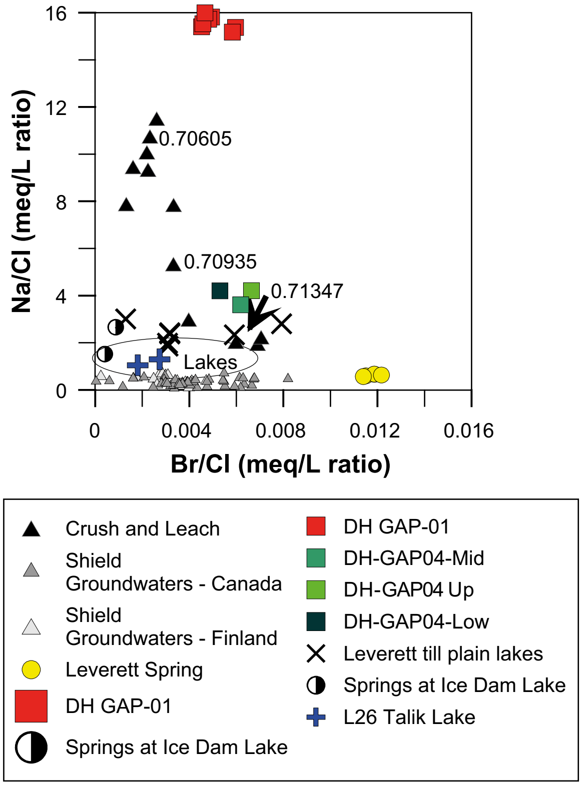

Figure 5-70. Br/Cl and Na/Cl ratios for groundwaters, lakes and crush and leach waters. Number values displaced on the plot indicate the $^{87}Sr/^{86}Sr$ values for crush and leach waters. Sea water has a Br/Cl ratio of 0.0016 and a Na/Cl ratio of 0.86, which is lower than any samples observed in the study area. The Talik lake, L26, is indicated separately in the stippled area that illustrates the range covered by lakes within the study area. DH-GAP04 values in Sect up and Sect-mid represent groundwaters contaminated with 38 and 33 % drilling waters, respectively.

Lakes have a range of $\delta^{34}S$ values for sulphate, indicating different sources and processes which are discussed in detail in Henkemans (2016) (Figure 5-71). These include the following:

- Sulphur produced from the oxidation of sulphides (L20) – this causes a small depletion (2 to 5.5 ‰) in $\delta^{34}S$ relative to the parent sulfides (Toran and Harris 1989, Fritz et al. 1994, Clark and Fritz 1997). Preliminary values for sulfides and sulphates from DH-GAP01 and DH-GAP04 core are found in Section 5.8 and indicate sulphide $\delta^{34}S$ in the range of 2–5 ‰. The $\delta^{34}S$ value for L20 was 0.35 ‰ when analysed in 2008 and −0.71 ‰ in 2011. This slight depletion compared to the rock sulphides, combined with the low pH (3.5) of L20, as well as sulphides observed in the lake basin, all suggest that sulphide oxidation is responsible for the sulphate found in L20. L18 may be influenced by sulphide oxidation as well (Figure 5-71).
- Sulphate has been found precipitated throughout the DH-GAP04 core and in several locations in DH-GAP01 as a fracture mineral, mainly in the form of gypsum. Preliminary analyses from DH-GAP01 and DH-GAP04 core (Section 5.8) indicate that $\delta^{34}S$ values for sulphate range from 2 to 6.5 ‰. On-going sulphur studies should provide more confidence in the range of values of fracture sulphates. L12 has a $\delta^{34}S$ of 3.82 ‰, indicating sulphate dissolution could be the source of sulphate.
- Sulphate-reducing bacteria can cause heavy enrichment of $\delta^{34}S$ in the residual sulphate (Fritz et al. 1989, 1994, Clark and Fritz 1997). A number of lakes, especially those in the Kellyville basin, show enrichment of $\delta^{34}S$ over the range described by sulphate minerals (Figure 5-72).
- While sulphate-reducing bacteria explain the heavy enrichment of $\delta^{34}S$ in the Kellyville basin lakes, the influence of marine sulphate from the nearby fjord may also contribute enriched sulphate to these lakes. Marine sulphate has a $\delta^{34}S$ value of 21 ‰ and is shown in Figure 5-71. It is not possible to determine the degree to which the enrichment of $\delta^{34}S$ is influenced by marine sulphate inputs when compared to bacterial sulphate reduction.

No geochemical indicator for groundwater discharge into lakes via taliks was found, and this is likely due to the fact that if taliks are discharging groundwater into lakes, the small volumes of groundwater entering the lakes would be insignificant compared to the volume of meteoric water. Taliks may be recharging or discharging, and likely both cases are found within the study area. Thus, it may be the case that many lakes harbour recharging taliks as well and would not show any indication of groundwater discharge.

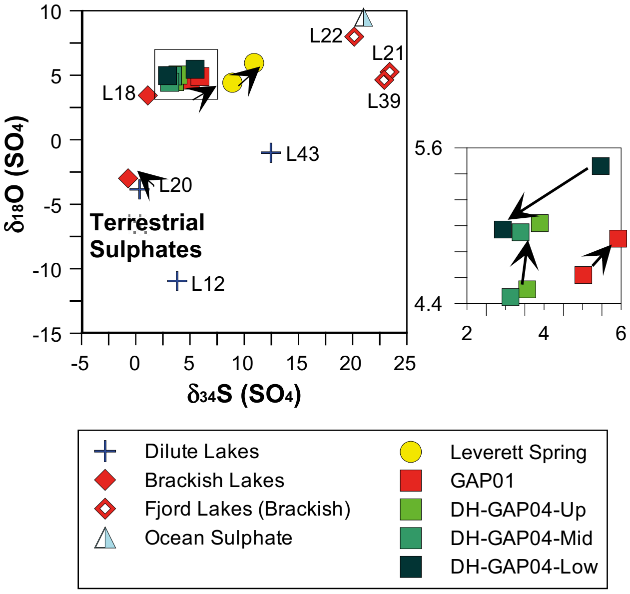

Figure 5-71. *$\delta^{34}S$ and $\delta^{18}O$ from sulphate for surface and groundwaters. Terrestrial sulphate range and ocean sulphate value is given in Clark and Fritz (1997). Arrows indicate samples from the same location at different times and the direction in which the sample shifted between the two measurements. An enlargement of the area covered by the groundwater samples from DH-GAP04 and DH-GAP01 showed the evolution of DH-GAP04 from the 2011 sampling to the 2013 sampling. The change is greatest in Sect-low which also showed the largest amount of recovery from drilling.*

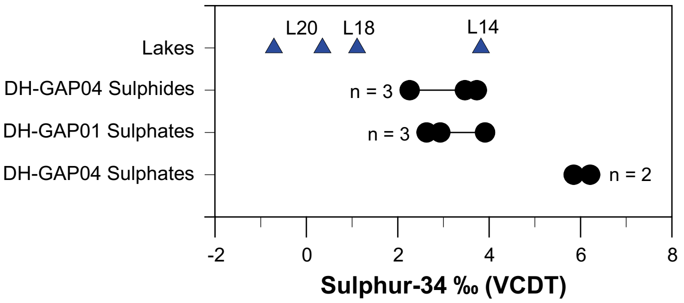

Figure 5-72. *δ^{34}S in lakes compared to preliminary sulphur mineral analyses (Section 5.8.2).*

5.7.3 Ice and meltwaters

Ice samples were collected from the GrIS in the summer of 2011. In general, the Holocene ice is much cleaner than the pre-Holocene ice due to increased atmospheric dust burden caused by high winds during colder, glacial periods (Ram and Koenig 1997). The divide between the "clean" and "dirty" ice is clear and a sample was taken from each area. However, no formal dating technique was used to confirm the age of the ice. Rather these samples provide some idea of the variability that exists within the glacier ice. The surface layer of ice was cleared away to reveal the pristine ice beneath and this was collected in bottles, melted and transferred into one bottle containing no head space for isotopic analyses.

Meltwater samples have been collected from a number of locations at Isunnguata Sermia (MW3, MW4, MW6, MW7, MW8), Leverett Glacier (MW1, MW2, MW5) and Russell Glacier (R-Ice, MW9) over the course of the GAP. For the locations, see Figure 5-73. Supraglacial samples indicate meltwater samples that were collected from meltwater flowing on top of the ice. Subglacial samples indicate smaller streams emerging from outflow tunnels along the ice margin. Samples labelled MW5 in Figure 5-73 were collected from the large meltwater river emerging from Leverett Glacier, and the GL11 samples were collected in SPB from the meltwater river at the terminus of Isunnguata Sermia (see Section 4.5). The caribou subglacial flow (river) samples were collected from the meltwater river beneath the DH-GAP04 drill site and, thus, are from Isunnguata Sermia; however, this is not the terminus river. The Qinquata Kuusua sample is from the river near Kangerlussuaq village.

Several samples were collected around Russell Glacier in the winter when outflow was still occurring. This includes samples at what was called "mini blood falls" (R-Ice in Figure 5-73) as the water contained iron and left red stained ice down the moraine. The iron staining is likely a result of the meltwater interaction with iron-bearing minerals in the glacially comminuted material, such as biotite, iron-sulphides, amphibole, garnet and pyroxene.

Meltwaters are of Ca-HCO_3 type; however, they are extremely dilute and the charge balance calculated for samples is often very poor. Meltwaters represent the most dilute waters found in the study area (Figure 5-67 and Figure 5-68).

The main diagnostic property of meltwaters is the heavily depleted δ^{18}O–δ^{2}H signature of meltwaters compared to other surface waters (Figure 5-66). There is a large range in δ^{18}O and δ^{2}H values for meltwaters, owing to the wide range in values of glacier ice through time. For example, there is a large difference between the two ice samples taken from the Holocene aged and Pleistocene aged ice. The large meltwater rivers emerging at the terminus of the glacier likely represent the best average values and are covered in much greater detail in Section 4.4.

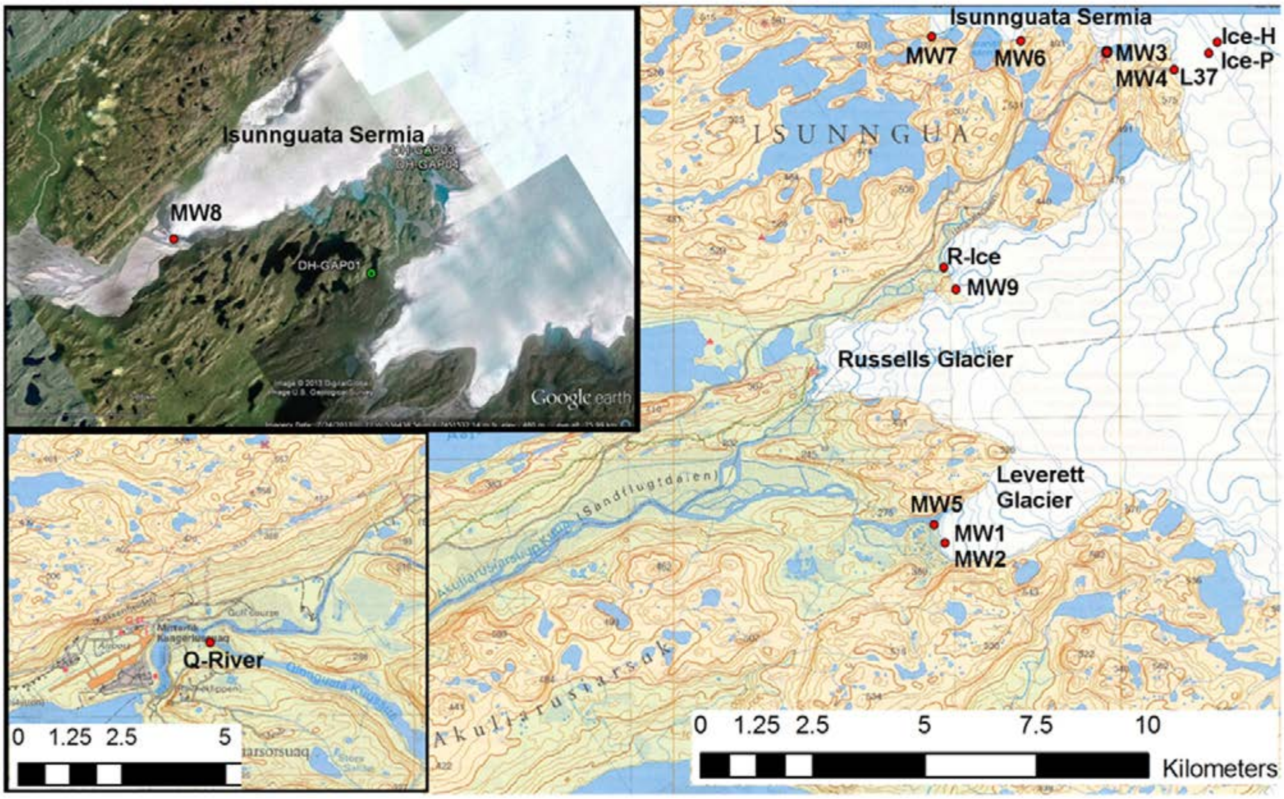

Figure 5-73. *Sampling locations for meltwater (MW) and ice samples.*

5.7.4 Groundwaters

5.7.4.1 Purpose of groundwater investigations

One of the main focuses of the GAP has been to increase knowledge about the interaction between ice sheets and groundwater. The bedrock boreholes drilled by SPC aimed to directly measure pressure, temperature, conductivity and chemistry of groundwater both beneath and in front of the ice sheet. The data from these boreholes could then be used to calibrate and compare groundwater models of glaciated systems. Such real-world data is extremely limited for these systems due to the difficult and expensive logistics of drilling in permafrost environments. The aims of the SPC hydrogeochemical survey were as follows.

1. Provide groundwater samples from a talik to increase understanding of the role of taliks in hydrogeological systems in continuous permafrost.
2. Provide temperature and pressure measurements from a talik for the purpose of thermal and hydrogeological modelling.
3. Enhance understanding of the geochemical evolution of groundwaters in a glacial environment, especially the influence of meltwater intrusion and permafrost formation. The achievement of these goals is aided by porewater and fracture mineral studies.
4. Measure pressures and temperatures in groundwater in the bedrock beneath the ice sheet by drilling at an angle from a location adjacent to the ice. In addition, continued monitoring of seasonal changes to allow evaluation of the relationship between the ice sheet and groundwater.
5. Determine pressures and water composition at typical repository depth (i.e. ~ 500 m b.g.s.).
6. Provide pressure and chemistry data for modelling of the hydrogeological system.
7. Improve understanding of the role of springs in the hydrogeological system. Similar to taliks beneath lakes, springs could be a potential focus point of contaminant discharge.

Water types considered representative of groundwaters include the talik related water in DH-GAP01, the deep waters in DH-GAP04, and the Leverett Spring water in front of Leverett Glacier (Figure 5-74).

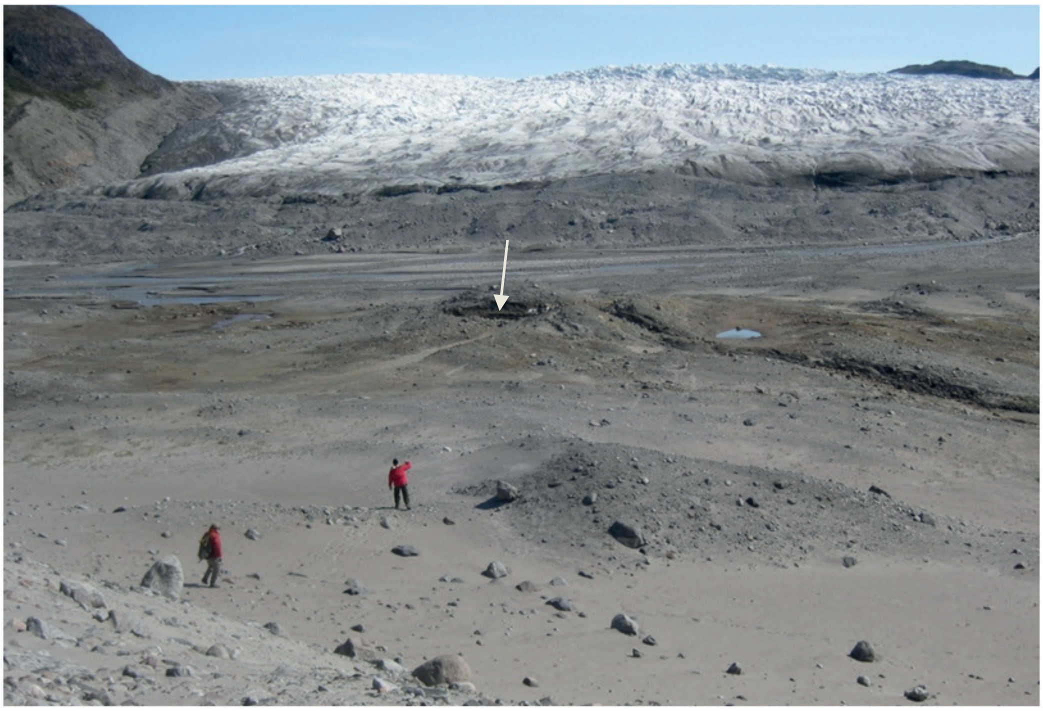

Figure 5-74. Leverett Spring (white arrow) in the moraine field in the proglacial area of the Leverett Glacier. Photo by Emily Henkemans.

5.7.4.2 Talik related waters

The waters collected by the sampling system in DH-GAP01 represent waters found in the talik beneath the Talik lake (L26). Water samples have been acquired beginning in September, 2009, and the borehole was fully recovered from drilling contamination by May of 2010. Subsequent sampling campaigns include September, 2010, and September, 2011. General chemistry is illustrated as various major elements plotted against chloride in Figure 5-67 and Figure 5-68.

DH-GAP01 waters are dominated by high sulphate concentrations, up to 393 mg/L. Salinity in the DH-GAP01 waters is likely derived from water-rock interaction, as indicated by the strontium isotopic values, which are similar to those derived from crush and leach experiments (Section 5.7.5.1). Additionally, high sulphate (and calcium) concentrations appear to be generated by gypsum – found as a fracture mineral. Gypsum was found as an occasional fracture mineral in the DH-GAP01 core and is much more ubiquitous in the DH-GAP04 core (Section 5.8.1). δ^{34}S of sulphate waters was similar to that of fracture sulphates analysed as part of a preliminary round of sulphur analyses (Figure 5-81). Elevated sulphate concentrations are not considered likely to have occurred due to freeze-out (i.e. concentration of solutes excluded from the process of ice formation in permafrost) (Zhang and Frape 2002).

Pressure measurements in the lake and DH-GAP01 indicate that the talik may currently be under recharge conditions, with flow from the lake to the borehole (Johansson et al. 2015b). Geochemical indicators that water is recharging from the lake through the talik, sampled by DH-GAP01, include: 1) mixing of the δ^{18}O/δ^{2}H signature of the groundwater with the evaporative signature of the lake water and 2) chloride concentrations and a δ^{37}Cl isotopic signature that indicate a surface water source for chloride (Henkemans 2016). At −0.05 ‰, the δ^{37}Cl signature of DH-GAP01 is isotopically depleted relative to the δ^{37}Cl value of deep groundwaters from DH-GAP04 (0.22 to 0.41 ‰). Groundwater from DH-GAP01 has similar Cl concentrations to those found in lake L26 (7.7 and 9.9 mg/L respectively). Lake L26 also has a similar δ^{37}Cl value at −0.07 ‰, which lends additional geochemical support that the groundwaters from the DH-GAP01 borehole are a mixture between groundwater and surface water recharging from Lake L26 (Henkemans 2016). DH-GAP01 waters fall slightly to the right of the GMWL (Figure 5-66), indicating a possible mixing scenario with recharging lake waters.

The geochemical evidence is supportive of the pressure measurement data that recharge (lake recharge to groundwater) conditions exist. If predicted values for DH-GAP04 (Figure 5-68) are used, then the $\delta^{18}O$ of the groundwater end member could be estimated to be around −24 ‰. The lake end member has a $\delta^{18}O$ of −12 ‰. For this mixing scenario, the DH-GAP01 groundwaters, with $\delta^{18}O$ of −21 ‰, would contain around 25 % surface water recharge. However, the low chloride concentrations found in the DH-GAP01 waters indicate that a more dilute groundwater end member must be mixing with the recharging surface waters (Henkemans 2016).

5.7.4.3 Deep groundwaters

Initial sampling of the DH-GAP04 borehole was conducted shortly after drilling in September, 2011. Samples at that time were heavily contaminated with drilling fluids, containing from 65 to 99 % drill fluid. Attempts to re-sample the borehole were unsuccessful until September, 2013. Figure 5-75 shows the relationship between the sodiumfluorescein tracer concentration and sample volume during the 2013 sampling campaign. Sect-low recovered rapidly and reached < 5 % drilling contamination on September 8, 2013, after purging 263 L. Sect-up and Sect-mid recovered less rapidly, and were estimated to contain 38 and 33 % drilling water, respectively, at the end of the 2013 sampling campaign.

Salinities and sulphate concentrations in the deep groundwaters sampled from DH-GAP04 are greater than those found in the talik waters. This may be due to the greater occurrence of gypsum as a fracture mineral in DH-GAP04 compared to DH-GAP01 (Section 5.8.1, Pere 2014). General chemistry for deep groundwaters is described in plots of major ions compared to chloride in Figure 5-67 and Figure 5-68. DH-GAP04 waters, being more saline, have higher concentrations of all major elements, but waters from both boreholes follow similar geochemical trends (Figure 5-67 and Figure 5-68) that are distinct from trends followed by lake waters. Ca and SO_4 dominate groundwater chemistry in the DH-GAP04 borehole, likely due to dissolution of gypsum.

Similar $^{87}Sr/^{86}Sr$ ratios between DH-GAP04 waters, DH-GAP01 waters and crush and leach derived waters indicate that the source of salinity in the groundwaters is water-rock interaction. Dissolution of fracture gypsum heavily influences the $^{87}Sr/^{86}Sr$ signature, as Sr and SO_4 concentrations increase together in a linear fashion (Figure 5-76) (Henkemans 2016). Celestite ($SrSO_4$) has also been observed within the rock matrix (Eichinger and Waber 2013), which increases both Sr and SO_4 concentrations during dissolution. Saturation indices can be calculated using PHREEQC for Sect-low. Groundwaters in Sect-low are at equilibrium with respect to gypsum and celestite.

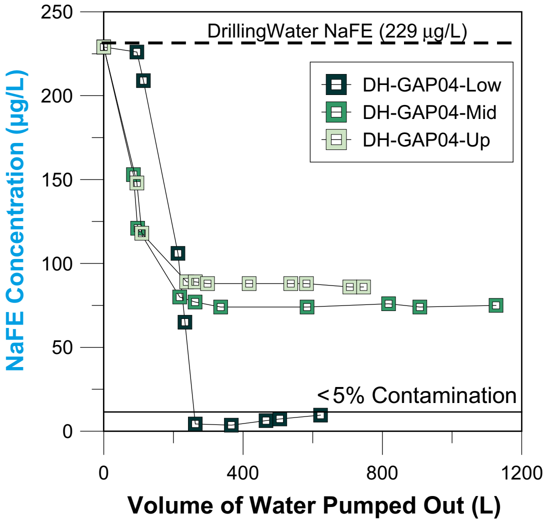

Figure 5-75. *Drilling tracer (sodiumfluorescein) concentrations in DH-GAP04 samples from September 2011 and 2013. DH-GAP04 Sect-low has < 5 % drilling water contamination while Sect-mid and Sect-up have not fully recovered.*

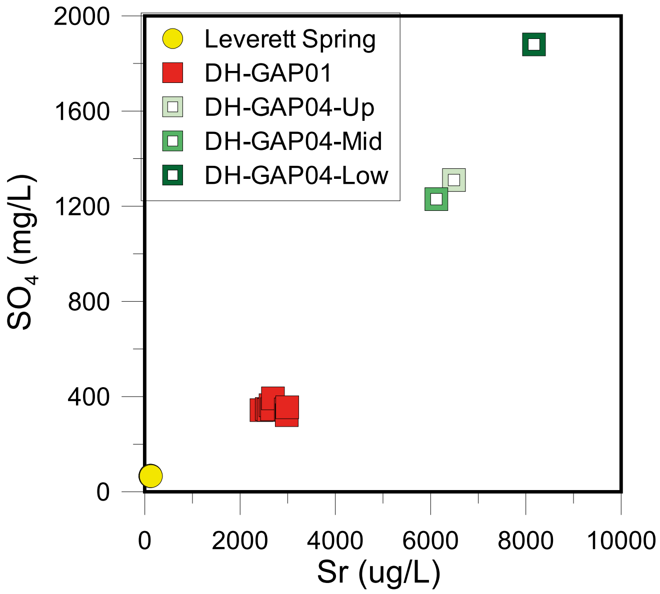

Figure 5-76. *Strontium vs. sulphate concentrations for groundwaters shows a positive linear relationship indicating a similar source, such as dissolution of gypsum and celestite.*

Strontium isotopic ratios of surface waters, including meltwaters, are more radiogenic than groundwaters. Sulphur ($\delta^{34}S$) and oxygen ($\delta^{18}O$) isotopes from sulphate were analysed for DH-GAP04. Considering the relatively minute amount of sulphate in the drilling waters compared to the borehole waters, the results of the sulphate isotope analyses should be representative of the groundwater. Figure 5-71 shows that the sulphate in DH-GAP01 and DH-GAP04 has a similar isotopic signature. This indicates that: 1) the source of sulphate in the two boreholes is likely the same, and 2) that likely there are no sulphate-reducing bacteria in DH-GAP04 that would cause fractionation and enrichment of $\delta^{34}S$ compared to DH-GAP01 (Henkemans 2016). Microbiological studies at DH-GAP01 have not observed sulphate-reducing bacteria in the talik waters (Section 5.7.7). Comparing the $\delta^{34}S$ of sulphate in groundwaters to the preliminary $\delta^{34}S$ from fracture sulphates, indicates that the groundwaters fall within a similar range as the fracture minerals (Figure 5-81). Small changes in $\delta^{34}S$ and $\delta^{18}O$ between the 2011 and 2013 sampling are likely related to dissolution of gypsum and do not appear to be related to bacterial sulphate reduction.

The $\delta^{37}Cl$ signature of DH-GAP04 groundwaters (0.22 to 0.41 ‰) fall within the reported ranges for groundwaters of the Canadian (−0.78 to 0.98 ‰) and Fennoscandian shields (−1.32 to 2.07 ‰) (Stotler et al. 2010).

In order to remove the effects of drilling water contamination, and to obtain the initial isotopic values for the deep groundwaters in Sect-up (38 % drilling water contamination) and Sect-mid (33 % drilling water contamination) of DH-GAP04, correction calculations were performed using a simple mixing model and the known tracer concentrations (Table 5-12) in the drilling water:

$$\delta_{sample} = \chi\delta_A + (1-\chi)\delta_B,$$

re-arranged to solve for the initial solution (δ_A):

$$\delta_A = \frac{\delta_{sample}-\delta_B(1-\chi)}{\chi}.$$

Where δ_A is the isotopic composition of the groundwater, δ_{sample} is the isotopic composition of the sample, δ_B is the isotopic composition of the drilling water and χ is the proportion of the sample that is drilling water based on the sodiumfluorescein concentration.

These calculated values are given in Table 5-12. Sect-low has recovered to tracer values < 5 % and, thus, does not need correction. Calculated values for δ^{18}O and δ^{2}H indicate that the deep groundwaters likely fall along the GMWL (see Figure 5-66) and are similar to values measured in the meltwater rivers emerging from the Isunnguata Sermia and Leverett glaciers.

Based on initial isotopic results from sampling in 2011 and the percentage of sodium fluorescein tracer, the projected isotopic composition of DH-GAP04 groundwaters was similar to the meltwater rivers and fell on the GMWL. Results from the 2013 sampling campaign show that groundwaters have evolved as predicted by the 2011 samples with uncontaminated Sect-low samples falling on the GMWL (Figure 5-77). δ^{18}O/δ^{2}H reslts from the 2013 sampling campaign indicate that meltwater is likely a significant component of the deep groundwater (Henkemans 2016). An exact mixing scenario cannot be predicted based on the large range in meltwater isotopic values (Figure 5-77).

Table 5-12. DH-GAP04 major chemistry and isotope results with calculated (blue font) final compositions from Sect-up and Sect-mid.

Section	Na mg/L	Ca mg/L	Mg mg/L	K mg/L	Cl mg/L	SO^4 mg/L	Alk mmol/L	pH	EC µS/cm	NaFE µg/L	^{18}O ‰	^{2}H ‰	^{3}H TU
Sect-up	257	368	23.1	3.64	93.8	1310	0.32	7.2	2580	86			3.0
Sect-mid	255	325	27.8	5.62	109	1230	0.35	7.4	2510	75	−15.75	−138.4	2.2
Sect-low	409	459	58.6	5.9	173	1880	0.4	7.4	3670	9.3	−23.85	−177.92	< 0.8
Drilling Water	5.20	12.3	7.85	3.74	5.9	3.8	1	7.6	160	229	−11.91	−116.9	8.7
Sect-up – calculated											−25.2	−190.6	
Sect-mid – calculated											−23.5	−181.7	

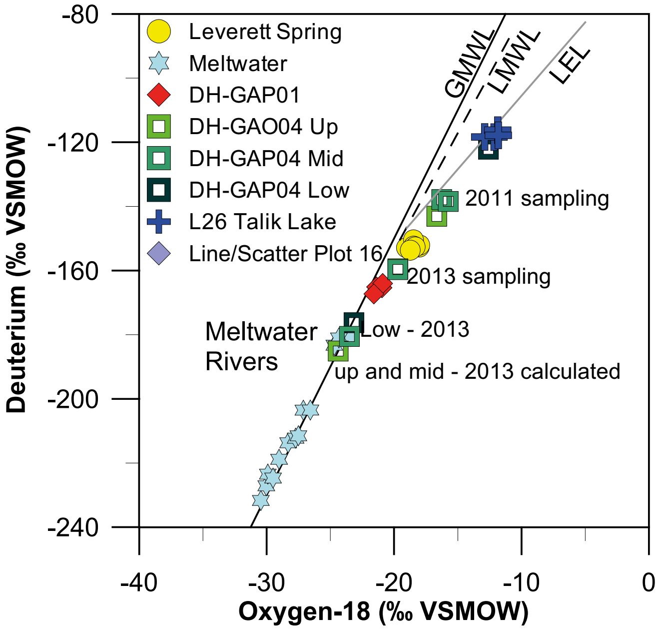

Figure 5-77. Oxygen-18 vs. deuterium for groundwaters, meltwaters and L26, the lake above DH-GAP01. Projected isotopic composition of DH-GAP04 waters are shown based on a simple linear mixing model. LEL is the evaporation line described by the dilute lakes, and the LMWL is based on IAEA precipitation data from Thule, Greenland.

The $^{36}Cl/Cl_{Total}$ ratios in the groundwater samples from DH-GAP04 sections were: Sect-up 14.3×10^{-14}, Sect-mid 12.7×10^{-14}, Sect-low 2.1×10^{-14}. A low $^{36}Cl/Cl_{Total}$ ratio in Sect-low indicates that the chloride found in the groundwater has been isolated from the atmosphere for a period of ~ 10^6 years or more. It should be noted that this residence time estimate concerns chloride ions, which may mostly originate from the rock matrix (e.g. in fluid inclusions) and may have been present much longer in the bedrock than the groundwater in fractures. The $^{36}Cl/Cl_{Total}$ ratios for Sect-up and Sect-mid are much higher than Sect-low, but they can be approximately explained by simple mixtures of a surface water (i.e. drilling fluid) and a groundwater having "old" chloride.

Gas sample results from DH-GAP04

Dissolved oxygen was measured simultaneously while pumping of DH-GAP04 using a portable dissolved oxygen sensor (accuracy ± 0.1 ppm) fitted into a plastic jar. Field measurements of dissolved O_2 were all below 0.1 ppm in the groundwaters being pumped from all three borehole sections. These results are however somewhat uncertain because both degassing and dilution with the N_2 gas initially present in the electrode chamber cannot be excluded. The laboratory analyses showed the presence of some dissolved O_2, probably from contamination during analysis, and therefore the results discussed below are corrected for air contamination.

Total dissolved gas content from DH-GAP04 (Sect-up) samples after oxygen correction in 2013 was 162 and 185 mL/L (in 25.0 °C and 101.3 kPa) in DH-GAP04(up)/1 and DH-GAP04(up)/2, respectively (Table 5-13). The concentration of hydrogen, helium and methane differs substantially between the samples which may be the result of the small water leakage that occurred at the beginning of the sampling of the DH-GAP04(up)/1 sample. The dominant gas in both samples was nitrogen (Figure 5-78). It must be kept in mind that the driving gas for purging was also nitrogen (technical grade, which often includes also minor amount of helium, argon and carbon dioxide), which will result in an increase in the overall nitrogen concentration. Helium was the second dominant gas measured, though the concentrations differ among samples. Hydrogen, argon, methane, carbon monoxide, carbon dioxide and ethene were observed in both samples. Other hydrocarbons measured (ethane, propane, propene, propyne) were all below detection limits. The driving gas, nitrogen, has not been analysed yet to determine the other possible gas phases involved. Thus, these results should be considered as tentative.

Table 5-13. Results of gas analyses on samples acquired from Sect-up in DH-GAP04.

Gas	DH-GAP04_up sample 1 (µL/L)	DH-GAP04_up sample 2 (µL/L)
H_2	22.1	1.07
He	964	3350
Ar	908	896
N_2	160 000	180 000
CO	1.94	1.52
CO_2	34.6	35.7
CH_4	204	37.7
C_2H_6	1.68	0.47
C_2H_4	< 0.48	< 0.48
C_2H_2	< 0.48	< 0.48
C_3H_8	< 0.48	< 0.48
C_3H_6	< 0.48	< 0.48
C_3H_4	< 0.96	< 0.96

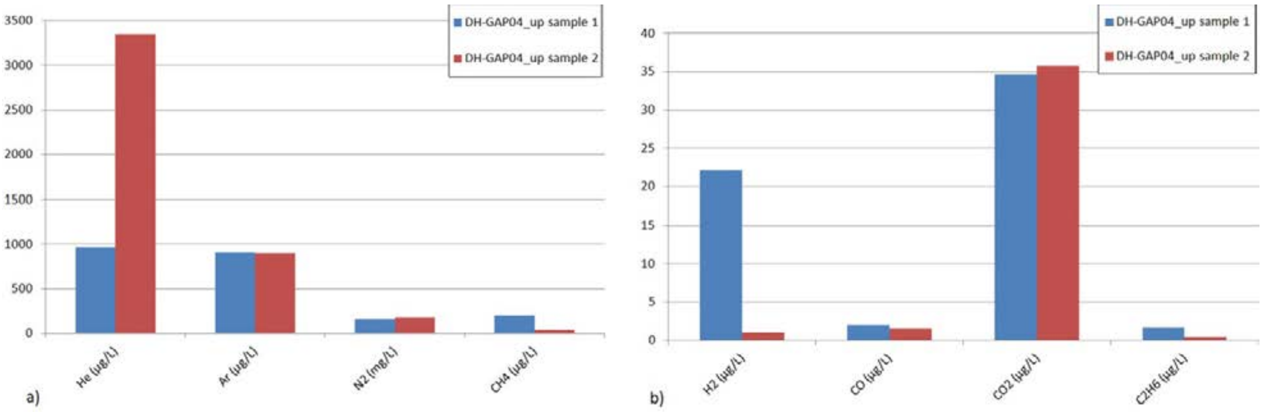

Figure 5-78. *Gas results from DH-GAP04 (Sect-up). Note that the nitrogen concentration is shown in mL/L while all others are in µL/L.*

5.7.4.4 Water and gas samples from Leverett Spring

Water from Leverett Spring has very different geochemical (Figure 5-67 and Figure 5-68) and isotopic properties when compared to the groundwaters sampled from the bedrock boreholes. Compared to the talik and deep groundwaters, the Leverett Spring waters are more isotopically enriched (Figure 5-66), plot to the right of the GMWL, are dilute, and contain more chloride and less sulphate (Figure 5-67). Leverett Spring waters have a high concentration of iron that is seasonally variable (between 4 and 14 mg/L) (Henkemans 2016).

The source of water for Leverett Spring is unlikely to be meltwater, despite its close proximity (< 200 m) to the ice sheet margin; the spring water is isotopically enriched compared to the meltwaters. It is not possible, with the data available at the time of reporting, to conclude what the source is of the water in the spring. Typical elements associated with hydrothermal systems, such as high fluoride concentrations, are lacking. The Leverett Spring is located at the transition from the Southern Nagssugtoqidian Orogen to the Archean Block, which may have an associated hydraulically conductive fault system. The spring system may be described as a hydrothermal talik (van Everdingen 1998), where pressurised flow at temperature greater than 0 °C forces water through permafrost and keeps the flow on-going year-round. Note that the term hydrothermal, in this case, does not necessarily imply that hydrothermal waters are involved, but that the talik formation is based on the heat supply of the flow.

Strontium values in spring water were higher (0.7428) than the Talik lake and deep groundwater (0.703–0.708) (Figure 5-69), likely indicating interaction between the spring water and thick glacial till in the Leverett Glacier valley where biotite weathering can rapidly impart a radiogenic signal (e.g. Blum and Erel 1997, Section 5.7.2.2). The δ^{37}Cl isotopic signature of the spring (0.02–0.06 ‰) is also indicative of interaction with surficial waters or materials where chloride from marine aerosols (δ^{37}Cl of 0 ‰) has been deposited.

Gas samples from the spring have a composition similar to atmospheric. The composition is dominated by nitrogen, with much smaller proportions of other gases. However, relative to atmospheric composition, there is higher content of carbon dioxide and lower content of oxygen (Table 5-14). The 2011 sample reveals a higher percentage of methane than was detected in previous sampling campaigns. δ^{13}C of methane (−69.33 and −71.57 ‰, Table 5-15) indicates that the methane is of biogenic origin. The range of δ^{13}C values for biogenic methane is −50 to −90 ‰ *Vienna Pee Dee Belemnite* (VPDB) (Barker and Fritz 1981, Clark and Fritz 1997). Gas sample results are given in Table 5-14 and Table 5-15. One explanation for the presence of gas in the spring could be that air has been trapped in bubbles and it has released during the melting of ice in the till around the Leverett pond. If this hypothesis were correct, this gas should have a composition near atmospheric, with oxygen consumed by redox reactions – such as the precipitation of Fe-oxide minerals that are abundant in and around the spring pond. Waller and Tuckwell (2005) reported that the moraine units at Leverett contain abundant layers and lenses of bubble-rich pure ice. The volumetric ice content was up to 50 % in all units in the ~ 15 m thick cross-section they could observe, except for the uppermost 2 m, which was ice free.

The gas samples from the spring contained small concentrations of O_2 (Table 5-14). Isotopic analysis indicated that the $\delta^{18}O$ value of the oxygen was −22 to −24 ‰, extremely depleted compared to atmospheric oxygen (+23 ‰). The possibility of lab error has been considered but ruled unlikely, however further sampling and analysis would be needed in order to fully exclude analytical error. The authors are unaware of any process that has been described in the scientific literature to produce such extreme values. At this time, any suggestion of process would be speculation.

Table 5-14. Results of gas analyses of samples acquired from the Leverett Spring.

	% O_2	% N_2	% CO_2	% CH_4	Total %
Atmosphere	20.95	78.08	0.04	0	99.07
Spring 2008	10.96	85.52	0.36	ND	96.83
Spring 2009 (Avg)	1.26	92.29	0.92	0.11	94.59
Spring 2010 (Avg)	1.53	93.69	1.88	0.03	97.13
Spring 2011(Avg)	1.83	88.7	0.625	0.65	91.81
Spring 2011 (Range)	1.56−2.10	86.9−90.5	0.60–0.65	0.65–0.65	90.25–93.36

Table 5-15. Isotopic results of Leverett Spring gas samples from 2011.

	$\delta^{18}O$	$\delta^{15}N$	$\delta^{13}C$	$\delta^{13}C$
	O_2	N_2	CH_4	CO_2
Spring 2011/1	−23.52	0.05	−71.57	−23.65
Spring 2011 /2	−22.36	0.12	−69.33	−22.86

5.7.4.5 Water samples from Ice dammed lake springs

The Ice dammed Lake (L38) located at the edge of Russell Glacier (Figure 5-65), periodically drains rapidly when the ice dam fails, resulting in a *jökulhlaup*. In the summer of 2011, the lake had drained to a low level, exposing a large part of the lake bed. Three springs were observed flowing from the lake bed, with two having discharge great enough to allow for the collection of water samples. The springs were located beneath drainage pathways leading down the eastern slope of the surrounding terrain above the lake.

Distinguishing features of these springs included depleted $\delta^{18}O$–$\delta^{2}H$ compositions (Figure 5-66) and relatively high nitrate concentrations. Nitrate concentrations generally are below detectable levels in the lakes and groundwaters, however, the Ice dammed Lake springs have concentrations of 3.6 and 5.4 mg/L. Tritium concentrations of 4.8 and 7.6 TU indicate a large component of modern meteoric waters. The location of the springs beneath the drainage pathways, the high nitrate concentrations, and the presence of moderate levels of tritium in the waters, led to the conclusion that the major component of these springs is flow through the active layer. Thus, the water chemistry likely represents shallow flow rather than deep groundwater discharge.

5.7.5 Porewater studies

Two methodologies have been used to investigate the matrix porewater end member and to observe possible long term changes in the groundwater system. The University of Waterloo applied the crush and leach technique, and porewater extraction has been applied in a method development study carried out at the University of Bern (Eichinger and Waber 2013).

The salts found in the crush and leach extracts (procedure described in next section) represent the readily available salts that can be weathered or leached from the rock into the groundwater regime by water-rock interaction (e.g. Frape et al. 2004, Waber and Smellie 2008, Stotler et al. 2009). As such, these results are useful for determining which waters in the study area have chemistry and isotope signatures that are the result of interaction between recharge groundwaters and the host rock. Crush and leach studies provide a porewater end member with which groundwaters can be compared (Section 5.7.4.3).

Eight drill core samples were collected for matrix porewater investigations during the drilling of DH-GAP04 in 2011. These samples were preserved immediately after retrieval at surface to avoid drying. All samples were collected below 377 m borehole length (Section 5.7.5.2).

5.7.5.1 Crush and leach studies

As a preliminary comparison for water-rock interaction studies, crush and leach experiments on sections of drill core were performed at the University of Waterloo in 2010. Eleven sections of core were used: 5 samples from DH-GAP01 and 6 from DH-GAP03. The sections of core were pulverised using a rock crusher, which was thoroughly cleaned between samples. Ultra-pure water (EC = 0.06–0.1 µS/cm) generated using a Millipore QPAK1 system (Millipore Corporation, Billerica, MA, USA), was added at a ratio of 1:1 mL water to mg rock. Samples were then placed on a shaker for 24 hours, after which the sediment was allowed to settle before waters were extracted for analyses. Samples for cation and anion analyses were prepared, as above, for surface water samples: cation samples were filtered using a 0.45 µm filter and acidified using ultra-pure nitric acid. Results were then corrected for the difference between the volume of water used for leaching compared to the volume of water found in the pore spaces using porosity and density values from petrophysical analyses (see Section 5.4.5, Harper et al. 2011). Uncorrected and corrected values are listed in Table 5-16. The use of porosity rather than a measured water content introduces error into porewater calculations. An estimate of this error is ~ 25 %, however it is not quantifiable.

Most of the crush and leach samples were dominated by Na^+. With respect to anions, the samples are dominated by either Cl or SO_4, with the majority being dominated by SO_4. Cl concentrations ranged from 0.5 to 8 g/L and SO_4 concentrations from 3 to 23 g/L. The porewater Cl concentration calculated from the out diffusion experiments (Eichinger and Waber 2013) ranged from 1 to 2.2 g/kg. Greater concentrations of Cl found in three of the crush and leach sections (Table 5-16) may be related to the incorporation of fluid inclusion waters due to crushing of the rock. Mass ratios of Br × 1000/Cl ranged from 13 to 40 in the crush and leach waters, the lower end of which is similar to groundwater Br × 1000/Cl mass ratios (10–14).

Gypsum was observed within the rock matrix during the porewater investigations by Eichinger and Waber (2013), and, for three of the four sections, porewaters were found to be at equilibrium with gypsum. The crush and leach waters for DH-GAP01 and DH-GAP03 were found to be saturated with respect to gypsum and often with celestite ($SrSO_4$) as well (Table 5-17), indicating these phases were likely present in the crush and leach sections as well as the DH-GAP04 sections used by Eichinger and Waber (2013). Dissolution of gypsum and celestite from the crush and leach sections has likely caused an over-estimate of the porewater corrected SO_4 and Ca concentrations.

Strontium ratios (Figure 5-69) analysed for a subset of the crush and leach derived waters were much less radiogenic (0.7061–0.7135) than those measured for surface waters (0.72–0.76, mean of 0.745). The $^{87}Sr/^{86}Sr$ ratios for the crush and leach waters agree well with strontium ratios measured for groundwaters from DH-GAP01 and DH-GAP04 (0.704–0.707), signifying that the groundwater salinity is likely derived from water-rock interaction, mainly involving gypsum and celestite.

Samples collected from DH-GAP04 drill core in 2012 were under preparation at the time when this report was written.

5.7.5.2 DH-GAP04 porewater analysis

Purpose and Sample Descriptions

As part of an NWMO work program (outside of the GAP) to document methodologies for porewater extraction and analysis from crystalline rock, porewaters were extracted and analysed from four DH-GAP04 core samples. The results are briefly summarised below, with emphasis on out-diffusion experiments performed to characterise porewater chemistry. For a comprehensive discussion of the analyses and results, please see the full report by Eichinger and Waber (2013).

Table 5-16. Chemistry for crush and leach derived waters. Uncorrected values are given in the upper table. Lower table provides values corrected for porewater volume.

Uncorrected values	Porosity	K mg/L	Ca mg/L	Fe mg/L	Mg mg/L	Na mg/L	S mg/L	Cl mg/L	SO_4 mg/L	Alk mmol/L	$^{87/86}$Sr
GAP-01 64.96–65.06	0.5	8.5	16.2	< 0.03	4.96	23	30.6	2	31.2	1.38	
GAP-01 64.96–65.06	0.5	9.18	16.2	< 0.03	4.97	22.9	30.6	1.98	31.1	–	
GAP-01 90.65–90.75	0.35	12.4	24.8	< 0.03	15.7	26.6	20.3	1.97	54	2.62	
GAP-01 149.90–150.00	0.44	11	12.7	2.29	1.98	27.8	3.12	18.5	7.8	1.41	0.71347
GAP-01 179.60–179.70	0.5	7.44	26.1	15.2	11.9	23.3	15.8	1.22	41.4	1.69	
GAP-01 188.98–189.08	0.42	25.8	12	12.3	7.46	18.3	13.6	6	19.4	1.29	
GAP-03 9.93–10.03	0.45	3.68	14.7	1.6	9.84	17.5	11.9	1.9	11.7	1.76	
GAP-03 41.50–41.60	0.53	19.9	15.2	1.25	4.92	36.2	6.19	27.2	12.8	1.99	
GAP-03 80.80–80.90	0.86	14.2	19.5	< 0.03	5.09	15.7	13.5	3.4	34.5	1.57	0.70935
GAP-03 139.75–139.80	0.4	5.84	19.2	< 0.03	7.15	23.7	9.56	2.68	21.5	2.09	0.70605
GAP-03 236.24–236.34	0.34	13.2	7.69	1.23	2.2	26.1	2.63	20	7.2	1.45	
GAP-03 302.44–302.54	0.39	1.2	6.8	1.69	3.69	32.8	6.99	2.27	19.5	1.66	

Volume corrected values	K mg/L	Ca mg/L	Fe mg/L	Mg mg/L	Na mg/L	S mg/L	Cl mg/L	SO_4 mg/L	Alk mmol/L
GAP-01 64.96–65.06	2594	4944		1514	7020	9339	610	9522	421
GAP-01 64.96–65.06	2802	4944		1517	6989	9339	604	9492	
GAP-01 90.65–90.75	5397	10 793		6833	11 576	8835	857	23 501	1140
GAP-01 149.90–150.00	3342	3859	696	602	8446	948	5621	2370	428
GAP-01 179.60–179.70	2323	8149	4746	3715	7275	4933	381	12 926	528
GAP-01 188.98–189.08	8563	3983	4082	2476	6074	4514	1991	6439	428
GAP-03 9.93–10.03	1203	4804	523	3216	5719	3889	621	3823	575
GAP-03 41.50–41.60	5022	3836	315	1242	9136	1562	6864	3230	502
GAP-03 80.80–80.90	2216	3044		794	2451	2107	531	5385	245
GAP-03 139.75–139.80	2184	7180		2674	8863	3575	1002	8040	782
GAP-03 236.24–236.34	5259	3064	490	877	10 398	1048	7968	2869	578
GAP-03 302.44–302.54	448	2539	631	1378	12 249	2610	848	7282	620

Table 5-17. Saturation indices for crush and leach derived waters, calculated using PHREEQC.

Section (borehole length)	Anhydrite	Calcite	Celestite	Gypsum
DH-GAP01, 64.96–65.06 m	0.44	2.69	0.45	0.64
DH-GAP01, 64.96–65.06 m	0.61		0.70	0.82
DH-GAP01, 90.65–90.75 m	0.87	3.28	0.91	1.05
DH-GAP01, 149.90–150.00 m	−0.21	2.64	−0.33	−0.01
DH-GAP01, 179.60–179.70 m	0.68	2.91	0.32	0.88
DH-GAP01, 188.98-189.08 m	0.16	2.59	0.10	0.36
DH-GAP03, 9.93–10.03 m	−0.02	2.77	−0.07	0.18
DH-GAP03, 41.50–41.60 m	−0.15	2.67	−0.38	0.05
DH-GAP03, 80.80–80.90 m	0.20	2.38	0.12	0.41
DH-GAP03, 139.75–139.80 m	0.38	3.01	0.25	0.57
DH-GAP03, 236.24–236.34 m	−0.31	2.61	−0.41	−0.12
DH-GAP03, 302.44–302.54 m	−0.01	2.51	−0.15	0.18

Out-diffusion experiments are based on the concept of chemical exchange between porewater residing in the rock matrix and a test solution of known composition surrounding the rock sample (Eichinger and Waber 2013). The goal of the experiments is to achieve equilibrium conditions between the two solution reservoirs (test water and porewater) for any solutes for which the porewater is the only source. The non-destructive nature of out-diffusion experiments prevents leakage of mineral fluid inclusions – which can perturb measured concentrations of chemical species, including conservative species such as Cl and Br (Eichinger and Waber 2013).

All samples prepared for porewater investigations are listed in Table 5-18, as well as their depth along borehole, their true vertical depth and the sample length. Analyses performed on these samples included petrological and mineralogical investigations, visualisation of pore space, density measurements, water content and water-loss (connected) porosity measurements (Eichinger and Waber 2013).

Table 5-18. List of DH-GAP04 samples used for porewater investigations.

Lab sample Nr.	Posiva sample Nr.	Interval along borehole		Av. bore-hole length	Av. vertical depth	Core length	Date sampled	Date received and prepared
		From m	To m	m BHL [1]	m b.s. [2]	m		
GAP04-1	DH-GAP04 501.35–501.61	501.4	501.61	501.48	473.4	0.26	25.6.2011	12.12.2011
GAP04-2	DH-GAP04 651.80–652.02	651.80	652.02	651.91	526.5	0.22	28.6.2011	12.12.2011
GAP04-3	DH-GAP04 557.59–557.78	557.6	557.78	557.69	572.8	0.19	26.6.2011	12.12.2011
GAP04-4	DH-GAP04 606.63–606.83	606.6	606.83	606.73	615.5	0.20	27.6.2011	12.12.2011

[1] BHL = along borehole

[2] b.s. = below surface

Methods

Out-diffusion experiments were performed on intact core samples with diameters between 50.5 mm and 50.6 mm, and lengths between 96.6 mm and 117.4 mm, in order to determine porewater Cl and Br concentrations and δ^{37}Cl isotopic signatures. During the experiments, the two water reservoirs (i.e. porewater and test water) were allowed to exchange until equilibrium was achieved, i.e. when the Cl and Br concentrations had reached a plateau and remained constant (within analytical error of ± 5 %) for at least 21 days. Continuous monitoring of all major ion concentrations was conducted by removing small volumes (0.5 mL) of solution (i.e. eluates) at regular intervals, initially every few days and later every few weeks, for major ion analysis by Ion Chromatography (IC). Following completion of the out-diffusion experiments, the final solutions were filtered and immediately analysed for pH and alkalinity.

Porewater Cl- and Br-concentrations are calculated by mass balance calculations using the mass of porewater determined gravimetrically.

Results and discussion

Mineralogical studies indicated that three of the DH-GAP04 samples were intermediate gneiss (IGN) and the fourth felsic gneiss (FGN). Gypsum occurred dispersed in the rock matrix and as micro-fracture infill to varying degrees in all samples. The results of the out-diffusion experiments suggest that gypsum dissolves readily and the newly formed pore space is replaced by test water. As a result, determination of the naturally saturated mass of the rock cores is a challenge. The mass of dissolved gypsum, and the volume of water filling the new pore space, were estimated for each core section by determination of the sulphate concentrations in the final solutions.

The final eluate solutions differ in composition and TDS between the intermediate gneiss and felsic gneiss samples. Solutions of the intermediate gneiss samples are of Ca-Na-SO_4 type, with Ca comprising more than 60 % and SO_4 comprising more than 90 % of the total cations and anions, respectively. The TDS of these solutions ranges between 2347 mg/L and 2929 mg/L. Saturation states indicate that the intermediate gneiss samples are affected by gypsum dissolution and related calcite precipitation during the experiment. In contrast, the final solution from the felsic gneiss sample is of Na-Ca-SO_4-HCO_3 type, with a TDS of 403 mg/L (Eichinger and Waber 2013). The final intermediate gneiss eluate solutions are in equilibrium or slightly oversaturated with respect to calcite, whereas the felsic gneiss solution is slightly undersaturated (Eichinger and Waber 2013). Eichinger and Waber (2013) reported that most of the carbon appears to come from the porewater and may be a major anion in the in situ porewater (in addition to SO_4 and Cl).

Cl and Br were the only major ions observed to behave conservatively. Considering both the conservative behaviour of Cl and Br, as well as the absence of Cl- and Br-bearing minerals in the rock, the porewater is the only source for dissolved Cl and Br in the experimental solution. For all samples, equilibrium was achieved with respect to Cl and Br, as shown by the Cl and Br elution curves (see Eichinger and Waber 2013). Between ~ 100 days and 250 days were required for Cl concentrations to reach equilibrium values (Eichinger and Waber 2013). Porewater Cl concentrations, as well as stable chlorine isotopic signatures, were determined on all four samples from DH-GAP04 (GAP04-1 through GAP04-4). Br could only be analysed in porewater from GAP04-4. High TDS of the eluate and final solutions for all other samples (GAP04-1 to GAP04-3) did not allow for undiluted measurement of the ion concentrations and, as a consequence, the detection limit for Br was a factor of ten higher in those samples.

The concentrations of Cl and Br in the porewaters were determined from the final solution composition by applying mass balance calculations. Using the mass of porewater in the rock samples, the Cl and Br concentrations could be calculated (see Table 5-19). The calculated Cl and Br concentrations were corrected for the mass and the concentration of removed eluate solutions as well. Final porewater Cl concentrations vary between 960 ± 220 and 2200 ± 480 mg/kg_{H2O} and show an increasing trend with depth. The large uncertainty attached to these values relates to difficulties in the determination of the original mass of porewater, which was modified from in situ conditions by: 1) desaturation between core recovery and sample reception in the lab, and 2) mineral dissolution (gypsum) during the experiment. The porewater Br concentration and Br × 1000/Cl ratio of sample GAP04-4 is 12.8 ± 2.8 mg/kg H_2O and 5.8 ± 1.8, respectively. Stable chlorine isotope ($\delta^{37}Cl$) signatures of the DH-GAP04 samples vary between −6.04 ± 0.08 and −2.89 ± 0.05 ‰ SMOC (see Table 5-19).

Table 5-19. Chloride and bromide concentrations, Br × 1000/Cl mass ratios and δ^{37}Cl values in porewater extracted from core samples of borehole DH-GAP04.

Sample	Depth m.b.TOC	Cl_{PW} mg/kg H_2O	Br_{PW} mg/kg H_2O	Br × 1000/Cl	δ^{37}Cl ‰SMOC
DH-GAP04-1	473.4	980 ± 200*	b.d.	–	−2.89 ± 0.05
DH-GAP04-2	572.8	1740 ± 420	b.d.	–	−4.03 ± 0.07
DH-GAP04-3	526.5	960 ± 220	b.d.	–	−6.04 ± 0.08
DH-GAP04-4	615.5	2200 ± 480	12.8 ± 2.8	5.8 ± 1.8	−5.49 ± 0.07

* errors are calculated by Gaussian error propagation (Eichinger 2009).
b.d. = below detection limit.

Discussion of uncertainties

For the calculation of the porewater Cl and Br concentrations, an exact determination of the mass of porewater is required. A factor that can influence the calculation of the porewater concentrations is the volume of test water, which can be influenced by evaporation from the time of sample recovery until preparation in the lab and/or, less so, by leakage during sub-sampling. The ingress of drilling fluid by stress release, and the formation of a drilling disturbed zone that might already result in dissolution of readily dissolvable minerals (e.g. gypsum) during drilling, can create pore space within the samples, leading to dilution of the Cl and Br concentrations of porewaters. Further dissolution of such minerals might then be induced during the out-diffusion experiment. To evaluate any potential disturbing effects, the weights of the core samples and the test water were determined both at the beginning and end of the out-diffusion experiments to allow for correction(s) due to changes in mass of the components. In addition to the factors above, the masses of the removed eluate solutions were recorded and all of these factors were considered in the determination of the final Cl and Br concentration estimates (Eichinger and Waber 2013).

5.7.6 Main conclusions from hydrogeochemical investigations

Taliks in this region are potentially either recharging or discharging, contributing at most only minor volumes of groundwater to the associated lakes. Lake chemistries do not indicate groundwater discharge as an important contribution to surface waters.

Processes involved in the sulphur system in lakes are not related to high sulphate groundwaters. Sulphate in lakes is derived from sulphide oxidation or sulphate mineral dissolution, and possibly marine sulphate. $\delta^{34}S$ may be significantly modified by bacterial sulphate reduction. While groundwater sulphate is likely derived from sulphate mineral dissolution (Section 5.8.2), it is not affected by bacterial sulphate reduction.

Meltwaters, despite covering a large range of values, have highly depleted $\delta^{18}O$-δ^2H signatures relative to modern meteoric water. As meltwaters are very dilute, and thus easily modified by interaction with fracture minerals and bedrock once recharged, it is difficult to use chemical composition to trace meltwater intrusion. The isotopic composition of the water provides a good tracer for meltwater intrusion into the subsurface because it is unlikely to be significantly altered in the subsurface, except by mixing with groundwaters.

Groundwaters have high sulphate concentrations, likely related to dissolution of sulphate minerals such as gypsum found as fracture minerals. Sulphate-reducing bacteria are not observed in DH-GAP01 and are presumed unlikely to be present in DH-GAP04 due to the similarity in $\delta^{34}S$ values between the two boreholes.

Groundwaters in DH-GAP01 may represent mixing between a groundwater end member, similar to what is observed in DH-GAP04, and surface waters; however, this has not been verified by a second geochemical tracer. A recharge scenario is supported by the pressure data. Groundwaters in DH-GAP04 likely have some component of meltwater based on similarities in isotopic composition between meltwaters and borehole waters. If DH-GAP04 waters are recharging meltwaters, they have evolved along the flow path from very dilute (EC < 5 µS/cm) to much higher salinities (EC > 900 µS/cm), and are dominated by SO_4 and Ca.

The Leverett Spring provides a unique view of natural groundwater discharge in the study area; it is likely a hydrothermal talik that may be related to a structural feature. Isotopic and chemical compositions differ from borehole groundwaters; thus, the spring is not likely related to the flow system represented by the boreholes.

Crush and leach studies indicate water-rock interaction is the main source of salinity in groundwaters from DH-GAP01 and DH-GAP04.

Groundwaters are similar to the chemistry of porewaters extracted in the out-diffusion experiment from the intermediate gneiss samples, in that they are of Ca-SO_4 type with moderate concentrations of Na^+ (up to 38 % of cations on a meq/L basis). Groundwaters in Sect-low were found to be at equilibrium with gypsum and saturated with respect to SO_4, similar to IGN porewaters. Porewater Br × 1000/Cl mass ratios of are between 5.8 ± 1.8 and 7.6 ± 2.6. Br/Cl ratios observed in groundwater are two times higher (10–14).

5.7.7 Microbial investigations

5.7.7.1 Objectives

The microbial investigations were conducted with the aim of characterising and classifying groundwater DNA signatures from DH-GAP01 at depths between 130 and 191 m and from the Talik lake. Microbial diversity was studied to evaluate the differences in DH-GAP01 groundwater and in the Talik lake water. Groundwater was sampled on two different occasions in July, 2009, and in September, 2010. Groundwater was collected from both DH-GAP01 and the Talik lake in 2009, and in 2010 groundwater was collected only from the borehole. Analyses were made at the Microbial Analytics Sweden AB laboratory.

5.7.7.2 Methods for characterising microbial communities

The methods used to determine the biomass were *quantitative PCR* (qPCR) and *total number of cells* (TNC) (Pedersen et al. 2014); PCR, cloning and sequencing (Jägevall et al. 2011, Pedersen et al. 2014) was used to characterise diversity and identify DNA signatures in the different samples.

DNA extractions were performed, as described by Jägevall et al. (2011). Five 50 mL groundwater samples were extracted for DNA from the borehole and pooled, and five samples of 50, 40, 40, 20 and 20 mL were extracted for DNA from the lake water and pooled. Numbers of bacteria and eukarya were determined based on known genetic information using quantitative PCR (qPCR) for 16S rRNA gene Bacteria, 16S rRNA gene Archaea, 18S rRNA gene Eukarya, apsA, fthfs, pmoA, mxaF, pvsA, narG1, narG2, nirK and ANME1, 2a and 2c in order to detect bacteria, archaea, eukarya, sulphate-reducing bacteria, acetogens, methanotrophs, methylotrophs, Pseudomonas fluorescens, nitrate-reducing bacteria and anaerobic methane oxidisers (Jägevall et al. 2011, Ginzinger 2002, Pedersen et al. 2010, Inagaki et al. 2004).

5.7.7.3 Classification of results

The borehole groundwater possessed a low diversity of microorganisms, while the lake water had a broad diversity. The composition of the microbial community differed completely between the borehole groundwater and the lake water; none of the DNA signatures (DNA sequences) found in the borehole were identical to the DNA signatures found in the lake water (Table 5-20 and Table 5-21).

DH-GAP01 groundwater

DNA signatures obtained from the cloned borehole groundwater were dominated by Clostridia, mostly Desulfosporosinus lacus (14/47 clones), Acetobacterium malicum (6/47 clones) and bacteriodetes (16/47 clones). Betaproteobacteria (6/47 clones), gammaproteobacteria (2/47 clones) and acidobacteria (1/47 clones) were less abundant compared to the dominant DNA signatures (Table 5-20).

Talik lake water

The lake water collected in September, 2010, was cloned and the sequences consisted primarily of DNA signatures from betaproteobacteria (9/44 clones), bacteriodetes (7/44 clones) and alphaproteobacteria (6/44 clones) (Table 5-21). Cyanobacterial DNA signatures were common as well (5/44 clones). Less frequent DNA signatures belonged to actinobacteria (2/44 clones), bulkholderiales (1/44 clones), cytophaga (1/44 clones), deltaproteobacteria (2/44 clones), flavobacterium (1/44 clones), flexibacter (3/44 clones) and verrucomicrobia (2/44 clones). No sequences were identical between the borehole and the lake water. One of the clones (HQ625536) resembled a clone (GQ240219) previously found in groundwater collected close to borehole KA1362A06 in the Äspö tunnel in Oskarshamn, Sweden.

Accession numbers

The sequence data from this study have been submitted to the GenBank database and were given the accession numbers HQ625523–HQ625563.

Classification by biomass

Biomass estimated by TNC from the second sampling occasion was somewhat higher in the borehole when compared to the lake (Table 5-22). qPCR for the 16S rRNA gene for bacteria was only performed for the first borehole sample and showed similar results, but the number of gene copies was about three times lower than the TNC measured for the second borehole sample. This may be due to filtration and RNA preservation solution, or due to substances inhibiting the qPCR. Eukarya DNA signatures were only measured in the DH-GAP01 groundwater sampled in July, 2009. Classification of groundwater DNA signatures from DH-GAP01 and the nearby lake, detected by cloning analyses, are discussed below because TNC and qPCR was used only for biomass estimations. The DH-GAP01 groundwater could be distinguished from the lake water easily, as they differed completely in microbial composition. From these results, it can be hypothesised that the borehole groundwater was not contaminated recently by Talik lake water (Section 5.7.4.2, Table 5-20 and Table 5-21). The following provides a description of the bacterial DNA signatures identified in the Talik lake and DH-GAP01 borehole groundwater samples:

Clostridia (Gram-positive bacteria) indicate anaerobic environments (Madigan and Martinko 2006). These spore-forming bacteria represent a significant difference between the borehole groundwater and lake water because the bacteria dominated in the borehole groundwater, but were absent in the lake.

Bacteriodetes DNA signatures include several different groups of bacteria (Madigan and Martinko 2006). They were common in the borehole groundwater and were found in the lake water as well. None of the DNA signatures from the borehole and the lake water shared identical sequences.

Alphaproteabacterial DNA signatures are found under aerobic conditions (Madigan and Martinko 2006). These DNA signatures differed greatly between groundwater from the borehole and the lake water. Several alphaproteobacterial DNA signatures were frequently found in the lake water, but not in the borehole groundwater.

Betaproteobacterial DNA signatures are found in aerobic or facultative aerobic environments and include several nitrogen-fixing bacteria (Madigan and Martinko 2006). Betaproteobacterial DNA signatures were more abundant in the lake water than in the DH-GAP01 groundwater.

Deltaproteobacterial DNA signatures are mostly sulphate-reducing bacteria using sulphate as an electron acceptor to produce hydrogen sulphide under anaerobic conditions (Madigan and Martinko 2006). In groundwater, where these signatures are found, sulphate reduction can be an on-going process. The lake water revealed two signatures, while the DH-GAP01 borehole groundwater revealed none.

Gammaproteobacterial DNA signatures are found in aerobic or anaerobic environments. They were widely distributed among groups of microbes (Madigan and Martinko 2006) and were found in the borehole DH-GAP01, but not in the lake.

Actinobacterial signatures are found mostly in aerobic environments (Ventura et al. 2007) and were found only in the lake water.

Acidobacterial DNA signatures are found in acidic environments (Barns et al. 2007). These DNA signatures were found in one clone in the borehole groundwater, but not in the lake.

Bulkholderiales DNA signatures are found in aerobic environments (Madigan and Martinko 2006) and were found solely in the lake water.

Cyanobacteria were found in the lake water, but not at all in borehole groundwaters. They generally are photosynthetic and require light (Madigan and Martinko 2006).

Cytophaga and Flexibacter are found in aerobic environments. Flexibacter can additionally be found in anaerobic environments (Madigan and Martinko 2006). These DNA signatures were found in the lake water, but not in the borehole groundwater.

Verrumicrobial DNA signatures were few, but were present in the lake water. They are aerobic or facultative anaerobic (Madigan and Martinko 2006).

Some DNA signatures were similar, but none of the sequences were identical between the DH-GAP01 groundwater and the lake water. Most DNA signatures indicated anaerobic conditions in the borehole and aerobic conditions in the lake. The borehole groundwater diversity was low compared to the lake water diversity.

Table 5-20. DNA signatures found by cloning the borehole DH-GAP01 groundwater sampled in September, 2010.

Phylum	Species	Id. Closest match GenBank (%)	Accession no GenBank	Number of clones
Bacteriodetes	Uncultured bacterium (HM141898)	97	HQ625528	16
Clostridia	*Desulfosporosinus lacus* (AJ582757)	96	HQ625530	14
Clostridia	*Acetobacterium malicum* (NR_026326)	98	HQ625524	6
Betaproteobacteria	*Herminiimonas fonticola* (AM989095)	99	HQ625525/27	2
Betaproteobacteria	*Polaromonas sp.* (EU106605/ FM955859)	93/99	HQ625531/32	2/1
Betaproteobacteria	*Polynucleobacter necessarius* (CP000655)	99	HQ625526	1
Gammaproteobacteria	*Pseudomonas peli* (HQ202835)	99	HQ625523	1
Acidobacteria	*Acidobacteria bacterium* (FR716684)	98	HQ625529	1
Gammaproteobacteria	*Pseudomonas anguilliseptica* (NR029319)	98	HQ625534	1
Unclassified	Uncultured bacterium (GU236035)	96	HQ625533	1
Unclassified	Uncultured bacterium (FM956230)	96	HQ625535	1

5.7.7.4 Evaluation of classification of data

Samples were collected from DH-GAP01 on two different occasions over a one year period and qPCR data, together with TNC, revealed a resemblance in the amount of biomass in groundwater samples over this time. qPCR performed on the borehole sample from the first sampling occasion in July, 2009, revealed low total biomass and, consequently, low numbers of bacteria, archaea, eukarya, sulfate-reducing bacteria, acetogens, methanotrophs, methylotrophs, ANME, nitrate-reducing bacteria and *Pseudomonas fluorescens*. Cloning and TNC were, for this reason, performed on samples collected during the second sampling occasion (September, 2010) instead of qPCR in order to characterise the diversity in DH-GAP01 and the Talik lake water.

5.7.7.5 Main conclusions from microbial investigations

The microbial investigations classified groundwater DNA signatures from DH-GAP01 (130–191 m) and the Talik lake, and aimed to determine microbial diversity in the sampled waters. Samples were collected on two different occasions in July, 2009, and September, 2010. The first groundwater sample was collected from DH-GAP01 directly from the pumped water, while the September, 2010, samples from DH-GAP01 were collected by filtering a large amount of water while pumping DH-GAP01. In September, 2010, the Talik lake water was sampled directly into the sample container (Harper et al. 2011).

The methods used to characterise biomass were qPCR and TNC (Pedersen et al. 2014). However, these methods can be used only for biomass estimations and DNA extractions; PCR, cloning and sequencing (Pedersen et al. 2014) was used to characterise diversity and identify DNA signatures in the different samples.

Analysis of the total numbers of microorganisms did not show a significant difference between DH-GAP01 groundwater and the Talik lake water. According to DNA signatures, the microorganisms in DH-GAP01 groundwater were mostly anaerobic or facultative anaerobic microorganisms. On the contrary, the Talik lake water contained aerobic microorganisms, including species of Cyanobacteria that typically require light for growth. The number of different DNA signatures found in the Talik lake water was higher than those observed for DH-GAP01 groundwater. None of the DNA signatures found in the Talik lake were found in the DH-GAP01 groundwater. These observations imply that the microbial communities differ between the borehole groundwater and the lake water.

Table 5-21. DNA signatures obtained by cloning of the Talik lake water sampled in September, 2010.

Phylum	Species	Id. Closest match GenBank (%)	Accession no GenBank	Number of clones
Bacteriodetes	Uncultured *Flectobacillus sp.* (FN668109)	99	HQ625542	4
Alphaproteobacteria	Uncultured bacterium (HM483831/EF667921/ GU305752)	99/92/99*	HQ625556/ HQ625553	3/1/1*
Betaproteobacteria	Uncultured bacterium (AM849432/EU802045/ GQ240219/FJ916348)	99/99/99/97*	HQ625555/ HQ625536/ HQ625546	3/1/1/1*
Cyanobacteria	Uncultured *Synechococcus sp.* (EU703425)	99	HQ625557	3
Bacteriodetes	Uncultured bacterium (EU640023/ EU703442)	100/99*	HQ625550/ HQ625548	2/1*
Actinobacteria	Uncultured bacterium (EU117782/88)	99/97*	HQ625551/58/	1/1*
Alphaproteobacteria	*Sphingomonas sp.* (AY584572)	99	HQ625541	1
Betaproteobacteria	*Methylibium petroleiphilum* (CP000555)	97	HQ625544	1
Betaproteobacteria	*Polynucleobacter acidiphobus* (AJ876403)	100	HQ625547	1
Betaproteobacteria	*Rhodoferax ferrireducens* (CP000267)	98	*	1
Bulkholderiales	Uncultured bacterium (EU803423)	98	*	1
Cyanobacteria	*Cyanobium sp.* (AM710378)	99	HQ625554	1
Cyanobacteria	*Synechococcus rubescens* (AF317076)	99	HQ625563	1
Cytophaga	Uncultured bacterium (AF361200)	94	*	1
Deltaproteobacteria	*Spirobacillus cienkowskii* (EU220836)	99	HQ625552	1
Deltaproteobacteria	Uncultured bacterium (EU449596)	94	HQ625543	1
Flavobacterium	Uncultured bacterium (FJ694511)	97	HQ625538	1
Flexibacter	Uncultured *Flexibacter sp.* (FN668178)	99	HQ625549	1
Flexibacter	Uncultured bacterium (AY509281/ AY509320)	97/97*	HQ625540/ HQ625537	1/1*
Unclassified	Uncultured bacterium (EU234313/ FN297294/353/459/ GU305849)	100/99/99/96/99*	HQ625539/HQ625559–HQ625562	1/1/1/1/1*
Verrucomicrobia	Uncultured bacterium (GQ347385/GU472738)	98/99*		1/1*

* Several similar clones were found and submitted and they are listed after each other and separated by /. Where no accession number is listed, the sequence failed quality tests and were not submitted.

Table 5-22. TNC and qPCR for 16S rRNA gene Bacteria and 18S rRNA Eukarya were detected for the DH-GAP01 borehole and Talik lake samples in July, 2009, and September, 2010.

Sample	TNC	Standard deviation	16S rRNA gene Bacteria qPCR		18S rRNA gene Eukarya qPCR		16S rRNA gene Archaea qPCR	
			Gene copy number (copies/mL)	Standard deviation	Gene copy number (copies/mL)	Standard deviation	Gene copy number (copies/mL)	Standard deviation
DH-GAP01 borehole 2009-07-12	*	*	4.9×10^3	3.8×10^3	3.3×10^5	1.6×10^5	< 100	< 100
DH-GAP01 borehole 2010-09-05	1.4×10^4	4.9×10^3	*	*	*	*	*	*
Talik lake 2010-09-05	8.8×10^3	1.6×10^3	*	*	*	*	*	*

* not analysed

5.8 Mineralogical studies

5.8.1 Fracture infillings

Physical and chemical characteristics of secondary minerals within fracture networks have been examined as part of GAP to provide insights into paleohydrological processes in bedrock (e.g. hydrothermal, metamorphic or glacial events). The work started with detailed drill core logging on the fractures and their infillings from DH-GAP01, DH-GAP03 and DH-GAP04, where numerous parameters were recorded. As a result, information became available on: the distribution of fracturing within the drill cores, the physical nature of the fractures, and the infilling mineralogy. The latter information is based primarily on visual identification during core logging, supported by some simple tests – such as hardness, or the acid test for carbonates. This information guided the sampling for detailed mineralogical and geochemical studies.

The drill core logging was conducted at Olkiluoto by Posiva (Pere 2014). Carbonate minerals and sulphates (gypsum) were studied for their mineralogy, isotope geochemistry and fluid inclusions at the University of Waterloo, Canada. Additionally, Terralogica AB and Linné University in Sweden and Helsinki University in Finland have performed detailed mineralogical and geochemical investigations on selected fracture surfaces.

5.8.1.1 Infilling mineralogy in drill cores

Fracture mineralogy in DH-GAP01, DH-GAP03 and DH-GAP04 is generally uniform for the majority of fractures. However, some specific differences exist between the cores. A type fracture for the area consists of a thin layer of chlorite on the fracture surface, with spots of calcite and, possibly, traces of clays on top. Total fracture filling thickness is typically ~ 0.2 mm. In DH-GAP04, gypsum is present as well (see Figure 5-24 and Figure 5-79). In some cases, it can be seen that the wall rock has been slightly altered (e.g. to epidote) in the immediate contact of the fracture (< 1 mm), but these were not considered as actual fillings. The fracture surfaces are typically undulated.

Specific features and differences in fracture mineralogy between the individual boreholes are discussed below after Pere (2014).

DH-GAP01

The main fracture filling minerals in DH-GAP01 are calcite (58 %, percentage of observations of all fractures), chlorite (47 %), unidentified clay minerals (34 %) and kaolinite (22 %). Some indications of gypsum were observed under microscope. Pyrite, hematite, quartz, biotite and feldspar are rare and occur in small amounts.

Figure 5-79. *Synchronous, practically mono-mineral gypsum fracture infillings sealing two fractures with different orientations (DH-GAP04, 533 m). The cross-fibrous texture is very common and indicates mineral growth during extensional conditions. Photograph by Tuomas Pere.*

Clear depth-related infilling trends cannot be identified in DH-GAP01, but, between 70–140 m borehole length, the number of fracture filling observations increases in accordance with a general increase in fracture frequency (see Figure 5-22). Similarly, between ~ 30–60 m, the absence of fracture fillings is related to an absence of fractures. Fracture infillings in DH-GAP01 are typically thin, varying between 0.1 and 10 mm, averaging 0.4 mm.

DH-GAP03

The main fracture filling minerals in DH-GAP03 are calcite (60 %), chlorite (54 %) and clay minerals (24 %). Kaolinite, epidote, pyrite, biotite, quartz, chalcopyrite and hematite are rare and occur in small amounts. Iron hydroxides (8 %) occur in the top section of the hole, above ~ 50 m borehole length (see Figure 5-23). Gypsum has not been detected in DH-GAP03 drill core, neither macro- nor microscopically. The fracture infillings in DH-GAP03 are variable, but typically thin, between 0.1 and 30 mm, with an average thickness of 0.4 mm.

DH-GAP04

The main fracture filling minerals in DH-GAP04 are chlorite (56 %), calcite (46 %), gypsum (34 %), and clays (13 %) (see Figure 5-24). Pyrite, pyrrhotite and kaolinite, as well as a number of other minerals, occur in small amounts as accessory fillings. Rusty fracture surfaces, with iron hydroxides, were predominantly observed in the upper parts of the hole, above 40 m. The presence of gypsum is a notable difference compared to the nearby borehole DH-GAP03, where gypsum has not been detected. In DH-GAP01, only traces of gypsum have been detected in association with calcitic infillings.

The fracture filling thicknesses in DH-GAP04 are thin and fractures with very thin fillings, on the order of 0.1–0.2 mm, are common. The thicknesses vary between 0.1 and 30 mm. The median thickness is 0.2 mm, averaging 0.5 mm. It is highly probable that the majority of fractures with thin fillings are not very continuous outside the borehole. However, thicker fillings, that indicate larger dimensions (Scholz 2002, Kim and Sanderson 2005), were observed in many fractures.

Chlorite and calcite occur rather evenly along the drill core. The amount of clay is slightly lower between 300 and 550 m borehole length.

The occurrence of gypsum shows distinct variation as function of depth. In the upper parts of the hole, gypsum is almost non-existent and its occurrence is limited to single fractures. Below ~ 300 m borehole length, the frequency of gypsum-bearing fractures increases substantially. In the lower parts of the hole, gypsum is the dominant fracture mineral. The increased abundance of gypsym coincides with the change of rock type from mafic to felsic/intermediate gneisses. Gypsum occurs as fibrous and/or flaky infillings (Figure 5-79). Detailed mineralogical information of the fracture infillings is scarce, but, typically, the fillings seem to be almost pure gypsum. Calcite, as a complex intergrowth with gypsum, is the most common accompanying mineral. The general appearance of the gypsum fillings (preferentially monomineral, fibrous or crystalline texture) suggest that gypsum has precipitated at high hydrothermal/metamorphic temperatures from a homogeneous fluid.

The isotope geochemistry of gypsum is discussed in Section 5.8.2.

5.8.1.2 Stable isotopes and fluid inclusions of calcite infillings

Two drill cores were sampled for fracture infillings in 2010. Calcite ($CaCO_3$) samples were selected based on the logging by Posiva geologists. The aim was to get a view of the mineralogical and isotopic variability at the site. X-ray diffraction was used to identify fracture minerals from DH-GAP01 and DH-GAP03.

Fracture infilling minerals are of interest because they can be used to characterise past fluid environments. Fracture mineral investigations on the drill cores are on-going, with preliminary findings presented in this report. Carbon ($\delta^{13}C$) and oxygen ($\delta^{18}O$) isotope geochemistry of carbonate fracture fillings are summarised in Table 5-23 and Table 5-24, and are plotted in Figure 5-80.

Powder x-ray diffraction was carried out using a Bruker D8 diffractometer, and each sample was analysed using a data collection time of one hour in order to characterise accessory phases present in the facture infillings. Carbon ($\delta^{13}C$) and oxygen ($\delta^{18}O$) isotope geochemistry of carbonate fracture fillings were collected at the Environmental Isotope Laboratory at the University of Waterloo and Isotope Tracer Technologies, following methods presented by Al-Aasm et al. (1990).

Fluid inclusion studies are being carried out, and preliminary results reveal a range of trapping temperatures between 100 and 200 °C. These results will be used for geothermometry calculations that will estimate the isotopic composition of the parent fluids from which these carbonates precipitated.

Table 5-23. Isotope geochemistry for fracture carbonates in DH-GAP01.

Borehole lenght (m)	Result (‰ -VPDB)		Std. Dev. (‰)	
	$\delta^{13}C$	$\delta^{18}O$	$\delta^{13}C$	$\delta^{18}O$
74.25	−6.29	−17.39	0	0.013
85.67	−6.72	−14.21	0.016	0.025
87.91	−7.95	−14.84	–	–
89.34	−9.30	−13.63	0.072	0.090
97.04	−7.12	−21.33	–	–
98.75	−6.04	−14.49	0.064	0.099
122.93	−6.83	−16.89	–	–
128.75	−6.91	−18.68	0.041	0.123
160.08	−9.91	−14.05	0.371	0.439
206.22	−9.20	−14.28	–	–

Table 5-24. Isotope geochemistry for fracture carbonates in DH-GAP03.

Borehole length (m)	Result (‰-VPDB)		Std. Dev. (‰)	
	$\delta^{13}C$	$\delta^{18}O$	$\delta^{13}C$	$\delta^{18}O$
15.80	−7.91	−15.42	–	–
28.54	−10.96	−14.14	–	–
40.04	−8.72	−13.63	–	–
47.08	−7.98	−17.23	0.011	0.048
77.50	−8.50	−15.89	–	–
83.15	−9.41	−16.03	0.070	0.089
90.15	−9.95	−14.37	0.016	0.158
117.43	−9.93	−16.86	0.048	0.136
142.39	−11.54	−16.07	0.109	0.202
158.74	−10.28	−12.99	0.135	0.082
173.72	−9.25	−15.32	0.007	0.157
184.92	−10.38	−14.38	0.095	0.055
208.73	−10.19	−14.70	0.062	0.007
218.89	−10.80	−15.41	0.022	0.116
221.38	−9.75	−13.97	0.020	0.152
246.73 (top)	−10.26	−14.40	–	–
246.73 (base)	−9.93	−9.96	–	–
260.46A	−12.00	−15.25	0.074	0.094
260.46B	−12.15	−12.92	–	–
260.46C	−11.15	−13.14	0.047	0.075
275.77	−10.11	−15.51	–	–
293.71A	−11.69	−14.47	0.019	0.078
293.71B	−10.54	−15.56	0.001	0.045
293.71C	−10.20	−16.57	0.084	0.042
305.6	−10.06	−14.41	0.211	0.329
328.84	−10.36	−14.51	–	–
328.91	−9.96	−13.03	–	–
335.12	−10.62	−14.21	–	–

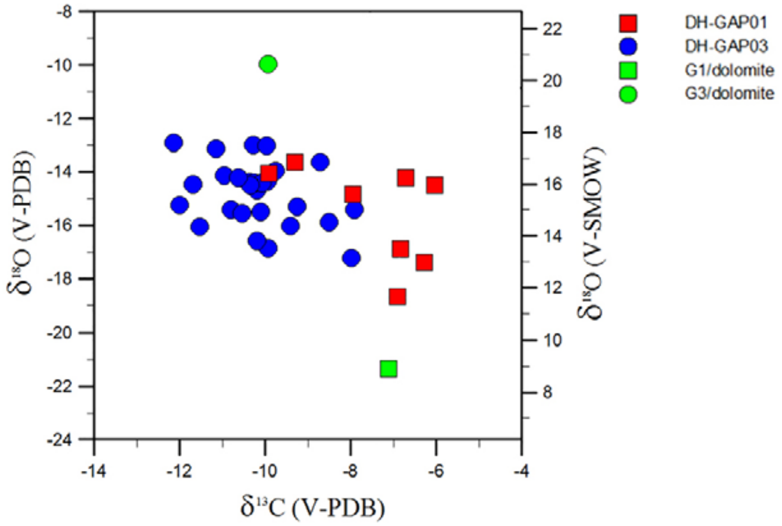

Figure 5-80. *$\delta^{13}C$ and $\delta^{18}O$ isotope signatures of carbonates sampled from GAP cores, with DH-GAP01 and DH-GAP03 fracture infillings identified using squares and circles, respectively. Carbonate fracture minerals were identified as calcite (red and blue) and dolomite (green).*

5.8.2 Preliminary isotope results on sulphate infillings

High sulphate concentrations are an important characteristic of groundwaters in the GAP. Gypsum ($CaSO_4$) is a highly soluble mineral that occurs as an infilling in fractures and pore spaces. If redox conditions change, this may initiate the microbial production of sulphide (Rosdahl et al. 2011). Understanding whether or not the high sulphate concentrations are a feature of periglacial environments (e.g. if they result from freeze-out), or if they are a result of geological conditions, is important. The sulphur mineral studies aim to determine which of the two previous scenarios are applicable in the GAP by providing isotopic fingerprinting of sulphur minerals to compare to groundwaters.

Sulphur-containing mineral samples were collected from DH-GAP01 and DH-GAP04 core using dental tools under a macroscope. $\delta^{34}S$ analyses were performed at the University of Waterloo Environmental Isotope Laboratory. Material was ground and then dissolved using ultra-pure water. $BaCl_2$ was used to precipitate $BaSO_4$ which was analysed on a Costech *element analyser* (EA) coupled with a Micro Mass Isochrom CF-IRMS (continuous flow isotope ratio mass spectrometer) after thermal reduction of $BaSO_4$ to sulphur dioxide. Only a small number of samples were analysed because additional core material was not available at the time. Additional sulphur studies are on-going at the University of Waterloo.

Preliminary results indicate that the $\delta^{34}S$ of groundwaters fall within a similar range as the sulphur minerals (Figure 5-81, Table 5-25). Oxidation of sulphide minerals produces a slight depletion in $\delta^{34}S$, as discussed in Section 5.7.2.2. Dissolution of sulphate seems most likely to occur for the high sulphate concentrations. On-going studies, aimed to provide more statistical significance to these results, are underway at the University of Waterloo. The range of $\delta^{34}S$ values covered by the sulphate minerals will be examined also. Further studies will aim to describe the source of the sulphate minerals found as fracture infillings.

Table 5-25. $\delta^{34}S$ from sulphates and sulphides found in DH-GAP01 and DH-GAP04.

Sample ID	$\delta^{34}S$ ‰ VCDT	Repeat	Repeat 2
DH-GAP04 A – sulphate	6.21		
DH-GAP04 B – sulphate	5.85	6.86	
DH-GAP01 C – sulphate	2.63	5.07	
DH-GAP01 D – sulphate	4.90	2.88	3.95
DH-GAP01 E – sulphate	2.93		
DH-GAP04 F – sulphide	3.73		
DH-GAP04 G – sulphide	3.47		
DH-GAP04 H – sulphide	2.26	2.54	

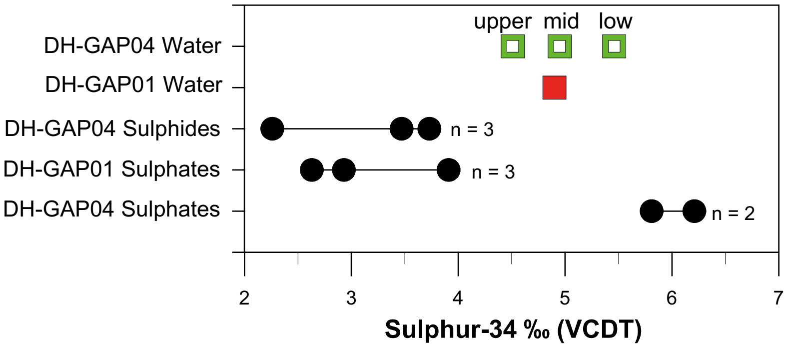

Figure 5-81. *$\delta^{34}S$ of sulphides, sulphates and groundwaters. Sulphide samples for DH-GAP04 come from a length along the borehole from 259.10 to 259.19 m. DH-GAP01 sulphates are from a fracture at 168.40 m. DH-GAP04 sulphates are from a fracture at 334.91 m.*

5.8.3 Observations on redox conditions based on fracture infillings

5.8.3.1 Background

The work reported in this section was conducted by an SKB and Posiva funded project entitled "Detection of the near-surface redox front". The leading partners are Terralogica AB and the Linné University, both from Sweden. ALS in Luleå provided the ICP analyses, the *Geological Survey of Sweden* (SGU) performed the *X-Ray diffraction* (XRD) analyses, and the SEM studies were performed by the Department of Geology, Earth Science Centre, Göteborg University. The Laboratory of Radiochemistry at Helsinki University, Finland, was responsible for the *Uranium series disequilibrium* (USD) analyses.

Components of glacial meltwater have been found in bedrock groundwaters at several hundred metres depth in the Baltic Shield e.g. Laxemar/Äspö (Laaksoharju et al. 2009) and Forsmark/SFR (Smellie et al. 2008) in Sweden, and at Olkiluoto (at a maximum depth of 300 m; Pitkänen et al. 1999) in Finland. This is consistent with hydrogeological models indicating that glacial meltwater can intrude to considerable depth in the bedrock during a deglaciation phase (Vidstrand et al. 2010). Some theoretical hydrochemical models (Glynn et al. 1999) suggest that glacial water is loaded with dissolved oxygen and its rapid transport into the bedrock can temporarily increase *redox potential* (Eh) at great depth. The aim of this investigation is to use mineralogy and geochemistry to determine possible changes in redox conditions from ground surface to the deep bedrock potentially caused by infiltrating glacial meltwater.

Drill core samples from assumed groundwater flow routes were analysed with emphasis on redox-sensitive minerals (Fe-oxyhydroxides and pyrite, and to a lesser degree Mn-oxyhydroxide), redox-sensitive elements (mainly Ce and U, but also Mn and Fe) and, for time contraints, USD. The data is collected to gain information about the depth of intrusion of oxygenated waters in the bedrock fractures (e.g. Dideriksen et al. 2010, Drake et al. 2009, Glynn et al. 1999, Guimerà et al. 1999, MacKenzie et al. 1992, Pérez del Villar et al. 2002, Spiessl et al. 2008, Suksi and Rasilainen 2002, Tullborg et al. 2003). Each of the parameters can provide indications of redox conditions individually. For example, findings of unoxidised pyrite strongly indicate that reducing conditions for Fe prevail, in contrast to findings of amorphous Fe- or Mn-oxyhydroxides, which indicates prevailing oxidising conditions with respect to Fe and Mn (Drake et al. 2009, Tullborg et al. 2008). U-series analyses can reveal if U has mobilised, which can be considered an indication of changes in groundwater flow conditions. Because U is redox-sensitive, mobilisation may indicate a change in redox conditions (oxidation of U(IV) to U(VI)) as well.

Interpretations of the redox front are not straightforward because specific physiochemical conditions in each fracture may have influenced different parameters in a different manner; e.g. mobilisation of U is not necessarily evidence of oxygenated conditions, because U(IV) oxidation to U(VI) can occur also in postoxic or mildly reducing conditions (cf. Berner 1981). Moreover, the redox front may have fluctuated over time. It is important to use several parameters in order to obtain thorough information from each fracture (here, the method successfully used for redox front studies at Laxemar, Sweden (Drake et al. 2009) is employed), and to understand whether the observed redox front corresponds to current conditions or is a fossil front – age constraints from USD, which approach secular equilibrium after a certain period of time depending on which isotope pair is studied (Gascoyne et al. 2002, MacKenzie et al. 1992, Osmond and Ivanovich 1992, Suksi 2001). The tiny amounts of fracture coatings, and relatively small drill core diameter, limits the number of methods to be carried out for each fracture (Tullborg et al. 2008). Another factor that has to be taken into account is the possible redox effect(s) that drilling and post-drilling handling activities may have caused. The latter is particularly important for DH-GAP04, where Fe-oxidation (rust) was found smeared (post-drilling deposited) on large sections of the unfractured core, due to introduction of oxygenated flushing water and metallic iron fragments originating from the drill bits/rods. Sometimes, this rust entered open fractures and care was taken to avoid these Fe-oxyhydroxides in the interpretation of pre-drilling redox conditions.

5.8.3.2 Methods

Fracture coating samples were collected from DH-GAP01, DH-GAP03 and DH-GAP04. The total number of samples was 13, 27 and 30 from each borehole, respectively. All samples were analysed using scanning electron microscopy for mineralogical characterisation; the same method was used for the characterisation of mineralogical changes (in thin sections) within the wall rock directly adjacent to a small number of near-surface fractures (DH-GAP01: 0, DH-GAP03: 5, DH-GAP04: 0). Bulk fracture coatings were scraped off of the fractures and analysed for chemical composition (6, 21, 21), USD analysis (3, 8, 13) and X-ray diffraction (3, 3, 0, mainly for detailed clay mineralogical composition).

SEM investigations

Thin sections, as well as fracture surfaces, from the samples were removed by sawing and were investigated using a Hitachi S-3400N scanning electron microscope, equipped with an Oxford Instruments energy dispersive system (SEM-EDS), in order to identify minerals and their weathering features. SEM-EDS analyses were performed at the Department of Earth Sciences, University of Gothenburg. The instrument was calibrated twice every hour using a cobalt standard linked to simple oxide and mineral standards. The acceleration voltage was 20 kV and the specimen current was about 1 nA. X-ray spectrometric corrections were made using on-line Oxford INCA software. The detection limit was 0.1 oxide% and Fe(II) and Fe(III) were not distinguished. Quantitative chemical analyses were not achieved for fracture surface samples due to the uneven surface of the samples. Minerals from these samples were identified by visual inspection and interpretation of X-ray spectra and/or element ratios.

X-ray diffraction

The XRD analyses were carried out by the SGU, Uppsala. The samples were separated into a coarse fraction and a fine fraction. The coarse fraction was ground in an agate mortar under acetone, and the powder was randomly oriented in the sample holder. The fine fraction was dispersed in distilled water, filtered and oriented according to Drever (1973). Measurements were carried out in three steps: 1) on the dried sample, 2) after saturation with ethylene glycol for 2 h, and 3) after heating to 400 °C for 2 h. A Siemens D5000 theta-theta-diffractometer with Cu-radiation, Cu Kα and graphite monochromator at 40 kV and 40 mA was used to produce difractograms. Coarse fraction scans were run from 2° to 65° (2-theta) without orientation of the samples. Fine fraction scans were run from 2° to 35° (2-theta) with a step size of 0.02° (2-theta) and counting time 1 s/step. The analyses were performed with a fixed divergence slit, a 2 mm anti-scatter slit and a 0.1 mm receiving slit. Bruker AXS DIFFRACPLUS 2.2 and EVA software were used for raw data evaluation. Minerals were identified using the PDF database (version 1994) and clay mineral data from Brindley and Brown (1980) and Jasmund and Lagaly (1993).

Chemical composition

The fracture coatings were analysed for major, minor and trace element contents by ALS AB, Sweden. 0.125 g samples were fused with 0.375 g LiBO2 and dissolved in dilute HNO3. Loss-on-ignition (LOI) was not carried out due to the small sample volumes. Concentrations of the elements were determined by ICP-AES and ICP-QMS. Analyses were carried out according to EPA methods (modified) 200.7 (ICP-AES) and 200.8 (ICP-QMS). The accuracy was 5–10 %. The analyses do not distinguish between Fe(II) and Fe(III).

U-series disequilibrium analyses

U-series studies refer to the analyses of the three longest-lived nuclides in the ^{238}U decay chain, ^{238}U, ^{234}U and ^{230}Th, to find out the state of radioactive equilibrium in the decay chain. Disequilibrium can be observed if U has moved relative to immobile Th, (i.e. measured ^{230}Th/^{238}U activity ratio deviates from unity). Nuclides were dissolved from fracture surface material in concentrated acid (HCl and HNO_3) and spiked with a known amount of yield tracers ^{236}U and ^{229}Th. Extraction solution was evaporated and the residue rinsed with dilute HCl for filtering. Filtrate was evaporated to dryness and residue dissolved in 9M HCl and loaded in a Dowex 1 × 4 anion exchange column for U/Th separation. In the procedure, U is fixed in the column while Th eluates with 9M HCl. Fixed U is eluated from the column with 0.1M HCl. The Th fraction is separated from other elements in a second ion exchange operation. Purified U and Th fractions were then prepared for α-spectrometry using the CeF_3 co-precipitation technique (Suksi 2001). Error bars for the determined nuclide activity ratios varied from 2.0–7.5 %, 4.0–8.5 % and 3.4–8.1 % for the ^{234}U/^{238}U, ^{230}Th/^{238}U and ^{230}Th/^{234}U activity ratios, respectively. Precision of the method was tested by analysing a U/Th reference sample DL-1a in which the U series is known to be in radioactive equilibrium (Steger and Bowman 1980). For samples with low U content (< 1 ppm) and a small sample amount, high resolution multi-collector (MC) MC-ICP-MS, with the same yield tracers was used. The device is situated in the Finnish Isotope Geoscience Laboratory at Geological Survey of Finland and has been used, among other things, for U-series dating since 2010 (FIGL 2009, Rinne 2010). Error bars are typically an order of magnitude lower than with α-spectrometry. It should be noted here that acid extraction may slightly dilute the USD signal because nuclides in radioactive equilibrium are extracted from rock forming minerals.

5.8.3.3 Results

The oxidative leaching of pyrite, and the formation of Fe-oxyhydroxide, indicates the position of the redox front as visible in the Fe system (Figure 5-82). Evidence of oxidising conditions is indicated by the presence of Fe-oxyhydroxides (mostly goethite) on many fracture surfaces from the upper 40 m (or less in DH-GAP01), whereas pyrite generally is absent. Goethite is abundant and shows characteristic spherulitic aggregates (mostly < 5 µm in diameter, Figure 5-83) of platy crystals. In addition, Mn-oxides (or oxyhydroxides), also indicative of oxidising conditions, are observed, but in much smaller amounts than goethite. Thin sections show that oxidising fluids have penetrated up to 6 mm into the wall rock in the near surface fractures, shown by goethite-filled microfractures and partial alteration of wall rock pyrite to goethite. At greater depths, pyrite, although present in small amounts, is fresh and unaltered on the fracture surfaces, and chlorite and clay minerals are common (XRD indicate the presence of swelling clay minerals of smectite type). In DH-GAP04, some deeper occurrences of goethite also exist, at depths about 160–162, 213 and 253–261 m. These occurrences show, in some cases, similar crystals to those near the surface, but generally are of another type (Figure 5-84). Instead, they are present as tiny crystals associated with sheared and slickensided chlorite-coatings, which shows that they were formed prior to a shearing event and are unlikely to have been formed recently. In all cases, the goethite occurrences are found within the section where permafrost prevails at present.

Results of the chemical composition of the bulk fracture coatings show trends representative of changes in redox conditions, going from oxidising conditions near surface to reducing conditions at greater depth. For example, Ce shows positive anomalies in the upper 40 m, indicative of Ce^{4+} (in DH-GAP03, Figure 5-85a), as well as leaching of U, which suggests U(IV) oxidation to more mobile U(VI) in the upper 20 m.

Mn concentrations are enhanced close to the surface, indicating the presence of Mn-oxyhydroxides (Figure 5-85b). At Laxemar, there were indications of relation between positive Ce-anomalies and Mn-oxyhydroxides (Drake et al. 2009). This relation is even more pronounced in the GAP cores and suggests a relatively well-developed redox front with well-developed crystals.

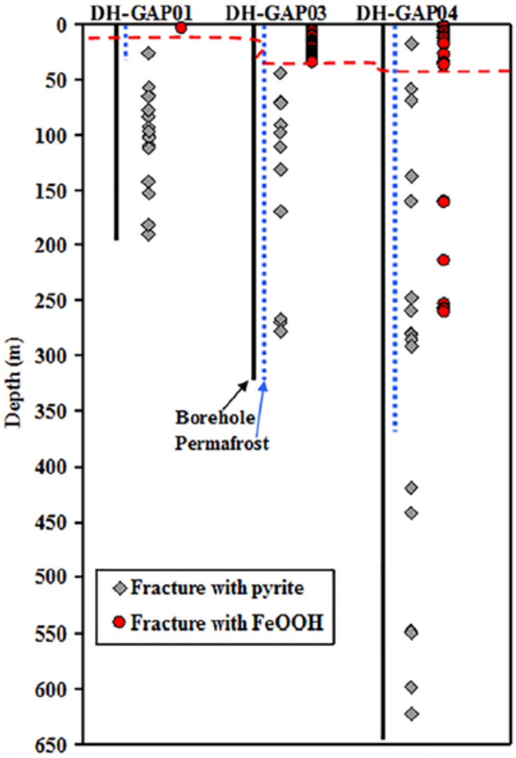

Figure 5-82. *Fracture coatings with, goethite (FeOOH) and pyrite vs. depth. On the x-axis, there is one column for each mineral in each of the boreholes. Y-axis shows vertical depth from TOC.*

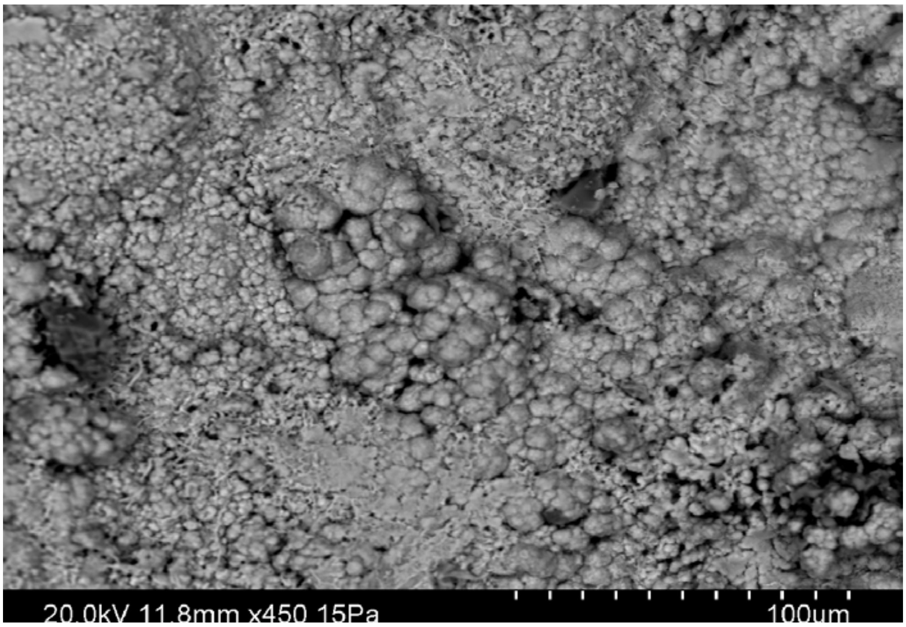

Figure 5-83. *Back-scattered SEM-image of spherulitical goethite aggregates from sample DH-GAP03: 34.65 m borehole length.*

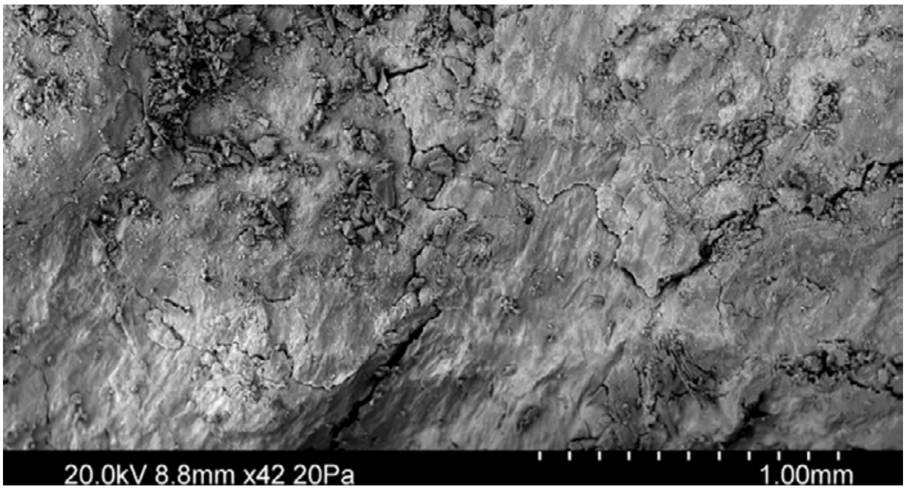

Figure 5-84. *Back-scattered SEM-image of fine-grained goethite crystals (bright), mixed with darker chlorite, which shows kinematic indication (slickensides) and, thus, pre-dates shearing of the fracture surface. Sample DH-GAP04: 273.30 m borehole length.*

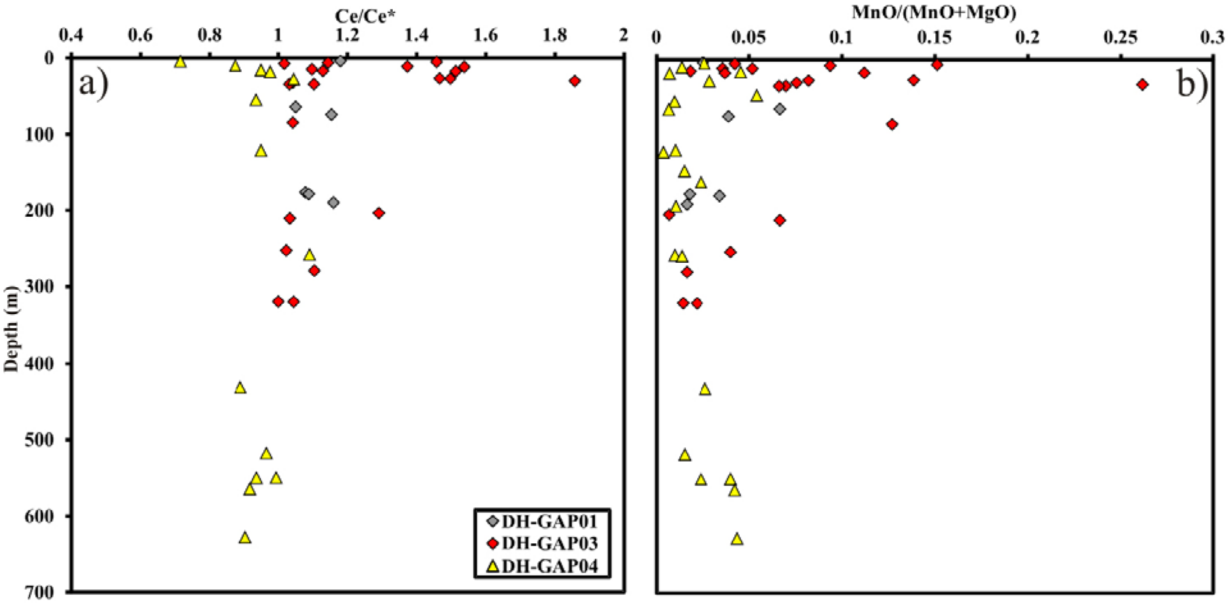

Figure 5-85. *a) Ce-anomalies (Ce/Ce*) in fracture coatings vs. depth. b) MnO/(MnO+MgO) vs. depth. Elevated Mn concentrations can be due to oxidation and accumulation in Mn-oxides or Mn-oxyhydroxides, as reported from Laxemar (Drake et al. 2009). Mn is a minor element in the common fracture minerals. In order to distinguish precipitated Mn-oxides, and to reduce the influence of chlorite/clay minerals, it was normalised to Mg, which is a major constituent of the latter. Mn-oxyhydroxides have readily precipitated above the near-surface redox front, within the upper 100 m.*

A subset of samples was selected for U-series analyses. The uranium content was very low (0.06 to 1.1 ppm) and the mobile part of the uranium presumably even lower. Due to this very low U content, and in order to complete alpha-spectrometry, high resolution multi-collector MC-ICP-MS was used to determine USD with good accuracy. Five samples were initially analysed with alpha spectrometry, and all 25 samples were analysed with MC-ICP-MS, providing a small methodological comparison with five samples. The results from the two methods show good correspondence (Figure 5-86), especially when taking into account the heterogeneity of the fracture samples. The results from MC-ICP-MS analyses are shown in Figure 5-87.

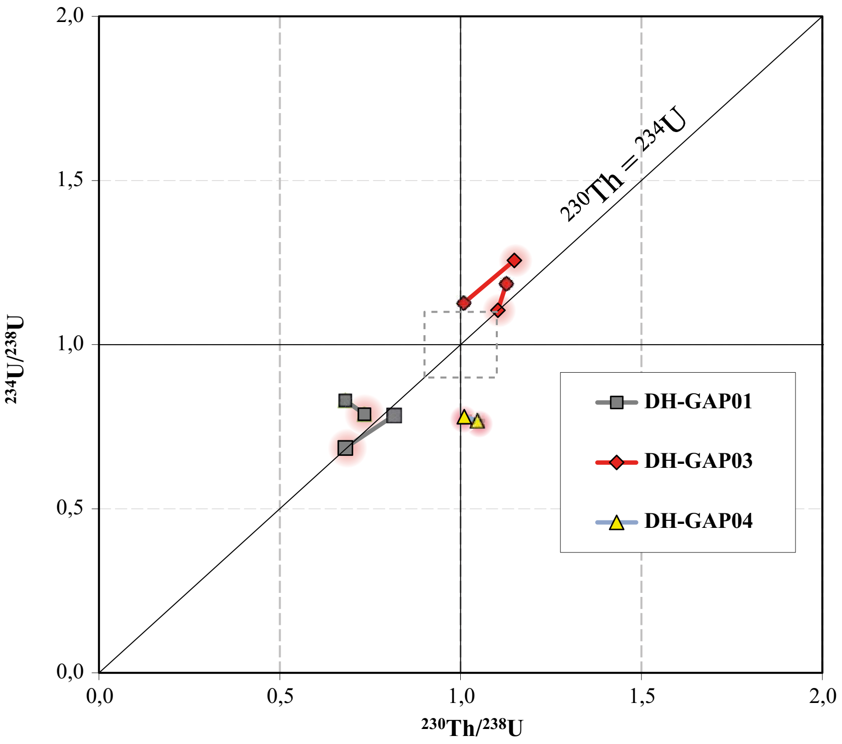

Figure 5-86. Comparison of alpha spectrometric and MC-ICP-MS analyses. Highlighted symbols represent alpha spectrometry. Sample material was not homogenised, which partially explains differences in activity ratios. Lines shown represent the different sectors in Figure 5-87.

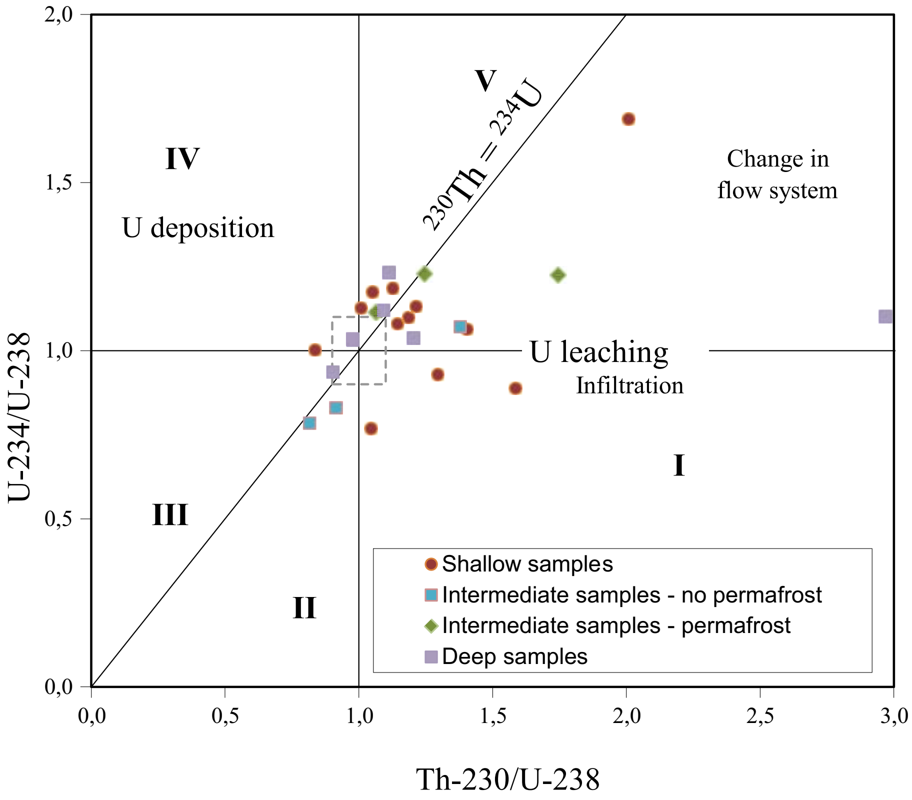

Figure 5-87. Interpretation of U-series data. The sectors from I to V represent different stages of U mobilisation/deposition when groundwater passes the redox-front. Part of the data plotted in the upper right sector indicate that these samples have experienced changed flow conditions, i.e. U-series disequilibria plotted in this sector cannot be created by a single event (see Figure 5-89 and text).

Activity ratios were plotted in a sector diagram (Figure 5-87) that describes U isotope behaviour according to Osmond et al. (1983). The meaning of the sectors is derived from a simple conceptual model of U mobility and Th immobility under water-rock interaction (Figure 5-88). In each sector, nuclide activity curves relative to immobile 230Th when groundwater passes the redoxfront from sector I to sector II and continues along the flow path. Activity ratios plotted in sector I are formed under bulk U leaching which is expected if Eh increases. Activity ratios from outcrops typically plot in sector I which suggests that leaching can also be very recent, even Holocene. Sectors II and III represent principal parts of U deposition (i.e. U occurs in excess of Th). Redox conditions in respective fractures strongly support stability of U. Transfer from sector II to sector III occurs via minor deposition of U. Sectors IV and V activity ratios are formed when more U is deposited sector IV representing younger (< 200 000 years) deposition. If redox transition exceeds sectors IV and V the resulting activity ratios will plot between sectors I and V, i.e. in the "sixth sector" .

Consequences of single event deposition of U for the evolution of the USD signatures are modelled in Figure 5-89.

Figure 5-87 indicates that the samples are from both sides of the redox-front in the flow system, showing both U deposition and mobilisation (depth distribution of samples from different sectors is shown in Figure 5-90). The fact that nearly all samples deviate from equilibrium indicates that the water-conducting fractures, where U movement has occurred within the last few hundreds of thousands of years (although they may have been sealed by permafrost for longer or shorter periods), were successfully sampled. It should be noted that most of the fractures mapped as open in the core log are probably not water-conducting, and parts of them may have been sealed originally. Results gathering along the $^{234}U{=}^{230}Th$ line, but deviating from the $^{234}U{=}^{238}U$ line, indicate that the fractures have been open to water circulation for a long time, at least during the last 1.5 Ma, but the hydrogeological activity during the last 200 000 years has, in many cases, been limited. Several exceptions exist where recent mobilisation is evident and these are described for each borehole below.

For DH-GAP01, (drilled to reach below a lake and assumed to represent a talik structure) a permafrost free scenario is suggested, except for the upper 20 m. Below this, one fracture coating sample from 190 m depth shows deposition of U probably during the last 200 000 years followed by recent leaching. The other two samples showed long term water-rock interaction under reducing conditions where ^{234}U is preferably leached. Concerning the USD results from DH-GAP03, possible recent (within the last 200 000 years) disturbances are indicated from two samples from relatively shallow depths (6 m and 17 m), the most shallow sample indicating U deposition ($^{230}Th/^{238}U$:0.83, $^{234}U/^{238}U$:1) and the others indicating dissolution ($^{230}Th/^{238}U$:1.4, $^{234}U/^{238}U$:1.06). Additional samples show some deposition of U, probably with limited recent mobility (< 200 000 years). One of the samples from greater depth (252 m) deviate significantly in showing first deposition (indicated by $^{234}U/^{238}U$:1.23), followed by leaching ($^{230}Th/^{238}U$:1.75). The latter process has been active during the last 200 000 years and, according to modelling using the DECSERVIS-2 simulation programme (Azzam et al. 2009), possibly within the last 100 000 years. This fracture is located within present-day permafrost.

In DH-GAP04, all but two samples deviate from secular equilibrium (or very close to). Most of the samples lines up along the $^{234}U{=}^{230}Th$ line, indicating that deposition (6 samples) occurred within the last 1.5 Ma, but during a time period before 200 000 years ago. Three samples from the upper part of the bedrock show clear signatures of U mobilisation, which could be relatively recent; these samples are from 9.5 m, 18 m and 27 m depth ($^{230}Th/^{238}U$:1.6, 1.3, 1.0, $^{234}U/^{238}U$:0.89, 0.93, 0.78). The sample from 55 m depth shows a typical signature for U deposition, but not a single continuous process (Figure 5-89). The deep samples beneath the permafrost represent depth from 431 m to 628 m, and show secular equilibrium (or close to) in 4 out of 6 samples. The other two show recent removal of U: significant in sample at 431 m ($^{230}Th/^{238}U$:2.97, $^{234}U/^{238}U$:1.1) and observable in fracture zone at 551 m ($^{230}Th/^{238}U$:1.21, $^{234}U/^{238}U$:1.04) (Figure 5-87). It is notable that the other sample from the same fracture zone shows secular equilibrium.

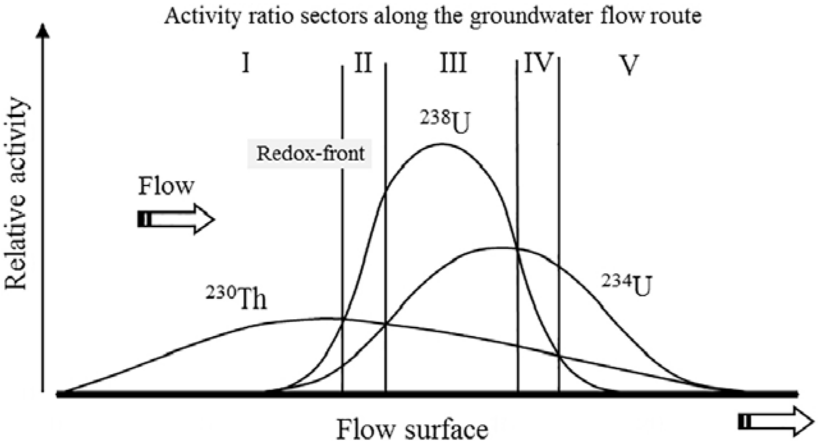

Figure 5-88. *Approximate distribution of ^{238}U, ^{234}U and ^{230}Th activities on fracture surfaces along groundwater flow route when water passes the redox-front (Modified from Osmond et al. 1983). Controlling factors for U and Th distribution are chemical properties of the elements, which cause leaching of U isotopes above the redox-front while ^{230}Th remains immobilised and accumulation of U in and after the front occurs. The decay of ^{238}U to ^{234}U and related processes enhance ^{234}U mobility, which shifts its activity curve during reducing conditions. Decay of ^{234}U to ^{230}Th causes stretching of the ^{230}Th peak as the ^{238}U and ^{234}U peaks advance. Displacements and shapes of the ^{238}U and ^{234}U peaks and displacement to the ^{230}Th peak are controlled by the groundwater flow rate and time, but the relative position of the peaks will remain.*

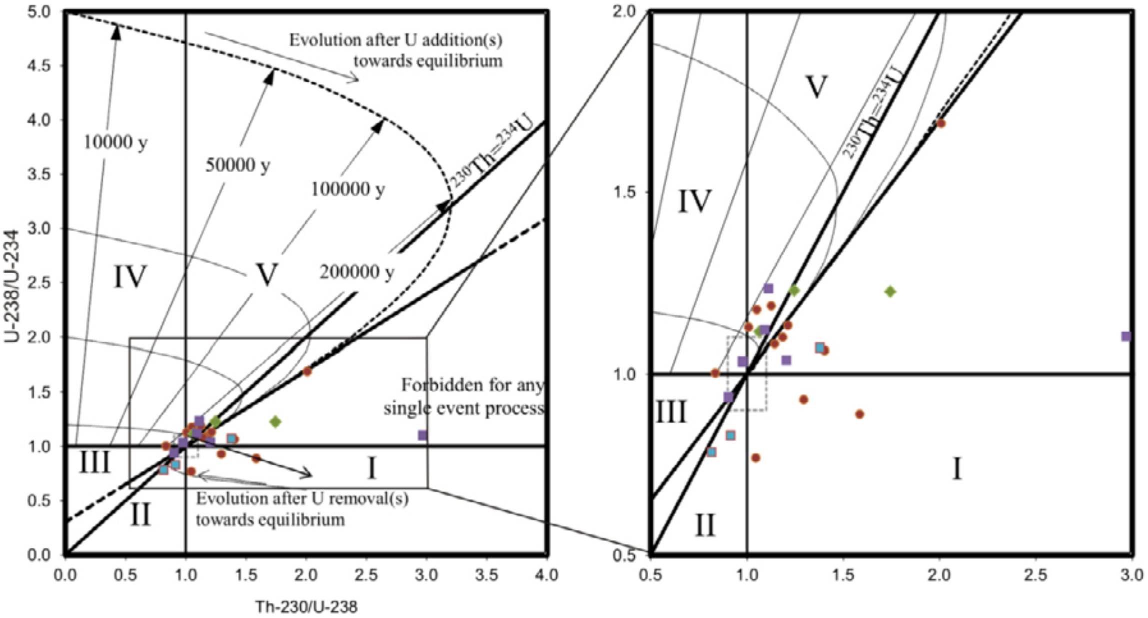

Figure 5-89. *Thiel diagram showing more detailed modelling of the evolution after addition of U, leading to USD signatures ending up in a small sector between sector V and the sector forbidden for any single event process. One of the shallow samples that ended up in the sector forbidden for any single event process (in Figure 5-87) is here indicated to be related to U deposition, whereas the others in the same sector definitely indicate leaching within the last 200 000 years. In the sector forbidden for any single event process, deposition of U has been followed by leaching of U within the last 200 000 years.*

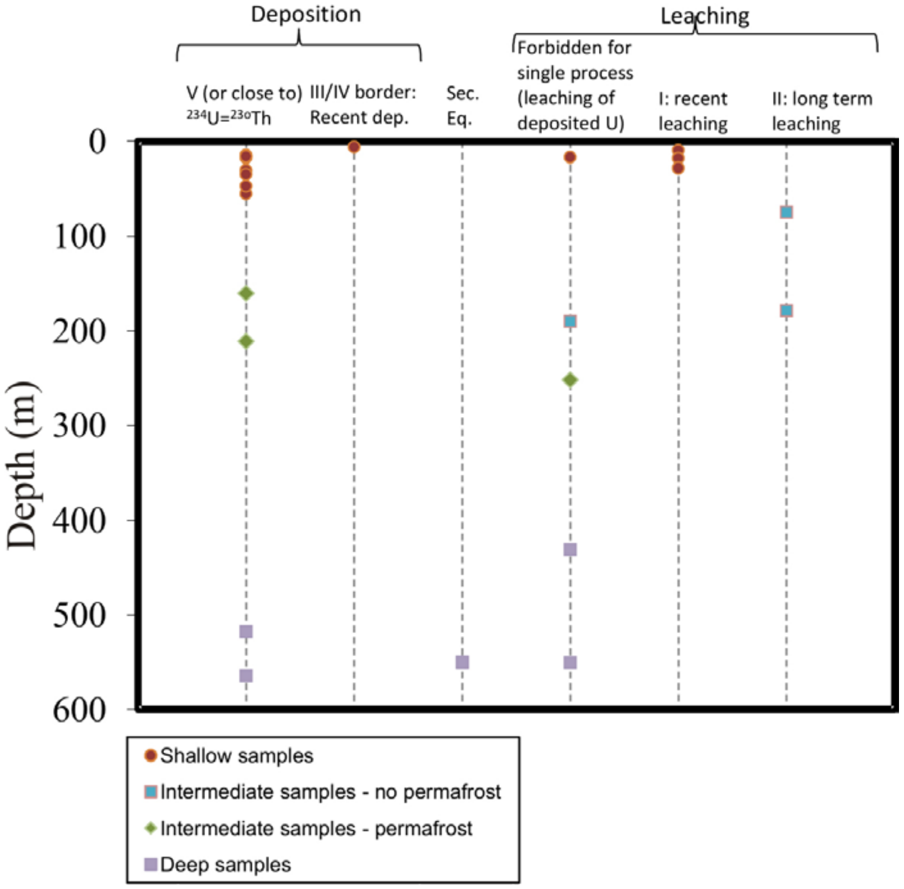

Figure 5-90. *Depth distribution of samples in the different sectors in Figure 5-87. The sector forbidden for a single process represent leaching within the last 200 000 years. For sector I, leaching may have occurred during the Holocene.*

The U-series data give indications of recent ingress of water capable of mobilising U into the bedrock at different depths. The presence and variation in permafrost thickness and ice sheet location during the same time interval make interpretations of the entire system challenging. Therefore, the interpretations are presented for three different depth intervals, where different scenarios are likely within the time-frame covered by the U-series data. These intervals are listed below:

1) the shallow system (0–70 m), where permafrost is presently prevailing in all samples except for most parts of DH-GAP01;
2) the intermediate system (70–300 m), which is currently within permafrost in DH-GAP03 and DH-GAP04, but not in DH-GAP01; and
3) the deep system (400–650 m), containing water-conducting fractures beneath the current permafrost (DH-GAP04 is the only borehole reaching these depths).

The shallow system

The USD results indicate that the very distinct near-surface redox-front expressed by the fracture infilling mineralogy may represent conditions that existed prior to the Holocene. Present conditions are less dynamic in most of the fractures analysed, which could be compatible with existing permafrost conditions. However, very few samples show secular equilibrium, which requires closed conditions for more than 1.5 Ma, indicating that groundwater movements have been active in the shallow fractures during the Quaternary, in a few cases within the last 10 000 years (Figure 5-87 and Figure 5-90). Some of these signatures may theoretically be due to seasonal variations, e.g. groundwater circulation in shallow fractures during summer (i.e. in the active layer of the permafrost), but, more importantly, it is known that the ice sheet has oscillated significantly in the area during the past 10 000 years. It is likely that during the Holocene Climate Optimum permafrost disappeared or at least receded to greater depths, allowing flow in the shallow system. Further support along these lines is offered by the fact that the FeOOH in the uppermost DH-GAP03 and DH-GAP04 fractures show quite well formed crystals, indicating that they were not precipitated recently. The findings in the DH-GAP samples are in contrast to the observations at Laxemar, where the near surface redox front (FeOOH and Ce-anomaly defined) is thought to correspond with present-day conditions (shown by USD, Drake et al. 2009) and where the FeOOH is less crystalline (i.e. it has not yet matured to well-formed crystals from the early stage low-temperature amorphous FeOOH; Dideriksen et al. 2010). Such a correspondence between the oxidation state in the Fe-minerals and the USD data is not found in the GAP samples.

The intermediate system

The fractures discussed here are either within present-day permafrost (DH-GAP03 and DH-GAP04) or below the Talik lake (DH-GAP01). Possible recent U mobilisation is indicated primarily in one sample within the permafrost (252 m DH-GAP03, Figure 5-87 and Figure 5-90). This disturbance may represent a period when the permafrost layer was thinner, e.g. when the ice sheet was larger and thicker and insulated the ground from low temperatures and permafrost formation. As the glacier is presently withdrawing, such a situation may have prevailed during the Holocene when warmer conditions than present prevailed during a period ~ 5000 years ago. The accumulation of U in the DH-GAP03 samples at depth of 15 m, 30 m, 35 m and 210 m, and at similar depths in DH-GAP04 (e.g. 16 m, 46 m, 55 m and 160 m) may be a result of groundwater circulation in the time span of 0.2 to 1 Ma. In DH-GAP01, one sample from a fracture where a significant drop in flushing water pressure was observed (indicating hydraulic conductivity within the unfrozen part of the borehole) at 190 m vertical depth shows that deposition of U has been followed by potentially recent leaching. The other two samples from DH-GAP01 in this interval show indications of long term leaching of U.

The deep system

In the deep system, beneath the permafrost in DH-GAP04, a dominance of samples showed ratios at, or close to, secular equilibrium, indicating limited groundwater circulation in these fractures within the last 200 000 years. However clear signatures of U mobilisation (as well as accumulation in two samples) confirm inflow of groundwater capable of mobilising U at these depths (431 and 550.70 m, Figure 5-87 and Figure 5-90), i.e. deposition followed by leaching within the last 300 000 years (Figure 5-89). The reason for the U mobilisation is intrusion of water with a significant content of complexing agents that can retain U in solution. The complexes in question are usually carbonate-uranyl complexes or, even more stable, Ca-carbonate-uranyl complexes (phosphate and others are possible, but less probable). U in the groundwater is dominantly U(VI), whereas U in the minerals are U(IV) and U(VI) in various proportions. It is possible that a Ca- and bicarbonate-containing water that enters into a fracture system can mobilise previously precipitated, oxidised U, or that the oxidation takes place at the same time as the intrusion of the water. Other redox indicators, e.g. the Fe-system, do not show evidence of late oxidation at these depths. This does not preclude that U can be oxidised, as this can take place under mildly reducing conditions as well (Berner 1981); the results indicate that the intrusion of O_2, if it has occurred, must have been limited. Hydrological observations indicate transport of water for long distances in horizontal fracture systems at these depths (see Section 5.6). The observed U-series disequilibrium may be related to transport of meltwater in the fracture system beneath the permafrost.

These signatures of U removal at great depth raise a question about whether or not the signatures are true or due to drilling and post-drilling handling. Different, and opposite, USD signatures obtained in this study show that drill core sampling (fracture surfaces) has not significantly affected fracture surfaces (disturbed during drilling or sampling), and, therefore, the USD results can be assumed to reflect the conditions in the bedrock aquifer. The very poor correlation between U concentrations and activity ratios indicate that the USD is not due to artificial handling, which would probably have led to notable disturbance in any U-poor samples (Figure 5-91). In addition, in one of the deep samples (DH-GAP04:550.70 m, vertical depth), two different fracture surfaces were analysed that showed U mobilisation in one fracture and secular equilibrium in the other, indicating that the flow path of oxidising waters has been more or less restricted to only one of these structures. Extensive influence from flushing water in the adjacent structures would have led to similar disequilibrium.

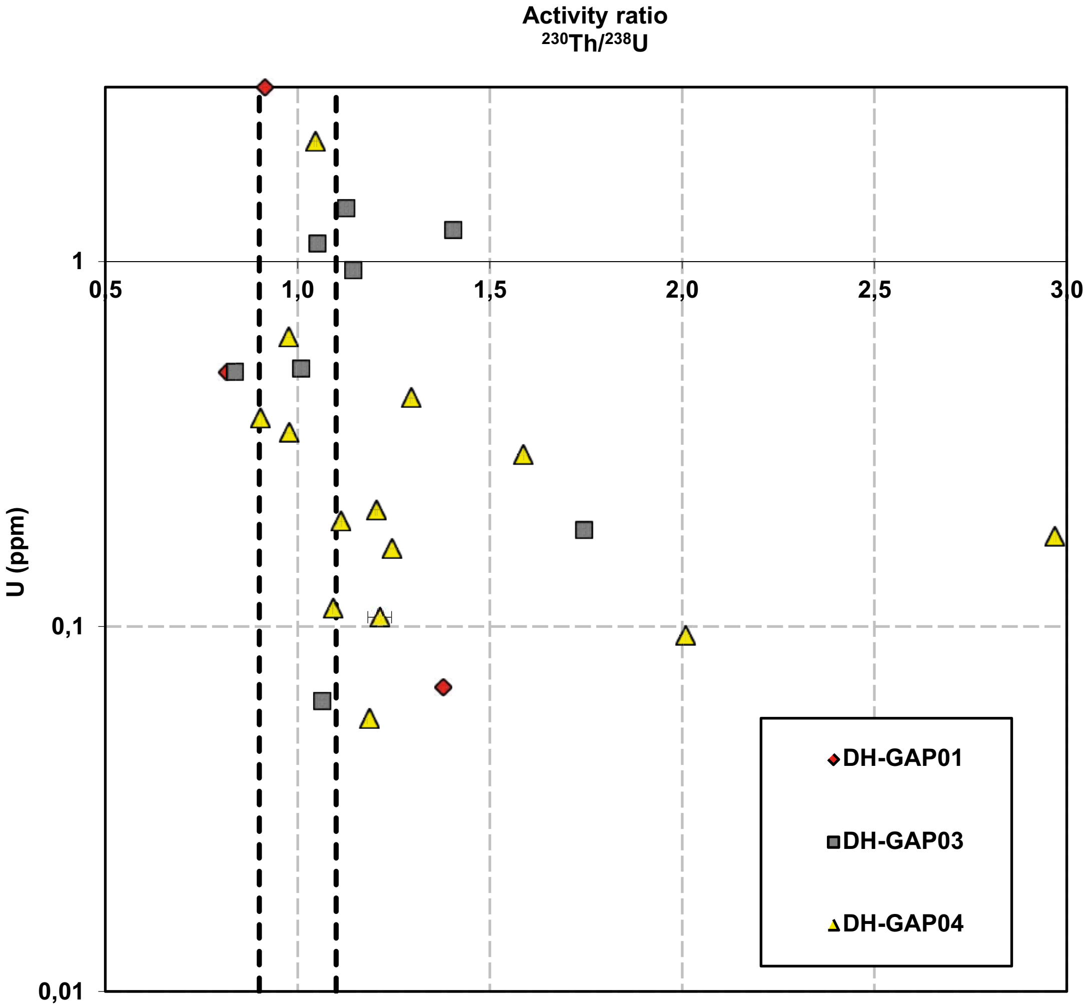

Figure 5-91. Activity ratio of ^{230}Th/^{238}U vs. U concentration. Vertical lines indicate secular equilibrium: 1 ± 0.1.

In contrast to the shallow system, where several independent proxies showed oxidation signatures (i.e. Ce, FeOOH, USD and Mn evidence), circulation of oxidative water in the deep system (> 400 m) is indicated solely by USD. One reason for this difference is that these proxies, in detail, reflect different *in situ* conditions and time-frames. Likely explanations are that the Eh is much lower at greater depth, and it is possible that only restricted, perhaps sporadic, events of more oxidative water have occurred in these fractures compared to the relict redox-front near the surface – where Eh has been higher and penetration of oxygenated waters has been continuous.

5.8.4 Main conclusions from the fracture infilling investigations

The majority of fracture mineralogy in the GAP drill cores is uniform. A typical fracture represented in these cores has a thin layer of chlorite coating, with spots of calcite and possibly traces of clays on top. Fluid inclusion studies carried out for fracture infilling calcites reveal a range of trapping temperatures between 100 and 200 °C. In DH-GAP04, gypsum is abundant and becomes the dominant fracture infilling below 300 m. This coincides with the change in rock type from mafic to intermediate or felsic. Gypsum forms practically mono-mineral infillings in fractures of variable orientation, although, occasionally, some calcite may be associated with the infill. Cross-fibrous texture commonly indicates mineral growth at extensional conditions (Passchier and Trouw 2005). Gypsum is found as microfracture infilling within the rock matrix also.

It is not well understood why gypsum is so abundant in DH-GAP04, while it is absent from nearby DH-GAP03 and is rare in DH-GAP01. The occurrence is assumed to be related to folding.

DH-GAP04 intersects the crest of a fold where opening of fractures takes place, providing routes for fluids. Another explanation could be sought from different depths and elevations of the boreholes. It can be argued that the reason for the scarcity of gypsum in DH-GAP01 and DH-GAP03 might be that they do not extend to depths exceeding 300 m, where gypsum becomes abundant in DH-GAP04. This depth control would imply that either gypsum has not originally precipitated at shallow depths, or it has been dissolved away. For comparison, studies carried out at SKB site in Laxemar (Drake and Tullborg 2009) indicate that the occurrence of gypsum increases at depths of 500 m or more.

The mineralogical textures in the gypsum infillings suggest high temperature (hydrothermal/metamorphic) formation from a homogenous fluid. Mineral formation in the fracture network, instead of a specific fracture generation and the occurrence of gypsum in rock matrix, is evidence of an intensive event. The origin of the sulphate-bearing fluids is not clear, but mineralogical, geochemical and isotope studies are on-going to provide insight into the source of the fracture gypsum.

Gypsum has several implications relevant for the hydrogeochemistry and hydrogeology of the site. Gypsum is a rather soluble mineral, and it is likely to contribute to the Ca and SO_4 composition of surface waters and groundwaters. It is a potential source for the sulphate in the DH-GAP04 groundwater. The relationship in DH-GAP01 is less evident due to the scarcity of gypsum infillings. The abundance of the soluble mineral in DH-GAP04 can also be taken as evidence that the conditions in the deep bedrock have remained largely unchanged since the formation of gypsum infillings.

All well-defined oxidation indications in the fracture infilling data are shallow (0–50 m) and from within the permafrost section and, thus, they cannot represent the current conditions (ice location). It is, however, possible that groundwater circulation have taken place in some of these fractures during the Holocene as indicated by U leaching (USD) i.a. activity ratios plotting in sector I, see Figure 5-90.

The deepest goethite samples (~ 260 m depth) have experienced shearing and may be of relatively old age. USD provides some indications of redox changes also in the deeper system, but they do not correspond to oxidation of Fe(II) suggesting a less oxidative nature of the redox transient.

5.9 Summary of understanding developed through SPC

5.9.1 Conceptual model for DH-GAP04 area

Figure 5-92 gives the N-S cross-section of the GAP drilling area extending from the Russell Glacier to Isunnguata Sermia. The 3D-model includes components assumed to contribute to the hydrogeology of the area and, especially to the hydrogeology of borehole DH-GAP04. Isunnguata Sermia occupies a deep valley, which is part of a major basal drainage system. The base of the ice sheet in this valley is at the elevation of −300 m b.s.l. while the drilling site elevation for DH-GAP04 is about 525 m a.s.l. Ice free areas are occupied by continuous permafrost, except for unfrozen zones (taliks) under larger/deeper lakes. The ice dammed lake at the northern flank of the Russell Glacier may support a talik, but it is not known if the talik is shallow or penetrates all the way through the deep permafrost. At least in some places permafrost likely extends laterally for some distance in under the ice sheet. The bedrock is cut by subvertical lineaments (yellow, lilac, blue, green and black lines in Figure 5-92) which have potential for water conductivity and routing groundwater flow within unfrozen bedrock.

5.9.2 Source areas for meltwater recharge

The bedrock in the GAP study area is Archaean-Proterozoic in age and has gone through various episodes of metamorphic and tectonic deformation. High-grade metamorphism has destroyed the primary features of the rocks and has left behind a gneissic appearance with cross-cutting veining of different size and composition. Only banding of mafic and felsic layers provide some hints about the original compositional variability of the volcanic-sedimentary precursors. Multi-phase folding, and both ductile and brittle deformations, have reworked the rocks and have resulted in major structures that are reflected in the present-day landscape. The Kangerlussuaq area is characterised by high bedrock ridges and deep stream valleys with a west-southwest to east-northeast trend. It is likely that

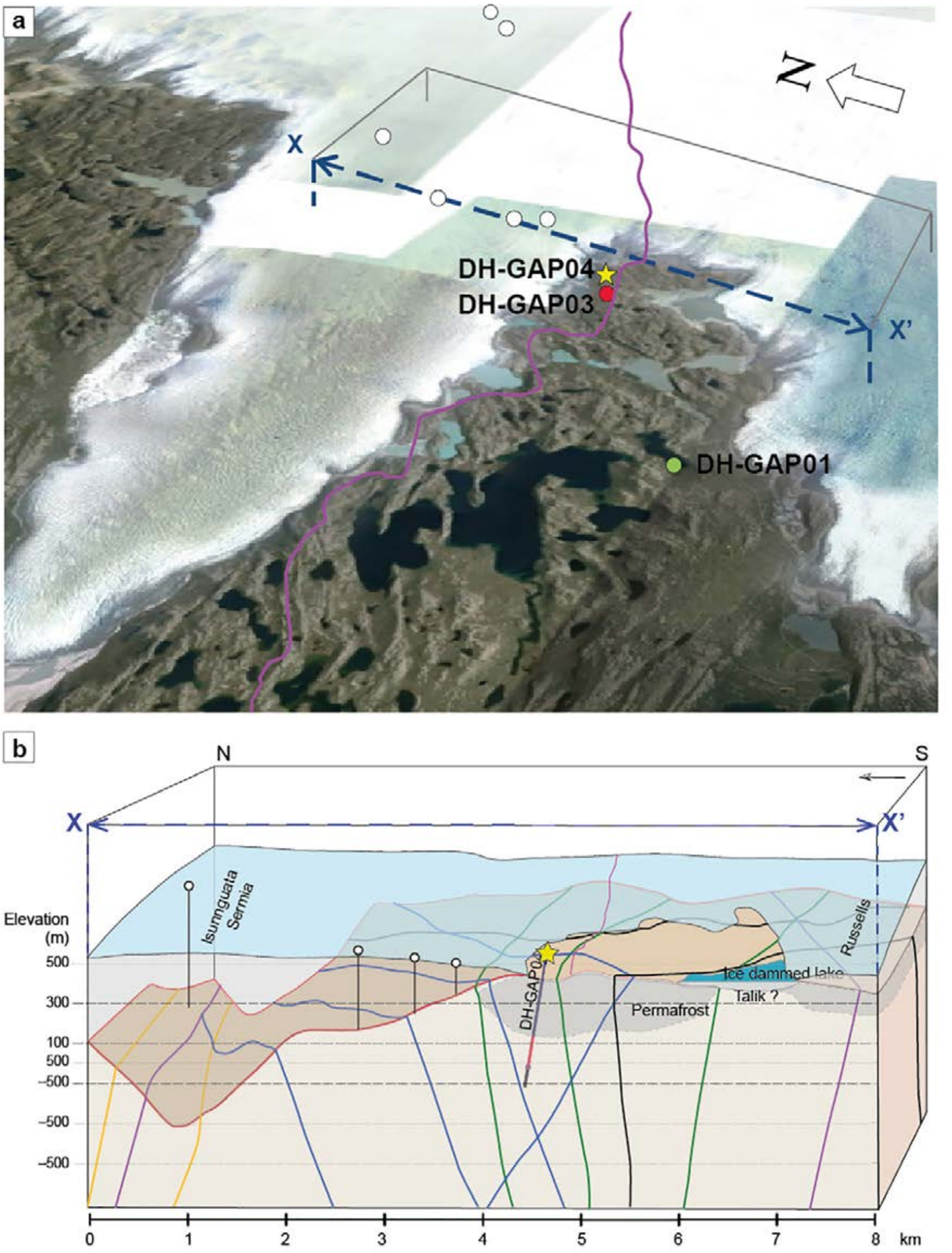

Figure 5-92. a) View showing the area between Isunnguata Sermia and Russell Glaciers. White spots indicate positions of six ice sheet boreholes. Green spot, blue spot and yellow star indicate positions of bedrock boreholes, DH-GAP01, DH-GAP03 and DH-GAP04, respectively. Purple line indicates the position of the border of the catchment (cf. Figure 3-59) b) Conceptual block model with the frontal plane parallel to blue dashed line (X to X') in a. Note the considerable bedrock undulations (100s of m) and the thick permafrost in the proglacial area and in DH-GAP04. Coloured solid lines indicates modelled lineaments.

oscillation of the continental ice sheet has further enforced these features by eroding preferentially brittle deformation zones. These major valleys, sub-parallel to ice movement, provide a continuous drainage system all the way from the ice sheet down to the fjords.

Typically the relief is a few tens of metres in the GAP area, although the highest summits, close to the ice margin, reach 600 m a.s.l. The same kind of relief seems to exist under the ice sheet, where the ice bed is locally depressed hundreds of metres below sea level (Section 3.5). For example, the difference in elevation from the DH-GAP04 drilling site to the topographical depression (−300 m) under Isunnguata Sermia to the north is about 800 m over a lateral distance of three kilometres. In comparision, the slope to the Kangerlussuaq fjord is about 500 m over a distance of 30 km.

The meltwater stream valleys in the proglacial area are filled with thick glaciolacustrine and glaciofluvial deposits, while only thin overburden is observed in elevated areas. Storms et al. (2012) reported pronounced sediment thicknesses from Sandflugtdalen at the Watson River (see Figure 2-2). The thickness of the deposits range from 40 to 80 m. Close to the Kangerlussuaq village, the sediments are typically 30 m thick.

It is plausible that the neoglacial re-advance has not been able to remove all sediments from the subglacial depressions, despite that the observations from the ice drillhole sites indicate bare bedrock conditions or only thin gravel cover (Section 4.5). If thicker sediment deposits occur in the depressions, the sediments are saturated with waters and provide space for meltwater storage, as well as pathways for flow between the ice sheet and the less porous bedrock below. During the melting season, large volumes of meltwater are formed and the majority of this meltwater is channelled through the basal drainage system or as supraglacial runoff into the stream system (see Section 3.3). A significant volumetric replenishment, with a temporary and spatially limited pressure pulse in connection with the formation of moulins, may occasionally increase the potential recharge rate to the basal drainage system for a short period (Sections 3.9.5 and 4.10). In winter, the surface freezes and surface water runoff is inhibited, implying that only groundwater runoff is present. In theory, the subglacial flow can continue for some time at the teminus along the deeper parts of the stream sediment deposits (i.e. if a deep active layer exists), or, if pressurised, possibly along the frozen sediment. Nevertheless, throughout the year, a variably pressurised meltwater source remains in contact with the bedrock and, via the fracture network, with the groundwaters as well.

There is no information available about the hydraulic properties of the deformation zones in Greenland. However, based on fracture mapping at the surface, and due to the multi-phase deformation history, it is plausible that brittle reactivation of the deformation zones has occurred on several occasions, providing pathways for water flow. Further, the analogue from Fennoscandia shows that in similar metamorphic terrains, with tectonic deformation structures, a water-conductive fracture network occupies the upper part of the bedrock (e.g. Follin et al. 2011). The major deformation zones in the Kangerlussuaq area are deep enough to extend through the thick (~ 350 m) confining permafrost and to provide pathways for sub-permafrost flow.

Based on the above discussion, the deep subglacial valleys and depressions filled with sediments overlying intensely fractured deformation zones are the most probable meltwater recharge areas (Sections 5.4, 5.6 and 5.7). It is less likely that the sparsely fractured subglacial bedrock ridges could effectively recharge meltwaters. It is not possible to pinpoint a single recharge area, but infiltration is likely to take place in favourable locations throughout the wet-based ice sheet (see Section 4.10). The most active surface melt zone (*surface runoff zone*), with significant volumes of surface meltwater input, extends about 100 km inland from the ice margin.

The question as to whether or not subglacial permafrost exists and how it affects infiltration and subglacial flow, is important as it has implications for groundwater flow. The GAP has shown that subglacial permafrost may exist close to the ice margin east of borehole DH-GAP04 and in the foreground of the ice margin (for more information see Sections 5.5.2 and 5.9.3 below). Consequently, the subglacial groundwater outflow entering this area must either flow above the permafrost in unfrozen sediment or along the base of the ice bed towards the outflow channels. Alternatively, if open fracture pathways exist, groundwater may flow downwards under the permafrost toward the sub-permafrost fracture network in the bedrock (see Figure 5-93). The hydraulic properties, and geometry of the local fracturing, determine the optimal flow directions. In favourable situations, continuous pressurised water flow can force channels through the permafrost as well (van Everdingen 1998). This is assumed to be the case with the Leverett Spring. However, there are no observations of such discharge points in the vicinity of Kangerlussuaq indicating that this may not be a common mechanism. There is not enough information to assess if discharge springs at the lake bottoms are more common than dry land springs.

The potentially very wide subglacial recharge areas, as suggested by the work in SPB, implies that the residence time for the meltwater in bedrock may become very long. The amount of meltwater at the base of the ice sheet is rather limited during winter. After the onset of the melting season, the surface input adds significant amounts of water into potential recharge areas (see Section 4.4). This likely results in a cyclic recharge behaviour and slightly different chemistries of the recharging waters (surface melt vs. basal melt at the contact with sediment at the ice bed). Additionally, it is possible that new recharge meltwater is continuously mixing with the initial recharge along the flow path. This would ensure that the chemistry remains dilute and would act to homogenise the stable isotope signatures, which are known to vary in the ice (see below).

5.9.3 The role of permafrost and taliks in the periglacial hydrogeology

The hydrogeology in periglacial environments is one of the key topics investigated in the GAP. Recharge of ice sheet derived meltwaters and the interaction of surface waters and deep groundwaters are controlled by the properties of the overburden and the bedrock. Geological investigations have shown that the bedrock is fractured, and it is reasonable to assume that there are flow paths from surface down to depth. The thick continuous permafrost occupying the area changes the conditions significantly and complicates the hydrogeological interpretations. As mentioned before, the presence of permafrost influences the entire flow system, from subglacial recharge to downstream hydrology.

Kangerlussuaq is located within the area of continuous permafrost. Prior to drilling of the GAP boreholes, there was little information about the actual thickness of the permafrost. Temperature data reported from shallow boreholes at Kangerlussuaq village indicated that the maximum thickness would be 158 m at sea level. The depth of the active layer depends on soil type and moisture. Close to the ice margin, depths of less than one metre have been reported for moist soils, while for dry sands it may be much deeper; and for outcrops active layer may extend down five metres. The development of the active layer in Kangerlussuaq begins in late May and continues until early October.

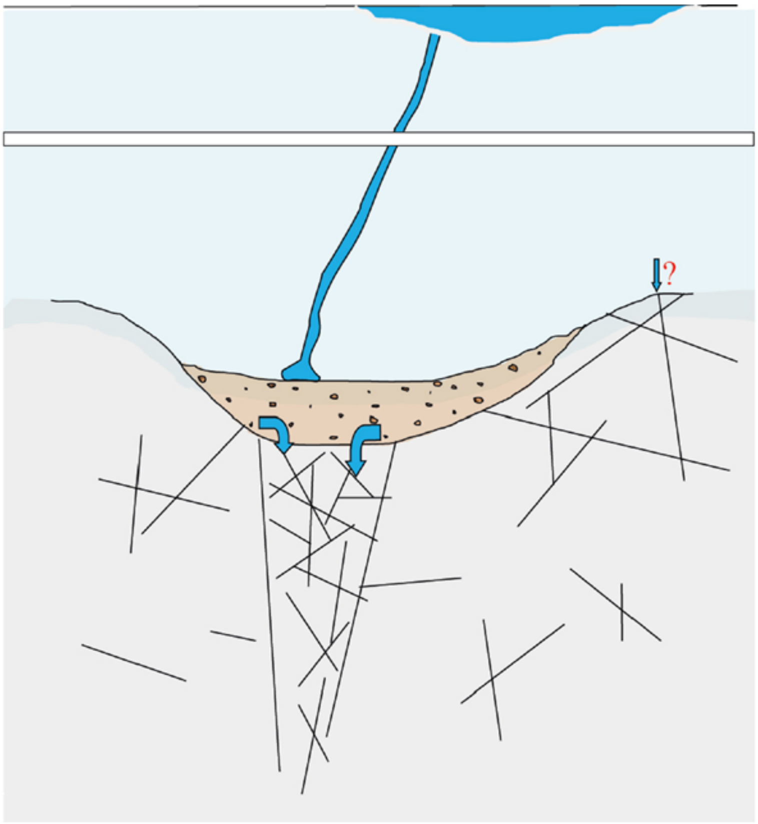

Figure 5-93. Potential recharge zone in a subglacial depression formed over a fractured deformation zone. Saturated porous sediment fill provides space for meltwater and flowpaths. Elevated bedrock areas are more likely to be less fractured and flushed bare.

The temperature profiles from the GAP bedrock boreholes suggest that the mean annual ground surface temperatures during the growth of permafrost have been up to 2–3 °C colder than presently observed, maybe as low as −5 to −6 °C (corresponding to about −7 to −9 °C MAAT). It cannot be ruled out that subglacial permafrost could exist for some kilometres in from the ice sheet margin. The relatively low temperature gradient and the low heat flux (27.2 ± 1.8 mW/m^2 for DH-GAP04 and 34.8 ± 1.9 mW/m^2 for DH-GAP03) in the upper bedrock favour the persistence of subglacial permafrost. The low heat flux is assumed to reflect cooling of the bedrock in Greenland as a result of continued glaciations(s) since the Pleistocene.

Temperature profiling in the GAP boreholes shows that close to the ice sheet margin, the permafrost thickness reaches 350–400 m, as measured in the DH-GAP03 and DH-GAP04 boreholes. Since temperature data from DH-GAP04 compared to DH-GAP03 does not indicate any obvious signs of thinning near the ice margin, it is possible that permafrost continues under the ice for some distance. However, no investigations of subglacial permafrost have been done in the area north of DH-GAP04. The results from electromagnetic soundings east of DH-GAP04 suggest that in this area, permafrost exists under the ice for two kilometres inland from the ice margin. It is reasonable to assume that this is the case also elsewhere in the GAP study area, although due to lacking field observations this cannot be confirmed. Because the geophysical method is not able to exactly define the base of permafrost, it is not known if the thickness is changing. Additionally, the soundings indicate that there is a thin unfrozen layer between the ice and the permafrost. This would be consistent with the temperature profiles from ice holes, which show that the temperature at the base of the ice is close to 0 °C at the ice margin and slightly negative farther up-glacier, where pressure melting conditions are reached (Section 4.4). SPB inferred from numerical modelling that the ice sheet is wet-based for ~ 250 km upstream from the margin. Seasonally, the most active surface melt zone extends about 100 km to the east from the margin (see Section 4.4), providing high energy transport to the base due to high flow rates, and leading to the development of an effective basal drainage system. In areas where meltwater flow is maintaining the basal temperature above the freezing point, the upper surface of the permafrost is expected to warm and, maybe, slightly thaw. Geothermal heat warms and eventually melts the bottom of the permafrost layer. Currently, it is unclear how deep the warming effect of the subglacial meltwater flow extends, and what the annual energy balance is, because flow at the base ceases during winter, leaving open questions related to the melting rate at the basal part of the permafrost.

The sealing effect of the frozen ground against the water flow is shown, for example, by the hydraulic testing in DH-GAP04 (see below). Infiltration and circulation of meteoric waters is limited to the active layer. Not even the deepest permafrost is able to close all hydraulic connections below the active layer. Vertical unfrozen structures and taliks, extending partially or entirely through the permafrost (through taliks), are reported to be typical features in periglacial areas. The structures typically exist under deep lakes and rivers, but also have been observed to exist, for example, beneath peat bogs. Their formation is based on the insulation effect of the water body or materials. If the cold air is insulated away from the ground year-round, the geothermal heat flow from below thaws a vertical temperate zone through the permafrost. Another possibility is that, if a lake basin already existed when the climate started to cool, the talik remained open throughout the freezing process.

Taliks penetrating through the whole permafrost layer (through taliks) are assumed to be common in the GAP study area. All larger, non-meltwater lakes, which do not freeze to the bottom, favour talik formation. Lakes of different sizes are typical of the periglacial landscape, most likely due to the presence of permafrost. Geothermal modelling shows that under the prevailing conditions in the GAP study area, the limiting size for a lake capable of supporting a through talik is 200 m in diameter (Section 5.5.3). A talik can form within a few hundreds of years, which is a short time compared to geological or glaciological cycles.

How taliks contribute to the hydrogeology depends on the properties of the lake bottom sediments, the underlying bedrock and the ambient hydraulic gradients (Figure 5-94). Taliks in fractured bedrock (e.g. within deformation zones) are more likely to be hydrogeologically active than taliks in sparsely fractured rock. Hydrogeology in a talik can be complicated both temporally and spatially in the dynamic system at the foreground of a continental ice sheet and is not understood very well. Nearby taliks can behave differently, and, even within the same talik, both discharge and recharge can occur in the different parts of the lake (Bosson et al. 2013, Vidstrand 2015[2]). Fluctuations of the hydraulic gradient in the course of the annual melting cycle, or in relation to the past movement of the ice margin, are likely and can change the direction in vertical flow systems.

The overall permafrost conditions in the GAP area since the Pleistocene have been variable, which has impacted the hydrogeology of the area. Deep permafrost in the proglacial area, as observed today, allows discharge/recharge through taliks only. Although numerous taliks do occur, the interaction between meteoric water and groundwater remains localised and restricted. During past permafrost-free periods, the interaction was much more intense, and due to the absence of sealing fracture ice, was controlled only by the availability of flowpaths and the hydraulic gradient. During warm periods, the amount of precipitation increased and the chemistry of recharging waters was different than during cool and arid periods (Follin et al. 2008). Considering the impacts on the evolution of the groundwaters, the relatively frequent changes in hydrogeological conditions may prevent the equilibration of the deep groundwater system, resulting in a situation where hydrogeochemically imbalanced water bodies of different residence times exist at different depths and in different hydrogeological compartments. Added to the large fluctuation in hydraulic gradients when the ice sheet oscillates over the area, it is imagined that the groundwater system near the ice margin is subject to continuous change.

5.9.4 Depth of meltwater penetration and flow in bedrock

Two questions to be assessed by the GAP, including the penetration depth of glacial meltwater and the subglacial hydraulic pressure driving groundwater flow, are directly linked to the bedrock structures and to the water-conducting fracture network. Geological structures, e.g. deformation zones, may provide pathways for the recharging meltwaters, provided that a connected network of transmissive fractures downward from the bedrock surface exists, in which case the prevailing hydraulic gradient determines the penetration depth of meltwaters.

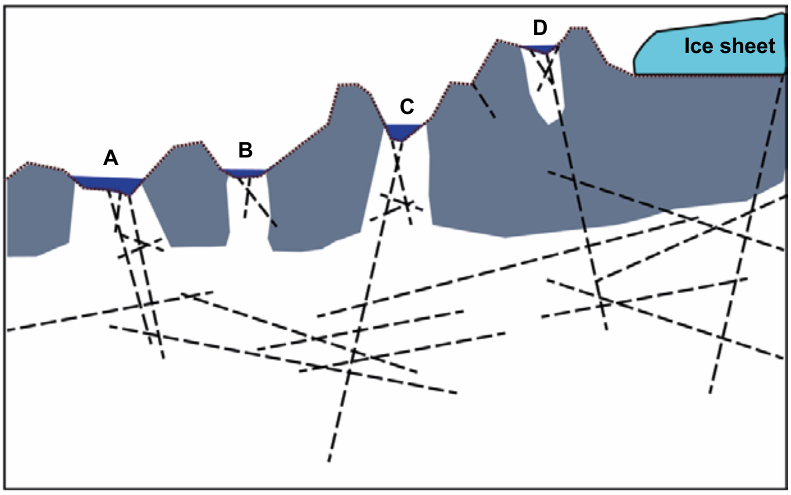

Figure 5-94. *Taliks contribute differently to hydrogeology, depending on their type, elevation and location relative to bedrock structures. Through taliks (A-C) extend through the permafrost and have potential for vertical flow, discharge or recharge, depending on the hydraulic gradient. However, if the fracture network is discontinuous (B), the talik is hydrogeologically inactive. It is the same for an open talik (D) which is open to surface, but confined by permafrost from all other sides. This type of talik forms under smaller lakes or ponds (diameter < 200–500 m). Regardless of potentially good hydraulic connections in the bedrock, the water circulation is limited to shallow depths. In rare cases, pressurised water flow could open routes through frozen bedrock and generate a hydrothermal talik.*

---

[2] Vidstrand P, in prep. Concept testing and site-scale groundwater flow modelling of the ice sheet marginal-area of the Kangerlussuaq region, Western Greenland. SKB R-15-01, Svensk Kärnbränslehantering AB.

The analysis of the geological and hydraulic data from the deep research borehole, DH-GAP04, provides an opportunity to investigate one part of the potential recharge system in detail. The geological information from the other two boreholes, DH-GAP01 and DH-GAP03, suggests that the geology, including the fracture network, varies from one location to another, depending on the geological setting (Figure 5-95A). Due to the presence of permafrost down to ~ 350 m vertical depth in DH-GAP04, no hydraulic test data were obtained from the upper part of the bedrock. The drill core showed that the observed fracture frequency is about the same throughout the borehole. An interesting observation, emphasizing the complexity of the fracture network, even at the borehole scale, is that vertical fractures are observed in the upper 300 m of the bedrock. Below 300 m, vertical fractures become rare and sub-horizontal fractures dominate. Temperature peaks observed in DH-GAP01 during the cooling stage, following hot water drilling, suggest that there are some water-conducting fractures in the upper 130 m of the bedrock. This is more or less expected and the lack of any hydraulic conductivity in the upper part of DH-GAP04 only demonstrates how effectively the permafrost seals the bedrock outside the taliks.

Hydraulic testing of DH-GAP04 with the PFL, (Pöllänen et al. 2012) revealed nine water-conducting zones below the permafrost. The hydraulic zones have variable PFL transmissivities and the fluid pressures vary as well. For sampling and monitoring purposes, the borehole was divided into three sections using a double packer system (i.e. Sect-up, Sect-mid and Sect-low). Sect-up is confined by permafrost at the top (~ 380 m vertical depth), and Sect-low extends to the end of the borehole (~ 650 m vertical depth). Sect-mid includes a 10 m section from 561 m to 571 m vertical depth.

The observed PFL transmissivities in the borehole are related to single fractures or to sets of a few fractures located close to each other. The hydraulic zones are separated by 4–35 m long drill core sections with sealed fractures. The orientation of the fracturing within the water-conducting zones is predominantly parallel to the foliation (i.e. sub-horizontal). Steeply dipping fractures are rare or missing from all hydraulic sections. This, together with an intact 34 m thick bedrock section between Sect-mid and Sect-low, explains the poor hydraulic connections and different hydraulic pressures between the two sections. On the other hand, the good hydraulic connection between the upper and middle sections is likely due to the two sub-horizontal fracture sets dipping in opposite directions and cross-cutting each other at an angle of 30–40 degrees.

Based on the above information it is possible to define three hydrogeological units in DH-GAP04 with different hydraulic properties:

- Unit A) ranges between 548–604 m of borehole length. It includes all the fractures with the highest PFL transmissivities. The internal fracturing responsible for the water conductivity is subhorizontal and either parallel to the foliation or cutting it. Monitoring sections Sect-up and Sect-mid are situated within this unit.
- Unit B) is a 34 m thick unit of intact rock, separating Unit A from the lower part of the borehole and provides a hydraulic and hydrogeochemical barrier (i.e. prevents mixing of groundwaters).
- Unit C) ranges between 638–687 m of borehole length. Observed PFL transmissivities within this unit are two orders of magnitude lower than in unit A and the water conductivity is strongly controlled by fracturing parallel to the foliation. Monitoring section Sect-low is situated within this unit.

DH-GAP04 intersects a large fold structure with a fold axis dipping gently towards NW. This implies that at the hinge area of the fold, the hydrogeological units dip gently to NW, i.e. towards the Isunnguata Sermia Glacier (Figure 5-95) suggesting that the upper sections of DH-GAP04 might be hydraulically connected to fractures outcropping beneath Isunnguata Sermia. The conjugate fracture system observed in Unit A can be linked to one of the main brittle lineaments (Type 5) in the area dipping either SE or NW. These type of lineaments intersect DH-GAP03 at the bottom of the borehole and at the upper part of DH-GAP04 (within permafrost). Thus the assumed hydraulic connections towards north may be controlled by the fold structure or the lineament, or a combination of these two. The cyclic behaviour of fluid pressures in Sect-up and Sect-mid provides support for this concept (see Sections 5.6.2 and 5.9.5). Correspondingly, the almost complete lack of steeply dipping fractures interescting Sect-low and the generally lower specific capacity values at depth in DH-GAP04 provides an explanation of why Sect-low lacks the pronounced cyclic pressure fluctuation and is characterised by lower hydraulic pressures and hydraulic heads.

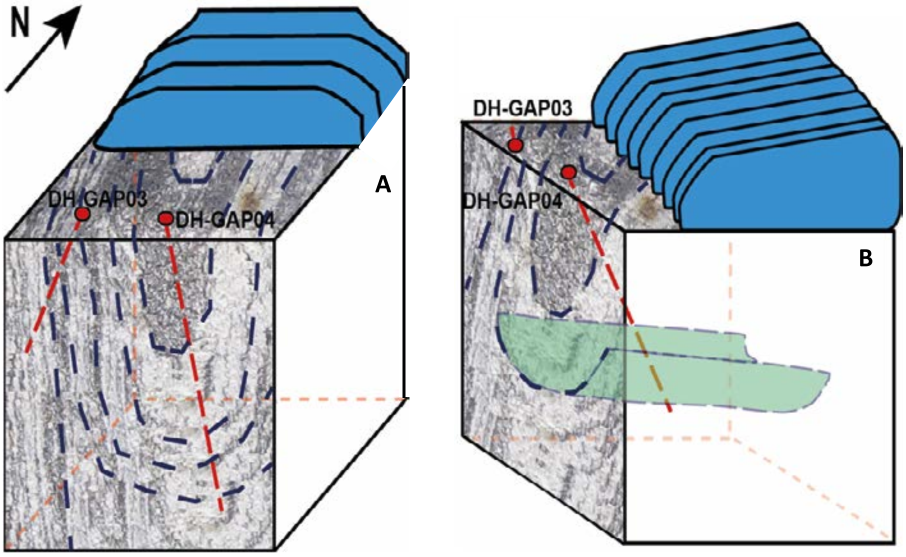

Figure 5-95. Schematic presentation of the location of boreholes DH-GAP03 and DH-GAP04 relative to the geological structure. Blue dashed lines depict the trends of foliation and the continuation of lithological units. A) DH-GAP03 intersects the limb of the fold and is, therefore, characterised by sub-vertical foliation. DH-GAP04 is drilled through the hinge of a synform fold, where the foliation turns to sub-horizontal. B) Same structure from a different angle, showing how the fold axis and the foliation planes are dipping gently towards the ice in the north. Because a major part of the fracturing within the hydraulic zones in DH-GAP04 is parallel to the foliation, it is plausible that hydraulic connection between the borehole and the base of the ice sheet is formed through this fracture system.

The observed variation in fracture frequency and orientation seem to create a hydraulic compartmentalisation around DH-GAP04. Sect-up and Sect-mid in DH-GAP04 are interacting and are situated within a confided location between the upper 'sealing' permafrost boundary and the lower ~ 30 m intact bedrock unit, while Sect-low is isolated from the rest of the borehole. It seems that the intact section in between is laterally extensive enough to prevent vertical flow anywhere in the vicinity of the borehole. Due to the complex geology in the study area, it is difficult to predict the continuation of the flowing features at greater distances. The observation that sub-horizontal fracturing is dominant in the vicinity of DH-GAP04 suggests that the hydraulic zones observed in the borehole have some lateral, although unknown, extents, and that the vertical connections are weak or non-existent. If correct, the assumption implies, among other things, that the meltwater component in the DH-GAP04 fracture water (see below) is not likely to be derived directly from above, but instead derived from a source farther inland. The subglacial permafrost possibly extending to some distance in under the ice margin, provides an additional obstacle for recharge at the immediate ice sheet margin. Presently, it seals off potential vertical flow even though vertical water conducting fracturing could exist.

The borehole data represents sparsely fractured bedrock between deformation zones. The data demonstrate that water flow occurs in fractures partly controlled by the foliation and that flow is confined by permafrost. Water conducting zones are few below 400 m depth. There is no evidence of post-glacial reactivation of fractures, although this could be expected due to the oscillations (advance and retreat) of the ice sheet and repeated subsidence-rebound cycles.

To conclude, the fracture network is well developed at least down to the observation depth of 650 m. Permafrost, fracture infillings and the geometry of the fracturing define which part of the fracture network is currently available for water flow. There are strong indications that there is a hydraulic connection from the base of the ice sheet down to the depth of 570 m (Section 5.9.5). This means that there is a potential flow path for meltwater recharge to this level.

It should be noted that the uncertainties related to the generalisation of these observations are significant because almost all of the information in 3D from this geologically complex area comes from a single borehole.

5.9.5 Hydraulic conditions in the bedrock

Flowing intervals in DH-GAP04 are related to single fractures or a few closely spaced fractures within the test intervals. Hydraulic testing using Posiva Flowlog (PFL) soon after drilling showed that the PFL transmissivities (specific capacity) within Sect-up and Sect-low are in the range of 10^{-7} to 10^{-6} m^2/s, and 10^{-9} to 10^{-8} m^2/s, respectively. These values are likely affected by the pressure transients after drilling, which means that the true values may be slightly higher. Hydraulic testing results consistently indicate flow toward the borehole in all flowing intervals, with the exception of the bottom of the borehole where a weak outflow was measured. Another test, using pumping and head recovery data, was conducted in the talik borehole, DH-GAP01. Total fracture transmissivity for the 71 m long sampling section at a depth of 131–191 m is $\sim 10^{-6}$ m^2/s. No other known hydraulic data for bedrock is available from the study site or from elsewhere in Greenland. DH-GAP01 and DH-GAP04 are far away from each other, and are situated in geologically and hydrogeologically different environments. The results provide an estimate of the hydraulic properties of the sparsely fractured bedrock in the area.

As mentioned previously, the obtained fluid pressure monitoring data from DH-GAP04 shows that Sect-up and Sect-mid are hydraulically connected, while Sect-low is isolated from the upper two sections. The calculated freshwater head in Sect-low is about 30 m lower than in Sect-up and Sect-mid. This is somewhat unexpected, but it is in an agreement with the PFL testing results, which showed out flow and also the lowest head at the bottom of the hole. Additional evidence that the head difference is real was obtained during the sealing of the borehole packers. The head in Sect-low decreased quickly following inflation, while Sect-up and Sect-low reacted much more slowly. Samplings in September, 2011, and September, 2013, showed that the pressure recovery in Sect-low is slow and that the pressure sensors responded normally to the numerous pumping cycles, exhibiting cyclic drawdown-recovery patterns. Continuous fluid pressure monitoring shows that there is a pronounced seasonal head variation (~ 10 m) in the upper two sections. The response pattern in Sect-low bears some similarities, but the head variation is only about one metre. The maximum error in the heads is less than ± 2.9 m (Appendix B).

In general, pressure monitoring in a borehole reveals whether or not flowing features are connected to a system subject to head variations. In permafrost environments, such systems can be taliks or the part of the subglacial meltwater network that connects to the groundwater systems.

In 2011–2012, heads in Sect-up and Sect-mid peaked in June and reached the lowest levels in October–December, respectively. Increasing heads in the upper and middle sections were observed from January, 2013, onward and the peak ocurred in July, indicating that similar head development is repeated from year to year. The timing may vary, as does the climatic forcing and the melting rate. Seasonal patterns suggest that the upper bedrock sections are in connection to the ice sheet basal drainage system (subglacial pressures, melting and ice velocity). Because of the sealing effect of the thick permafrost in the proglacial area, and the reversed correlation between precipitation and the bedrock pressures, it is difficult to envision any meteoric forcing. The isotopic composition of the water samples collected from the upper sections indicate a meltwater component, giving credibility to the ice-bedrock connection. The differences in head between the upper and middle sections and the lower section are interpreted to be due to observed differences in structural-hydraulic properties with depth, e.g. differences in fracture intensity, orientations and transmissivities.

The relatively quick decline in heads after the peak in July is lagged compared to the onset of the melting season, but coincides with seasonal change in glacioseismic activity. Although the majority of the glacial earthquakes are geographically associated with major outlet glaciers, it is interesting to note that the pronounced increase in the annual earthquake frequency coincides with the peaking of the hydraulic heads in the bedrock boreholes (Kanao et al. 2012).

The pressure response is not necessarily linked to instant changes in the water chemistry (i.e. the dynamic pulse does not generate the movement of groundwater). However, it has not been possible to observe this aspect in detail yet due to the persistent drilling water contamination. The EC sensors in the monitoring sections provide continuous data of the salinity of the water. The EC in Sect-up stabilised in late 2012, but the water salinity in the other two sections remains transient. Pumping in association with sampling in 2013 had a strong impact on Sect-low by removing practically all drilling water and almost doubling the groundwater EC. The other two sections still have more than 30 % drilling water. Based on the slow rate at which the upper sections are cleaning, the groundwater flow and associated advective velocities in the bedrock around the DH-DAP04 monitoring sections are considered to be relatively slow.

In comparison with the observed head change in Sect-up and Sect-mid the barometric impact is very small, although observable despite the thick confining permafrost. Thus, the barometric pressure variations do not explain the head fluxuation in the borehole. Nevertheless, a 100 % barometric correction is applied for the borehole pressure data. To be able to confirm the timing and the rates of the cyclic behaviour of the pressures, and to identify the subglacia/glacial process possibly causing the observed pressure behaviour deep in the bedrock, additional monitoring data over the next few years along with numerical modelling is required. Integration of the present structural, hydraulic and glaciological information (i.e. from SPA and SPB) gives support for the following conceptual model (Figure 5-96).

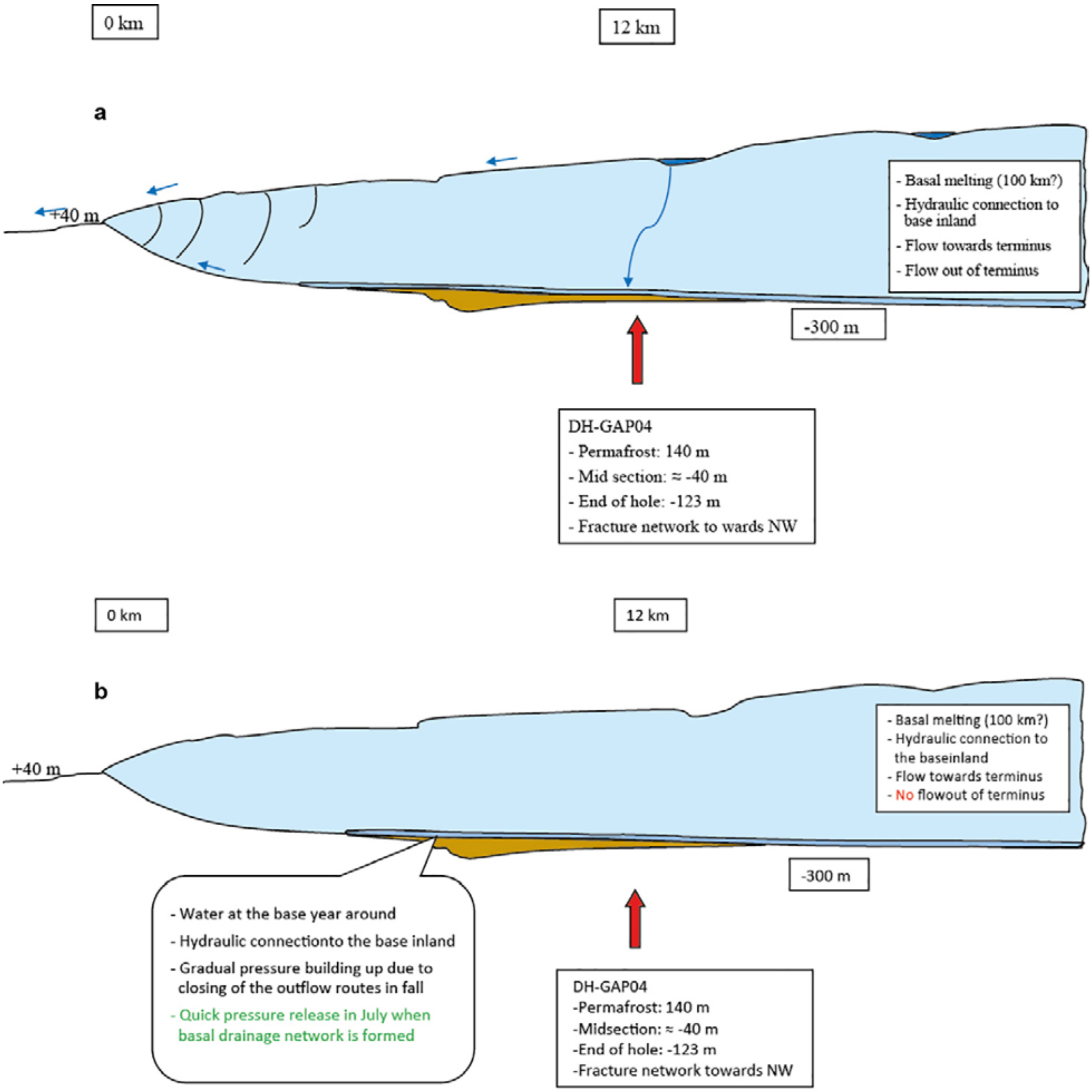

***Figure 5-96.** Conceptual model describing the hydraulic interaction between the bedrock groundwaters and the ice sheet of Isunnguata Sermia. a) Melting season. b) Winter.*

The bedrock is significantly depressed under Isunnguata Sermia. Radar investigations conducted by SPA suggest that the elevation at the centre trough is −300 m (in front of the terminus the river plain is at the elevation of about 40 m) and can be followed eastward in under the ice for considerable distances. It is assumed to form one of the most important regional basal drainage systems in the GAP area. The depression is controlled by a major deformation zone which is seen as a lineament in the proglacial area. For comparison, the elevation at the end of DH-GAP04 is −123 m and at the Sect-mid the elevation is 40 m. As noted above, the hydraulic units are dipping toward the trough depression and likely connect to the ice bed of Isunnguata Sermia directly or via the fracture network within the underlying deformation zone.

From spring to fall the ice sheet is hydrologically active to varying degrees. Surface melting generates large volumes of meltwater, which is channelled away by surface runoff or is collected into SGLs. Occasionally these lakes drain through moulins and reach the ice sheet bed. The ice sheet in this area is wet-based due to basal melting, and the basal pressures are controlled, in part, by the outflow at the terminus.

In late fall, the surface melting terminates, but the basal melting continues and so does the flow toward the terminus. Due to the gradual closing of the basal drainage system at the terminus, the basal pressures start to build up and the process continues throughout the cold season. This pressure increase is observed in Sect-up and Sect-mid and to a smaller extent in Sect-low, implying hydraulic connection to bedrock somewhere under Isunnguata Sermia. In May–June surface melting initiates, but because it takes some time before the basal drainage system is developed, the borehole heads continue to increase. Just before or at peak melting the deeper part of the ice sheet is activated and the basal drainage system changes from inefficient to efficient; a relatively rapid drop of ice borehole pressures followed by a drop in basal pressures are observed at this time (Figure 5-59 and Figure 5-60). It is interesting to note that a similar pressure release pattern is observed at approximately the same time in the ice holes drilled ~ 30 km inland from the ice margin, suggesting that the pressure drop may be linked to a large-scale change in basal conditions (Figure 4-14).

5.9.6 Surface water evolution in periglacial environment

The role of surface water bodies, and their impact on groundwater in the GAP area, has been studied by a variety of means. Theoretical papers have been written on the role of cryogenic solute concentration in cold climate terrains (e.g. Herut et al. 1990, Starinsky and Katz 2003). In these scenarios, the concept of freeze-out or solute exclusion near a glacial ice front leads to highly concentrated lakes in the region of the foreland bulge and the recharge of these highly saline solutions into the underlying rock mass; the origin of concentrated crystalline brines was attributed to this mechanism by these authors. After glacial retreat, the emplaced brines move back toward the surface, creating saline lakes. Investigations of surface lakes and the Leverett Spring were made to assess the salinity of surface water bodies and the origin and fate of solutes in these waters in terms of the geochemical and hydrologic budget.

Overall, it was found that the lakes are dilute to brackish. In the immediate proglacial area, lakes are dominated by Ca^{2+}, whereas lakes in areas less recently deglaciated may be dominated by Ca^{2+}, Mg^{2+} or Na^{+}. Generally, lakes dominated by Na^{+} are saline lakes (salinity < 5 g/L, Na-Cl types located near fjord). Interaction of water with bedrock and glacial sediments, as well as loess, contribute to the salinity, to various extents, during travel in streams and the active layer and during residence time in lakes. Glacially comminuted sediment exposed to the air provides faster reaction times for minerals, such as biotite, than would be observed in intact bedrock (e.g. Blum and Erel 1997).

Although bicarbonate is the dominant anion in fresh water lakes, some do have noticeable concentrations of SO_4 or Cl. Oxidation of sulphides found in bedrock, as well as dissolution of sulphate minerals and recycling of sulphate through yearly cycles of precipitation and dissolution, are important processes related to lake sulphur. In the area around the fjord, sea salt aerosols and sulphide-reducing bacteria influence lake chemistry as well. Sulphide-reducing bacteria may be found in lakes between the fjord and the ice margin. Chloride is generally dominant only in the region around the fjord where sea-salt aerosols may have a greater impact on lake composition. The role of paleo-sea water intrusion in the past, due to sea level fluctuations, may have added to the salinity in the shallow bedrock and glacial deposits near the fjord. Ten Brink (1974) reported the highest marine clays at an elevation of 40 ± 5 m in the Kangerlussuaq area. Storms et al. (2012) pointed out that the clays define only the minimum elevation for the marine limit because they do not refer to the palaeo coastline position. Thus, the influence of sea water may be observed at elevations somewhat higher than 40 m.

While lake water chemical composition is derived from the processes above, salinity is mainly determined by the presence or absence of outflow from the lake basin, and is primarily the result of evaporative concentration. Salinity is not hypothesised to be caused by the upwelling of saline waters as a result of cryogenic concentration of sea water (Starinsky and Katz 2003) or the upwelling of subsurface brines (Frape et al. 1994, Henkemans 2016).

5.9.7 Meltwater characteristics

When analysing the influence of meltwater recharge on the groundwater system, the most useful parameters are $\delta^{18}O$ and $\delta^{2}H$ due to the heavy depletion of these isotopes in glacial meltwater. Meltwaters cover a wide range of depleted $\delta^{18}O$ and $\delta^{2}H$ values and it is thus difficult to calculate mixing scenarios based on these isotopes alone.

If the waters in DH-GAP04 are recharging meltwaters, as suggested by the depleted $\delta^{18}O$ and $\delta^{2}H$ values, they have evolved along the flow path from very dilute (EC < 5 µS/cm) to much higher salinities (EC > 900 µS/cm). These waters are dominated by SO_4 and Ca from gypsum dissolution. Sulphate-reducing bacteria are not observed in DH-GAP01 and are presumed unlikely to be present in DH-GAP04 due to the similarity in $\delta^{34}S$ values between the two boreholes.

At the ice-bed interface, dissolved oxygen may be present in high concentrations (Section 4.5.4). Studies on redox-sensitive fracture infilling minerals and chemical elements (Ce, U, Mn, Fe) provide no evidence of deep penetration of oxygenated waters. This would suggest that high oxygen concentrations in meltwater are attenuated rapidly in the subsurface. However, obvious mineralogical or geochemical signs of oxidation readily attributed to meltwater recharge into the upper part of the fracture network have not been observed. The 40 m deep redox front in DH-GAP03 is assumed to be related to ancient infiltration of some type of oxic waters.

5.9.8 Deep groundwater evolution and penetration of meltwater

If the measured values in Sect-low, and the groundwater isotopic values corrected for drilling contamination for Sect-up and Sect-mid from DH-GAP04 are applied, depletion relative to modern meteoric water (4 to 6 ‰ in $\delta^{18}O$) is apparent and the waters have an isotopic composition similar to meltwaters. The results indicate that the groundwaters sampled in DH-GAP04 originate from glacial meltwaters down to 570 m depth based on $\delta^{18}O$–$\delta^{2}H$ (Figure 5-77); however, it is not possible to determine a mixing scenario because the meltwaters cover a broad range of $\delta^{18}O$–$\delta^{2}H$ values (−23 to −35 ‰) and because any other end members are unknown. Components of glacial meltwater have been documented in the deep bedrock aquifers of the Baltic Shield, e.g. the Laxemar/Äspö (Laaksoharju et al. 2009) and Forsmark/SFR (Smellie et al. 2008) sites in Sweden and Olkiluoto in Finland (Pitkänen et al. 1999).

The seasonal pressure response in Sect-up and Sect-mid in DH-GAP04 supports the concept that these sections are connected to the ice sheet basal drainage system. Sect-low shows different hydraulic behaviour, and appears also to be connected to the ice sheet basal drainage system but does not appear to be connected to the Sect-up and Sect-mid flow systems.

Due to geologic (Section 5.4), permafrost (Section 5.5), hydrogeological (Section 5.6) and geochemical (Section 5.7) evidence, along with concepts of subglacial flow developed by SPA (Section 3.9) and SPB (Section 4.10), a general understanding of the evolution of groundwater in DH-GAP04 could be as described below:

Meltwater infiltration into the subsurface occurs beneath the ice sheet within some distance (up to ~ 130 km) from the ice margin. Subglacial permafrost prevents recharge at the immediate ice margin (Section 5.5), (Figure 5-97). Recharging meltwater is dilute and assumed to be oxygenated. Within the near surface of the bedrock, the oxygen is consumed by oxidation reactions with various minerals, such as pyrite and biotite, in the glacial sediment and the bedrock (Section 5.8; Section 5.9.4).

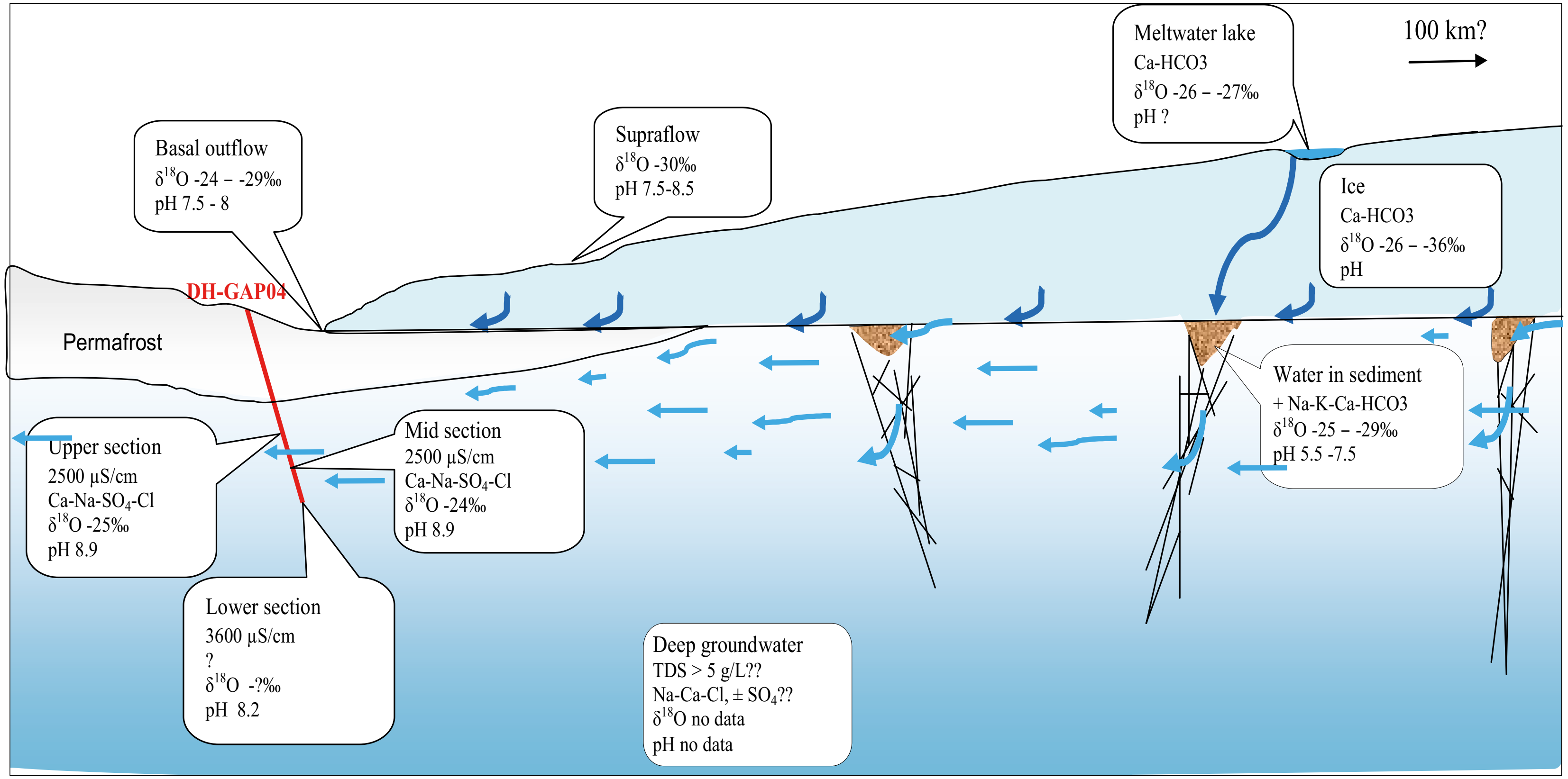

***Figure 5-97.** Hydrogeochemical conceptual model including the different components contributing to the groundwater evolution in the research area. It is suggested that the subglacial recharge is taking place in favourable locations along the whole length of active surface melt zone, which extends about 100 km inland from the ice margin (Figure 4-52). Due to the chemical nature of the meltwater, the recharge tends to dilute the groundwaters and to maintain light stable isotope composition.*

Dilute waters interact with glacial sediment and the bedrock and fracture minerals. Dissolution of fracture gypsum contributes high concentrations of Ca^{2+} and SO_4^{2-}. Calcite dissolution occurs as well, but calcite occurs in smaller quantities than gypsum in DH-GAP04. The groundwater in Sect-low is in equilibrium with gypsum and celestite. Due to contamination with drilling water, it cannot yet be confirmed whether or not Sect-mid and Sect-up are in equilibrium with gypsum and celestite as well. Interaction with silicate minerals, which are considerably less soluble than gypsum, contributes to groundwater chemistry to a lesser extent. At the depths representative for a repository, meltwaters are no longer oxygenated or dilute, but still possess an isotopic signature similar to meltwater. Due to a lack of sulphate-reducing bacteria (Section 5.7.7), sulphate would not be converted into H_2S in at low temperatures (e.g. Machel et al. 1995).

In summary, the general concept for the evolution of deep groundwaters at DH-GAP04, as presented here, is reflecting the geological conditions present in the study area, particularly the presence of gypsum as a fracture mineral.

Gypsum is found only in small quantities within the DH-GAP01 cores, resulting in overall lower SO_4 concentrations than those found in DH-GAP04, where gypsum is abundant. This may be attributed to the different relative positions of the boreholes compared to folds with DH-GAP01, occurring on the limb of a fold and DH-GAP04 at the apex. Whether fractures were open or closed in the past (or present) can determine the depositional history of fracture mineralisation and the longevity and dissolution history of highly soluble mineral phases, such as gypsum, today. The openness of the fracture system with time can only be addressed in a relative sense, such that a highly soluble mineral phase (gypsum) presently exists in abundance (> 200 fractures) throughout the DH-GAP04 core, and in a few places in other cores. Studies are on-going to try to understand more about the sulphate mineralogy and the origin and evolution of this system in the area.

The Leverett Spring provides a unique view of natural groundwater discharge in the study area. It is likely a hydrothermal talik and may be related to a structural feature. Isotopic and chemical composition differ from borehole groundwaters and the spring is likely not related to the deeper groundwater flow system represented by the boreholes, providing evidence that pathways through the permafrost may exist where warm and/or pressurised systems form taliks.

5.9.9 Geochemistry of talik waters

The hydrogeological history of DH-GAP01 is likely complex and transient due to the advance and retreat of the ice sheet, supported by previous studies on the complexity of the hydrogeology of taliks (e.g. Bosson et al. 2013). DH-GAP01 has a chemistry that differs from the talik-forming lake above the borehole in terms of the chemical composition and isotopic signatures, as well as microbial communities. However, the δ^2H and $\delta^{18}O$ values from the DH-GAP01 waters show a slight evaporation signature which indicates that DH-GAP01 waters are a mixture of groundwater (likely recharged glacial meltwaters) and Talik lake waters. Recharge of lake waters is also supported by the simlar $\delta^{37}Cl$ isotopic signature of the talik waters and groundwaters. Low Cl^- concentrations suggest a more dilute groundwater end member is mixing with the recharging lake waters.

6 Summary of GAP datasets and key outputs

This concluding chapter summarises the datasets collected during the GAP and the key findings from each of the three subprojects (A, B and C).

6.1 Subproject A (SPA)

The aim of research activities in SPA was to improve the current understanding of ice sheet hydrology and its relationship to subglacial hydrology and groundwater dynamics. To obtain information on the parts of the ice sheet which contribute water for groundwater infiltration, primarily indirect observations from the ice sheet surface of the basal hydrological system were employed. A brief description of the methods employed and the findings from each type of investigation are summarised below.

6.1.1 Remote sensing

Archived remotely sensed data from satellite and aerial platforms (optical and radar sensors) were used to determine fluxes of surface meltwater to the bed of the ice sheet, and the extent to which catchment-wide spatial and temporal variations in ice sheet velocity are linked to these changes in meltwater flux.

Key outputs

The storage and drainage of ~ 200 seasonally occurring *supraglacial lakes* (SGLs) across the GAP study area were quantified. Although the SGLs in the study area occupy a relatively small portion of the catchment (2 %), they store a disproportionate large volume of bulk runoff (13 %) of annual surface meltwater production. They have important implications for the ice dynamics through the release of surface meltwater into the subglacial hydrological system via rapid in situ drainage or through overflow into moulins.

Structural mapping reveals that patterns of foliation on the ice surface are longitudinally extended in areas of faster ice flow corresponding to the location of subglacial troughs. This suggests that the spatial patterns of ice flow can be attributed to the slope of both the ice sheet surface and the underlying bedrock, acting in unison to determine subglacial hydrological pathways.

Spatial and temporal variations in ice velocity are complex. Although they are influenced by the amount of water that is routed from the surface to the bed of the ice sheet and the rate of flow of that water from the surface to the bed, other factors, such as bedrock topography, are of importance and need to be taken into account.

6.1.2 Automatic weather station network

A network of automatic weather stations (AWS) on the ice sheet surface was used to quantify the energy exchange at snow and ice surfaces, and surface energy balance models (SMB) were subsequently used to determine the total surface meltwater production in the area.

Key outputs

The SMB results demonstrate that nearly all melt in the GAP study area takes place during the three summer months (June–August). Interannual variability is large though, both in length of the melt season and the melt intensity. Most of the meltwater drains from the ice sheet surface during the four year monitoring period, implying that only a smaller portion refroze in snow and firn. The portion of water which refreezes increases with increasing elevation.

6.1.3 GPS measurements of ice motion

Measurements of ice motion were made using geodetic-quality GPS receivers deployed across the ice sheet in the GAP study area. The purpose was to explore seasonal and diurnal velocity cycles, SGL drainage events, rainfall events, and the influence of moulins on drainage and on the basal hydrogeology of the ice sheet.

Key outputs

The seasonal velocity cycle of ice motion in the GAP study area is characterised by an initial maximum at melt onset (the so called 'spring event') followed by a gradual decline to an all year minimum in the autumn.

A drainage event of a SGL was successfully captured in 2010 where the GPS stations recorded the opening and closure of the fractures through which the lake was drained, The event lasted 2 hours and accounted for 7.4×10^6 m^3 of rapid meltwater drainage showing that SGLs can rapidly deliver large volumes of water to the ice-bed interface.

Surface velocity measurements from the GPS station high up on the ice sheet, well above the *equilibrium line altitude* (ELA) (location s10/KAN_U), show a year-on-year increase in annual velocity, from 51.78 ± 0.01 m/yr in 2009 to 52.92 ± 0.01 m/yr in 2012, or a net increase of 2.2 %. This may suggest increased penetration of water to the ice-bed interface, which drives faster ice motion at high elevations on the GrIS.

6.1.4 Ground-penetrating radar

Approximately 1500 km of radar profiles were collected using two *ground-based impulse radar* (GPR) surveys. This dataset was used together with other available datasets (IceBridge and Danish Technical University datasets) to generate Digital Elevation Models (DEMs) of ice thickness and bed topography.

Key outputs

As expected, the results show that the ice thickness generally increases towards the ice divide. The maximum ice depth noted in the study area is 1460 m, whereas the mean ice thickness is 830 m. The bed shows a highly variable subglacial topography resembling the landscape in front of the ice sheet. The major subglacial valleys are aligned in a NE-SW or SE-NW direction, likely following the dominant zones of geological weakness. The deepest troughs are found under the Isunnguata Sermia outlet glacier with an elevation of 510 m below the WGS-84 (World Geodetic System 1984) ellipsoid. This corresponds to 544 m b.s.l. At this location there is a vertical distance of of ~ 1000 m between the valley floor and the elevated areas on each side. The highest subglacial peak in the area reaches 1060 m above the ellipsoid (1026 m a.s.l.). The relief of the bed topography decreases towards the ice divide, but is generally variable throughout the area.

6.1.5 Seismics – reflection and passive seismics

Seismic reflection data was collected at four sites on the ice sheet to study the elastic properties of the ice sheet subsurface and to determine the geometry and characteristics of the material at the ice-bed interface in the study area.

Key outputs

Reflection seismic data collected from the four sites (five measurement locations) indicate a widespread occurrence of till with varying material characteristics. Soft till is found in basins to the south (SHBAM) and north (PLOP) of the F-lake field site, whereas at a third site near the lake (F-lake) the results indicate the presence of lodged till. Closer to the ice sheet terminus, analysis of seismic data from site SHR suggests that weak and wet (although not dilating) subglacial sediment is present.

The acquired passive seismic data, combined with SGL water pressure and GPS motion data provide the first direct evidence for the initiation and propagation of both a hydrofracture and the reactivation of a moulin to the bed of the GrIS. A rapid lake drainage event involving ice tectonic deformation, hydrofracturing and consequent drainage of water was characterised. Drainage occurred through a number of step-like hydraulic fractures with the ice deforming as semi-independent tectonic blocks. The displacement of these blocks during rapid drainage triggered the drainage of adjacent SGLs through longitudinal stress coupling, which was coincident with and possibly led to regional subglacial flooding on the order of 7×107 m^3 over a few days. Once meltwater accessed the subglacial environment, it was transferred over 70 km to the ice sheet margin along major subglacial pathways determined by basal relief where it had a discernible impact on ice flow dynamics.

6.2 Subproject B (SPB)

In SPB, ice drilling and direct studies of basal conditions were conducted to improve the understanding of ice sheet hydrology and groundwater formation. These direct observations of the basal hydrological system were then paired with numerical ice sheet modelling. To assess drainage, water flow, basal conditions and water pressures at the interface between the ice and bed, multiple holes were drilled through the ice in three regions on the ice sheet:

1. **Margin** represents ice sheet basal conditions near the margin, where the ice is thinner and the climate is warmer relative to the ice sheet interior. A total of 15 boreholes were drilled in this region, located between 100 m to ~ 3 km from the ice margin, providing information on the near-field boundary conditions for the deep bedrock borehole (DH-GAP04, see Section 6.3.4) drilled near the margin.
2. **Interior** represents ice sheet basal conditions beneath thicker ice (~ 460 m) away from the margin. The seven holes drilled are located between 15 and 30 km away from DH-GAP04, providing information on the far-field boundary conditions for the deep bedrock borehole.
3. **Interior trough** represents deep basal conditions, where water is potentially routed along the bed to the subglacial trough beneath the ice sheet. This region is located 15 km inland from the ice margin and is distinctly different from the nearby interior region in that it overlies a deep bedrock trough, with an increase in ice thickness to ~ 700 m. A total of four boreholes were drilled to the bed in this region.

6.2.1 Summary of testing in SPB

Testing conducted in the ice boreholes drilled in all three case-study regions included:

- **Basal water pressure measurements** to provide a direct measure of hydraulic pressure within the basal hydrogeological system.
- **Borehole impulse tests** to provide information on the state of the hydrological system at the base of the ice sheet and its ability to respond to transient perturbations.
- **Basal water and sediment chemistry** to investigate water flow processes at the bed, as well as chemical conditions at the groundwater/ice interface. In the margin case-study, water samples collected from streams at the terminal outlet of the Isunnguata Sermia outlet glacier were also collected, representing a natural averaging of subglacial conditions.
- **Ice surface velocity measurements** to provide information on temporal changes in sliding velocity. Although known to be poorly constrained, these measurements can provide an indication of changing basal hydrological conditions.
- **Surface meteorology measurements** to provide data which can be directly compared to meltwater generation and the effects of meltwater forcing on basal processes.
- **Ice temperature measurements** provide data for comparison with output from numerical simulations, including simulations used to investigate the distribution and effects of frozen versus melted conditions at the ice sheet bed.

Also as part of SPB, numerical ice sheet simulations of basal temperature and basal water production were conducted for comparison with field observations and to provide boundary conditions for groundwater modelling.

6.2.2 Key outputs from SPB

Basal water pressures

Basal water pressure was observed in boreholes from each of the study regions, with a similar seasonal cycle defined by marked differences between summer and winter behaviour. Relatively high water pressure persisted during the winter months, with pressure changing by no more than a few percent of overburden ice pressure over time periods lasting weeks to months. In contrast, summer variations in bed water pressure were rapid and substantial. Pressures changed over time periods as short as hours, and in some cases changed by > 50 % of ice overburden pressure on a repeated daily cycle. During the fall and spring transition periods, the pressure underwent unsystematic pressure variations on time scales of hours to days. The distinct differences between winter and summer behaviour were observed in all study regions despite other important differences between the locations.

The data collected for the GrIS demonstrate that the basal drainage system of the investigated part of the ice sheet maintained a high mean pressure, averaging near ice overburden water pressure. Pressures falling below 80 % of overburden ice pressure (on diurnal cycle or during spring and fall seasons) were only observed within a few km of the ice sheet margin. The low pressures in this area were not necessarily uniform across the bed, but were limited to well-connected and highly transmissive areas of the bed, such as areas influenced by a drainage conduit. Areas between these transmissive parts remain at ice overburden pressure, even less than 1 km from the margin.

The highest pressures measured were ~ 110 % of overburden ice pressure. This high pressure corresponds to a water column equal to the thickness of the ice. It is concluded that the maximum possible pressure in the study regions is 110 % of overburden, though this pressure limit is rare in both time and space. In terms of overburden ice pressure, the lowest pressure measured was 25 % of overburden. This was observed in more than one borehole, but was limited to boreholes located near the ice margin. In those sites located within a few km of the margin, relatively low water pressures (in terms of percentage of overburden ice pressure) were not persistent when averaged over the annual seasonal cycle. Low pressures (i.e. < 30 % below overburden) were common on a diurnal cycle during mid-summer or during brief periods of erratic variations in the fall or spring seasonal transitions. Overburden pressure was most common over time; most of the year, near overburden pressure was present at all study sites.

Borehole pressure observations indicate the existence of meltwater flowing in a basal drainage system at the ice/bed interface from the margin to at least 30 km toward the interior of the ice sheet. Flowing water is revealed by basal water pressure variations, which imply the presence of a basal drainage system capable of transmitting relatively large volumes of water. Several other lines of evidence support the inference that a high capacity basal drainage system is present at the study sites: 1) drill breakthrough tests show the drainage system can transport > 3000 litres in less than 3 minutes when the drill hole suddenly connects with the bed; 2) pumping tests show the existing basal drainage system has a high capacity for water transmission, as it can accommodate the addition of 300 L/min; 3) diurnal water pressure variations imply fast response to surface melt in a highly connected hydrologic system; and 4) concomitant diurnal velocity variations imply a large fraction of the bed is connected.

Borehole impulse tests

Boreholes < 30 m apart commonly exhibited opposing type responses during slug testing. Large magnitude pressure pulses associated with drilling breakthrough tests exhibited the capacity to influence water levels in some adjacent boreholes, but not in others. Long duration pumping tests in boreholes showed heterogeneous connectivity to adjacent boreholes. This variability was generally consistent across all drilling sites. The spatial variability among all three types of impulse tests conducted suggests that, at the local scale, water may flow largely through discrete pathways in the basal hydrologic network as opposed to more diffusive, laminar flow through a homogenous till layer.

Near the ice sheet margin, drilling breakthrough tests and borehole video confirm the presence of englacial features that may act as water storage reservoirs or active transport pathways. While inland boreholes provide a limited sample size, and surface-to-bed water routing moulins are prevalent throughout the ablation zone, no evidence for an extensive englacial fracture network was evident in drill breakthrough tests away from the margin.

Basal water and sediment chemistry

The chemistry of boreholes and outlet waters is consistent with an environment where dissolved CO_2 facilitates the weathering of silicate minerals. A silicate source for most of the dissolved constituents is suggested by the relatively high abundance of Si, K and Na in the water. Bicarbonate is the dominate anion and is present in excess of Ca sourced from carbonate, implying CO_2 as the primary acid. The measurable depletion of base cations, and the enrichment of silica in the sediment compared to rock, suggests that the bedrock is losing mass to chemical weathering reactions. For such mass loss to occur in a subglacial environment, the residence times of the subglacial sediment are likely to be relatively long.

Concentrations of dissolved constituents were observed to vary considerably between boreholes drilled tens of metres apart. This small scale variation is of a large enough magnitude that it dampens any larger scale or regional variation in dissolved load. This suggests regions where water is able to cycle very quickly through the basal hydraulic system, as well as regions of far greater water residence times existing in close proximity to each other.

Ice surface velocity

All GPS stations revealed surface velocities with strong seasonal variability, as evidenced by higher daily average velocities in early summer than in late summer or autumn. Diurnal velocity variations were also observed at the two ice sheet interior stations. The diurnal velocity variations were present only during the middle of summer.

Conclusions relevant to the basal hydrological system that can be inferred from the ice surface measurements include: 1) surface meltwater reaches the bed of the ice sheet over widespread areas and without substantial delay; 2) this meltwater flux causes the basal drainage system to undergo evolutionary changes on time scales that vary from diurnal to seasonal; 3) the resulting changes in drainage system geometry lead to changes in ice/bed coupling and sliding speed; and 4) complicated feedbacks between sliding speed, and drainage system geometry and pressure, cause additional change to the drainage system. Each of these results is inferred from surface velocity and are not a direct measurement of the drainage system. Further, the general conclusion that the basal boundary to groundwater flow cannot be considered to be static is robust, as there is no other way to explain the velocity variations.

Surface meteorology

Atmospheric conditions and surface melt at all of the sites show, as expected, strong seasonal influence. Diurnal swings in temperature and solar radiation are also present, which results in diurnal swings in the rate of ice melt at each of the study regions.

Ice temperatures

The marginal ice, for several kilometres inland, is approximately isothermal and at the pressure melting point temperature. Farther inland, as far as the deepest holes, the basal ice remains at the pressure melting point and water is present at the bed. The thickness of the warm ice (i.e. at the pressure melting point) at the base of the ice sheet decreases up-glacier, going from the full depth near the margin to ~ 140 m thickness (or 30 % of ice depth) at 15 km up-glacier. At the highest site, only 30–40 m of basal ice is warm, which is only a few percent of the ice column. Assuming the thickness of warm basal ice continues to decrease up-glacier, the ice sheet becomes cold-based and free water will no longer be present at the bed. The existence of a cold based area under the central parts of the ice sheet is also consistent with results from GAP radar soundings and numerical modelling.

Above the basal layer of warm ice, the ice continuously becomes colder up-glacier as the ice thickness increases. At the deepest, highest site, the bulk ice temperature drops to −13.8 °C and is expected to get somewhat colder farther up-glacier. Warming surface temperatures at lower elevations, in combination with a warm basal ice, often create the observed cold core at depth, originating from the horizontal advection of cold ice from up-glacier. These temperature profiles are useful for input, validation and comparison with numerical models.

The full depth warm ice at the margin facilitates vertical water motion that drains meltwater from the surface to the bed because less energy is required to melt a pathway when ice is already at the melting point. Although the melt rate near the margin is high, and surface streams abound, the streams tend to be short and small and often disappear into moulins or crevasses before reaching the margin. Farther up-glacier, the cold core of the ice presents a thermal barrier to meltwater migration from the surface to the bed. Based on the presence of moulins, and the drainage of surface lakes, the region of basal water extends up to 50 km up-glacier from the highest drill site; thus, water in this region is freely available at the ice-bedrock interface.

Numerical simulations

The spatial distribution of frozen/melted basal conditions of ice sheets has been studied for a long time, and with considerable uncertainties. Prior to the GAP, direct measurement of thermal bed conditions along the ice marginal areas were essentially non-existent, and modelling efforts were poorly constrained by observational data. However, the key factors dictating basal thermal conditions have long been recognised: 1) atmospheric temperature, 2) ice thickness and 3) geothermal heat flux, and 4) heat produced by the ice flow (from internal deformation and basal sliding).

The findings of this study exemplify that these factors, alone, are insufficient for describing basal melt conditions for the portion of the GrIS examined by GAP. Other factors, also related to ice flow dynamics, are here demonstrated to be important in dictating basal thermal conditions. In particular, latent heat transfer is a key process for heat transfer that is not well understood or represented in current ice sheet models.

A significant (nearly 2 degrees centigrade) mismatch between model and observed temperature profiles indicates that a stronger role is played by the refreezing of surface meltwater than previously assumed for ice sheets. There are currently no ice sheet models that properly represent this process. Future studies should focus on correctly parameterising the bulk hydraulic conductivity of ice, as well as the rate of heating that occurs given the difference in temperatures between ice and meltwater.

The quantity of basal meltwater being generated annually can be highly variable. The mm/yr of basal melt is dwarfed by the m/year of surface melt that penetrates to the bed over certain parts of the ice sheet. Consequently, for general conceptualisation of summer-time behaviour at the GAP study area, detailed ice energy budgets are unnecessary. However, in winter, it is likely that the basal melt rates are dominated by the ice sheet energy balance, and in this case, numerical simulations become important.

6.3 Subproject C (SPC)

Field investigations conducted by SPC in the proglacial part of GAP study area focused on groundwater flow dynamics, including evidence on the depth of permafrost, redox conditions and the infiltration of glacial meltwater into the bedrock. Key findings from the geological, geophysical and surface water investigations are presented first, followed by those from the bedrock borehole investigations.

6.3.1 Bedrock geology

Detailed geological mapping focused on a transect from Kangerlussuaq to the ice margin and a smaller subarea surrounding the area selected for drilling of three cored bedrock boreholes. As part of the bedrock borehole investigations (see Section 6.3.4 below), detailed fracture characterisation, lithological mapping, and mapping of foliations and deformation zones was conducted on drill cores.

Key outputs

The bedrock geology in the GAP study area is complex and several episodes of deformation have reworked the rocks. The lineament model and the fieldwork confirmed that six different types of lineaments are found within the GAP study area. The lineaments can be expanded to a larger area that extends significant distances and covers areas currently beneath the ice sheet. The lineaments represent different structural features and all except one type represent typical brittle structures.

There is no information available about the hydraulic properties of the regional deformation zones. Based on the fracture observations at surface, and the multi-phase deformation history of the region, it is plausible that brittle reactivation of the zones has occurred on several occasions, providing pathways for water flow. No signs of postglacial faulting have been observed, although such faulting could be expected in an area of oscillating ice margin. The depth and length extension of the deformation zones define them as regional hydrogeological features, which have been active also below the thick confining permafrost. The fact that they extend beneath the ice sheet, forming deep subglacial and possibly sediment filled valleys (see Section 3.5), increases their importance as potential zones for meltwater recharge and flow.

6.3.2 Geophysics

A wide-band frequency-domain electromagnetic sounding (SAMPO) system was used to measure a total of 260 sounding points on the ice and in front of the ice sheet, in order to test the applicability of this method to detect permafrost both in the proglacial area and under the ice sheet.

Key outputs

The SAMPO profiles from the GAP study area provided a consistent cryogenic structure for the soil and crystalline bedrock in front of the ice sheet, which included: 1) a low resistivity active layer, 2) highly resistive permafrost, and 3) lower resistivity bedrock beneath including a weak, deep (550–750 m deep) conductor. In the investigated ice-covered area (i.e. the area directly east of borehole DH-GAP04), four layers were preliminarily distinguished: 1) glacier ice, 2) an unfrozen layer, 3) permafrost, and 4) a low-resistivity feature at depth, i.e. the same deep conductor as observed in the proglacial areas. The weak conductor at depth, seen in almost all of the GAP profiles at 550–750 m depth, could possibly indicate the base of the permafrost. However, based on the temperature profiling in the GAP boreholes, it is known that the permafrost in the GAP study area extends to depths of 350–400 m. The most likely explanation of the weak, deep conductor is that it coincides with the depth where the salinity of groundwater exceeds a certain threshold level and becomes observable.

In the area where the SAMPO survey was carried out, no supporting information or data exist to help in elucidating the presence or absence of subglacial permafrost in the ice-covered area.

6.3.3 Surface water characterisation

Waters from springs, rivers, glacial meltwaters from several locations, ice and over 40 lakes were sampled for analyses of the main chemical and isotopic parameters. This information was used to define end-member water compositions, which were then applied to interpret groundwater characteristics.

Key outputs

Processes involved in the sulphur system in lakes are not related to high sulphate groundwaters. The δ^{34}S isotopic signature of sulphate in lakes suggests that lake sulphate may be variably impacted by oxidation of sulphides, marine sulphate and bacterial sulphate reduction.

Meltwaters, despite covering a wide range of values, have highly depleted δ^{18}O– δ^{2}H signatures relative to modern meteoric water. As meltwaters are very dilute, and thus easily modified by interaction with fracture minerals and bedrock once recharged, it is difficult to use chemical composition to trace meltwater intrusion. The isotopic composition of the water provides a good tracer for meltwater intrusion into the subsurface because it is unlikely to be significantly altered in the subsurface, except by mixing with groundwaters.

6.3.4 Bedrock borehole investigations

Three deep and inclined boreholes were drilled into the bedrock and through the permafrost in the vicinity of the ice sheet margin. Two of the boreholes were hydraulically tested and instrumented to allow hydrogeologic and hydrogeochemical monitoring. Testing included:

1. **Drill core investigations**
   - Drill core logging of lithologies, fractures and fracture infillings, orientation of planar structural features.
   - Petrophysical measurements to provide an overview of the variations in rock physical properties, such as porosity, density and thermal conductivity.
   - Fracture infilling investigations, including mineralogical and stable isotope studies on calcite, sulphur and sulphate phases, and observations of redox conditions.
2. **Downhole measurements**
   - The Posiva Flow Log method (PFL) was used to conduct hydraulic testing in the borehole DH-GAP04 to find the best location for the downhole instrument system, and also for hydrogeological characterisation of the tested bedrock volume.
   - Slug tests were used in DH-GAP01 to measure transmissivity of fractures and hydraulic conductivity of the rock mass.
   - Temperature monitoring. The boreholes DH-GAP01, DH-GAP03 and DH-GAP04 were equipped with optical fibres that allow accurate, high-resolution temperature profiling utilizing the Distributed Temperature Sensing (DTS) technique.
   - Monitoring of water pressure and electrical conductivity in DH-GAP01 and DH-GAP04.
3. **Groundwater and porewater analyses**
   - Groundwater samples from DH-GAP01 and DH-GAP04 were analysed for major ions and stable isotopes. Matrix porewater was studied using crush and leach of core samples and by porewater extraction from preserved core samples.
   - Microbial investigations were conducted in DH-GAP01 with the aim of characterising and classifying microbial DNA signatures in groundwater and to provide information on the anaerobic or aerobic nature of the groundwater.

Key outputs considering results from multiple bedrock boreholes

Bedrock geology: The rock observed in the boreholes can be divided into four main types: felsic gneiss, mafic gneiss, intermediate gneiss and granitic pegmatite. The relative amount of mafic/felsic minerals have been used as a guideline when defining the rock types. DH-GAP01 is situated in foliated felsic gneiss which has both mafic and intermediate layers. In DH-GAP03 alternating layers of felsic and mafic gneisses dominate. DH-GAP04 is dominated by mafic garnet gneiss in the upper 300 m, with more foliated intermediate to felsic gneiss below.

One of the fracture sets in all drill cores is parallel to the foliation. Because the three boreholes intersect different parts of large folds, the geometry of fracturing is different. A steeply dipping fracture set is dominant in DH-GAP01 and DH-GAP03, whereas sub-horizontal fracturing is characteristic for DH-GAP04. An interesting feature in DH-GAP04 is that the fracture orientations change with depth, whereas the foliation remains constant along the length of the borehole. Vertical fractures are common in the upper 300 m of the bedrock. Below 300 m, vertical fractures become rare and sub-horizontal fractures dominate. The fracture network is well developed, at least down to the observation depth of 600 m. The presence of permafrost, fracture infillings and the geometry of the fracturing determine which part of the fracture network is currently available for water flow.

Petrophysical studies: The felsic and mafic rock types from the GAP cores have different densities, as expected. In general, the felsic and mafic rocks have similar matrix porosities. In DH-GAP01 and DH-GAP03 matrix porosities range from 0.2 to 0.6 %, averaging around 0.45 %, whereas the range for the matrix porosities in DH-GAP04 is 0.2 to 1.32 %. This broader range is related to a group of felsic rocks, with matrix porosities of 0.9 to 1.32 %, occurring between 500–650 m borehole lengths in DH-GAP04. The reasons for these higher porosities are currently unknown. The range of porosities for intact rock is relatively wide (0.2–1.32 %).

The average radiogenic heat production for felsic rocks in DH-GAP04 is 0.36 $\mu W/m^3$, whereas the average for the mafic rocks is 0.22 $\mu W/m^3$. The thermal conductivity does not appear to correlate with rock type, and the calculated average of 2.50 W/mK for all three drill cores is considered to be representative for all rock types in the research area. The results suggest that the geology in the area has only a minor impact on permafrost thickness due to its relatively uniform thermal properties.

Heat Flux Density (or geothermal heat flux): Model calculations, DTS temperature profiling and petrophysical data from DH-GAP03 and DH-GAP04 were used to obtain the first estimates of Heat Flux Density (HFD) for the site. The HFD value for DH-GAP03 is 34.8 ± 1.9 mW/m^2, whereas the HFD from the deeper DH-GAP04 borehole is 27.2 ± 1.8 mW/m^2. The HFD difference between the boreholes could be related to the different climatic history of the borehole sites, since the ground surface at each site has been ice-free for different periods of time since deglaciation (DH-GAP03 has been ice-free for a longer time than DH-GAP04). The calculated HFD values are considerably lower than previous HFD estimates for this part of Greenland. The new HFD values are not corrected for climatic effects, i.e. long term palaeoclimatic variations have not been considered. If a climate correction were to be made, the values would be somewhat higher, although still not as high as previous estimates. Furthermore, the difference between the new and old values is well within the large expected variability of HFD values in this type of geologic setting. Sensitivity analysis suggests that the difference between the new and old HFD values is of significant importance in ice sheet modelling for this portion of the GrIS.

Fracture infilling investigations: The majority of fracture mineralogy in the GAP drill cores is uniform. A typical fracture represented in these cores has a thin layer of chlorite coating, with spots of calcite and possibly traces of clays on top. Fluid inclusion studies carried out for fracture infilling calcites reveal a range of trapping temperatures between 100 and 200 °C. In DH-GAP04, gypsum is abundant and becomes the dominant fracture infilling below 300 metres. This coincides with the change in rock type from mafic to intermediate or felsic. Gypsum forms practically mono-mineral infillings in fractures of variable orientation, although, occasionally, some calcite may be associated with the infill. Gypsum is also found as microfracture infilling within the rock matrix. The mineralogical textures in the gypsum infillings suggest high temperature (hydrothermal/metamorphic) formation from a homogenous fluid. Mineral formation in the fracture network, instead of a specific fracture generation and the occurrence of gypsum in rock matrix, is evidence of an intensive hydrothermal/metamorphic event.

All well-defined oxidation indications in the fracture infilling data are shallow (0–50 m) and from within the permafrost section and, thus, they cannot represent the current conditions (ice location). It is possible that groundwater circulation has taken place in some of these fractures during the Holocene as indicated by U leaching (inferred from U contents in the fracture minerals as a function of depth, and from uranium-series data). The deepest goethite samples (~ 260 m depth) have experienced shearing and may be of relatively old age. *Uranium-series disequilibrium* (USD) provides some indications of redox changes also in the deeper system, but they do not correspond to oxidation of Fe(II) thus suggesting less oxidative nature of the redox transient.

Permafrost: The base of the permafrost (0 °C isotherm) was measured at a vertical depth of 335 ± 14 m in DH-GAP03 (based on 2010 measurements) and at 405 ± 10 m in DH-GAP04 (based on 2013 measurements). To account for differences in the ground surface topography between the two drill sites, the elevation of a point on the ice margin directly north of DH-GAP04 was determined and used as a reference point to calculate permafrost thickness at each location. Using this approach, permafrost thickness is ~ 315 m at DH-GAP03 and ~ 350 m at DH-GAP04. The small, observed difference in permafrost thickness between the two borehole sites may be related to differences in geology, differences in local surface conditions over time, slight differences in instrument calibration procedures, or a combination of these factors.

Key outputs for DH-GAP01

This borehole was drilled to investigate the hydrogeological, geochemical and thermal conditions under a proglacial lake, to assess if areas of unfrozen ground within the permafrost (taliks) may act as potential pathways for exchange of deep groundwater and surface water.

Pressure response test: Two pressure response tests associated with water withdrawal from borehole DH-GAP01 were performed. Pressure recovery following water removal was evaluated, allowing calculation of transmissivity and hydraulic conductivity using methods for slug tests. The tests had short durations and involved small water volumes, implying that the evaluated parameters relate to the rock immediately surrounding the borehole. The results of the evaluation of the two pressure response tests suggest a total transmissivity for the tested section (71 m in length) of the DH-GAP01 borehole of ~ 10^{-6} m^2/s.

Temperature profiling: As soon as DH-GAP01 was advanceed beneath the lake, the bedrock temperature increased to values above 0 °C. The temperature was continuously above 0 °C from ~ 20 m vertical depth down to the bottom of the borehole. A separate temperature sensor at a vertical depth of 140 m maintained a temperature of 1.3 ± 0.2 °C from mid-July, 2009. These observations show the absence of permafrost and the presence of a talik under the lake. Furthermore, these results, combined with observations of the lake water chemistry and groundwater sampled within boreholes DH-GAP-01 and DH-GAP-04, indicate that the talik constitutes a through talik, i.e. it stretches through the full thickness of the permafrost, allowing for exchange between surface water and deep groundwater. This evidence for the existence of a through talik in a proglacial area characterised by continuous permafrost, in close proximity to a continental-scale ice sheet, is a key finding.

Pressure monitoring: The lake level varied from a minimum of –5.6 m (during winter 2011–2012) to a maximum of –5.3 m (in June, 2013) relative to the TOC of DH-GAP01 during the monitoring period. During the same time period, the water level in the borehole varied from a minimum of –8.5 m (in July, 2011) to a maximum of –6.6 m (in June, 2010) relative to TOC of DH-GAP01. Thus, the hydraulic head in the monitoring section of the borehole (h = ~ 367 m) is lower than the hydraulic head in the lake (h = ~ 369 m) at all times. This indicates recharge from the Talik lake to the bedrock where the sampling section in DH-GAP01 is positioned. The lake head and borehole head showed some similarity in terms of timing of increase and decrease of head values, although the magnitudes of variation were different, with larger variations in the borehole head. The similar timing is likely due to the fact that both lake and borehole head vary according to seasonal changes.

Groundwater analyses: Groundwaters in DH-GAP01 may represent mixing between Talik lake waters and a groundwater end member with an isotopic composition similar to meltwaters and similar to what is observed in DH-GAP04 (see Section 6.3.5 below). However, this has not been verified by a second geochemical tracer. Recharge from the lake to groundwater is supported by the pressure data.

Microbial investigations: Analysis of the total numbers of microorganisms did not show a significant difference between DH-GAP01 groundwater and the Talik lake water. However, according to DNA signatures, the microorganisms in DH-GAP01 groundwater were mostly anaerobic or facultative anaerobic microorganisms. In contrast, the Talik lake water contained aerobic microorganisms, including species of Cyanobacteria that typically require light for growth. The number of different DNA signatures found in the Talik lake water was higher than observed in DH-GAP01 groundwater. None of the DNA signatures found in the Talik lake were found in the DH-GAP01 groundwater. These observations imply that the microbial communities differ between the borehole groundwater and the lake water. Most DNA signatures indicated anaerobic conditions in the DH-GAP01 borehole and aerobic conditions in the lake.

Key outputs for DH-GAP03

This borehole was drilled in order to define the depth of permafrost close to the ice margin, prior to drilling the deep bedrock borehole that was to be instrumented (DH-GAP04). Due to technical problems during installation, only a fibre optical DTS cable could be successfully installed in this borehole.

Temperature profiling was completed to estimate the maximum permafrost depth in the region close to the ice margin. Measurements completed in 2010 indicate that at this location, the base of the permafrost (i.e. the 0-degree isotherm) is located at a vertical depth of 335 ± 14 m. However, it is probable that these temperature measurements still remained affected by the drilling conducted in 2009.

Key outputs for DH-GAP04

This inclined, deep borehole was drilled to investigate the geological, hydrogeological and geochemical conditions in the bedrock directly at the ice sheet margin.

Posiva Flow Log: The PFL testing identified nine flowing features. The measured specific capacities (flow rate in m^3/s per metre of head change) in these flowing features indicate a range of transmissivities from 1.6×10^{-9} to 3.3×10^{-6} m^2/s. In addition to the PFL testing, further hydraulic evaluations of pressure data collected during water sampling campaigns in September, 2011 and September 2013 were conducted.

Distributed temperature profiling: Bedrock temperatures in DH-GAP04 have been measured continuously since July 2011, with different temporal measurement intervals depending on the purpose of the monitoring. The borehole was initially cooling following the hot water drilling campaign. More stable temperature profiles were observed after December 2012, when the effect of the drilling could be considered small. However, due to the heat added during drilling, and during the subsequent groundwater sampling campaigns, the borehole is still ~ 0.2 °C from being completely thermally recovered. The base of the permafrost is located at a vertical depth of 405 ± 10 m.

Pressure monitoring: Time series measurements show that the water level is ~ 40 m below the TOC in Sect-low (h = ~ 486 m) and 5 to 14 m below TOC (h = ~ 521 m to 512 m) in Sect-up and Sect-mid. Seasonal head variation, in particular the heads at 500 m depth in Sect-up and Sect-mid, clearly show that these sections are affected by the ice sheet and regional ice sheet runoff, and provide, for the first time, evidence of a dynamic coupling between the bedrock and ice sheet. In contrast, the time series data show a consistently lower head in Sect-low and also reveal a significantly weaker correlation to the seasonal changes in the regional runoff. This difference is attributed to the almost complete lack of steeply dipping fractures intersecting Sect-low, and by the generally lower specific capacity values at depth in DH-GAP04.

6.3.5 Groundwater and porewater characterisation

Groundwaters were sampled from boreholes DH-GAP01 and DH-GAP04 and from Leverett Spring, and were analysed for major ions and stable isotopes, in particular, δ18O and δ2H. The results suggest that groundwaters likely have some component of meltwater based on similarities in isotopic composition between meltwaters and borehole waters. If the waters in DH-GAP04 are recharging meltwaters, they have evolved along the flow path from very dilute (EC < 5 µS/cm) to much higher salinities (EC > 900 µS/cm), and are dominated by SO_4 and Ca from gypsum dissolution. Sulphate-reducing bacteria were not observed in DH-GAP01 and are presumed to be absent also in DH-GAP04 due to the similarity in $\delta^{34}S$ values between the two boreholes.

The Leverett Spring provides a unique view of natural groundwater discharge in the study area, since it is likely a hydrothermal talik that may be related to a structural feature. Isotopic and chemical compositions differ from borehole groundwaters; thus, the spring is not likely related to the deeper groundwater flow system represented by the boreholes.

Porewater analyses: Crush and leach studies indicate that water-rock interaction is the main source of salinity in groundwaters from DH-GAP01 and DH-GAP04. The chemistry of porewaters extracted in the out-diffusion experiment from the intermediate gneiss samples is similar to the groundwaters, in that they are of Ca-SO_4 type with moderate concentrations of Na+ (up to 38 % of cations on a molar equivalent basis).

Acknowledgement

The success of the Greenland Analogue Project is a result of huge amounts of work, research and dedication. Still, this would not have been possible without the support of many individuals. Therefore we would like to extend our sincere gratitude to all of you - the research leading to the results presented in this report would not have been possible to accomplish without your support.

First of all we are thankful to: GEUS , Basse Vaengtoft (Kangerlussuaq International Science Support), Per Mikkelsen (JMM Gruppen), Jørgen Mårtensen, the DMI-office in Kangerlussuaq, Kathy Young and Robin Abbot(Polarfield), Ed, Sparky and the greater CH2MHill-team at KISS, for their logistical support and for providing essential guidance concerning project implementation.

We are also grateful to: the GRASP-team, Jennifer McKelvie and Andrew Parmenter (NWMO), Ulf Brising (SWECO), Fredrik Hartz, Thomas Ingeman-Nielsen (DTU), Joakim Stoor, Jan Sundberg, Kent Hansson, John Olausson, Mikael Ericsson (Geosigma, Uppsala, Sweden), Jani Mantila, Harri Rautakoski, Henri Vuollet, Pekka Ämmälä, Vesa Matti Ämmälä, Juha Kärkkäinen, Juha Hirvi and Rauli Kuokkanen, Matti Rautakoski (Oy KATI Ab Kalajoki, Finland), Ismo Aaltonen, Tiina Lamminmäki, Jyrki Liimatainen and Antti Mustonen (Posiva Oy), Tomi Laakso (TVO), Ilmo Kukkonen (GTK/Helsinki University), Lars Andersson, Mats Lundgren and Cecilia Berg (SKB), Brandon Stackhouse (Princeton University), Dalton Hardisty, Bruce Douglas (Indiana University), Sara Jägevall, Karsten Pedersen (Micans), Barry Freifeld (Lawrence Berkeley National Laboratory), Sam Johansson, José Acuna, Sten Berglund (Hydroresearch), Julie Klint, Jari Lehtinen, Bernd Kulessa (Swansea University), Marion Bougamont and Poul Christoffersen (Cambridge University) and the Posiva Flow Log-team (Petri Heikkinen, Pöyry Oy and Juha Taskinen, Posiva Oy), for provision of expertise, and technical and logistical support during the project period. Your superior knowledge and experience has been essential for the project.

We would also like to acknowledge the guidance provided throughout the project by the GAP Technical Coordination Committee: Jens-Ove Näslund, Ignasi Puigdomenech and Jan-Olof Selroos (SKB), Peter Jansson (Stockholm University), Marjut Vähänen, Petteri Pitkänen and Petri Korkeakoski (Posiva), Nuria Marcos (Saanio & Riekkola Oy), and Sarah Hirschorn, Eric Sykes, Andre Vorauer and Monique Hobbs (NWMO).

References

SKB's (Svensk Kärnbränslehantering AB) publications can be found at www.skb.se/publications.

Aaltonen I, Douglas B, Claesson Liljendahl L, Frape S, Henkemans E, Hobbs M, Klint K E, Lehtinen A, Lintinen P, Ruskeeniemi T, 2010. The Greenland Analogue Project, Sub-Project C, 2008, Field and data report. Posiva Working Report 2010-62, Posiva Oy, Finland.

Abdalati W, Steffen K, 2001. Greenland ice sheet melt extent: 1979–1999. Journal of Geophysical Research: Atmospheres, 106, 33983–33988.

Abdalati W, Krabill W, Frederick E, Manizade S, Martin C, Sonntag J, Swift R, Thomas R, Wright W, Yungel J, 2001. Outlet glacier and margin elevation changes: near-coastal thinning of the Greenland ice sheet. Journal of Geophysical Research: Atmospheres 106, 33729–33741.

Aebly F A, Fritz, S C, 2009. Palaeohydrology of Kangerlussuaq (Søndre Strømfjord), West Greenland during the last ~ 8000 years. Holocene 19, 91–104.

Al-Aasm I S, Taylor B E, South S, 1990. Stable isotope analysis of multiple carbonate samples using selective acid extraction. Chemical Geology 80, 119–125.

Alley R B, Koci B R, 1990. Recent warming in central Greenland. Annals of Glaciology 14, 6–8.

Alley R B, Dupont T K, Parizek B R, Anandakrishnan S, 2005. Access of surface meltwater to beds of sub-freezing glaciers: preliminary insights. Annals of Glaciology 40, 8–14.

Anderson N, Leng M, 2004. Increased aridity during the early Holocene in West Greenland inferred from stable isotopes in laminated-lake sediments. Quaternary Science Reviews 23, 841–849.

Anderson N J, Harriman R, Ryves D B, Patrick S T, 2001. Dominant factors controlling variability in the ionic composition of west greenland lakes. Arctic, Antarctic, and Alpine Research 33, 418–425.

Anderson S P, 2005. Glaciers show direct linkage between erosion rate and chemical weathering fluxes. Geomorphology 67, 147–157.

Anderson S P, Drever J I, Humphrey N F, 1997. Chemical weathering in glacial environments. Geology 25, 399–402.

Aschwanden A, Bueler E, Khroulev C, Blatter H, 2012. An enthalpy formulation for glaciers and ice sheets. Journal of Glaciology 58, 441–457.

Azzam S, Suksi J, Ammann M, 2009. DECSERVIS-2: a tool for natural decay series mass flow simulation. Applied Radiation and Isotopes 67, 1992–1997.

Baiocchi C, Brezzi F, Franca L P, 1993. Virtual bubbles and Galerkin-least-squares type methods (Ga.L S.). Computer Methods in Applied Mechanics and Engineering 105, 125–141.

Balay S, Brown J, Buschelman K, Eijkhout V, Gropp W, Kaushik D, Knepley M, Curfman McInnes L, Smith B, Zhang H, 2013. PETSc Users manual, Revision 3.3. Oak Ridge, TN: U.S. Department of Energy.

Bamber J L, Layberry R L, Gogineni S P, 2001. A new ice thickness and bed dataset for the Greenland ice sheet: 1. Measurement, data reduction, and errors. Journal of Geophysical Research: Atmospheres 106, 33773–33780.

Bamber J L, Griggs J A, Hurkmans R T W L, Dowdeswell J A, Gogineni S P, Howat I, Mouginot J, Paden J, Palmer S, Rignot E, Steinhage D, 2013a. A new bed elevation dataset for Greenland. Cryosphere 7, 499–510.

Bamber J L, Siegert M J, Griggs J A, Marshall S J, Spada G, 2013b. Paleofluvial mega-canyon beneath the central Greenland ice sheet. Science 341, 997–999.

Barker J A, Black J H, 1983. Slug tests in fissured aquifers. Water Resources Research 19, 1558–1564.

Barker J F, Fritz P, 1981. The occurrence and origin of methane in some groundwater flow systems. Canadian Journal of Earth Science 18, 1802–1816.

Barns S M, Cain E C, Sommerville L, Kuske C R, 2007. *Acidobacteria* phylum sequences in uranium-contaminated subsurface sediments greatly expand the known diversity within the phylum. Applied and Environmental Microbiology 73, 3113–3116.

Bartholomaus T C, Anderson R S, Anderson S P, 2008. Response of glacier basal motion to transient water storage. Nature Geoscience 1, 33–37.

Bartholomew I, Nienow P, Mair D, Hubbard A, King M A, Sole A, 2010. Seasonal evolution of subglacial drainage and acceleration in a Greenland outlet glacier. Nature Geoscience 3, 408–411.

Bartholomew I, Nienow P, Sole A, Mair D, Cowton T, King M, Palmer S, 2011. Seasonal variations in Greenland Ice Sheet motion: inland extent and behaviour at higher elevations. Earth and Planetary Science Letters 307, 271–278.

Bartholomew I, Nienow P, Sole A, Mair D, Cowton T, King M A, 2012. Short-term variability in Greenland Ice Sheet motion forced by time-varying meltwater drainage: implications for the relationship between subglacial drainage system behavior and ice velocity. Journal of Geophysical Research 117, F03002. doi:10.1029/2011JF002220

Bartoli G, Sarnthein M, Weinelt M, Erlenkeuser H, Garbe-Schönberg D, Lea D W, 2005. Final closure of Panama and the onset of northern hemisphere glaciation. Earth and Planetary Science Letters 237, 33–44.

Bassis J N, Fricker H A, Coleman R, Bock Y, Behrens J, Darnell D, Okal M, Minster J-B, 2007. Seismicity and deformation associated with ice-shelf rift propagation. Journal of Glaciology 53, 523–536.

Bennike O, Björck S, 2002. Chronology of the last recession of the Greenland Ice Sheet. Journal of Quaternary Science 17, 211–219.

Bense V F, Ferguson G, Kooi H, 2009. Evolution of shallow groundwater flow systems in areas of degrading permafrost. Geophysical Research Letters 36. doi:10.1029/2009GL039225

Bentley C R, Koci B R, 2007. Drilling to the beds of the Greenland and Antarctic ice sheets: a review. Annals of Glaciology 47, 1–9.

Bentley C R, Lord N, Liu C, 1998. Radar reflections reveal a wet bed beneath stagnant Ice Stream C and a frozen bed beneath ridge BC, West Antarctica. Journal of Glaciology 44, 149–156.

Berman E S F, Levin N E, Landais A, Li S, Owana T, 2013. Measurement of $\delta^{18}O$, $\delta^{17}O$ and ^{17}O-excess in water by off-axis integrated cavity output spectroscopy and isotope ratio mass spectrometry. Analytical Chemistry 85, 10392–10398.

Berner R A, 1981. A new geochemical classification of sedimentary environments. Journal of Sedimentary Petrology 51, 359–365.

Bindschadler R A, Nowicki S, Abe-Ouchi A, Aschwanden A, Choi H, Fastook J, Granzow G, Greve R, Guowski G, Herzfeld U, Jackson C, Johnson J, Khroulev C, Levermann A, Lipscomb W H, Martin M A, Morlighem M, Parizek B R, Pollard D, Price S F, Ren D, Saito F, Saito T, Seddik H, Seroussi H, Takahashi K, Walker R, Wang W L, 2013. Ice-sheet model sensitivities to environmental forcing and their use in projecting future sea level (the SeaRISE project). Journal of Glaciology 59, 195–224.

Blomqvist R, Ruskeeniemi T, Kaija J, Paananen M, Ahonen L, Smellie J, Grundfelt B, Bruno J, Pérez del Villar L, Rasilainen K, Pitkänen P, Casanova J, Suksi J, 2000. The Palmottu natural analogue project: phase II: Transport of radionuclides in a natural flow system at Palmottu: final report. EUR 19611, European Commission.

Blum J D, Erel Y, 1997. Rb–Sr isotope systematics of a granitic soil chronosequence: the importance of biotite weathering. Geochimica et Cosmochimica Acta 61, 3193–3204.

Blyth A, Frape S, Ruskeeniemi T, Blomqvist R, 2004. Origins, closed system formation and preservation of calcites in glaciated crystalline bedrock: evidence from the Palmottu natural analogue site, Finland. Applied Geochemistry 19, 675–686.

Booth A D, Clark R A, Kulessa B, Murray T, Carter J, Doyle S, Hubbard A, 2012. Thin-layer effects in glaciological seismic amplitude-versus-angle (AVA) analysis: implications for characterising a subglacial till unit, Russell Glacier, West Greenland. Cryosphere 6, 909–922.

Bosson E, Sassner M, Sabel U, Gustafsson L-G, 2010. Modelling of present and future hydrology and solute transport at Forsmark. SR-Site Biosphere. SKB R-10-02, Svensk Kärnbränslehantering AB.

Bosson E, Selroos J-O, Stigsson M, Gustafsson L-G, Destouni G, 2013. Exchange and pathways of deep and shallow groundwater in different climate and permafrost conditions using the Forsmark site, Sweden, as an example catchment. Hydrogeology Journal 21, 225–237.

Bougamont M, Price S, Christoffersen P, Payne A J, 2011. Dynamic patterns of ice stream flow in a 3-D higher-order ice sheet model with plastic bed and simplified hydrology. Journal of Geophysical Research: Earth Surface 116. doi: 10.1029/2011JF002025

Bougamont M, Christoffersen P, Hubbard A L, Fitzpatrick A A, Doyle S H, Carter S P, 2014. Sensitive response of the Greenland Ice Sheet to surface melt drainage over a soft bed. Nature Communications 5, 5052. doi:10.1038/ncomms6052

Boulton G S, Zatsepin S, Maillot B, 2001. Analysis of groundwater flow beneath ice sheets. SKB TR-01-06, Svensk Kärnbränslehantering AB.

Boulton G S, Lunn R, Vidstrand P, Zatsepin S, 2007. Subglacial drainage by groundwater-channel coupling, and the origin of esker systems: part II – theory and simulation of a modern system. Quaternary Science Reviews 26, 1091–1105.

Boulton G S, Hagdorn M, Maillot P B, Zatsepin S, 2009. Drainage beneath ice sheets: groundwater-channel coupling, and the origin of esker systems from former ice sheets. Quaternary Science Reviews 28, 621–638.

Bouwer H, Rice R C, 1976. A slug test for determining hydraulic conductivity of unconfined aquifers with completely of partially penetrating wells. Water Resources Research 12, 423–428.

Box J E, Fettweis X, Stroeve J C, Tedesco M, Hall D K, Steffen K, 2012. Greenland ice sheet albedo feedback: thermodynamics and atmospheric drivers. The Cryosphere 6, 821–839.

Brindley G W, Brown G (eds), 1980. Crystal structures of clay minerals and their X-ray identification. London: Mineralogical Society.

Brinkerhoff D J, Johnson J V, 2013. Data assimilation and prognostic whole ice-sheet modelling with the variationally derived, higher-order, open source, and fully parallel ice sheet model VarGlaS. The Cryosphere Discussions 7, 1029–1074.

Brinkerhoff D J, Meierbachtol T W, Johnson J V, Harper J T, 2011. Sensitivity of the frozen/melted basal boundary to perturbations of basal traction and geothermal heat flux: Isunnguata Sermia, western Greenland. Annals of Glaciology 52, 43–50.

Brooks A N, Hughes T J R, 1982. Streamline upwind/Petrov-Galerkin formulations for convection dominated flows with particular emphasis on the incompressible Navier-Stokes equations. Computer Methods in Applied Mechanics and Engineering 32, 199–259.

Brown R J E, Pewe T L, 1973. Distribution of permafrost in North America and its relationship to the environment: a review, 1963–1973. In Permafrost: The North American Contribution to the Second International Conference, Yakutsk, U.S.S.R., 13–28 July 1973. Washington DC: National Academy of Sciences, 71–100.

Bursey G G, 1990. Geochemical and isotopic investigations in a watershed of the eastern Arctic, Northwest Territories. MSc thesis. University of Waterloo, Ontario, Canada.

Cappelen J (ed), 2012. Weather and climate data from Greenland 1958–2011 – Observation data with description. Technical Report 12-15, Danish Meteorological Institute.

Cappelen J (ed), 2013. Weather observations from Greenland 1958–2012 – Observation data with description. Technical Report 13-11, Danish Meteorological Institute.

Cappelen J, Jørgensen B V, Laursen E V, Stannius L S, Thomsen R S, 2001. The observed climate of Greenland, 1958–99 – with climatological standard normal, 1961–90. Technical Report 00-18, Danish Meteorolorogical Institute.

Carter S P, Fricker H A, Blankenship D D, Johnson J V, Lipscomb W, 2011. Modeling 5 years of subglacial lake activity in the MacAyeal Ice Stream (Antarctica) catchment through assimilation of ICESat laser altimetry. Journal of Glaciology 57, 1098–1112.

Catania G A, Neumann T A, Price S F, 2008. Characterizing englacial drainage in the ablation zone of the Greenland ice sheet. Journal of Glaciology 54, 567–578.

Chandler D M, Wadham J L, Lis G P, Cowton T, Sole A, Bartholomew I, Telling J, Nienow P, Bagshaw E B, Mair D, Vinen S, Hubbard A, 2013. Evolution of the subglacial drainage system beneath the Greenland Ice Sheet revealed by tracers. Nature Geoscience 6, 195–198.

Charalampidis C, van As D, Box J E, van den Broeke M R, Colgan W T, Doyle S H, Hubbard A L, MacFerrin M, Macguth H, Smeets C J P P, 2015. Changing surface-atmosphere energy exchange and refreezing capacity of the lower accumulation area, West Greenland. The Cryosphere 9, 2163–2181.

Chen G, 1999. GPS kinematic positioning for the airborne laser altimetry at Long Valley, California. PhD thesis. Massachusetts Institute of Technology.

Christensen E L, Reeh N, Forsberg R, Jørgensen J H, Skou N, Woelders K, 2000. Instruments and methods: a low-cost glacier-mapping system. Journal of Glaciology 46, 531–537.

Christiansen H H, Humlum O, 2000. Permafrost. In Topografisk atlas, Grønland. Jakobsen B H, Böcher J, Nielsen N, Guttesen R, Humlum O, Jensen O (eds). Det Kongelige Geografiske Selskab og Kort og Matrikelstyrelsen, 32–35.

Christl M, Vockenhuber C, Kubik P W, Wacker L, Lachner J, Alfimov V, Synal H-A, 2013. The ETH Zurich AMS facilities: performance parameters and reference materials. Nuclear Instruments and Methods in Physics Research Section B: Beam Interactions with Materials and Atoms 294, 29–38.

Chu V W, 2013. Greenland ice sheet hydrology: a review. Progress in Physical Geography 38, 19–54.

Clark I D, Fritz P, 1997. Environmental isotopes in hydrogeology. Boca Raton, FL: Lewis Publishers.

Clark P U, Alley R B, Pollard D, 1999. Northern Hemisphere ice-sheet influences on global climate change: Science 286, 1104–1111.

Clarke G K C, 1987. Subglacial till: a physical framework for its properties and processes. Journal of Geophysical Research: Solid Earth 92, 9023–9036.

Clauser C (ed), 2003. Numerical simulation of reactive flow in hot aquifers. SHEMAT and Processing SHEMAT. Berlin: Springer.

Cooper H H, Bredehoeft J D, Papadopulos I S, 1967. Response of a finite-diameter well to an instantaneous charge of water. Water Resources Research 3, 263–269.

Cooper R J, Wadham J L, Tranter M, Hodgkinds R, Peters N E, 2002. Groundwater hydrochemistry in the active elayer of the proglacial zone, Finsterwalderbreen, Svalbard. Journal of Hydrology 269, 208–223.

Cowton T, Nienow P, Bartholomew I, Sole A, Mair D, 2012. Rapid erosion beneath the Greenland ice sheet. Geology 40, 343–346.

Cowton T, Nienow P, Sole A, Wadham J, Lis G, Bartholomew I, Mair D, Chandler D, 2013. Evolution of drainage system morphology at a land-terminating Greenland outlet glacier. Journal of Geophysical Research 118, 29–41.

Csatho B, van der Veen C J, Tremper C, 2005. Trimline mapping from multispectral Landsat ETM+ imagery. Géographie Physique et Quaternaire 59, 49–62.

Cuffey K M, Paterson W S B, 2010. The physics of glaciers. 4th rev. ed. Amsterdam: Butterworth-Heinemann.

Cuffey K M, Clow G D, Alley R B, Stuiver M, Waddington E D, Saltus R W, 1995. Large Arctic temperature change at the Wisconsin-Holocene glacial transition. Science 270, 455–458.

Cuffey K M, Conway H, Hallet B, Gades A M, Raymond C F, 1999. Interfacial water in polar glaciers and glacier sliding at –17 °C Geophysical Research Letters 26, 751–754.

Dahl-Jensen D, Mosegaard K, Gundestrup N, Clow G D, Johnsen S J, Hansen A W, Balling N, 1998. Past temperatures directly from the Greenland ice sheet. Science 282, 268–271.

Dahl-Jensen D, Gundestrup N, Gogineni S P, Miller H, 2003a. Basal melt at NorthGRIP modeled from borehole, ice-core and radio-echo sounder observations. Annals of Glaciology 37, 207–212.

Dahl-Jensen D, Johnsen S, Willerslev E, Miller H, Thorsteinsonn T, 2003b. Basal water at the NorthGRIP drill site. In Proceedings of Third International Conference on Mars Polar Science and Exploration, Alberta, Canada, 13–17 October 2003, 13–17.

Das S B, Joughin I, Behn M D, Howat I M, King M A, Lizarralde D, Bhatia M P, 2008. Fracture propagation to the base of the Greenland Ice Sheet during supraglacial lake drainage. Science 320, 778–781.

Deuflhard P, 2004. Newton methods for nonlinear problems: affine invariance and adaptive algorithms. Berlin: Springer. (Springer Series in Computational Mathematics 35)

Dickin A P, 2005. Radiogenic isotope geology. 2nd ed. Cambridge: Cambridge University Press.

Dideriksen K, Christiansen B C, Frandsen C, Balic-Zunic T, Mørup S, Stipp S L S, 2010. Paleo-redox boundaries in fractured granite. Geochimica et Cosmochimica Acta 74, 2866–2880.

Dietrich R, Rülke A, Scheinert M, 2005. Present-day vertical crustal deformations in West Greenland from repeated GPS observations. Geophysical Journal International 163, 865–874.

Dow J M, Neilan R E, Rizos C, 2009. The International GNSS Service in a changing landscape of Global Navigation Satellite Systems. Journal of Geodesy 83, 191–198

Dow C F, Hubbard A, Booth A D, Doyle S H, Gusmeroli A, Kulessa Y B, 2013. Seismic evidence of mechanically weak sediments underlying Russell Glacier, West Greenland. Annals of Glaciology 54, 135–141.

Doyle S H, Hubbard A L, Dow C F, Jones G A, Fitzpatrick A, Gusmeroli A, Kulessa B, Lindback K, Pettersson R, Box J E, 2013. Ice tectonic deformation during the rapid in situ drainage of a supraglacial lake on the Greenland Ice Sheet. The Cryosphere 7, 129–140.

Doyle S H, Hubbard A, Fitzpatrick A A W, van As D, Mikkelsen A B, Pettersson R, Hubbard B, 2014. Persistent flow acceleration within the interior of the Greenland Ice sheet. Geophysical Research Letters 41, 899–905.

Drake H, Tullborg E-L, 2009. Paleohydrogeological events recorded by stable isotopes, fluid inclusions andtrace elements in fracture minerals in crystalline rock, Simpevarp area, SE Sweden. Applied Geochemistry 24, 715–732.

Drake H, Tullborg E-L, MacKenzie A B, 2009. Detecting the near-surface redox front in crystalline bedrock using fracture mineral distribution, geochemistry and U-series disequilibrium. Applied Geochemistry 24, 1023–1039.

Drever S I, 1973. The preparation of oriented clay mineral specimens for X-ray diffraction analysis by a filter-membrane peel technique. American Mineralogist 58, 553–554.

Dukowicz J K, 2011. Reformulating the full-Stokes ice sheet model for a more efficient computational solution. The Cryosphere Discussions 5, 1749–1774.

Echelmeyer K, Wang Z, 1987. Direct observation of basal sliding and deformation of basal drift at sub-freezing temperatures. Journal of Claciology 33, 83–98.

Eggenkamp H G M, Kreulen R, Koster Van Groos A F, 1995. Chlorine stable isotope fractionation in evaporites. Geochimica et Cosmochimica Acta 59, 5169–5175.

Eichinger F, 2009. Matrix porewater – fracture groundwater interaction in crystalline bedrock based on natural tracers: an archive for long-term hydrogeological evolution. PhD thesis. Institute of Geological Sciences, University of Bern, Switzerland.

Eichinger F, Waber H N, 2013. Matrix porewater in crystalline rocks: extraction and analysis. NWMO TR-2013-23, Nuclear Waste Management Organization, Canada.

Engelhardt H, Humphrey N, Kamb B, Fahnestock M, 1990. Physical conditions at the base of a fast moving Antarctic ice stream. Science 248, 57–59.

Engström J, Klint K E S, 2014. Continental collision structures and post-orogenic geological history of the Kangerlussuaq area in the southern part of the Nagssugtoqidian orogen, Central West Greenland. Geosciences 4, 316–334.

Engström J, Paananen M, Klint K E, 2012. The Greenland Analogue Project. Geomodel version 1 of the Kangerlussuaq area on Western Greenland. Posiva Working Report 2012-10, Posiva Oy, Finland.

Epstein S, Mayeda T K, 1953. Variation of the ^{18}O content of waters from natural sources. Geochimica Cosmochimica Acta 4, 213–224.

Ettema J, van den Broeke M R, van Meijgaard E, van de Berg W J, Bamber J L, Box J E, Bales R C, 2009. Higher surface mass balance of the Greenland ice sheet revealed by high-resolution climate modelling. Geophysical Research Letters 36. doi:10.1029/2009GL038110

Fausto R S, Ahlstrøm A P, van As D, Bøggild C E, Johnsen S J, 2009. A new present-day temperature parameterization for Greenland. Journal of Glaciology 55, 95–105.

Fettweis X, Belleflamme A, Erpicum M, Franco B, Nicolay S, 2011. Estimation of the sea level rise by 2100 resulting from changes in the surface mass balance of the Greenland ice sheet. In Blanco J, Kheradmand H (eds). Climate change: geophysical foundations and ecological effects. Rijeka, Croatia: InTech, 503–520.

Fettweis X, Hanna E, Lang C, Belleflamme A, Erpicum M, Gallée H, 2013. Brief communication "Important role of the mid-tropospheric atmospheric circulation in the recent surface melt increase over the Greenland ice sheet". The Cryosphere 7, 241–248.

FIGL, 2009. Finland Isotope Geoscience Laboratory, Annual report 2009. Geological Survey of Finland. Available at: http://en.gtk.fi/export/sites/en/research/infrastructure/isotopegeology/SIGL_2009_AnnualReport.pdf

Fitzpatrick A A W, Hubbard A, Joughin I, Quincey D J, van As D, Mikkelsen A P B, Doyle S H, Hasholt B, Jones G A, 2013. Ice flow dynamics and surface meltwater flux at a land-terminating sector of the Greenland Ice Sheet. Journal of Glaciology 59, 687–696.

Fitzpatrick A A W, Hubbard A L, Box J E, Quincey D J, van As D, Mikkelsen A P B, Doyle S H, Dow C F, Hasholt B, Jones G A, 2014. A decade (2002–2012) of supraglacial lake volume estimates across Russell Glacier, West Greenland. The Cryosphere 8, 107–121.

Follin S, Johansson P-O, Hartley L, Jackson P, Roberts D, Marsic N, 2007. Hydrogeological conceptual model development and numerical modelling using CONNECTFLOW, Forsmark modelling stage 2.2. SKB R-07-49, Svensk Kärnbränslehantering AB.

Follin S, Stephens M B, Laaksoharju M, Nilsson A-C, Smellie J A T, Tullborg E-L, 2008. Modelling the evolution of hydrochemical conditions in the Fennoscandian Shield during Holocene time using multidisciplinary information. Applied Geochemistry 23, 2004–2020.

Follin S, Stigsson M, Rhén I, Engström J, Klint K E, 2011. Greenland Analogue Project – Hydraulic properties of deformation zones and fracture domains at Forsmark, Laxemar and Olkiluoto for usage together with Geomodel version 1. SKB P-11-26, Svensk Kärnbränslehantering AB.

Forman S L, Van Der Veen C, Tremper C, Csatho B, 2007. Little Ice Age and neoglacial landforms at the inland ice margin, Isunguata Sermia, Kangerlussuaq, west Greenland. Boreas 36, 341–351.

Fountain A G, Walder J S, 1998. Water flow through temperate glaciers. Reviews of Geophysics 36, 299–328.

Fox Maule C M, Purucker E, Olsen N, 2009. Inferring magnetic crustal thickness and geothermal heat flux from crustal magnetic field models, Report 09-09, Danish Meteorological Institute. Available at: http://www.dmi.dk/dmi/dkc09-09.pdf

Frampton A, Painter S, Lyon S W, Destouni G, 2011. Non-isothermal, three-phase simulations of near-surface flows in a model permafrost system under seasonal variability and climate change. Journal of Hydrology 403, 352–359.

Franco B, Fettweis X, Erpicum M, 2013. Future projections of the Greenland ice sheet energy balance driving the surface melt. The Cryosphere 7, 1–18

Frape S K, Fritz P, McNutt R H, 1984. Water–rock interaction and chemistry of groundwaters from the Canadian Shield. Geochimica et Cosmochimica Acta 48, 1617–1627.

Frape S K, Blyth A, Blomqvist R, McNutt R H, Gascoyne M, 2004. Deep fluids in the continents: II. Crystalline rocks. In Holland H D, Turekian K K (eds), Treatise on Geochemistry. Vol. 5, Surface and ground water, weathering, and soils. Amsterdam: Elsevier, 541–580.

Freifeld B M, Trautz R C, Kharaka Y K, Phelps T J, Myer L R, Hovorka S D, Collins D J, 2005. The U-tube: a novel system for acquiring borehole fluid samples from a deep geologic CO_2 sequestration experiment. Journal of Geophysical Research 110, B10203. doi:10.1029/2005JB003735

Freifeld B M, Finsterle S, Onstott T C, Toole P, Pratt L M, 2008. Ground surface temperature reconstructions: using in situ estimates for thermal conductivity acquired with a fiber-optic distributed thermal perturbation sensor. Geophysical Research Letters 35. doi:10.1029/2008GL034762

French H M, 2007. The periglacial environment. 3rd ed. Chichester: Wiley.

Fritz P, Basharmal G M, Drimmie R J, Ibsen J, Qureshi R M, 1989. Oxygen isotope exchange between sulphate and water during bacterial reduction of sulphate. Chemical Geology 79, 99–105.

Fritz P, Frape S K, Drimmie R J, A leyard E C, 1994. Sulfate in brines in the crystalline rocks of the Canadian Shield. Geochimica et Cosmochimica Acta 58, 57–65.

Funder S (co-ordinator), 1989. Quaternary geology of the ice free areas and adjacent shelves of Greenland. In Fulton R J (ed). Quaternary geology of Canada and Greenland. Geological Survey of Canada, Geology of Canada 1 (also Geological Society of America, The Geology of North America K-l), 741–792.

Funder S, Hansen L, 1996. The Greenland Ice Sheet – a model for its culimination and decay during and after the last glacial maximum. Bulletin of the Geological Society of Denmark 42, 137–152.

Funk M, Echelmeyer K, Iken A, 1994. Mechanisms of fast flow in Jakobshavns Isbræ, West Greenland: Part II. Modelling of englacial temperatures. Journal of Glaciology 40, 569–585.

Gades A M, Raymond C F, Conway H, Jacobel R W, 2000. Bed properties of Siple Dome and adjacent ice streams, West Antarctica, inferred from radio-echo sounding measurements. Journal of Glaciology 46, 88–94.

Garde A A, Hollis J A, 2010. A buried Palaeoproterozoic spreading ridge in the northern Nagssugtoqidian orogen, West Greenland. In Kusky T M, Zhai M-G, Xiao W (eds). The evolving continents: understanding processes of continental growth. London: Geological Society. (Geological Society Special publications 338), 213–234.

Garde A A, Marker M, 2010. Geological map of Greenland, 1:500 000, Kangerlussuaq/Søndre Strømfjord – Nuussuaq, Sheet 3. 2nd edition. Copenhagen: Geological Survey of Denmark and Greenland.

Gascoyne M, Miller N H, Neymark L A, 2002. Uranium-series disequilibrium in tuffs from Yucca Mountain, Nevada, as evidence of pore-fluid flow over the last million years. Applied Geochemistry 17, 781–792.

Gercek H, 2007. Poisson's ratio values for rocks. International Journal of Rock Mechanics and Mining Sciences 44, 1–13.

Ginzinger D G, 2002. Gene quantification using real-time quantitative PCR: an emerging technology hits the mainstream. Experimental Hematology 30, 503–512.

Glen J W, 1955. The creep of polycrystalline ice. Proceedings of the Royal Society of London A 228, 519–538.

Glynn P D, Voss C I, Provost A M, 1999. Deep penetration of oxygenated meltwaters from warm based ice-sheets into the Fennoscandian Shield. In Use of hydrochemical information in testing groundwater flow models: technical summary and proceedings of a workshop organised by the NEA Co-ordinating Group on Site Evaluation and Design of Experiments for Radioactive Waste Disposal (SEDE), Borgholm, Sweden, 1–3 September 1997, 201–241.

Goldberg D N, Sergienko O V, 2011. Data assimilation using a hybrid ice flow model. Cryosphere 5, 315–327.

Grant F S, West G F, 1965. Interpretation theory in applied geophysics. New York: McGraw-Hill.

Greve R, 2005. Relation of measured basal temperatures and the spatial distribution of the geothermal heat flux for the Greenland ice sheet. Annals of Glaciology 42, 424–432.

Gudmundsson G H, Raymond M, 2008. On the limit to resolution and information on basal properties obtainable from surface data on ice streams. The Cryosphere Discussions 2, 413–445.

Guimerà J, Duro L, Jordana S, Bruno J, 1999. Effects of ice melting and redox front migration in fractured rocks of low permeability. SKB TR-99-19, Svensk Kärnbränslehantering AB.

Gundestrup N S, Hansen B L, 1984. Bore-hole survey at Dye 3, south Greenland. Journal of Glaciology 30, 282–288.

Gundestrup N S, Dahl-Jensen D, Hansen B L, Kelty J, 1993a. Bore-hole survey at Camp Century, 1989. Cold Regions Science and Technology 21, 187–193.

Gundestrup N S, Dahl-Jensen D, Johnsen S J, Rossi A, 1993b. Bore-hole survey at dome GRIP 1991. Cold Regions Science and Technology 21, 399–402.

Habashi W G, Dompierre J, Bourgault Y, Ait-Ali-Yahia D, Fortin M, Vallet M-G, 2000. Anisotropic mesh adaptation: towards user-independent, mesh-independent and solver-independent CFD Part I: general principles. International Journal for Numerical Methods in Fluids 32, 725–744.

Habermann M, Maxwell D, Truffer M, 2012. Reconstruction of basal properties in ice sheets using iterative inverse methods. Journal of Glaciology 58, 795–807.

Hanna E, Huybrechts P, Steffen K, Cappelen J, Huff R, Shuman C, Irvine-Flynn T, Wise S, Griffiths M, 2008. Increased runoff from melt from the Greenland ice sheet: A response to global warming, Journal of Climatology 21, 331–341.

Hanna E, Mernild S H, Cappelen J, Steffen K, 2012. Recent warming in Greenland in a long-term instrumental (1881–2012) climatic context: I Evaluation of surface air temperature records. Environmental Research Letters 7, 045404. doi:10.1088/1748-9326/7/4/045404

Hansen B L, Langway C C, 1966. Deep core drilling in ice and core analysis at Camp Century Greenland, 1961–1966. Antarctic Journal of the United States 1, 207–208.

Harper J T, Humphrey N F 1995. Borehole video analysis of a temperate glacier's englacial and subglacial structure; implications for glacier flow models, Geology 23, 901–904.

Harper J T, Humphrey N F, Pfeffer W T, Fudge T, O'Neel S, 2005. Evolution of subglacial water pressure along a glacier's length. Annals of Glaciology 40, 31–36.

Harper J T, Humphrey N F, Pfeffer T W, Lazar B, 2007. Two modes of accelerated glacier sliding related to water. Geophysical Research Letters 34, L12503. doi:10.1029/2007GL030233

Harper J, Humphrey N, Pfeffer W T, Brown J, Fettweis X, 2012. Greenland ice-sheet contribution to sea-level rise buffered by meltwater storage in firn. Nature 491, 240–243.

Harper J, Hubbard A, Ruskeeniemi T, Claesson Liljedahl L, Lehtinen A, Booth A, Brinkerhoff D, Drake H, Dow C, Doyle S, Engström J, Fitzpatrick A, Frape S, Henkemans E, Humphrey N, Johnson J, Jones G, Joughin I, Klint KE, Kukkonen I, Kulessa B, Landowski C, Lindbäck K, Makahnouk M, Meierbachtol T, Pere T, Pedersen K, Pettersson R, Pimentel S, Quincey D, Tullborg E-L, van As D, 2011. The Greenland Analogue Project Yearly Report 2010. Posiva Working Report 2012-16, Posiva Oy Finland. SKB R-11-23, Svensk Kärnbränslehantering AB.

Harper J, Hubbard A, Ruskeeniemi T, Claesson Liljedahl L, Lehtinen A, Booth A, Brinkerhoff D, Drake H, Dow C, Doyle S, Engström J, Fitzpatrik A, Frape S, Helanow C, Henkemans E, Humphrey N, Johnson E, Johnson J, Jones G, Klint K E, Kulessa B, Landowski C, Lindbäck K, Luckman A, Maddoc L, Makahnouk M, Meierbachtol T, Pere T, Petterson R, Pimentel S, Quincey D, Tullborg E-L, van As D, 2015. The Greenland Analogue Project Yearly Report 2011. Posiva Working Report 2012-79, Posiva Oy, Finland.

Hasholt B, Bech Mikkelsen A, Holtegaard Nielsen M, Dahl Larsen A M, 2013. Observations of runoff and sediment and dissolved loads from the Greenland ice sheet at Kangerlussuaq, West Greenland, 2007 to 2010. Zeitschrift für Geomorphologie, Supplementbände 57, 3–27.

Helm V, Humbert A, Miller H, 2014. Elevation and elevation change of Greenland and Antarctica derived from CryoSat-2. The Cryosphere 8, 1–21.

Henkemans E, 2016. Geochemical characterization of groundwaters, surface waters and water–rock interaction in an area of continuous permafrost adjacent to the Greenland ice sheet, Kangerlussuaq, Southwest Greenland. PhD thesis. University of Waterloo, Canada.

Henriksen N, Higgins A K, Kalsbeek F, Pulvertaft T C R, 2000. Greenland from Archean to Quaternary: descriptive text to the geological map of Greenland, 1:2 500 000. Geology of Greenland Survey Bulletin 185.

Heroux M A, Bartlett R A, Howle V E, Hoekstra R J, Hu J J, Kolda T G, Lehoucq R B, Long K R, Pawlowski R P, Phipps E T, Salinger A G, Thornquist H K, Tuminaro R S, Willenbring J M, Williams A, Stanley K S, 2005. An overview of the Trilinos project. ACM Transactions on Mathematical Software 31, 397–423.

Herut A, Katz A, Bein A, 1990. The role of seawater freezing in the formation of subsurface brines. Geochimica et Cosmochimica Acta 54, 13–21.

Hindmarsh R C A, 2006. Stress gradient damping of thermoviscous ice flow instabilities. Journal of Geophysical Research, Solid Earth, 111. doi:10.1029/2005JB004019

Hooke R LeB, 1989. Englacial and subglacial hydrology: A qualitative review. Arctic and Alpine Research 21, 221–233.

Howat I M, Negrete A, Scambos T, Haran T, 2012. A high-resolution elevation model for the Greenland Ice Sheet from combined stereoscopic and photoclinometric data. Available at: http://bpcrc.osu.edu/gdg/data/gimpdem

Howat I M, de la Peña S, van Angelen J H, Lenaerts J T M, van den Broeke M R, 2013. Expansion of meltwater lakes on the Greenland Ice Sheet. The Cryosphere 7, 201–204.

Howat I M, Negrete A, Smith B E, 2014. The Greenland Ice Mapping Project (GIMP) land classification and surface elevation datasets. The Cryosphere 8, 1509–1518.

Hubbard A, Blatter H, Nienow P, Mair D, Hubbard B, 1998. Comparison of a three-dimensional model for glacier flow with field data from Haut Glacier d'Arolla, Switzerland. Journal of Glaciology 44, 368–378.

Huggel C, Kääb A, Haeberli W, Teysseire P, Paul F, 2002. Remote sensing based assessment of hazards from glacier lake outbursts: a case study in the Swiss Alps. Canadian Geotechnical Journal 39, 316–330.

Humphrey N, Echelmeyer K, 1990. Hot-water drilling and bore-hole closure in cold ice. Journal of Glaciology 36, 287–298.

Humphrey N F, Harper J T, Pfeffer W T, 2012. Thermal tracking of meltwater retention in Greenland's accumulation area. Journal of Geophysical Research: Earth Surface (2003–2012), 117. doi:10.1029/2011JF002083

Hutter K, 1982. A mathematical model of polythermal glaciers and ice sheets. Geophysical & Astrophysical Fluid Dynamics 21, 201–224.

Huybrechts P, 1996. Basal temperature conditions of the Greenland ice sheet during the glacial cycles. Annals of Glaciology 23, 226–236.

Hvorslev M J, 1951. Time lag and soil permeability in ground-water observations. Bulletin 36, Waterways Experiment Station, Corps of Engineers, U.S. Army.

Hyder Z, Butler J J, McElwee C D, Liu W, 1994. Slug tests in partially penetrating wells. Water Resources Research 30, 2945–2957.

IAEA, 2012. IAEA annual report. Vienna: International Atomic Energy Agency.

Iken A, 1981. The effect of the subglacial water pressure on the sliding velocity of a glacier in an idealized numerical model. Journal of Glaciology 27, 407–421.

Iken A, Bindschadler R A, 1986. Combined measurements of subglacial water pressure and surface velocity of Findelengletscher, Switzerland: conclusions about drainage system and sliding mechanism. Journal of Glaciology 32, 101–119.

Iken A, Echelmeyer K, Harrison W, Funk M, 1993. Mechanisms of fast flow in Jakobshavns Isbræ, West Greenland. I: Measurements of temperature and water level in deep boreholes. Journal of Glaciology 39, 15–25.

Inagaki F, Tsunogai U, Suzuki M, Kosaka A, Machiyama H, Takai K, Nunoura T, Nealson K H, Horikoshi K, 2004. Characterization of C_1-metabolizing prokaryotic communities in methane seep habitats at the Kuroshima Knoll, Southern Ryukyu Arc, by analyzing pmoA, mmoX, mxaF, mcrA, and 16S rRNA genes. Applied and Environmental Microbiology 70, 7445–7455.

Ingersoll L R, Plass H J, 1948. Theroy of the ground pipe heat source for the heat pump. Transactions of the American Society of Heating and Ventilating Engineers 54.

Irving J D, Knoll M D, Knight R J, 2007. Improving crosshole radar velocity tomograms: a new approach to incorporating high-angle traveltime data. Geophysics 72, J31–J41.

IPCC-WGI, 2007. Climate change 2007. Contribution of Working Group I to the Fourth Assessment Report of the Intergovernmental Panel on Climate Change. Cambridge: Cambridge University Press.

IPCC, 2013. Climate change 2013: the physical science basis: summary for policymakers. Contribution of Working Group I to the Fifth Assessment Report of the Intergovernmental Panel on Climate Change. Cambridge: Cambridge University Press.

Isaaks E H, Srivastava R M, 1989. An introduction to applied geostatistics. Oxford: Oxford University Press.

Jacobel R W, Welch B C, Osterhouse D, Pettersson R, MacGregor J A, 2009. Spatial variation of radar-derived basal conditions on Kamb Ice Stream, West Antarctica. Annals of Glaciology 51, 10–16.

Jansson P, 1995. Water pressure and basal sliding on Storglaciären, northern Sweden. Journal of Glaciology 41, 232–240.

Jansson P, 2010. Ice sheet hydrology from observations. SKB TR-10-68, Svensk Kärnbränslehantering AB.

Jasmund K, Lagaly G (eds), 1993. Tonminerale und Tone: Struktur, Eigenschaften, Anwendungen und Einsatz in Industrie und Umwelt. Darmstadt: Steinkopff.

Johannessen O M, Khvorostovsky K, Miles M W, Bobylev L P, 2005. Recent ice-sheet growth in the interior of Greenland. Science 310, 1013–1016.

Johansson E, Berglund S, Lindborg T, Petrone J, van As D, Gustafsson L-G, Näslund J-O, Laudon H, 2015a. Hydrological and meteorological investigations in a periglacial lake catchment near Kangerlussuaq, west Greenland – presentation of a new multi-parameter dataset. Earth System Science Data 7, 93–108.

Johansson E, Gustafsson L-G, Berglund S, Lindborg T, Selroos J-O, Claesson Liljedahl L, Destouni G, 2015b. Data evaluation and numerical modeling of hydrological interactions between active layer, lake and talik in a permafrost catchment, Western Greenland. Journal of Hydrology 527, 688–703.

Jol H M, (ed) 2009. Ground penetrating radar: theory and applications. Amsterdam: Elsevier Science.

Jones G A, Kulessa B, Doyle S H, Dow C F, A Hubbard, 2013. An automated approach to the location of icequakes using seismic waveform amplitudes. Annals of Glaciology 54, 1–9.

Joughin I, 2002. Ice-sheet velocity mapping: a combined interferometric and speckle-tracking approach. Annals of Glaciology 34, 195–201.

Joughin I, Das S B, King M A, Smith B E, Howat I M, Moon T, 2008. Seasonal speedup along the western flank of the Greenland Ice Sheet. Science 320, 781–783.

Joughin I, Smith B E, Howat I M, Scambos T, Moon T, 2010. Greenland flow variability from ice-sheet-wide velocity mapping. Journal of Glaciology 56, 415–430.

Joughin I, Das S B, Flowers G E, Behn M D, Alley R B, King M A, Smith B E, Bamber J, van den Broeke M R, van Angelen J H, 2013. Influence of supraglacial lakes and ice-sheet geometry on seasonal ice-flow variability The Cryosphere Discussions 7, 1101–1118.

Jägevall S, Rabe L, Pedersen K, 2011. Abundance and diversity of biofilms in natural and artificial aquifers of the Äspö Hard Rock Laboratory, Sweden. Microbial Ecology 61, 410–422.

Jørgensen A S, Andreasen F, 2007. Mapping of permafrost surface using ground-penetrating radar at Kangerlussuaq Airport, western Greenland. Cold Regions Science and Technology 48, 64–72.

Kanao M, Tsuboi S, Butler R, Anderson K, Dahl-Jensen T, Larsen T, Nettles M, Voss P, Childs D, Clinton J, Stutzman E, Himeno T, Toyokuni G, Tanaka S, Tono Y, 2012. Greenland Ice Sheet dynamics and glacial earthquake activities. In Müller J, Koch L (eds). Ice sheets: dynamics, formation and environmental concerns. Nova Science Publishers, 93–120.

Kane D L, Yoshikawa K, McNamara J P, 2013. Regional groundwater flow in an area mapped as continuous permafrost, NE Alaska (USA). Hydrogeology Journal 21, 41–52.

Kaufman R S, Long A, Bentley H, Davis S, 1984. Natural chlorine isotope variations. Nature 309, 338–340.

Kern-Hansen C, 1990. Data basis for permafrost studies in Greenland. In Proceeding of POLARTECH '90: International Conference on Development and Commercial Utilization of Technologies in Polar Areas, Copenhagen, 14–16 August 1990. Hørshelm, Denmark: Danish Hydraulic Institute, 635–644.

Kim Y-S, Sanderson D J, 2005. The relationship between displacement and length of faults: a review. Earth-Science Reviews 68, 317–334.

King M, 2004. Rigorous GPS data-processing strategies for glaciological applications. Journal of Glaciology 50, 601–607.

Kleiven H F, Jansen E, Fronval T, Smith T H, 2002. Intensification of Northern Hemisphere glaciations in the circum Atlantic region (3.5–2.4 Ma) – ice-rafted detritus evidence. Paleogeopgraphy, Paleoclimatology, Paleoecology 184, 213–223.

Kleman J, Stroeven A P, Lundqvist J, 2008. Patterns of Quaternary ice sheet erosion and deposition in Fennoscandia and a theoretical framework for explanation. Geomorphology 97, 73–90.

Korhonen K, Ruskeeniemi T, Paananen M, Lehtimäki J, 2009. Frequency domain electromagnetic soundings of Canadian deep permafrost. Geophysica 45, 77–92.

Krabill W, Abdalati W, Frederick E, Manizade S, Martin C, Sonntag J, Swift R, Thomas R, Wright W, Yungel J, 2000. Greenland ice sheet: high-elevation balance and peripheral thinning. Science 289, 428–430.

Krawczynski M J, Behn M D, Das S B, Joughin, I. 2009. Constraints on the lake volume required for hydro-fracture through ice sheets. Geophysical Research Letters 36. doi:10.1029/2008gl036765

Laaksoharju M, Smellie J, Tullborg E-L, Wallin B, Drake H, Gascoyne M, Gimeno M, Gurban I, Hallbeck L, Molinero J, Nilsson A-C, Waber N, 2009. Bedrock hydrogeochemistry Laxemar. Site descriptive modelling, SDM-Site Laxemar. SKB R-08-93, Svensk Kärnbränslehantering AB.

Lampkin D J, 2011. Supraglacial lake spatial structure in western Greenland during the 2007 ablation season. Journal of Geophysical Research, Earth Surface 116. doi:10.1029/2010JF001725

Landowski C, 2012. Geochemistry and subglacial hydrology of the West Greenland Ice Sheet. MSc thesis. University of Wyoming.

Larour E, Rignot E, Joughin I, Aubry D, 2005. Rheology of the Ronne Ice Shelf, Antarctica, inferred from satellite radar interferometry data using an inverse control method. Geophysical Research Letters 32. doi:10.1029/2004GL021693

Larour E, Seroussi H, Morlighem M, Rignot E, 2012. Continental scale, high order, high spatial resolution, ice sheet modelling using the Ice Sheet System Model (ISSM). Journal of Geophysical Research: Earth Surface 117. doi:10.1029/2011JF002140

Layberry R L, Bamber J L, 2001. A new ice thickness and bed dataset for the Greenland ice sheet: 2. Relationship between ice dynamics and basal topography. Journal of Geophysical Research: Atmospheres 106, 33781–33788.

Le Brocq A M, Payne A J, Siegert M J, Alley R B, 2009. A subglacial water-flow model for West Antarctica. Journal of Glaciology 55, 879–888.

Lemieux J-M, Sudicky E A, Peltier W R, Tarasov L, 2008. Simulating the impact of glaciations on continental groundwater flow systems: 1. relevant processes and model formulation. Journal of Geophysical Research: Earth Surface 113, F03017. doi:10.1029/2007JF000928.

Leng M J, Anderson N J, 2003. Isotopic variation in modern lake waters from western Greenland. The Holocene 13, 605–611.

Leng W, Ju L, Gunzburger M, Price S, Ringler T, 2012. A parallel high-order accurate finite element nonlinear Stokes ice sheet model and benchmark experiments. Journal of Geophysical Research: Earth Surface 117. doi:10.1029/2011JF001962

Leuschen C, Allen C, 2010. IceBridge MCoRDS L2 Ice Thickness, 2010-2012, Boulder, Colorado NASA DAAC National Snow Ice Data Centre. Available from: http://nsidc.org/data/irmcr2

Levy L B, Kelly M A, Howley J A, Virginia R A, 2012. Age of the Ørkendalen moraines, Kangerlussuaq, Greenland: constraints of the extent of the southwestern margin of the Greenland Ice Sheet during the Holocene. Quaternary Science Reviews 52, 1–5.

Lindbäck K, Pettersson R, Doyle S H, Helanow C, Jansson P, Kristensen S S, Stenseng L, Forsberg R, Hubbard A I, 2014. High-resolution ice thiskness and bed topography of a land-terminating section of the Greenland Ice Sheet. Earth System Science Data 6, 331–338.

Lindbäck K, Pettersson R, 2015. Spectral roughness and glacial erosion of a land-terminating section of the Greenland Ice Sheet. Geopmorphology 238, 149-159.

Livingstone S J, Clark C D, Woodward J, Kingslake J, 2013. Potential subglacial lakes and meltwater drainage pathways beneath the Antarctic and Greenland ice sheets. The Cryosphere 7, 1721–1740.

Logg A, Mardal K-A, Wells G, 2012. Finite element assembly. In Logg A, Mardal K-A, Wells G (eds). Automated solution of differential equations by the finite element method: the FEniCS book. Heidelberg: Springer. (Lecture notes in computational science and engineering 84), 141–146.

Lowry C S, Walker J F, Hunt R J, Anderson M P, 2007. Identifying spatial variability of groundwater discharge in a wetland stream using a distributed temperature sensor. Water Resources Research 43. doi: 10.1029/2007WR006145

Ludvigson J-E, Hansson K, Rouhiainen P, 2002. Methodology study of Posiva difference flow meter in borehole KLX02 at Laxemar. SKB R-01-52, Svensk Kärnbränslehantering AB.

Luthi M, Funk M, Iken A, Gogineni S, Truffer M, 2002. Mechanisms of fast flow in Jakobshavn Isbræ, West Greenland: Part III. Measurements of ice deformation, temperature and cross-borehole conductivity in boreholes to the bedrock. Journal of Glaciology 48, 369–385.

Lyons R G, 2004. Understanding digital signal processing. 2nd ed. Upper Saddle River, NJ: Prentice Hall.

Lythe M B, Vaughan D G, 2001. BEDMAP: A new ice thickness and subglacial topographic model of Antarctica. Journal of Geophysical Research: Solid Earth 106, 11335–11351.

MacAyeal D R, Bindschadler R A, Scambos T A, 1995. Basal friction of ice stream E, West Antarctica. Journal of Glaciology 41, 247–262.

Macgregor J A, Winebrenner D P, Conway H, Matsuoka K, Mayewski P A, Clow G D, 2007. Modeling englacial radar attenuation at Siple Dome, West Antarctica, using ice chemistry and temperature data. Journal of Geophysical Research: Earth Surface 112, F03008. doi 10.1029/2006JF000717

Machel H G, Krouse H R, Sassen R, 1995. Products and distinguishing criteria of bacterial and thermochemical sulphate reduction. Applied Geochemistry 10, 373–389.

MacKenzie A B, Scott R D, Linsalata P, Miekeley N, 1992. Natural decay series studies of the redox front system in the Poços de Caldas uranium mineralization. Journal of Geochemical Exploration 17, 289–322.

Madigan M T, Martinko J M, 2006. Brock biology of microorganisms. 11th ed. Upper Saddle River, NJ: Pearson Prentice Hall.

Mandl G, Harkness R, 1987. Hydrocarbon migration by hydraulic fracturing. In Jones E, Preston R M F (eds). Deformation of sediments and sedimentary rocks. Geological Society Special Publications 29, 39–53.

Maslin M A, Mikkelsen M, Vilela C, Haq B, 1998. Sea-level and gas-hydrate controlled catastrophic sediment failures of the Amazonas Fan. Geology 26, 1107–1110.

Matsuoka K, 2011. Pitfalls in radar diagnosis of ice-sheet bed conditions: lessons from englacial attenuation models. Geophysical Research Letters, 38. doi: 10.1029/2010GL046205

Matsuoka K, Morse D, Raymond C F, 2010. Estimating englacial radar attenuation using depth profiles of the returned power, central West Antarctica. Journal of Geophysical Research: Earth Surface 115, F02012. doi 10.1029/2009jf001496

Mayborn K R, Lesher C E, 2006. Origin and evolution of the Kangâmiut mafic dyke swarm, West Greenland. Geological Survey of Denmark and Greenland Bulletin 11 , 61–86.

McNutt R H, Frape S K, Fritz P, Jones M G, MacDonald I A, 1990. The ^{87}Sr/^{86}Sr values of Canadian Shield brines and fracture minerals with a lications to groundwater mixing, fracture history, and geochronology. Geochimica et Cosmochimica Acta 54, 205–215.

Meese D A, Gow A J, Alley R B, Zielinski G A, Grootes P M, Ram M, Taylor K C, Mayewski P A, Bolzan J F, 1997. The Greenland Ice Sheet Project 2 depth-age scale: methods and results. Journal of Geophysical Research 102, 26411–26423.

Meier D, 2012. Matrix pore water in crystalline rocks at Olkiluoto, Finland: chemical and transport properties and artefacts induced by drill core sampling. MSc thesis. University of Bern, Switzerland.

Meierbachtol T, Harper J, Humphrey N, 2013. Basal drainage system response to increasing surface melt on the Greenland ice sheet. Science 341, 777–779.

Mernild S H, Liston G E, van den Broeke M R, 2012. Simulated internal storage buildup, release, and runoff from Greenland ice sheet at Kangerlussuaq, West Greenland. Arctic, Antarctic, and Alpine Research 44, 83–94.

Mitchell A C, Brown G H, 2007. Diurnal hydrological–physicochemical controls and sampling methods for minor and trace elements in an Alpine glacial hydrological system. Journal of Hydrology 332, 123–143.

Mikkelsen A B, Hasholt B, Knudsen N T, Nielsen M H, 2013. Jökulhlaups and sediment transport in Watson River, Kangerlussuaq, West Greenland. Hydrology Research 44, 58–67.

Morlighem M, Rignot E, Seroussi H, Larour E, Ben Dhia H, Aubry D, 2010. Spatial patterns of basal drag inferred using control methods from a full-Stokes and simpler models for Pine Island Glacier, West Antarctica. Geophysical Research Letters 37, L14502. doi:10.1029/2010GL043853

Morrison J, Fallick T, Donelly T, Leossen M, St.Jean G, Drimmie R J, 1996. δ^{34}S measurements of standards from several laboratories by continuous flow isotope ratio mass spectrometry. Technical Note TN309, CF-IRMS. Micromass UK, Ltd.

Morrison J T, Brockwell T, Merren T, Fourel F, Phillips A M, 2001. On-line high precision stable hydrogen isotopic analyses on nanoliter water samples. Analytical Chemistry 73, 3570–3575.

Moser H (ed), 1978. Jahresbericht 1977: Institut für Radiohydrometrie. Munich: Gesellschaft für Strahlen- und Umweltforschung. (In German.)

Murray T, 1998. Assessing the paradigm shift: deformable glacier beds. Quaternary Science Reviews 16, 995–1016.

Natural Resources Canada, 2013. CSRS-PPP: On-Line GNSS PPP Post-Processing Service (WWW Document). Availbale at: http://webapp.geod.nrcan.gc.ca/geod/tools-outils/ppp.php [1 October 2013].

Navarro F J, Eisen O, 2009. Ground penetrating radar. In Pellikka P, Rees W G (eds). Remote sensing of glaciers: techniques for topographic, spatial and thematic mapping. London: Taylor & Francis, 195–229.

Nghiem S V, Hall D K, Mote T L, Tedesco M, Albert M R, Keegan K, Shuman C A, DiGirolamo N E, Neuman G, 2012. The extreme melt across the Greenland ice sheet in 2012. Geophysical Research Letters 39, L20502. doi:10.1029/2012GL053611

Nienow P, Sharp M, Willis I, 1998. Seasonal changes in the morphology of the subglacial drainage system, Haut Glacier d'Arolla, Switzerland. Earth Surface Processes and Landforms 23, 825–843.

Nippress S, Rietbrock A, Heath A, 2010. Optimized automatic pickers: application to the ANCORP dataset. Geophysical Journal International 181, 911–925.

Nocedal J, Wright S J, 1999. Numerical optimization. New York: Springer.

NWMO, 2012. Adaptive phased management. Used fuel repository conceptual design and postclosure safety assessment in crystalline rock. Pre-project report NWMO TR-2012-16, Nuclear Waste Management Organization, Canada.

Näslund J-O, Jansson P, Fastook J L, Johnson J, Andersson L, 2005. Detailed spatially distributed geothermal heat-flow data for modeling of basal temperatures and meltwater production beneath the Fennoscandian ice sheet. Annals of Glaciology 40, 95–101.

Osmond J K, Ivanovich M, 1992. Uranium-series mobilization and surface hydrology. In Ivanovich M, Harmon R S (eds). Uranium-series disequilibrium: applications to earth, marine, and environmental sciences. 2nd ed. Oxford: Clarendon, 259–289.

Osmond J K, Cowart J B, Ivanovich M, 1983. Uranium isotopic disequilibrium in groundwater as an indicator of anomalies. The International Journal of Applied Radiation and Isotopes 34, 282–308.

Paananen M, Ruskeeniemi T, 2003. Permafrost at Lupin: interpretation of SAMPO electromagnetic soundings at Lupin. Report YST-117, Geological Survey of Finland.

Palmer S, Shepherd A, Nienow P, Joughin I, 2011. Seasonal speedup of the Greenland Ice Sheet linked to routing of surface water. Earth and Planetary Science Letters, 302, 423–428.

Palmer S J, Dowdeswell J A, Christoffersen P, Young D A, Blankenship D D, Greenbaum J S, Benham T, Bamber J, Siegert M J, 2013. Greenland subglacial lakes detected by radar. Geophysical Research Letters 40, 6154–6159.

Parizek B R, Alley R B, 2004. Implications of increased Greenland surface melt under global-warming scenarios: ice-sheet simulations. Quaternary Science Reviews 23, 1013–1027.

Parkhomenko E I, 1967. Electrical properties of rocks [transl. from Russian and edited by George V. Keller]. New York.

Passchier C W, Trouw R A J, 2005. Microtectonics. 2nd ed. Berlin: Springer.

Pattyn F, 2003. A new three-dimensional higher-order thermomechanical ice sheet model: basic sensitivity, ice stream development, and ice flow across subglacial lakes. Journal of Geophysical Research: Solid Earth 108. doi:10.1029/2002JB002329

Pattyn F, Perichon L, Aschwanden A, Breuer B, de Smedt B, Gagliardini O, Gudmundsson G H, Hindmarsh R, Hubbard A, Johnson J V, Kleiner T, Konovalov Y, Martin C, Payne J, Pollard D, Price C, Rückamp M, Saito F, Souček O, Sugiyama S, Zwinger T, 2008. Benchmark experiments for higher-order and full Stokes ice sheet models (ISMIP-HOM). The Cryosphere Discussions 2, 111–151.

Pedersen K, 2008. Microbiology of Olkiluoto groundwater, 2004–2006. Posiva 2008-02, Posiva Oy, Finland.

Pedersen K, Arlinger J, Edlund J, Eriksson S, Jägevall S, Rabe L, 2010. Microbiology of Olkiluoto and ONKALO groundwater. Results and interpretations, 2008–2009. Posiva Working Report 2010-60, Posiva Oy, Finland.

Pedersen K, Bomberg M, Itävaara M, 2014. Summary report. Microbiology of Olkiluoto and ONKALO groundwater. Posiva 2012-42, Posiva Oy, Finland.

Peltoniemi M, 1988. Maa- ja kallioperän geofysikaaliset tutkimusmenetelmät. Espoo: Otakustantamo. (In Finnish.)

Pere T, 2014. Geological logging of the Greenland Analogue Project drill cores DH-GAP01, 03 and 04. Posiva Working Report 2013-59, Posiva Oy, Finland.

Pérez del Villar L, Bruno J, Campos R, Gómez P, Cózar J S, Garralón A, Buil B, Arcos D, Carretero G, Ruiz Sánchez-Porro J, Hernán H, 2002. The uranium ore from Mina Fe (Salamanca, Spain) as a natural analogue of processes in a spent fuel repository. Chemical Geology 190, 395–415.

Peters M E, Blankenship D D, Morse D L, 2005. Analysis techniques for coherent airborne radar sounding: application to West Antarctic ice streams. Journal of Geophysical Research: Solid Earth 110. doi:10.1029/2004JB003222

Phillips T P, 2010. The characterization of the cryo-hydrologic system of the Sermeq Avannarleq Glacier in Greenland and its influence on ice temperature. PhD thesis. University of Colorado at Boulder, Boulder, Colorado.

Phillips T, Rajaram H, Steffen K, 2010. Cryohydrologic warming: a potential mechanism for rapid thermal response of ice sheets. Geophysical Research Letters 37. doi:10.1029/2010GL044397

Phillips T, Colgan W, Rajaram H, Steffen K, 2013. Evaluation of cryo-hydrologic warming as an explanation for increased ice velocities near the equilibrium line, Southwest Greenland. Geophysical Research Letters, Earth Surface 118, 1241-1256.

Pidwirny M, 2006. Periglacial processes and landforms. In Fundamentals of physical geography. 2nd ed. Available at: http://www.physicalgeography.net/fundamentals/10ag.html

Pitkäranta R, 2009. Pre-late Weichselian podzol soil, permafrost features and lithostratigraphy at Penttilänkangas, western Finland. Bulletin of the Geological Society of Finland 81, 53–74.

Pitkänen P, Luukonen A, Ruotsalainen P, Leino-Forsman H, Vuorinen U, 1999. Geochemical modelling of groundwater evolution and residence time at the Olkiluoto site. Posiva 98–10, Posiva Oy, Finland.

Posiva, 2012. Safety case for the disposal of spent nuclear fuel at Olkiluoto. Formulation of radionuclide release scenarios 2012. Posiva 2012-08, Posiva Oy, Finland.

Price S F, Payne A J, Howat I M, Smith B E, 2011. Committed sea-level rise for the next century from Greenland ice sheet dynamics during the past decade. Proceedings of the National Academy of Sciences of the United States of America 108, 8978–8983.

Pritchard H D, Arthern R J, Vaughan D G, Edwards L A, 2009. Extensive dynamic thinning on the margins of the Greenland and Antarctic ice sheets. Nature 461, 971–975.

Pöllänen J, Heikkinen P, Lehtinen A, 2012. Difference flow measurements in Greenland, borehole DH-GAP04 in July 2011. Posiva Working Report 2012-13, Posiva Oy, Finland.

Raiswell R, 1984. Chemical models of solute acquisition in glacial melt waters. Journal of Glaciology 30, 49–57.

Ram M, Koenig G, 1997. Continuous dust concentration profile of pre-Holocene ice from the Greenland Ice Sheet Project 2 ice core: dust stadials, interstadials, and the Eemian. Journal of Geophysical Research 103, 26641–26648.

Rees C E, Holt B D, 1991. The isotopic analysis of sulphur and oxygen. In Krouse H R, Grinenko A (eds). Stable isotopes in the assessment of natural and anthropogenic sulphur in the environment, SCOPE. John Wiley & Sons, 43–64.

Rignot E, Kanagaratnam P, 2006. Changes in the velocity structure of the Greenland ice sheet. Science 311, 986–990.

Rinne K, 2010. User manual for U-series MC-ICPMS dating. Geological Survey of Finland.

Rippin D M, 2013. Bed roughness beneath the Greenland ice sheet. Journal of Glaciology 59, 724–732.

Rippin D M, Vaughan D G, Corr H F J, 2011. The basal roughness of Pine Island Glacier, West Antarctica. Journal of Glaciology 57, 67–76.

Rosdahl A, Pedersen K, Hallbeck L, Wallin B, 2011. Investigation of sulphide in core drilled boreholes KLX06, KAS03 and KAS09 at Laxemar and Äspö. Chemical-, microbiological- and dissolved gas data from groundwater in four borehole sections. SKB P-10-18, Svensk Kärnbränslehantering AB.

Ruskeeniemi T, Paananen M, Ahonen L, Kaija J, Kuivamäki A, Frape S, Moren L, Degnan P, 2002. Permafrost at Lupin: Report of Phase 1. Report YST-112, Geological Survey of Finland, Nuclear Waste Disposal Research.

Russell A J, 2007. Controls on sedimentology of an ice-contact jökulhlaup-dominated delta, Kangerlussuaq, west Greenland. Sedimentary Geology 193, 131–148.

Russell A J, Aitken J F, de Jong C, 1990. Observations on the drainage of an ice-dammed lake in West Greenland. Journal of Glaciology 36, 72–74.

Russell A J, Carrivick J L, Ingeman-Nielsen T, Yde J C, Williams M, 2011. A new cycle of jökulhlaups at Russel Glaicier, Kangerlussuaq, West Greenland. Journal of Glaciology 57, 238–246.

Röthlisberger H, 1972. Water pressure in intra- and subglacial channels. Journal of Glaciology 11, 177–203.

Sambridge M, Kennett B L N, 1986. A novel method of hypocenter location. Geophysical Journal International 87, 679–697.

Savin S M, 1980. Oxygen and hydrogen isotope effects in low temperature mineral–water interactions. In Fritz P, Fontes J C (eds). Handbook of environmental isotope geochmiestry. Amsterdam: Elsevier, 283–328.

Schanze T, 1995. Sinc interpolation of discrete periodic signals. Signal Processing, IEEE Transactions 43, 1502–1503.

Scholz C H, 2002. The mechanics of earthquakes and faulting. 2nd ed. Cambridge: Cambridge University Press.

Scholz H, Baumann M, 1997. An “open system pingo” near Kangerlussuaq (Søndre Strømfjord), West Greenland. Geology of Greenland Survey Bulletin 176, 104–108.

Schoof C, 2010. Ice-sheet acceleration driven by melt supply variability. Nature 468, 803–806.

Schuenemann K C, Cassano J J, 2010. Changes in synoptic weather patterns and Greenland precipitation in the 20th and 21st centuries: 2. Analysis of 21st century atmospheric changes using self-organizing maps. Journal of Geophysical Research 115, D05108. doi:10.1029/2009JD011706

Scott W J, Sellmann P V, Hunter J A, 1990. Geophysics in the study of permafrost. In Ward S H (ed). Geotechnical and environmental geophysics. Vol 1. Tulsa, OK: Society of Exploration Geophysicists, 355–384.

Selker J S, Thévenaz L, Huwald H, Mallet A, Luxemburg W, van de Giesen N, Stejskal M, Zeman J, Westhoff M, Parlange M B, 2006. Distributed fiber-optic temperature sensing for hydrologic systems. Water Resources Research 42, W12202. doi:10.1029/2006WR005326

Selmes N, Murray T, James T, 2011. Fast draining lakes on the Greenland Ice Sheet. Geophysical Research Letters 38, L15501. doi:10.1029/2011GL047872

Selmes N, Murray T, James T D, 2013. Characterizing supraglacial lake drainage and freezing on the Greenland Ice Sheet. The Cryosphere Discussions 7, 475–505.

Shapiro N M, Ritzwoller M H, 2004. Inferring surface heat flux distributions guided by a global seismic model: particular application to Antarctica. Earth and Planetary Science Letters 223, 213–224.

Shepherd A, Hubbard A, Nienow P, King M, McMillan M, Joughin I, 2009. Greenland ice sheet motion coupled with daily melting in late summer. Geophysical Research Letters 36. doi: 10.1029/2008GL035758

Shouakar-Stash O, Drimmie R J, Frape S K, 2005a. Determination of inorganic chlorine stable isotopes by continuous flow isotope ratio mass spectrometry. Rapid Communication in Mass Spectrometry 19, 121–127.

Shouakar-Stash O, Frape S K, Drimmie R J, 2005b. Determination of bromine stable isotopes using continuous-flow isotope ratio mass spectrometry. Analytical Chemistry 77, 4027–4033.

Shreve R L, 1972. Movement of water in glaciers. Journal of Glaciology 11, 205–214.

Siegert M J, Taylor J, Payne A J, 2005. Spectral roughness of subglacial topography and implications for former ice-sheet dynamics in East Antarctica. Global and Planetary Change 45, 249–263.

SKB, 2010a. Climate and climate-related issues for the safety assessment SR-Site. SKB TR 10-49, Svensk Kärnbränslehantering AB.

SKB, 2010b. The Greenland analogue project. Yearly report 2009. SKB R-10-59, Svensk Kärnbränslehantering AB.

SKB, 2011. Long term safety for the final repository for spent nuclear fuel at Forsmark. Main report of the SR-Site project. SKB TR-11-01, Svensk Kärnbränslehantering AB.

Smeets C J P P, van den Broeke M R, 2008. Temporal and spatial variation of momentum roughness length in the ablation zone of the Greenland ice sheet. Bounder-Layer Meteorology 128, 315–338.

Smellie J, Tullborg E-L, Nilsson A-C, Gimeno M, Sandström B, Waber N, Gascoyne M, 2008. Explorative analysis of major components and isotopes. SDM-Site Forsmark. SKB R-08-84, Svensk Kärnbränslehantering AB.

Soininen H, Jokinen T, 1991. SAMPO, a new wide-band electromagnetic system. In Technical programme and abstracts, EAEG 53rd meeting and technical exhibition, Florence, Italy, 26–30 May 1991, 366–367.

Sole A J, Mair D W F, Nienow P W, Bartholomew I D, King M A, Burke M J, Joughin I, 2011. Seasonal speedup of a Greenland marine-terminating outlet glacier forced by surface melt-induced changes in subglacial hydrology. Journal of Geophysical Research 116, F03014. doi:10.1029/2010JF001948

Sole A, Nienow P, Bartholomew I, Mair D, Cowton T, Tedstone A, King M A, 2013. Winter motion mediates dynamic response of the Greenland Ice Sheet to warmer summers. Geophysical Research Letters 40, 3940–3944.

Spiessl S M, MacQuarrie K T B, Mayer K U, 2008. Identification of key parameters controlling dissolved oxygen migration and attenuation in fractured crystalline rocks. Journal of Contaminant Hydrology 95, 141–153.

Starinsky A, Katz A, 2003. The formation of natural cryogenic brines. Geochimica et Cosmochimica Acta 67, 1475–1484.

Steger H F, Bowman W S, 1980. Reference uranium-thorium ore DL-1a, certificate of analysis. CANMET Report 80-10E, Energy, Mines and Resources Canada.

Stenberg L, Håkansson N, 2007. Oskarshamn site investigation. Revision of borehole deviation measurements in Oskarshamn. SKB P-07-55, Svensk Kärnbränslehantering AB.

Stephens M B, Fox A, La Pointe P, Simeonov A, Isaksson H, Hermanson J, Öhman J, 2007. Geology Forsmark. Site descriptive modelling Forsmark stage 2.2. SKB R-07-45, Svensk Kärnbränslehantering AB.

Stibal M, Šabacká M, Žárský J, 2012. Biological processes on glacier and ice sheet surfaces. Nature Geoscience 5, 771–774.

Stolt R H, 1978. Migration by Fourier transform. Geophysics 43, 23–48.

Storms J E A, de Winter I L, Overeem I, Drijkoningen G G, Lykke-Andersen H, 2012. The Holocene sedimentary history of the Kangerlussuaq Fjord-valley fill, West Greenland. Quaternary Science Reviews 35, 29–50.

Stotler R L, Frape S K, Ruskeeniemi T, Ahonen L, Onstott T C, Hobbs M Y, 2009. Hydrogeochemistry of groundwaters in and below the base of thick permafrost at Lupin, Nunavut, Canada. Journal of Hydrology 373, 80–95.

Stotler R L, Frape S K, Ahonen L, Clark I, Greene S, Hobbs M, Johnson E, Lemieux J-M, Peltier R, Pratt L, Ruskeeniemi T, Sudicky E, Tarasov L, 2010. Origin and stability of a permafrost methane hydrate occurrence in the Canadian Shield. Earth and Planetary Science Letters 296, 384–394.

Stotler R L, Frape S K, Ruskeeniemi T, Pitkänen P, Blowes D W, 2012. The interglacial–glacial cycle and geochemical evolution of Canadian and Fennoscandian Shield groundwaters. Geochimica et Cosmochimica Acta 76, 45–67.

Suksi J, 2001. Natural uranium as a tracer in radionuclide geosphere transport studies. PhD thesis. University of Helsinki.

Suksi J, Rasilainen K, 2002. Isotope fractionation of U in rocks reflecting redox conditions around a groundwater flow route. In Hart K P, Lumpkin G R (eds). Scientific basis for nuclear waste management XXIV: symposium held in Sydney, Australia, 27–31 August 2000. Warrendale, PA: Materials Research Society. (Materials Research Society Symposium Proceedings 663), 961–969.

Sundal A V, Shepherd A, Nienow P, Hanna E, Palmer S, Huybrechts P, 2011. Melt-induced speed-up of Greenland ice sheet offset by efficient subglacial drainage. Nature 469, 521–524.

Tarasov L, Peltier R W, 2002. Greenland glacial history and local geodynamic consequences. Geophysical Journal International 150, 198–229.

Taylor C B, 1977. Tritium enrichment of environmental waters by electrolysis: development of cathodes exhibiting high isotopic separation and precise measurements of tritium enrichment factors. In Povinec P, Usačev S (eds). Low-radioactivity measurements and applications. Bratislava: Slovenski Pedagogicke Nakladatelstvo, 131–140.

Taylor J, Siegert M J, Payne A J, Hubbard B, 2004. Regional-scale bed roughness beneath ice masses: measurement and analysis. Computers & Geosciences 30, 899–908.

Taylor P L, 1984. A hot water drill for temperate ice. CRREL Special Report 84–34, US Army Cold Regions Research and Engineering Laboratory, 105–117.

Tedesco M, Fettweis X, Alexander P, Green G, Datta T, 2013. MAR Greenland Outputs.

1958–2013 ver. 3.2, CCNY Digital Archive. Available at: https://www.aoncadis.org/dataset/CPL_MAR.html.

Ten Brink N W, 1974. Glacio-isostacy: new data from west Greenland and geophysical implications. Geological Society of America Bulletin 85, 219–228.

Ten Brink N W, 1975. Holocene history of the Greenland Ice Sheet based on radiocarbon-dated moraines in West Greenland. Bulletin Grønlands Geologiske Undersøgelse 113.

Ten Brink N, Weidick A, 1974. Greenland Ice Sheet history since the last deglaciation. Quaternary Research 4, 429–440.

Terzaghi R D, 1965. Sources of errors in joint surveys. Géotechnique 15, 287–304.

Thiem G, 1906. Hydrologische methoden. Leipzig: Gebhardt. (In German.)

Thomas R, Csatho B, Davis C, Kim C, Krabill W, Manizade, McConnell S J, Sonntag J, 2001. Mass balance of higher-elevation parts of the Greenland ice sheet. Journal of Geophysical Research 106, 33707–33716.

Thomsen H H, 1988. Mass balance, ice velocity and ice temperature at the Inland Ice margin northeast of Jakobshavn, central West Greenland. Rapport Grønlands Geologiske Undersøgelse 140, 111–114.

Thomsen H H, Braithwaite R J, 1987. Use of remote-sensing data in modelling run-off from the greenland ice sheet. Annals of Glaciology, 9, 215–217.

Thomsen H H, Olesen O B, Braithwaite T J, Bøggild C E, 1991. Ice drilling and mass balance and basal water pressure at Pakitsoq, Jakobshavn, central West Greenland. Rapport Grønlands Geologiske Undersøgelse 152, 80–84.

Toran L, Harris R F, 1989. Interpretation of sulfur and oxygen isotopes in biological and abiological sulfide oxidation. Geochimica et Cosmochimica Acta 53, 2341–2348.

Tranter M, Sharp M J, Lamb H R, Brown G H, Hubbard B P, Willis I C, 2002. Geochemical weathering at the bed of Haut Glacier d'Arolla, Switzerland – a new model. Hydrological Processes 16, 959–993.

Truffer M, Harrison W D, March R S, 2005. Correspondence: Record negative glacier balances and low velocities during the 2004 heatwave in Alaska, USA: implications for the interpretation of observations by Zwally and others in Greenland. Journal of Glaciology 51, 663–664.

Tulaczyk S, Kamb W B, Engelhardt H F, 2000. Basal mechanics of Ice Stream B, west Antarctica 2. Undrained plastic bed model. Journal of Geophysical Research: Solid Earth 105, 483–494.

Tullborg E-L, Smellie J A T, MacKenzie A B, 2003. The use of natural uranium decay series studies in support of understanding redox conditions at potential radioactive waste disposal sites. In Oversby V M, Werme L O (eds). Scientific basis for nuclear waste management XXVII: symposium held in Kalmar, Sweden, 15–19 June 2003. Warrendale, PA: Materials Research Society. (Materials Research Society Symposium Proceedings 807), 571–576.

Tullborg E-L, Drake H, Sandström B, 2008. Palaeohydrogeology: a methodology based on fracture mineral studies. Applied Geochemistry 23, 1881–1897.

Tyler S W, Selker J S, Hausner M B, Hatch C E, Torgersen T, Thodal C E, Schladow S G, 2009. Environmental temperature sensing using Raman spectra DTS fiber-optic methods. Water Resources Research 45. doi:10.1029/2008WR007052

Vaittinen T, Ahokas H, Komulainen J, Nummela J, Pentti E, Turku J, Karvonen T, Aro S, 2014. Results of monitoring at Olkiluoto in 2013. Hydrology and hydrogeology. Posiva Working Report 2014-43, Posiva Oy, Finland.

van Angelen J H, Lenaerts J T M, Lhermitte S L, Fettweis X, Kuipers Munneke P, van den Broeke M R, van Meijgaard E, Smeets C J P P, 2012. Sensitivity of Greenland Ice Sheet surface mass balance to surfacealbedo parameterization: a study with a regional climate model. The Cryosphere 6, 1175–1186.

van As D, 2011. Warming, glacier melt and surface energy budget from weather station observations in the Melville Bay region of northwest Greenland. Journal of Glaciology 57, 208–220.

van As D, Hubbard A L, Hasholt B, Mikkelsen A B, van den Broeke M R, Fausto R S, 2012. Large surface meltwater discharge from the Kangerlussuaq sector of the Greenland ice sheet during the record-warm year 2010 explained by detailed energy balance observations. The Cryosphere 6, 199–209.

van As D, Fausto R S, Colgan W T, Box J E, PROMICE project team, 2013. Darkening of the Greenland ice sheet due to the melt-albedo feedback observed at PROMICE weather stations. Geological Survey of Denmark and Greenland Bulletin 28, 69–72.

van den Broeke M R, Gallée H, 1996. Observation and simulation of barrier winds at the western margin of the Greenland ice sheet. Quarterly Journal of the Royal Meteorological Society 122, 1365–1383.

van den Broeke M R, van As D, Reijmer C H, van de Wal R S W, 2004. Assessing and improving the quality of unattended radiation observations in Antarctica. Journal of Atmospheric and Oceanic Technology 21, 1417–1431.

van den Broeke M R, Bamber J, Lenaerts J, Rignot E, 2011. Ice sheets and sea level: thinking outside the box. Surveys of Geophysics, proceedings of the ISSI workshop on the Earth's Cryosphere and Sea Level Change, Bern, Switzerland, 22–26 March 2011.

van der Veen C J, 2001. Greenland ice sheet response to external forcing. Journal of Geophysical Research 106, 34047–34058.

van der Veen C J, 2007. Fracture propagation as means of rapidly transferring surface meltwater to the base of glaciers. Geophysical Research Letters 34. doi:10.1029/2006gl028385

van de Wal R S W, Boot W, van der Broeke M R, Smeets C J P P, Reijmer C H, Donker J J A, Oerlemans J, 2008. Large and rapid melt-induced velocity changes in the ablation zone of the Greenland Ice Sheet. Science 321, 111–113.

van de Wal R S W, Boot W, Smeets C J P P, Snellen H, van den Broeke M R, Oerlemans J, 2012. Twenty-one years of mass balance observations along the K-transect, West Greenland. Earth System Science Data 4, 31–35.

van de Wal R S W, Smeets C J P P, Boot W, Stoffelen M, van Kampen R, Doyle S H, Wilhelms F, van den Broeke M R, Reijmer C H, Oerlemans J, Hubbard A, 2015. Self-regulation of ice flow varies across the ablation area in south-west Greenland. The Cryosphere 9, 603–611.

van Everdingen R O (ed), 1998. Multi-language glossary of permafrost and related ground-ice terms. Boulder, CO: National Snow and Ice Data Center/World Data Center for Glaciology.

van Gool J A M, Connelly L N, Marker M, Mengel F C, 2002. The Nagssugtoqidian orogen of West Greenland: tectonic evolution and regional correlation from a West Greenland perspective. Canadian Journal of Earth Sciences 39, 665–686.

van Tatenhove F G M, Olesen O B, 1994. Ground temperature and related permafrost characteristics in West Greenland. Permafrost and Periglacial Processes 5, 199–215.

van Tatenhove F G M, van der Meer J J M, Huybrechts P, 1995. Glacial geological/geomorphological research in west Greenland used to test an ice sheet model. Quaternary Research 44, 317–327.

van Tatenhove F G M, van der Meer J J M, Koster E A, 1996. Implications for deglaciation chronology from new AMS age determinations in central west Greenland. Quaternary Research 45, 245–253.

Ventura M, Canchaya C, Tauch A, Chandra G, Fitzgerald G F, Chater K F, van Sinderen D 2007. Genomics of Actinobacteria: tracing the evolutionary history of an ancient phylum. Microbiology and Molecular Biology Reviews 71, 495–548.

Vaughan D G G, Marshall J, Connolley W M, Parkinson C, Mulvaney R, Hodgson D A, King J C, Pudsey C J, Turner J, 2003. Recent rapid regional climate warming on the Antarctic Peninsula. Climate Change 60, 243–274.

Vidstrand P, Follin S, Zugec N, 2010. Groundwater flow modelling of periods with periglacial and glacial climate conditions – Laxemar. SKB R-09-25, Svensk Kärnbränslehantering AB.

Vizcaíno M, Mikolajewicz U, Jungclaus J, Schurgers G, 2010. Climate modification by future ice sheet changes and consequences for ice sheet mass balance. Climate Dynamics 34, 301–324.

Waber H N, Smellie J A T, 2008. Characterisation of pore water in crystalline rocks. Applied Geochemistry 23, 1834–1861.

Wahlgren C-H, Curtis P, Hermanson J, Forssberg O, Öhman J, Fox A, La Pointe P, Drake H, Triumf C-A, Mattsson H, Thunehed H, Juhlin C, 2008. Geology Laxemar. Site descriptive modelling, SDM-Site Laxemar. SKB R-08-54, Svensk Kärnbränslehantering AB.

Wahr J, van Dam T, Larson K, Francis O, 2001. Geodetic measurements in Greenland and their implications. Journal of Geophysical Research: Atmospheres 106, 16567–16581.

Waller R I, Tuckwell G W, 2005. Glacier–permafrost interaction and glaciotectonic landform generation at the margin of the Leverett Glacier, West Greenland. In Harris C, Murton J B (eds). Cryospheric systems: glaciers and permafrost. London: Geological Society. (Geological Society Special publications 242), 39–50.

Weaver J, 2003. Assessment of sub-permafrost groundwater conditions at the Red Dog Mine, Alaska. In Permafrost: proceedings of the Eighth International Conference on Permafrost, Zurich, Switzerland, 21–25 July 2003. Lisse: A. A. Balkema, 1223–1228.

Weertman J, 1968. Comparison between measured and theoretical temperature profiles of the Camp Century, Greenland, borehole. Journal of Geophysical Research 73, 2691–2700.

Weertman J, 1983. Creep deformation of ice. Annual Review of Earth and Planetary Science Letters 11, 215-240.

Weidick A, 1968. Observations on some Holocene glacier fluctuations in West Greenland. Meddelelser om Grønland 165.

Weidick A, 1993. Neoglacial change of ice cover and the related response of the Earth's crust in west Greenland. Rapport Grønlands Geologiske Undersøgelse 159, 121–126.

Weidick A, 1996. Late Holocene and historical changes of glacier cover and related relative sea level in Greenland. Zeitschrift fur Gletscherkunde und Glazialgeologie 32, 217–224.

Weis M, Greve R, Hutter K, 1999. Theory of shallow ice shelves. Continuum Mechanics and Thermodynamics 11, 15–50.

White D, Hinzman L, Alessa L, Cassano J, Chambers M, Falkner K, Francis J, Gutowski W J, Holland M, Holmes R, Huntington H, Kane D, Kliskey A, Lee C, McClelland J, Peterson B, Ru T S, Straneo F, Steele M, Woodgate R, Yang D, Yoshikawa K, Zhang T, 2007. The arctic freshwater system: changes and impacts. Journal of Geophysical Research: Biogeosciences 112, G04S54. doi:10.1029/ 2006JG000353

Willemse N W, Koster E A, Hoogakker B, van Tatenhove F G M, 2003. A continuous record of Holocene Aeolian activity in West Greenland. Quaternary Research 59, 322–334.

Wilson R W, Klint K E S, van Gool J A M, McCaffrey K J W, Holdsworth R E, Chalmers J A, 2006. Faults and fractures in central West Greenland: onshore expression of continental break-up and sea-floor spreading in the Labrador – Baffin Bay Sea. Geological Survey of Denmark and Greenland Bulletin 11, 185–204.

Winebrenner D P, Smith B E, Catania G A, Conway H B, Raymond C F, 2003. Radio-frequency attenuation beneth Siple Dome, West Antarctica, from wide-angle and profiling radar observations. Annals of Glaciology 37, 226–232.

Yilmaz Ö, 2001. Seismic data analysis: processing, inversion, and interpretation of seismic data. 2nd ed. Tulsa, OK: Society of Exploration Geophysicists.

Zhang M, Frape S K, 2002. Permafrost: evolution of shield groundwater compositions during freezing. Report 06819-REP-01200-10098-R00, Ontario Power Generation, Nuclear Waste Management Division, Canada.

Zhou H-W, 1994. Rapid three-dimensional hypocentral determination using a master station method. Journal of Geophysical Research: Solid Earth 99, 15439–15455.

Zwally H J, Abdalati W, Herring T, Larson K, Saba J, Steffen K, 2002. Surface melt-induced of Greenland acceleration ice-sheet flow. Science 297, 218–222.

Zwally H J, Li J, Brenner A C, Beckley M, Cornejo H G, DiMarzio J, Giovinetto M B, Neumann T A, Robbins J, Saba J L, Yl D, Wang W, 2013. Greenland ice sheet mass balance: distribution of increased mass loss with climate warming; 2003–07 versus 1992–2002. Journal of Glaciology 57, 88–102.

Öhberg A, 2006. Investigation equipment and methods used by Posiva. Posiva Working Report 2006-81, Posiva Oy, Finland.

Appendix A

Measured variables from automatic weather stations KAN_L, KAN_M and KAN_U, respectively.

Dirk van As, Geological Survey of Greenland and Denmark.

KAN_L

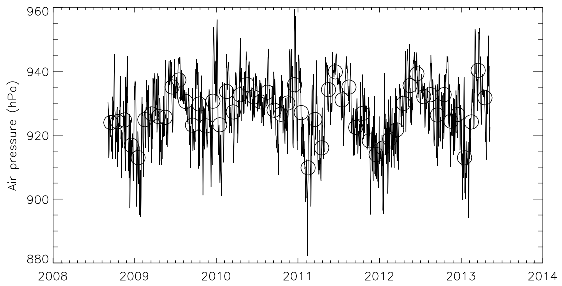

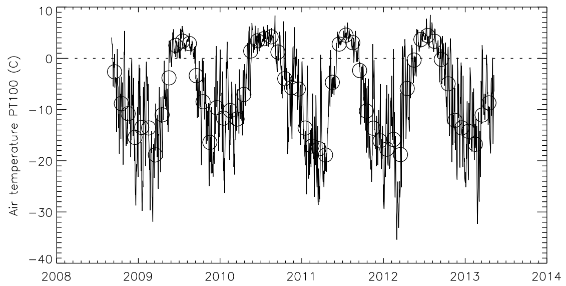

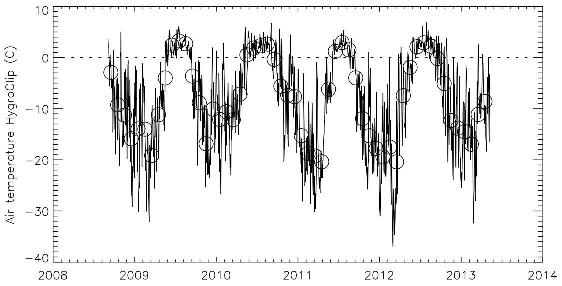

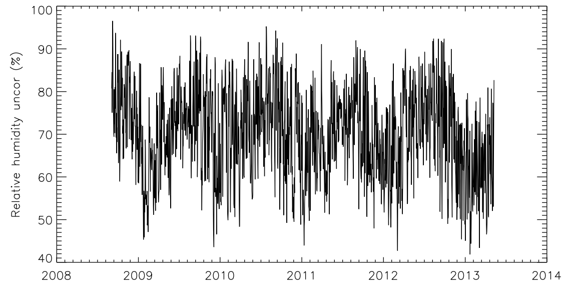

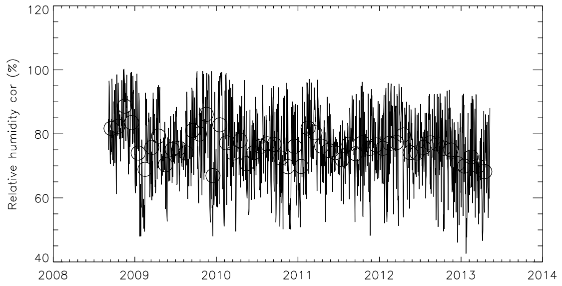

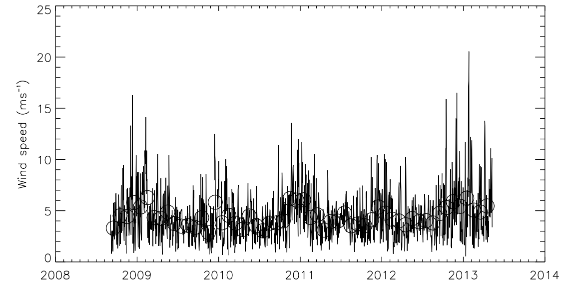

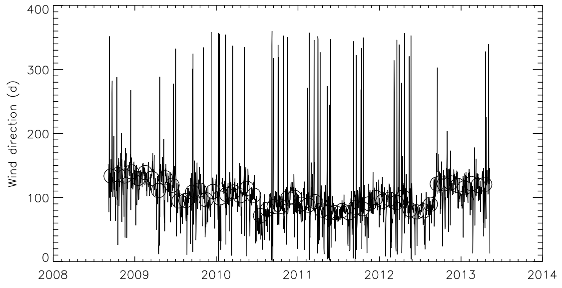

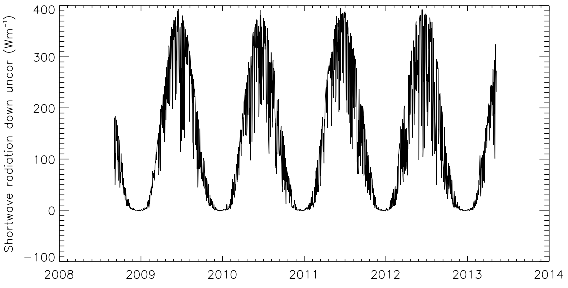

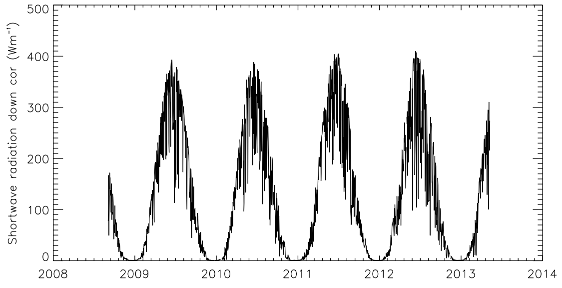

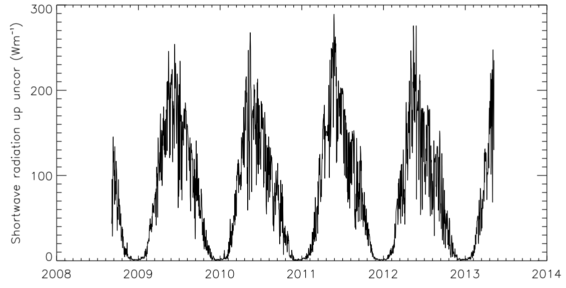

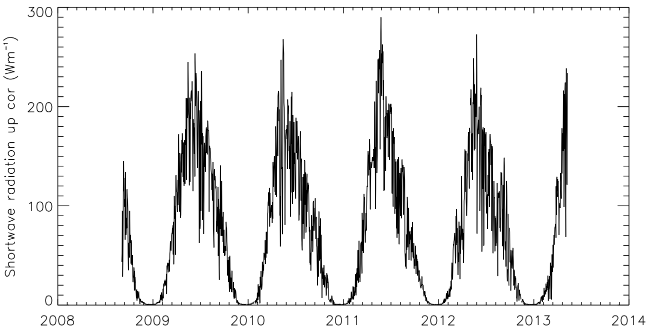
Shortwave radiation up cor (Wm⁻¹)
0
100
200
300
2008
2009
2010
2011
2012
2013
2014

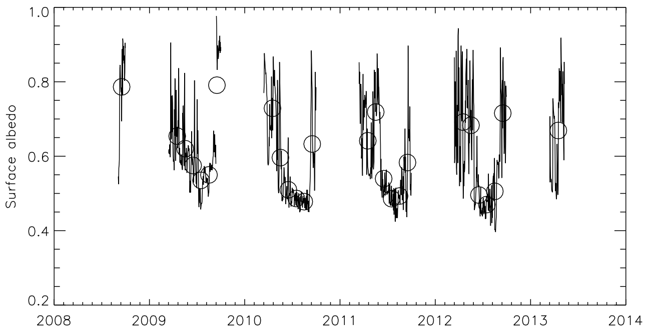
Surface albedo
0.2
0.4
0.6
0.8
1.0
2008
2009
2010
2011
2012
2013
2014

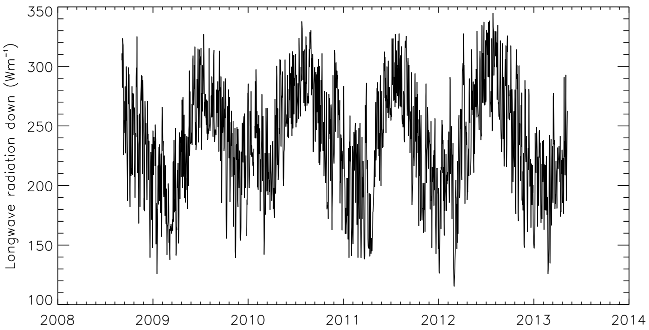
Longwave radiation down (Wm⁻¹)
100
150
200
250
300
350
2008
2009
2010
2011
2012
2013
2014

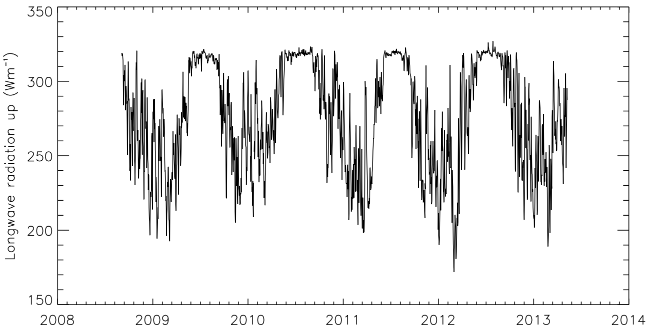
Longwave radiation up (Wm⁻¹)
150
200
250
300
350
2008
2009
2010
2011
2012
2013
2014

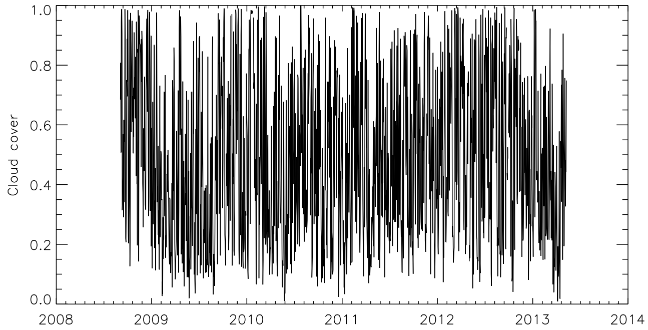
Cloud cover
0.0
0.2
0.4
0.6
0.8
1.0
2008
2009
2010
2011
2012
2013
2014

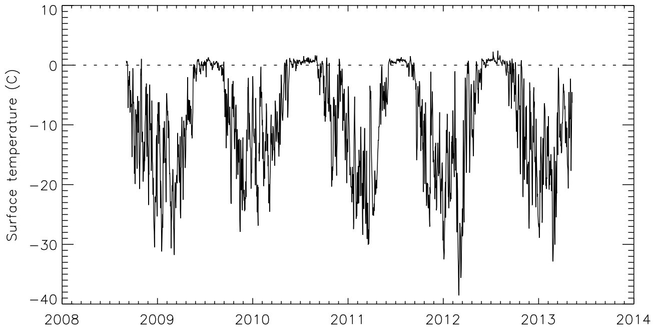
Surface temperature (C)
−40
−30
−20
−10
0
10
2008
2009
2010
2011
2012
2013
2014

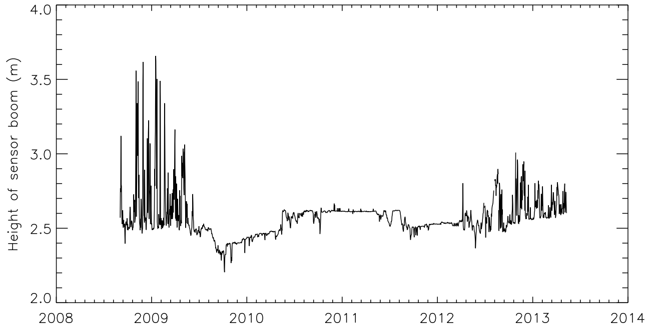
Height of sensor boom (m)
2.0
2.5
3.0
3.5
4.0
2008
2009
2010
2011
2012
2013
2014

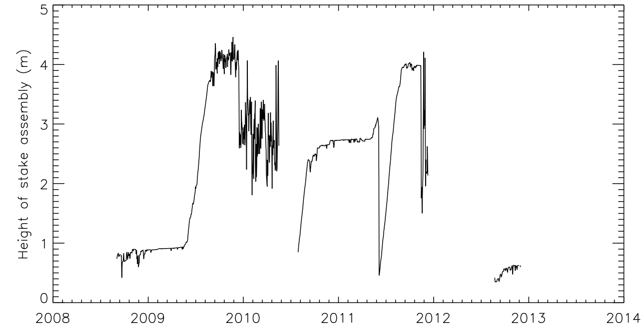
Height of stake assembly (m)
0
1
2
3
4
5
2008
2009
2010
2011
2012
2013
2014

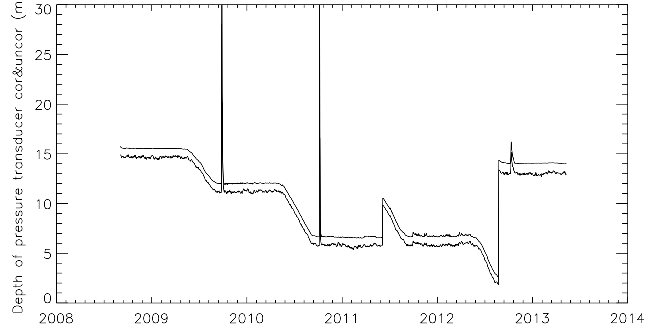
Depth of pressure transducer cor&uncor (m)
0
5
10
15
20
25
30
2008
2009
2010
2011
2012
2013
2014

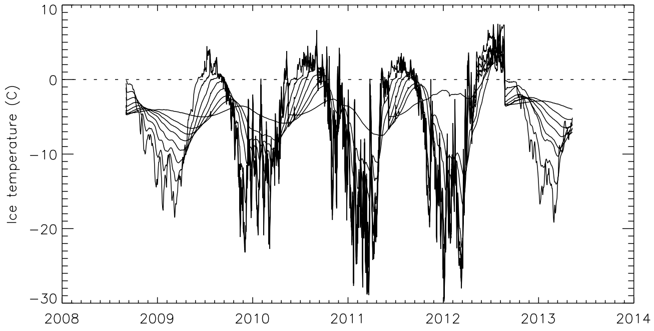
Ice temperature (C)
−30
−20
−10
0
10
2008
2009
2010
2011
2012
2013
2014

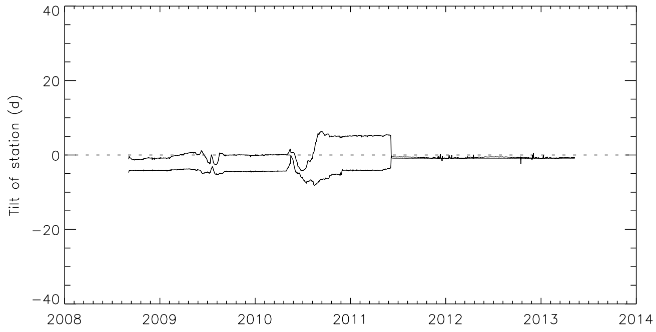
Tilt of station (d)
40
20
0
−20
−40
2008
2009
2010
2011
2012
2013
2014

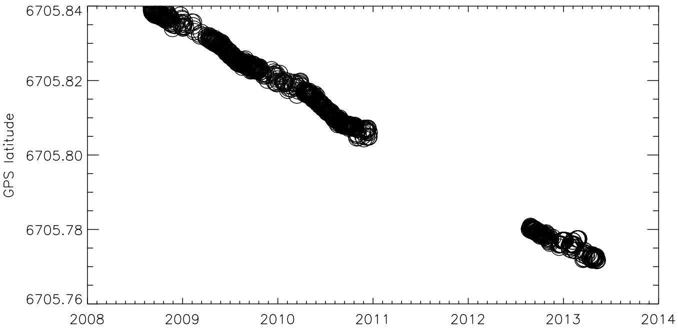
GPS latitude
6705.84
6705.82
6705.80
6705.78
6705.76
2008
2009
2010
2011
2012
2013
2014

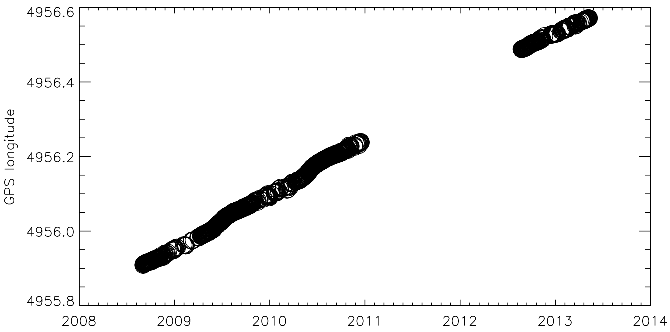
GPS longitude
4956.6
4956.4
4956.2
4956.0
4955.8
2008
2009
2010
2011
2012
2013
2014

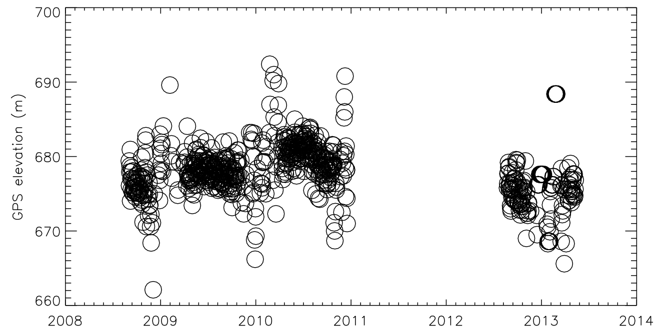
GPS elevation (m)
700
690
680
670
660
2008
2009
2010
2011
2012
2013
2014

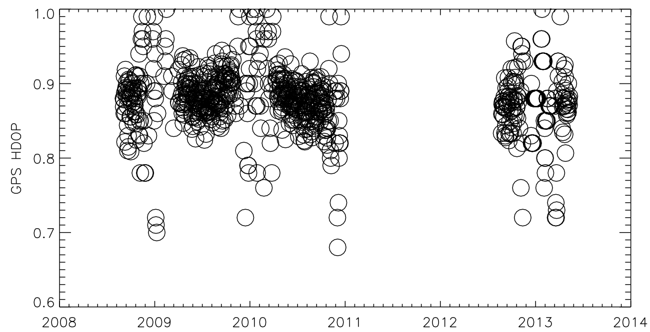
GPS HDOP
1.0
0.9
0.8
0.7
0.6
2008
2009
2010
2011
2012
2013
2014

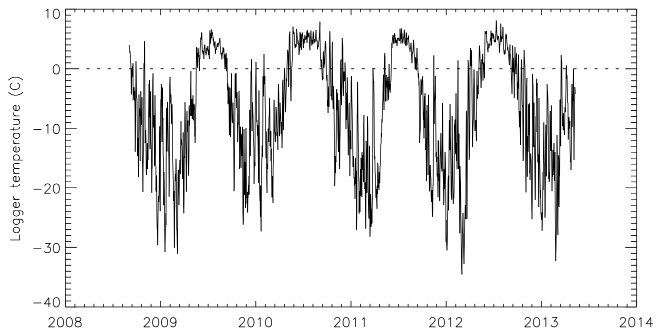
Logger temperature (C)
10
0
−10
−20
−30
−40
2008
2009
2010
2011
2012
2013
2014

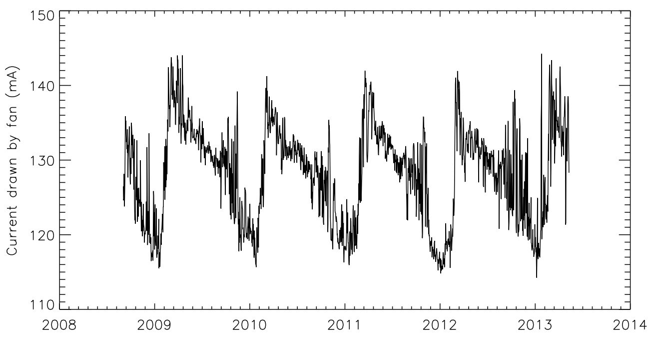
Current drawn by fan (mA)
150
140
130
120
110
2008
2009
2010
2011
2012
2013
2014

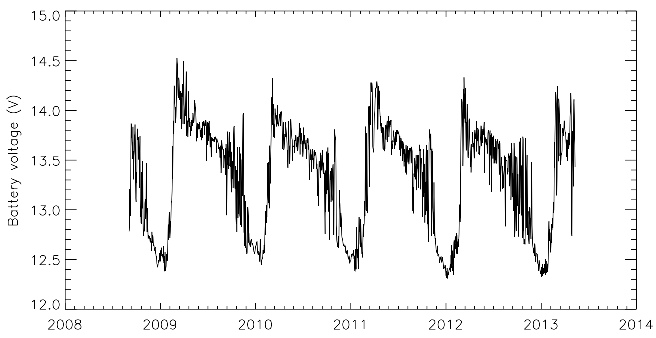
Battery voltage (V)
15.0
14.5
14.0
13.5
13.0
12.5
12.0
2008
2009
2010
2011
2012
2013
2014

KAN_M

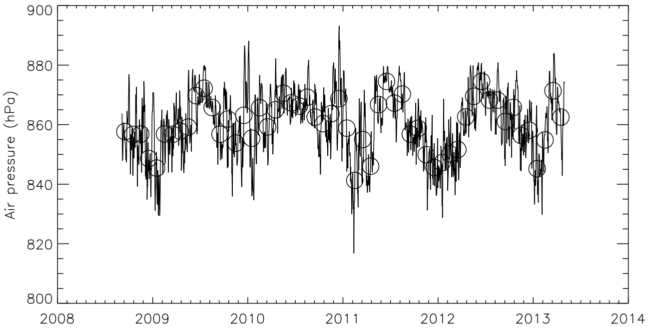
Air pressure (hPa)
800
820
840
860
880
900
2008
2009
2010
2011
2012
2013
2014

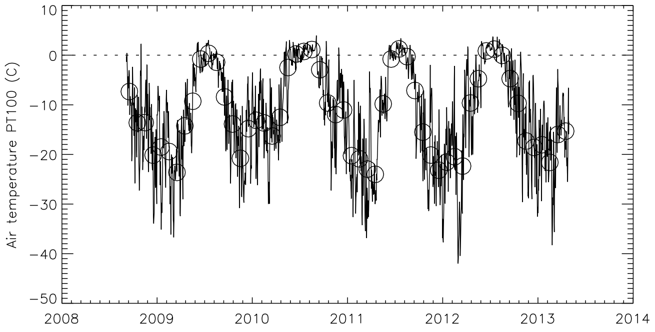
Air temperature PT100 (C)
−50
−40
−30
−20
−10
0
10
2008
2009
2010
2011
2012
2013
2014

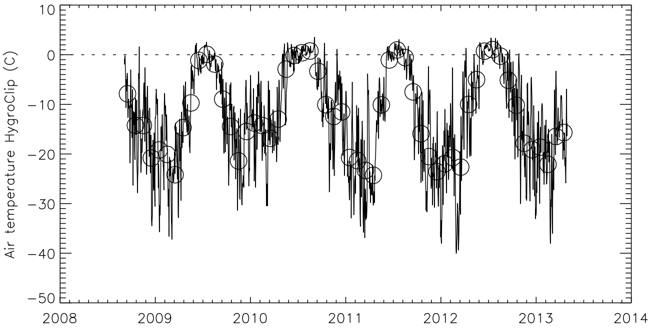
Air temperature HygroClip (C)
−50
−40
−30
−20
−10
0
10
2008
2009
2010
2011
2012
2013
2014

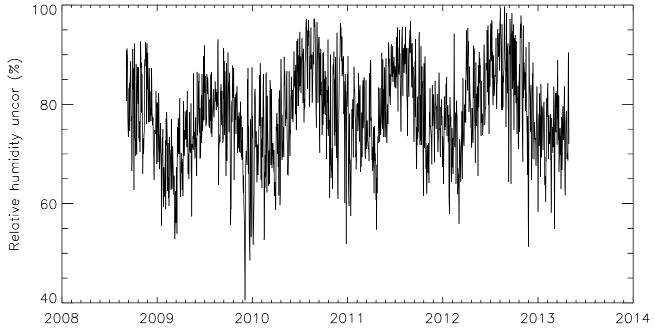
Relative humidity uncor (%)
40
60
80
100
2008
2009
2010
2011
2012
2013
2014

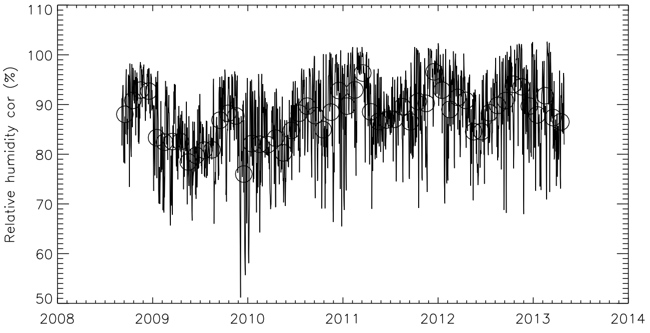
Relative humidity cor (%)
50
60
70
80
90
100
110
2008
2009
2010
2011
2012
2013
2014

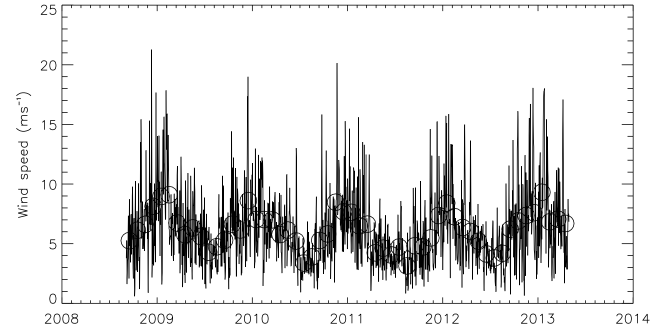
Wind speed (ms^{-1})
0
5
10
15
20
25
2008
2009
2010
2011
2012
2013
2014

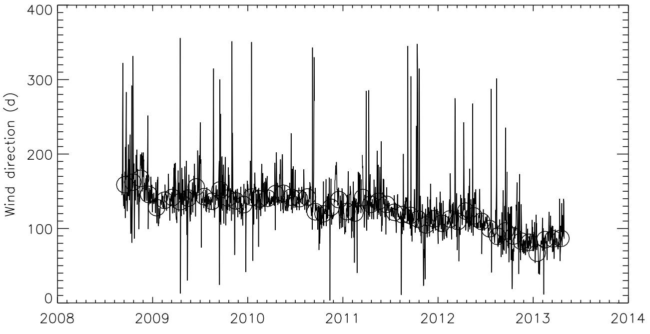
Wind direction (d)
0
100
200
300
400
2008
2009
2010
2011
2012
2013
2014

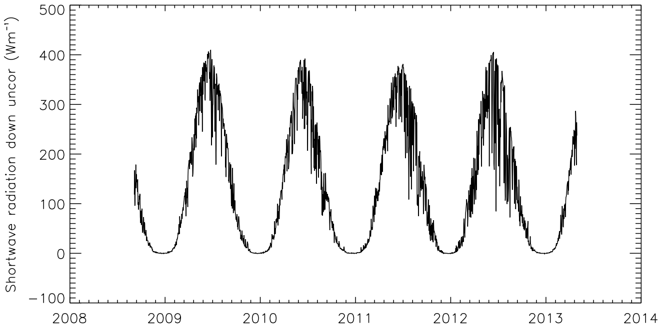
Shortwave radiation down uncor (Wm^{-1})
−100
0
100
200
300
400
500
2008
2009
2010
2011
2012
2013
2014

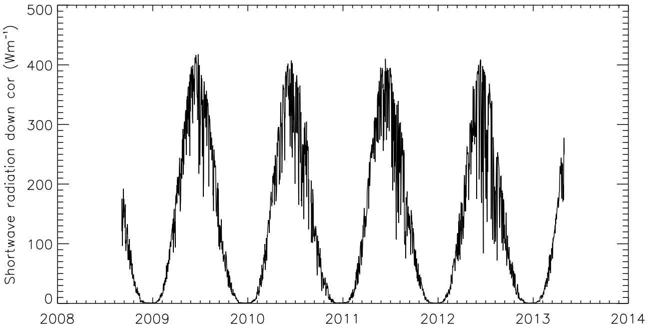
Shortwave radiation down cor (Wm^{-1})
0
100
200
300
400
500
2008
2009
2010
2011
2012
2013
2014

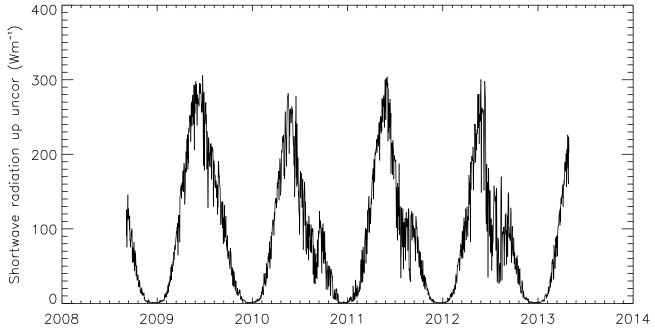
Shortwave radiation up uncor (Wm^{-1})
0
100
200
300
400
2008
2009
2010
2011
2012
2013
2014

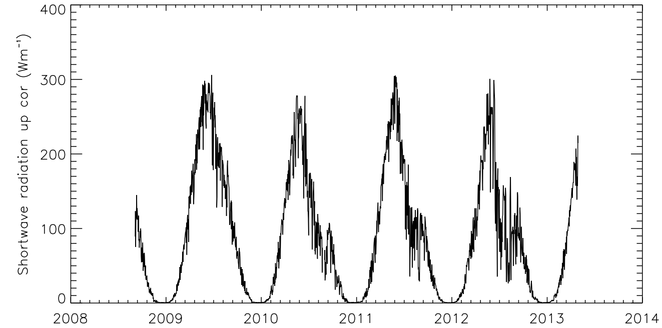
Shortwave radiation up cor (Wm⁻¹)
400
300
200
100
0
2008
2009
2010
2011
2012
2013
2014

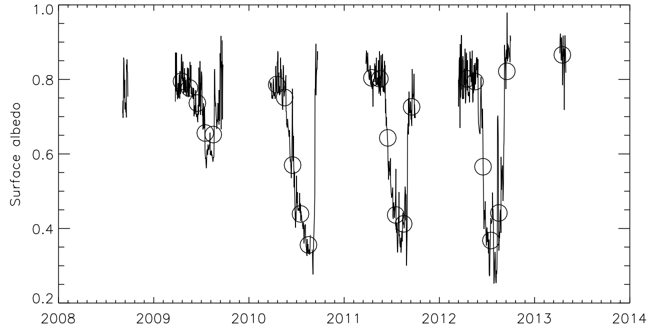
Surface albedo
1.0
0.8
0.6
0.4
0.2
2008
2009
2010
2011
2012
2013
2014

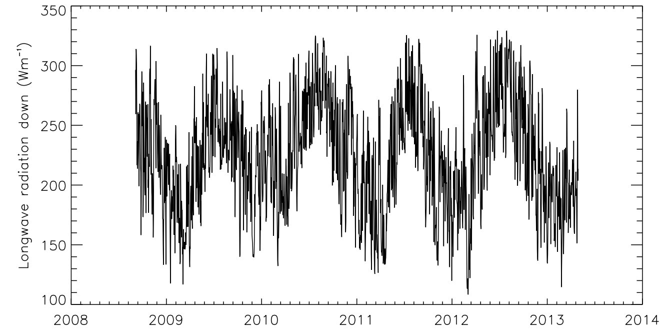
Longwave radiation down (Wm⁻¹)
350
300
250
200
150
100
2008
2009
2010
2011
2012
2013
2014

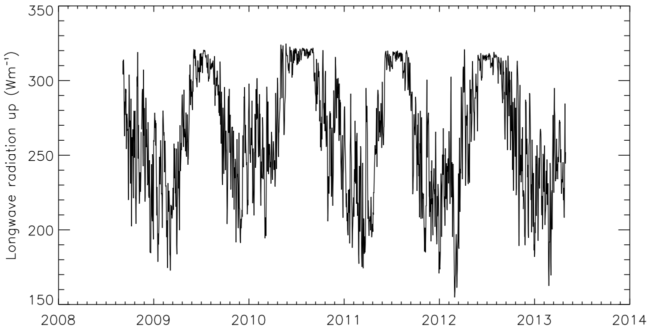
Longwave radiation up (Wm⁻¹)
350
300
250
200
150
2008
2009
2010
2011
2012
2013
2014

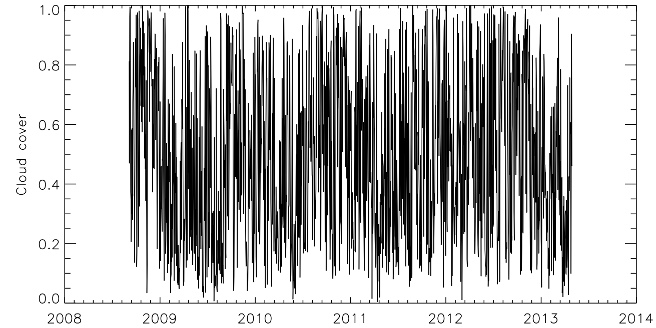
Cloud cover
1.0
0.8
0.6
0.4
0.2
0.0
2008
2009
2010
2011
2012
2013
2014

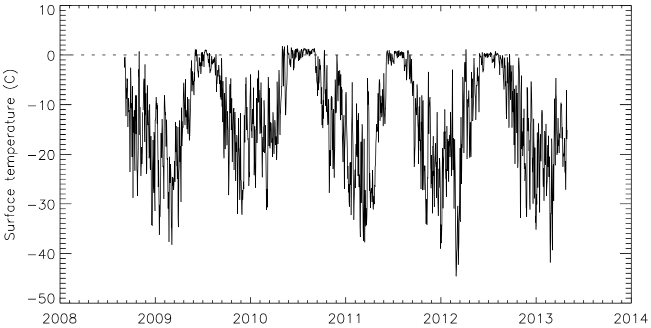
Surface temperature (C)
10
0
−10
−20
−30
−40
−50
2008
2009
2010
2011
2012
2013
2014

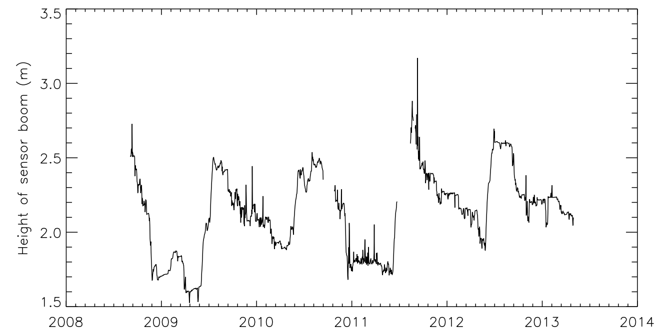
Height of sensor boom (m)
3.5
3.0
2.5
2.0
1.5
2008
2009
2010
2011
2012
2013
2014

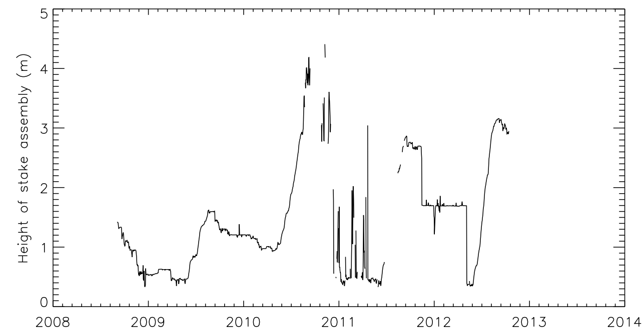
Height of stake assembly (m)
5
4
3
2
1
0
2008
2009
2010
2011
2012
2013
2014

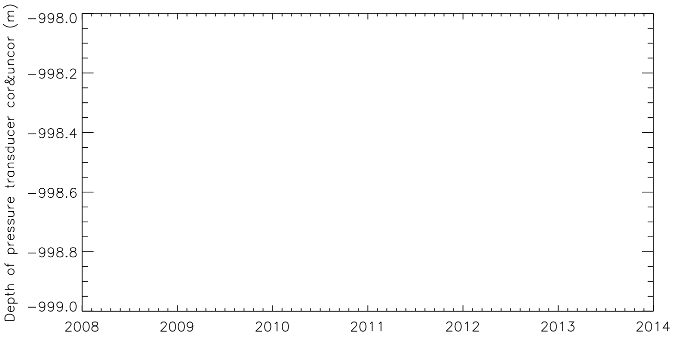
Depth of pressure transducer cor&uncor (m)
−998.0
−998.2
−998.4
−998.6
−998.8
−999.0
2008
2009
2010
2011
2012
2013
2014

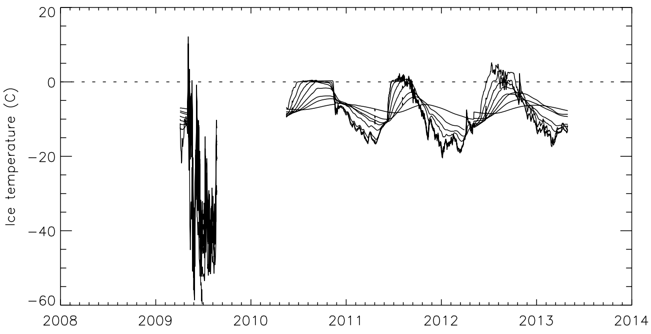
Ice temperature (C)
20
0
−20
−40
−60
2008
2009
2010
2011
2012
2013
2014

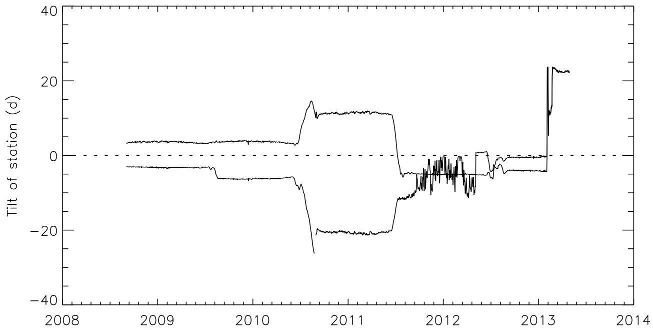
Tilt of station (d)
40
20
0
−20
−40
2008
2009
2010
2011
2012
2013
2014

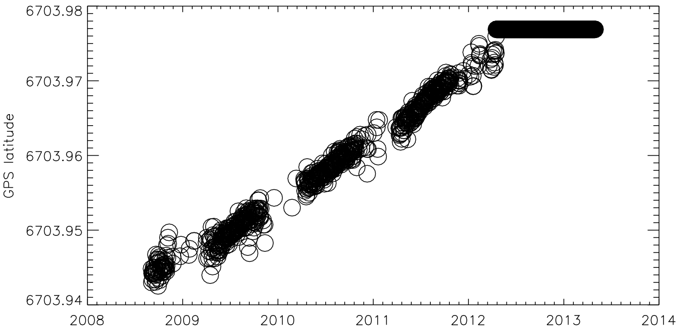
GPS latitude
6703.98
6703.97
6703.96
6703.95
6703.94
2008
2009
2010
2011
2012
2013
2014

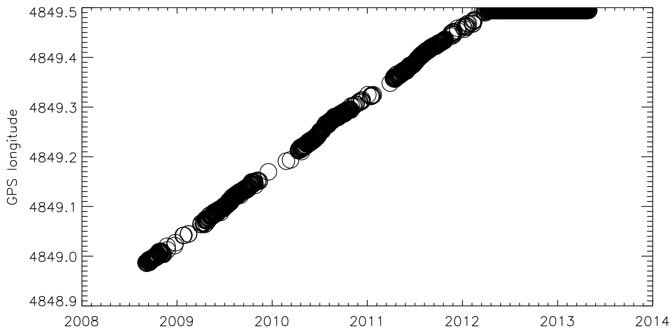
GPS longitude
4849.5
4849.4
4849.3
4849.2
4849.1
4849.0
4848.9
2008
2009
2010
2011
2012
2013
2014

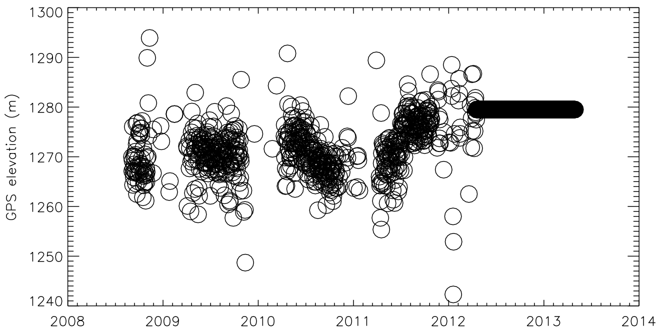
GPS elevation (m)
1300
1290
1280
1270
1260
1250
1240
2008
2009
2010
2011
2012
2013
2014

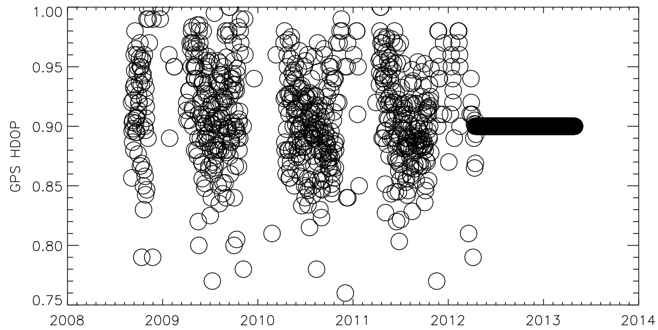
GPS HDOP
1.00
0.95
0.90
0.85
0.80
0.75
2008
2009
2010
2011
2012
2013
2014

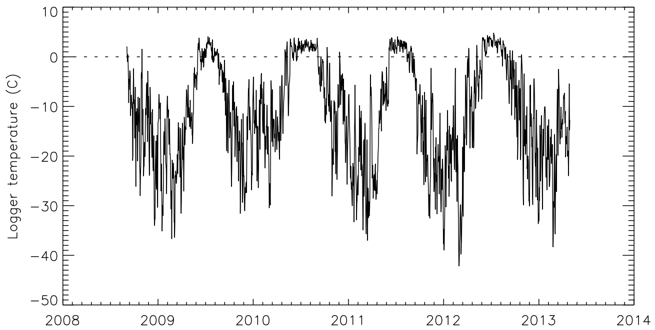
Logger temperature (C)
10
0
−10
−20
−30
−40
−50
2008
2009
2010
2011
2012
2013
2014

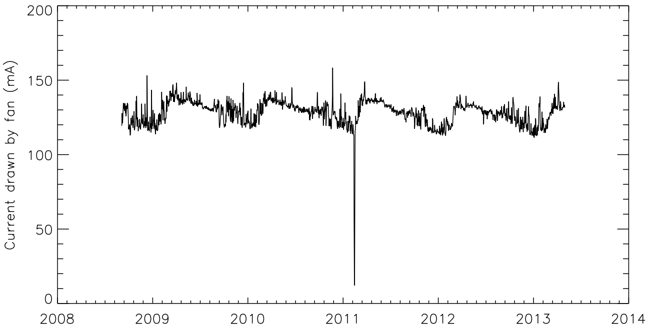
Current drawn by fan (mA)
200
150
100
50
0
2008
2009
2010
2011
2012
2013
2014

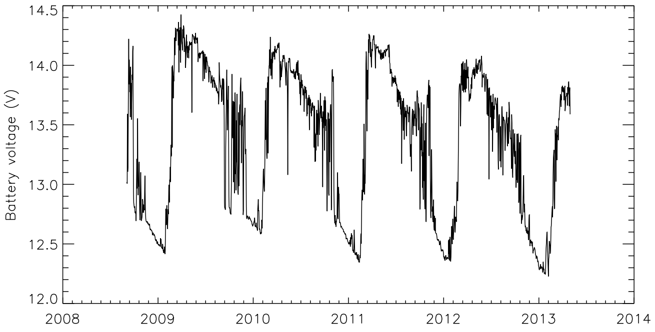
Battery voltage (V)
14.5
14.0
13.5
13.0
12.5
12.0
2008
2009
2010
2011
2012
2013
2014

KAN_U

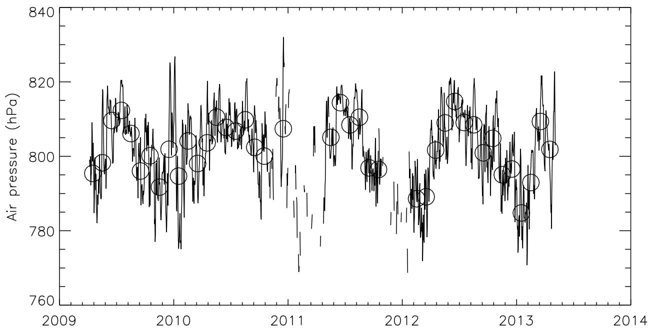
Air pressure (hPa)
840
820
800
780
760
2009
2010
2011
2012
2013
2014

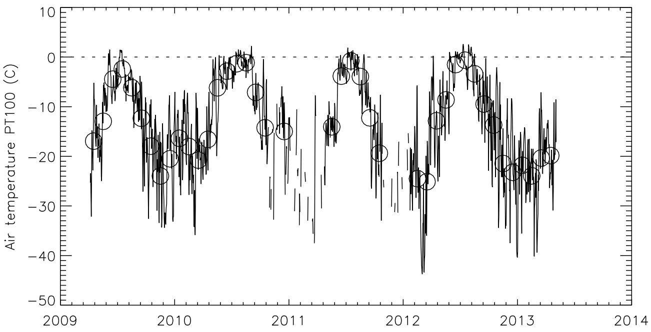
Air temperature PT100 (C)
10
0
−10
−20
−30
−40
−50
2009
2010
2011
2012
2013
2014

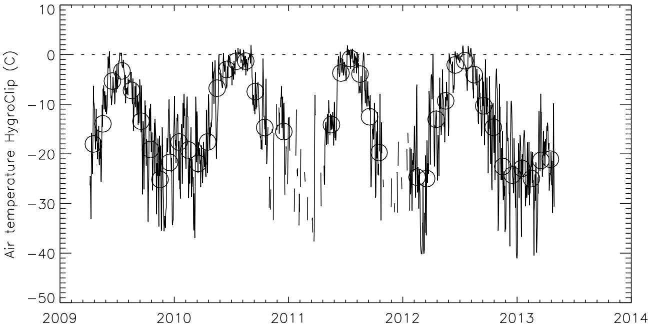
Air temperature HygroClip (C)
10
0
−10
−20
−30
−40
−50
2009
2010
2011
2012
2013
2014

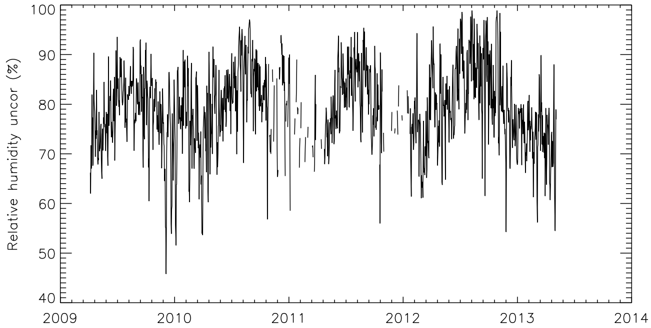
Relative humidity uncor (%)
100
90
80
70
60
50
40
2009
2010
2011
2012
2013
2014

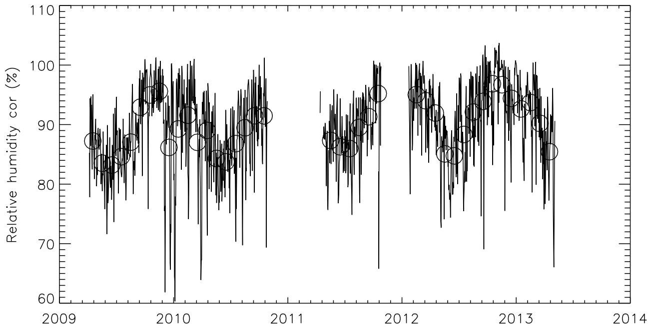
Relative humidity cor (%)
110
100
90
80
70
60
2009
2010
2011
2012
2013
2014

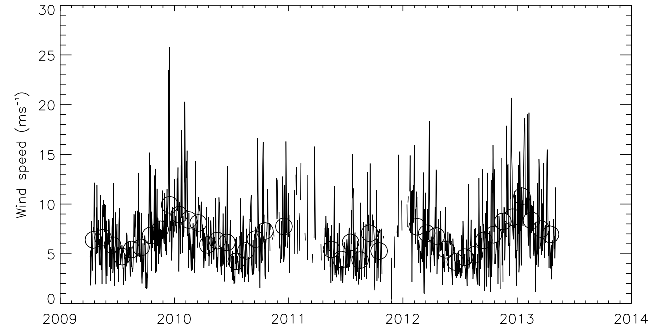
Wind speed (ms⁻¹)
30
25
20
15
10
5
0
2009
2010
2011
2012
2013
2014

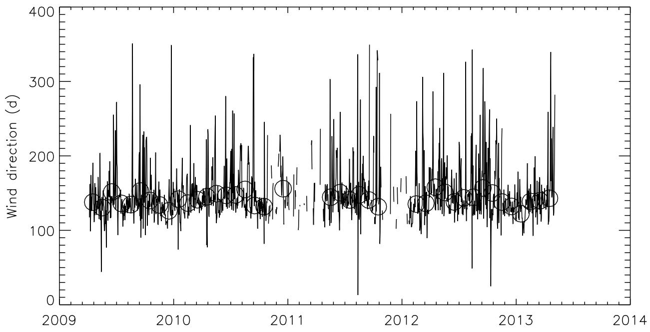
Wind direction (d)
400
300
200
100
0
2009
2010
2011
2012
2013
2014

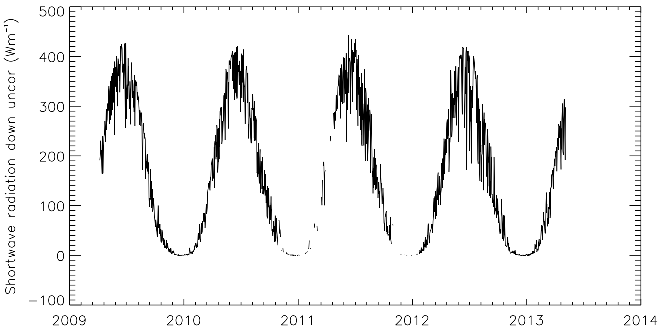
Shortwave radiation down uncor (Wm⁻¹)
500
400
300
200
100
0
−100
2009
2010
2011
2012
2013
2014

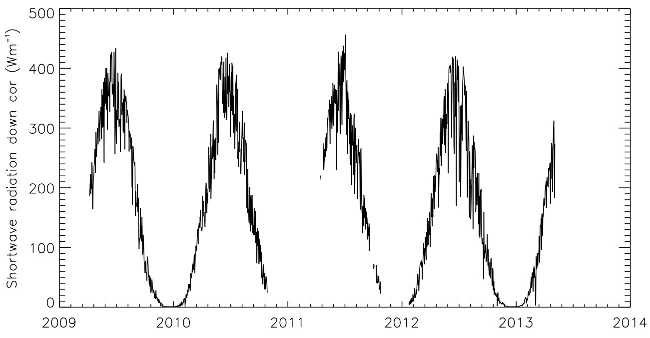
Shortwave radiation down cor (Wm⁻¹)
500
400
300
200
100
0
2009
2010
2011
2012
2013
2014

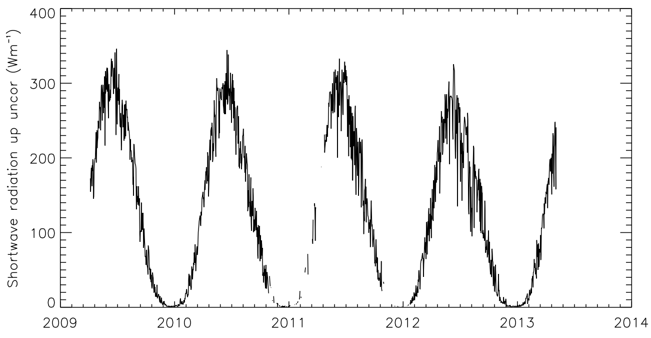
Shortwave radiation up uncor (Wm⁻¹)
400
300
200
100
0
2009
2010
2011
2012
2013
2014

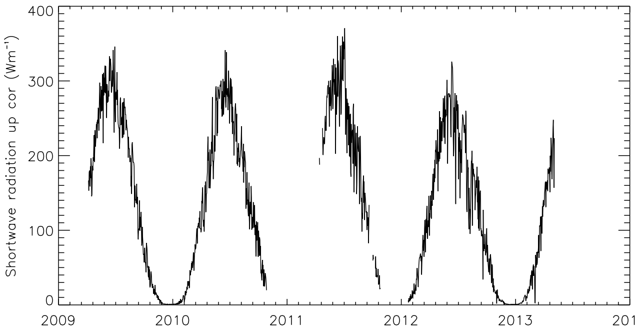
Shortwave radiation up cor (Wm⁻¹)
0
100
200
300
400
2009
2010
2011
2012
2013
2014

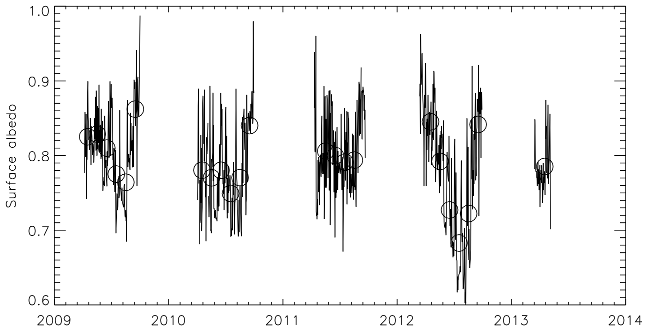
Surface albedo
0.6
0.7
0.8
0.9
1.0
2009
2010
2011
2012
2013
2014

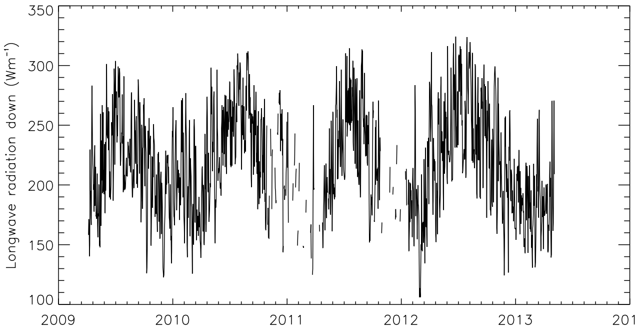
Longwave radiation down (Wm⁻¹)
100
150
200
250
300
350
2009
2010
2011
2012
2013
2014

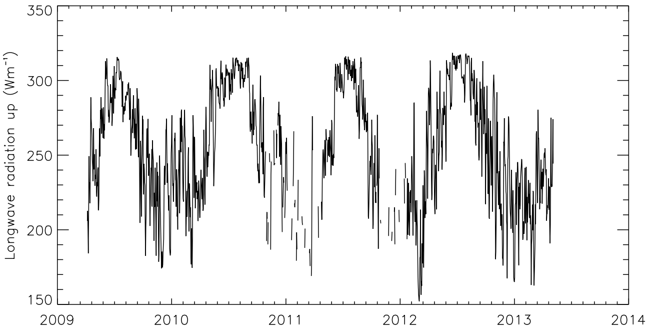
Longwave radiation up (Wm⁻¹)
150
200
250
300
350
2009
2010
2011
2012
2013
2014

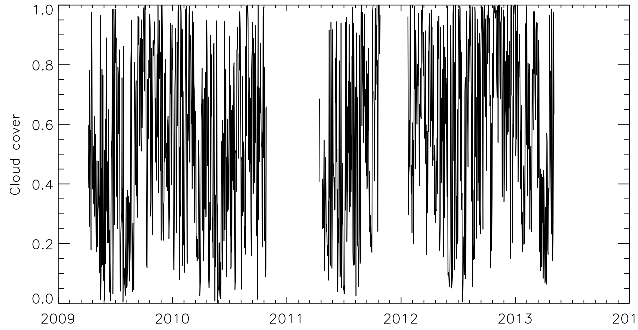
Cloud cover
0.0
0.2
0.4
0.6
0.8
1.0
2009
2010
2011
2012
2013
2014

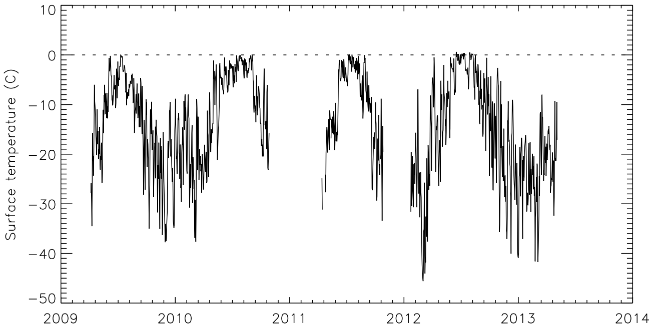
Surface temperature (C)
−50
−40
−30
−20
−10
0
10
2009
2010
2011
2012
2013
2014

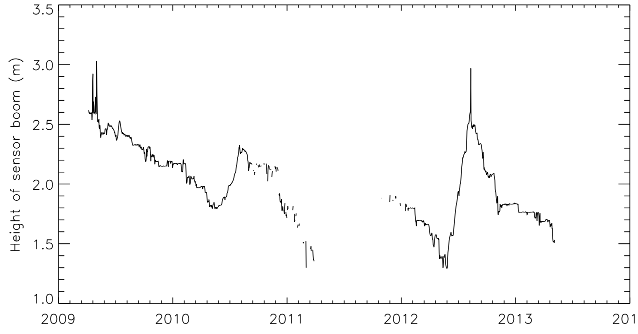
Height of sensor boom (m)
1.0
1.5
2.0
2.5
3.0
3.5
2009
2010
2011
2012
2013
2014

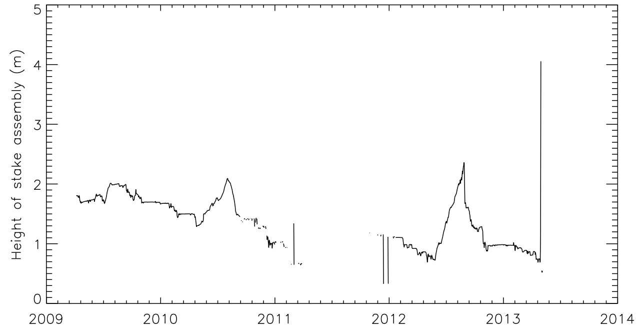
Height of stake assembly (m)
0
1
2
3
4
5
2009
2010
2011
2012
2013
2014

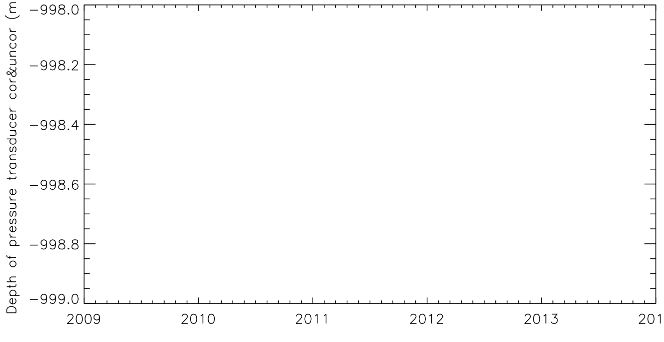
Depth of pressure transducer cor&uncor (m)
−999.0
−998.8
−998.6
−998.4
−998.2
−998.0
2009
2010
2011
2012
2013
2014

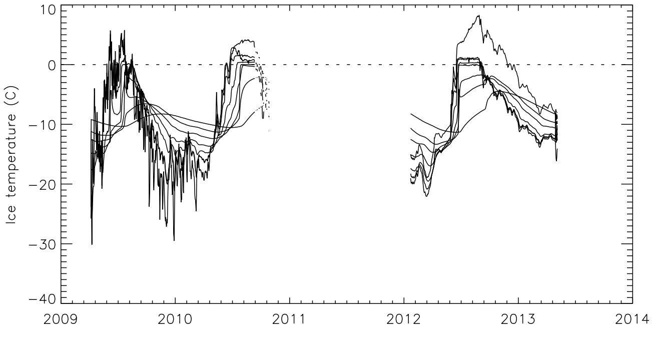
Ice temperature (C)
−40
−30
−20
−10
0
10
2009
2010
2011
2012
2013
2014

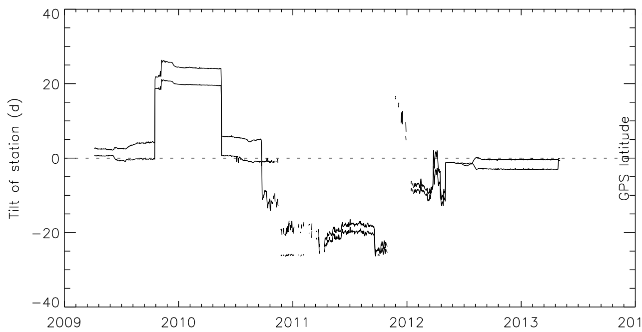
Tilt of station (d)
40
20
0
−20
−40
2009
2010
2011
2012
2013
2014

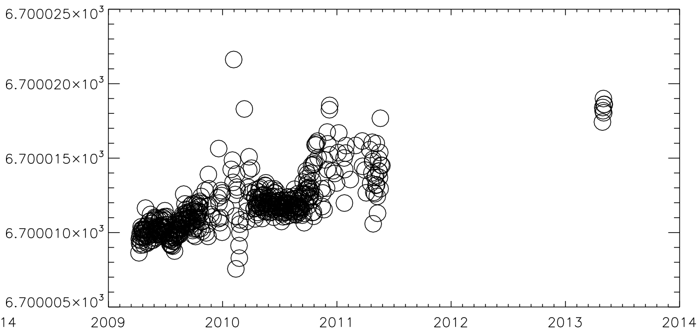
GPS latitude
6.700025×10³
6.700020×10³
6.700015×10³
6.700010×10³
6.700005×10³
2009
2010
2011
2012
2013
2014

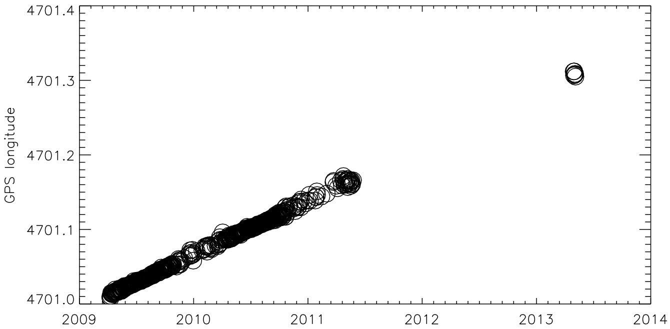
GPS longitude
4701.4
4701.3
4701.2
4701.1
4701.0
2009
2010
2011
2012
2013
2014

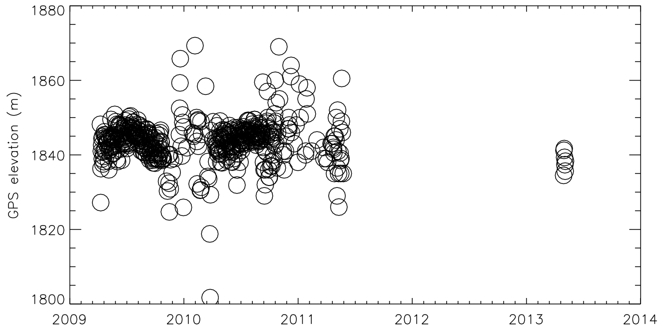
GPS elevation (m)
1880
1860
1840
1820
1800
2009
2010
2011
2012
2013
2014

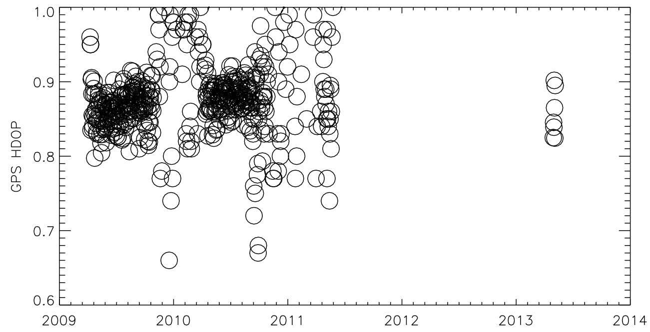
GPS HDOP
1.0
0.9
0.8
0.7
0.6
2009
2010
2011
2012
2013
2014

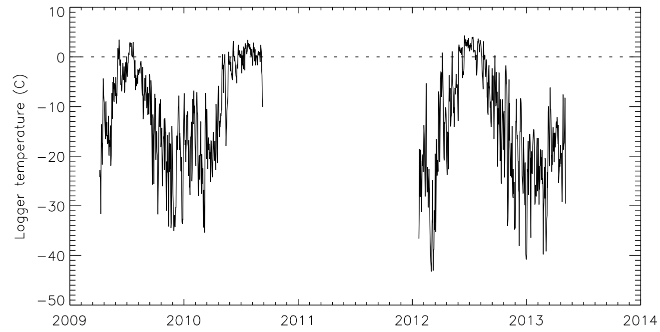
Logger temperature (C)
10
0
−10
−20
−30
−40
−50
2009
2010
2011
2012
2013
2014

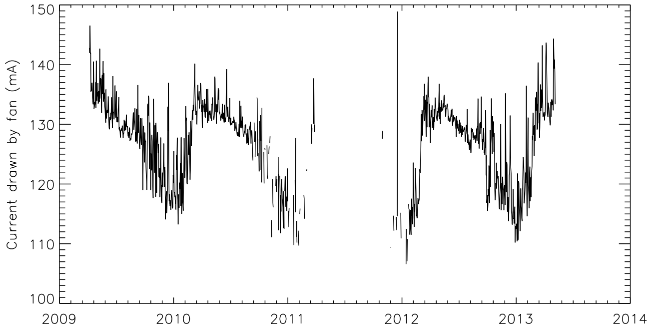
Current drawn by fan (mA)
150
140
130
120
110
100
2009
2010
2011
2012
2013
2014

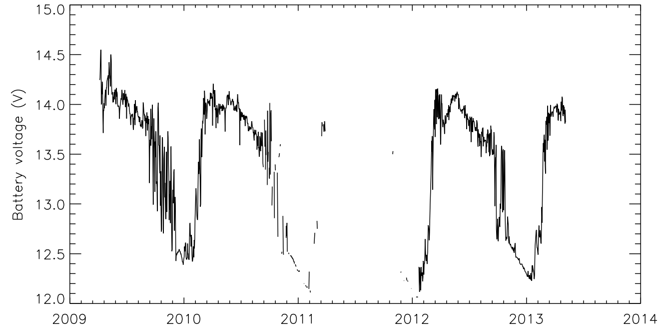
Battery voltage (V)
15.0
14.5
14.0
13.5
13.0
12.5
12.0
2009
2010
2011
2012
2013
2014

Appendix B

Borehole DH-GAP04 monitoring equipment, installation of the instruments and uncertainties related to pressures and evaluated heads.

Kent Hansson and Jan Sundberg, Geosigma AB.

B1 Introduction

Within the Greenland Analogue Project (GAP), an ~ 690 m long and 650 m deep borehole (DH-GAP04) was drilled in SW Greenland in June 2011, see Figure B1-1.

The borehole was drilled close to the Greenland Ice Sheet (GrIS) margin with an inclination of 70 degrees and a bearing of 9 degrees relative to North. The end of borehole (EOB) is about 650 m below the ground surface at the drill site, which corresponds to a level of ~ 560 m below the ice sheet, equivalent to 123 m b.s.l., see Table B1-1, Figures B1-2 and B1-3.

Table B1-1. Coordinates (UTM/D-WGS84) of reference for borehole DH-GAP04.

Coordinate	Easting	Northing	Elevation
Start (TOC)	540 732.20	7 449 003.90	526.17
End (EOB)	540 810.77	7 449 213.83	−122.90
Ground surface	540 732.23	7 449 004.09	525.64
Ice sheet margin	540 708.68	7 449 192.69	474.63

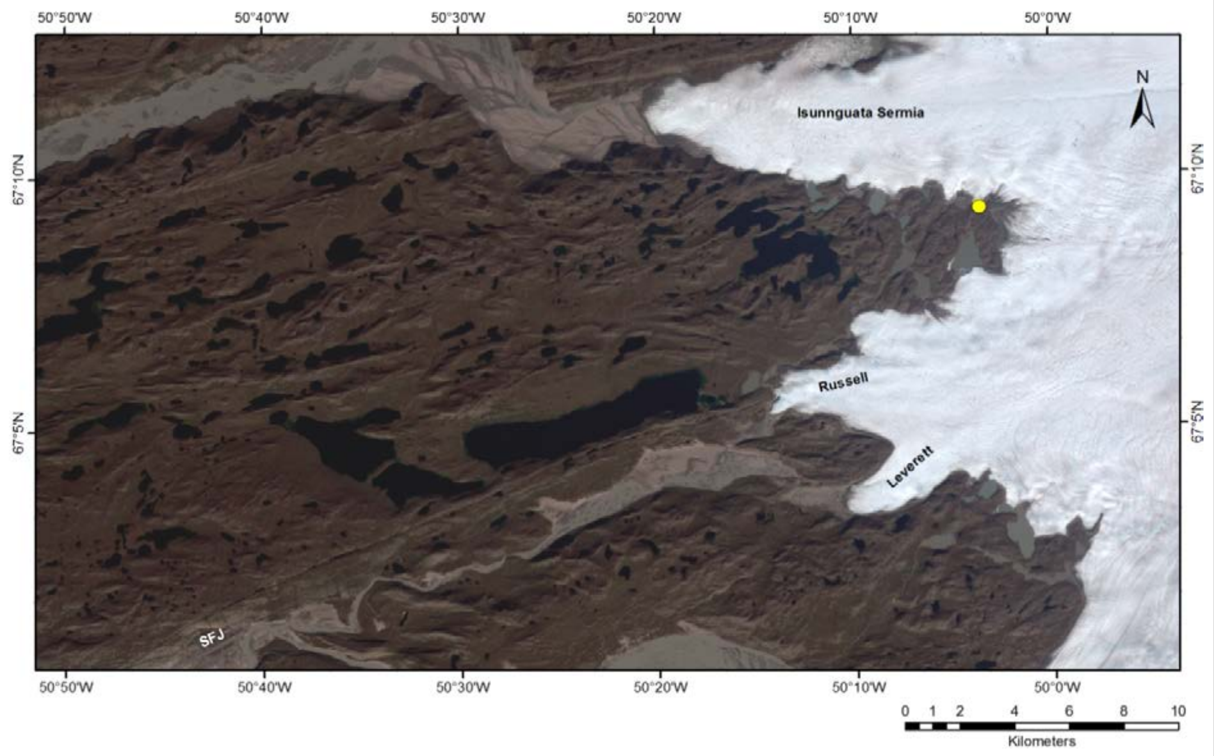

Figure B1-1. Map of the study area in southwestern Greenland showing the location of borehole DH-GAP04 (yellow circle). The main outlet glaciers in the area are indicated.

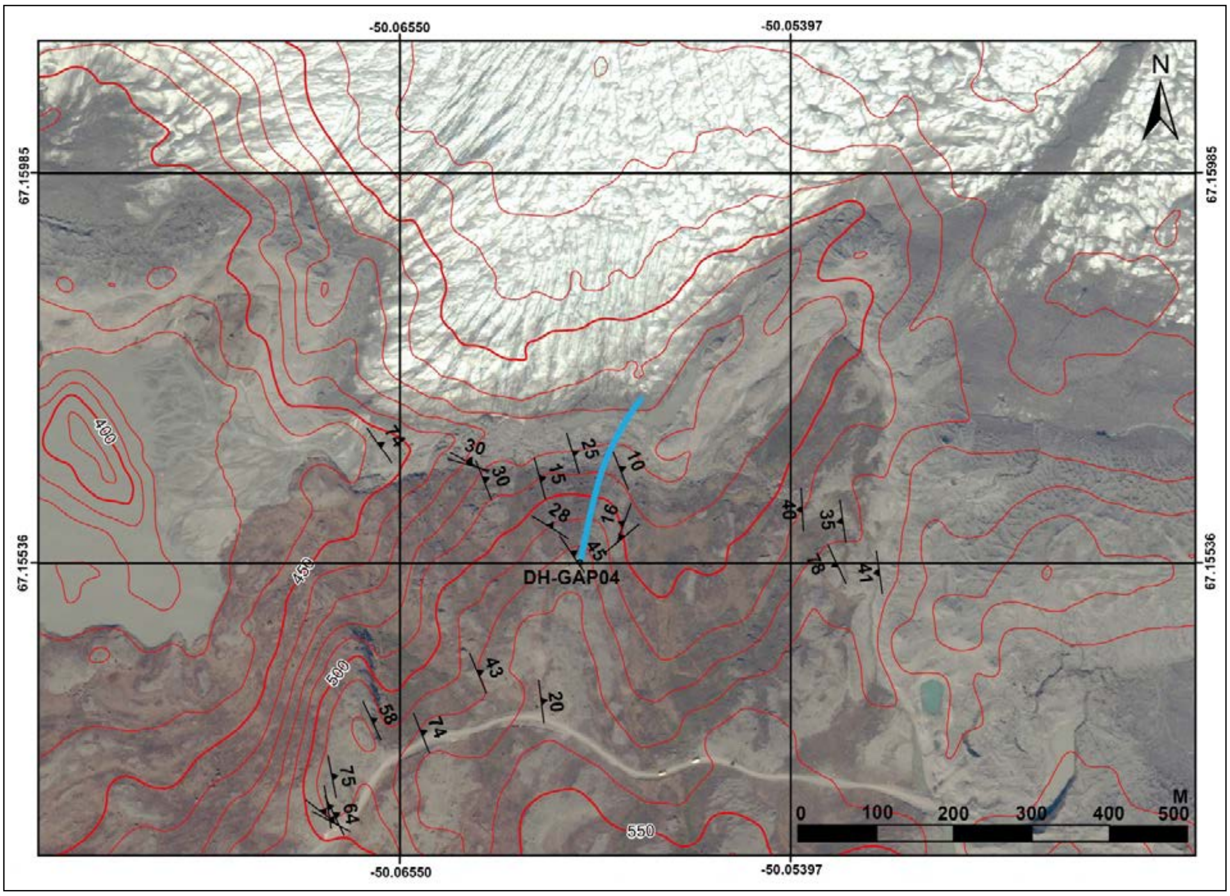

Figure B1-2. Quickbird satellite image acquired July 4, 2011, showing the study site and the trace of borehole DH-GAP04 (in blue) and elevation contours in red.

The aim with the borehole and its instrumentation is to obtain information about the hydrological and hydrogeochemical conditions (i.e. flow conditions for groundwater, thermal conditions, and the chemical properties of the groundwater) at ~ 500 m depth relative to the ice sheet margin. The time table showing the drilling and borehole activities (e.g. heating and Posiva Flow Log (PFL) measurements) are presented in Table B1-2.

Table B1-2. Time table showing the activities in the borehole.

Activity	Date (YYYY/MM/DD)	Duration (days)	Duration (hours)*	Flow rate (liters/min)**
Drilling	2011-06-18–2011-06-28	11	231	21.7
Deviation measurement	2011-06-29	1		
Heating of the borehole	2011-06-29–2011-07-01	2	47	12.4
Posiva Flow Log measurements	2011-07-01–2011-07-02	2		
Circulation of hot water in the borehole	2011-07-02–2011-07-07	5	112	29.6
Installation of multipacker system involving packer sealing	2011-07-07	1		
Heating and water sampling	2013-08-30–2013-09-25	27		
Heating and water sampling	2014-08-30–2014-09-14	16		

* Duration in hours is provided for the activities prior to the installation of the multipacker system, i.e. for the periods when the borehole was circulated with hot water.

**Flow rate is given as the average flow rate. The total water consumption was 535 m^3, where 301 m^3 was used for actual drilling and 234 m^3 for keeping the borehole warm until instrumentation.

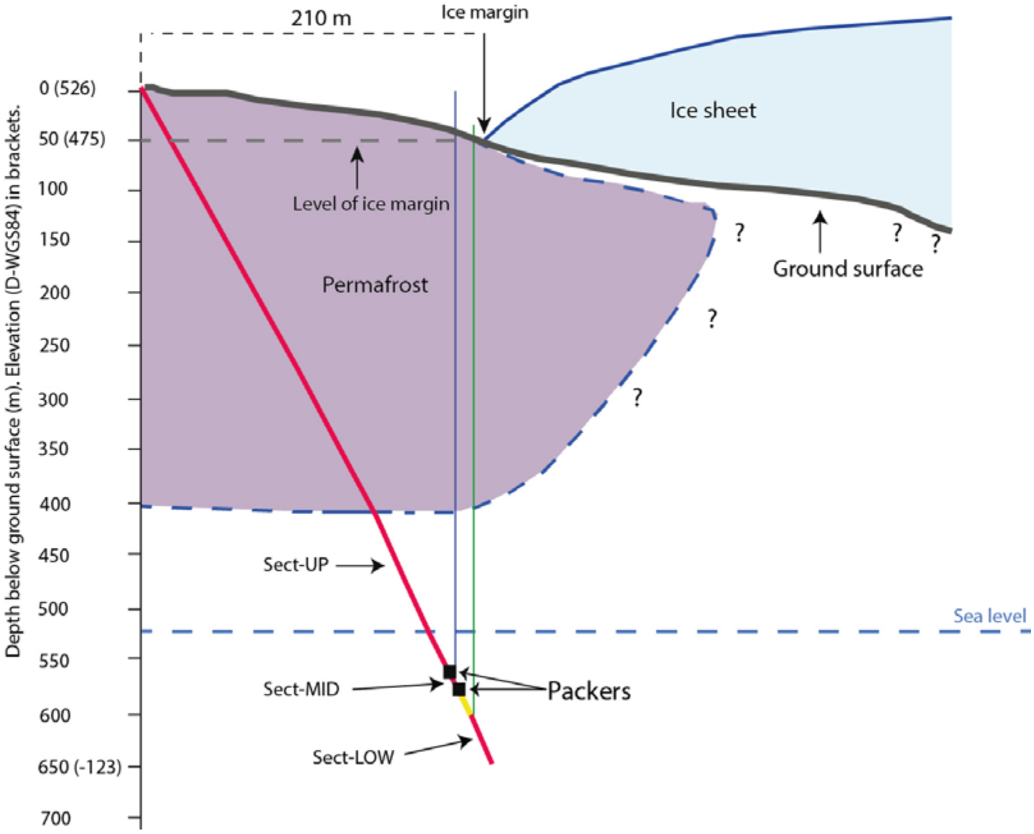

***Figure B1-3.** Schematic cross-sectional view of borehole DH-GAP04. Yellow field below the lower packer represents a ~ 30 m intact rock unit.*

B2 Selection of sections for the monitoring equipment

Three monitoring sections were installed (Figure B1-3). The precondition for emplacement of the 10 m long middle section (Sect-mid) was that it should contain at least one transmissive fracture, that it is located at a depth comparable to repository depths (i.e. ~ 500 m) and that the two packers are placed in intact rock sections. The chosen packer positions of Sect-mid were based on the preliminary core mapping that was made on site in combination with the results of PFL measurements (Pöllänen et al. 2012).

Figure B2-1 shows the borehole with the position of the PFL flow anomalies and the corresponding drill core photos showing fractures potentially related to the flow. There may be discrepancies in the actual position of the PFL anomalies, since there is a degree of uncertainty of which fracture(s) correspond to the PFL anomalies.

Positions for the installed equipment in the borehole are described in Chapter 4. A summary of the results of the PFL measurements and evaluation of pressure recovery data are presented in Chapter 7. The geological information and the core photos from sections coinciding with the PFL anomalies presented here were compiled by Tuomas Pere, Posiva Oy. A complete presentation of the core log of DH-GAP04 is presented in Pere (2014).

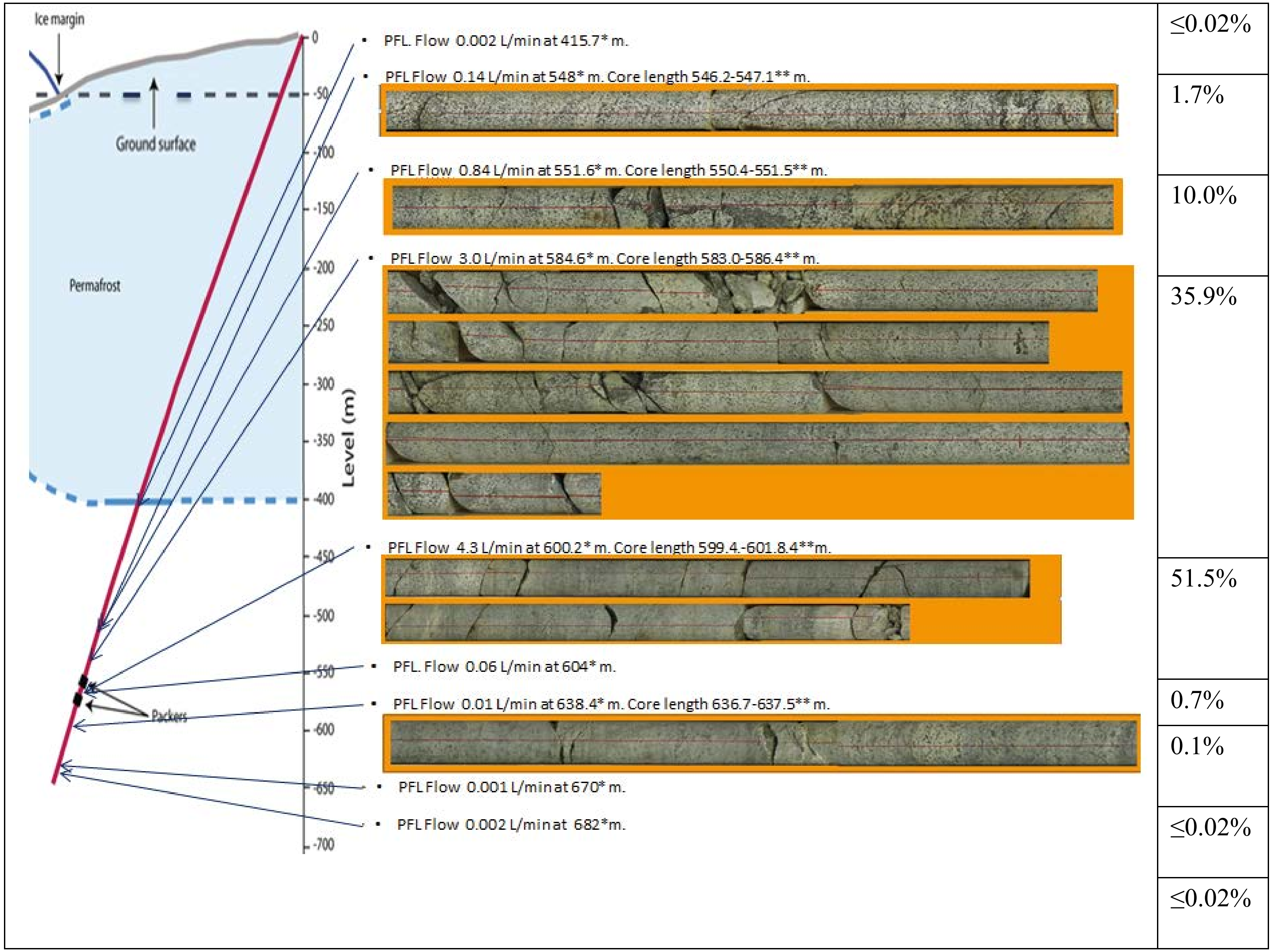

Figure B2-1. *Nine PFL anomalies and example photos of cores in associated sections along the borehole based on the preliminary core mapping made on site.*Relative to top of casing (TOC). **Relative to ground surface. TOC is 0.5 m above ground surface, see Table B1-1. The percentages in the right column show the percentages of the total flow of the nine flow anomalies (8.355 L/min).*

B3 Monitoring equipment

The monitoring equipment was designed to meet the following conditions:

- A borehole length of ~ 700 m and an inclination of ~ 70 degrees with a diameter of 76 mm.
- Sealing of the borehole in three monitoring sections.
- The upper part of the borehole will consist of frozen ground (i.e. the upper ~ 300–350 m of the borehole will be drilled in permafrost).
- The two packer systems will be placed at a depth of ~ 500 to 550 m below TOC.
- Air temperatures down to −40 °C, which limits the choice of sensors and data loggers at surface.
- Pressure durability.

The monitoring equipment for the borehole was constructed such that it is possible to:

- Monitor the temperature along the entire borehole using the DTS (distributed temperature sensing) technique.
- Monitor the temperature in the middle section (an independent reference sensor).
- Monitor the absolute pressure in each section, and air (atmospheric?) pressure at surface.
- Monitor the electrical conductivity of the water in each section.
- Melt the ice in the upper part of the sample tubes/borehole in order to enable the water chemistry sampling.
- Collect water samples (both pressurised and non-pressurised) in each section.
- Collect and distribute the data to Sweden, Finland and Canada via satellite.

The manufactured equipment may be divided into:

- Equipment on the ground surface.
- Equipment in the borehole.

Equipment on the ground surface

Equipment on the ground surface is mounted in a steel container which is placed over the borehole, see Figure B3-1.

The equipment in the container consists of:

- Control system for packer inflation, including pressure transmitters for the control system.
- Pressure transmitter for air pressure and temperature sensor for the air temperature (inside the container).
- Data logger for the sensors in the container and in the borehole.
- Satellite modem.
- DTS instrument (Sensornet, ORYX) to monitor temperature along the borehole.
- Power supply including solar panel and wind generator for datalogger, sensors, satellite modem and DTS optical fiber for temperature monitoring.
- Control system for water sampling, including pressure transmitters.
- Control system for the heating cable in the borehole.
- Nitrogen gas vessels.

A generator providing power to melt the sampling tubes during water sampling is placed outside the container.

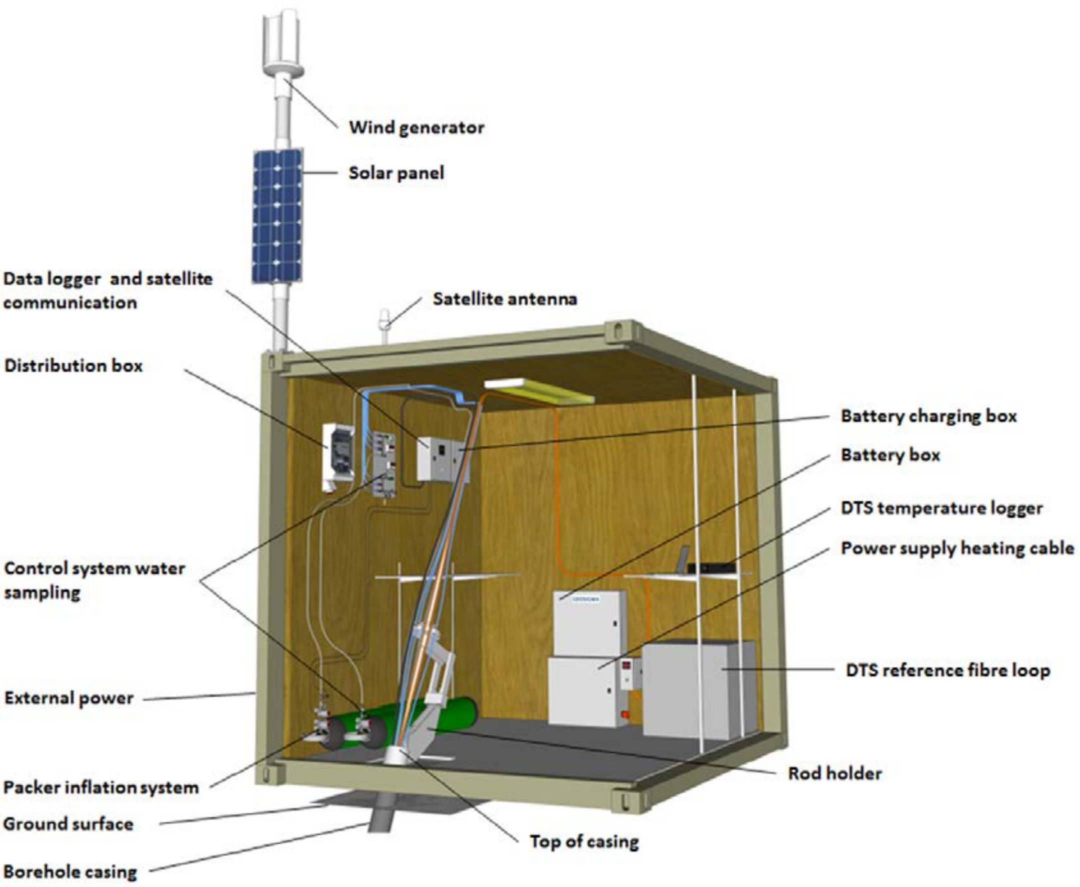

Figure B3-1. *Container with the surface equipment.*

Equipment in the borehole

The equipment in the borehole is shown in Figure B3-2.

The equipment in borehole consists of:

- Stainless and aluminium rods (16 mm diameter) for: maintaining the desired distance between the components in the borehole, hold up the pipes and cables along the borehole and pushing and pulling the equipment if it gets stuck during installation.
- Rope for lowering the equipment.
- Optical fibre for DTS temperature measurements along the borehole, down to about 2 m below the lower packer.
- Stainless steel pipe (outer diameter, OD, 6 mm, inner diameter, ID, 2 mm) for packer inflation.
- Two stainless steel pipes (OD 6 mm, ID 2 mm) allowing water sampling each of the three sections.
- Signal cable for the sensors in borehole.
- Two heating cables installed down to a borehole length of ~ 480 m below TOC (corresponding to a vertical depth of ~ 450 m relative to TOC).
- A double packer system with a section length of 10 m and packer length of 1 m are installed at 594.50–604.50 m below TOC (borehole length). This corresponds to a vertical depth of 558–568 m relative to TOC.
- Filter for water sampling.
- Additional heating cable down to a depth of 20 m.

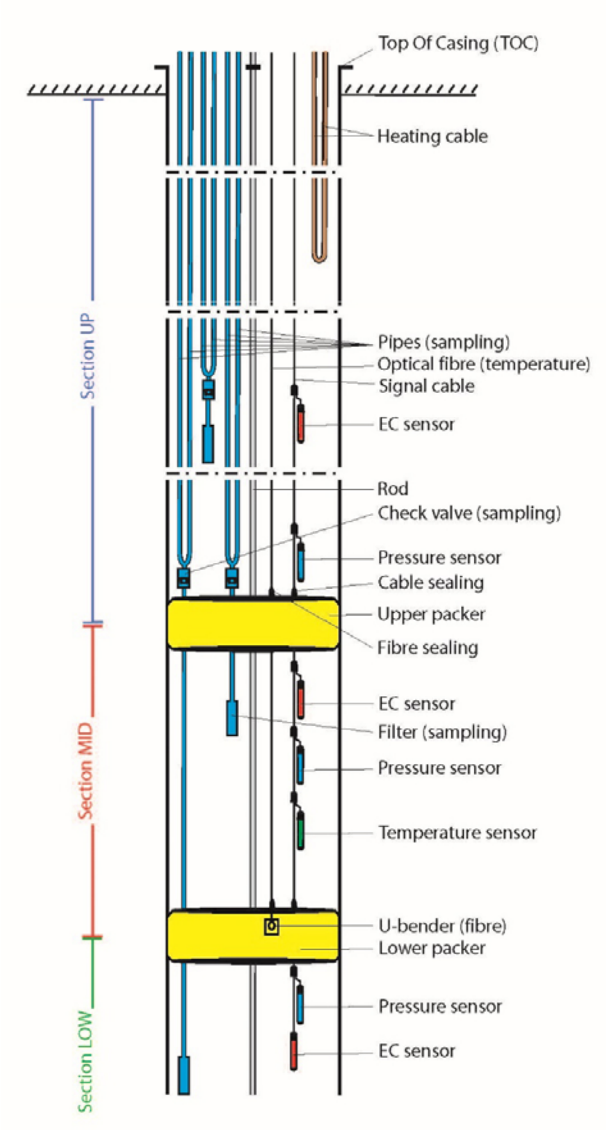

***Figure B3-2.** Equipment in borehole DH-GAP04. Each packer is 1 m long. The upper 400 m of the hole is within the permafrost and are naturally sealed from the bottom part of the hole. The top of the upper packer is located at a depth of 561 m below TOC. The top of the lower packer is located at a depth of 571 m below TOC. Sect-up is ~ 190 m and extends from the base of the permafrost to the uppermost packer, its volume is 840 L. Sect-mid is isolated by the two packers and is 10 m long and has a volume of 44 L. Sect-low is 80 m long and extends from the lowermost packer to the bottom of the hole with a volume of 350 L. A heating cable is installed to a depth of ~ 450 m allowing melting of the water sample tubings for water sampling campaigns.*

Section-up

Approximately 50 m above the upper packer, the following is installed:

- electrical conductivity transmitter,
- filter for water sampling,
- check valve with Y-coupling.

The pressure transmitter is installed just above the upper packer.

Section-mid

In section-mid the following is installed:

- electrical conductivity transmitter,
- filter for water sampling,
- pressure transmitter,
- temperature transmitter.

Check valve with Y-coupling is installed just above the upper packer.

Section-low

About two metres below the lower packer the following is installed:

- pressure transmitter,
- electrical conductivity transmitter,
- filter for water sampling.

Check valve with Y-coupling is installed just above the upper packer.

The levels and depth below TOC for all components are presented in Table B4-1.

B4 Installations

The installations in the borehole are shown schematically in Figure B3-2. Coordinates and elevations for the installations are presented in Table B4-1. Parameters monitored are listed in Table B4-2.

The length of the borehole from the TOC is ~ 688 m. The length between TOC and ground surface (along the borehole) is 0.56 m.

Table B4-1. Coordinates, lengths, and depths to the different components in the borehole.

Sensors, etc.	Length along borehole (m)*	North (m)*	East (m)*	Level UTM/D_WGS84 (m)	Depth below TOC (m)
Top of casing	0.00	7 449 003.90	540 732.20	526.17	0.00
Ground surface	0.56	7 559 004.09	570 732.23	525.62	0.48
U-bender, heating cable	479.75	7 449 155.95	540 774.42	73.29	−452.88
EC sect-up	541.32	7 449 173.87	540 783.64	15.10	−511.07
Filter sect-up.	541.70	7 449 173.98	540 783.70	14.74	−511.43
Pressure sect-up	592.01	7 449 188.27	540 792.13	−32.75	−558.92
Sect-mid upper limit	594.50	7 449 188.97	540 792.56	−35.10	−561.27
EC sect-mid	595.70	7 449 189.30	540 792.77	−36.23	−562.40
Filter sect-mid	596.08	7 449 189.40	540 792.84	−36.59	−562.76
Pressure sect-mid	596.74	7 449 189.58	540 792.96	−37.21	−563.38
Temperature sect-mid	597.47	7 449 189.78	540 793.09	−37.90	−564.07
Sect-mid_lower limit	604.50	7 449 191.72	540 794.36	−44.54	−570.71
U-bender, optical fibres	605.52	7 449 192.00	540 794.54	−45.50	571.67
Pressure sect-lo	606.90	7 449 192.38	540 794.80	−46.81	−572.98
EC sect-lo	607.52	7 449 192.54	540 794.92	−47.39	−573.56
Filter sect-lo	607.60	7 449 192.57	540 794.92	−47.47	−573.64
Deepest, deviation measurement	687.56	7 449 213.83	540 810.77	−122.9	−649.07

* According to the manufacturer, the accuracy of the dip is ± 0.2 degrees. The accuracy of the gyroscopically measured direction varies by the hole length. According to the manufacturer, the accuracy of the direction is ± 0.5 degrees for an 800 m long hole, when measured in 40 min.

Table B4-2. Parameters monitored in DH-GAP04.

Parameter	Name on the logger	Unit
Air pressure	Pair	kPa
Air temperature (inside the logger box)	Tair	° C
Pressure in gas bottle	Pgasbottle	kPa
Packer pressure	Ppack	kPa
Section pressure (upper section)	Psect-up	kPa
Section pressure (middle section)	Psect-mid	kPa
Section pressure (lower section)	Psect-lo	kPa
Temperature (Middle Section)	Tsect-mid	° C
Electrical conductivity (upper section)	Esect-up	µS/cm
Electrical conductivity (middle section)	Esect-mid	µS/cm
Electrical conductivity (lower section)	Esect-lo	µS/cm
Battery capacity	Bat	Volt

B5 Measurement methodology for the monitoring equipment

The measurement methodology used to collect data from the borehole is based on the advice received from the agent for the data logger (Campbell Scientific) as well as from manufacturers of the downhole sensors. In the measurement programs (WINTER, SUMMER and WATER SAMPLING) measurements are done every four hours and recording of measurements are done after a 'warm up' time of 40 seconds.

A schematic chart showing the data acquisition system set up is shown in Figure B5-1. Power supply via the signal cable from the DC/DC Out is connected to sensors in the borehole. The' low-side' on the measuring resistance to the three EC-channels is connected to earth (GND) via 1 kohm resistor to connect floating channels to ground.

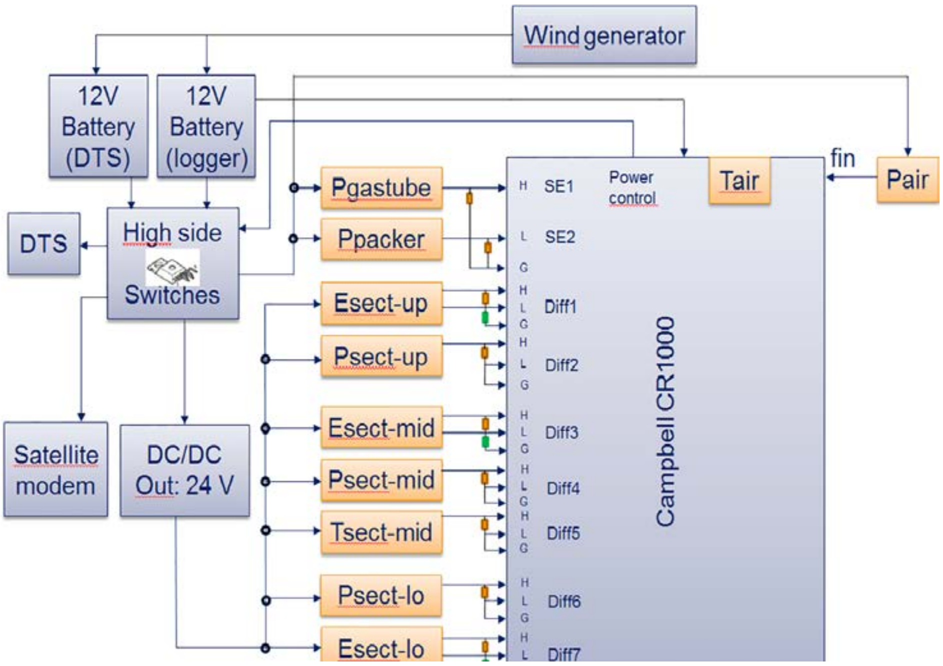

Figure B5-1. *Schematic figure of the data acquisition system and connection of sensors. The 1 kohm resistors between the low-side of the measuring resistances and GND, on the three EC-channels, is highlighted in green.*

B6 Uncertainties of measurement with respect to pressures and evaluated heads

The obtained pressure results and calculated hydraulic heads in DH-GAP04 do not increase with depth (i.e. the pressure and the hydraulic head in the lowermost section are lower than in the upper and middle sections). Experience from pressure monitoring in fractured rock indicates that pressures in different fractures are related to connectivity rather than to depth alone. Still, it is valid to ask: 1) are the sensors correctly connected to the logger (i.e. are they positioned where they should be); and, 2) were the sensors damaged during installation or during packer inflation? When analysing data and calculating hydraulic head it is important to have an understanding of how large the associated errors can be.

To check that the sensors are 1) connected correctly, 2) positioned at the correct level, and 3) functioning properly after lowering of the equipment to the planned depth and after expansion of packers, the following checks were carried out.

Following lowering of the equipment to the planned depth, and before inflating the packers, the following pressures were measured:

Section	Gauge pressure in kPa
Sect-up	5.518
Sect-mid	5.560
Sect-low	5.648

The pressures increase with depth, indicating that the sensors are connected to the appropriate section. If the pressure differences between the sensors are converted to water column height differences, and these are compared to the calculated level differences of the sensors based on the deviation survey, the following is obtained:

Sections	Calculated height differences expressed as metre water	Calculated differences in elevation of the sensors expressed in metres
Sect-up – Sect-mid	4.3	5.5
Sect-mid – Sect-lo	9.0	9.6

This indicates that the values from the pressure sensors are in good agreement, and that they are positioned as they should be.

When the packers were inflated, and the hole was still open (i.e. not frozen in the upper part), the following was noted:

- the pressure did not change in the Sect-up,
- the pressure in Sect-mid increased during the initial time following inflation, and
- the pressure was significantly lowered in Sect-low.

These observations support that the pressure sensor in the lower section is not affected by inflation of the packers and is adequately connected. Once the hole freezes, the pressure in Sect-up drops after some time. The fact that the water is flowing above (artesian behavior) the TOC immediately after drilling is likely due to the influence of drilling.

The uncertainties with respect to the estimated hydraulic heads (i.e. fresh water head) are calculated for a theoretical section and a pressure that approximately matches that of Sect-mid. The following equation was used when transferring pressure to water column at a certain point:

$H=P_{corr}/(\varrho \times g)$

Where:

H = vertical depth of the fluid at a certain depth (m)

P_{corr} = Fluid pressure at a certain point (Pa), pressure is reduced for air pressure

g = acceleration of gravity at the actual site (m/s^2)

ϱ = density (kg/m^3).

Table B6-1 shows the results of the uncertainty analysis based on the assumed parameters. The acceleration of gravity and measured/assumed pressures have not been varied.

In the uncertainty calculations, the following assumptions were made.

- **Acceleration of gravity** – according to the Geological survey of Denmark and Greenland (GEUS), g is 9.8235 m/s^2 at the Kangerlussuaq village. In order to get the g for the local elevation, 0.00003 m/s^2 for each metre of height is subtracted. This gives a local gravity constant of 9.813 m/s^2 at DH-GAP01 and 9.808 m/s^2 at DH-GAP04.
- The **pressure** – correction for barometric pressure is determined to be 5000 kPa. The measured pressures in the three sections varied between ~ 5200–5500 kPa
- **Density** of (pure) water at different temperatures are from "Handbook of Chemistry and Physics 53rd Edition, p. F4." The following densities were used 999.94 kg/m^3 (at +2 °C) and 997.04 kg/m^3 (at +25 °C). The temperature at 500 m depth in the borehole is +2 °C. When calculating density variations due to pressure variations the compressibility of water was assumed to be 4.6×10^{-10} 1/Pa.
- **Compression of the water column** is based on water compressibility and the height of the water column.
- **Pressure sensors** – based on sensor specifications, calibrations and adopted changes with time, the accuracy has been set to ± 0.3 % of full scale.
- **Air pressure** ± 0.3 % of full scale, which is based on sensor specifications and calibrations.
- **Position of the hole** in D-WGS84 elevation. The accuracy of the elevation of the TOC and the accuracy of the deviation measurement is ± 0.7 m at the assumed measuring point.

In Table B6-1 the calculations using different assumptions, including the use of a water density of 1004 kg/m^3, which is based on the analysis/measurement of water density of samples from September, 2011 from DH-GAP04.

Table B6-1. Calculation of water column heights at different assumptions.

	Water column heights (m)
Distilled water at +25 C Density constant throughout the water column Measured pressure 5000 kPa	510.68
Distilled water at +2 C Density constant throughout the water column Measured pressure 5000 kPa	509.20
Density of 1004 kg/m^3 throughout the water column at a water temperature of +2 C	507.14
Distilled water at +25 C Density of the water column was increased due to the weight of the water Measured pressure 5000 kPa	510.39
Distilled water at +25 C Density of the water column was increased due to the weight of the water Measured pressure 5000 kPa + 0.3 % of measuring range	512.82
Distilled water at +25 C Density of the water column was increased due to the weight of the water Measured pressure 5000 kPa – 0.3 % of measuring range	508.53

Fresh water head

The results presented in Table B6-2 were made using the following assumptions:

- Water temperature of + 2 °C.
- Water is of distilled type.
- Density of water was adjusted to the depth based on the weight of the water column.
- The measured pressure in the section (corrected for barometric pressure) is 5000 kPa.
- The accuracy of the pressure sensors is set to ± 0.3 % of full scale.

Table B6-2. Calculations of water column height based on the assumptions above.

	Water column height (m)
Distilled water at a temperature of +2 °C Density of water was increased due to the weight of the water column. Measured pressure was 5000 kPa + 0.3 % of full measuring range	511.04
Distilled water at a temperature of +25 °C Density of water was increased due to the weight of the water column. Measured pressure 5000 kPa −0.3 % of the full measuring range.	506.77

To be able to estimate the uncertainty in fresh water head related to UTM/D-WGS84 knowledge of the uncertainty of following is required:

- Determination of the elevation of the TOC of DH-GAP04.
- Borehole deviation uncertainties.
- Position of the sensors along DH-GAP04.

The uncertainty of the determination of the top of casing is ± 0.10 m.

The elevation uncertainty, based on measured borehole deviations, using a borehole length representative for a depth of 500 m is ~ ± 0.6 m. The calculation is based on the following equation from Stenberg and Håkansson (2007):

$$\Delta Z_n = \sum_{i=1}^{n} (L_i - L_{i-1}) \times \sin(\Delta I) \times \cos(I_i)$$

Uncertainty of elevation determination caused by errors in length during installations is based on the length tolerance of the rods used during installation and the characteristics of the rod material. Manufacturing tolerance of the 2 m rods used in borehole DH-GAP04 is ± 1 mm, which means that on a rod assembly length of 530 m the uncertainty is ± 0.27 m**.**

Thermal changes of the rods at 18 degrees temperature difference (difference between the manufacturing temperature +20 °C and the downhole temperature of +2 °C) will cause a length reduction of 0.22 for a rod assembly of 530 m.

Length extension of the rods caused by their weight is calculated from the weight in water of the aluminium rods and the inclination of the borehole. A rod assembly of 530 m weighs 180 k and will be extended by 0.04 m. Given the actual borehole inclination this represents a length difference of +0.08–0.42 m.

Table B6-3 summarises the uncertainties of the values in Table B6-2 with the calculated uncertainties above.

Table B6-3. Calculated and summarised uncertainties.

	Water column height (m)
Distilled water at a temperature of +2 °C Density of water was increased due to the weight of the water column. Measured pressure was 5000 kPa + 0.3 % of full measuring range Determination of borehole deviation, top of casing etc. (+0.08 m)	511.78
Distilled water at a temperature of +25 °C Density of water was increased due to the weight of the water column. Measured pressure 5000 kPa −0.3 % of the full measuring range. Determination of borehole deviation, top of casing etc. (+0.08 m)	505.65

The errors in the estimated fresh water head for the actual measurement points in DH-GAP04, should be considered a summation of the maximal errors, and is not greater than ± 2.9 m.

The uncertainties are with respect to point water head. The calculations are based on the existence of a relationship between EC in the water and the density at a given pressure and temperature. In the calculations, the EC-interval is taken from measurements in the three sections. The results indicate that the point water head is ~ 1.5 m lower than the freshwater head, but the calculated maximal error is the same at ± 2.9 m. Based on a similar approach, the summation of the maximal errors in fresh water head for the actual measurement points is ± 0.9 m.

B7 Hydraulic transmissivity along the borehole

The hydraulic transmissivity (specific capacity) of flowing test sections along the borehole have been determined by the following two methods:

- PFL, which was done before the installation of the packer and the monitoring system.
- Stationary and transient evaluations of pressure data measured during the water sampling in the three sections in September 2011 and September 2013.

Posiva Flow Log (PFL).

The main purpose of the PFL survey was to detect the positions of flow anomalies to support the decision on where to place the two packer system for monitoring pressure, temperature and EC and to allow water sampling. The data from the PFL survey could also be used for the general hydrogeological interpretation of the rock volume.

Pöllänen et al. 2012 describe the flow logging measurements carried out with the function of Posiva Flow Log (in borehole DH-GAP04). The method is based on inflow measurements during abstraction (pumping), where the flows from the rock are measured in defined sequential sections along borehole. Measurements are usually made at two different pressure conditions in the borehole. Usually, one measurement is made at natural groundwater head and the other one at a certain drawdown of the water table by pumping. With the flow meter, it is theoretically possible to measure flow rates between 0.5 to 6000 mL/min, corresponding to 8.3×10^{-10} to 1×10^{-5} m^2/s for a head change of 10 m. By combining the two measurements, it is possible to calculate the transmissivity and natural groundwater head of the flowing sections.

- Before the PFL-measurements were made the pressure head in the open borehole and the flow out of the hole was measured. The measurement of the pressure level was made by attaching a nylon tube to the casing since the borehole was artesian. The level in the tube was about 3.52 m over the ground (2.99 m above TOC). The overflow at the top of casing, i.e, was estimated to about 2.85 L/min.
- Flow logging measurements were conducted using a device setup with a 10 m section length when the borehole was not pumped and in pumped conditions. In these measurements the probe was deployed in 2 m steps.
- During the measurements under natural conditions the ground water level was located at top of the casing and the overflow at the casing was about the same as reported in the point above.

- During the measurements under pumped conditions the ground water level was kept about 12 m (vertical depth) below TOC. The pumping rate varied from 16.5 L/min to 10.0 L/min. The measurements were made along the borehole from borehole length 275 m to the bottom of the borehole. The reasons for this strategy were that the rock in the upper part of the borehole was frozen and the time limitation during installation. These data indicate a hydraulic transmissivity for the entire borehole of about 1.1 to 1.8×10^{-5} m^2/s.

The measurements were carried out partially in a transient flow condition, since the flow measurements began two days after drilling. Due to the borehole freezing risk there was no time to await steady state flow conditions. The results from the PFL-measurements are presented in Table B7-1.

Table B7-1. Length along the borehole, measured flow rates and groundwater head together with calculated transmissivity and natural groundwater head of the detected flow anomalies by PFL.

Length (m)	Head0 (m)	Flow0 (mL/h)	Flow 0 (m^3/s)	Head1 (m)	Flow 1 (mL/h)	Flow1 (m^3/s)	T (m^2/s)	Head of fracture (m)	Comment's
415.7	526.41	–	–	514.35	103	2.9E−8	2.35E−09	–	*
548	527	3340	9.3E−7	515.05	8390	2.3E−6	1.16E−07	534.90	
551.6	526.98	16 300	4.5E−6	515.01	50 500	1.4E−5	7.86E−07	532.69	
584.6	527.09	73 500	2.0E−5	515.2	182 000	5.1E−5	2.51E−06	535.14	
600.2	527.23	119 000	3.3E−5	515.67	257 000	7.1E−5	3.29E−06	537.20	
604	527.18	1040	2.9E−7	515.25	3570	9.9E−7	5.82E−08	532.08	*
638.4	527.34	214	5.9E−8	515.43	653	1.8E−7	1.01E−08	533.15	
670	527.53	–	–	515.61	68	1.9E−8	1.57E−09	–	*
682	528.1	−179**	−5.0E−8	516.25	140	3.9E−8	7.40E−09	521.45	*

* Uncertain fracture. The flow rate is less than 30 mL/h or the flow anomalies are overlapping or unclear because of noise.

** Negative flow means flow out from the borehole.

Description of columns:
Length (m) = Length along the bore borehole from reference to the fracture (m)
Head0 (m) = Head in the bore borehole without pumping (m)
Flow0 (mL/h) = Flow from the fracture to the bore borehole without pumping
Head1 (m) = Head in the borehole at pumping (m)
Flow1 (mL/h) = Flow from the fracture to the borehole at pumping
T (m^2/s) = Transmissivity of the fracture
Head of fracture (m) = Natural groundwater head of the fracture

Sect-up: 🟥
Sect-mid: 🟦
Sect-low: 🟩

The sum of all measured flows along the borehole without pumping was 3.6 L/min. There was only one negative flow (flow out from the bore borehole, see 682 m in Table B6-1). The measured flow over the casing was 2.85 L/min.

The pumping rate varied during the measuring period between about 16.5−10 L/min. The sum of all measured flows during pumping was 8.4 L/min. The differences compared to the measurements without pumping may be due to flows in individual sections of hole not measured at the same time. There may be flows at the unmeasured parts of the borehole but the largest flows were probably detected.

The summarised transmissivities of the PFL-anomalies in the three monitoring sections are presented in the Table B7-2.

Table B7-2. Summed transmissivities of the PFL-anomalies in the three monitoring sections.

Section	Transmissivity (m^2/s)
Sect-up	3.4E−06
Sect-mid	3.3E−06
Sect-lo	1.9E−08

Evaluation of transmissivity from pumping in September 2011 and 2013

The performance of the water sampling was not designed for evaluation of the transmissivity. The borehole is divided into three sections. The subdivision of the sections and the equipment for water sampling are described earlier in this appendix.

Pumping cycles during the first field visit in September 2011:

- The water volume pumped up during each pumping cycle was ~ 5 liters.
- The duration of a pump cycle ranged between 25 to 30 minutes, including five minutes to pump up the water sample in the pipe to the surface.
- A total of 68 pumping cycles, of which the number of cycles for each section varied from 20 to 27.

Due to the long scanning time (5 minutes) for the measurements it was not possible to evaluate each pumping cycle separately (by slug test analysis).

Pressure responses in the sections during water sampling are shown in Figures B7-1 to B7-3

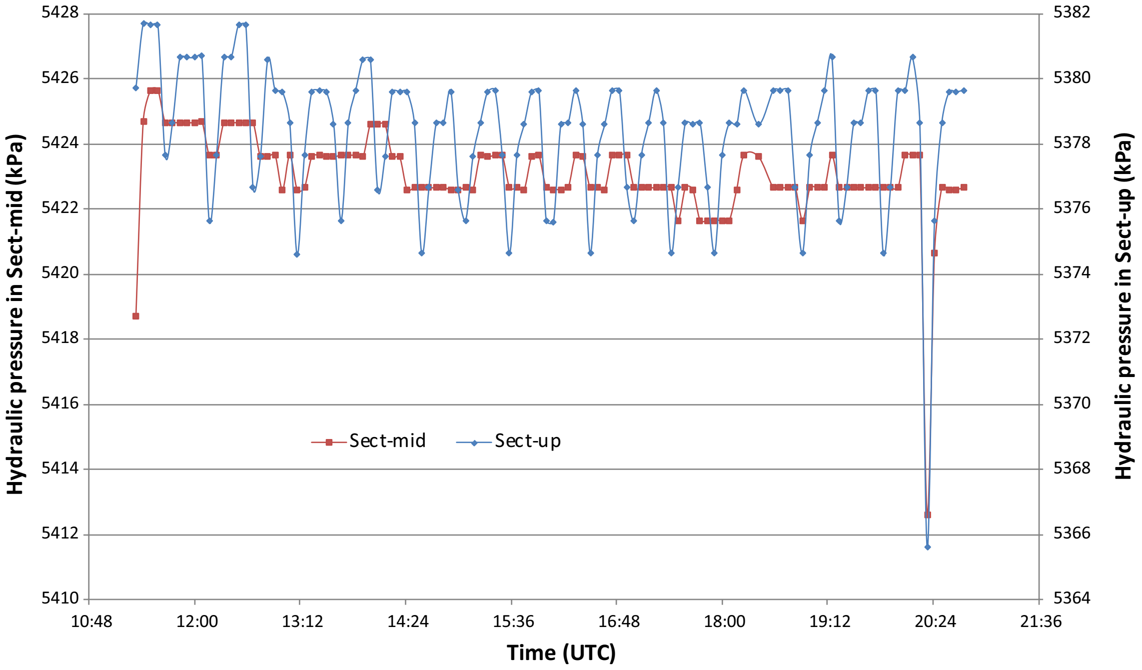

Figure B7-1. Pressure responses in Sect-up and Sect-mid during pumping in Sect-up, September 10, 2011.

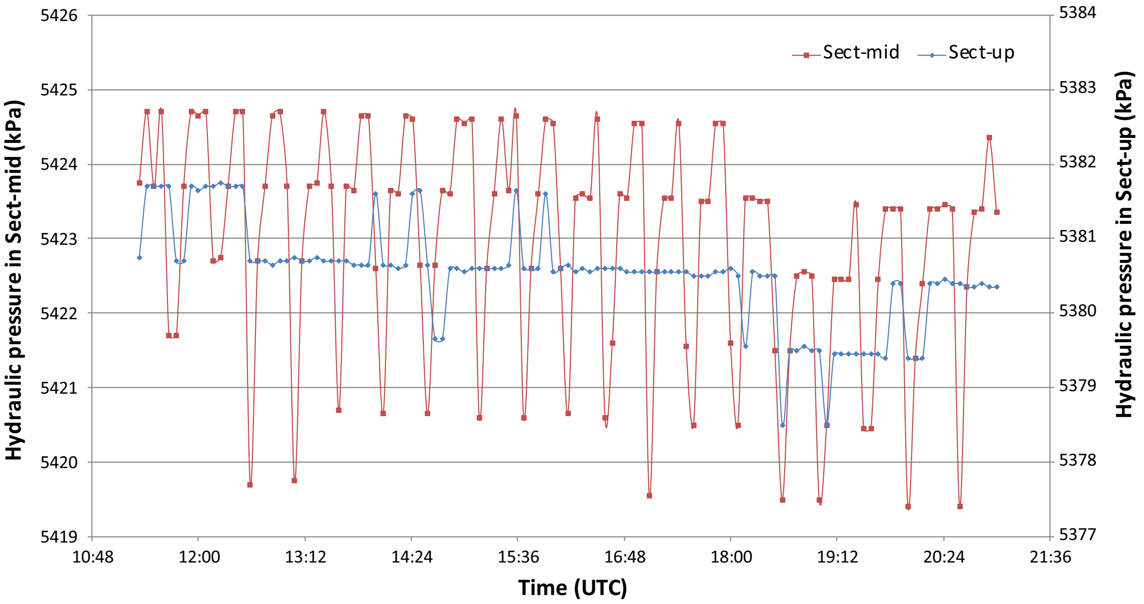

Figure B7-2. *Pressure responses in Sect-up and Sect-mid during pumping in Sect-mid, September 9, 2011.*

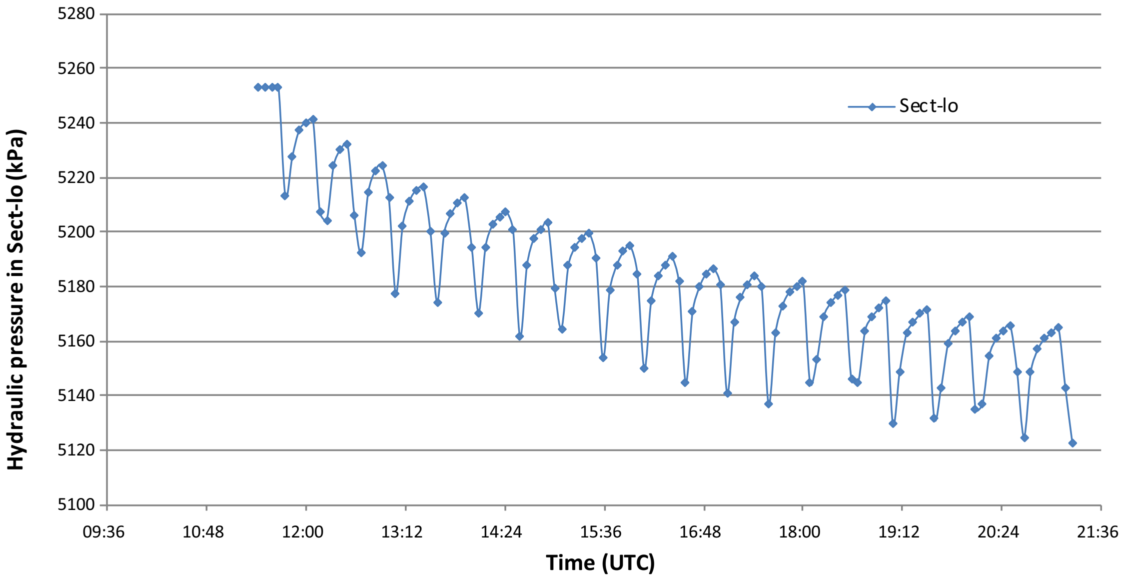

Figure B7-3. *Pressure responses in Sect-low during pumping in Sect-low, September 8, 2011.*

Results

The calculation of the test section transmissivities/specific capacity has been made as follows:

- Evaluation of the specific capacity Q/s assuming steady state conditions. This type of evaluation is made for all three sections, see, Table B7-3.
- Evaluation of transmissivity during the transient recovery. This type of evaluation is made for Sect-low section only.

Transmissivity in Sect-lo evaluated from the recovery phase

The estimated transmissivity (from transient analysis) from the recovery phase in Sect-lo is ~ 1.7×10^{-7} m^2/s, see Figure B7-4.

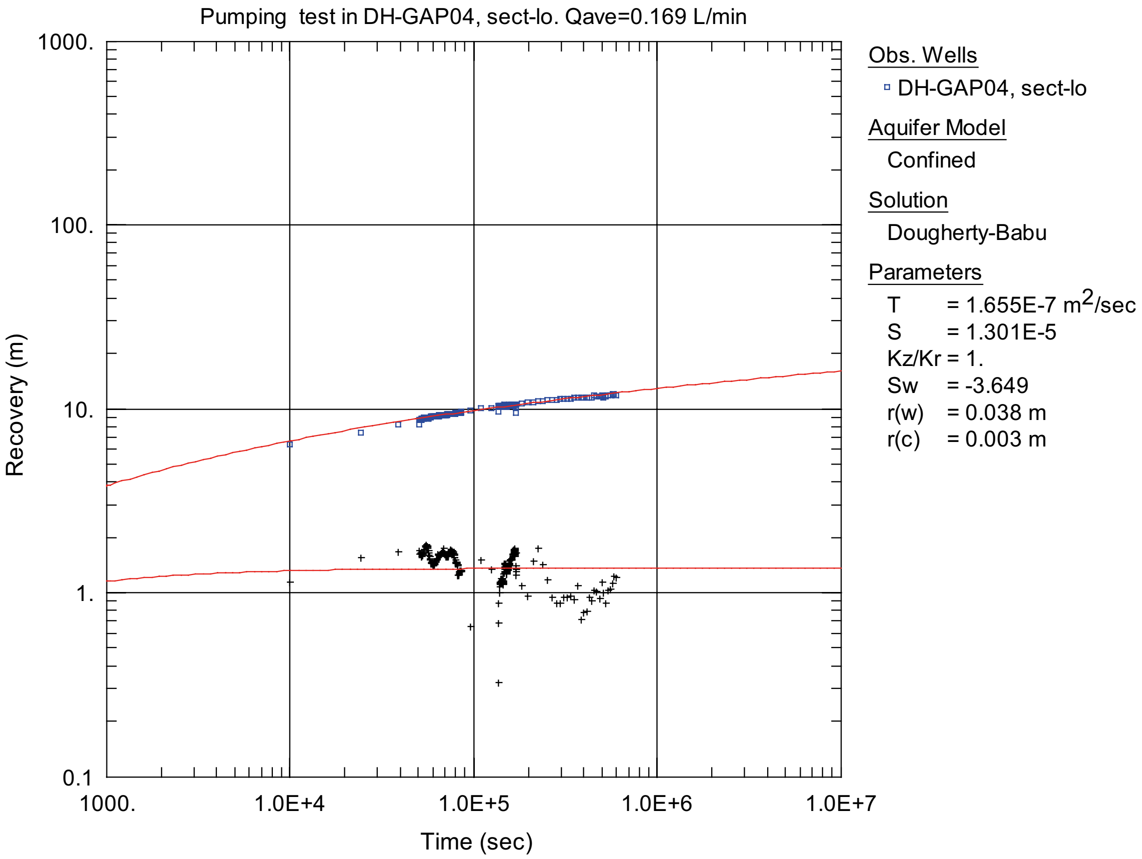

Figure B7-4. *Evaluation curves from Sect-low, recovery phase. □=Pressure. += Pressure derivate.* Q_{ave} *is calculated as total pump volume divided with total pump time.*

Table B7-3. Specific capacity Q/s in the monitoring sections.

Section	Drawdown (m)	Average flow rate (m^3/s)	Specific capacity (m^2/s)
Sect-up	Approx 0.1	2.90×10^{-6}	3×10^{-5}*
Sect-mid	Approx 0.15	3.03×10^{-6}	2.0×10^{-5}*
Sect-low	9.0	2.86×10^{-6}	3.2×10^{-7}**

* The stationary evaluation of the pumping has been made in a transient stage. The used drawdown is very small and has been made with the assumption that no other pressure changes occurred during pump periods. Estimated values of specific capacities are too high due to assumed hydraulic contact between Sect-up and Sect-mid and due to the uncertain values of the actual drawdown.

** The stationary evaluation of the pumping has been made in a transient stage. The used drawdown is very small and has been made with the assumption that no other pressure changes occurred during pump periods.

Evaluation of transmissivity from the pumping in September 2013.

The performance of the water sampling was not designed for evaluation of the transmissivity. The borehole is divided into three sections; the section subdivision and equipment for water sampling are described earlier in this appendix.

Pumping cycles during the field visit in September 2013:

- The water volume pumped up during each pumping cycle was ~ 5 liters.
- The duration of a pump cycle ranged between 25 to 30 minutes, including five minutes to pump up the water sample in the pipe to the surface.
- For the hydraulic evaluation five pumping cycles were made in each section before the water sampling.

The scanning time was 6 seconds. Although the scanning time was 6 seconds it was not possible to evaluate each pumping cycle separately (by slug test analysis). The head variations in the sections during the pumping are shown in Figures B7-5 to B7-7.

Results

The calculation of the test section transmissivity/specific capacity has been made as follows:

- Evaluation of the specific capacity Q/s assuming steady state conditions. This type of evaluation is made for two sections, see Table B7-4.
- Evaluation of transmissivity during the transient recovery. This type of evaluation is made for Sect-lo section only.

Table B7-4. Specific capacity Q/s in the monitoring sections.

Section	Drawdown (m)	Average flow rate (m^3/s)	Specific capacity (m^2/s)
Sect-up	Approx 0.17	3.1×10^{-6}	2×10^{-5}*
Sect-mid	–	–	–**
Sect-low	3.6	2.8×10^{-6}	7.8×10^{-7}***

* The stationary evaluation of the pumping has been made in a transient stage. The used drawdown is very small and has been made with the assumption that no other pressure changes occurred during pump periods. Estimated values of specific capacities are too high due to assumed hydraulic contact between Sect-up and Sect-mid and due to the uncertain values of the actual drawdown.

** The values from the section are not evaluated because of uncertainties regarding impact of other factors than pumping.

*** The stationary evaluation of the pumping has been made in a transient stage. The used drawdown is very small and has been made with the assumption that no other pressure changes occurred during pump periods.

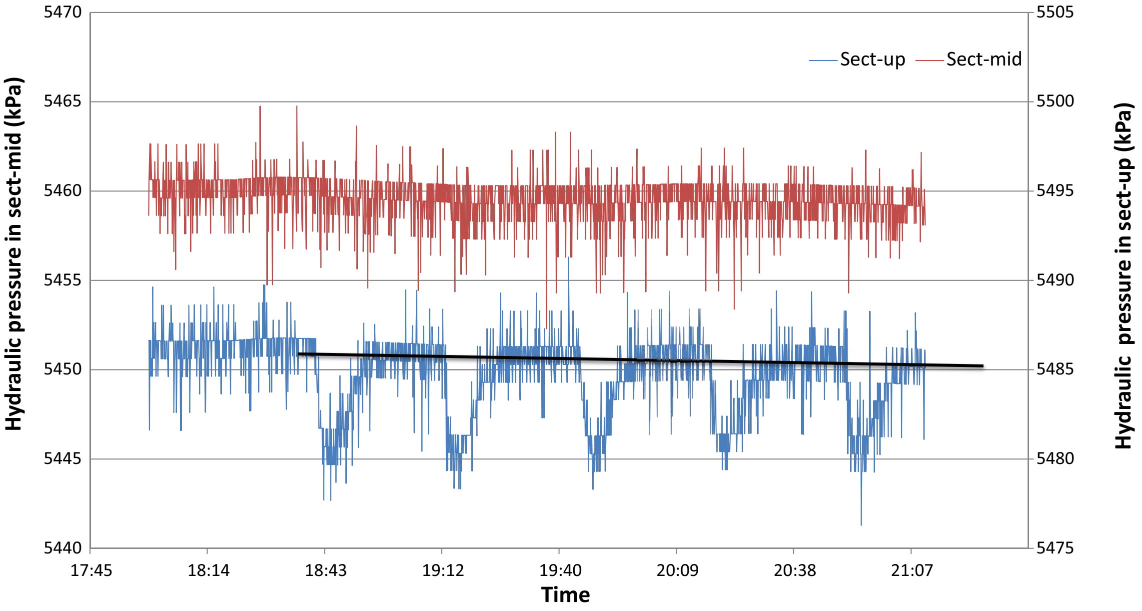

Figure B7-5. *Pressure responses in Sect-up and Sect-mid during pumping in Sect-up, September 4, 2013. Black line represents the pressure decrease during pumping.*

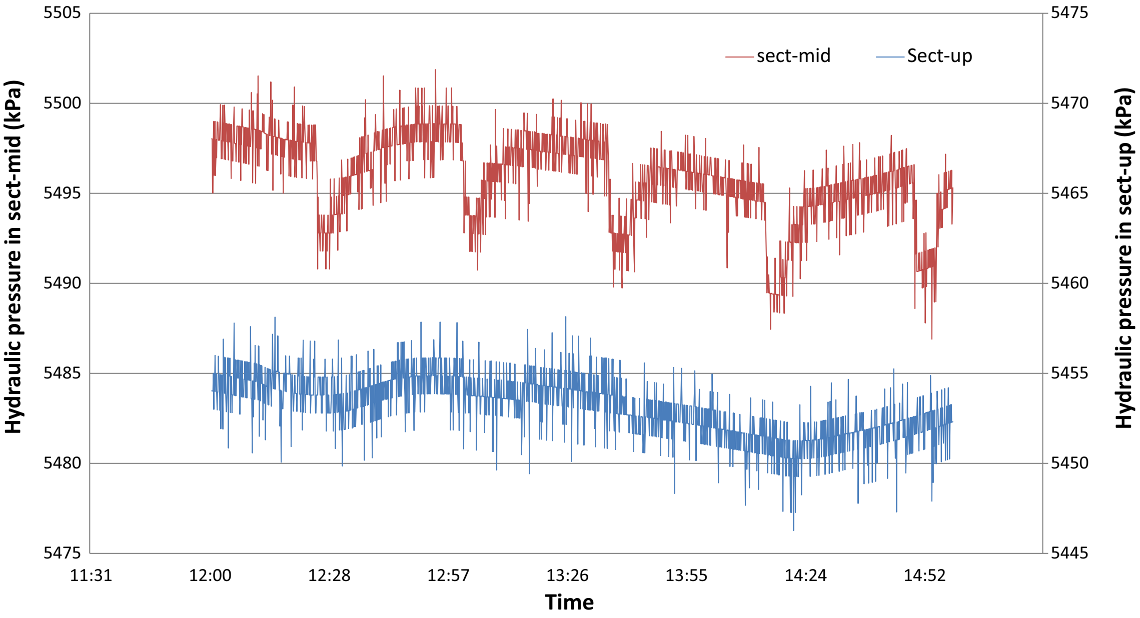

Figure B7-6. *Pressure responses in Sect-up and Sect-mid during pumping in Sect-mid, September 4, 2013. The pumping seems to be affected by some other external pressure disturbance. The air pressure is only decreasing about 0.5 kPa during the pump period.*

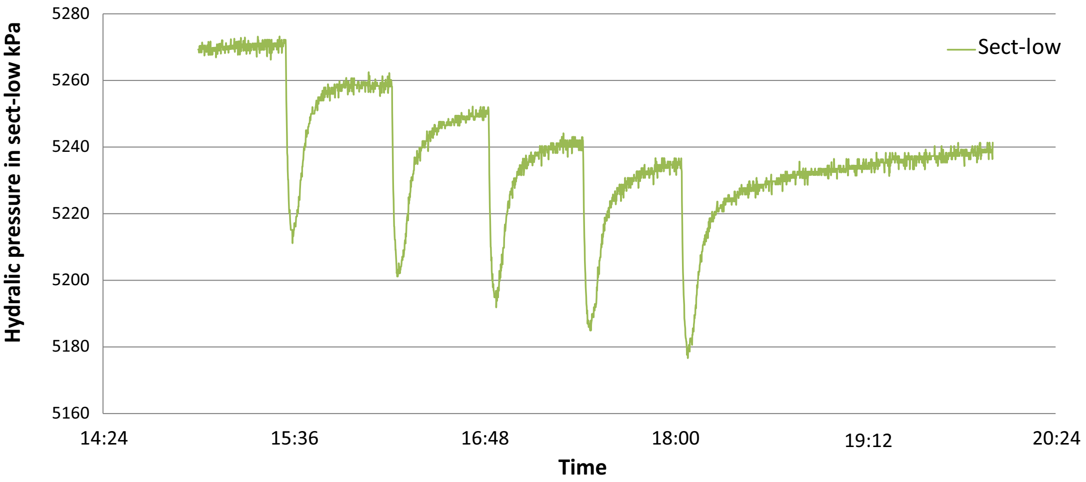

Figure B7-7. *Pressure responses in Sect-low during pumping in Sect-low, September 4, 2013.*

Discussion

It was noted that there are significant differences between the two sets of data (calculated specific capacity from the water sampling and the PFL data, respectively).

The PFL measurement represents generally radial flow conditions in the vicinity of the hole, but it is possible that the PFL-data is affected by the transients from the drilling.

By the evaluation of the data from water sampling a spherical flow regime could be anticipated for the Sect-up and Sect-mid measurements. This is because in sections Sect-up and Sect-mid there are high transmissivities very close to each other, and only separated by a one metre long packer. Estimated values of specific capacity are too high because the stationary evaluation was made during transient conditions and assumed good hydraulic contact between Sect-up and Sect-mid and due to the uncertain values of the actual drawdown. Thus, the real values in these two sections would probably be closer to the transmissivity values evaluated from PFL.

The specific capacity, which is a rough estimate of transmissivity, estimated from the water sampling in Sect-low is approximately about one order of magnitude greater than the transmissivity from the PFL-measurements. The reason for the differences may be the effect of the pressure transients from drillings or/and a potential PFL-anomaly not detected at the bottom of the borehole.

The reason of the differences of about a factor two between the stationary evaluation of specific capacity between the water sampling in September 2011 and in September 2013 is that the pumping time was much longer in September 2011 and because the drawdown was larger. But none of the pumping tests reached stationary conditions.

The transmissivity was also estimated from the water sampling in Sect-low by transient evaluation. The difference between specific capacity and transmissivity from the transient evaluation during the water sampling in September 2011 is less than a factor 2. In September 2013 the difference was about factor 5.

To conclude, the differences in the transient evaluations between September 2011 and September 2012 were very small.

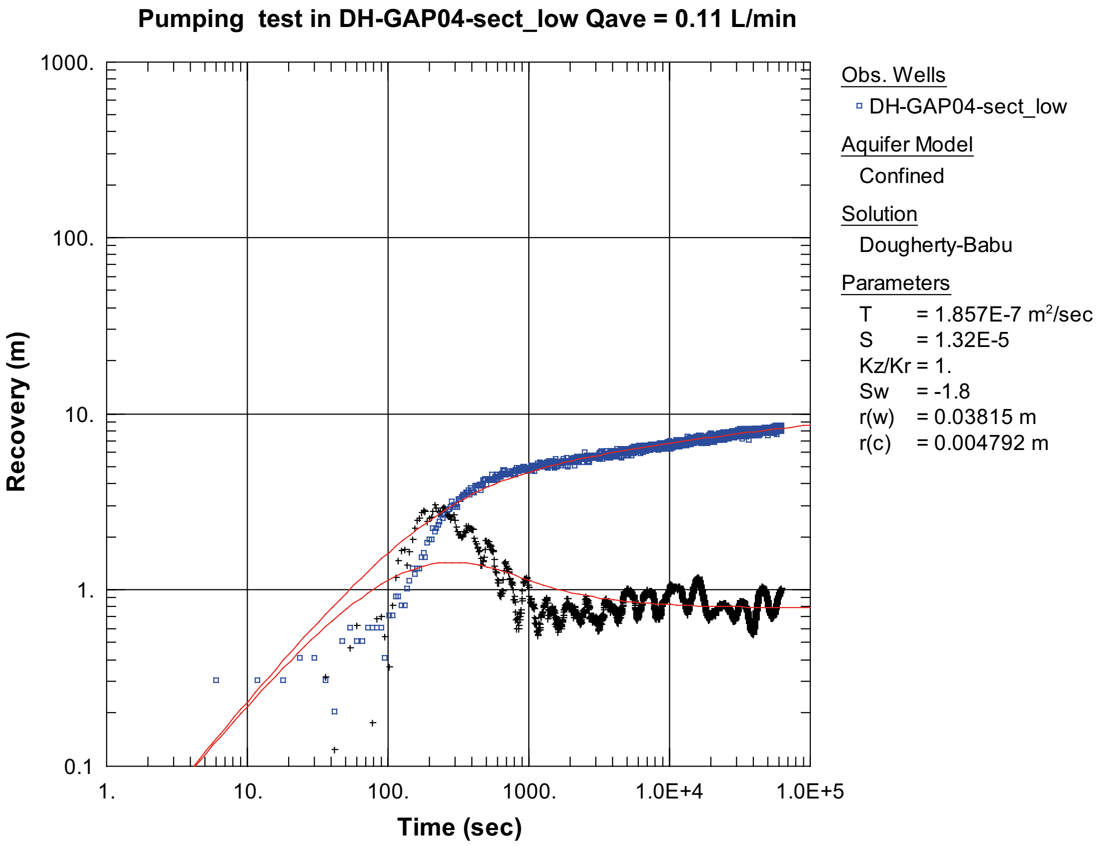

Figure B7-8. *Evaluation curves from Sect-low, recovery phase. □=Pressure. += Pressure derivate. Q_{ave} is calculated as total pump volume divided with total pump time.*

List of abbreviations

2D	Two-dimensional
3D	Three-dimensional
AD	Anno Domini
AECL URL	Atomic Energy of Canada Limited Underground Research Lab
ArcGIS	ESRI's geographic information system (GIS) tool for working with maps and geographic information
AMS	Accelerator Mass Spectrometry
ARSF	Airborne Research and Survey Facility
ASTER	Advanced Spaceborne Thermal Emission and Reflection Radiometer
AVA	Amplitude versus angle
AWI	Alfred Wegener Institute
AWS	Automatic Weather Stations
BHL	Borehole Length
BP	Before Present
CF-IRMS	Continuous Flow Isotope Ratio Mass Spectrometer
CHW	Cryo-Hydrologic Warming
CISM	Community Ice Sheet Model
CReSIS	Center for Remote sensing of Ice and Snow
DGR	Deep Geological Repository
DH	Drillhole
DEM	Digital Elevation Model
DMI	The Danish Meteorological Institute
DNA	Deoxyribonucleic acid
DOY	Day of the year
DTS	Distributed Temperature Sensing
DTU	Danish Technical University
EC	Electrical conductivity
EDT	Equal Distance Time
Eh	Redox potential
ELA	Equilibrium Line Altitude
EOH	End of Hole
ESRI	ArcGIS platform, software and product supplier
FFT	Fast Fourier Transform
FGN	Felsic gneiss
FMB	Frozen/melted boundary
Ga	Billion years
GAP	Greenland Analogue Project
GEUS	Geological Survey of Denmark and Greenland
GIMP	Greenland Mapping Project
GMWL	Global Meteoric Water Line
GPR	Ground-Penetrating Radar
GPS	Global Positioning System
GRASP	Greenland Analogue Surface Project
GrIS	Greenland Ice Sheet
HFD	Heat Flux Density
IC	Ion Chromatograph
Ice2Sea	A European Union FP7 project between 2009-2013 studying projections of the contribution of ice to future sea-level rise.
ICEBridge	A NASA program of airborne remote sensing measurements over the Earth's polar ice to bridge the gap in measurements between the end of the ICESat-1 mission and the launch of ICESat-2.

ICP-AES	Inductively Coupled Plasma Atomic Emission Spectroscopy
ICP-MS	Inductively Coupled Plasma Mass Spectrometry
ICP-OES	Inductively Coupled Plasma Optical Emission Spectrometry
IDL springs	Ice dammed lake springs
IMAU	Institute for Marine and Atmospheric Research in Utrecht
ISG	Isunnguata Sermia Glacier
ISMIP-HOM	Ice Sheet Model Intercomparison Project - Higher Order Model
ka	Thousand years
KBS-3/KBS-3H	A multi-barrier deep geologic repository concept for disposal of high-level radioactive waste developed in Sweden by Svensk Kärnbränslehantering AB (SKB).
KISS	Kangerlussuaq International Science Support centre
L	Litre(s)
LEL	Local Evaporation Line
LGM	Last Glacial Maximum
LIA	Little Ice Age
LMWL	Local Meteoric Water Line
LTA	Long Term Average
M3	Multivariate Mixing and Mass balance calculations
Ma	Million years
MAAT	Mean Annual Air Temperature
MAGT	Mean Annual Ground Temperature
MAR	Modèle Atmosphérique Régional, the name of a specific regional climate model
m a.g.s.	Metres above ground surface
m b.g.s.	Metres below ground surface
m a.s.l.	Metres above sea level
m b.s.l.	Metres below sea level
MODIS	The Moderate-resolution Imaging Spectroradiometer
NWMO	Nuclear Waste Management Organization
P	Pressure
PFL	Posiva Flow Log
Posiva	Posiva Oy, Finland
PHREEQC	Geochemical thermodynamic modelling code
qPCR	quantitative Polymerase Chain Reactor
RACMO2	Regional Atmospheric Climate Model, the name of another specific regional climate model (version 2)RMS
SAMPO	Wide-band frequency-domain electromagnetic sounding system
Sect-low	Lower section of borehole DH-GAP04
Sect-mid	Middle section of borehole DH-GAP04
Sect-up	Upper section of borehole DH-GAP04
SEM	Scanning Electron Microscope
SEM-EDS	Scanning Electron Microscope-energy dispersive system
SF6	Sulphur hexafluoride
SFJ	Kangerlussuaq International Airport
SFR	The low- and intermediate level radioactive waste underground repository located in the vicinity of the Forsmark nuclear power plant
SGL	Supraglacial lake(s)
SGU	Swedish Geological Survey
SKB	Svensk Kärnbränslehantering AB, Sweden
SMB	Surface energy balance models
SPOT	Satellite Pour l'Observation de la Terre
STA	Short Term Average
T	Temperature (in °C)

TDS	Total Dissolved Solids
TIMS	Thermal ionization mass spectometry
TNC	Total number of cells
TOC	Top of Casing
TVO	Teollisuuden Voima Oyj
TU	Tritium unit(s)
UTC	Coordinated Universal Time
UofT GSM	University of Toronto Glacial Systems Model
USD	Uranium Series Disequilibrium
VSMOW	Vienna Standard Mean Ocean Water
VSLAP	Vienna Standard Light Antarctic Precipitation
WGS-84	World Geodetic System from 1984
WRA	Whiteshell Research Area
XRD	X-Ray Diffraction